

**Control Strategies for Grid-Connected Inverters Enabling Power Quality Improvement  
and Increased Penetration of Renewable Energy Resources  
in Low Voltage Distribution Networks**

**Regelstrategieën voor netgeconnecteerde invertoren voor verbetering van de netkwaliteit  
en verhoogde penetratiegraad van hernieuwbare energiebronnen  
in laagspanningsdistributienetten**

**Dimitar Bozalakov**

Promotoren: prof. dr. ir. L. Vandeveld, prof. dr. ir. A. Van den Bossche  
Proefschrift ingediend tot het behalen van de graad van  
Doctor in de ingenieurswetenschappen: werktuigkunde-elektrotechniek



Vakgroep Elektrische Energie, Metalen, Mechanische Constructies en Systemen  
Voorzitter: prof. dr. ir. L. Dupré  
Faculteit Ingenieurswetenschappen en Architectuur  
Academiejaar 2019 - 2020

ISBN 978-94-6355-299-8  
NUR 959, 961  
Wettelijk depot: D/2019/10.500/107



Ghent University  
Faculty of Engineering and Architecture (FEA)  
Department of Electrical Energy, Metals, Mechanical  
Constructions and Systems (EEMMeCS)  
Electrical Energy Laboratory (EELAB)

# Control strategies for grid-connected inverters enabling power quality improvement and increased penetration of renewable energy resources in the low voltage distribution networks

---

Dimitar V. Bozalakov

PhD dissertation submitted to obtain the degree of  
Doctor of Electromechanical Engineering

Promoters:

Prof. dr. ir. Lieven Vandeveldde (UGent)

Prof. dr. ir. Alex Van den Bossche (UGent)

Chairman:

Ereprof. dr. ir. Ronny Verhoeven (eredecaan)

Exam Commission:

Prof. dr. Bruno François (Ecole Centrale de Lille, France)

Prof. dr. ir. Geert Deconinck (KU Leuven)

Dr. ir. Jan Van de Vyver (Fluvius)

Prof. dr. ir. Chris Develder (UGent)

Prof. dr. ir. Jan Desmet (UGent)

Prof. dr. ir. Jeroen De Koning (UGent)



# Thanks

I would like to express my gratitude to my promoters prof. Lieven Vandevelde and Alex Van den Bossche who gave me the opportunity to do my PhD degree in the field of electromechanical engineering. This achievement would not be possible without their valuable advises, patience and faith in me during this journey.

I acknowledge the contribution of my tutors Tine Vandoorn and Bart Meersman for their valuable guidance and instructions. Without their academic support this thesis would not have reached its present form. I will not forget the weekly meeting in the beginning of the thesis during which we had fruitful discussions which led to many inspirations and ideas.

I am grateful to prof. Jan Desmet and his team (more particularly Jurgen Van Ryckeghem and Agkaton Bottenberg) for their technical support during my experimental work in the Laboratory of LEMKO, Kortrijk. Their practical knowledge in renewable energy resources made my work less difficult during the experimental period of my thesis.

Thanks to my office mates Kristof De Koker and Pieter Nguyen Phuc for the nice and interesting dialogues. They helped in creating a pleasant environment which made the working process very easy.

I extend my sincere thanks to all members of EELAB, and all those who contributed directly or indirectly to the dissertation. Thanks to my colleagues for the interesting discussion in the halls and during coffee breaks. You supported me greatly and were always willing to help me.

Last but not the least I would like to my wife for her unconditional support and constant encouragement over the years. She always supported me and help me to overcome difficulties without complaining. Thanks to my parents and brother who originally generated my love for science and their moral support. I undoubtedly could not have finished this without you.

*Gent, August 2019  
Dimitar V. Bozalakov*



# Table of Contents

|  |            |
|--|------------|
| <b>Thanks</b>  | <b>i</b>   |
| <b>1 Introduction</b>  | <b>1-1</b> |
| 1.1 Introduction . . . . .   | 1-1        |
| 1.2 Conclusions . . . . .  | 1-6        |
| <b>2 Overview of control strategies for inverter-connected renewable energy units in low voltage grids</b> | <b>2-1</b> |
| 2.1 Power quality problems due to the increased penetration level of DERs . . . . .                        | 2-1        |
| 2.1.1 Numerical example of the neutral point shifting . . . . .  | 2-4        |
| 2.2 Solutions for preventing overvoltages and voltage unbalance . . . . .                                  | 2-6        |
| 2.2.1 Distribution grid reinforcement . . . . .  | 2-6        |
| 2.2.2 Voltage profile support by dedicated equipment . . . . .   | 2-6        |
| 2.2.3 Voltage control by means of reactive power . . . . .   | 2-6        |
| 2.3 Conventional control strategies for DERs . . . . .   | 2-10       |
| 2.3.1 Single-phase control strategy . . . . .  | 2-11       |
| 2.3.2 Three-phase positive-sequence control strategy . . . . .   | 2-12       |
| 2.4 Discussion . . . . .   | 2-13       |
| 2.5 Voltage-based droop control . . . . .  | 2-13       |
| 2.6 Voltage unbalance mitigation control strategies . . . . .  | 2-17       |
| 2.7 Conclusions . . . . .  | 2-20       |
| <b>3 Local control strategies for distributed energy resources connected to LV grids</b>                   | <b>3-1</b> |
| 3.1 Introduction . . . . .   | 3-1        |
| 3.1.1 Integrating the VBDC in the single-phase and positive-sequence control strategies . . . . .          | 3-4        |
| 3.1.2 Integration of the VBDC in the three-phase damping control strategy . . . . .                        | 3-5        |
| 3.2 Validation of the proposed control algorithms by means of simulations . . . . .                        | 3-7        |
| 3.2.1 Classical control strategies used in the simulation model under examination . . . . .                | 3-9        |
| 3.2.2 Single-phase control strategy with variable PF . . . . .   | 3-9        |

|          |  |            |
|----------|--|------------|
| 3.2.3    | Positive-sequence control strategy with variable PF . . . . .  | 3-11       |
| 3.2.4    | Comparison between the positive-sequence and the maximum of phase voltages . . . . .                                     | 3-12       |
| 3.2.5    | Comparison between different control strategies - scenario 13-14   |            |
| 3.2.6    | Comparison between different control strategies - scenario 23-27   |            |
| 3.3      | Experimental validation of the modified damping control strategy   | 3-30       |
| 3.3.1    | Obtained experimental results for case 1 . . . . .   | 3-32       |
| 3.3.2    | Obtained experimental results for case 2 . . . . .   | 3-34       |
| 3.3.3    | Obtained experimental results for case 3 . . . . .   | 3-35       |
| 3.3.4    | Discussion . . . . .   | 3-36       |
| 3.4      | Conclusions . . . . .  | 3-38       |
| <b>4</b> | <b>Operation modes of the three-phase damping control strategy</b>   | <b>4-1</b> |
| 4.1      | Mathematical model examination . . . . .   | 4-1        |
| 4.1.1    | Case 1: Three-phase damping control strategy under voltage variations in phase $a$ . . . . .                             | 4-4        |
| 4.1.1.1  | Sub-case 1: Three-phase damping control strategy with zero input power and variable phase voltage $v_a$ . . . . .        | 4-4        |
| 4.1.1.2  | Sub-case 2: Three-phase damping control strategy under nominal input power at variable phase voltage $v_a$ . . . . .     | 4-10       |
| 4.1.1.3  | Sub-case 3: Three-phase damping control strategy under nominal consumed power and variable phase voltage $v_a$ . . . . . | 4-16       |
| 4.1.2    | Case 2: Phase angle $\theta_a$ variation . . . . .   | 4-20       |
| 4.1.2.1  | Sub-case 1: Phase angle $\theta_a$ variation under zero input power . . . . .  | 4-20       |
| 4.1.2.2  | Sub-case 2: Phase angle $\theta_a$ variation under nominal input power . . . . .   | 4-24       |
| 4.1.2.3  | Sub-case 3: Phase angle $\theta_a$ variation under nominal consumed power . . . . .                                      | 4-31       |
| 4.1.3    | Case 3: Phase voltage $v_a$ and phase angle $\theta_a$ variation . . . . .   | 4-37       |
| 4.1.3.1  | Sub-case 1: Phase voltage $v_a$ and phase angle $\theta_a$ variation under zero input power . . . . .                    | 4-37       |
| 4.1.3.2  | Sub-case 2: Phase voltage $v_a$ and phase angle $\theta_a$ variation under nominal input power . . . . .                 | 4-39       |
| 4.1.3.3  | Sub-case 3: Phase voltage $v_a$ and phase angle $\theta_a$ variation under nominal consumed power . . . . .              | 4-41       |
| 4.2      | Limits of the damping conductance values based on the current ratings of the power electronic inverter . . . . .         | 4-43       |
| 4.2.1    | Practical considerations of the damping conductance when DER is subjected to a voltage dip of Type B . . . . .           | 4-46       |
| 4.2.2    | Practical considerations of the damping conductance when DER is subjected to a voltage dip of Type D . . . . .           | 4-50       |

|          |   |      |
|----------|---|------|
| 4.2.3    | Discussion and future work . . . . .  | 4-54 |
| 4.3      | Validation of the discussed case studies in a distribution network<br>by means of simulations on a real LV feeder . . . . . | 4-55 |
| 4.3.1    | Verification of zero-powered DERs in an LV distribution<br>network by means of simulations . . . . .                        | 4-55 |
| 4.3.2    | Verification of dc-bus loaded DER on an LV distribution<br>network by means of simulations . . . . .                        | 4-62 |
| 4.3.3    | Discussion . . . . .  | 4-69 |
| 4.4      | Performance assessment of the considered control strategies on an-<br>annual basis . . . . .                                | 4-69 |
| 4.4.1    | Data of 78 node LV grid . . . . .   | 4-70 |
| 4.4.2    | Loads, DERs and irradiation data . . . . .  | 4-70 |
| 4.4.3    | Three-phase damping control strategy with segregate<br>negative- and zero-sequence mitigation . . . . .                     | 4-73 |
| 4.4.4    | Description of the Open DSS model . . . . .   | 4-74 |
| 4.4.5    | Simulation results . . . . .  | 4-76 |
| 4.4.6    | Discussion and future work . . . . .  | 4-82 |
| 4.5      | Experimental validation of the conducted theoretical analysis . . .   | 4-83 |
| 4.5.1    | Experimental validation of case 1 sub-case 2 . . . . .  | 4-85 |
| 4.5.2    | Experimental validation of case 1 sub-case 1 . . . . .  | 4-89 |
| 4.5.3    | Experimental validation of case 1 sub-case 3 . . . . .  | 4-93 |
| 4.5.4    | Discussion . . . . .  | 4-96 |
| 4.6      | Future work . . . . .   | 4-96 |
| 4.7      | Conclusions . . . . .   | 4-96 |
| <b>5</b> | <b>Practical implementation of the three-phase damping control strategy 5-1</b>   |      |
| 5.1      | Three-phase damping control strategy . . . . .  | 5-1  |
| 5.2      | Sampling of the different variables . . . . .   | 5-3  |
| 5.3      | Phase angle and voltage magnitude extraction . . . . .  | 5-4  |
| 5.3.1    | Sampling of phase voltages $v_a$ , $v_b$ and $v_c$ . . . . .  | 5-9  |
| 5.3.2    | Sampling of $g_1$ . . . . .   | 5-10 |
| 5.3.3    | Sampling of the damping conductance $g_d$ . . . . .   | 5-12 |
| 5.3.4    | Midpoint stabilisation . . . . .  | 5-12 |
|          | 5.3.4.1 Midpoint stabilisation by using a split dc controller   | 5-17 |
|          | 5.3.4.2 Reference current offset . . . . .  | 5-18 |
|          | 5.3.4.3 Experimental validation . . . . .   | 5-20 |
| 5.3.5    | Discussion . . . . .  | 5-22 |
| 5.3.6    | Current controller . . . . .  | 5-23 |
| 5.3.7    | Duty ratio feed-forward . . . . .   | 5-23 |
| 5.4      | Simulation results of the obtained model . . . . .  | 5-25 |
| 5.4.1    | Case studies . . . . .  | 5-25 |
| 5.4.2    | Case study 1 . . . . .  | 5-27 |
| 5.4.3    | Case study 2 . . . . .  | 5-30 |
| 5.4.4    | Case study 3 . . . . .  | 5-33 |
| 5.4.5    | Discussion . . . . .  | 5-34 |

|          |  |            |
|----------|--|------------|
| 5.5      | Experimental validation of the modified three-phase damping control strategy in a laboratory environment . . . . .         | 5-34       |
| 5.5.1    | Laboratory test . . . . .  | 5-35       |
| 5.5.2    | Feeder modelling in Matlab & Simulink . . . . .  | 5-36       |
| 5.5.3    | Experimental verification of the three-phase damping control strategy . . . . .  | 5-38       |
| 5.5.3.1  | Model accuracy assessment at variable phase voltage $v_a$ and zero input power . . . . .                                   | 5-39       |
| 5.5.3.2  | Model accuracy assessment at variable phase voltage $v_a$ and nominal input power . . . . .                                | 5-43       |
| 5.5.3.3  | Model accuracy assessment at variable phase voltage $v_a$ and 66% consumed power . . . . .                                 | 5-46       |
| 5.5.4    | Discussion . . . . .   | 5-49       |
| 5.6      | Conducted field trial in Graz, Austria . . . . .   | 5-49       |
| 5.7      | Conclusions . . . . .  | 5-54       |
| <b>6</b> | <b>Battery storage incorporation in the three-phase damping control strategy</b>   | <b>6-1</b> |
| 6.1      | Introduction . . . . .   | 6-2        |
| 6.2      | Control strategies description . . . . .   | 6-3        |
| 6.2.1    | Active power drooping . . . . .  | 6-3        |
| 6.2.2    | Controller for the battery energy storage system . . . . .   | 6-4        |
| 6.2.3    | Positive-sequence control strategy . . . . .   | 6-8        |
| 6.2.4    | Three-phase damping control strategy . . . . .   | 6-9        |
| 6.3      | Simulation results . . . . .   | 6-11       |
| 6.3.1    | Model description . . . . .  | 6-11       |
| 6.3.1.1  | Grid data . . . . .  | 6-11       |
| 6.3.1.2  | DER, BESS and load data . . . . .  | 6-11       |
| 6.3.1.3  | Short description of the Simulink model . . . . .  | 6-14       |
| 6.3.1.4  | Integration of BESS into DER . . . . .   | 6-14       |
| 6.3.2    | Simulation results . . . . .   | 6-15       |
| 6.3.2.1  | BESS controller operating principle . . . . .  | 6-17       |
| 6.3.2.2  | Performance assessment of the different cases and sub-cases . . . . .  | 6-21       |
| 6.4      | Discussion . . . . .   | 6-30       |
| 6.5      | Centralised energy storage by using voltage unbalance mitigation control strategies to improve the power quality . . . . . | 6-30       |
| 6.6      | Comparison between positive-sequence and damping control strategies . . . . .  | 6-31       |
| 6.6.1    | Droop controller . . . . .   | 6-31       |
| 6.6.2    | Damping controller . . . . .   | 6-33       |
| 6.6.3    | Practical implementation . . . . .   | 6-35       |
| 6.7      | Experimental results . . . . .   | 6-36       |
| 6.8      | Discussion . . . . .   | 6-42       |
| 6.9      | Conclusions . . . . .  | 6-43       |

---

|          |   |            |
|----------|---|------------|
| <b>7</b> | <b>Voltage dips</b>   | <b>7-1</b> |
| 7.1      | Introduction . . . . .  | 7-2        |
| 7.2      | Voltage dip characterisation . . . . .  | 7-4        |
| 7.2.1    | Immunity curve of equipment . . . . .   | 7-8        |
| 7.2.2    | Short overview existing technologies for voltage dip mitigation . . . . .         | 7-11       |
| 7.3      | Voltage dip analysis . . . . .  | 7-14       |
| 7.4      | Analytical comparison between the positive and damping control strategy . . . . . | 7-15       |
| 7.4.1    | Positive-sequence control strategy . . . . .                                      | 7-15       |
| 7.4.2    | Three-phase damping control strategy . . . . .                                    | 7-15       |
| 7.4.3    | Analytical analysis of voltage dips in LV feeders . . . . .                       | 7-20       |
| 7.4.4    | Simulation results . . . . .  | 7-22       |
| 7.4.5    | Examination of voltage dips at nominal input power . . . . .                      | 7-24       |
| 7.4.6    | Examination of voltage dips at zero input power . . . . .                         | 7-31       |
| 7.4.7    | Examination of voltage dips at nominal consumed power . . . . .                   | 7-38       |
| 7.4.8    | Discussion . . . . .  | 7-45       |
| 7.5      | Voltage dip mitigation in an extended low voltage distribution feeder . . . . .   | 7-45       |
| 7.5.1    | Voltage dip characterisation algorithms . . . . .                                 | 7-45       |
| 7.5.2    | Simulation results of a 7 node LV feeder and multiple DERs connection . . . . .   | 7-50       |
| 7.6      | Conclusions . . . . .   | 7-58       |
| <b>8</b> | <b>Conclusions and future work</b>  | <b>8-1</b> |
| 8.1      | Concluding remarks . . . . .  | 8-1        |
| 8.2      | Future research . . . . .   | 8-3        |
|          | <b>Bibliography</b>   | <b>8-5</b> |
| <b>A</b> | <b>Additional measurements conducted in Chapter 3</b>                             | <b>A-1</b> |
| <b>B</b> | <b>Developed inverter prototype and experimental set-up</b>                       | <b>B-1</b> |
| <b>C</b> | <b>Price comparison of BESS and PV inverters</b>                                  | <b>C-1</b> |



# List of Figures

|      |  |      |
|------|--|------|
| 1.1  | Global CO <sub>2</sub> emissions and economy relationship . . . . .                                  | 1-3  |
| 1.2  | Global energy consumption for 2011-2018 period . . . . .   | 1-4  |
| 1.3  | Installed renewable energy capacities until 2015 . . . . .   | 1-5  |
| 2.1  | Medium and low voltage tolerances set by EN50160 and IEC 60038                                       | 2-2  |
| 2.2  | Typical low voltage feeder topology . . . . .  | 2-3  |
| 2.3  | Voltage control in LV by using an OLTC . . . . .   | 2-7  |
| 2.4  | Variable power factor control . . . . .  | 2-7  |
| 2.5  | Volt-Var control . . . . .   | 2-9  |
| 2.6  | Voltage source inverter topology used by the voltage-based droop control strategy . . . . .          | 2-14 |
| 2.7  | Block diagram of the voltage-based droop control strategy . . . .                                    | 2-14 |
| 2.8  | Variable power factor control . . . . .  | 2-16 |
| 3.1  | Hierarchical control for increasing the penetration level of renewable energy resources . . . . .    | 3-2  |
| 3.2  | Active power drooping based on the VBDC . . . . .  | 3-4  |
| 3.3  | Damping-based droop control . . . . .  | 3-6  |
| 3.4  | Damping conductance dependency on the maximum value among the voltages in the three phases . . . . . | 3-6  |
| 3.5  | Cable equivalent model used in the simulations . . . . .   | 3-8  |
| 3.6  | 19 node LV feeder . . . . .  | 3-9  |
| 3.7  | Simulation results comparison between the three case studies . . .                                   | 3-13 |
| 3.8  | Voltage profiles obtained when different control strategies are examined . . . . .                   | 3-16 |
| 3.9  | Voltage profiles obtained with the different control strategies are examined . . . . .               | 3-20 |
| 3.10 | Negative- and zero-sequence unbalance factors . . . . .  | 3-21 |
| 3.11 | Total injected power from the DERs for the different cases . . . .                                   | 3-22 |
| 3.12 | Injected power per DER for the different cases . . . . .   | 3-22 |
| 3.13 | Total feeder losses . . . . .  | 3-24 |
| 3.14 | Total feeder losses . . . . .  | 3-28 |
| 3.15 | Negative- and zero-sequence unbalance factors at initial voltage of 1.06 p.u. . . . .                | 3-30 |
| 3.16 | Experimental set-up configuration . . . . .  | 3-32 |

---

|      |  |      |
|------|--|------|
| 3.17 | Voltage profiles obtained with the different control strategies . . .  | 3-37 |
| 4.1  | Connection diagram of DER and LV grid . . . . .  | 4-2  |
| 4.2  | Exchanged phase currents as a function of the phase voltage $v_a$ and the damping conductance $g_d=1$ p.u. when the input power $p_{dc}=0$ p.u. and the phase angles are perfectly shifted at $120^\circ$ electrical degrees . . . . . | 4-6  |
| 4.3  | Fundamental input conductance dependency as a function of the phase voltage $v_a$ and $g_d$ at nominal phase angles and zero input power $p_{dc} = 0$ p.u. . . . .   | 4-8  |
| 4.4  | Phase currents dependency on the variation of the phase voltage $v_a$ and the damping conductance $g_d$ at nominal phase angles and zero input power $p_{dc} = 0$ p.u. . . . .   | 4-9  |
| 4.5  | Relationship between the phase voltage $v_a$ and the damping conductance $g_d = 1$ p.u. when the input power $p_{dc} = -1$ p.u. and the phase angles are perfectly shifted at $120^\circ$ electrical degrees . . . .                   | 4-12 |
| 4.6  | Fundamental input conductance dependency on the variation of the phase voltage $v_a$ and damping conductance $g_d$ at nominal phase angles and nominal input power $p_{dc} = -1$ p.u. . . . .  | 4-13 |
| 4.7  | Phase currents dependency on the variation of the phase voltage $v_a$ and damping conductance $g_d$ at nominal phase angles and nominal input power $p_{dc} = -1$ p.u. . . . .   | 4-14 |
| 4.8  | Relationship between the phase voltage $v_a$ and the damping conductance $g_d = 1$ p.u. when the input power $p_{dc} = 1$ p.u. and the phase angles are perfectly shifted at $120^\circ$ electrical degrees . . . .                    | 4-16 |
| 4.9  | Fundamental input conductance dependency on the variation of the phase voltage $v_a$ and damping conductance $g_d$ at nominal phase angles and nominal input power $p_{dc} = 1$ p.u. . . . .   | 4-18 |
| 4.10 | Phase currents magnitudes and current angles dependency on the variation of the phase angle $\theta_a$ and the damping conductance $g_d$ and nominal input power $p_{dc} = 1$ p.u. . . . .   | 4-19 |
| 4.11 | Three-phase damping control strategy performance under variable phase angle $\theta_a$ , zero input power $p_{dc} = 0$ and damping conductance $g_d = 1$ p.u. . . . .  | 4-23 |
| 4.12 | Three-phase damping control strategy performance under variable phase angle $\theta_a$ , nominal input power $p_{dc} = -1$ p.u. and damping conductance $g_d = 0$ p.u. . . . .   | 4-26 |
| 4.13 | Three-phase damping control strategy performance under variable phase angle $\theta_a$ , nominal input power $p_{dc} = -1$ p.u. and damping conductance $g_d = 1$ p.u. . . . .   | 4-27 |
| 4.14 | Three-phase damping control strategy performance under variable phase angle $\theta_a$ , nominal input power $p_{dc} = -1$ p.u and damping conductance $g_d = 5$ p.u . . . . .   | 4-28 |
| 4.15 | Phase currents magnitudes and current angles dependency on the variation of the phase angle $\theta_a$ and the damping conductance $g_d$ .   | 4-30 |

---

|      |   |      |
|------|---|------|
| 4.19 | Phase currents magnitudes and current angles dependency as a function of the phase angle $\theta_a$ and the damping conductance $g_d$ at $p_{dc} = 1$ p.u. . . . .                                      | 4-33 |
| 4.16 | Three-phase damping control strategy performance under variable phase angle $\theta_a$ , nominal input power $p_{dc} = 1$ p.u. and damping conductance $g_d = 0$ p.u. . . . .                           | 4-34 |
| 4.17 | Three-phase damping control strategy performance under variable phase angle $\theta_a$ , nominal input power $p_{dc} = 1$ p.u. and damping conductance $g_d = 1$ p.u. . . . .                           | 4-35 |
| 4.18 | Three-phase damping control strategy performance under variable phase angle $\theta_a$ , nominal input power $p_{dc} = 1$ p.u. and damping conductance $g_d = 5$ p.u. . . . .                           | 4-36 |
| 4.20 | Phase currents dependency on the variation of the phase voltage $v_a$ and the phase angle $\theta_a$ at zero input power $p_{dc} = 0$ p.u. and damping conductance $g_d = 1$ p.u. . . . .               | 4-38 |
| 4.21 | Phase currents dependency on the variation of phase voltage $v_a$ , phase angle $\theta_a$ at nominal input power $p_{dc} = -1$ p.u. and damping conductance $g_d = 1$ p.u. and $g_d = 10$ p.u. . . . . | 4-40 |
| 4.22 | Exchanged phase currents as a function of phase voltage $v_a$ , phase angle $\theta_a$ at nominal consumed power $p_{dc} = 1$ p.u. and damping conductance $g_d = 1$ p.u. and $g_d = 10$ p.u. . . . .   | 4-42 |
| 4.23 | Dips classification where - - - - represents the nominal phase magnitudes and angles while — represents the residual phase voltages and angles during a voltage dip . . . . .                           | 4-45 |
| 4.24 | Phase currents exchange dependency under Type B voltage dip and $g_d$ in generation ( $p_{dc} = -1$ ) and consumption ( $p_{dc} = 1$ p.u.) . . . .  | 4-48 |
| 4.25 | Voltage dip evolution from HV to LV level through two Dy transformers . . . . .   | 4-51 |
| 4.26 | Phase currents exchange dependency under Type D voltage dip and $g_d$ in generation ( $p_{dc} = -1$ ) and consumption ( $p_{dc} = 1$ p.u.) . . . .  | 4-53 |
| 4.27 | Phase voltage results comparison between the four case studies when $p_{dc} = 0$ p.u. is used . . . . .   | 4-56 |
| 4.28 | Symmetrical components voltage comparison between the four case studies when $p_{dc} = 0$ p.u. is used . . . . .  | 4-58 |
| 4.29 | Voltage unbalance factors profiles comparison between the four case studies when $p_{dc} = 0$ p.u. is used . . . . .  | 4-59 |
| 4.30 | Per phase active power injection by the different DERs . . . . .  | 4-60 |
| 4.31 | Per phase reactive power injection by the different DERs . . . . .  | 4-60 |
| 4.32 | Total feeder losses when $p_{dc} = 0$ p.u. is applied . . . . .   | 4-62 |
| 4.33 | Phase voltage results comparison between the four case studies when $p_{dc} = 0.666$ . . . . .  | 4-64 |
| 4.34 | Symmetrical components voltage comparison between the four case studies when $p_{dc} = 0.666$ . . . . .   | 4-65 |
| 4.35 | Voltage unbalance factors profiles comparison between the four case studies when $p_{dc} = 0.666$ . . . . .   | 4-66 |

|      |  |      |
|------|--|------|
| 4.36 | Per phase active power injection by the different DERs . . . . .   | 4-67 |
| 4.37 | Per phase reactive power injection by the different DERs . . . . .   | 4-67 |
| 4.38 | Total feeder losses when $p_{dc} = 0.67$ p.u. . . . .  | 4-68 |
| 4.39 | Feeder topology used to access the performance the examined control strategies . . . . .   | 4-71 |
| 4.40 | Aggregated load profile of all loads . . . . .   | 4-72 |
| 4.41 | Solar irradiation profile used in the simulation model . . . . .   | 4-73 |
| 4.42 | Concatenated results of the entire LV grid when case <i>C0</i> is examined   | 4-76 |
| 4.43 | Concatenated voltage results of the entire LV grid when cases <i>C1</i> to <i>C4</i> are examined . . . . .  | 4-77 |
| 4.44 | Concatenated voltage results of the entire LV grid when cases <i>C5</i> to <i>C8</i> are examined . . . . .  | 4-78 |
| 4.45 | Concatenated VUFs results of the entire LV grid when cases <i>C1</i> to <i>C4</i> are examined . . . . .   | 4-79 |
| 4.46 | Concatenated VUFs results of the entire LV grid when cases <i>C5</i> to <i>C8</i> are examined . . . . .   | 4-80 |
| 4.47 | Total annual injected power by DERs when different control strategies are applied . . . . .  | 4-82 |
| 4.48 | Total feeder losses when different control strategies are applied . .  | 4-83 |
| 4.49 | Connection of DER in the laboratory experimental set-up . . . . .  | 4-85 |
| 4.50 | Phase currents and angles dependency on the variation of the phase voltage $v_a$ at nominal input power $p_{dc} = -1$ p.u. and different values of the damping conductance $g_d$ . . . . .   | 4-86 |
| 4.51 | Phase voltages and angles dependency on the variation of the phase voltage $v_a$ at nominal input power $p_{dc} = -1$ p.u. and different values of the damping conductance $g_d$ . . . . .   | 4-88 |
| 4.52 | Phase currents and angles dependency on the variation of the phase voltage $v_a$ at zero input power $p_{dc} = 0$ p.u. and different values of the damping conductance $g_d$ . . . . .       | 4-90 |
| 4.53 | Phase voltage and angle errors dependency on the variation of the phase voltage $v_a$ at zero input power $p_{dc} = 0$ p.u. and different values of the damping conductance $g_d$ . . . . .  | 4-91 |
| 4.54 | Phase currents and angles dependency on the variation of the phase voltage $v_a$ at consumed power $p_{dc} = 0.66$ p.u. and different values of the damping conductance $g_d$ . . . . .      | 4-94 |
| 4.55 | Phase voltages and angles dependency on the variation of the phase voltage $v_a$ at zero consumed power $p_{dc} = 0.66$ p.u. and different values of the damping conductance $g_d$ . . . . . | 4-95 |
| 5.1  | Simplified connection diagram of the damping control strategy . .  | 5-2  |
| 5.2  | Block diagram of the modified three-phase damping control strategy . . . . .   | 5-3  |
| 5.3  | Structure of the T/4 based PLL . . . . .   | 5-5  |
| 5.4  | Simulation results of the the T/4 PLL . . . . .  | 5-8  |

|      |  |      |
|------|--|------|
| 5.5  | Zero-crossing detection of the PLL voltage used for sampling and hold of the rms value of the phase voltages . . . . .   | 5-10 |
| 5.6  | Input conductance sampling method . . . . .  | 5-11 |
| 5.7  | Different fourth leg topologies used in practice to form the neutral . . . . .   | 5-15 |
| 5.8  | Block diagram of the split dc-bus controller - concept . . . . .   | 5-17 |
| 5.9  | Block diagram of the split dc-bus controller concept for midpoint stabilisation . . . . .  | 5-17 |
| 5.10 | Midpoint stabilisation by offsetting the reference currents - concept . . . . .  | 5-18 |
| 5.11 | Block diagram of midpoint stabilisation by offsetting the reference currents . . . . .   | 5-18 |
| 5.12 | Test set-up used to validate the midpoint stabilisation algorithms . . . . .   | 5-19 |
| 5.13 | Phase voltages and dc-bus voltages at the inverter terminals . . . . .   | 5-21 |
| 5.14 | Injected phase currents by the DER . . . . .   | 5-21 |
| 5.15 | The input conductance when two dc-bus controllers are used . . . . .   | 5-22 |
| 5.16 | Input conductance and compensation current waveforms when reference current offset is used . . . . .   | 5-22 |
| 5.17 | Block diagram of the used duty-ratio feed-forward . . . . .  | 5-24 |
| 5.18 | Connection diagram of the DER used to investigate the performance of the local control under unbalanced voltages and different input power . . . . .   | 5-26 |
| 5.19 | DER reaction when $g_d$ is set from 0 to 12 p.u. . . . .   | 5-28 |
| 5.20 | DER reaction when $g_d$ is set from 0 to 12 p.u. . . . .   | 5-29 |
| 5.21 | DER reaction when the input power changes from 0 to $-1$ p.u. and back to 0 p.u. are applied and the full local control is enabled . . . . .   | 5-31 |
| 5.22 | Exchanged active power by the DER when the input power changes from 0 to $-1$ p.u. and back to 0 p.u. are applied and the full local control is enabled . . . . .                                | 5-32 |
| 5.23 | DER reaction when the input power changes from 1 to $-1$ p.u. and back to 1 p.u. when the full local control is enabled . . . . .  | 5-33 |
| 5.24 | Exchanged active power by the DER when the input power changes from 1 to $-1$ p.u. and back to 1 p.u. are applied and the full local control is enabled . . . . .                                | 5-34 |
| 5.25 | LV feeder measurements . . . . .   | 5-37 |
| 5.26 | Phase currents and angle errors dependency on the variation of the phase voltage $v_a$ at zero input power $p_{dc} = 0$ p.u. and different values of the damping conductance $g_d$ . . . . .     | 5-41 |
| 5.27 | Phase voltage and angle errors dependency on the variation of the phase voltage $v_a$ at zero input power $p_{dc} = 0$ p.u. and different values of the damping conductance $g_d$ . . . . .      | 5-42 |
| 5.28 | Phase currents and angle errors dependency on the variation of the phase voltage $v_a$ at nominal input power $p_{dc} = -1$ p.u. and different values of the damping conductance $g_d$ . . . . . | 5-44 |

|      |  |      |
|------|--|------|
| 5.29 | Phase voltages and angle errors dependency on the variation of the phase voltage $v_a$ at nominal input power $p_{dc} = -1$ p.u. and different values of the damping conductance $g_d$ . . . . .   | 5-45 |
| 5.30 | Phase currents and angle errors dependency on the variation of the phase voltage $v_a$ at nominal input power $p_{dc} = 0.66$ p.u. and different values of the damping conductance $g_d$ . . . . . | 5-47 |
| 5.31 | Phase voltages and angle errors dependency on the variation of the phase voltage $v_a$ at nominal input power $p_{dc} = 0.66$ p.u. and different values of the damping conductance $g_d$ . . . . . | 5-48 |
| 5.32 | Connection diagram of the original set up used to test the three-phase damping control strategy in a real LV grid . . . . .  | 5-50 |
| 5.33 | PV inverters, available at the 10 <sup>th</sup> floor of the field trial building . . . . .  | 5-51 |
| 5.34 | Connection diagram of the field set-up where the three-phase damping control strategy is implemented by using three single-phase inverters . . . . .   | 5-52 |
| 5.35 | Connection diagram of the field set-up where the three-phase damping control strategy is implemented by using three single-phase inverters . . . . .   | 5-53 |
| 5.36 | Comparison between the positive-sequence and three-phase damping control strategy obtained by the field trial . . . . .  | 5-53 |
| 6.1  | Active power drooping based on the VBDC . . . . .  | 6-4  |
| 6.2  | Active power droop controller and BESS controller used for the integration in the examined control strategies . . . . .  | 6-8  |
| 6.3  | Feeder topology used to access the performance the examined control strategies . . . . .   | 6-12 |
| 6.4  | Solar irradiation and load profiles used in the simulation model . . . . .   | 6-14 |
| 6.5  | Integration of BESS into the DER . . . . .   | 6-15 |
| 6.6  | Voltage profile of phase b during an entire day when the positive-sequence and three-phase damping (under two values of $g_d$ ) control strategies and storage capacities are examined . . . . .   | 6-18 |
| 6.7  | Reaction of the BESS controllers when positive-sequence ( $g_d = 0$ ) p.u. and three-phase damping control ( $g_d = 20$ ) p.u. strategies are examined at different time instances . . . . .       | 6-19 |
| 6.8  | Injected power and SOC of all DER when the positive-sequence and the three-phase damping control strategies are examined ( <i>CIS1</i> , <i>CIS2</i> and <i>CIS3</i> ) . . . . .                   | 6-23 |
| 6.9  | Injected power and SOC of all DER when the the three-phase damping control strategy is examined ( <i>CIS4</i> and <i>CIS5</i> ) . . . . .  | 6-24 |
| 6.10 | Injected power and SOC of all DER when the positive-sequence and the three-phase damping control strategies are examined ( <i>C2IS1</i> , <i>C2S2</i> and <i>C2S3</i> ) . . . . .                  | 6-25 |
| 6.11 | Injected power and SOC of all DER when the the three-phase damping control strategy is examined ( <i>CIS4</i> and <i>CIS5</i> ) . . . . .  | 6-26 |

|      |  |      |
|------|--|------|
| 6.12 | Total losses of renewable energy due to drooping of active power of all DER when different test cases are studied . . . . .  | 6-27 |
| 6.13 | Feeder topology used to access the performance the examined control strategies . . . . .   | 6-28 |
| 6.14 | Full cycle of the droop controller when charging (—) and discharging the BESS (—) . . . . .  | 6-34 |
| 6.15 | Full cycle of the damping controller when charges (---) and discharges the BESS (---) . . . . .  | 6-34 |
| 6.16 | Three-phase four-wire inverter used by the three-phase damping control strategy . . . . .  | 6-36 |
| 6.17 | Connection diagram of the experimental set-up . . . . .  | 6-36 |
| 6.18 | Phase voltages measured at the inverter terminals when the damping conductance value is 0 p.u. . . . .   | 6-38 |
| 6.19 | Phase currents injected by the three-phase damping control strategy when operating in discharge mode under two initial values of the $g_d = 0$ and 5 p.u. Note that the high frequency noise is due to the measurements. . . . . | 6-38 |
| 6.20 | Phase voltages measured at the inverter terminals in charging mode when the damping conductance value is 0 p.u. . . . .  | 6-39 |
| 6.21 | Phase currents drawn by the three-phase damping control strategy when operating in charging mode under two values of the $g_d = 0$ and 5 p.u. . . . .  | 6-40 |
| 7.1  | Financial losses due to power quality issues . . . . .   | 7-3  |
| 7.2  | Research articles about voltage dips found in Web of Science database with key words "voltage dips" and "voltage sags" . . . . .   | 7-4  |
| 7.3  | Dips classification where ---- represents the nominal phase magnitudes and angles while — represents the residual phase voltages and angles during a voltage dip . . . . .   | 7-5  |
| 7.4  | Grid topology used to demonstrate the propagation of the different types of voltage dips through the electrical grid . . . . .   | 7-7  |
| 7.5  | Immunity curves of computer equipment set by different standards   | 7-10 |
| 7.6  | Voltage divider model used to investigate the residual voltage at the PCC . . . . .  | 7-14 |
| 7.7  | Equivalent circuit of the positive-sequence control strategy, expressed by symmetrical components . . . . .  | 7-16 |
| 7.8  | Calculation of the reference currents at voltage dips . . . . .  | 7-18 |
| 7.9  | Equivalent circuit of the three-phase damping control strategy, expressed by symmetrical components . . . . .  | 7-19 |
| 7.10 | Set-up configuration to test voltage dip Type B . . . . .  | 7-23 |
| 7.11 | Phase voltages and injected phase currents by the positive-sequence and three-phase damping control strategies at $p_{dc} = -1$ p.u. when voltage dip Type B is investigated . . . . .   | 7-25 |
| 7.12 | Positive and negative dc-bus voltages at $g_d = 0$ p.u. and 12 p.u. . .  | 7-26 |

---

|      |   |      |
|------|---|------|
| 7.13 | dc-bus voltages transient, rms current injection and voltage unbalance factor dependency on the damping conductance and residual voltages caused by a dip Type B at $p_{dc} = -1$ p.u. . . . . .        | 7-27 |
| 7.14 | Phase voltages and injected phase currents by the positive-sequence and three-phase damping control strategies at $p_{dc} = -1$ p.u. when voltage dip Type D is investigated . . . . .                  | 7-29 |
| 7.15 | dc bus voltages transient, rms current injection and voltage unbalance factor dependency on the damping conductance and residual voltages caused by a dip Type D at $p_{dc} = -1$ p.u. . . . . .        | 7-30 |
| 7.16 | Phase voltages and injected phase currents by the positive-sequence and three-phase damping control strategies at $p_{dc} = 0$ p.u. when voltage dip Type B is investigated . . . . .                   | 7-32 |
| 7.17 | dc bus voltages transient, rms current injection and voltage unbalance factor dependency on the damping conductance and residual voltages caused by a dip Type B at $p_{dc} = 0$ p.u. . . . . .         | 7-35 |
| 7.18 | Phase voltages and injected phase currents by the positive-sequence and three-phase damping control strategies at $p_{dc} = 0$ p.u. when voltage dip Type D is investigated . . . . .                   | 7-36 |
| 7.19 | dc bus voltages transient, rms current injection and voltage unbalance factor dependency on the damping conductance and residual voltages caused by a dip Type D at $p_{dc} = 0$ p.u. . . . . .         | 7-37 |
| 7.20 | Phase voltages and injected phase currents by the positive-sequence and three-phase damping control strategies at $p_{dc} = 1$ p.u. when voltage dip Type B is investigated . . . . .                   | 7-39 |
| 7.21 | dc bus voltages transient, rms current injection and voltage unbalance factor dependency on the damping conductance and residual voltages caused by a dip Type B at $p_{dc} = -1$ p.u. . . . . .        | 7-41 |
| 7.22 | Phase voltages and injected phase currents by the positive-sequence and three-phase damping control strategies at $p_{dc} = 1$ p.u. when voltage dip Type D is investigated . . . . .                   | 7-42 |
| 7.23 | RMS current injection, residual phase voltages and voltage unbalance factors dependency on the damping conductance and residual voltages caused by a dip Type D at $p_{dc} = 1$ p.u. . . . . .          | 7-43 |
| 7.24 | Voltage dip detection block diagram . . . . .   | 7-48 |
| 7.25 | Voltage dip detection performance of the improved algorithm . . . . .   | 7-48 |
| 7.26 | Voltage dip detection block diagram . . . . .   | 7-49 |
| 7.27 | Damping conductance reduction during voltage dips . . . . .   | 7-49 |
| 7.28 | Voltage dip detection performance of the improved algorithm . . . . .   | 7-50 |
| 7.29 | Feeder topology used to access the performance the examined control strategies . . . . .  | 7-51 |
| 7.30 | Phase voltages during pre-fault, fault and post-fault conditions when cases No DER, positive-sequence and three-phaser damping control strategies are applied without dip detection algorithm . . . . . | 7-53 |

---

|      |  |      |
|------|--|------|
| 7.31 | Injected currents by the DERs during pre-fault, fault and post-fault conditions when cases No DER, positive-sequence and three-phaser damping control strategies are applied without dip detection algorithm . . . . . | 7-54 |
| 7.32 | Injected currents by the DERs during pre-fault, fault and post-fault conditions when cases No DER, positive-sequence and three-phaser damping control strategies are applied with dip detection algorithm . . . . .    | 7-56 |
| 7.33 | Phase voltages during pre-fault, fault and post-fault conditions when cases No DER, positive-sequence and three-phaser damping control strategies are applied with dip detection algorithm . . . . .                   | 7-57 |
| B.1  | Three-phase inverter prototype used for the experimental validation of the proposed control algorithms . . . . .   | B-2  |
| B.2  | Block diagram of the developed DSP-based controller used in the experimental set-up . . . . .  | B-3  |
| B.3  | A picture of the developed DSP-based controller used in the experimental set-up . . . . .  | B-4  |



## List of Tables

|      |   |      |
|------|---|------|
| 2.1  | Standard requirements for DERs under normal and abnormal conditions . . . . .   | 2-5  |
| 3.1  | Full cable impedance matrix including the earth impedance [ $\Omega/\text{km}$ ] . . . . .  | 3-7  |
| 3.2  | Load connection and parameters used in the simulation model . . . . .   | 3-9  |
| 3.3  | DER data used to compare the two active power drooping cases . . . . .  | 3-10 |
| 3.4  | DER data used in the simulation model . . . . .   | 3-15 |
| 3.5  | Initial and actual values of the damping conductance for the different test cases . . . . .   | 3-19 |
| 3.6  | Segregated feeder losses . . . . .  | 3-23 |
| 3.7  | Summarised simulation data in of the exchanged rms currents in phase quantities by the different DERs . . . . .   | 3-25 |
| 3.8  | Summarised simulation data of the voltages, currents and power in symmetrical components . . . . .  | 3-27 |
| 3.9  | Summarised simulation data of voltages, currents, power, etc. that are exchanged by the DERs (red values means power quality problem, i.e., overvoltages) . . . . . | 3-29 |
| 3.10 | <i>Case 1</i> :Obtained phase voltage and voltage unbalance factors by means of experiments at $v_a = 1.057$ p.u. (114V) . . . . .                                  | 3-33 |
| 3.11 | <i>Case 1</i> :Obtained phase currents and injected power by means of experiments at $v_a = 1.039$ p.u. (114.3V) . . . . .  | 3-33 |
| 3.12 | Obtained phase voltage and voltage unbalance factors by means of experiments at $v_a = 1.057$ p.u. (116.3V) . . . . .   | 3-35 |
| 3.13 | Obtained phase currents and injected power by means of experiments at $v_a = 1.057$ p.u. (116.3V) . . . . .   | 3-35 |
| 3.14 | Obtained phase voltage and voltage unbalance factors by means of experiments at $v_a = 1.075$ p.u. (118.3V) . . . . .   | 3-36 |
| 3.15 | Obtained phase currents and injected power by means of experiments at $v_a = 1.075$ p.u. (118.3V) . . . . .   | 3-36 |
| 4.1  | VUF <sub>2</sub> of voltage dip propagation in a typical transmission/distribution grid configuration and residual voltage of 50%for star connected load. . . . .   | 4-45 |
| 4.2  | Injected phase currents by DER <sub>11</sub> , DER <sub>18</sub> and DER <sub>19</sub> . . . . .  | 4-62 |

---

|      |  |      |
|------|--|------|
| 4.3  | Initial and calculated values by the damping controllers values of the damping conductance used by DER <sub>11</sub> , DER <sub>18</sub> and DER <sub>19</sub> . . . | 4-63 |
| 4.4  | Injected phase currents by DER <sub>11</sub> , DER <sub>18</sub> and DER <sub>19</sub> . . . . .   | 4-69 |
| 4.5  | Initial and calculated damping conductance by the damping controllers of DER <sub>11</sub> , DER <sub>18</sub> and DER <sub>19</sub> . . . . .                       | 4-69 |
| 4.6  | Nominal power of DERs . . . . .  | 4-72 |
| 5.1  | Test set-up parameters . . . . .   | 5-19 |
| 5.2  | Settings of the dc-bus PI controllers . . . . .  | 5-20 |
| 5.3  | Obtained measurements under unbalanced current injection . . . .   | 5-22 |
| 5.4  | Prototype parameters . . . . .   | 5-35 |
| 5.5  | Full cable impedance matrix . . . . .  | 5-36 |
| 5.6  | Comparison between the obtained simulation and measured values of the test set-up feeder and power supply . . . . .  | 5-37 |
| 6.1  | Properties of the LV feeder. . . . .   | 6-12 |
| 6.2  | Nominal power of DER and storage capacity . . . . .  | 6-13 |
| 6.3  | Examined test cases . . . . .  | 6-13 |
| 6.4  | Nominal power of the loads and type of connection . . . . .  | 6-14 |
| 6.5  | Maximum current ratings of the power electronic inverters as a function of the damping conductance and storage . . . . .   | 6-28 |
| 6.6  | Test set-up parameters . . . . .   | 6-37 |
| 6.7  | Voltages measured at the inverter terminals when operating in charge mode . . . . .  | 6-41 |
| 6.8  | Currents measured at the inverter terminals when operating in charge mode . . . . .  | 6-41 |
| 6.9  | Voltages measured at the inverter terminals when operating in discharge mode . . . . .   | 6-42 |
| 6.10 | Currents measured at the inverter terminals when operating in discharge mode . . . . .   | 6-42 |
| 7.1  | Voltage dip propagation in a typical transmission/distribution grid configuration and residual voltage of 50% for star connected load. . . . .                       | 7-7  |
| 7.2  | Standard test residual voltage levels according to IEC 61000-4-11 and IEC 61000-4-34. . . . .  | 7-10 |
| 7.3  | Comparison between voltage dips Type D and Type C in terms of residual voltages and phase jumps . . . . .  | 7-28 |
| 7.4  | Most commonly used voltage dip characterization algorithms . . . .   | 7-47 |
| 7.5  | Properties of the LV feeder. . . . .   | 7-51 |
| 7.6  | Nominal power of the loads and type of connection . . . . .  | 7-52 |
| 7.7  | Nominal power of DERs and node connection . . . . .  | 7-52 |
| A.1  | Zero- and negative-sequence voltage unbalance factors, measured at the PCC when $p_{dc} = -1$ p.u. . . . .   | A-2  |

---

|     |  |     |
|-----|--|-----|
| A.2 | Zero- and negative-sequence voltage unbalance factors, measured at the PCC when $p_{dc} = 0$ p.u. . . . .                | A-2 |
| A.3 | Zero- and negative-sequence voltage unbalance factors, measured at the PCC when $p_{dc} = 0.6666$ p.u. . . . .           | A-2 |
| C.1 | Maximum current ratings of the power electronic inverters as a function of the damping conductance and storage . . . . . | C-2 |



# List of Acronyms

|          |                                  |
|----------|----------------------------------|
| APC      | Active Power Curtailment         |
| APF      | Active Power Filters             |
| ASD      | Adjustable Speed Drives          |
| BESS     | Battery Energy Storage System    |
| DD       | Dip Detection                    |
| DER      | Distributed Energy Resource      |
| DFF      | Discrete Fourier Transform       |
| DG       | Distributed Generation           |
| DSTATCOM | Distribution Static Compensator  |
| DSO      | Distribution System Operator     |
| DSP      | Digital Signal Processor         |
| DVR      | Dynamic Voltage Restorer         |
| EC       | European Commission              |
| EU       | European Union                   |
| EV       | Electric Vehicle                 |
| EKF      | Extended Kalman Filter           |
| FACTS    | Flexible AC Transmission System  |
| FT       | Fourier Transform                |
| FFT      | Fast Fourier Transform           |
| HEV      | Hybrid Electric Vehicle          |
| IT       | Information Technology           |
| LV       | Low Voltage                      |
| MPC      | Model-based Predictive Control   |
| MRST     | Multi-resolution S-Transform     |
| MV       | Medium Voltage                   |
| NMSD     | Numerical Matrix Sag Detector    |
| OLTC     | On Load Tap Changer              |
| P        | Proportional controller          |
| PCC      | Point of Common Coupling         |
| PF       | Power Factor                     |
| PFC      | Power Factor Corrector           |
| PI       | Proportional Integral controller |
| PLC      | Programmable Logic Controller    |
| PLL      | Phase Locked Loop                |
| PV       | Photo Voltaic                    |
| PVDQ     | Peak Vector DQ Transformation    |

|           |                              |
|-----------|------------------------------|
| PVEM      | Peak Value Evaluation Method |
| REM (rms) | RMS Evaluation Method        |
| RMS (rms) | Root Mean Square             |
| STATCOM   | Static Compensator           |
| THD       | Total Harmonic Distortions   |
| VBDC      | Voltage-based Droop Control  |
| VSI       | Voltage Source Inverters     |
| WA        | Wavelet Analysis             |





# Summary

The concerns about climate change and uncertain prices of fossil fuels are leading to an increased penetration of renewable energy resources in electrical distribution grids. Although distributed energy resources have many advantages compared to the classical centralised energy supply, the fit-and-forget approach of connecting them to distribution grid is not an appropriate solution because of power quality problems. In areas with high penetration of renewable energy resources, overvoltages do occur, and they are considered as the main stopper of further integration of new renewables in the distribution grid. Besides overvoltages, voltage unbalance is also present in the distribution feeders. To solve the above listed power quality issues and thus to increase the penetration level of renewable energy resources in the distribution grids, more sophisticated control strategies for controlling the injected power by the renewables are needed. In this dissertation, new control algorithms are proposed that control their exchanged power based on local measurements such as phase voltages and currents. The control algorithm takes different actions if overvoltages or voltage unbalance are present at the inverter terminals by altering the injected power into the grid.

In the introductory chapter an overview of the greenhouse gas emissions is presented.

Chapter 2 provides an overview of the existing solutions targeting the most common power quality problems in areas with increased penetration of renewable energy resources. In addition, currently used control strategies used in the distribution energy resources units are also given and their drawback of providing sufficient voltage control and handling high penetration of renewables are also pointed out. Therefore, to provide a better voltage control and improve the power quality in the distribution grid, a combination of the voltage-based droop control and the three-phase damping control strategy are considered for further examination.

Chapter 3 forms the core of this dissertation. It combines the active power

drooping of the communicationless voltage-based droop control strategy and the three-phase damping control strategy. The active power drooping is part of the voltage-based droop control and is responsible for the active power injection by the renewable energy resource unit based on the rms values of the grid voltages. The voltage unbalance mitigation, provided by the three-phase damping control strategy, is further improved by implementing a damping controller by calculating the damping conductance as function of the grid voltages. By combining the active power droop controller and the damping controller, the full local control is formed. By measuring the grid voltages, the distribution energy resource unit injects current into the grid without deteriorating the power quality at the point of common coupling.

In Chapter 4, the three-phase damping control strategy is theoretically examined and based on the mathematical model, three different operating modes are defined, i.e., injection mode, consumption mode and zero-powered inverter. The theoretical study covers different operating scenarios and based on the outcome some practical limits regarding the sizing of the power electronic inverter of the renewable energy resource unit are defined for the different modes in §4.2. In section §4.3, the local control in consumption mode and zero-powered inverter modes are tested by means of simulations on a real low voltage feeder. The results show that the local control together with the three-phase damping control strategy are capable of improving the power quality by mitigating voltage unbalance and over-voltages which can be beneficial to implement the proposed algorithm in different applications such as three-phase loads, battery storage systems, etc.

Chapter 5 provides some guidelines of the practical implementation of the three-phase positive-sequence and three-phase damping control strategies. A sampling strategy is implemented in order to use all measured signals at the appropriate time instance such that the generated reference currents are not polluted with harmonics. Since the three-phase damping control strategy requires a four-wire inverter, a split dc-bus capacitor voltage balancing scheme is proposed which ensures normal operation of the control strategy. Some recommendations are also given regarding the time responses of the different controllers which are part of the local control. In addition, some scenarios are examined to demonstrate the transient response of the local control.

Chapter 6 discusses integrating a decentralised battery storage system together with the local control, positive-sequence and three-phase damping control strategies with the ultimate purpose to minimise lost renewable energy due to curtailment, to improve the power quality and the grid performance. A separate battery storage controller is added to the control strategy which also relies on local mea-

surements to determine whether storage should source or sink power from the dc-bus of the inverter. The better voltage unbalance mitigation by the three-phase damping control strategy compared to the positive-sequence control strategy has a beneficial effect on the storage capacity as well as longer charging and discharging times, allowing for a better grid support. A battery storage controller is proposed for centralised storage applications together with an adapted curve of the damping controller. The advantageous performance in terms of voltage unbalance mitigation of the three-phase damping control strategy draws less power from the storage which is beneficial for the cost of the centralised storage system.

Since voltage dips are considered to be among the most harmful power quality issues in practice, Chapter 7 examines the behaviour of the positive-sequence and three-phase damping control strategies when subjected to voltage dips. The performance of both control strategies is further examined when different voltage dips are considered. In addition, the proposed dc-bus stabilisation algorithm in Chapter 5 is also tested and its performance is assessed. In this chapter it is also proposed that a voltage detection algorithm is incorporated in the control strategy in order to temporarily reduce the value of the damping conductance such that the exchange of excessive currents are limited during the dip. Finally, the proposed combination is tested on a real low voltage feeder, and the results showed that the proposed solution is able to decrease the exchanged phase currents and therefore only 30 % oversizing of the power electronic inverter is required which is less costly for the prosumer.

Chapter 8 draws the conclusions of this PhD dissertation and outlines some possibilities for further research.



# Samenvatting

De bezorgdheden omtrent de klimaatsverandering en de onzekere prijzen van fossiele brandstoffen geven aanleiding tot een verhoogde penetratie van hernieuwbare energiebronnen in de elektrische distributienetwerken. Hoewel de verdeelde energiebronnen veel voordelen opleveren in vergelijking met de klassieke gecentraliseerde energieproductie, is het verbinden van deze energiebronnen met het net volgens de “fit-and-forget” methode geen gepaste oplossing wegens de voortvloeiende problemen in netkwaliteit. Overspanningen kunnen zich manifesteren in gebieden met hoge penetratie van hernieuwbare energiebronnen, en worden beschouwd als het belangrijkste obstakel voor verdere integratie van nieuwe hernieuwbare energiebronnen in het distributienet. Naast overspanningen kunnen zich eveneens spanningsonbalansen voordoen in de distributielijnen. Om de bovengestane problemen in spanningskwaliteit op te lossen en op die manier het penetratieniveau van hernieuwbare energiebronnen te verhogen, is er nood aan complexere controlestrategieën om het geïnjecteerd vermogen van de hernieuwbare bronnen beter te kunnen regelen. In dit proefschrift worden nieuwe controlealgoritmen voorgesteld die het uitgewisselde vermogen sturen op basis van lokale metingen zoals fasespanningen en stromen. Het controle-algoritme reageert op overspanningen en spanningsonbalansen die zich voordoen aan de invertorterminals door het vermogen geïnjecteerd in het net aan te passen.

Het inleidend hoofdstuk presenteert een overzicht van de broeikasgasuitstoot.

Hoofdstuk 2 biedt een overzicht van de bestaande oplossingen die gericht zijn op de meest voorkomende netkwaliteitsproblemen in gebieden met verhoogde penetratie van hernieuwbare energiebronnen. Verder worden de huidige controlestrategieën die gebruikt worden in de energieproductie-eenheden uitgelegd, en wordt er gewezen op de nadelen in het streven naar voldoende spanningsregeling en verwerking van de hoge penetratie aan hernieuwbare bronnen. Om een betere spanningsregeling te bekomen en de netkwaliteit in het distributienet te verbeteren, wordt een combinatie van de spanningsgebaseerde droopregeling en de driefasige dependende regeling verder in detail onderzocht.

Hoofdstuk 3 vormt de kern van dit proefschrift. Het combineert de droopregeling gebaseerd op actief vermogen van de communicatieloze spanningsgebaseerde droopregeling met de driefasige dempende regeling. Actief-vermogen-droopregeling maakt deel uit van de spanningsgebaseerde droopregeling en regelt de hernieuwbare energiebron bij de injectie van het actief vermogen gebaseerd op de rms waarden van de netspanningen. De limitering van de spanningsonbalans, die wordt geboden door de driefasige dempende regeling, wordt verder aangescherpt door het implementeren van een dempende regeling die de dempingsgeleidbaarheid berekent als functie van de netspanningen. De combinatie van de actief-vermogen droopregeling en de dempende regeling vormt de volledige lokale regeling. Door het meten van de netspanningen kan de energieproductie-eenheid stroom in het net injecteren zonder de netkwaliteit op het punt van gemeenschappelijke koppeling te doen verlagen.

In Hoofdstuk 4 wordt de driefasige dempende regeling theoretisch onderzocht. Men definieert drie verschillende werkingsmodi op basis van het wiskundig model: de injectiemodus, de verbruiksmodus en de zero-powered inverter modus. De theoretische studie beschouwt verschillende werkingsscenario's, waarbij enkele praktische limieten omtrent de dimensionering van de vermogens-elektronische omvormer van de hernieuwbare energie-eenheid worden gedefinieerd voor de verschillende modi §4.2. In Sectie §4.3 wordt de lokale regeling in verbruiksmodus en zero-powered inverter modus getest met simulaties gebruik makende van een bestaande lagespanningslijn. De resultaten tonen aan dat de lokale regeling in combinatie met de driefasige dempende regeling in staat is om de spanningskwaliteit te verhogen door spanningsonbalansen en overspanningen te limiteren. Dit maakt het gunstig om het voorgestelde algoritme te implementeren in verschillende toepassingen, waaronder driefasige lasten, batterij-opslag, etc.

Hoofdstuk 5 biedt enkele richtlijnen voor de praktische implementatie van de driefasige symmetrische regeling en driefasige dempende regeling. Een benoemingsstrategie werd gecomplementeerd om de meetsignalen op de geschikte ogenblikken te gebruiken zodat de gegenereerde referentiestromen vrij zijn van harmonische vervuiling. Gezien de driefasige dempende regeling een vierdraads omvormer nodig heeft, wordt een schema vooropgesteld om de condensatorspanning van een gesplitste dc-bus te balanceren. Dit verzekert een normale werking van de regeling. Verder worden enkele aanbevelingen aangereikt omtrent de reactietijd van de verschillende regelingen die deel uitmaken van de lokale regeling. Ten slotte worden enkele scenario's onderzocht om de transiënte respons van de lokale regeling te demonstreren.

In Hoofdstuk 6 volgt een bespreking van de integratie van een gedecentraliseerd batterij-opslagsysteem in combinatie met de lokale regeling, symmetrische regeling en driefasige dempende regeling. Het einddoel is het minimaliseren van het energieverlies wegens beperking van de hernieuwbare energiebron, het verbeteren van de netkwaliteit en de prestatie van het net. Aan de regeling werd een aparte regeling voor batterij-opslag toegevoegd om te bepalen of de opslag als bron al dan niet als afvoer (sink) moet fungeren ten opzichte van de dc-bus van de omvormer. De aparte regeling is hierbij ook afhankelijk van lokale metingen. De driefasige dempende regeling gaat gepaard met een verbeterde limitering van spanningsonbalansen in vergelijking met de symmetrische regeling. De dempende regeling heeft daarmee een gunstig effect op zowel opslagcapaciteit als de laad- en ontladtijd: een langere laad- en ontladtijd laat immers een betere ondersteuning van het net toe. Een regeling voor batterij-opslag wordt voorgesteld voor toepassingen met gecentraliseerde opslag, in combinatie met een aangepaste curve van de dempende regeling. De gunstige performantie van de driefasige dempende regeling met betrekking tot de limitering van spanningsonbalansen zorgt ervoor dat er minder vermogen uit de opslag wordt getrokken, wat bevorderlijk is voor de kost van het gecentraliseerde opslagsysteem.

Gezien spanningsdips in de praktijk beschouwd worden als een van de meest schadelijke fenomenen voor de netkwaliteit, wordt in Hoofdstuk 7 het gedrag van de symmetrische regeling en de driefasige dempende regeling onderzocht in aanwezigheid van verscheidene soorten spanningsdips. Verder wordt ook het voorgestelde algoritme in Hoofdstuk 5 voor stabilisatie van de dc-bus getest en diens performantie vastgesteld. In Hoofdstuk 7 wordt tevens voorgesteld om een algoritme voor spanningsdetectie in de regeling te implementeren om tijdelijk de waarde van de dempende geleidbaarheid te verlagen. Dit zorgt ervoor dat de uitwisseling van buitensporige stromen begrensd blijft gedurende de dip. Ten slotte wordt de voorgestelde combinatie getest op een bestaande lagespanningslijn: de resultaten tonen aan dat de voorgestelde oplossing in staat is om de uitgewisselde fasestromen te doen afnemen, wat op zijn beurt toelaat om de nodige overdimensionering te verkleinen.

In Hoofdstuk 8 worden de conclusies van dit doctoraatsproefschrift getrokken en worden de grote lijnen van mogelijke pistes voor toekomstig onderzoek voorgesteld.



# 1

## Introduction

### 1.1 Introduction

Over the past decades, CO<sub>2</sub> emissions have increased significantly, which has led to more extreme climate conditions. On the 11<sup>th</sup> of December 1997, a meeting was held in Kyoto in Japan, during which the “Kyoto Protocol” was ratified and adopted in COPs (Conference of the Parties). This is the first document with legally binding obligations for limits and reductions to the greenhouse gas emissions. The Kyoto protocol is based on the scientific consensus that (1) global warming is occurring and (2) it is extremely likely that human-made CO<sub>2</sub> emissions have predominantly caused it. The period of applicability was set for the years 2008 to 2012 (1<sup>st</sup> obligation period) and 2013 to 2020 (2<sup>nd</sup> obligation period) [1].

The Kyoto Protocol is seen as an important first step towards global emission reduction strategy that will stabilise GHG emissions. This protocol has binding conditions until 2020 as the second obligation period ends. Therefore, a new climate agreement was required to maintain the international climate protection after 2020. This was adopted in 2015 at the COP in Paris as the “Paris Agreement”. For the first time such an agreement includes a specific target for limiting global warming to less than 2°C compared the pre-industrial level of 1750. All different ratified countries set their individual targets and every 5 years a review and strengthening of the climate protection efforts will be conducted. In October 2016, the required number of at least 55 ratified countries, which are responsible for at least 55 %

of the global greenhouse gas emissions, was reached, which meant the agreement could enter into force.

As it stands, the European Union (EU) is aiming to reduce greenhouse gas emissions by 20% by 2020 compared to 1990 and by 40% by 2030 [2]. To achieve these goals by 2020 the EU has set targets for the renewable energy sources and energy efficiency:

- 20% improvement in energy efficiency
- 20% of EU energy from renewables

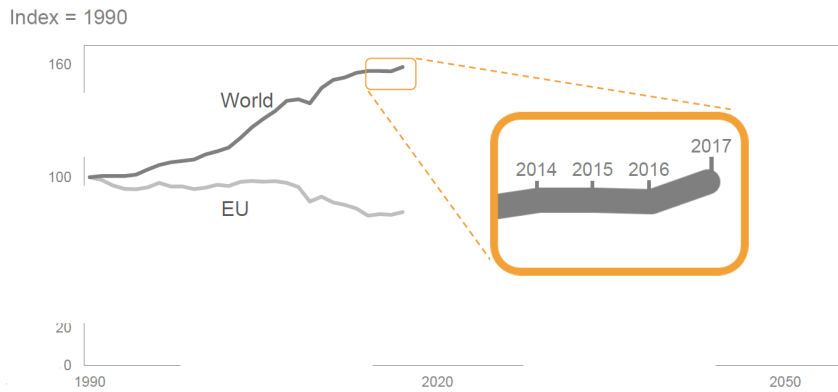
The more ambitious goal of 40% reduction will be achieved by the same means but different target values:

- At least 32.5% improvement in energy efficiency
- At least 32.5% share for renewable energy

Saving energy through energy efficiency measures in buildings, industry and the transport sectors helps to reduce greenhouse emissions and effectively fight climate change while boosting the economy, creating jobs and improving living conditions of the citizens. The energy efficiency includes besides measures as co-generation of heat and power, heating and cooling, energy efficient buildings (insulation, lighting, smart sensors, etc.) as well as promoting of rational use of energy. The later one includes actions such as informing customers and raise their awareness about how to use energy more economically, energy-efficient appliances and ways in which they can construct and renovate in an energy-aware manner.

On the other hand, the green low carbon technologies produce electricity from renewable sources such as solar, wind, dams, wave, tidal and so on. These technologies can be successfully used to de-carbonise the electricity sector because the ratio of produced kWh per invested energy in CO<sub>2</sub> equivalent is very low. Depending on the photovoltaic technology: poly-crystalline, mono-crystalline, thin film, etc., give typical values of about 20 to 50 gCO<sub>2</sub> per kWh. Wind power has even lower ratios than the photovoltaic. Typical values of on shore wind farms are 5 to 15 gCO<sub>2</sub>/kWh while for off-shore wind farms these values are about 4 to 10 gCO<sub>2</sub>/kWh.

Fig. 1.1 (a) shows that there is a general downward trend to emissions during the 1990-2019 period (aside from the big peak in 1996, when a cold winter led to an increase in heating requirements). In the period from 1999 to 2006 the trend of greenhouse gas emissions within the EU remained relatively unchanged. In the year 2009, a sharp drop in emissions can be observed as a consequence of the global financial and economic crisis which has led to global economy decrease with 6% (see Fig. 1.1 (b)) which resulted in shrinking of industrial activities. During 2010 the emissions increased and decreased again from 2011 onward. Emissions increased by 0.7 % (30 million tonnes of CO<sub>2</sub>-equivalents) between 2016



(a) Global CO<sub>2</sub> Emissions from 1990 to 2017 (in percentage)



(b) Global economy fluctuations from 1990 to 2017 (in percentage)

Figure 1.1: Global CO<sub>2</sub> emissions and economy relationship <sup>1</sup>

and 2017. The measures of energy efficiency and renewable energy integration has led to a decrease of greenhouse emissions and according to [2] the EU has already reached the target of 20% reduction.

In the same figure the global greenhouse gas emissions are depicted. Unlike the EU trends, the world curve is steadily increasing. The drop in 2009, is present as well due to the same reasons. Nevertheless, the difference in emissions during 2015 and 2016 were negligibly small which gave the impression that the green-

<sup>1</sup>Source [3]

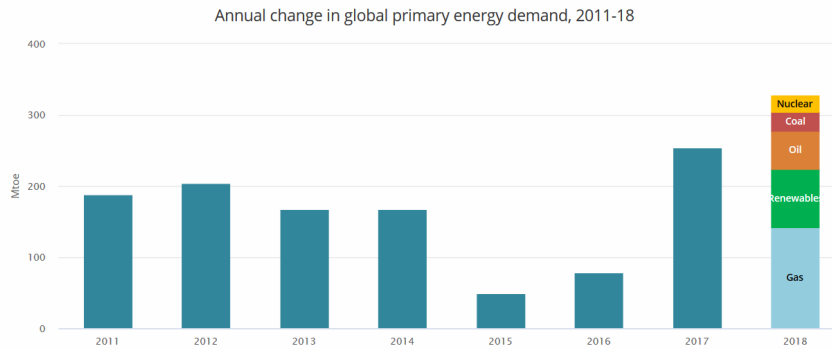


Figure 1.2: Global energy consumption for 2011-2018 period<sup>2</sup>

house gas emissions are at their peak and they will start to decrease in the future. However, this plateau was caused by the lack of economy growth during these years. In 2017, CO<sub>2</sub> emission have slightly risen.

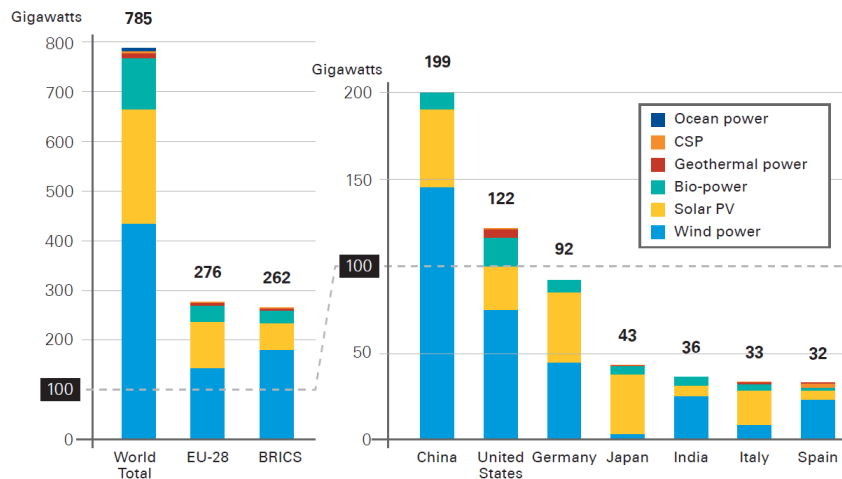
According to [4], the world energy consumption has grown by 2.3% in 2018, which is more than 33% average rate of growth since 2011 (see Fig.1.2). This energy consumption (in Mtoe – million tons of oil equivalent) is driven by a robust global economy growth of 3.7%. According to the same source, almost a fifth of the increase in global energy demand is due to weather conditions last year. Historical temperatures records were approached or exceeded during the summer and winter seasons in 2018. The cold periods drove demand for heating and, more significantly, hotter summer temperatures pushed up demand for cooling. This figure is probably one of the clearest examples of how extreme weather conditions can cause higher energy consumption, therefore more CO<sub>2</sub> emissions, which causes a chain reaction towards global warming.

As a consequence of the higher energy consumption, CO<sub>2</sub> emissions increased to 33.1 Gt CO<sub>2</sub>, which is almost 1.7% as reported in [4]. More than 30% of the energy related emissions are due to coal-fired power generation plants and they continue to be the single largest emitter of CO<sub>2</sub> related emissions.

What is remarkable is that almost 25% of the energy comes from renewable energy resources such as bio, concentrated solar, wind, solar ocean and geothermal plants. Fig. 1.3 shows the total installed power of renewable energy resources until 2015 worldwide. Almost 800 GW have been installed by the end of this year and the EU share of it is about 276 GW. The same figure also shows the segregated data of the different types of renewables and as it can be seen wind accounts for almost half of it while the solar is a little bit over 1/3 of the total amount.

In addition, projects delivering energy from renewable sources have become credible low-carbon alternatives to carbon-intensive fossil fuel based projects. In

<sup>2</sup>Source [4]



The five BRICS countries are Brazil, the Russian Federation, India, China and South Africa.

Figure 1.3: Installed renewable energy capacities until 2015<sup>3</sup>

the last ten years a dramatic drop in the prices of renewable energy projects is shown as experience and scale increased. Furthermore, reference [5] reports levelised cost of electricity produced by PV of about 0.1\$ while the wind energy reaches down to 0.05\$ per kWh. In the same reference levelized cost of electricity produced by concentrated solar power plants, dams and geothermal can also be found. These results seem very promising to reduce the greenhouse gas emissions, however, to reach the 2030 EU target of 32.5% renewable energy significant efforts by the distribution system operators must be done also on a technical level. This high penetration of renewables causes power quality problems which can lead to malfunction of equipment and endanger the security of energy supply.

The goal of this thesis is to provide solutions to the distribution system operators to solve these problems. The solutions are integrated in the distributed energy resources which rely on local measurements to take respective actions and thus to prevent possible problems. The solutions are focused on low voltage distribution grids. This decision is driven by the fact that the distribution system operators have a better control on the medium voltage grids because very often they consist of 10 to 30 nodes which can be easily monitored and controlled. Unlike the medium voltage grids, the low voltage ones have more nodes – between 50 and 200 (or more) and the distribution system operators have very limited number of measurements in these grids. Usually smart meters are installed at the step down transformer and at distributes generation units with relatively high power (> 10kW) to

<sup>3</sup>Source [6]

monitor and send out data to the distribution system operators. In case of power quality problems, the distribution system operator takes respective actions.

## **1.2 Conclusions**

In this chapter, a brief overview of the carbon emissions is given. To meet the European targets for 2030, significant effort must be done in order to integrate 32.5% of renewables in the existing grids. This thesis proposes control schemes which are able to increase the penetration level of renewables and help the distribution system operators to maintain the power quality standards in their grids.

# 2

## Overview of control strategies for inverter-connected renewable energy units in low voltage grids

In this chapter, based on the current standards and regulations the main power quality problems that occur in areas with high penetration of distributed energy resources (DERs) are discussed. A literature overview is conducted and it identified that overvoltages and voltage unbalance are the most common problems in low voltage distribution grids. An overview of different solutions for decreasing the overvoltages and voltage unbalance problems are given, based on grid reinforcement, using dedicated equipment and reactive power support at both low voltage (LV) grid and DERs levels.

### **2.1 Power quality problems due to the increased penetration level of DERs**

Originally, the power flow in the distribution grids was unidirectional from the power plants to the end user and problems such as overvoltages were not a pronounced phenomenon. Due to environmental and economic concerns, the interest in distributed energy resources (DER) is continuously growing and in some feeders has already led to a bidirectional power flow from low voltage (LV) to medium voltage (MV) grid during peak generation and low consumption periods. Hence,

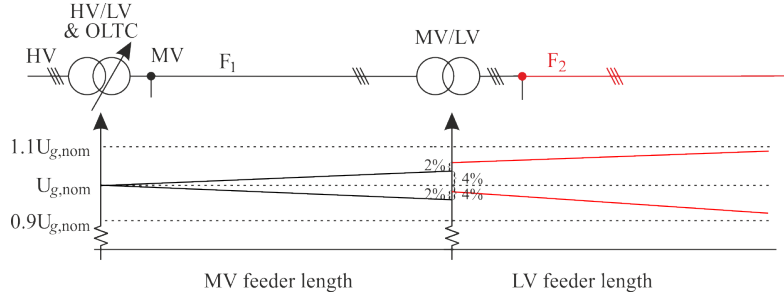


Figure 2.1: Medium and low voltage tolerances set by EN50160 and IEC 60038<sup>1</sup>

power quality problems such as overvoltages and voltage unbalance occur [7].

According to the current standards EN50160 [8], IEC60038 [9] the permissible voltage levels in MV and LV networks are limited to  $\pm 10\%$  from the nominal value as shown in Fig. 2.1. Previously the distribution system operators (DSO) did split the voltage tolerance of 10% as follows: 4% MV, 2% for the LV/MV transformer (in practice this setting is between 2 and 4%) and 4% for the LV grid [10], where the secondary voltage of the MV/LV transformer was set to be 2% higher to overcome the voltage drop of the feeder and thus guarantee appropriate voltage levels for the user at the end of the feeder. However, with increasing the penetration level of DERs in MV and LV grids, the split tolerances have become fuzzy and grid codes such as BDEW [11] have introduced technical guide line for DERs connected to MV (later some requirements were adopted for LV grids) to ensure safe, secure and economic functioning of the electric system. In [11], it is recommended that the maximum power of DER, injected to a specific point in the MV grid, is linked to the voltage change that the DER is allowed to cause and it is set to be 2% of the nominal voltage at the point of common coupling (PCC). As a result, the shares of the MV and LV voltage levels became different and the DSOs have to do more efforts to maintain the tolerances of  $\pm 10\%$ .

To explain the impact of DERs on an LV feeder a fictitious three-phase LV radial feeder is used and it is depicted in Fig. 2.2. It consists of loads  $R_{a,1}$ ,  $R_{b,2}$ ,  $R_{b,3}$ ,  $R_{c,3}$  and  $R_{b,4}$ . The feeder impedances connecting the different nodes are denoted with  $Z_x$  and three DERs are connected to this feeder. Parameters  $V_{x,0}$  notate the phase voltage coming out of the MV/LV transformer and  $V_{x,y}$  indicates the phase voltage of each node. Index “x” denotes the respective phase and index “y” the specific node. If the power produced from DERs is not consumed by the local loads, then it will be injected to the MV grid and it will cause a voltage increase in the LV grid. The change in the voltage level, in a particular node, depends on the amount of the injected currents by DERs and the equivalent grid

<sup>1</sup>Source [8] and [9]

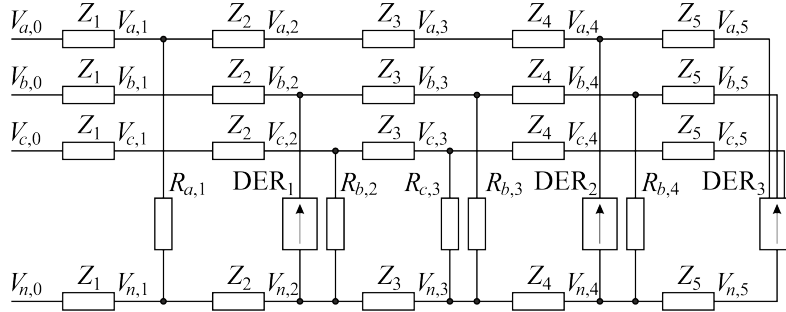


Figure 2.2: Typical low voltage feeder topology

impedance at the specific node. Usually all electrical equipment connected to the grid is designed to withstand some voltage deviation from its nominal value  $V_{g,\text{nom}}$  but still, the variations of  $V_g$  need to remain in a tolerated voltage band, for example 90% to 110% of the nominal grid voltage  $V_{g,\text{nom}}$  [12–14]. The voltage levels recommended by the different standards are listed in Table 2.1. If  $V_g$  by some reason rises above  $V_{g,\text{max}}$  then the DERs are disconnected from the LV grid in order to prevent damage on the other electrical equipment, connected to the same LV grid.

Furthermore, due to the asymmetrical loading of the three-phase systems the phase voltages differ from each other. This asymmetry becomes higher due to the mainly single-phase connections of the rooftop photovoltaic installations. Moreover, the single-phase DERs differ in power ratings and they are not uniformly distributed over the three phases and feeder length. The three-phase voltage asymmetry is known as voltage unbalance and it has a negative impact on the three-phase system and equipment such as transformers, induction machines, distribution feeder losses, etc. In order to limit the negative impact of the voltage unbalance and ensure safe operation of electrical equipment, a maximum allowable limit is set by the standards listed in Table 2.1 with which the DSO must comply.

Unequal loading and distribution of DERs has an impact on the neutral potential and this effect is known as neutral point shifting and it is studied in [15]. Basically, this effect is a voltage potential shifting of the neutral conductor because of the mutual influence between the three phase voltages due to the current flowing through the neutral conductor. The potential of the neutral shifts to the most loaded phase, which results in decreasing the voltage potential in it and increasing the voltage potential in the most unloaded phase. The effect is even strongly pronounced when single-phase DERs are present, especially in the most unloaded phase, due to the additional neutral current.

### 2.1.1 Numerical example of the neutral point shifting

A brief numerical example is given by considering the grid presented in Fig. 2.2. Suppose that a load at node 4 a load  $R_{b,4} = 23\Omega$  (approximate active power consumption of 2 kW), the sum of the line impedances  $Z_1$  to  $Z_4$  is  $0.5 + j.0.266\Omega$  (typical impedance for the consumers at the end of the feeders in LV grids), the initial phase voltages  $V_{x,0}=230$  V (perfectly phase shifted at  $\frac{2\pi}{3}$  radians) and no other loads or DERs are connected to the feeder. The current that flows in phase  $a$  is:

$$\underline{I}_a = \frac{V_{a,0}}{Z_a} A$$

where  $Z_a$  is the equivalent impedance of the load and twice the line impedance. Using the above data, the phase current value is then:

$$\underline{I}_a = \frac{V_{a,0}\sqrt{2}\exp(j\theta_a)}{Z_a} = 13.47 \angle 1.17^\circ$$

Then the voltage at the load ( $R_{b,4} = 23\Omega$ ) terminals becomes:

$$\underline{V}_{a,4} = \underline{I}_a R_{b,4} = 311.66 - j6.901V$$

The neutral potential of  $\underline{V}_{n,4}$  compared to  $\underline{V}_{n,0}$  is then:

$$\underline{V}_{n,4} = \underline{I}_a Z_n = \underline{I}_a (0.5 + j.0.266) = 6.73 + j3.31 V$$

The impedance of the earthing systems is neglected because of its high impedance, which is between 5 to 30  $\Omega$  compared to the neutral impedance, which is assumed to be 0.5  $\Omega$ . Considering that phases  $b$  and  $c$  are lightly loaded such that the current in phases  $b$  and  $c$  can be neglected, the phase voltages at  $\underline{V}_{b,4}$  and  $\underline{V}_{c,4}$  then can be written as:

$$\begin{aligned} \underline{V}_{b,4} &= \underline{V}_{b,0} - \underline{V}_{n,4} = \\ &= (162.5 + j281.458) - (6.73 + j3.31) = -169.23 - j284.768 V \end{aligned}$$

$$\begin{aligned} \underline{V}_{c,4} &= \underline{V}_{c,0} - \underline{V}_{n,4} = \\ &= (162.5 - j281.458) - (6.73 + j3.31) = -169.166 + j278.01 V \end{aligned}$$

The obtained data for the phase voltages at node 4 can be summarised in phasors and rms values as follows:

| phase     | Phasor  | rms                  | $\Delta V$ |
|-----------|---|----------------------|------------|
| phase $a$ | $\underline{V}_{a,4} = 311.736 V \angle 1.27^\circ$   | $V_{a,4} = 220.43 V$ | -4.77%     |
| phase $b$ | $\underline{V}_{b,4} = 331.25 V \angle -120.72^\circ$ | $V_{b,4} = 234.29 V$ | +1.45%     |
| phase $c$ | $\underline{V}_{c,4} = 325.43 V \angle +121.32^\circ$ | $V_{c,4} = 230.11 V$ | -0.4%      |

In the opposite case where the same current is being injected into the grid at node 4, the obtained data for the phase voltages at node 4 can be summarised in phasors and rms values as follows:

| phase          | Phasor  | rms                  | $\Delta V$ |
|----------------|---|----------------------|------------|
| phase <i>a</i> | $\underline{V}_{a,4} = 338.4 V \angle 1.27^\circ$     | $V_{a,4} = 239.28 V$ | +3.61%     |
| phase <i>b</i> | $\underline{V}_{b,4} = 312.46 V \angle -118.51^\circ$ | $V_{b,4} = 220.94 V$ | -4.34%     |
| phase <i>c</i> | $\underline{V}_{c,4} = 324.74 V \angle +118.67^\circ$ | $V_{c,4} = 229.62 V$ | -0.6%      |

As can be seen, the asymmetrical consumption and injection forces the neutral potential to shift and it has significant impact of the voltage levels on the loaded phase as well as the unloaded ones although phases *b* and *c* are unloaded or lightly loaded.

Due to the above listed problems, in some LV feeders, where the penetration level of DERs is high, overvoltage problems can occur and the DERs must be disconnected from the grid for a certain amount of time (see Table 2.1). Therefore, the DSO has difficulties with further integration of new DERs due to capacity constraints of the existing LV network infrastructure [16]. Consequently, increasing the DER penetration level is not possible without improving and operating the LV network and the DERs in an appropriate way [17, 18].

| IEEE 1547                                 | IEC 61727             | VDE 0126 1-1  | EN50160            |
|---|-----------------------|---------------|--------------------|
| Permissible voltage levels in LV grids    |                       |               |                    |
| 88% < $V_g$ < 110%                        | 85% < $V_g$ < 110%    | -             | 90% < $V_g$ < 110% |
| Under-voltage disconnection times         |                       |               |                    |
| 88% < $V_g$ 2 sec                         | 85% < $V_g$ 2 sec     | -             | 90% < $V_g$ 2 sec  |
| Over-voltage disconnection times          |                       |               |                    |
| $V_g$ < 110% 1 sec                        | $V_g$ < 110% 1 sec    | -             | $V_g$ < 110% 1 sec |
| Reconnection time after abnormal tripping |                       |               |                    |
| no time specified                         | minimum delay of 3min | not specified | 15 min             |
| Voltage unbalance limits                  |                       |               |                    |
| -   | 2% or 3%              | -             | 2 %                |

Table 2.1: Standard requirements for DERs under normal and abnormal conditions

## **2.2 Solutions for preventing overvoltages and voltage unbalance**

### **2.2.1 Distribution grid reinforcement**

One of the possible approaches concerning increasing the penetration level of DERs, reducing the overvoltages and voltage unbalance problems in LV networks is increasing the cross section of the cables of the distribution feeders in the existing infrastructure. However, with increasing further the installation of new DERs, voltage problems might appear again or current congestion of the MV/LV transformer will occur [19]. Hence, the DSO has to make another investment of changing the MV/LV transformer. Therefore, this approach is not preferable on a wide scale because of its financial aspect.

### **2.2.2 Voltage profile support by dedicated equipment**

Another approach that can be used to maintain the voltage levels in the LV distribution feeder, involves the use of network components like on-load tap changers (OLTC) and autotransformers. However, the OLTC can solve overvoltage problems in one feeder as shown in Fig. 2.3 by tapping down a few steps, but it can cause undervoltage problems in others due to lack of DERs and heavy loading [20, 21]. In addition, not all MV/LV transformers are equipped with an OLTC due to the additional cost. Furthermore, the majority of the OLTC can only solve overvoltage problems because the tapping is performed on all phases at the same time and the voltage imbalance, especially at the end of the line, where this problem is most prominent, remains an issue.

On the other hand, autotransformers are connected in the middle of the distribution feeders and they can maintain both the overvoltages and the voltage unbalance because they allow regulating the voltage levels per phase. However, this approach adds additional failure points and also significant cost in the grid, therefore, it is also not preferable [22].

### **2.2.3 Voltage control by means of reactive power**

The third approach involves the use of reactive power for voltage control, similar to HV and MV grids where the voltage control is generally managed by the reactive power provided by the large centralised generators. This is based on the natural linkage between reactive power and voltage in the, mainly inductive, HV and MV grids. For maintaining the voltage profiles within limits the transmission system operator (TSO) and DSO use flexible ac transmission system devices (FACTS), such as static Var (SVAR) compensators and static compensator STATCOM. In MV networks more dominant are distribution static compensator devices

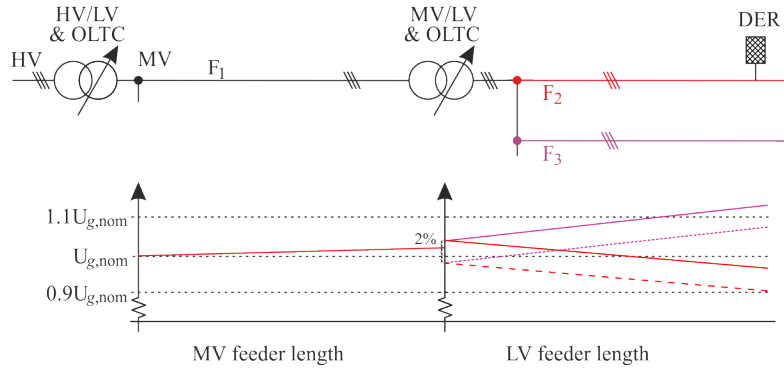


Figure 2.3: Voltage control in LV by using an OLTC

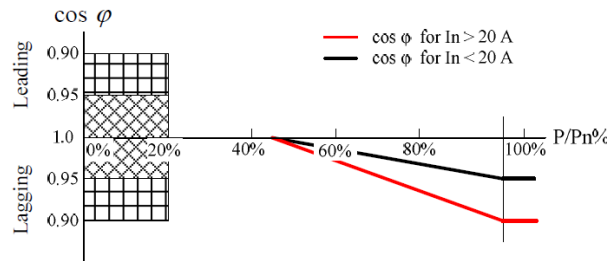


Figure 2.4: Variable power factor control<sup>2</sup>

D-STATCOM. These devices, due to their cost (device cost, maintenance and installation cost), are used in very rarely.

On the other hand, the voltage control can be performed by reactive power that can be delivered from the DERs themselves, which is a more economically viable solution compared to the above listed ones. Recent studies [23–27] show that the reactive power support has advantages compared to the approaches listed above, because it is “effective” and additional investments are not needed. Typical control strategies that use reactive power are shown in Fig. 2.4 and Fig. 2.5.

The first control strategy is depicted in Fig. 2.4 and is called variable power factor (PF) control, where the reactive power is in function of the inverter real power injection. If the ratio between the injected active power over the inverter nominal power is greater than 50% then the inverter starts consuming reactive power. This means that during periods with high renewable energy production, reactive power will be always consumed.

The second control strategy is called Volt-var control. The inverter injects or consumes reactive power depending on the rms value of the voltage  $V_g$  at the PCC.

<sup>2</sup>Source [11]

If this value is greater than 250V (1.086 pu) at the PCC, the control strategy considers this as an overvoltage condition and the inverter starts consuming reactive power (lagging - under excitation). The slope of the reactive power curve is determined by the two voltages where the starting point is 250V and the end point is 265V. Above the upper threshold the reactive power is maintained constant. The maximum value of the power factor must be limited to 0.95 for DERs that inject current less than 20A per phase and 0.85 for DERs the inject current greater than 20A. The same is valid when the rms value at the PCC is smaller than 220V (0.956 p.u.), then the inverter starts injecting reactive power (leading - over excitation). The advantage of the Volt-var control is that the inverter can rely on its terminal measurements and provide custom var response [28]. In [28, 29], the authors proposed adaptive Volt-var control for each DER and the result showed that the voltage deviation can be reduced by applying this control. In [30], the authors suggested a combination of local and centralised control in order to keep the power quality in the distribution grid.

In [31], an analytical methodology is developed that is used to calculate the inverter power ratings in order to provide additional reactive power support to the grid and increase the annual yield. In areas with high DERs penetration more oversizing of the power electronic inverter will be needed, therefore this will lead to a higher initial cost of the plant.

Furthermore, the  $R/X$  ratio in LV networks is often high, typically between 3 and 5, hence 3 to 5 times more reactive power than active power is needed in order to achieve the same effect on the voltage level [18, 32]. Overall, the voltage control in LV grids by means of reactive power can increase the penetration level of DERs but it has two limitations i) the inverter reactive power support, which is constrained by its kVA capacity and ii) limited impact due to high  $R/X$  ratio. Furthermore, the reactive power support introduces additional losses in the mainly resistive LV feeders.

Despite the reactive power support provided from DERs, in residential areas with high penetration of renewable energy resources, overvoltages can occur due to low loading and high peak generation [33]. When the grid voltage reaches a certain threshold the inverter encounters abnormal conditions and an overvoltage protection embedded in the inverter trips and the DER is disconnected from the utility grid. The disconnection times are listed in Table 2.1. This leads to a sudden decrease of the phase voltage but the inverter remains disconnected for a few minutes. This voltage drop depends on the LV feeder properties and on the disconnected power at that moment. When the inverter is reconnected and starts injecting again, then it will cause overvoltages and again it will turn off. This effect is studied in [33] and it has been observed in Oostende, West Flanders, Belgium in [34]. This may happen several times during the peak generation period. This is known as hard active power curtailment (APC) and it can lead to poor power quality due

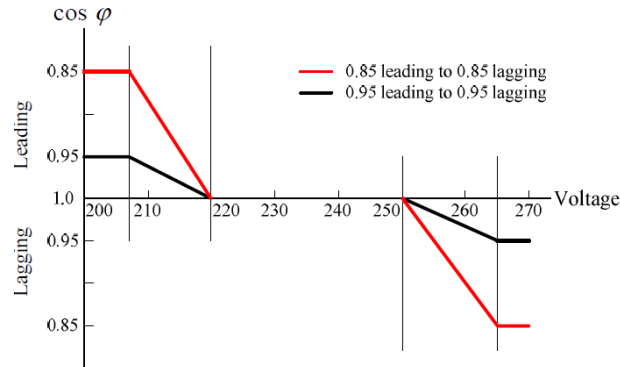


Figure 2.5: Volt-Var control<sup>3</sup>

to on-off oscillations and huge loss of renewable energy due to the disconnection periods [24, 33].

Another way of controlling DERs involves droop law curves, as proposed in the voltage-based droop control studied in [33, 36]. Above a certain threshold of the grid voltage, the inverter control reduces the exchanged power with a certain amount but the DER remains connected to the utility grid and still exchanges power. Thus, the control of the voltage level will be much more effective in LV networks due to the high  $R/X$  ratio. Although the active power is reduced, the revenue loss will be small. Overall, the loss of renewable energy can even be lower compared with the case of traditional connection of DERs [32, 33, 37], because these units should remain disconnected for a minimum amount of time after being turned off due to overvoltages. Hence, the soft APC became more attractive. Recent studies [23], [38, 39] that use centralised control also show that the penetration level of DER along the feeder can be increased by active power curtailment with a minimised loss of revenue. In [38] and [40], an equalised active power curtailment among the DERs connected to one feeder is implemented and results show that more renewable energy is exchanged with the LV network compared to On-Off control. Despite the fact that centralised control increases the annual renewable harvesting the necessity of communication reduces the reliability of this solution.

On the other hand, it is difficult to solve the voltage unbalance problems by means of reactive power. The majority of the DERs in urban areas are single-phase rooftop DERs, which are most often not equal in power and not uniformly distributed over the feeder and the phases. Together with the single-phase loads big voltage unbalance problems can occur in periods of peak generation and low loading. The negative impact of the voltage unbalance of the grid losses and grid equipment is widely studied in [18], [41] and many more. As it was mentioned above, the neutral point shifting also influences the voltage magnitudes in a three-

<sup>3</sup>Sources [11] and [35]

phase system because it leads to higher potential shifting of the least loaded phase compared to the other two phases, which leads to more reactive power injection of the DERs connected to that phase or even worse, disconnecting the DERs due to overvoltages. The voltage unbalance can be reduced or eliminated completely if dedicated equipment such as Active Power Filters (APF), unified power quality conditioner, etc. is used but the initial and maintenance cost is high. In [42] and [43], an approach to limit the voltage unbalance by injecting reactive power was proposed. Although the voltage magnitudes were converging to each other, the zero- and the negative-sequence voltage components were increased. The authors also proposed an algorithm based on Pareto optimisation for reconnecting the single-phase DERs among different phases in order to decrease the voltage unbalance. The results showed that the phase voltage magnitudes are converging to each other very well and voltage unbalance is decreased. There are a few disadvantages of this approach such as full knowledge of the grid under consideration is needed to perform a simulation and when new load and/or DER has to be included in the grid, a new power flow simulation is needed and also a new reconnection of the installed DERs.

### 2.3 Conventional control strategies for DERs

The DERs are controlled via a control strategy that ensures proper operation of the power electronic inverter, maintains the power balance between the renewable energy source (dc side) and the grid (ac side) and provides some functionalities and flexibilities. The current regulation concerning the DERs connection with different power ratings states that the maximum allowable power that can be injected from a single-phase DER is 5kVA in Belgium [44]. DERs that have higher power ratings the connection must be two or three phase. In this section, a detailed description of the most used control strategies will be given. Two assumptions will be made such that the DERs operate in steady state mode and also harmonic distortions will not be considered, and also further on, complex values (and thus only fundamental components) are used, thus the pu value of the phase voltage  $\underline{v}_x$  can be written in complex form as:

$$\underline{v}_x = |\underline{v}_x| \exp(j\theta_x) \quad (2.1)$$

with  $|\underline{v}_x|$  the amplitude of  $\underline{v}_x$  and  $x$  is the phase of connection. Then the power balance between the dc side and the ac side can be written as:

$$p_{ac} = \eta \Re(\underline{v}_a \underline{i}_a^* + \underline{v}_b \underline{i}_b^* + \underline{v}_c \underline{i}_c^*) \quad (2.2)$$

where  $\eta$  is the efficiency of the inverter and for simplicity it will be assumed to be 100%,  $\Re$  stands for real part of the power and  $\underline{i}_x^*$  is the complex conjugate of the injected phase currents.

### 2.3.1 Single-phase control strategy

The majority of the single-phase DERs are interfaced to the grid via a power electronic inverter, that is controlled via a single-phase control strategy, which is part of the unity PF family [41, 45]. The phase current that is being injected to the grid by this control strategy can be written as:

$$i_x(t) = g_1 \cos(\omega t + \theta_x) \quad (2.3)$$

where  $\omega t = 2\pi f t$ ,  $t$  is the time interval under consideration,  $f$  is the grid frequency,  $x$  represents the corresponding phase connection,  $\theta_x$  the respective phase angle and  $g_1$  represents the fundamental input conductance of the VSI. For analytical analysis, the fundamental input conductance is calculated when (2.3) is substituted in (2.2) and solved as:

$$g_1 = \frac{p_{dc}}{|v_x|} \quad (2.4)$$

where  $p_{dc}$  is the dc power available from the renewable energy source and the denominator is the rms values of the phase voltage to which the DER is connected. In practice, the fundamental input conductance signal is obtained by using a dc-bus controller and more information can be found in Chapter 5.

In case of a three-phase connection, using three single-phase inverters with a common dc bus the phase currents is:

$$\underline{i}_x = g_1 \exp(j\theta_x) \quad (2.5)$$

where  $x$  represents the corresponding phase connection,  $\theta_x$  the respective phase angle and  $g_1$  represents the fundamental input conductance of the VSI if an assumption is made that  $v_x = 1$  p.u. By applying the reverse Fortesque transformation on (2.5), then from  $(a, b, c)$  to  $(0, 1, 2)$  the control strategy can be expressed by symmetrical components as follows:

$$\begin{aligned} \underline{i}_0 &= \frac{1}{3} g_1 \{ \exp(j\theta_a) + \exp(j\theta_b) + \exp(j\theta_c) \} \\ \underline{i}_1 &= \frac{1}{3} g_1 \left\{ \exp(j\theta_a) + \exp\left(j\left(\theta_b + \frac{2\pi}{3}\right)\right) + \exp\left(j\left(\theta_c - \frac{2\pi}{3}\right)\right) \right\} \\ \underline{i}_2 &= \frac{1}{3} g_1 \left\{ \exp(j\theta_a) + \exp\left(j\left(\theta_b - \frac{2\pi}{3}\right)\right) + \exp\left(j\left(\theta_c + \frac{2\pi}{3}\right)\right) \right\} \end{aligned} \quad (2.6)$$

where  $\theta_x$  is the respective phase angle of the phase voltage,  $g_1$  is the fundamental output conductance and the indexes 0, 1 and 2 are the zero-, positive-, and the negative-sequence components. Then, the fundamental input conductance in p.u. of this control strategy can be written as:

$$g_1 = \frac{p_{dc}}{|v_a| + |v_b| + |v_c|} \quad (2.7)$$

If a DER is connected via a single-phase connection, then the fundamental conductance  $g_1$  and the injected current  $i_x$  are calculated with the respective phase voltage.

From the mathematical description provided above, in case of unbalance voltages at the PCC it can be seen from (2.3) that the triple single-phase control strategy will inject currents with approximately equal magnitudes. Although (2.6) proves that zero- and negative-sequence currents are injected, the impact towards the voltage unbalance at the PCC is rather limited and uncontrolled by the control strategy whatsoever.

### 2.3.2 Three-phase positive-sequence control strategy

The most common practice for controlling three-phase inverters connected to the utility grid is exchanging only positive-sequence current. This comes from the fact that the most of the phase angle detection techniques are based on phase locked loop (PLL) algorithms using synchronous reference frame [45]. In other words the three-phase PLLs use a coordinate transformation from  $abc \rightarrow dq$  [46] and, therefore, the output signals of these PLLs have phase angles corresponding to the positive-sequence component of the grid voltage [46–49].

The analytical model can be written in the following manner. The phase angles of the phase voltages are assumed to be:

$$\theta_a = 0, \theta_b = \theta_a - \frac{2\pi}{3}, \theta_c = \theta_a + \frac{2\pi}{3}$$

Then the injected phase currents can be written as:

$$\underline{i}_x = g_1 \exp(j\theta_x) \quad (2.8)$$

where  $x$  represents the corresponding phase a, b or c. Substituting (2.8) in (2.2) and solving for  $g_1$ , the following expression is obtained:

$$g_1 = \frac{p_{dc}}{3|\underline{v}_1|} = \frac{1}{3} \frac{p_{dc}}{|\underline{v}_a| + |\underline{v}_b| \cos(\theta_b - \theta_a + \frac{2\pi}{3}) + |\underline{v}_c| \cos(\theta_c - \theta_a - \frac{2\pi}{3})} \quad (2.9)$$

Obtaining the symmetrical components representation for the injected currents is made by the inverse Fortesque transformation and it yields to:

$$i_0 = 0, i_1 = g_1, i_2 = 0 \quad (2.10)$$

where the indexes  $(0,1,2)$  are the zero-, positive-, and the negative-sequence components.

This control strategy together with the reactive power support, is easily implementable by using rotary reference frame  $dq$  control or stationary reference frame  $\alpha\beta$  as well as  $abc$  control as demonstrated in [45]. In case of a combination with

the reactive power support the resultant control strategy will provide limited impact on the voltage magnitude at the PCC. Furthermore, the control strategy only injects positive-sequence currents and the phase currents are invariant of the difference between the phase voltages, therefore, under unbalanced voltages at the PCC, the control strategy will have no impact on the zero- and the negative-sequence components whatsoever. Furthermore, the reactive power injected from the two control strategies is equally divided among the phases and they do not provide the flexibility of equalising the voltages by injecting different reactive power in the different phases.

## 2.4 Discussion

From the literature overview of the current standards and grid codes and the state-of-the-art control algorithms it is evident that they are unable to give effective solutions for further DERs penetration while maintaining the power quality and the losses of the distribution grid in acceptable levels. Although the control strategies based on reactive power injection improve the voltage profile they lead to additional losses and the overview shows that the effect of the reactive power in LV grids is limited due to their mainly resistive properties. Furthermore, the reactive power support, provided by DERs, faces the limitations of the inverter VA ratings and significant oversizing is needed. It was also discussed the impact of the reactive power on the voltage unbalance and the results are rather limited and poorly performing. The coordinated APC provides good annual harvesting of renewable energy while increasing the penetration level of DERs and keeps the power quality within limits. The disadvantage of the coordinated APC is the necessity of communication between the DERs and central control. Therefore, a control strategy for grid-connected inverter-based DERs that is capable of operating in areas with penetration of renewable energy resources and improves the power quality in the distribution grid is needed.

## 2.5 Voltage-based droop control

The voltage-base droop (VBD) control is developed in [50] and it is originally designed for islanded micro-grids. A typical architecture of the connection diagram used by a DER equipped with the VBD control strategy is shown in Fig. 2.6. The primary energy source must have the properties of a dc current source and it is connected to the dc-bus of the power electronic inverter, which is a voltage source inverter (VSI). The capacitor  $C_{dc}$  provides transient storage capabilities while the power electronic inverter driven by the VBD control strategy converts the dc into ac current. The output filter implemented by the components  $L$  and  $C$  filters out

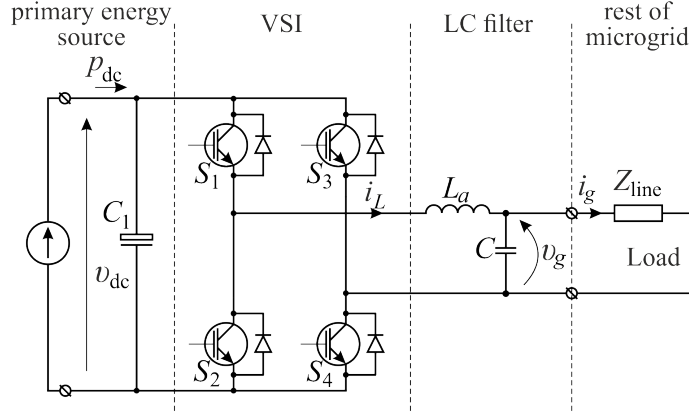


Figure 2.6: Voltage source inverter topology used by the voltage-based droop control strategy

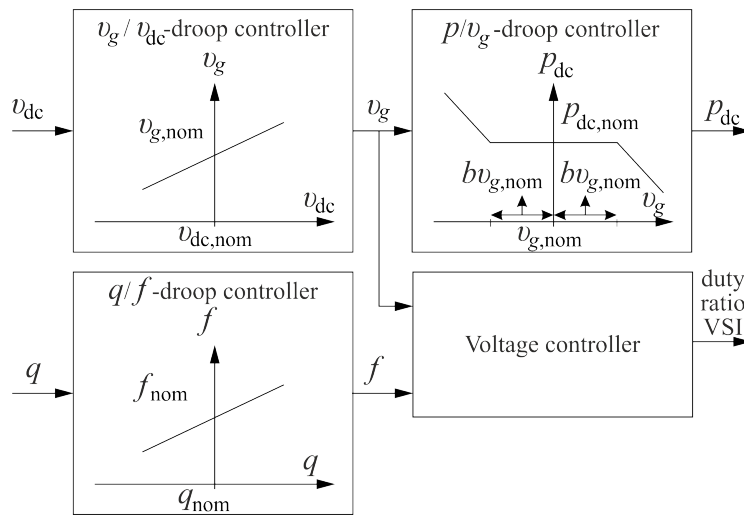


Figure 2.7: Block diagram of the voltage-based droop control strategy

the modulation high frequency components and thus the current from the renewable energy source is injected into the micro-grid.

This control strategy is composed of four different control algorithms named  $p/v_g$  droop controller,  $v_g/v_{dc}$  droop controller,  $q/f$  droop controller and voltage controller. The block diagram of the VBD control strategy is depicted in Fig. 2.7. The primary function of the  $p/v_g$  droop controller is to ensure the power balance between the dc and the ac side of the power electronic inverter that interfaces the renewable energy source to the grid similar to (2.2). The secondary function is to limit the dc-bus voltage to its nominal or set value and ensure optimal operational conditions for the power electronic inverter. In general, the  $v_g/v_{dc}$  droop control

strategy delays changing the output power of the generators by slightly varying  $v_g$ . In the low-voltage grids, which are more resistive grids, there is a linkage between active power and grid voltage. Hence, a  $p_{dc}/v_g$  droop controller is used that changes  $p_{dc}$  according to  $v_g$ , thus the need of communication and central controllers are completely avoided. Changing  $p_{dc}$  can be realised in several ways. For instance,  $p_{dc}$  can be decreased by storage charging (if storage is involved), by lowering the generated power  $p_{gen}$ , by a load increase or by using dump loads. For an increase of  $p_{dc}$ , battery discharge, demand-side management (potentially driven by the emerging smart grid concept) or an increase of  $p_{gen}$  can be incorporated in the control. The method of changing the power delivered to the dc-link does not inherently change the control method and can be determined according to the specific application [50].

The  $p_{dc}/v_g$  droop controller only operates when the terminal voltage of the DER exceeds a certain threshold value, which is determined by the adjustment voltages  $v_{g,up} = v_{g,nom}(1 + b)$  and  $v_{g,low} = v_{g,nom}(1 - b)$ . In case these adjustment voltages are not exceeded,  $p_{dc}$  remains unchanged and only the  $v_g/v_{dc}$  droop control strategy is used. This operating mode is called constant-power operation. The total width of the constant-power band equals  $h = 2b = v_{g,up} + v_{g,low}$ . The parameter “b” is called “the constant-power bandwidth” and a symmetrical constant-power band ( $h = 2b$ ) is considered. Summarised, the  $p_{dc}/v_g$  droop controller operates according to:

$$p_{dc} = \begin{cases} p_{dc,nom} - K_p (v_g - (1 + b) \cdot v_{g,nom}) & \text{if } v_g > (1 + b) \cdot v_{g,nom} \\ p_{dc,nom} & \text{if } (1 - b) \cdot v_{g,nom} < v_g < (1 + b) \cdot v_{g,nom} \\ p_{dc,nom} - K_p (v_g - (1 - b) \cdot v_{g,nom}) & \text{if } v_g < (1 - b) \cdot v_{g,nom} \end{cases} \quad (2.11)$$

where  $p_{dc}$  is the current power from the renewable source,  $p_{dc,nom}$  is the nominal power from the renewable source but necessarily equal to the maximum power,  $K_p$  is the droop coefficient,  $v_g$  is the rms value of the grid voltage and b is a constant. Fig. 2.8 illustrates how the VBD control operates and when each of the controllers is activated.

These two blocks ( $p/v_g$  and  $v_g/v_{dc}$ ) are of main interest for the modification of the control strategy from micro-grid to grid-connected operation. In islanded micro-grid mode the DERs can be connected in grid former mode or grid follower mode. Therefore, the voltage controller in grid connected mode is not needed and it is omitted. Since the frequency of the distribution grid is controlled by the big power plants inertia the  $q/f$  droop controller algorithm can be modified in order to comply with the requirement of different standards such as VDE-V-0126 [51], IEC-61727-SE [14] and EN 50160 [8]. This can be done by replacing  $q$  with  $p$  and applying power drooping in function of the grid frequency. This is an interesting feature of the VBD control connected in grid connected mode but this is future work and it will be out of scope of the current thesis.

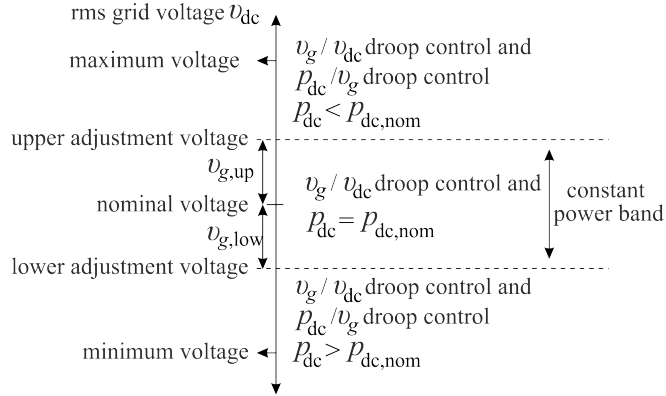


Figure 2.8: Variable power factor control

In grid connected mode the  $p_{dc}/v_g$  droop controller can be modified to comply with a specific standard or the grid code of the respective country. According to Table 2.1 three standards set the maximum and the minimum allowable values of the phase voltage of the grid voltage. If the grid voltage is lower than  $v_{g,nom}$ , then the  $p_{dc}/v_g$  droop controller operates in the second quadrant of the coordinate system. When the phase voltage decreases below the rms value prescribed by the respective standard and no storage is considered, then the inverter stops exchanging power with the grid thus  $v_{g,low}$  is directly equal to  $v_{g,min}$ . As it was mentioned above, the current regulations concerning DERs control states that if the grid voltage exceeds 110% then the inverter must be disconnected from the grid for a certain period of time. In all listed standards the maximum grid voltage value is 110% then this equals the  $v_{g,max}$ . The parameters  $v_{g,up}$  and  $v_{g,low}$  according to the VBD control depend on the ability of the DERs to deliver constant power for a certain band width and these parameters will be elaborated and discussed in details further in this thesis. The advantages of the VBD control strategy are the following:

- $v_g/v_{dc}$  droop controller, ensures the power balancing between the dc and ac side of the VSI
- $p_{dc}/v_g$  droop controller, ensures voltage limitation by preventing overvoltages in peak generation periods (less loading periods) and also provides a delay to active power changed compared with the conventional on-off control, which improves the power quality
- The VBD control strategy relies on local measurements at the inverter terminals and take corresponding measures based on them thus the necessity of communication between the different DERs is omitted, which ensures reliability of the distribution grid

- It can react fast (in order of several grid cycles) on voltage perturbation

The disadvantages is:

- The VBD control strategy is not able to solve voltage unbalance problems.

## 2.6 Voltage unbalance mitigation control strategies

Besides the overvoltages, the areas with high penetration of DERs encounter voltage unbalance problems due to the presence of single-phase distributed generation units and single-phase loads [17, 18, 52]. Furthermore, in LV grids the penetration of DERs is currently limited by voltage unbalance, which is caused by the high number of the mainly small roof-top single-phase connected DERs.

Many control strategies have been recently developed, which are capable of voltage unbalance mitigation [17, 52, 53]. These control strategies are capable of diminishing the negative-sequence component in the grid but the zero-sequence component remains an issue due to neutral point shifting caused by single-phase loads and DERs [18]. In [54,55], the authors proposed a control strategy for power factor correction converters that is able to damp harmonics by consuming harmonic currents with opposite sign of the harmonics in the grid voltage. Later [46] and [56] extend this research to control strategies for single-phase grid connected inverters named single-phase damping control strategy. The authors in [18] propose a similar approach to triple single-phase control strategy where three single-phase inverters are connected to a common dc-bus but each inverter is controlled by the single-phase damping control strategy. The research in [18] showed that the newly developed triple single-phase damping control strategy reacts resistively to the zero- and the negative-sequence components and therefore it is capable of reducing the voltage unbalance at the PCC. In [18] and [41], the authors propose the three-phase damping control strategy that is interfaced to the grid via three-phase four-wire inverter and studies the impact of the triple single-phase, positive-sequence, triple single-phase damping and the three-phase damping control strategies over the voltage profile of a particular LV feeder. The results showed that the three-phase damping control strategy has superior performance on improving the voltage profile in a LV feeder, compared to the other control strategies. Therefore, the three-phase damping control strategy seems a very promising solution in areas with high penetration on of DERs that experience voltage unbalance problems. The idea behind the three-phase damping control strategy is as follows: the desired reaction of the three-phase damping control strategy is the ability to behave resistively towards the zero- and negative-sequence voltage components in LV networks [18,41]. Then the damping control strategy can be described mathematically by the following set of equations:

$$\begin{bmatrix} \underline{i}_0 \\ \underline{i}_1 \\ \underline{i}_2 \end{bmatrix} = \begin{bmatrix} g_d & 0 & 0 \\ 0 & g_1 & 0 \\ 0 & 0 & g_d \end{bmatrix} \begin{bmatrix} \underline{v}_0 \\ \underline{v}_1 \\ \underline{v}_2 \end{bmatrix} \quad (2.12)$$

where  $\underline{v}_0$ ,  $\underline{v}_1$  and  $\underline{v}_2$  are the zero-, positive- and the negative-sequence voltage components,  $g_d$  is the fundamental damping conductance of the inverter, which has an opposite sign of  $g_1$  in case of power injection to the grid. Eq. (2.12) can be transformed into phase values by using:

$$\begin{bmatrix} \underline{i}_a \\ \underline{i}_b \\ \underline{i}_c \end{bmatrix} = T^{-1} \begin{bmatrix} g_d & 0 & 0 \\ 0 & g_1 & 0 \\ 0 & 0 & g_d \end{bmatrix} T \begin{bmatrix} \underline{v}_a \\ \underline{v}_b \\ \underline{v}_c \end{bmatrix} \quad (2.13)$$

where  $T$  is the transformation matrix from phase quantities ( $a, b, c$ ) to symmetrical components ( $0, 1, 2$ ). Consequently, the following equations for the phase currents are obtained:

$$\begin{aligned} \underline{i}_a &= \frac{1}{3} \{ \underline{v}_a (g_1 + 2g_d) + a\underline{v}_b (g_1 - g_d) + a^2\underline{v}_c (g_1 - g_d) \} \\ \underline{i}_b &= \frac{1}{3} \{ a^2\underline{v}_a (g_1 - g_d) + \underline{v}_b (g_1 + 2g_d) + a\underline{v}_c (g_1 - g_d) \} \\ \underline{i}_c &= \frac{1}{3} \{ a\underline{v}_a (g_1 - g_d) + a^2\underline{v}_b (g_1 - g_d) + \underline{v}_c (g_1 + 2g_d) \} \end{aligned} \quad (2.14)$$

with  $a = e^{j2\pi/3}$ .

If (2.1) is substituted in (2.14), the following equations for the phase currents are obtained:

$$\begin{aligned} \underline{i}_a &= \frac{1}{3} \left\{ g_1 \left[ |\underline{v}_a| e^{j\theta_a} + |\underline{v}_b| e^{j(\theta_b + \frac{2\pi}{3})} + |\underline{v}_c| e^{j(\theta_c - \frac{2\pi}{3})} \right] \right. \\ &\quad \left. + g_d \left[ 2|\underline{v}_a| e^{j\theta_a} - |\underline{v}_b| e^{j(\theta_b + \frac{2\pi}{3})} - |\underline{v}_c| e^{j(\theta_c - \frac{2\pi}{3})} \right] \right\} \\ \underline{i}_b &= \frac{1}{3} \left\{ g_1 \left[ |\underline{v}_b| e^{j\theta_b} + |\underline{v}_a| e^{j(\theta_a - \frac{2\pi}{3})} + |\underline{v}_c| e^{j(\theta_c + \frac{2\pi}{3})} \right] \right. \\ &\quad \left. + g_d \left[ 2|\underline{v}_b| e^{j\theta_b} - |\underline{v}_a| e^{j(\theta_a - \frac{2\pi}{3})} - |\underline{v}_c| e^{j(\theta_c + \frac{2\pi}{3})} \right] \right\} \\ \underline{i}_c &= \frac{1}{3} \left\{ g_1 \left[ |\underline{v}_c| e^{j\theta_c} + |\underline{v}_a| e^{j(\theta_a + \frac{2\pi}{3})} + |\underline{v}_b| e^{j(\theta_b - \frac{2\pi}{3})} \right] \right. \\ &\quad \left. + g_d \left[ 2|\underline{v}_c| e^{j\theta_c} - |\underline{v}_a| e^{j(\theta_a + \frac{2\pi}{3})} - |\underline{v}_b| e^{j(\theta_b - \frac{2\pi}{3})} \right] \right\} \end{aligned} \quad (2.15)$$

where terms in (2.15) related to  $g_1$  can be interpreted as the steady-state value of the fundamental component of the injected current. These terms are adapted by the

dc bus-voltage controller in order to balance the power exchanged with the grid. Since the bus voltage controller is slow,  $g_1$  is slowly varying. The terms related to  $g_d$  emulate the resistive behaviour towards the zero- and negative-sequence voltage components.

In practice, the power balance between the dc side and the utility grid is maintained by using the dc-bus controller whose output is the fundamental conductance of the inverter  $g_1$  [36]. In order to incorporate the fundamental conductance into a simulation model, the following equation can be used:

$$g_1 = \frac{3 p_{dc}}{\sum |v_x|^2 + 2 \sum_{x \neq y} |v_x| |v_y| \cos(\theta_x - \theta_y - \frac{2\pi}{3})} - 2g_d \frac{\sum |v_x|^2 - \sum_{x \neq y} |v_x| |v_y| \cos(\theta_x - \theta_y - \frac{2\pi}{3})}{\sum |v_x|^2 + 2 \sum_{x \neq y} |v_x| |v_y| \cos(\theta_x - \theta_y - \frac{2\pi}{3})} \quad (2.16)$$

where  $p_{dc}$  is available power at the dc bus. The term determined by the first fraction describes the exchanged active power with the grid and the term determined by the second fraction compensates the power of the zero-sequence and the negative-sequence components [18]. This control strategy mitigates the voltage unbalance by injecting higher currents in the phase with lower voltage and lower current in the phase with higher voltage. The damping capabilities of this control strategy are determined by the damping conductance  $g_d$ , which can be calculated by using the nominal ratings of the inverter:

$$G_d = \frac{P_{DC_{ref}}}{V_{ref}^2} \quad (2.17)$$

where  $P_{DC_{ref}}$  is the reference power of the inverter and  $V_{ref}$  is the nominal grid voltage.

From (2.17) it can be seen that the value of the damping conductance plays important role for the resistive behaviour towards the zero- and the negative-sequence voltage components. In [18, 41, 46, 54–56], the authors used a fixed value of the damping conductance and it was chosen to be 1 p.u. Therefore, further investigation of the value of this parameter can be made in order to improve the performance of the three-phase damping control strategy.

The advantages are:

- It is capable of mitigating the voltage unbalance at the point of common coupling.
- It reacts fast on perturbations (in order of several grid cycles) on voltage perturbation.
- It is based on symmetrical components so the voltage unbalance is mitigated naturally .

The disadvantage is:

- The three-phase damping control strategy control strategy is not able to solve overvoltage problems.

## 2.7 Conclusions

In this chapter, an overview of some existing control strategies for DERs is conducted. The control strategies are analytically described and from the conducted analysis their advantages and disadvantages are pointed out. The comparison concludes that the considered control strategies alone are not able to target multiple power quality problems. Therefore, a combination of control strategies is needed in order to solve overvoltage and voltage unbalance power quality issues.

The proposed solution in this thesis is a combination of two control strategies. The first one is the voltage-based droop control, which is able to maintain the voltage at the PCC within acceptable levels by applying APC. The second one is the three-phase damping control strategy, which is able to reduce the voltage unbalance at the PCC by emulating resistive behaviour towards the zero- and negative-sequence components. Both control strategies rely on local measurements at the inverter terminals and take respective actions based on them. This ensures adequate reaction towards grid disturbances and also avoids the necessity of communication between the units and also a centralised controller.

# 3

## Local control strategies for distributed energy resources connected to LV grids

In this chapter, a detailed description of the combination of the voltage-based droop control strategy with the positive-sequence and the three-phase damping control strategy is given. Furthermore, an additional control strategy is proposed that is based on the VBDC and the three-phase damping control strategy but the value of the damping conductance is dependent on the voltages at the inverter terminal. The performance of all control strategies is evaluated by means of simulation based on a laboratory LV feeder with 19 nodes and high penetration of DERs.

### 3.1 Introduction

To meet the European 20-20-20 targets, the share of renewable energy needs to be 20 % of the total energy use in 2020 and 50 % by 2050 [57]. This ambitious objective needs a significant increase of the number of DERs at the LV grid and installation of wind or solar power plants at the MV level. Consequently, the DSOs face the challenge to connect and integrate an ever increasing amount of renewable energy sources, and also to guarantee the high level of power quality to their customers. Grid operators today already face problems to dispatch the distribution grid with the currently installed DERs [58] and the connection of new production units is at risk to be cancelled (or at the very least significantly delayed) because it

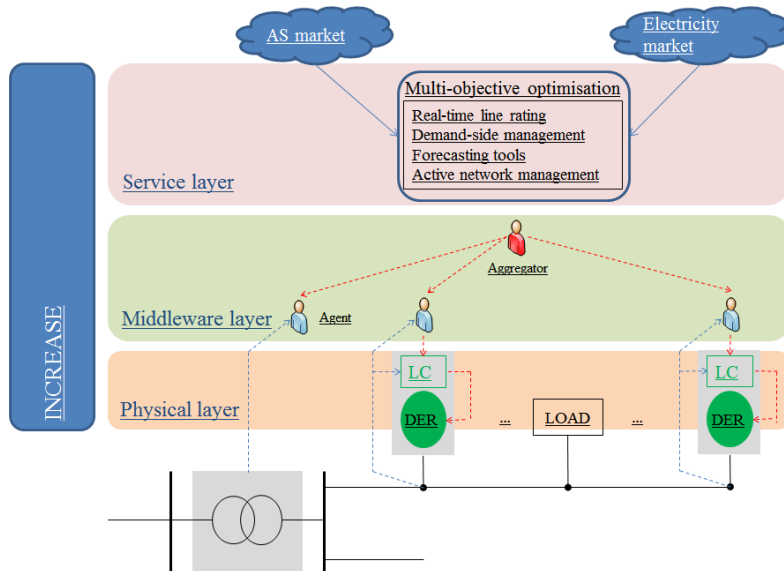


Figure 3.1: Hierarchical control for increasing the penetration level of renewable energy resources

requires expensive and time-consuming investments to extend the hosting capacity of the grid. A possible solution for managing the problem with the increasing penetration DERs is proposed in the project INCREASE [59] where the goal is to maximise the penetration level of DERs while not violating the power quality requirements and bring maximum benefit to the prosumers (consumers that also produce energy) by providing ancillary services to the DSO. The adopted bottom-up approach is consists of three levels.

1. The first one is the so-called Physical layer, which is consisted of DERs that are equipped with local control strategies, which react on perturbation in the order of a few grid cycles. This local control strategy uses both local parameters (e.g., grid voltage(s), injected phase currents and available power measured at the inverter terminal). The local control is targeting voltage unbalance mitigation, over/under voltage control and grid support in case of disturbances and faults. This control strategy thus enables an intelligent control of the voltage profile and improves the reliability of distribution grid in times of disturbances and grid faults.
2. In the second (Middleware) layer a multi agent system (MAS) is used for dynamic load flow optimisations, system stability, voltage control and congestion management. It is consisted of agents (software entities) that are embedded in each asset (such as DERs, On Load Tap Changers, etc.) and is able to autonomously react to changes in that environment with response

time of 10 to 15 min basis. It handles three functional aspects: management, coordination and execution of actions with the ultimate goal of reaching an optimal system performance [19].

3. The third (Service) layer has the highest hierarchical level and it is responsible for multi-objective optimisation such as real-time line rating, active network management, demand side management, etc. These solutions are provided to the DSO and TSO as ancillary crevices. More information can be found on [60,61].

This work focusses on developing an intelligent and sophisticated control at the physical layer, that is able to:

- maintain the grid stability and reliability
- ensure a secure operation of the system even if there is no connection with the higher level i.e. Middleware
- maximise the penetration of DERs (i.e. increases the hosting capacity in LV grids but with combination with the MAS, which is out of the scope of this thesis) and at the same time keeps or even improves the power quality requirements set by the current standards

In the previous chapter, a detailed description of the existing control strategies was made and it was found out that as a most promising solution for mitigating overvoltages is the voltage-based droop control strategy and a promising solution for voltage unbalance mitigation is the three-phase damping control strategy.

As mentioned in the previous chapter, only two controllers will be used from the VBDC namely  $p/v_g$ -droop controller and  $v_g/v_{dc}$  - droop controller. The  $p/v_g$ -droop controller operates at fixed dc-bus voltage while the  $v_g/v_{dc}$  operates in the first and the second quadrant of the coordinate system. For grid-connected applications VBDC can be further simplified as shown in Fig. 3.2. Since undervoltages are not considered in this chapter they will be neglected in the further analysis. For the sake of completeness, however, the second quadrant is also depicted. The droop that will be used from the local control is located in the first quadrant and it is split in three different regions. Region I allows the DER to inject all available power delivered from the renewable energy source and it ranges from the nominal grid voltage  $v_{g,nom}$  to the constant power band voltage  $v_{cpb}$ . Region II ranges from  $v_{cpb}$  to the maximum allowable grid voltage  $v_{g,max}$  and droops the injected power in a linear law. If the grid voltage is above  $v_{g,max}$  then the DER is being disconnected from the grid and all renewable power is curtailed. Then (2.11) can be further simplified to less complex droop curve that can be mathematically described by the following piecewise function:

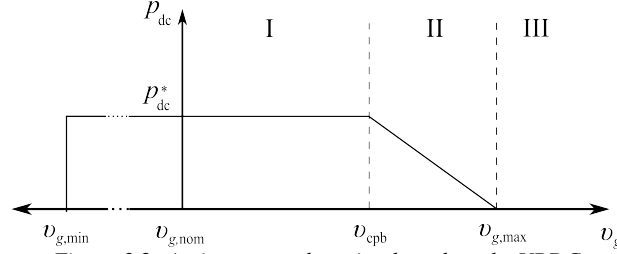


Figure 3.2: Active power drooping based on the VBDC

$$p_{dc}^{\bullet} = \begin{cases} 0, & \text{if } v_g < v_{g,\min} \\ p_{dc}, & \text{if } v_g \leq v_{cpb} \\ p_{dc} \left( 1 - \frac{v_g - v_{cpb}}{v_{g,\max} - v_{cpb}} \right), & \text{if } v_{cpb} < v_g \leq v_{g,\max} \\ 0, & \text{if } v_g > v_{g,\max} \end{cases} \quad (3.1)$$

In this chapter it is assumed that the power electronic inverter has 100% efficiency and then the available power at the dc side is equal to the injected power at the ac side, hence,  $p_{dc}^{\bullet} = p_{ac}$ . Index “•” denotes the calculated power by (3.1), which can vary from 0 to  $p_{dc,nom}$ , depending on the available power from the primary source (photovoltaic system, wind turbine,  $\mu$ CHP, etc.). The conditioning algorithm that ensures maximum power harvesting, called a maximum power point tracking algorithm, is also neglected because it is out of the scope of this work. For simplicity, it will be assumed that the DERs operate under their nominal power.

### 3.1.1 Integrating the VBDC in the single-phase and positive-sequence control strategies

The combination of the VBDC droop curve into the described control strategies in Chapter 2, i.e., single-phase (triple single-phase) and the positive-sequence control strategies can be made by substituting the drooping law curve (3.1) in (2.4) and (2.9), respectively. If the single-phase control strategy is used in DERs then the droop controller uses the rms value of the phase voltage that the DER is connected to it. Nowadays, the majority of the installed three-phase DERs inject positive-sequence currents synchronised with the positive-sequence voltage so this value could be used by the droop controller as well. Another possibility is using the maximum voltage among the three phases and this value could be used by the droop controller to droop the injected power accordingly.

### 3.1.2 Integration of the VBDC in the three-phase damping control strategy

The combination of the VBDC and the three-phase damping control strategy is not as straightforward as the single-phase and the positive-sequence control strategies. According to the mathematical description of the power balance of the three-phase damping control strategy it can be seen that the drooping cannot be implemented by replacing the term  $p_{dc}^\bullet$  with (3.1), because when overvoltages occur ( $v_g > v_{g,max}$ ) then all the available active power will be drooped. Hence, the fundamental input conductance  $g_1$  calculated by Eq. (2.16) calculated at  $p_{dc}^\bullet = 0$  becomes:

$$g_{1,(p_{dc}^\bullet=0)} = -2g_d \frac{\sum |v_x|^2 - \sum_{x \neq y} |v_x| |v_y| \cos(\theta_x - \theta_y - \frac{2\pi}{3})}{\sum |v_x|^2 + 2 \sum_{x \neq y} |v_x| |v_y| \cos(\theta_x - \theta_y - \frac{2\pi}{3})} \quad (3.2)$$

By using the new calculated value of  $g_1$  back in (2.15) it will result in reverse power flow from the phase with the highest voltage and injecting it back in the phases with the lowest voltages, however, according to [8] the DERs must be disconnected from the grid if  $v_g \geq v_{g,max}$ .

Therefore, in order to comply with the standard EN50160 [8],  $g_d$  must be also drooped and it can be performed in the same manner as the active power drooping:

$$g_d^\bullet = \begin{cases} 0, & \text{if } v_g < v_{g,min} \\ g_d, & \text{if } v_g \leq v_{cpb} \\ g_d \left(1 - \frac{v_g - v_{cpb}}{v_{g,max} - v_{cpb}}\right), & \text{if } v_{cpb} < v_g \leq v_{g,max} \\ 0, & \text{if } v_g > v_{g,max} \end{cases} \quad (3.3)$$

As it was mentioned above, the damping capabilities of the three-phase damping control strategy depend entirely on the damping conductance  $g_d$ . Further improvement of this beneficial quality towards the power quality improvement of the voltage at PCC can be a droop controller that is incorporated in the control strategy such that the damping conductance is dependable on the grid voltage. The proposed concept is presented in Fig. 3.3. The equation that describes the proposed damping-based droop curve is:

$$g_d^\bullet = \begin{cases} g_d, & \text{if } v_x \leq v_{cdb} \\ g_d + g_d \frac{v_x - v_{cdb}}{v_{cpb} - v_{cdb}}, & \text{if } v_x > v_{cdb} \end{cases} \quad (3.4)$$

where  $v_{cdb}$  is the constant damping band area. The damping-based droop control is split in four different regions in which the DER operates in different modes. The first region ranges from 1 p.u. to  $v_{cdb}$  and represents the case when the grid voltage is within limits and no specific actions are necessary to be taken by control strategy, i.e.,  $g_d$  is kept constant and it is calculated via (2.17). The second region ranges

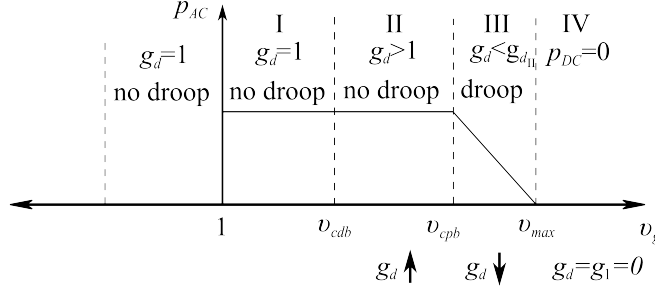


Figure 3.3: Damping-based droop control

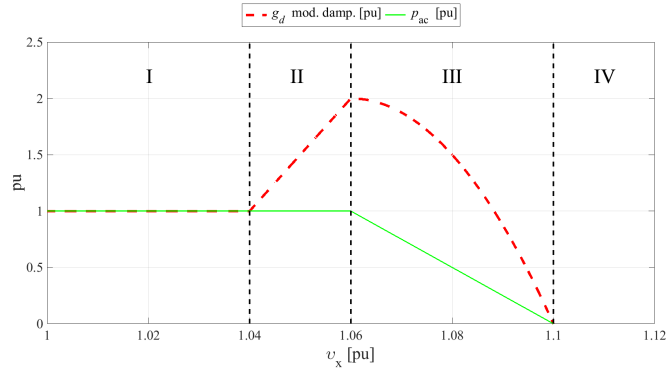


Figure 3.4: Damping conductance dependency on the maximum value among the voltages in the three phases

from  $v_{cdb}$  to  $v_{cpb}$  and it is used when the grid voltage is close to the drooping point of the power droop curve (in the first and the second region all available power is exchanged). In this region the control strategy increases the damping conductance, which is calculated by (2.17) and (3.4). By doing so, the control strategy tries to inject as much as possible power with the other two phases before the grid voltage with the highest voltage exceeds  $v_{cpb}$  or said in other words the DERs will exchange less power in the phase(s) where the voltage is higher and more power in the phase(s) where the grid voltage is lower. The third region starts from  $v_{cpb}$  to  $v_{g,max}$  and it is active when the DER operates in the drooping region. Then active power drooping is applied according to (3.1) in order to maintain the grid voltage within limits. The damping conductance is decreasing and it is recalculated again with the new injected power in (2.17) and (3.4). The fourth region describes the case when the grid voltage exceeds the maximum permissible value set by [8] hence,  $g_1$  and  $g_d$  are zero and the exchanged power is equal to 0. Recalculating the damping conductance via the drooped power prevents the reverse power flow and makes the proposed control strategy compatible with the current standards. The final equation for calculating  $g_d$  is:

$$g_d^\bullet = \begin{cases} 0, & \text{if } v_x < v_{g,\min} \\ g_d, & \text{if } v_x \leq v_{cdb} \\ g_d \left( 1 + \frac{v_x - v_{cdb}}{v_{cpb} - v_{cdb}} \right), & \text{if } g_d < v_x \leq v_{cpb} \\ g_d \left( 1 - \frac{v_x - v_{cpb}}{v_{g,\max} - v_{cpb}} \right) \left( 1 + \frac{v_x - v_{cdb}}{v_{cpb} - v_{cdb}} \right), & \text{if } v_{cpb} < v_x \leq v_{\max} \\ 0 & \text{if } v_x > v_{\max} \end{cases} \quad (3.5)$$

and the obtained profile of  $g_d$  as a function of the grid voltage is presented in Fig. 3.4. The damping controller as well as the active power drooping controller take actions based on the local measurements. The possibilities for the “ $x$ ” axis voltage are the same as for the droop controller i.e. positive-sequence and the maximal voltage of the three-phases. More information of the practical implementation of the positive-sequence and modified three-phase damping control strategies is given in Chapter 5.

### 3.2 Validation of the proposed control algorithms by means of simulations

In this section, a validation of the proposed algorithms will be made and their impact on the voltage profile, power quality (voltage unbalance and overvoltages) and the grid losses will be examined. A simulation model is used, which is based on an LV feeder setup available in the power quality laboratory at Lemcko UGent, Kortrijk [62]. Instead of an MV/LV transformer, a programmable three-phase voltage source Spitzenberger&Spies is used, which is able to deliver 80 kVA per phase or in total 240 kVA. These power ratings are comparable with the power ratings of a typical MV/LV transformer. Another advantage of using the power source is that its output voltages are stabilised, which helps to avoid the voltage variation that is coming from the MV grid. The set-up and the simulation model consist of three main feeders, each one with a length of 173 m. The three feeders can be connected in different configurations by means of a contactor matrix but the most interesting connection that will be used in this work is the configuration where the feeder has the biggest length of 479 m as shown in Fig. 3.6. The feeder cable type is

|                  |                  |                  |                  |
|------------------|------------------|------------------|------------------|
| 0.2553 + j0.7395 | 0.0493 + j0.6820 | 0.0493 + j0.6499 | 0.0493 + j0.6820 |
| 0.0493 + j0.6820 | 0.2553 + j0.7395 | 0.0493 + j0.6820 | 0.0493 + j0.6499 |
| 0.0493 + j0.6499 | 0.0493 + j0.6820 | 0.2553 + j0.7395 | 0.0493 + j0.6820 |
| 0.0493 + j0.6820 | 0.0493 + j0.6499 | 0.0493 + j0.6820 | 0.2553 + j0.7395 |

Table 3.1: Full cable impedance matrix including the earth impedance [ $\Omega/\text{km}$ ]

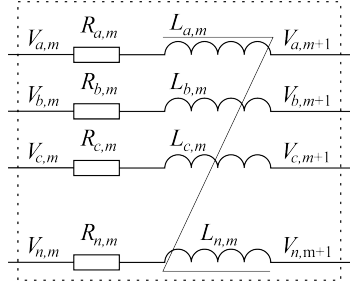


Figure 3.5: Cable equivalent model used in the simulations

EAXVB4x150 mm<sup>2</sup> and its equivalent circuit used in the model is depicted in Fig. 3.2 where  $m$  is the  $m^{\text{th}}$  segment of the grid feeder and also the mutual impedances between the different conductors have been taken into account as used in [63]. Unbalanced power flow analyses however, require a full cable model in order to represent the cable properties as accurately as possible. On top of that, the earth resistance also plays a crucial role on the cable impedance. In [64, 65] a cable model is described that is based on Carson's approach for earth modelling. Taking into account the geometry of the used cable and also the fundamental frequency of the investigated system the full matrix of the cable impedance including the earth effect is listed in Table 3.1. Therefore, the real and imaginary part are added to the datasheet parameters  $R_{x,m}$  and  $j\omega L_{x,m}$  so that the earth effect is included. The cable sections are implemented in Simulink by using a mutual inductor with four windings and the impedance matrix, multiplied by the distance of the respective feeder segment is used in the inductor properties.

The voltage levels from the ac power supply are set to 1.04 p.u. (assuming that the primary is 1 p.u.) because this is a typical setting made by the DSO to compensate the feeder voltage drop and in this way guarantees that the voltage levels at the end of the feeder will be in the standard limits [66]. The node distances and connections over the feeder are also depicted in Fig. 3.6. The loads that are used in this simulation model and the respective node connection are listed in Table 3.2. In [67] (p. 8), is stated that the majority of the single-phase loads have unity PF. However, due to the large cable cross section the power ratings of the loads are close to the maximum allowed limit for single-phase connection and the power factor is chosen to be PF = 0.9, which is typical value used in power flow simulations. For simplicity, the loads are chosen to be linear ones. In order to evaluate the performance of the examined control strategies, some voltage unbalance is introduced in the feeder. Although the programmable power supply allows unequal phase voltage settings it is better to create the voltage unbalance naturally by means of unequal loading hence, the loads are connected to phases  $b$  and  $c$  as listed in Table 3.2.

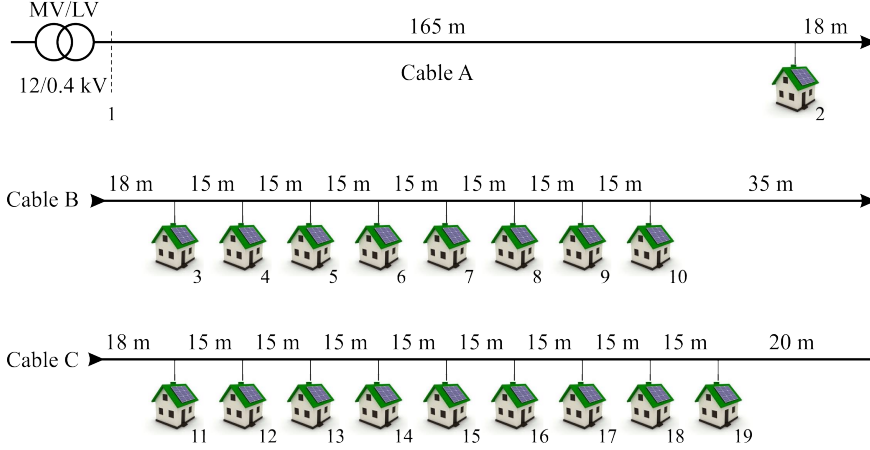


Figure 3.6: 19 node LV feeder

| Node             | N4  | N6  | N6  | N7  | N11 | N12 | N15 | N17 | N18 | N19 |
|------------------|-----|-----|-----|-----|-----|-----|-----|-----|-----|-----|
| $S_{Load}$ [kVA] | 5   | 5   | 5   | 5   | 5   | 5   | 5   | 5   | 5   | 5   |
| PF               | 0.9 | 0.9 | 0.9 | 0.9 | 0.9 | 0.9 | 0.9 | 0.9 | 0.9 | 0.9 |
| Phase connection | b   | c   | b   | c   | c   | b   | b   | c   | b   | c   |

Table 3.2: Load connection and parameters used in the simulation model

### 3.2.1 Classical control strategies used in the simulation model under examination

In order to make the single-phase and the positive-sequence controls strategies described in §2.3.1 and §2.3.2 comply to the current standards, a reactive power support with variable PF must be included. By doing so, a precise comparison and better performance evaluation can be made between the existing control and the proposed control strategies.

### 3.2.2 Single-phase control strategy with variable PF

Usually single-phase and three-phase control strategies are implemented by using the stationary dq reference frame [45] where the reactive power exchange can be set easily due to the nature of the dq transformation. Since the control strategies described in Chapter 2 are implemented in the natural reference frame then the reactive power support will be implemented in the natural reference frame as well. The reactive power support can be implemented in the analytical model of the single-phase control strategy described in §2.3.1 with some minor changes in the equations. The active current injection remains the same as (2.3):

$$i_{x,p}(t) = g_1 \sin(\omega t + \theta_x) \quad (3.6)$$

| Node                   | N9    | N10   | N11   | N13   | N16   | N18   | N19   |
|------------------------|-------|-------|-------|-------|-------|-------|-------|
| $P_{\text{DER}}$ [kW]  | 3     | 3     | 25    | 2     | 3     | 50    | 50    |
| $S_{\text{DER}}$ [kVA] | 3.33  | 3.33  | 27.77 | 2.22  | 3.33  | 55.55 | 55.55 |
| PF                     | 1/0.9 | 1/0.9 | 1/0.9 | 1/0.9 | 1/0.9 | 1/0.9 | 1/0.9 |
| Phase connection       | a     | a     | abcn  | a     | a     | abcn  | abcn  |

Table 3.3: DER data used to compare the two active power drooping cases

where index “p” denotes the active power. The reactive currents that the DER must exchange with the grid are written as:

$$i_{x,q}(t) = g_{1,q} \cos(\omega t + \theta_x) \quad (3.7)$$

where  $x$  represents the corresponding phase connection, index “q” denotes that this is a reactive current,  $\theta_x$  the respective phase angle and  $g_{1,q}$  represents the virtual reactive power fundamental input conductance of the VSI. Unlike  $g_1$  that has a physical meaning for the DER, the reactive power fundamental input conductance  $g_{1,q}$  is a set value that depends on the injected active power and it has no physical meaning to the system. This is why it is called virtual input conductance. The parameter  $g_{1,q}$  is calculated similar to  $g_1$ :

$$g_{1,q} = \frac{q^\bullet}{\sum |v_x|} \quad (3.8)$$

where  $q^\bullet$  is the set value of the reactive power that has to be exchanged (consumed/injected) by the DER. The reactive power is calculated based on the injected active power and power factor PF. The drooping of the PF is implemented according to Fig. 2.4 and in the current simulation model, the following piece wise function is used:

$$\text{PF}^\bullet = \begin{cases} 1, & \text{if } p_{\text{ac}}^\bullet \leq \frac{1}{2} p_{\text{nom}} \\ 1 - \frac{p_{\text{ac}}^\bullet - \frac{1}{2} p_{\text{nom}}}{p_{\text{nom}} - \frac{1}{2} p_{\text{nom}}} \Delta \text{PF}, & \text{if } p_{\text{ac}}^\bullet > \frac{1}{2} p_{\text{nom}} \end{cases} \quad (3.9)$$

where  $p_{\text{nom}}$  is the nominal power of the renewable source and  $\Delta \text{PF}$  is the slope of the desired PF drooping. Then the amount of reactive power that needs to be exchanged is calculated as follows:

$$q^\bullet = \begin{cases} +p_{\text{ac}}^\bullet \cos(\tan(\text{PF})) & \text{if } |v_g| < v_{g,\text{nom}} \\ -p_{\text{ac}}^\bullet \cos(\tan(\text{PF})) & \text{if } |v_g| \geq v_{g,\text{nom}} \end{cases} \quad (3.10)$$

where the signs “+” or “-” show whether the reactive power has to be injected or consumed. Then the total injected current becomes:

$$i_x = i_{x,p} + i_{x,q} \quad (3.11)$$

This modified analytical model of the single-phase control strategy together with the original model described in §2.3.1 will be used in the simulation model and further examined.

### 3.2.3 Positive-sequence control strategy with variable PF

The reactive power support can be implemented in the analytical model of the positive-sequence control strategy described in §2.3.2 similar to the single-phase control strategy. The injected active current remains the same as the one in §2.3.2:

$$\underline{i}_{x,p} = g_1 \exp(j\theta_x) \quad (3.12)$$

but for more clarity an index “p” is added to denote that the current is related to the active power injection. The reactive current that has to be exchanged with the grid is:

$$\underline{i}_{x,q} = g_{1,q} \exp\left(j\left(\theta_x + \frac{\pi}{2}\right)\right) \quad (3.13)$$

where  $x$  represents the corresponding phase  $a$ ,  $b$  or  $c$ . Similar to the active power balance (2.2), the reactive power balance can be expressed as:

$$q_{ac} = \eta \Im(\underline{v}_a \underline{i}_a^* + \underline{v}_b \underline{i}_b^* + \underline{v}_c \underline{i}_c^*) \quad (3.14)$$

By substituting (3.13) in (3.14), and solving for  $g_{1,q}$ , the following expression for  $q_{ac}$  is obtained:

$$g_{1,q} = \frac{1}{3} \frac{q^\bullet}{|\underline{v}_a| + |\underline{v}_b| \sin\left(\theta_b - \theta_a + \frac{2\pi}{3}\right) + |\underline{v}_c| \cos\left(\theta_c - \theta_a - \frac{2\pi}{3}\right)} \quad (3.15)$$

which yields a solution that has the same denominator as the power balance for the active power (2.9).

The amount of the reactive power that needs to be exchanged with the grid is calculated as (3.9) and (3.10). Obtaining the symmetrical components representation for the injected currents is made by the inverse Fortesque transformation and it yields to:

$$\underline{i}_0 = 0, \underline{i}_{1,p} = g_1 \exp(j\theta_a), \underline{i}_2 = 0 \quad (3.16)$$

where the indices 0, 1 and 2 are the zero-, positive-, and the negative-sequence components. The reactive positive-sequence current that has to be injected in the grid is written as:

$$\underline{i}_0 = 0, \underline{i}_{1,q} = g_{1,q} \exp\left(j\left(\theta_a + \frac{\pi}{2}\right)\right), \underline{i}_2 = 0 \quad (3.17)$$

Hence, the total injected positive-sequence current can be expressed as:

$$\underline{i}_1 = \underline{i}_{1,p} + \underline{i}_{1,q} \quad (3.18)$$

This modified analytical model of the positive-sequence control strategy together with the original model described in §2.3.2 will be used in the simulation model to further examine performance of the DERs equipped with variable PF control strategy.

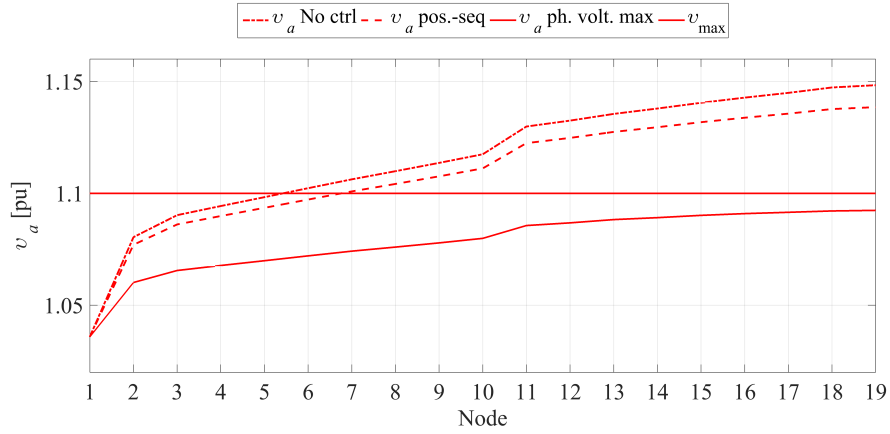
### 3.2.4 Comparison between the positive-sequence and the maximum of phase voltages

Before starting with the performance evaluation of the above listed DER control strategies, a short comparison of two possible variables of drooping controllers will be made. As it was mentioned above there were two options for active power drooping. One of the options is using the positive-sequence voltage and the other is using the maximum rms value of the three-phase voltages. Such a comparison is interesting due to the fact that the majority of the three-phase DERs is driven by the positive-sequence control strategy and the aim of this case study is to show whether this value can or cannot be used for active power drooping purposes.

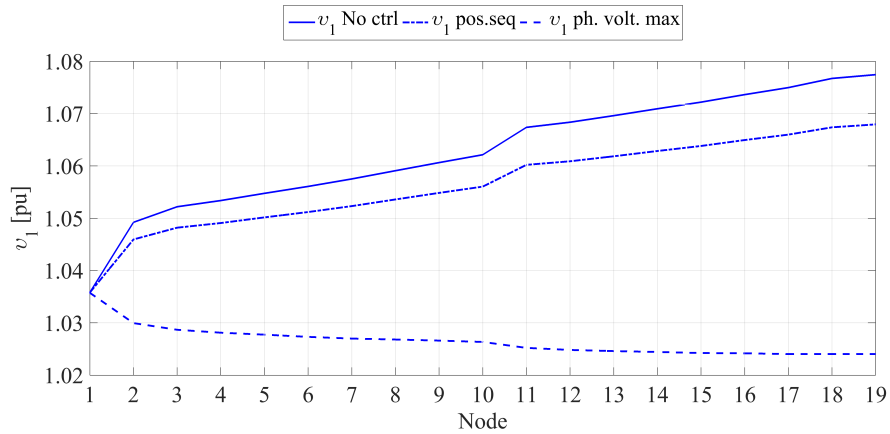
The set-up topology is the same as shown in Fig. 3.6 and the load nodes and phase connections are listed in Table 3.2. The DER parameters (nominal power, PF and phase connections) are listed in Table 3.3. The rated power of the DERs connected to node 18 and node 19 is chosen such that overvoltages occur at the end of the feeder when no voltage control is applied to the DERs. Additionally, some voltage unbalance is introduced by connecting single-phase DERs with small rated power to phase *a*. The power drooping will be tested on the three-phase DERs while the single-phase ones will be uncontrolled and they will inject all available power. In addition, the single phase DERs will inject only active power.

The asymmetrical power flow simulation is based on a time domain model in Matlab&Simulink and it reaches steady state regime after 1.5 s. However, to ensure that the obtained results will not be influenced by the transients of the model, the simulation time is set to 2 s. Then the data are extracted from the workspace and the last readings are used to present the obtained simulation results. Three case studies are simulated. In the first case study, no control is present, i.e., all DERs inject all available power. In the second case, the droop controller uses the positive-sequence voltage to calculate the necessary power drooping, while in the last case the power drooping is based on the maximum rms voltage value among the three phase voltages. The value of the constant power band voltage is chosen to be  $v_{cpb}=1.06$  p.u. and  $v_{g,max}=1.1$  p.u.

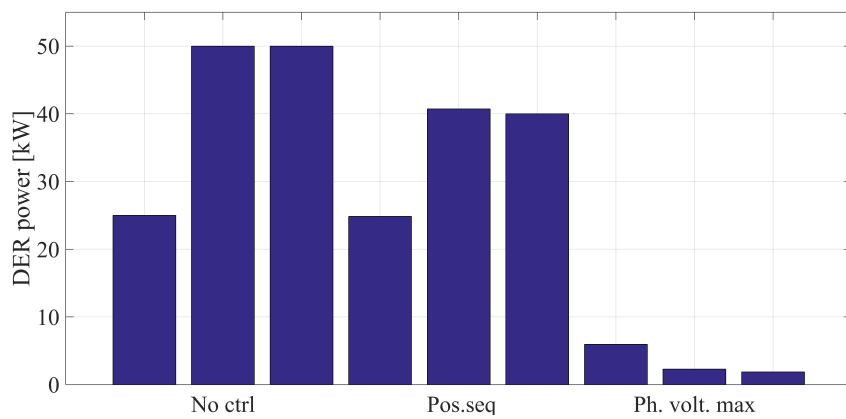
Taking into account this distribution of loads, their phase connections and DERs, it is obvious that phase *a* is the most unloaded one and overvoltages will be present in it due to the neutral point shifting [15], which makes the voltage profiles in phase *b* and *c* less interesting for this case study. The simulation results of the voltage profile in phase *a* are shown in Fig. 3.7 (a). As can be seen from the simulation results, the no control case “*No ctrl*” results in overvoltages from Node 6 till Node 19, where at the end of the LV feeder the voltage in phase *a* exceeds 1.15 p.u. while the limit  $v_{g,max}$  is 1.10 p.u.



(a) Voltage profile of phase  $a$  across the 19 node feeder



(b) Positive-sequence voltage profile across the 19 node feeder



(c) Injected power of the three case studies

Figure 3.7: Simulation results comparison between the three case studies

The second case study “*pos.-seq*” where the active power is drooped according to the positive-sequence, yields to slightly better results compared to the previous case but still overvoltages are present from Node 7 till Node 19. This is because the value of the positive-sequence voltage is rather low compared to the maximum voltage and it more or less resembles an average value of the three phase voltages. In the last case “*ph. volt. max*” the active power is drooped according to the maximum among the phase voltages and all droop controllers are activated because the phase voltage is  $v_g > v_{c_{pb}}$  and it can be seen that the voltage profile of the entire LV feeder is kept below the maximum of 1.1 p.u.

The positive-sequence voltage profile of the same LV feeder is depicted in Fig. 3.7 (b). Even in the case where no control is present the positive-sequence voltage hardly reaches 1.08 p.u. When active power drooping is applied according to the positive-sequence value all droop controllers are activated as well, but the amount of the drooped power is not sufficient to prevent overvoltages.

When drooping according to the phase voltages is applied the positive-sequence voltage profile is decreasing whereas in the previous two cases it is increasing. The injected renewable power by the three DERs of the different cases is shown in Fig. 3.7 (c). The first case “*No ctrl*” is used as a reference to compare the amount of the drooped power. Columns 1–3 per case, represent the injected power by DER<sub>11</sub>, DER<sub>18</sub> and DER<sub>19</sub>, respectively. The drooping according to the positive-sequence voltage does not droop enough active power and therefore overvoltages occur. On the other hand, the drooping according to the phase voltages droops enough active power such that it is able to maintain the voltage levels successfully within limits.

As can be seen from the conducted simulations, the active power drooping as a function of the to the positive-sequence voltage is not capable of maintaining the voltages across the feeder within limits. Despite the fact that the active power drooping as a function of the maximum rms value droops more active power, it is able to maintain the voltage profiles without violating the limits set by the standard EN50160. Hence, this drooping principle will be used further on in the thesis.

### 3.2.5 Comparison between different control strategies - scenario 1

In this subsection, the newly proposed control algorithms for DERs, i.e., drooped positive-sequence, drooped damping and modified damping control strategies will be compared with the damping control strategy proposed in [41, 68, 69], the classical positive-sequence and the single-phase control strategies. For more accurate comparison between the proposed and the existing control strategies, reactive power support based on variable PF is added to the classical control strategies, which makes them compatible with the current regulations and standards. The used LV feeder is depicted in Fig. 3.6 and the consumed power by the loads, node

| Node                    | N9    | N10   | N11   | N13   | N16  | N18   | N19   |
|-------------------------|-------|-------|-------|-------|------|-------|-------|
| $P_{\text{Load}}$ [kW]  | 3     | 3     | 25    | 2     | 3    | 20    | 20    |
| $S_{\text{Load}}$ [kVA] | 3.33  | 3.33  | 27.77 | 2.22  | 3.33 | 22.22 | 22.22 |
| PF                      | 1/0.9 | 1/0.9 | -     | 1/0.9 | -    | -     | -     |
| Phase connection        | a     | a     | abcn  | a     | a    | abcn  | abcn  |

Table 3.4: DER data used in the simulation model

and phase connections are listed in Table 3.2. The DERs power and connection type are listed in Table 3.4. The power is chosen such that, when any classical voltage control is applied to the DERs, overvoltages occur at the end of the feeder, which means that the hosting capacity of the LV network is reached. The three-phase DERs, which are connected at nodes 11, 18 and 19 are equipped with these control strategies and different cases are formulated. In addition, five single-phase DERs with small power ratings are connected to phase *a* to introduce additional voltage unbalance. The small DERs, besides the first case (i) (described below), are always driven by the single-phase control strategy with variable PF, which is used in the single-phase inverters available on the market and they are not subjected to power drooping. By doing so, more accurate comparison between the available and the proposed control strategies can be made.

Similar to the previous simulation case, here as well the simulation time is set to be 2 s, the data are extracted from the workspace and the last readings are used to present the obtained simulation results. Seven different cases are simulated, starting from case (i) no control “*No ctrl*” where the single-phase DERs are equipped with the single-phase control strategy, which is described in §2.3.1 and the three-phase DERs with the positive-sequence control strategy, which is described in §2.3.2. Case (ii) “*Q ctrl*” is where a variable PF control is applied to all DERs (single- and three-phase) with apparent power ratings listed in Table 3.4 and the analytical models from §3.2.2 and §3.2.3 are used. From this case to all that follow next, the single-phase DERs will be equipped with the single-phase control strategy with the variable PF and the three-phase DERs with the control strategies under study unless otherwise mentioned. Case (iii) “*D ctrl*” is the case where the three-phase damping control strategy is used and analytically described in §2.6. Case (iv) is the drooped positive-sequence control strategy “*Dr ctrl*”, described in §3.1.1 and no reactive power support is included. In cases (v) -“*MD  $g_d=1$* ”, (vi)“*MD  $g_d=7$* ” and (vii) “*MD  $g_d=20$* ” the modified three-phase damping control strategy is used but the only difference is that the  $g_d$  assumes different values such as 1, 7 and 20 p.u, respectively. In this particular case, the value selection is done so that there is a significant difference between them. Thus the impact of it on the power quality and injected currents can be evaluated.

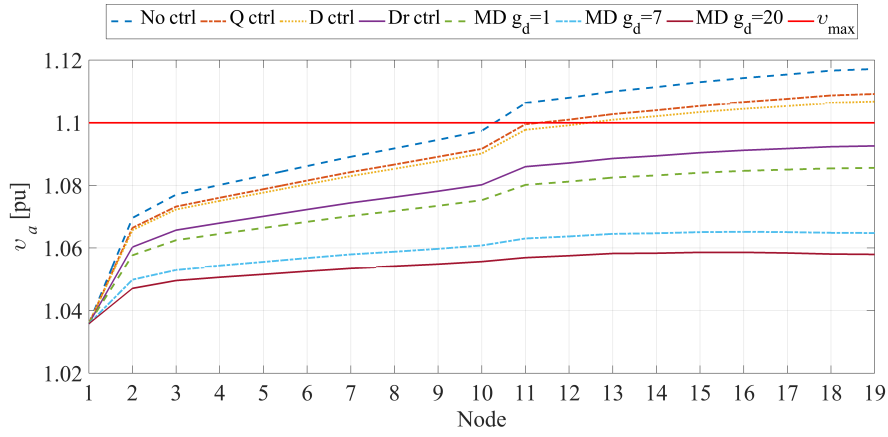
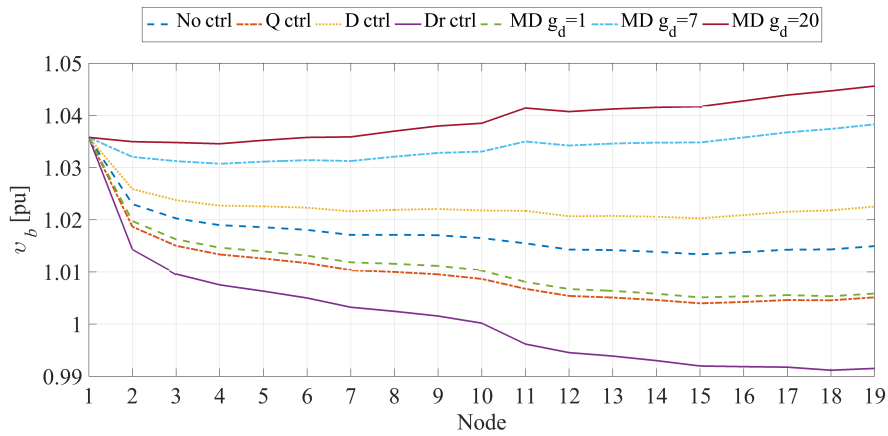
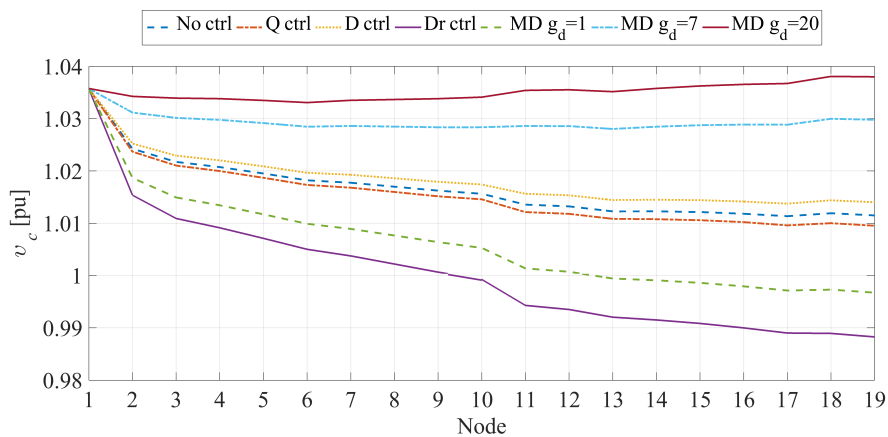
(a) Voltage profile in phase  $a$ (b) Voltage profile in phase  $b$ (c) Voltage profile in phase  $c$ 

Figure 3.8: Voltage profiles obtained when different control strategies are examined

The parameters of the active power drooping needed for (3.1) are chosen to be  $v_{cpb}=1.06$  p.u and  $v_{g,max}=1.1$  p.u. The parameters needed for the damping controller are the same as in the drooping controller but the constant damping band is  $v_{cpb}=1.04$  p.u. and is used in (3.3). Note that these values can vary, depending on the grid properties such as DER location in the feeder (closer or further from the MV/LV transformer), the MV/LV transformer and the feeder properties. In this case study, the phase voltage profiles will be examined as well as the symmetrical components profiles. Further examinations are also conducted on the negative- and zero- voltage unbalance factors  $VUF_2$  and  $VUF_0$ . In addition, the grid losses are investigated and compared when different control strategies are used. The voltage profiles of phase  $a$  are depicted in Fig. 3.8 (a). For more clarity, a red line referred as  $v_{max}$  draws the upper limit set by EN50160. When no control (i) is present, the DERs inject only active power and as can be seen overvoltages are present from Node 10 to Node 19. In test case (ii), the variable PF is investigated and its ability to provide voltage control in LV grids. Since all DERs operate at their maximum power ratings, the PF is equal to 0.9 and it can be seen that the voltage profile is slightly lower compared to the previous case but still overvoltage problem is present. Therefore, this control strategy is not capable of providing sufficient voltage control in LV grids despite the reactive power support. In test case (iii), the three-phase damping control strategy [46] is used.

The damping conductance in this case is calculated by (2.17) and turned in p.u. values. As it was mention above, due to the resistive behaviour towards the zero- and the negative-sequence voltage components, the three-phase damping control strategy injects higher current in the phase(s) with the lower voltage and lower current(s) in the phase(s) with the highest voltage and thus, the voltage unbalance is mitigated. In this case however, the three-phase damping control strategy is unable to mitigate the voltage unbalance sufficiently and still overvoltages are present. Note that in cases (i) to (iii) the active power is not drooped and all of them lead to overvoltages. Hence, the overvoltage protection would have tripped and all DERs would have been disconnected from the grid. Sudden disconnections of DERs can cause big variation of the rms voltage values and lead to poor power quality, where the variations depend on the disconnected power and feeder properties. A similar scenario has been observed in Ostende, Belgium and it is reported in [33]. In case (iv) the active power drooping sufficiently decreases the injected power and overvoltage problems are prevented. When the modified damping with  $g_d= 1$  p.u. is used - case (v), the voltage profile is even lower compared to the previous cases but the lowest profiles are achieved when case (vi) and (vii) are used. It is remarkable to point out that when an initial value of  $g_d=20$  p.u. is used, the voltage profile does not cross the  $v_{cpb}$  value, hence no active power drooping is applied to any of the DERs and maximum renewable energy harvesting is achieved.

The sharp changes in all voltage profiles between the nodes 1 to 2 and nodes

10 to 11 are due to the fact that the nodes are not uniformly distributed over the feeder. In this particular LV network, the distance between Node 1 and Node 2 is 165 m (Node 10 to Node 11 the distance is 53 m) while the distance between the other nodes is 15 m.

The simulation results of the voltage profile in phase *b* are depicted in Fig. 3.8 (b). When no control is applied (case (i)) the voltage profile decreases towards the last node but it is within the standard limits. In case (ii), the reactive power support gives lower profile compared to the previous one. Due to the voltage unbalance mitigation (iii) the voltage profile is slightly higher compared to the previous cases. Case (iv) provides the lowest profile of all cases due to the fact that too big amount of active power is drooped and the loads are supplied mainly by the programmable voltage source. Case (v) represents the modified damping control strategy where the initial  $g_d=1$  p.u. is used and it results in a voltage profile similar to case (ii). Up to this point all cases have decreasing voltage profile, which means the local demand of the loads is provided by the programmable voltage source. When cases (vi) and (vii) are applied, due to the higher damping conductance, which means an improved resistive behaviour towards the zero- and the negative-sequence components is present, the power flow changes its direction and it leads to a voltage profile that increases towards the last node.

The simulation results of the voltage profile in phase *c* are shown in Fig. 3.8 (c). The obtained results have similar arrangements as in phase *b* but there are two major differences. First, the modified damping control strategy with  $g_d=1$  p.u. performs more poorly and it provides the secondly lowest voltage profile and second, the inverse power flow is achieved only when the case (vii) is used. The rest of the results are the same as in phase *b*.

The simulation results of the positive-sequence voltage profile across the feeder are depicted in Fig. 3.9 (a). The lowest positive-sequence profile is obtained when case (iv) is used (i.e. the drooped positive-sequence control strategy) because the amount of the drooped power is incredibly high. Although the balancing abilities are improved by the modified damping control strategy, it provides the second lowest profile because the amount of the drooped active power remains high, which is the result of case (v). The reactive power support (ii) provides relatively higher profile and it is led by the modified damping control strategy with  $g_d=7$  p.u. The obtained results for the remaining cases (i), (iii) and (vii) have similar performance providing the same results and the profiles overlap. The reason for this effect is that the first two cases do not droop any active power because they are not equipped with a droop controller and the last case (vii) avoids active power drooping by mitigating the voltage unbalance so intensively that the active power is distributed among the other two phases.

The simulation results of the zero-sequence voltage profile are presented in Fig. 3.9 (b). Since cases (i), (ii) and (iv) cannot influence the zero-sequence volt-

| case/Node                     | Node 11  | Node 18  | Node 19  |
|-------------------------------|----------|----------|----------|
| Case (v) MD $g_d = 1$ p.u.    | 1/1.49   | 1/1.19   | 1/1.18   |
| Case (vi) MD $g_d = 7$ p.u.   | 7/13.88  | 7/13.73  | 7/13.74  |
| Case (vii) MD $g_d = 20$ p.u. | 20/35.57 | 20/36.45 | 20/36.32 |

(initial value/final value)

Table 3.5: Initial and actual values of the damping conductance for the different test cases

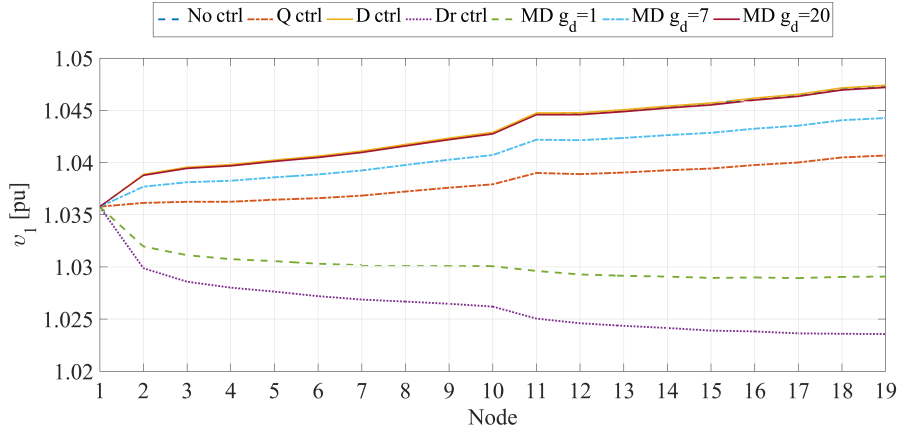
age component, the voltage profiles are similar and very close to each other. When the three-phase damping control strategy is used - case (iii), the voltage profile is lower compared to the previous cases due to the introduced resistive behaviour towards the zero-sequence voltage component. Although the modified damping control strategy with  $g_d = 1$  p.u. has a power drooping controller, the zero-sequence voltage profile is slightly lower compared to case (iii) where the three-phase damping control strategy is used with a fixed  $g_d = 1$  p.u. The reason for the better performance is that the damping controller has increased the values of the damping conductance as listed in Table 3.5. The two cases (vi) and (vii) provide outstanding performance compared to the previous cases because  $g_d$  is increased significantly, hence the resistive behaviour is improved. Case (vii) decreases the zero-sequence voltage with a factor of 6 compared to case (i), (ii) and (iv). Finally, the obtained initial and the final values of the damping conductance  $g_d$  in the performed simulation for cases (vi) and (vii), are listed in Table 3.5.

The simulation results of the negative-sequence voltage profile are presented in Fig. 3.9 (b). Cases (i), (ii) and (iv) do not influence the negative-sequence voltage component and the voltage profiles are similar and also very close to each other. Furthermore, cases (iii) and (iv) also have a very poor performance despite the introduced resistive behaviour. The two cases (vi) and (vii) provide very good performance compared to the previous cases because  $g_d$  is increased significantly while case (vii) decreases the zero-sequence voltage with almost a factor of 3 compared to case (i) and (v).

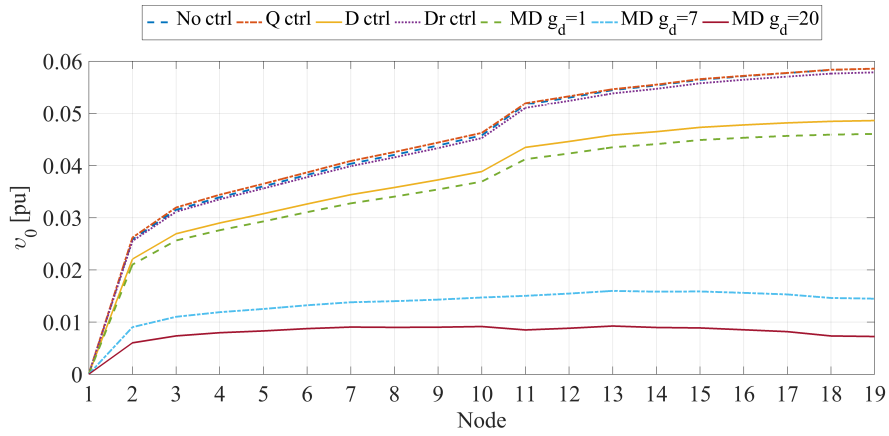
According to standard EN50160 [8] the negative-sequence voltage unbalance factor may not exceed 2% and it is calculated as:

$$\text{VUF}_2 = \frac{V_2}{V_1} \cdot 100[\%] \quad (3.19)$$

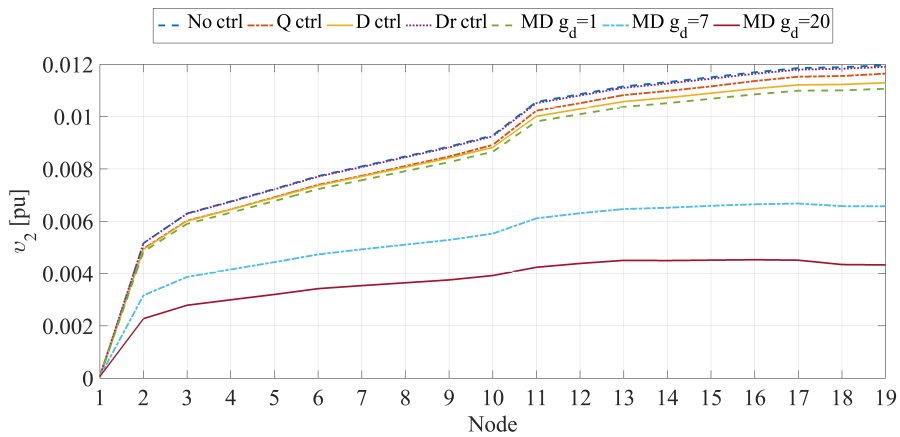
The negative-sequence voltage unbalance factor across the distribution feeder is presented in Fig. 3.10 (a). The highest  $\text{VUF}_2$  occurs when droop control is present - case (iv). Since the positive-sequence voltage is being reduced by the active power drooping, the negative-sequence voltage remains the same and this results in higher  $\text{VUF}_2$  values. In cases (i) and (iii), the voltage unbalance factor still remains high.



(a) Positive-sequence voltage profile

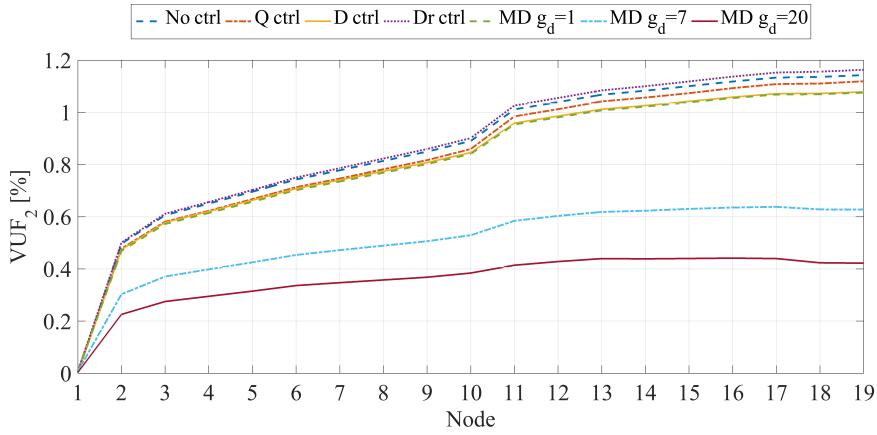


(b) Zero-sequence voltage profile

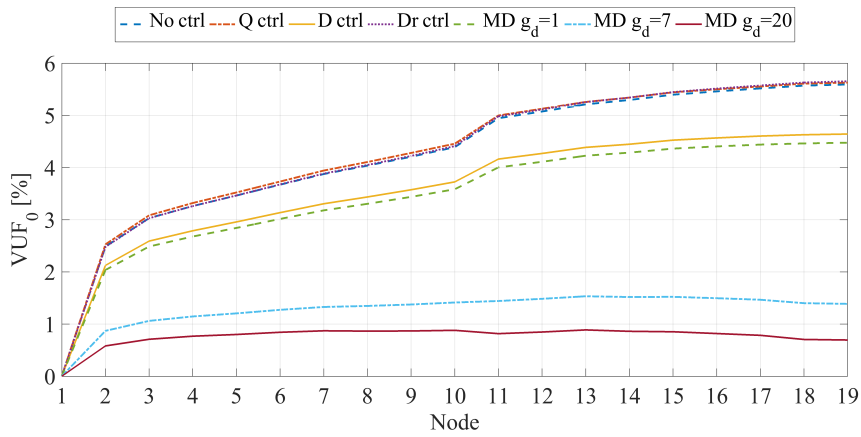


(c) Negative-sequence voltage profile

Figure 3.9: Voltage profiles obtained with the different control strategies are examined



(a) Negative-sequence unbalance factor



(b) Zero-sequence unbalance factor

Figure 3.10: Negative- and zero-sequence unbalance factors

When the three-phase damping control strategy: case (iii) and the modified damping control strategy with  $g_d = 1$  p.u. (case (v)) are used,  $VUF_2$  is slightly lower but it still gives high values that are close to the previous cases. The lowest negative-sequence unbalance factors are achieved when cases (vi) and (vii) are used due to the higher values of the damping conductance  $g_d$ .

Similar to  $VUF_2$  the zero-sequence voltage unbalance factor  $VUF_0$  is calculated in the same manner:

$$VUF_0 = \frac{V_0}{V_1} \cdot 100[\%] \quad (3.20)$$

The performance of the studied cases towards the  $VUF_0$  resembles the explanation of the  $VUF_2$ . Cases (i), (ii) and (iv) do not have any impact on the

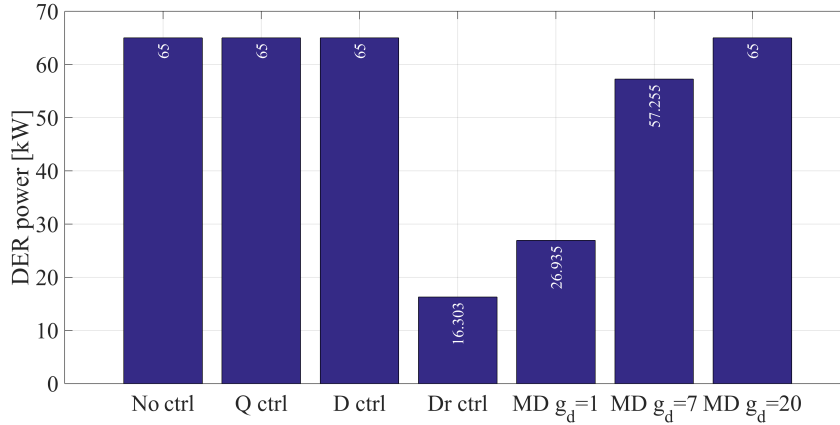


Figure 3.11: Total injected power from the DERs for the different cases

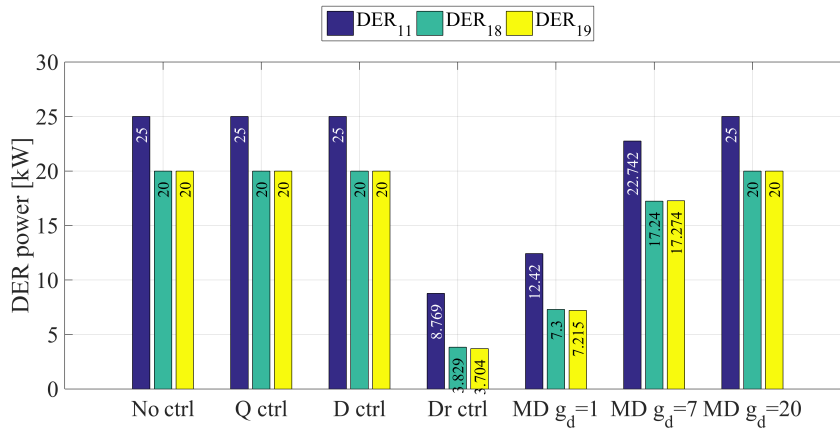


Figure 3.12: Injected power per DER for the different cases

zero-sequence and the  $VUF_0$  profiles are close to each other and assume high values. Case (iii) and case (v) provide similar results and lower profile but the lowest profiles are again achieved in cases (vi) and (vii).

Unfortunately EN50160 does not include a limit for the zero-sequence unbalance factor. However, it is important to reduce this component because it has an impact of the grid losses and especially when the MV/LV transformer is used in  $\Delta - Y$  connection. Last but not least, it has a direct impact on the penetration level of the DERs due to the neutral point shifting. This impact depends on the zero-sequence impedance of the feeders as well as the loads and DERs, which exchange zero-sequence current.

Fig. 3.11 shows the total injected active power from all three-phase DERs. In cases (i - "No ctrl"), (ii - "Q ctrl") and (iii - "D ctrl"), the DERs inject all available power but overvoltages are present and as it was mentioned earlier in such circum-

| Case/Feeder        | Phase <i>a</i> | Phase <i>b</i> | Phase <i>c</i> | Neutral | Total  | Deviation |
|--------------------|----------------|----------------|----------------|---------|--------|-----------|
| No control [kW]    | 0.8805         | 0.1020         | 0.047          | 1.0981  | 2.129  | 100%      |
| Q control [kW]     | 1.1930         | 0.5036         | 0.332          | 1.1083  | 3.137  | 147.38%   |
| D control [kW]     | 0.7482         | 0.0942         | 0.0588         | 0.7791  | 1.680  | 78.94%    |
| Dr control [kW]    | 0.1288         | 0.3021         | 0.4455         | 1.0725  | 1.9489 | 91.56%    |
| MD $g_d = 1$ [kW]  | 0.1612         | 0.1534         | 0.2616         | 0.7026  | 1.2788 | 60.08%    |
| MD $g_d = 7$ [kW]  | 0.2464         | 0.0681         | 0.0945         | 0.1192  | 0.5283 | 24.82%    |
| MD $g_d = 20$ [kW] | 0.2345         | 0.1161         | 0.1219         | 0.0630  | 0.5354 | 25.15%    |

Table 3.6: Segregated feeder losses

stances, the on-off control will be activated, which will lead to a disconnection of the DERs from the grid. When the droop control is applied (iv - “*Dr ctrl*”), the amount of curtailed power is extremely high and around 4 times less power is injected compared to the previous cases. When case (v) is used the, curtailed power is less and it is approximately 2.4 times less compared to the original power. In case (vi), the drooped power is considerably smaller (1.13 times the original) compared to the previous two cases. When the modified damping control strategy with  $g_d=20$  p.u. is used, all available power is injected and no drooping is applied. The reason for this beneficial effect is that the control strategy has redistributed the available power over the phases *b* and *c* and less power has been injected in phase *a*.

The actual exchanged renewable power by the DER<sub>11</sub>, DER<sub>18</sub> and DER<sub>19</sub> is shown in Fig 3.12. The DERs in the middle of the feeder, inject more power due to the smaller impedance to the MV/LV transformer. In case (vi) however, DER<sub>19</sub> injects slightly more power than DER<sub>18</sub>. This is because DER<sub>19</sub> additionally lowers the voltage profile in phase *a* thus allowing more power injection to the grid. Although in this particular case study a strong radial feeder is examined, the interpretation of the obtained results can be applied also for softer or even stronger feeders. The higher feeder impedance will cause more power drooping for the DERs at the middle and end of the feeder. The voltage unbalance mitigation capabilities of the control strategy will be also influenced by the feeder properties. Stronger feeders tend to have less voltage unbalance and thus the three-phase damping control strategy will have less impact on the voltage unbalance mitigation for the same value of the damping conductance. The same can be stated also for the DER location in the feeder. Usually if DER is closer to the MV/LV transformer (as it is the case for DER<sub>1</sub>), the overvoltages are less prominent as well as the voltage unbalances. In soft grids or DERs connected farther from the MV/LV transformer, overvoltages will be higher and more renewable power will be curtailed but also the voltage unbalance will be more impacted for the same damping conductance value.

This LV feeder is based on a sectioned four-wire cable. In [70], the effect of the earth in LV underground cables is studied. If the earth effect is neglected,

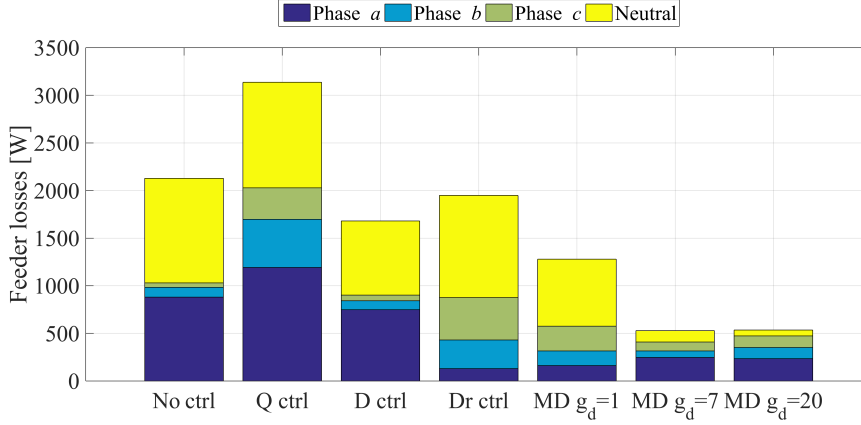


Figure 3.13: Total feeder losses

the results show that the worst possible error of the phase-to-neutral voltages is below 0.0025 p.u., which in absolute value is 0.577 V. In addition, some further examination is carried out in [71] where the earth effect is included in the cable properties and the results showed that the earth effect has a negligible impact on the results when sectioned cables are used. Therefore, the earth effect can be neglected and the total feeder losses are calculated by summing up the different section losses:

$$P_{tl} = \sum_{l_a=1}^{l_a=18} R_{l,a} i_{l,a}^2 + \sum_{l_b=1}^{l_b=18} R_{l,b} i_{l,b}^2 + \sum_{l_c=1}^{l_c=18} R_{l,c} i_{l,c}^2 + \sum_{l_n=1}^{l_n=18} R_{l,n} i_{l,n}^2 \quad (3.21)$$

where,  $l$  is the corresponding section number,  $R_{l,x}$  is the corresponding section ohmic resistance and  $x$  is the respective phase  $a, b, c$  and the neutral  $n$ . The currents flowing through a section  $l$  are  $i_{l,x}$ . Case (i) will be used as a reference case to evaluate the performance of the other 6 cases. The losses in the feeder for each case study are depicted in Fig. 3.13 and detailed data are listed in Table 3.6. The classical voltage control by means of reactive power support (case (ii)) performs poorly when used for voltage control in LV grids and as expected it leads to extra losses of 47% in the feeder compared to case (i). The three-phase damping control strategy - case (iii) is able to decrease the feeder losses with 21% compared to case (i), by redistributing the active power among the phases. The drooping control strategy case (iv) provides similar total losses as the reference case but the segregation shows that the losses in the other two phases are increased. Due to the increased damping conductance in case (v) the losses are decreased with 40%. When the modified damping control strategy with  $g_d=7$  p.u. (case (vi)) is used the losses are decreased down to 75.2% while in case (vii) the losses are decreased to 74.8%. The difference in losses between these two cases is rather small but due to fact that

| Cases      | DER <sub>11</sub> |       |       | DER <sub>18</sub> |       |       | DER <sub>19</sub> |       |       |
|------------|-------------------|-------|-------|-------------------|-------|-------|-------------------|-------|-------|
|            | $I_a$             | $I_b$ | $I_c$ | $I_a$             | $I_b$ | $I_c$ | $I_a$             | $I_b$ | $I_c$ |
| Case (i)   | 34.59             | 34.29 | 34.91 | 27.62             | 27.33 | 27.91 | 27.61             | 27.29 | 27.94 |
| Case (ii)  | 38.58             | 38.54 | 38.63 | 30.82             | 30.76 | 30.88 | 30.81             | 30.72 | 30.91 |
| Case (iii) | 31.9              | 35.99 | 36.2  | 24.62             | 29.28 | 29.37 | 24.61             | 29.27 | 29.37 |
| Case (iv)  | 14.47             | 14.38 | 14.55 | 7.26              | 7.21  | 7.31  | 7.10              | 7.04  | 7.15  |
| Case (v)   | 15.53             | 21.81 | 21.48 | 8.39              | 14.34 | 13.96 | 8.30              | 14.24 | 13.82 |
| Case (vi)  | 17.32             | 42.38 | 38.29 | 9.63              | 34.72 | 0.10  | 9.90              | 34.97 | 29.69 |
| Case (vii) | 13.53             | 48.73 | 42.70 | 8.52              | 40.80 | 34.45 | 9.38              | 41.24 | 33.19 |

Table 3.7: Summarised simulation data in of the exchanged rms currents in phase quantities by the different DERs

case (vi) droops small amount of power while case (vii) injects it all. This leads to slightly bigger reverse power flow to the programmable power source hence higher losses. As it can be seen the neutral losses are significantly reduced when cases (vi) and (vii) are used, hence the neutral current is reduced as well. In [72–74], the authors have investigated eventual ancillary services such as reactive power support, harmonic mitigation, voltage unbalance, etc. that DERs could provide to the DSO. From the conducted examinations it can be clearly seen that the modified three-phase damping control strategy has a great potential to provide ancillary services such as voltage control and also voltage unbalance mitigation. All case studies are performed by using a time domain model under the assumption that the DERs are operating at their maximum power. The cases demonstrate the differences in the applied control strategies but in practice the DERs operate under variable input power and grid conditions. In Chapter 4, more comprehensive analyses are conducted where the impact of the control strategies is evaluated on an annual basis by means of simulations on an existing LV grid.

The simulation data, needed for a better performance evaluation of the different control algorithms, are listed in Table 3.8. The data are in absolute values and represent the obtained phase voltages, phase active currents, injected active power per phase, injected total power by the DER, injected reactive power per phase, injected total reactive power by the DER, apparent power per phase, total apparent power and the power factor per phase. From the presented simulation results in Fig. 3.8 it is evident that cases (vi) and (vii) have excellent performance in terms of overvoltage and voltage unbalance mitigation. This effect is achieved by injecting smaller current in phase  $a$  and bigger current in phase  $b$  and  $c$ , where the values of exchanged active currents can be seen in Table 3.7. In practice, for a 20 kWp PV installation, the power ratings of an off-the-shelf should also take the PF into account:

$$I_{\text{nom}} = \frac{P_{\text{nom}}}{\text{PF} \times n \times V_{\text{nom}}} = \frac{20\text{kW}}{0.9 \times 3 \times 230.94\text{V}} = 32.07[\text{A}] \quad (3.22)$$

with  $P_{\text{nom}}$  the nominal active power of the inverter,  $V_{\text{nom}}$  the nominal grid voltage,  $n$  number of phases and PF the required power factor. The modified damping

control strategies with  $g_d=7$  p.u. and  $g_d=20$  p.u. (case (vi) and (vii)) inject bigger active current in phase  $b$  with current of 34.97 A and 41.24 A with a unity power factor. This way the active current can be assumed to be the output rms current. Compared to the result of (3.22) with cases (vi) and (vii), the needed oversizing is 8.5% and 22.1%, respectively. Hence, all three phases must be oversized with these ratios in order to cover all different possible voltage scenarios. The apparent power needed when case (ii) is used is 22.22 kVA whereas in case (vii) the total apparent power will be 28.48 kVA. That makes a difference of 6.28 kVA, which is not that much considering the overall performance and the significant improvement of the power quality and the feeder loss reduction.

Initially, cases (i) and (iv) are supposed to inject only active power and the obtained simulation results show that the reactive power is negligibly small and the PF is close to unity. Hence, the models are properly developed and perform according to the analytical models presented in the beginning of this chapter. Case (ii) operates under PF=0.9 and it can be seen that the PF differs slightly from 0.9 for the different phases. Nevertheless, the average power factor is exactly 0.9 (small deviations are possible due to number rounding). Therefore, the developed Simulink models, perform in a good agreement with the analytical models.

Since the grid parameters differ from grids to grids, in practice the value of the damping conductance can be selected by means of simulation in the worst case scenarios based on the inverter power ratings and a present voltage unbalance at the PCC of 2%. As of the constant power band voltage ( $v_{cpb}$ ), in this work it is chosen to be 1.06 p.u., which is based on previous research conducted in [33,50,75]. However, this fixed value leads to unfair power curtailment for the different DERs. In practice, this value can be chosen based on the initial transformer voltage, positive-sequence impedance of the feeder, the injected positive-sequence current by the DER and some reserve of 1 to 2%. Nevertheless, the goal of the local control is to ensure power quality in LV grids with or without a secondary control layer. Further optimisations regarding the fair power sharing can be done in the second control layer by sending different power setpoints to all DERs and also changing the constant power band voltage as done in [76, 77].

All cases that are based on the three-phase damping control strategy exchange some small amount of reactive power with the grid. The reason for this reactive power flow is due to the small differences of the phase angles of the three-phase voltages at the PCC. This difference is multiplied by the damping conductance value, which results in reactive power consumption and injection. However, this reactive power is a result of the symmetrical components theory, while in case (ii) it is intentionally introduced by the currently active standards to provide voltage control. Despite the reactive power flow in cases (vi) and (vii) the feeder losses are significantly reduced as shown in Fig. 3.13.

The symmetrical components values of the voltages, injected currents and

| Cases      | Param. | DER <sub>11</sub> |       |       | DER <sub>18</sub> |       |       | DER <sub>19</sub> |       |       |
|------------|--------|-------------------|-------|-------|-------------------|-------|-------|-------------------|-------|-------|
|            |        | 0                 | 1     | 2     | 0                 | 1     | 2     | 0                 | 1     | 2     |
| Case (i)   | U [V]  | 2.44              | 241.3 | 11.93 | 2.7460            | 241.8 | 13.47 | 2.764             | 241.9 | 13.52 |
| Case (ii)  |        | 2.362             | 239.9 | 11.99 | 2.668             | 240.3 | 13.48 | 2.689             | 240.3 | 13.52 |
| Case (iii) |        | 2.313             | 241.3 | 10.04 | 2.594             | 241.8 | 11.19 | 2.609             | 241.9 | 11.23 |
| Case (iv)  |        | 2.429             | 236.7 | 11.79 | 2.732             | 236.4 | 13.31 | 2.749             | 236.4 | 13.36 |
| Case (v)   |        | 2.267             | 237.8 | 9.52  | 2.541             | 237.6 | 10.6  | 2.556             | 237.7 | 10.64 |
| Case (vi)  |        | 1.411             | 240.7 | 3.47  | 1.519             | 241.1 | 3.38  | 1.518             | 241.2 | 3.35  |
| Case (vii) |        | 0.979             | 241.2 | 1.96  | 1.003             | 241.8 | 1.70  | 1.0               | 241.8 | 1.67  |
| Case (i)   | I[A]   | 0.01              | 34.54 | 0     | 0.01              | 27.57 | 0     | 0.01              | 27.56 | 0     |
| Case (ii)  |        | 0.003             | 38.59 | 0     | 0.002             | 30.82 | 0     | 0.002             | 30.82 | 0     |
| Case (iii) |        | 0.523             | 34.64 | 2.27  | 0.587             | 27.69 | 2.53  | 0.59              | 27.69 | 2.54  |
| Case (iv)  |        | 0.002             | 12.27 | 0     | 0.002             | 5.33  | 0     | 0.002             | 5.15  | 0     |
| Case (v)   |        | 0.765             | 17.64 | 3.21  | 0.686             | 10.46 | 2.86  | 0.683             | 10.34 | 2.85  |
| Case (vi)  |        | 4.448             | 32.34 | 10.9  | 4.683             | 24.7  | 10.44 | 4.681             | 24.75 | 10.34 |
| Case (vii) |        | 6.418             | 34.71 | 14.16 | 6.535             | 27.71 | 11.8  | 6.397             | 27.69 | 11.41 |
| Case (i)   | P [kW] | 0                 | 8.335 | 0     | 0                 | 6.666 | 0     | 0                 | 6.667 | 0     |
| Case (ii)  |        | 0                 | 9.258 | 0     | 0                 | 7.406 | 0     | 0                 | 7.406 | 0     |
| Case (iii) |        | 0.001             | 8.359 | 0.022 | 0.002             | 6.695 | 0.028 | 0.002             | 6.698 | 0.029 |
| Case (iv)  |        | 0                 | 2.904 | 0     | 0                 | 1.26  | 0     | 0                 | 1.218 | 0     |
| Case (v)   |        | 0.002             | 4.195 | 0.031 | 0.002             | 2.485 | 0.03  | 0.002             | 2.458 | 0.030 |
| Case (vi)  |        | 0.006             | 7.784 | 0.038 | 0.007             | 5.955 | 0.035 | 0.007             | 5.969 | 0.035 |
| Case (vii) |        | 0.006             | 8.372 | 0.028 | 0.007             | 6.70  | 0.02  | 0.006             | 6.695 | 0.019 |

Table 3.8: Summarised simulation data of the voltages, currents and power in symmetrical components

powers are listed in Table 3.8. The analytical models of case (i), (ii) and (iv) show that these cases are not able to impact the zero- and negative-sequence voltage components. The obtained simulation results show negligibly small values of zero-sequence currents, which can be neglected and complete absence of negative-sequence currents. Hence it can be concluded that the developed Simulink time domain models perform according to the analytical ones. It can be also seen that a significant power quality improvement can be achieved with relatively small injection of zero- and negative-sequence currents as demonstrated by the simulation results of cases (vi) and (vii).

### 3.2.6 Comparison between different control strategies - scenario 2

In the previous scenario, the initial voltage supplied by the three-phase programmable voltage source was set to 1.04 p.u., which is a typical setting value by the DSO where the primary voltage is assumed to be 1 p.u. According to the German grid code BDEW, the maximum voltage rise at the PCC that can be caused by a DER, which is connected to the MV grid, must be limited to 2%. Hence, a scenario shown in Fig. 3.14 is possible in reality. The HV is assumed as a slack bus and the HV/MV transformer is equipped with an OLTC. In this scenario, a DER is connected to Feeder F<sub>1</sub> in the vicinity of the MV/LV transformer and it causes some reverse power flow that leads to a voltage rise up to 1.02 p.u. To simplify

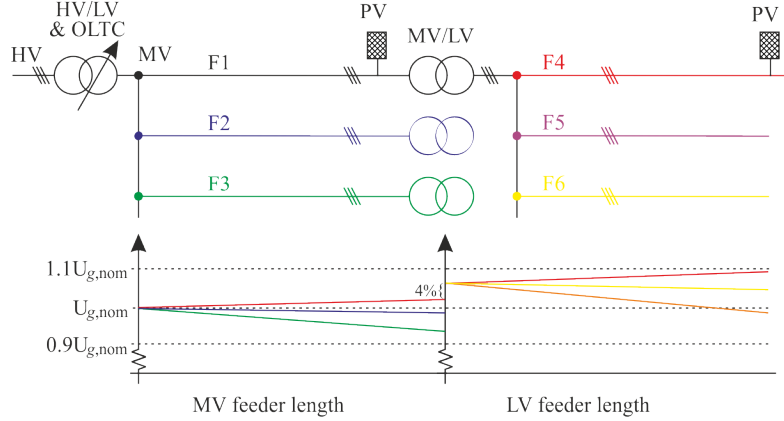


Figure 3.14: Total feeder losses

this scenario and avoid the voltage rise due the reverse power flow coming from the LV grid, an assumption is made such that all produced power in the LV grid is consumed locally by the loads in feeders F<sub>5</sub> and F<sub>6</sub> where no DERs are present (as well as in F<sub>2</sub> and F<sub>3</sub>). Taking into account the initial margin of 0.04 p.u. and the voltage rise due to DER, which is connected at the MV level, then the secondary voltage of the MV/LV transformer becomes 1.06 p.u. Similar cases are described in [21] and [78], where the impact on DERs and electric vehicles to the power quality is studied.

Since this is a scenario that can occur in practice, it is interesting to investigate further the behaviour of the proposed control strategies with this higher initial voltage of 1.06 p.u. The simulation settings are the same as in the previous scenario (LV network topology, load powers and connection and DERs power and connection). Since the previous scenario was designed such that case (i) leads to overvoltages at the end of the feeder, in this scenario the overvoltages will be even higher, therefore, it is not interesting for a further discussion. The simulation results obtained in the previous scenario showed that case (ii) and (iii) also lead to overvoltages, so these cases will not be discussed, either.

The obtained simulation results are summarised in Table 3.9. In case (iv), DER<sub>11</sub> droops almost all available power and injects only 417W. Nevertheless, the voltages at the point of common coupling are within limits (lower than 254V) while the other controllable DER<sub>18</sub> and DER<sub>19</sub> do not inject any active power. Although all power from the last two controllable DERs is drooped, the uncontrollable DERs and the asymmetrical loading pushes the voltage profile in phase *a* to overvoltages. Similar results are obtained for case (v) where the modified damping control strategy with  $g_d=1$  p.u. is used. In cases (vi) and (vii), due to the high damping conductance, hence better current distribution over the phases,

| Cases      | Param.   | DER <sub>11</sub> |       |       | DER <sub>18</sub> |              |              | DER <sub>19</sub> |              |              |
|------------|----------|-------------------|-------|-------|-------------------|--------------|--------------|-------------------|--------------|--------------|
|            |          | a                 | b     | c     | a                 | b            | c            | a                 | b            | c            |
| Case (iv)  | U [V]    | 253.9             | 233.0 | 232.6 | <b>255.1</b>      | <b>231.6</b> | <b>231.1</b> | <b>255.2</b>      | <b>231.7</b> | <b>230.9</b> |
| Case (v)   |          | 253.8             | 233.0 | 232.6 | <b>255.1</b>      | <b>231.7</b> | <b>231.1</b> | <b>255.1</b>      | <b>231.7</b> | <b>231.0</b> |
| Case (vi)  |          | 248.8             | 241.6 | 240.0 | 249.0             | 241.9        | 240.0        | 248.9             | 242.1        | 239.9        |
| Case (vii) |          | 246.8             | 243.4 | 242.7 | 246.8             | 243.9        | 243.1        | 246.8             | 244.1        | 243.1        |
| Case (iv)  | I [A]    | 0.58              | 0.58  | 0.58  | 0                 | 0            | 0            | 0                 | 0            | 0            |
| Case (v)   |          | 0.50              | 0.91  | 0.90  | 0                 | 0            | 0            | 0                 | 0            | 0            |
| Case (vi)  |          | 7.77              | 30.9  | 26.99 | 3.21              | 26.65        | 22.05        | 3.45              | 27.02        | 21.8         |
| Case (vii) |          | 4.91              | 40.45 | 34.32 | 2.48              | 33.84        | 27.67        | 3.31              | 34.53        | 26.52        |
| Case (iv)  | P [kW]   | 0.147             | 0.134 | 0.134 | 0                 | 0            | 0            | 0                 | 0            | 0            |
|            |          | 0.417/25.0        |       |       | 0/20.0            |              |              | 0/20.0            |              |              |
| Case (v)   |          | 0.126             | 0.212 | 0.21  | 0                 | 0            | 0            | 0                 | 0            | 0            |
|            |          | 0.548/25.0        |       |       | 0/20.0            |              |              | 0/20.0            |              |              |
| Case (vi)  |          | 1.933             | 7.466 | 6.478 | 0.800             | 6.446        | 5.293        | 0.858             | 6.543        | 5.229        |
|            |          | 15.88/25.0        |       |       | 12.54/20.0        |              |              | 12.63/20.0        |              |              |
| Case (vii) |          | 1.211             | 9.846 | 8.328 | 0.611             | 8.253        | 6.727        | 0.817             | 8.43         | 6.447        |
|            |          | 19.39/25.0        |       |       | 15.59/20.0        |              |              | 15.69/20.0        |              |              |
| Case (iv)  | Q [kVar] | 0.121             | -0.24 | 0.335 | 0.100             | -0.22        | 0.295        | 0.981             | -0.22        | 0.298        |
|            |          | 0.696             |       |       | 0.618             |              |              | 0.618             |              |              |
| Case (v)   |          | 0.008             | 0.046 | 0.043 | 0                 | 0            | 0            | 0                 | 0            | 0            |
|            |          | 1.323             |       |       | 1.103             |              |              | 1.09              |              |              |
| Case (vi)  |          | -0.18             | -1.21 | 1.533 | -0.31             | -1.02        | 1.45         | -0.37             | -0.97        | 1.45         |
|            |          | 2.921             |       |       | 2.776             |              |              | 2.784             |              |              |
| Case (vii) |          | -0.41             | -1.25 | 1.84  | -0.61             | -0.54        | 1.296        | -                 | -            | 1.266        |
|            |          | 3.499             |       |       | 2.444             |              |              | 2.382             |              |              |
| Case (iv)  | S [kVA]  | 0.190             | 0.275 | 0.360 | 0.100             | 0.222        | 0.295        | 0.098             | 0.223        | 0.297        |
|            |          | 0.827             |       |       | 0.618             |              |              | 0.618             |              |              |
| Case (v)   |          | 0.126             | 0.217 | 0.214 | -                 | 0            | -            | 0                 | 0            | 0            |
|            |          | 0.559             |       |       | 0                 |              |              | 0                 |              |              |
| Case (vi)  |          | 1.941             | 7.563 | 6.657 | 0.857             | 6.527        | 5.487        | 0.933             | 6.614        | 5.426        |
|            |          | 16.16             |       |       | 12.87             |              |              | 12.97             |              |              |
| Case (vii) |          | 1.276             | 9.925 | 8.529 | 0.861             | 8.270        | 6.851        | 1.117             | 8.437        | 6.567        |
|            |          | 19.7              |       |       | 15.98             |              |              | 16.12             |              |              |
| Case (iv)  | PF       | 0.771             | 0.489 | 0.374 | 0                 | 0            | 0            | 0                 | 0            | 0            |
| Case (v)   |          | 0.998             | 0.977 | 0.979 | -                 | -            | -            | -                 | -            | -            |
| Case (vi)  |          | 0.996             | 0.987 | 0.973 | 0.933             | 0.988        | 0.965        | 0.919             | 0.989        | 0.964        |
| Case (vii) |          | 0.949             | 0.992 | 0.977 | 0.709             | 0.998        | 0.982        | 0.731             | 0.999        | 0.981        |

Table 3.9: Summarised simulation data of voltages, currents, power, etc. that are exchanged by the DERs (red values means power quality problem, i.e., overvoltages)

the voltage profile in phase *a* is lowered to a safer level. Furthermore, the injected power is significantly increased compared to cases (iv) and (v).

The negative-sequence voltage unbalance factor is presented in Fig. 3.15 (a) and the zero-sequence voltage unbalance factor is presented in Fig. 3.15 (b). The unbalance factor profiles look very similar to scenario 1 (Fig. 3.10 (a) and (b)) but differ only in magnitude especially in cases (vi) and (vii) where the difference is more clear. This difference is due to the increased positive-sequence component and since the unbalanced factors are inversely proportional to it, this leads to lower values for  $VUF_0$  and  $VUF_2$ .

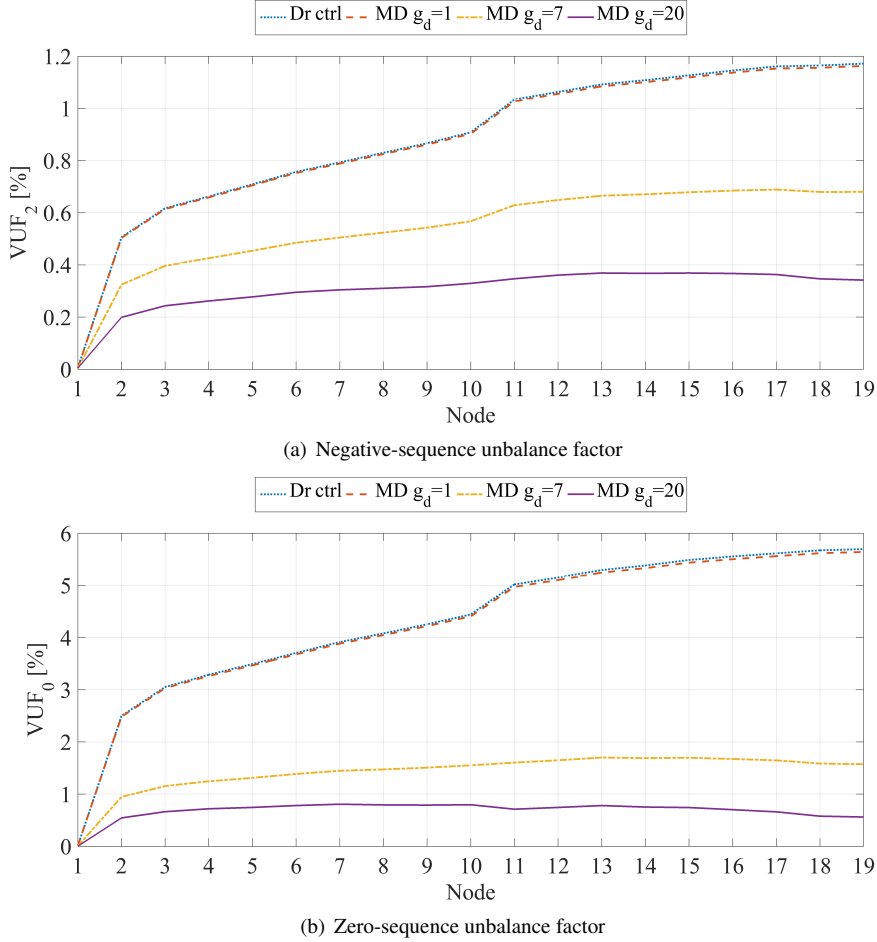


Figure 3.15: Negative- and zero-sequence unbalance factors at initial voltage of 1.06 p.u.

### 3.3 Experimental validation of the modified damping control strategy

The proposed three-phase damping based control strategy is tested in a controllable laboratory environment. The connection diagram of the set-up is shown in Fig. 3.16 where the DER comprise of a three-phase four-wire inverter, controller and a programmable dc power supply. The controller is responsible for generating the reference currents based on the local measurements, maintaining the dc-bus voltages according to their reference values and also giving new power set points to the programmable dc power supply. The DER is connected to the LV grid

through a power analyser PM3000, which provides accurate measurements of the exchanged currents and the voltages at the PCC. The LV grid is implemented by using a cable with an impedance of  $Z = 0.47 + j0.201\Omega$  and three-phase programmable ac power supply Spitzenberger & Spies, which is able to provide 5 kVA per phase in all four quadrants (sourcing and sinking mode).

The voltage unbalance is introduced by setting one of the phase voltages higher by the ac source. In §3.2.5 and §3.2.6, it was assumed that the loads will introduce the voltage unbalance, however in this particular set-up the power ratings are rather limited and this approach would overload or even damage the equipment. By setting one phase voltage higher than the other two phases, similar conditions as §3.2.5 and §3.2.6 will be recreated and the DER will have to mitigate both voltage unbalance and overvoltages, simultaneously.

As it was shown in §3.2.5, the reactive power has an insignificant impact to the voltage profile in LV grids, hence it will not be further investigated. The positive-sequence and damping control strategies with a fixed damping conductance value are not able to provide power drooping if overvoltages are present, hence they will be also omitted. On the other hand, the drooped positive-sequence and the modified three-phase damping control strategies are capable of power drooping. Therefore, the performance of the DER will be examined when the positive-sequence and the modified damping control strategies with three values of the damping conductance are taken into consideration. Four sets of experiments are conducted in this section where three different values of the phase voltage  $a$  are used:

- *case 1* phase voltages values  $V_a = 114$  V,  $V_b = 108$  V and  $V_c = 108$  V
- *case 2* phase voltages values  $V_a = 116$  V,  $V_b = 108$  V and  $V_c = 108$  V
- *case 3* phase voltages values  $V_a = 118$  V,  $V_b = 108$  V and  $V_c = 108$  V

The value of phase voltage  $V_a$  is chosen such that the DER operates within the different regions of the power droop and damping droop (see Fig. 3.4). For safety reasons the dc bus voltage is limited to 400V and the nominal rms value of the phase voltages to 110V.

In addition, The chosen values for the  $v_{cdb} = 1.04$  p.u. and  $v_{cpb} = 1.06$  p.u. are the same as the chosen in the performed simulations in §3.2.5 and §3.2.6. In absolute values, the exact thresholds become 114.4 V and 116.6V, respectively.

The nominal power of the inverter is 1.2 kVA, with an average efficiency of 94%. However, the efficiency of those inverters as a function of the current (at constant switching frequency and dc bus voltages), which will lead to a bit lower efficiency in the phase, which injects lower currents and vice versa for the phases that inject higher currents. In addition, the different commercial brands inverter brands have different efficiency curves. Therefore, the efficiency variation must be further examined when a selection of an inverter is made. Therefore, in this case

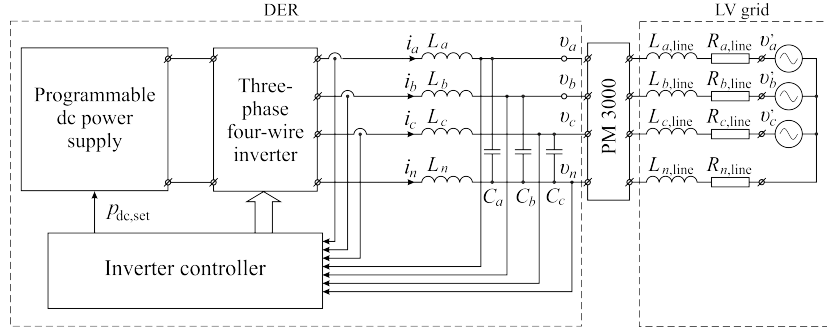


Figure 3.16: Experimental set-up configuration

is better to use the solution provided by (3.1) as an estimate of the droop power. By doing so the obtained experimental results become invariant to the efficiency of the inverter. The parameters of the inverter, which is used in the conducted experiments are as follows:

$$\begin{array}{llll}
 I_{\text{ref}} = 10 \text{ A} & I_{\text{nom}} = 3.3 \text{ A} & V_{\text{g,ref}} = 170 \text{ V} & V_{\text{g,nom}} = 110 \text{ V ac} \\
 P_{\text{ac}} = 3 \text{ kVA} & V_{\text{dc,ref}} = 600 \text{ V} & V_{\text{dc,nom}} = 400 \text{ V} & P_{\text{dc}} = 1.2 \text{ kW} \\
 C_{\text{dc}} = 1000 \mu\text{F} & L_n = 2 \text{ mH} & L_x = 0.666 \text{ mH} & C_x = 5 \mu\text{F}
 \end{array}$$

### 3.3.1 Obtained experimental results for case 1

In this case, the first measurements are performed without connecting the DER to the grid. Then the phase voltages and phase angles are measured and used as reference case. The obtained experimental results for the phase voltages and the phase currents are listed in Table 3.10 and Table 3.11, respectively. Based on the measured data, the voltage unbalance factors  $\text{VUF}_0$  and  $\text{VUF}_2$  are calculated and listed in Table 3.10. When DER equipped with the positive-sequence control strategy is connected to the feeder, it causes a phase voltage rise at the PCC with almost 1.9 V per phase and the phase angles remain unchanged. Phase voltage  $V_a$  is still below  $v_{\text{cpb}}$  and the droop controller does not droop any active power. The voltage unbalanced factors however, have decreased because the positive-sequence component has increased (a similar case was described above). The injected phase currents listed in Table 3.11 are equal in rms values, which indeed corresponds to the positive-sequence control strategy. The phase angles of the injected currents are  $180^\circ$  phase shifted, which corresponds to a current injection mode and these angles deviate with a maximum of  $0.2^\circ$  from the voltage angles, which means that they are very well locked to the grid voltage and very little reactive power is being exchanged.

| Parameter | $g_d^*$ | $V_a$ [V] | $V_b$ [V] | $V_c$ [V] | $\theta_a$ [°] | $\theta_b$ [°] | $\theta_c$ [°] | VUF <sub>0</sub> | VUF <sub>2</sub> |
|-----------|---------|-----------|-----------|-----------|----------------|----------------|----------------|------------------|------------------|
| No load   | -       | 114.3     | 108.3     | 108.3     | 0              | -120.2         | 119.8          | 1.817            | 1.817            |
| PS        | 0       | 115.9     | 110       | 109.9     | 0              | -120.2         | 119.8          | 1.774            | 1.778            |
| $g_d = 1$ | 1.62    | 115.6     | 110.1     | 110.1     | 0              | -120.3         | 119.9          | 1.543            | 1.741            |
| $g_d = 4$ | 5.49    | 115.1     | 110.4     | 110.3     | 0              | -120.4         | 120.1          | 1.168            | 1.667            |
| $g_d = 8$ | 9.79    | 114.7     | 110.6     | 110.5     | 0              | -120.4         | 120.1          | 0.989            | 1.489            |

Table 3.10: Case 1: Obtained phase voltage and voltage unbalance factors by means of experiments at  $v_a = 1.057$  p.u. (114V)

| Parameter | $g_d^*$ | $I_a$ [A] | $I_b$ [A] | $I_c$ [A] | $\theta_{i,a}$ [°] | $\theta_{i,b}$ [°] | $\theta_{i,c}$ [°] | $P_{dc}$ | $P_{exc}$ |
|-----------|---------|-----------|-----------|-----------|--------------------|--------------------|--------------------|----------|-----------|
| PS        | 0       | 3.14      | 3.324     | 3.332     | -180.1             | 59.6               | -60.3              | 1        | 1         |
| $g_d = 1$ | 1.62    | 3.075     | 3.438     | 3.458     | -180.2             | 59.8               | -60.3              | 1        | 1         |
| $g_d = 4$ | 5.49    | 2.607     | 3.671     | 3.701     | -180.7             | 61                 | -61.2              | 1        | 1         |
| $g_d = 8$ | 9.79    | 2.236     | 3.851     | 3.907     | -181.2             | 62.6               | -62.4              | 1        | 1         |

Table 3.11: Case 1: Obtained phase currents and injected power by means of experiments at  $v_a = 1.039$  p.u. (114.3V)

When DER is controlled by the three-phase modified damping control strategy with  $g_d = 1$  p.u. the phase voltage  $V_a$  is slightly decreased whereas  $V_b$  and  $V_c$  are increased. Due to the present voltage unbalance, the reaction of the three-phase damping control strategy is to mitigate it and it also injects some reactive currents, which slightly changes the angles of the phase voltages. Phase voltage  $V_a$  is still below  $v_{cpb}$  but higher than  $v_{cdb}$ , which enables the damping controller and the final value of the  $g_d$ , which is used to calculate the reference currents is 1.62 p.u. The impact of the control strategy on the voltage unbalance factors is clearly noticeable especially on the zero-sequence component. This impact is achieved by redistributing the phase currents over the phases. In this particular case, lower current is being injected in phase  $a$  and higher in phases  $b$  and  $c$ . The exact values are listed in Table 3.11 where it can be also seen that the current angles start to differ from their nominal values.

When DER is controlled by the three-phase modified damping control strategy and higher initial values for the damping conductance are chosen such as  $g_d = 4$  p.u. and  $g_d = 8$ , the phase voltage  $V_a$  is significantly decreased whereas  $V_b$  and  $V_c$  are increased. The phase angles have slightly changed as well. Phase voltage  $V_a$  is still below  $v_{cpb}$  but higher than  $v_{cdb}$ , which again enables the damping controller and the final values of the  $g_d$  are 5.49 p.u. and 9.79 p.u. respectively. The impact of the control strategy on the voltage unbalance factors is even more significant compared to the positive-sequence control strategy and when  $g_d = 1$  p.u. were used. This impact is achieved by the better redistribution of the phase currents over

the phases. The exact values are listed in Table 3.11 where it can be also seen that the current angles start to differ from their nominal values in comparison with the positive-sequence control strategy. Overall,  $VUF_0$  is decreased by approximately 46% and  $VUF_2$  by 19%.

### 3.3.2 Obtained experimental results for case 2

In this case, the initial value of phase voltage  $a$  is set to 116V while phase voltages  $b$  and  $c$  remain the same. The no load voltage measurements are listed in Table 3.12 and similarly to *case 1* the voltage unbalance factors are calculated based on the measured phase voltages and angles. The injected phase currents and their angles are listed in Table 3.13 and as it can be seen, despite the active power drooping, the rms values are equal in magnitude, which indeed corresponds to drooped positive-sequence control strategy. When DER is equipped with the positive-sequence control strategy, the potential at the PCC of phase  $a$  rises up to 117.5V, which is higher than  $v_{cpb}$  and the drooping controller is activated. Since  $V_a$  is the highest among the phase voltages, the damping and drooping controllers react based on  $V_a$ . The drooping controller sends a new power set-point to the programmable dc power supply based on the obtained local measurements and thus, the active power is being reduced. In this particular experiment, the positive-sequence control strategy is able to inject only 74 % of the available power. Furthermore, the positive-sequence component is reduced and it can be seen from Table 3.12 that both voltage unbalance factors are very close to the no load measurements.

When DER is controlled by the three-phase modified damping control strategy with  $g_d = 1$  p.u., the phase voltage  $V_a$  is decreased by 0.3V whereas  $V_b$  and  $V_c$  are increased by 0.4V. The phase angles are also slightly changed as well. The measured rms phase voltage  $V_a$  is 117.2V, which is still greater than  $v_{cpb}$  and also  $v_{cdb}$ , which enables both controllers to adjust the damping conductance and the active power injection. In this case, the DER is able to inject 83% of the available power at final value of  $g_d = 1.94$  p.u. and this is achieved due to the better current distribution over the phases with the lower voltages. The exact rms values of the injected phase currents and their angles are listed in Table 3.13. Since the DER is equipped with the modified three-phase damping control strategy, which allows for an improved resistive behaviour towards the zero- and negative-sequence voltage components, the voltage unbalance factors are decreased as listed in Table 3.12.

When an initial value of  $g_d = 4$  p.u. is considered, the phase voltage  $V_a$  rises up to 116.5V, which is only 0.2V higher compared to the no load case and the other two phases have risen by 2.5V. This value is very close to  $v_{cpb}$ , which means that the damping controller almost does not droop any active power. Moreover, the damping controller gives maximum damping conductance value, which has a bigger impact on the zero- and negative-sequence voltage components and there-

| Parameter | $g_d^*$ | $V_a$ [V] | $V_b$ [V] | $V_c$ [V] | $\theta_a$ [°] | $\theta_b$ [°] | $\theta_c$ [°] | VUF <sub>0</sub> | VUF <sub>2</sub> |
|-----------|---------|-----------|-----------|-----------|----------------|----------------|----------------|------------------|------------------|
| No load   | -       | 116.3     | 108.4     | 108.3     | 0              | -120.2         | 119.8          | 2.389            | 2.392            |
| PS        | 0       | 117.5     | 109.6     | 109.5     | 0              | -120.2         | 119.8          | 2.364            | 2.366            |
| $g_d = 1$ | 1.94    | 117.2     | 110       | 109.9     | 0              | -120.3         | 119.9          | 2.054            | 2.254            |
| $g_d = 4$ | 7.99    | 116.5     | 110.7     | 110.6     | 0              | -120.5         | 119.2          | 1.824            | 2.082            |
| $g_d = 8$ | 14.27   | 115.9     | 111.1     | 110.9     | 0              | -120.5         | 119.2          | 1.104            | 1.804            |

Table 3.12: Obtained phase voltage and voltage unbalance factors by means of experiments at  $v_a = 1.057$  p.u. (116.3V)

| Parameter | $g_d^*$ | $I_a$ [A] | $I_b$ [A] | $I_c$ [A] | $\theta_{i,a}$ [°] | $\theta_{i,b}$ [°] | $\theta_{i,c}$ [°] | $P_{dc}$ | $P_{exc}$ |
|-----------|---------|-----------|-----------|-----------|--------------------|--------------------|--------------------|----------|-----------|
| PS        | 0       | 2.474     | 2.455     | 2.468     | -179.3             | 60.3               | -59.5              | 1        | 0.74      |
| $g_d = 1$ | 1.94    | 2.334     | 2.893     | 2.912     | -179.7             | 60.3               | -60.1              | 1        | 0.83      |
| $g_d = 4$ | 7.99    | 1.973     | 3.864     | 3.906     | -181.3             | 60.3               | -62.6              | 1        | 0.99      |
| $g_d = 8$ | 14.27   | 1.41      | 4.267     | 4.326     | -183.3             | 65.8               | -65.1              | 1        | 1         |

Table 3.13: Obtained phase currents and injected power by means of experiments at  $v_a = 1.057$  p.u. (116.3V)

fore, the voltage unbalance factors. The drooped power in this particular case is around 1% and VUF<sub>0</sub> and VUF<sub>2</sub> are reduced by approximately 24% and 13%, respectively.

In the last experiment of this case, the initial damping conductance value is set to 8 p.u. This high  $g_d$  is able to decrease phase voltage  $V_a$  down to 115.9V, which is below the measured value at no load test and even below  $v_{cpb}$ . This means that the droop controller is disabled, hence, the DER injects all available power into the grid. These results are achieved due to the higher final value of  $g_d = 14.27$  p.u. The phase angles are also influenced by the higher value of the damping conductance due to the improved resistive behaviour. The rms values of the injected currents are listed in Table 3.13 as well as their respective angles. As can be seen the angle of  $I_a$  is lagging with  $3.6^\circ$  (compared to the positive-sequence current), which leads to some under excitation in phase  $a$  whereas the currents  $I_b$  and  $I_c$  have phase leading of around  $5^\circ$ , which helps increasing the rms voltage levels in these phases. The voltage unbalanced factors are strongly decreased compared to the no load case by around 54% and 24.5%, respectively.

### 3.3.3 Obtained experimental results for case 3

In the last case,  $V_a$  is set to 118V while the other two voltages remain unchanged. The measured voltages at the PCC at no load and when DER is equipped with the different control strategies are listed in Table 3.14. Since the initial voltage in phase  $a$  is greater than  $v_{cpb}$  the droop controller in the positive-sequence control

| Parameter | $g_d^*$ | $V_a$ [V] | $V_b$ [V] | $V_c$ [V] | $\theta_a$ [°] | $\theta_b$ [°] | $\theta_c$ [°] | VUF <sub>0</sub> | VUF <sub>2</sub> |
|-----------|---------|-----------|-----------|-----------|----------------|----------------|----------------|------------------|------------------|
| No load   | -       | 118.3     | 108.4     | 108.3     | 0              | -120.2         | 119.8          | 2.972            | 2.974            |
| PS        | 0       | 119       | 109.1     | 109       | 0              | -120.2         | 119.8          | 2.953            | 2.955            |
| $g_d = 1$ | 1.74    | 118.7     | 109.5     | 109.3     | 0              | -120.4         | 119.9          | 2.61             | 2.91             |
| $g_d = 4$ | 7.26    | 117.8     | 110.4     | 110.2     | 0              | -120.6         | 120.2          | 1.387            | 2.082            |
| $g_d = 8$ | 15.6    | 117.1     | 111.2     | 111       | 0              | -120.6         | 120.4          | 1.275            | 2.267            |

Table 3.14: Obtained phase voltage and voltage unbalance factors by means of experiments at  $v_a = 1.075$  p.u. (118.3V)

| Parameter | $g_d^*$ | $I_a$ [A] | $I_b$ [A] | $I_c$ [A] | $\theta_{i,a}$ [°] | $\theta_{i,b}$ [°] | $\theta_{i,c}$ [°] | $P_{dc}$ | $P_{exc}$ |
|-----------|---------|-----------|-----------|-----------|--------------------|--------------------|--------------------|----------|-----------|
| PS        | 0       | 1.428     | 1.402     | 1.413     | -176.8             | 62.6               | -57.3              | 1        | 0.43      |
| $g_d = 1$ | 1.47    | 1.272     | 1.811     | 1.83      | -176.8             | 62.1               | -58.7              | 1        | 0.48      |
| $g_d = 4$ | 7.26    | 0.8128    | 3.008     | 3.035     | -178               | 64.5               | -63.2              | 1        | 0.70      |
| $g_d = 8$ | 15.6    | 0         | 4.126     | 4.117     | 0                  | 68.7               | -67.5              | 1        | 0.86      |

Table 3.15: Obtained phase currents and injected power by means of experiments at  $v_a = 1.075$  p.u. (118.3V)

strategy is immediately enabled and droops the active power, thus preventing further overvoltages at the PCC. In this case, phase voltage  $V_a$  rises only by 0.7V up to 119V and the positive-sequence control strategy is able to inject only 43% of the available power.

The performance of the modified three-phase damping control strategy is similar with *case 1* and *case 2*. When an initial value of  $g_d = 1$  p.u. is used, the DER is able to decrease  $v_a$  by 0.3 V and by doing so, the exchanged power is increased to 48% of the nominal. When initial value of  $g_d = 4$  p.u. is used, the modified damping control strategy decreases  $V_a$  by 0.5 V compared to the no load measurement. This effect is already explained in *case 2*. The injected power has risen up to 70% of the nominal one. A remarkable performance is achieved when the value of the damping conductance is set to  $g_d = 8$  p.u. In this experimental case, the control strategy decreases  $V_a$  by 1.2 V, which is accomplished by injecting zero current in phase  $a$  as can be seen in Table 3.15. Although the control strategy is able to inject only 86% of the nominal power, the impact on VUF<sub>0</sub> and VUF<sub>2</sub> is very impressive. Overall, the voltage unbalance factors are decreased by 57% and 24%, respectively, compared to the *No load* results.

### 3.3.4 Discussion

As can be seen from the obtained experimental results, the modified damping control strategy has superior performance compared to the classical positive-sequence control strategy by decreasing the drooping power with 23% compared to *case 2*

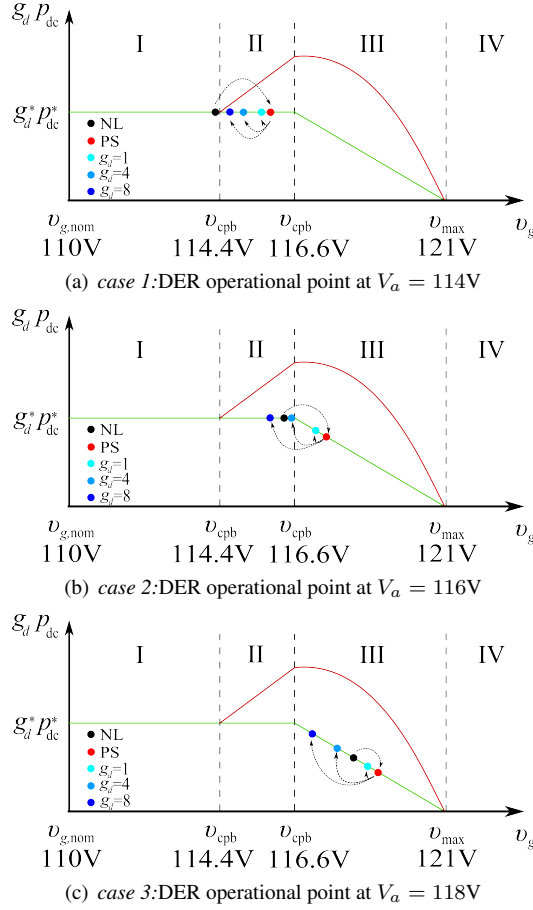


Figure 3.17: Voltage profiles obtained with the different control strategies

and with 43% in case 3. In Fig. 3.17 the operational points of the DER, when equipped with the control strategies under consideration, are depicted. The operating points of Case 1 are presented in Fig. 3.17 (a) where the black dot is the no load measurement, the red dot shows the DER state when the positive-sequence is equipped and with the three nuances of blue dots, the modified damping control strategy with different initial values of  $g_d$  are represented. When the positive-sequence control strategy is used, the DER operational point moves from I to II region where no active power is drooped but still the operational point is close to  $v_{cpb}$ . When the three-phase damping control strategy is used, the operational point of the DER moves closer to I region especially at high values of  $g_d$ .

The operating points of DER, when case 2 is considered, are depicted in Fig. 3.17 (b). The colour arrangement is the same however, the operational points are

located in a different way. The no load measurement shows that phase voltage  $V_a$  is almost at the end of region II and when the positive-sequence control strategy injects currents, the operating point is shifted in region III where active power drooping is applied to prevent overvoltages. The three-phase damping control strategy with an initial value of  $g_d = 1$  p.u. is able to move the operating point backwards but it is still located within region III. If  $g_d = 4$  p.u. or higher is used, the operating point is pushed completely back into region II, which allows the DER to inject all available dc power.

The obtained operating points of DER when *case 3* is considered are depicted in Fig. 3.17 (c). The measured no load voltage is already in the middle of region III, which forces the positive-sequence control strategy to droop significant amount of power. The modified damping control strategy with an initial value of  $g_d = 1$  p.u. performs slightly better but the drooped power still remains high. Setting  $g_d = 4$  p.u. leads to lowering phase voltage  $V_a$  compared to the no load measurement, which leads to less active power drooping but the lowest power drooping is achieved when  $g_d = 8$  p.u. is applied. In summary, in this case all points are located in region III. However, it can be concluded that the modified three-phase damping control strategy has superior performance compared to the positive-sequence control strategy in terms of drooped power and voltage unbalance mitigation.

### 3.4 Conclusions

The modified damping control strategy combines the best properties of the VBDC and the three-phase damping control strategy. The modified damping control strategy does not require communication between the different units and/or a supervisory control, which makes it a robust and self sustainable solution in areas with increased penetration of DERs. In the examined scenarios, it was illustrated by means of simulations that the modified damping control strategy is able to prevent overvoltages and significantly improves voltage profiles compared to the classical control strategies and the variable PF control strategy, which is currently recommended by the standards. Therefore, the DSOs could benefit from the installation of these inverter instead of investing into grid reinforcement.

Furthermore, a comparison between different control strategies is performed and their impact on the power quality in an LV feeder is assessed. From the examined case studies, it can be seen that the reactive power support used for voltage control has negligible impact on the voltage levels in LV grids and it just introduces additional losses in the feeders. Incorporating the active power drooping with the positive-sequence control strategy is able to prevent the overvoltages but unfortunately leads to enormous power drooping, which eventually will lead to more renewable energy curtailment, higher  $VUF_0$  and  $VUF_2$  values and delaying

the revenue for the prosumer. The modified damping control strategy has the most beneficial voltage profiles when high values of the damping conductance are used such as 7 and 20 p.u. Thus, smaller (or none) amount of renewable power is been curtailed while improving the power quality by successfully mitigating overvoltages and voltage unbalance, which eventually can be used to provide ancillary services to the DSO. In addition, a significant reduction of the feeder losses is achieved, which improves the grid efficiency. This beneficial effect is achieved with less than 22% oversizing of the power electronic inverter compared to the classical positive-sequence control strategy with PF control. This makes the modified damping control strategy more suitable for areas with increased penetration of renewable energy resources and power quality problems compared to the positive-sequence control strategy with a variable PF control and the drooped positive-sequence control strategies.



# 4

## Operation modes of the three-phase damping control strategy

In this chapter, a study of the three-phase damping control strategy under different conditions is conducted. In the first part of the chapter, a theoretical examination of the behaviour of the control strategy is performed under different input power values, phase voltages, phase angles and different values of the damping conductance. The theoretical examination is done by using the mathematical model of the control strategy and numerical simulations in Matlab & Simulink. Based on the obtained results, three different operating modes of the control strategy are defined namely zero-power mode, injection mode and consumption mode. Practical limits of the damping conductance value based on three different power ratings (oversizing of 30%, 100% and 200%) of the power electronic inverter are defined. Finally, the zero-power, injection mode and consumption modes are experimentally validated for different values of the damping conductance and phase voltages by using a laboratory set-up.

### 4.1 Mathematical model examination

The purpose of this study is to investigate the behaviour of a DER equipped with the three-phase damping control strategy and the impact on the exchanged currents as a function of different variables. The study is conducted in three stages:

1. In the first one, the exchanged currents are investigated by using only the

mathematical model with certain simplifications and assumptions.

2. The second stage includes investigation in a simulation model where the DER is connected to a real feeder and the impact of the control strategy on the voltage profiles is examined.
3. Finally, the theoretical study is experimentally verified by means of laboratory experiments.

The first stage, is a purely theoretical study of the three-phase damping control strategy, based on the mathematical model of Chapter 2. The outcome of this examination will be used later as a guideline to set practical limits of the damping conductance as well as the physical implementation of the control strategy. The DER is connected to ideal voltage sources  $v_a$ ,  $v_b$  and  $v_c$  through a line impedance  $Z_{x,\text{line}} = \sqrt{R_{x,\text{line}}^2 + X_{Lx,\text{line}}^2}$ , as shown in Fig 4.1. In order to avoid the influence of the line impedance, which leads to voltage changes at the PCC, the former one is set to a negligibly small value. Hence, the voltages at the PCC  $v_a$ ,  $v_b$  and  $v_c$  are equal to the phase voltages of the three-phase source  $v_a$ ,  $v_b$  and  $v_c$ . The voltage unbalance is characterised by the difference in magnitude between the phase voltages as well as difference in the phase angles [18, 79]. Therefore, three case studies are formed as follows:

- Case 1: one of the phase voltages is variable, the other two phase voltages and all angles are fixed and perfectly phase shifted at  $120^\circ$ :

$$\begin{aligned} \underline{v}_a(n) &= |\underline{v}_a|(n) \exp(j(\theta_a)), \text{ where } |\underline{v}_a|(n) \in [0..2.5] \text{ p.u. } \theta_a = 0 \\ \underline{v}_b &= |\underline{v}_b| \exp(j(\theta_b)), \text{ where } |\underline{v}_b| = 1.0 \text{ p.u. } \theta_b = -\frac{2\pi}{3} \\ \underline{v}_c &= |\underline{v}_c| \exp(j(\theta_c)), \text{ where } |\underline{v}_c| = 1.0 \text{ p.u. } \theta_c = +\frac{2\pi}{3} \end{aligned}$$

- Case 2: one of the phase angles is variable, the other two phase angles and

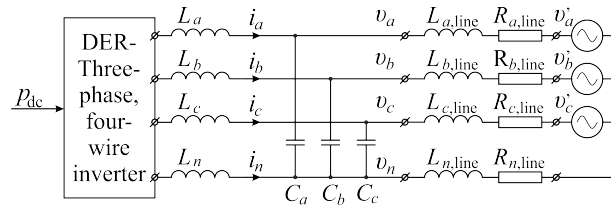


Figure 4.1: Connection diagram of DER and LV grid

all voltages are equal to their nominal values:

$$\underline{v}_a = |\underline{v}_a| \exp(j(\theta_a(m))), \text{ where } |\underline{v}_a| = 1.0 \text{ p.u. } \theta_a(m) \in [-\pi.. + \pi]$$

$$\underline{v}_b = |\underline{v}_b| \exp(j(\theta_b)), \text{ where } |\underline{v}_b| = 1.0 \text{ p.u. } \theta_b = -\frac{2\pi}{3}$$

$$\underline{v}_c = |\underline{v}_c| \exp(j(\theta_c)), \text{ where } |\underline{v}_c| = 1.0 \text{ p.u. } \theta_c = +\frac{2\pi}{3}$$

- Case 3: phase voltage  $v_a$  and phase angle  $\theta_a$  are variables, while the other two phase angles and all voltages are fixed:

$$\underline{v}_a(n, m) = |\underline{v}_a(n)| \exp(j(\theta_a(m))), \text{ where } v_a(n) \in [0..2.5] \text{ p.u. } \theta_a(m) \in [-\pi.. + \pi]$$

$$\underline{v}_b = |\underline{v}_b| \exp(j(\theta_b)), \text{ where } |\underline{v}_b| = 1.0 \text{ p.u. } \theta_b = -\frac{2\pi}{3}$$

$$\underline{v}_c = |\underline{v}_c| \exp(j(\theta_c)), \text{ where } |\underline{v}_c| = 1.0 \text{ p.u. } \theta_c = +\frac{2\pi}{3}$$

The combination of two phase voltages and angles variation will increase significantly the volume of the theoretical study and the added value of it would be relatively small because the reaction of the control strategy could be explained well enough with the cases described above.

Due to the intermittent nature of the renewable resources, the injected power into the grid is not constant and it varies between its zero and nominal value. In [18], it is stated that the value of  $g_1$  is negative and the value  $g_d$  has an opposite sign in case that the three-phase damping control strategy is used in current injection mode. In [69, 79], it is demonstrated that the three-phase damping control strategy can be used as an active rectifier where the value of  $g_1$  is positive, as well as the value of  $g_d$ . In the active rectifier mode, the control strategy consumes less current(s) from the phase(s) with the lower voltage and consumes higher currents (current) from the phases (phase) with the higher voltages (voltage). This feature of the three-phase phase damping control strategy can be very useful when a battery storage system is incorporated and the consumption mode could be used to charge the storage system while mitigating the voltage unbalance at the PCC in unbalanced grids. Hence, examining the extremes would be useful to evaluate the performance of the three-phase damping control strategy and three sub-case studies under zero, nominal input power and nominal output power will be further examined.

Assumptions:

- For simplicity, in this study the efficiency of the power electronic inverter is assumed to be 100%.

- Since the reactive power has a negligible impact on the voltage profiles in LV grids, as demonstrated in Chapter 3, only active power is considered.
- Harmonic distortions are also not considered in this study, which means only the fundamental components are used.
- The DER (the power electronic inverter) is able to exchange infinite phase currents.

In this thesis, it is adopted that the consumed power has a positive sign and the injected power has a negative sign therefore, in case of generation,  $p_{dc}$  is varying between -1 and 0 p.u. and in case of consumption 1 and 0 p.u.

### 4.1.1 Case 1: Three-phase damping control strategy under voltage variations in phase $a$

In this case, the behaviour of the three-phase damping control strategy will be studied under variation of phase voltage  $v_a$  while the other two phase voltages will be kept constant at their nominal values and the phase angles are shifted to  $120^\circ$ . Due to the intermittent nature of the renewable energy resources, the DER will not constantly operate at full power. In addition, there will be periods when the primary source will not deliver any power to the DER. Furthermore, in the near future the electric vehicles, hybrid electric vehicles and battery storage systems will play significant role as flexible loads in the distribution grid. Based on these objectives, Case 1 is split in three sub-cases where further examinations are conducted. More specifically, the control strategy is examined under zero input power, nominal input power and nominal consumed power.

#### 4.1.1.1 Sub-case 1: Three-phase damping control strategy with zero input power and variable phase voltage $v_a$

In this sub-case, the voltage in phase  $a$  is chosen to vary from 0 to 2.5 p.u. Not all values in this range have a practical meaning but they will help to obtain a better understanding of the behaviour of the three-phase damping control strategy. The power balance (2.2) always holds and in this particular sub-case it is written as:

$$\Re(v_a i_a^* + v_b i_b^* + v_c i_c^*) = p_{dc} = 0 \quad (4.1)$$

The mathematical equations that describe the three-phase damping control strategy, which are initially explained in details in Chapter 2, can be rewritten by substituting (4.1) in (2.16). The fundamental input conductance at  $p_{dc} = 0$  p.u. can be written as:

$$g_{1p_{dc}=0, v_a(n)} = -2g_d \frac{|v_a(n)|^2 + |v_b|^2 + |v_c|^2 - A}{|v_a(n)|^2 + |v_b|^2 + |v_c|^2 + 2A} \quad (4.2)$$

where A is:

$$\begin{aligned} A = & |v_a(n)||v_b| \cos(\theta_a - \theta_b - \frac{2\pi}{3}) \\ & + |v_b||v_c| \cos(\theta_b - \theta_c - \frac{2\pi}{3}) \\ & + |v_c||v_a(n)| \cos(\theta_c - \theta_a - \frac{2\pi}{3}) \end{aligned} \quad (4.3)$$

Since  $p_{dc} = 0$  p.u. then the fundamental input conductance only depends on the second term of (2.16). Using the new value of  $g_{1p_{dc}=0, v_a(n)}$  back in the phase currents calculation (2.15) results in:

$$\begin{aligned} \dot{i}_a(n) = & \frac{1}{3} \left\{ g_{1p_{dc}=0, v_a(n)} \left[ |v_a(n)|e^{j\theta_a} + |v_b|e^{j(\theta_b + \frac{2\pi}{3})} + |v_c|e^{j(\theta_c - \frac{2\pi}{3})} \right] \right. \\ & \left. + g_d \left[ 2|v_a(n)|e^{j\theta_a} - |v_b|e^{j(\theta_b + \frac{2\pi}{3})} - |v_c|e^{j(\theta_c - \frac{2\pi}{3})} \right] \right\} \\ \dot{i}_b(n) = & \frac{1}{3} \left\{ g_{1p_{dc}=0, v_a(n)} \left[ |v_b|e^{j\theta_b} + |v_a(n)|e^{j(\theta_a - \frac{2\pi}{3})} + |v_c|e^{j(\theta_c + \frac{2\pi}{3})} \right] \right. \\ & \left. + g_d \left[ 2|v_b|e^{j\theta_b} - |v_a(n)|e^{j(\theta_a - \frac{2\pi}{3})} - |v_c|e^{j(\theta_c + \frac{2\pi}{3})} \right] \right\} \\ \dot{i}_c(n) = & \frac{1}{3} \left\{ g_{1p_{dc}=0, v_a(n)} \left[ |v_c|e^{j\theta_c} + |v_a(n)|e^{j(\theta_a + \frac{2\pi}{3})} + |v_b|e^{j(\theta_b - \frac{2\pi}{3})} \right] \right. \\ & \left. + g_d \left[ 2|v_c|e^{j\theta_c} - |v_a(n)|e^{j(\theta_a + \frac{2\pi}{3})} - |v_b|e^{j(\theta_b - \frac{2\pi}{3})} \right] \right\} \end{aligned} \quad (4.4)$$

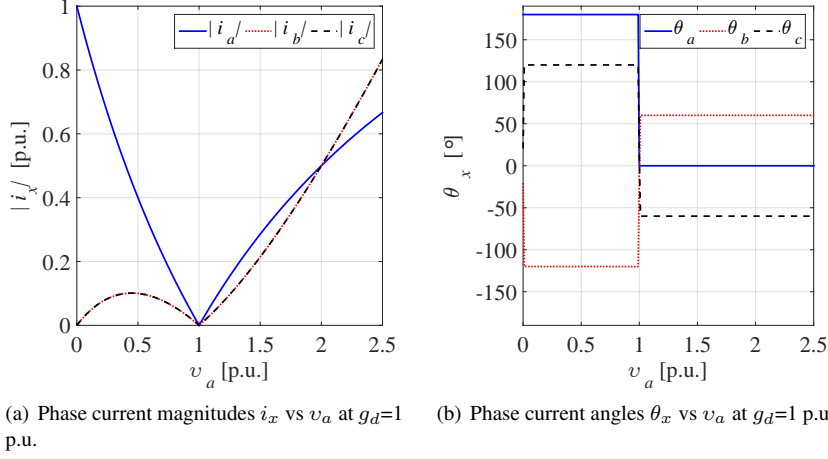
From (4.2) it is evident that if  $g_d = 0$  p.u. (which corresponds to positive-sequence control strategy),  $g_1$  will be zero as well. Also the injected phase currents of (4.4) will be zero. This means that the positive-sequence control strategy will not inject any currents into the grid. Another special case is when there is no voltage unbalance at the PCC then the numerator of (4.2) is zero, which means no power flow occurs between the DER and the grid. In all other cases, the numerator differs from zero, hence  $g_1 \neq 0$  and if  $g_d > 0$  p.u. there is power exchange between the DER and the grid is present.

Taking into account that  $v_b = v_c = 1$  p.u. and solving for  $v_a$ , a further simplification of (4.4) can be done and it leads to an equation that is easier to be interpreted:

$$\dot{i}_a(v_a) = \frac{2g_d(v_a - 1)}{v_a + 2} \quad (4.5)$$

$$\dot{i}_b(v_a) = \dot{i}_c(v_a) = -\frac{g_d v_a^2 - g_d v_a}{v_a + 2} \quad (4.6)$$

Local extrema can be found by using the first derivative of the equations above. However, Eq. (4.5) is a first order (odd function) equation so there are no local extrema. Eq. (4.6) is a second order equation (even function) and in the investigated range  $0 \leq v_a \leq 2.5$  p.u. this quadratic function has one extremum, which can be found by the root of the first derivative of (4.6). Since the phase voltages are



(a) Phase current magnitudes  $i_x$  vs  $v_a$  at  $g_d=1$  p.u. (b) Phase current angles  $\theta_x$  vs  $v_a$  at  $g_d=1$  p.u.

Figure 4.2: Exchanged phase currents as a function of the phase voltage  $v_a$  and the damping conductance  $g_d=1$  p.u. when the input power  $p_{dc}=0$  p.u. and the phase angles are perfectly shifted at  $120^\circ$  electrical degrees

shifted at exactly  $120^\circ$  the influence of the phase angles can be neglected and the final result is:

$$i'_b(v_a) = -g_d \frac{(v_a^2 + 4v_a - 2)}{(v_a + 2)^2} \quad v_a \in [0 \dots 2.5] \text{ p.u.}, g_d = 1 \text{ p.u.} \quad (4.7)$$

Eq. (4.6) has three roots: (i)  $v_a = -2$  from the denominator, which is out of the investigated range and (ii)  $v_a = 0$  and (iii)  $v_a = 1$ . Eq. (4.7) has an extremum for the given region, which is a minimum of  $i_{b,\min} = -0.101$  p.u. at  $v_a = 0.4495$  p.u. This equation also shows that the roots are invariant to the value of the damping conductance  $g_d$ . These three points will be used for splitting the obtained results into three regions  $0 \leq v_a \leq 0.4495$ ,  $0.4495 \leq v_a \leq 1$  and  $1 \leq v_a \leq 2.5$ , which will bring more clarity during the interpretation of the obtained results.

As mentioned in [69] in case of power injection, the fundamental input conductance  $g_1$  has a negative sign and the damping conductance  $g_d$  has a positive sign. If the damping control strategy is used in active rectification mode, both parameters have a positive sign. Consequently, the injected active current is shifted  $180^\circ$  with respect to the voltage and  $0^\circ$  in case of current consumption. This holds for all phase currents. The relationships between the phase currents and phase angles versus the variation of phase voltage  $v_a$  are depicted in Fig. 4.2. The simulation results are obtained under  $p_{dc} = 0$  and  $g_d = 1$  p.u.

- interval  $0 \leq v_a \leq 0.4495$ : When the voltage  $v_a$  tends to 0, phase currents  $i_b$  and  $i_c$  tend to zero as well, whereas phase current  $i_a$  is at its maximum.

When  $v_a$  is increasing then  $i_a$  starts decreasing while  $i_b$  and  $i_c$  are increasing because the denominator becomes dominant in this region. According to (4.6) phase currents  $i_b$  and  $i_c$  have a minimum but due to the fact that in Fig. 4.2 (a) the absolute values are used, the results appear as a local maximum. However, the phase angles are depicted in Fig. 4.2 (b), which shows the actual sign of the currents. In this range of phase voltage  $v_a$ , the denominator is dominant and the currents tend to the local minimum. Fig. 4.2 (b) shows that current  $i_a$  is phase shifted at  $180^\circ$ , which corresponds to current injection, whereas phase current  $i_b$  and  $i_c$  are  $0^\circ$  shifted, which corresponds to current consumption from the grid. When  $v_a = 0.4495$  is reached phase currents  $i_b$  and  $i_c$  reach their minimum, too. Despite the big difference in the magnitudes between phase current  $i_a$  and  $i_b = i_c$  the power balance always holds and in this region is expressed as:

$$\Re(v_a i_a^*) = -\Re(v_b i_b^* + v_c i_c^*) \quad (4.8)$$

where the injected power in phase  $a$  is the sum of the consumed power from phases  $b$  and  $c$ . This shows that the control strategy has two modes of operations, i.e., grid consumption mode and grid injection mode and both modes can be present simultaneously in the different phases despite that the sign of  $g_1$  is negative and  $g_d$  positive.

- interval  $0.4495 < v_a \leq 1$ : When phase voltage  $v_a$  is in this range, the numerator becomes dominant and phase currents  $i_b$  and  $i_c$  are increasing while phase current  $i_a$  is still decreasing. All currents are equal to zero at  $v_a = 1$  p.u. because the phase voltages at the PCC become balanced. This state will be called the “border mode” and it will be used further in this thesis. In this region, the signs of the injected currents are the same as the previous region and the power balance corresponds to (4.8).
- interval  $1 < v_a \leq 2.5$ : When phase voltage  $v_a$  is within this region, phase current  $i_a$  changes its sign and a transition occurs from grid injection mode to grid consumption mode and vice versa for phase currents  $i_b$  and  $i_c$ . The power balance (4.8) still holds but in this region power is being consumed from phase  $a$  and injected back into the grid via phases  $b$  and  $c$ .

The conducted analyses, which are presented in Fig. 4.2 (a) and (b) are performed only under one value of the damping conductance ( $g_d = 1$  p.u.). Chapter 3 demonstrated that the damping conductance  $g_d$  plays a crucial role for the performance of the three-phase damping control strategy towards the voltage unbalance mitigation. In the next simulations, a more comprehensive analysis is performed where both phase voltage  $v_a$  and the damping conductance  $g_d$  are considered as variables. In Fig. 4.3 the values of  $g_1$  are calculated by using (4.2) and in this

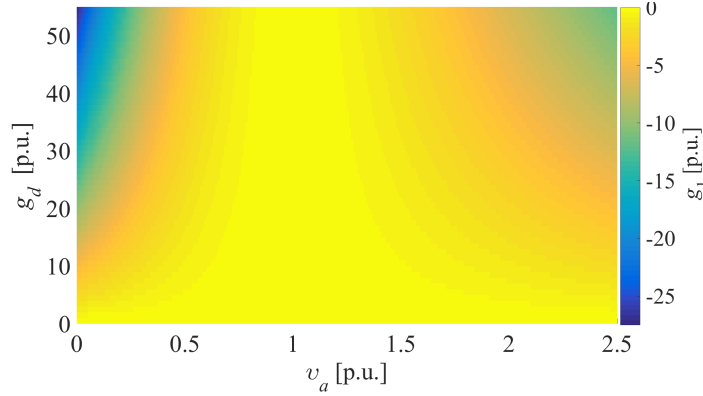
(a)  $g_1$  as a function of  $v_a$  and  $g_d$ 

Figure 4.3: Fundamental input conductance dependency as a function of the phase voltage  $v_a$  and  $g_d$  at nominal phase angles and zero input power  $p_{dc} = 0$  p.u.

simulation  $g_d$  varies from 0 to 55 p.u. When  $g_d$  is equal to zero, the input conductance  $g_1$  is also equal to zero and this is valid for the entire range of  $v_a$ . With the increase of the damping conductance  $g_d$ , the input conductance  $g_1$  increases as well, especially in the regions where the highest voltage unbalance is present i.e. in the extreme values of  $v_a$ , which will lead to high phase currents (almost 55 p.u.).

The magnitude of the phase currents  $i_a$ ,  $i_b$  and  $i_c$  that flow between the DER and grid are depicted in Fig 4.4 (a), (c) and (e), respectively. Their corresponding phase angles  $\theta_{i,a}$ ,  $\theta_{i,b}$  and  $\theta_{i,c}$  are depicted in Fig 4.4 (b), (d) and (f). In these different intervals the magnitudes and the phase angles of the exchanged phase currents can be described as:

- interval  $0 \leq v_a \leq 0.4495$ : when the voltage  $v_a$  tends to zero and  $g_d$  equals zero, then all currents are equal to zero for the entire range of  $v_a$ . When  $g_d$  increases, the phase currents  $i_a$  and  $i_b$  increase too because as can be seen from (4.5) and (4.6) they are proportional to  $g_d$ . At high values of  $g_d$  and  $v_a$  tending to zero, phase current  $i_a$  assumes very high values close to 55 p.u. while  $i_b$  and  $i_c$  are tending to zero. Although the difference in the currents is very big, the power balance still obeys on (4.8). With increasing  $v_a$ , phase current  $i_a$  starts decreasing while  $i_b$  and  $i_c$  are increasing until they reach the local maximum at  $v_a = 0.4495$  p.u. The obtained phase angles are depicted in Fig. 4.4 (b), (c) and (d). As it can be seen in this range phase current  $i_a$  is  $180^\circ$  shifted with respect to  $v_a$ , which corresponds to phase injection mode and currents  $i_b$  and  $i_c$  are  $0^\circ$  shifted, which corresponds to current consumption mode. This holds for the entire range of  $g_d$  and it can be seen from Fig. 4.4 (b), (d) and (e) as well as (4.5) and (4.6).

- interval  $0.4495 < v_a \leq 1$ : When phase voltage  $v_a$  is in this range, the numerator of (4.5) becomes dominant and phase currents  $i_b$  and  $i_c$  are increasing while phase current  $i_a$  is still decreasing. Although  $g_d$  can assume high values, all currents are equal to zero at  $v_a = 1$  p.u. because the phase voltages at the PCC are balanced, which is the border mode of the control strategy where no power is being injected.

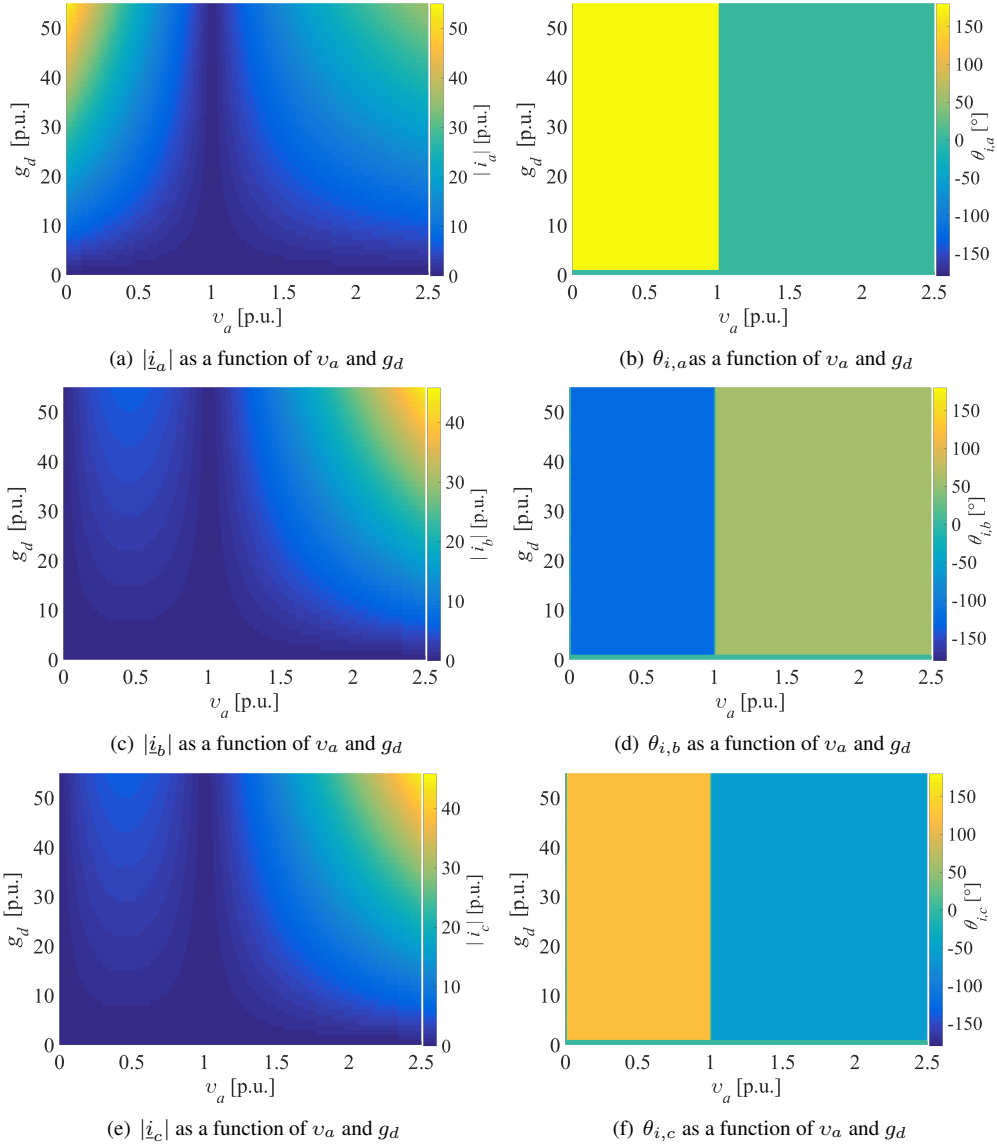


Figure 4.4: Phase currents dependency on the variation of the phase voltage  $v_a$  and the damping conductance  $g_d$  at nominal phase angles and zero input power  $p_{dc} = 0$  p.u.

- interval  $1 < v_a \leq 2.5$ : The transition from current injection to consumption or vice versa under  $p_{dc} = 0$  p.u. condition is present when  $v_a = 1$  p.u. then all phase currents  $i_a = i_b = i_c = 0$  p.u. and it holds for the entire range for the damping conductance i.e.  $0 \leq g_d \leq 55$ . From the moment when  $v_a$  passes the threshold 1.0 p.u. all phase currents shift their phase angles independently of the value of  $g_d$  (this is true if  $g_d \neq 0$ ). The power balance (4.8) still holds but in this region power is being consumed from phase  $a$  and injected back into the grid via phases  $b$  and  $c$ . The magnitudes of the injected and consumed currents are proportional to the damping conductance  $g_d$ .

In this example, the three-phase damping control strategy is not supplied with any input power but the results show that it possesses the ability to balance the voltages at the PCC by consuming current from the phase with the highest voltage and injects it back in the phases with the lowest voltages. The balancing properties are proportional to the damping conductance  $g_d$  and this ability is present for the entire range of  $v_a$  (except  $v_a = 1$  p.u.) and for the entire range of  $g_d$  (except for  $g_d = 0$  p.u.). This valuable property of the three-phase damping control strategy to improve the power quality at the PCC can be used during periods with low production or even zero production coming from the primary source (PV, wind,  $\mu$ CHP, etc.).

#### 4.1.1.2 Sub-case 2: Three-phase damping control strategy under nominal input power at variable phase voltage $v_a$

The tests of this sub-case are performed under the same conditions as the previous one ( $0 \leq v_a \leq 2.5$  p.u.  $g_d = 1$  p.u. and ideal phase shift between the three phase voltages) except that the input power is set to be equal to its nominal value i.e.  $p_{dc} = -1$  p.u., which corresponds to a DER that will inject maximum power to the grid. Therefore, the fundamental input conductance at this conditions can be written as:

$$g_{1p_{dc}=1, v_a(n)} = \frac{3p_{dc}}{|v_a(n)|^2 + |v_b|^2 + |v_c|^2 + 2A} - 2g_d \frac{|v_a(n)|^2 + |v_b|^2 + |v_c|^2 - A}{|v_a(n)|^2 + |v_b|^2 + |v_c|^2 + 2A} \quad (4.9)$$

where  $A$  is the same as (4.3) and the injected currents are calculated by using (4.4). In this sub-case, phase currents  $i_b$  and  $i_c$  have the same magnitude for the entire range of  $v_a$  because  $v_b = v_c = 1$  p.u. Hence, expanding (2.15), simplifying further and solving it for  $v_a$ ,  $g_d$  and  $p_{dc}$  it yields to:

$$\dot{i}_b = -\frac{g_d v_a^2 - g_d v_a - p_{dc}}{v_a + 2} \quad (4.10)$$

Eq. (4.10) has three roots  $v_{a,1} = -2$  from the denominator and two complex roots from the numerator:  $v_{a,2} = 0.5 - i0.866$  and  $v_{a,3} = 0.5 + i0.866$ . The first two roots are out of the investigated range of  $v_a$  and the third root  $v_{a,3}$  shows the current magnitude and angle. As opposed to (4.6), equation (4.10) does not bring sufficient information concerning different operational regions. However, in this equation the magnitudes of the phase currents  $i_b$  and  $i_c$  are proportionally dependent on the damping conductance  $g_d$  as well as the input power  $p_{dc}$  while in the previous sub-case only  $g_d$  contributed for the current magnitudes. Furthermore, this quadratic function has an extremum in the investigated range  $0 \leq v_a \leq 2.5$  p.u. and it can be found by the first derivative of (4.10). Since the phase voltages at the PCC are perfectly phase shifted at  $120^\circ$ , the influence of the phase angles can be neglected and the final expression for the first derivative can be written as:

$$i_b'(v_a) = -\frac{(g_d v_a^2 + 4g_d v_a - 2g_d + p_{dc})}{(v_a + 2)^2}$$

$$v_a \in [0 \dots 2.5] \text{ p.u.}, g_d = 1 \text{ p.u.}, p_{dc} = -1 \text{ p.u.} \quad (4.11)$$

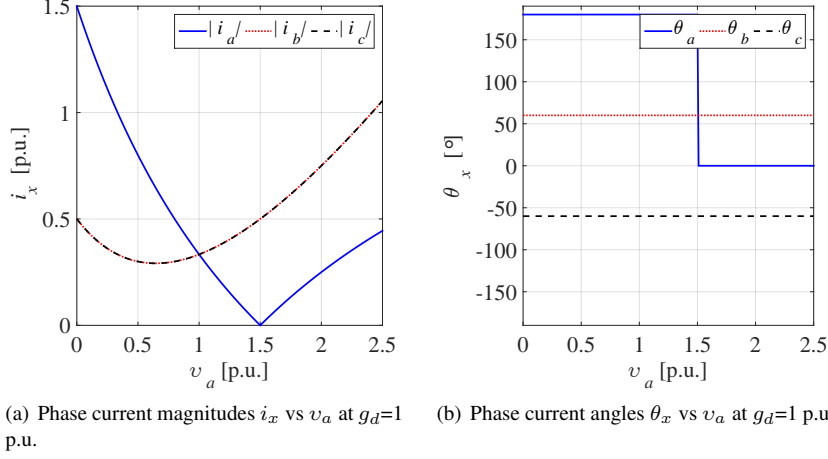
Solving (4.11) for the given region when using  $g_d = 1$  p.u. and  $p_{dc} = -1$  p.u. shows that the current  $i_b$  has a minimum of 0.2915 p.u. at  $v_a = 0.6458$  p.u. This point will be used later for explaining in details how the control strategy behaves when  $v_a$  assumes values between 0 and 0.6458 p.u.

The magnitude of phase current  $i_a$  is obtained in the same manner i.e by expanding (2.15), simplifying and solving it for  $v_a$ ,  $g_d$  and  $p_{dc}$ :

$$i_a = \frac{2g_d v_a - 2g_d + p_{dc}}{v_a + 2} \quad (4.12)$$

Eq. (4.12) has one root at  $v_{a,2} = 1.5$  in the investigated range for  $v_a$  when  $g_d = 1$  p.u. and  $p_{dc} = -1$  p.u. Consequently, the investigated ranges in this sub-case are formulated as follows:  $0 \leq v_a \leq 0.6458$ ,  $0.6458 < v_a \leq 1.5$  and  $1.5 < v_a \leq 2.5$ . The obtained simulation results for the magnitudes of the phase currents  $i_a$ ,  $i_b$  and  $i_c$ , as well as the corresponding phase angles  $\theta_{i,a}$ ,  $\theta_{i,b}$  and  $\theta_{i,c}$  are shown in Fig. 4.5 (a) and (b), respectively. The different regions are described as follows:

- $0 \leq v_a \leq 0.6458$ : When  $v_a$  tends to zero, the injected phase current in phase  $a$  is  $i_a = 1.5$  p.u. and the other two currents are  $i_b = i_c = 0.5$  p.u. With the increasing of  $v_a$  up to 0.6458 p.u. all currents are decreasing and as it was mentioned above, this is the local minimum for  $i_b = i_c$ , while  $i_a$  continuous to decrease. When phase voltage  $v_a$  is within this interval, all phase currents are phase shifted at  $180^\circ$  therefore, all phase currents are being injected into the grid and the DER mitigates the voltage unbalance at the PCC by relying on the renewable power delivered by the primary source. The power balance for this region is described by (2.2).



(a) Phase current magnitudes  $i_x$  vs  $v_a$  at  $g_d=1$  p.u. (b) Phase current angles  $\theta_x$  vs  $v_a$  at  $g_d=1$  p.u.

Figure 4.5: Relationship between the phase voltage  $v_a$  and the damping conductance  $g_d = 1$  p.u. when the input power  $p_{dc} = -1$  p.u. and the phase angles are perfectly shifted at  $120^\circ$  electrical degrees

- $0.6458 < v_a \leq 1.5$ : In this interval, phase current  $i_a$  is still decreasing and phase currents  $i_b$  and  $i_c$  are increasing with the increasing of  $v_a$ . In this interval, as well as in the previous one, the DER mitigates the voltage unbalance at the PCC by relying on the renewable power delivered by the primary source and the power balance is described by (2.2). Up to this point all phase angles are phase shifted at  $180^\circ$  with respect to their phase voltage, hence DER injects currents into the grid. When  $v_a = 1.5$  p.u. then phase current  $i_a$  becomes zero and all available power is being injected into phases  $b$  and  $c$ . Unlike the previous case, here the border mode occurs in only one phase, which is the one with the highest voltage.
- $1.5 < v_a \leq 2.5$ : In this region, the phase currents are increasing with the increasing  $v_a$  but  $i_a$  changes its phase angle and from current injection this phase switches to current consumption mode. This means that the control strategy tries to mitigate the voltage unbalance at the PCC by the power delivered by the primary source in combination with the consumed power from phase  $a$ . Hence, the power balance in this region can be expressed as:

$$p_{dc} + \Re(\underline{v}_a \underline{i}_a^*) = -\Re(\underline{v}_b \underline{i}_b^* + \underline{v}_c \underline{i}_c^*) \quad (4.13)$$

These simulation results were obtained with a damping conductance of 1 p.u. The next examination shows the influence of different values of the damping conductance on the phase currents magnitudes and their phase angles. In this simulation, the phase voltage is within the range of  $0 \leq v_a \leq 2.5$  p.u. as well as

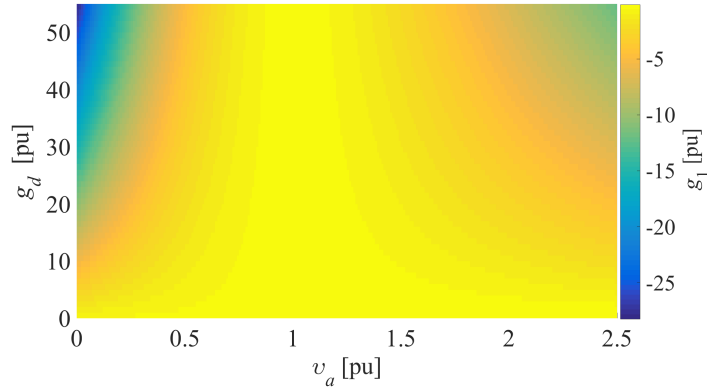


Figure 4.6: Fundamental input conductance dependency on the variation of the phase voltage  $v_a$  and damping conductance  $g_d$  at nominal phase angles and nominal input power  $p_{dc} = -1$  p.u.

the damping conductance, which varies between  $0 \leq g_d \leq 55$  p.u. In Fig. 4.6 (a) is shown the fundamental input conductance  $g_1$  and its dependency on  $g_d$  and  $v_a$ . As can be seen it is very similar to Fig. 4.3 with the only difference that the initial value of  $g_1$  is not 0 but 0.333 p.u., which is the nominal value of  $g_1$  when the control strategy operates under nominal phase voltage values and balanced grid conditions.

The obtained results for the phase currents are depicted in Fig. 4.7 (a), (c) and (e) and their corresponding angles are shown in Fig. 4.7 (b), (d) and (f), respectively. Here as well the behaviour of the damping control strategy will be described in the different regions that were used above:

- $0 \leq v_a \leq 0.6458$ : When  $v_a$  is in this region, phase current  $i_a$  is approximately equal to the value of  $g_d$  and this can be seen in (4.12) while the values of phase currents  $i_b$  and  $i_c$  are determined entirely by the input power  $p_{dc}$ , which can be seen in (4.10). When  $v_a$  is within this region and  $g_d$  is low, phase current  $i_a$  is also low and increases proportionally with the increase of  $g_d$ , which corresponds to (4.12). The phase angle  $\theta_{i,a}$  is  $180^\circ$  phase shifted with respect to  $\theta_a$  for the entire range of  $g_d$ . Hence, the control strategy operates in a current injection mode. By further increasing  $g_d$ , the phase currents  $i_b$  and  $i_c$  are decreasing and become zero at  $g_d = 4$  p.u. and  $v_a = 0.6458$  where the two roots, which are determined by the numerator of (4.10) are  $v_{a,2} = v_{a,3} = 0.5$ . Therefore, the border mode for these two currents is reached and further increase of  $g_d$  will lead to a sign change of  $i_b$  and  $i_c$ . The exact value of the border mode occurrence in this region is set by the second root  $v_{a,2}$  of (4.10) and it can be seen that when  $g_d$  assumes high values  $v_{a,2} \rightarrow 0$  and the border mode occurs at smaller values of  $v_a$  and at

high values of  $g_d$ . The power balance in this region can be mathematically described as follows:

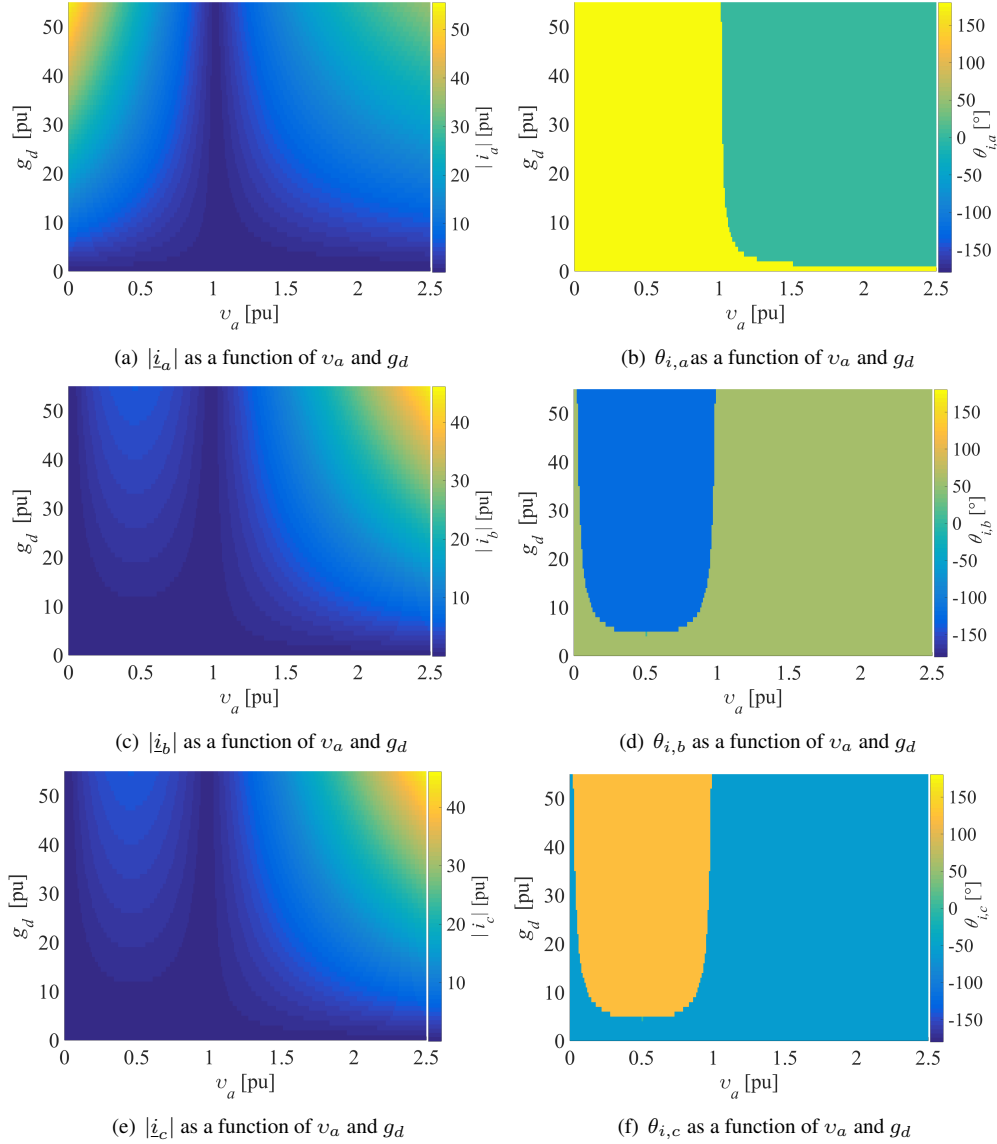


Figure 4.7: Phase currents dependency on the variation of the phase voltage  $v_a$  and damping conductance  $g_d$  at nominal phase angles and nominal input power  $p_{dc} = -1$  p.u.

- if  $i_b < v_{a,2}$  in the investigated intervals  $0 \leq v_a \leq 0.6458$  and  $0 \leq g_d \leq 55$ , the power balance is described as (2.2).
- If  $i_b = v_{a,2}$  in the investigated intervals  $v_a = 0.6458$  and  $g_d = 4$ , then

$i_b = i_c = 0$  and the power balance is described as:

$$p_{dc} = \Re(\underline{v}_a \underline{i}_a^*) \quad (4.14)$$

– If  $i_b > v_{a,2}$  in the investigated intervals  $0 \leq v_a \leq 0.6458$  and  $4 \leq g_d \leq 55$ , the power balance is described as (4.13).

- $0.6458 < v_a \leq 1$ : As in the previous region, in this one as well, phase current  $i_a$  is still decreasing with increasing  $v_a$  but its angle remains unchanged. Phase currents  $i_b$  and  $i_c$  decrease with the increasing of  $g_d$  up to 4 p.u. but by increasing the damping conductance the border mode occurs at higher values of  $v_a$ . The border mode in this region is determined by  $v_{a,3}$  and its exact value can be calculated via (4.10). From (4.10) it can be also seen that if  $g_d \rightarrow \infty$  then  $v_{a,3} \rightarrow 1$ . When  $v_a = 1$  p.u. all phase currents are equal in magnitude and they are invariant to the value of the damping conductance. The power balance in this region is described as:

– If  $i_b < v_{a,3}$  in the investigated intervals  $0 \leq v_a \leq 0.6458$  and  $0 \leq g_d \leq 55$ , the power balance is described as (4.13) .

– If  $i_b = v_{a,3}$  in the investigated intervals  $v_a = 0.6458$  and  $g_d = 4$ , then  $i_b = i_c = 0$  and the power balance is described as:

$$p_{dc} = \Re(\underline{v}_a \underline{i}_a^*) \quad (4.15)$$

– If  $i_b > v_{a,3}$  in the investigated intervals  $0.6458 < v_a \leq 1$  and  $0 \leq g_d \leq 55$ , the power balance is described as (2.2).

- $1 < v_a \leq 2.5$ : In this region, the angles of phase currents  $i_b$  and  $i_c$  remain  $180^\circ$  phase shifted with respect to their phase voltages, which corresponds to a current injection mode. On the other hand, the phase angle  $\theta_{i,a}$  of phase current  $i_a$  is strongly dependable on  $g_d$  and  $v_a$ . The exact values of border mode where  $i_a = 0$  at different values of  $g_d$  and  $v_a$  can be calculated via (4.12) and they are equal to the second root  $v_{a,2}$ , which can be seen in Fig. 4.7 (b). Above this value, phase angle  $\theta_{i,a}$  is no longer phase shifted at  $180^\circ$  with respect to  $v_a$  and the control strategy starts consuming power from phase  $a$  and injecting it back into the grid via phases  $b$  and  $c$ . The power balance in this region is:

– If  $i_a < v_{a,2}$  in the investigated intervals  $1 < v_a \leq 2.5$  and  $0 \leq g_d \leq 55$ , the power balance is described as (2.2) .

– If  $i_a = v_{a,2}$  in the investigated intervals  $1 < v_a \leq 2.5$  and  $0 \leq g_d \leq 55$ , then  $i_a = 0$  and the power balance is described as:

$$p_{dc} = \Re(\underline{v}_b \underline{i}_b^* + \underline{v}_c \underline{i}_c^*) \quad (4.16)$$

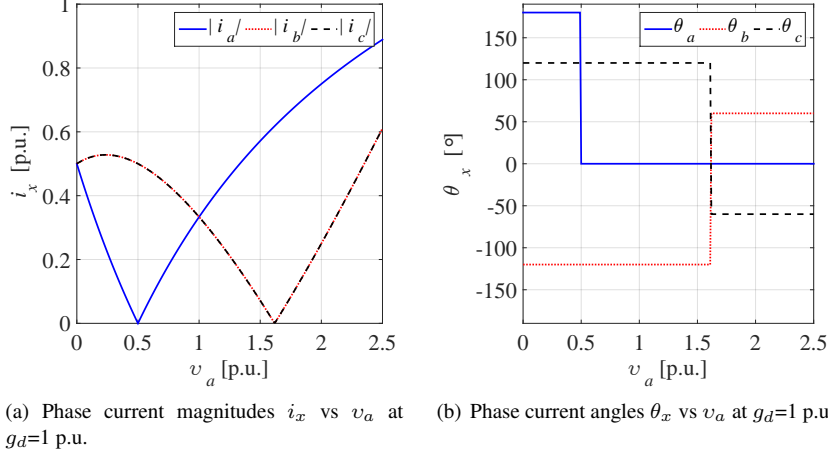


Figure 4.8: Relationship between the phase voltage  $v_a$  and the damping conductance  $g_d = 1$  p.u. when the input power  $p_{dc} = 1$  p.u. and the phase angles are perfectly shifted at  $120^\circ$  electrical degrees

- If  $i_a > v_{a,a}$  in the investigated intervals  $1 < v_a \leq 2.5$  and  $0 \leq g_d \leq 55$ , the power balance is described as (4.13).

From the obtained results in sub-case 2 can be concluded that unlike the positive-sequence control strategy, the three-phase damping control strategy is able to mitigate the voltage unbalance at the PCC by redistributing the available renewable power among the phases. Furthermore, at high values of  $g_d$ , the control strategy starts consuming power from the phase with the higher voltage and injecting it back into the grid through the other two phases.

#### 4.1.1.3 Sub-case 3: Three-phase damping control strategy under nominal consumed power and variable phase voltage $v_a$

In this sub-case, the three-phase damping control strategy is examined in a consumption mode. To decrease the curtailed energy in areas with high penetration of DERs, big battery banks are used absorb the excessive power and later source it back to the grid. These centralised battery storage banks are usually connected at strategic points in the LV grid targeting, besides less drooped power, but also some specific power quality problems. This mode of the three-phase damping control strategy could be used to supply a load at the dc side such as a centralised battery storage system as studied in [69], decentralised storage applications of it can be integrated in three-phase battery chargers for EV and plug-in HEV as studied in [80].

The input power then is set to  $p_{dc} = 1$  p.u., which corresponds to power consumption and to achieve voltage unbalance mitigation, the damping conductance is also set to be positive ( $g_d = 1$  p.u.). The obtained simulation results for the magnitudes of the phase currents  $i_a$ ,  $i_b$  and  $i_c$ , as well as the corresponding phase angles  $\theta_{i,a}$ ,  $\theta_{i,b}$  and  $\theta_{i,c}$  are shown in Fig. 4.8 (a) and (b), respectively. By making (4.10) and (4.12) into characterisation equations the border mode can be found for the different phase voltage values. Eq. (4.12) has one root at  $v_a = 0.5$  p.u. and eq. (4.10) has two roots but only one root at  $v_a = 1.6180$  p.u., which is within the investigated range of  $v_a$ . In addition, the first derivative of (4.10) gives an extremum at  $v_a = 0.2361$  p.u. All different regions can now be defined, starting from  $0 \leq v_a < 0.236$  p.u.  $0.236 \leq v_a < 0.5$  p.u.  $0.5 \leq v_a < 1$  p.u.  $1 \leq v_a < 1.618$  p.u. and  $1.618 \leq v_a \leq 2.5$  p.u.

- $0 \leq v_a < 0.236$ : In this interval, phase current  $i_a$  is decreasing while phase currents  $i_b$  and  $i_c$  are increasing. Fig. 4.8 (b), shows that the phase angle  $\theta_{i,a}$  is  $180^\circ$  shifted compared to  $\theta_a$  therefore, due to the low values of  $v_a$ , the control strategy tries to mitigate the voltage unbalance at the PCC by consuming power from phases  $b$  and  $c$  and injects it back into phase  $a$ . The power balance obeys (4.13).
- $0.236 \leq v_a < 0.5$ : All phase currents are decreasing in this interval and  $i_a$  tends to 0 when  $v_a$  is close to 0.5 p.u. The power balance still obeys (4.13).
- $0.5 \leq v_a < 1$ : At  $v_a = 0.5$  p.u. occurs the border mode of phase  $a$ . From this point on,  $i_a$  increases and all phases consume power from the grid. With the increase of  $v_a$  all phase currents tend to their nominal values of 0.333 p.u. The power balance obeys (2.2).
- $1 \leq v_a < 1.618$ : When  $v_a = 1$  p.u. all phase currents equal their nominal value of 0.333 p.u. and with the further increase of  $v_a$ , phase current  $i_a$  increases, while phase currents  $i_b$  and  $i_c$  are decreasing. The former ones decrease up to the point where  $v_a = 1.618$  p.u. In this region, the power balance also obeys to (2.2).
- $1.618 \leq v_a \leq 2.5$ : In the last region, the border mode of phase currents  $i_b$  and  $i_c$  occurs when  $v_a = 1.618$  p.u. Further increase of  $v_a$  leads to an angle shift of  $\theta_{i,b}$  and  $\theta_{i,c}$  with respect to their phase voltages and power is being consumed from phase  $a$  and injected back into phases  $b$  and  $c$ . The power balance in this region can be described by using (4.13).

From the obtained results up to this point can be concluded that the three-phase damping control strategy when employed in power consumption mode, is able to mitigate the voltage unbalance at the PCC also by consuming more current from the phase with the highest voltage and less current from the phases with the

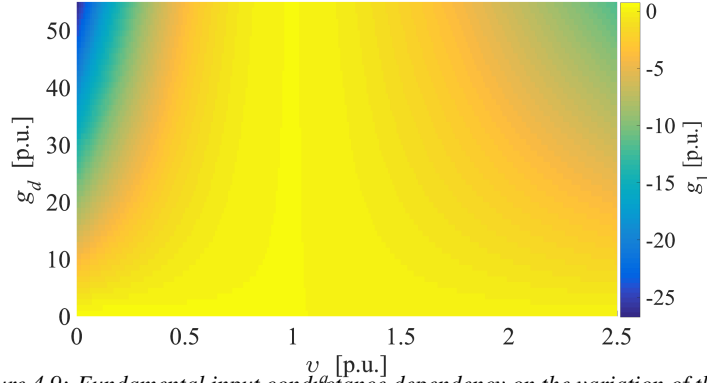


Figure 4.9: Fundamental input conductance dependency on the variation of the phase voltage  $v_a$  and damping conductance  $g_d$  at nominal phase angles and nominal input power  $p_{dc} = 1$  p.u.

lowest voltages. In contrast, the positive-sequence control strategy will consume only positive-sequence current and will not impact the zero- and negative-sequence voltage components.

These simulation results were obtained with a damping conductance  $g_d = 1$  p.u. The next study shows the influence of different values of the damping conductance over the phase currents magnitudes and phase angles. In this simulation, the phase voltage  $0 \leq v_a \leq 2.5$  pu. as well as the damping conductance, which varies between  $0 \leq g_d \leq 55$  p.u.

In Fig. 4.9 is shown the fundamental input conductance  $g_1$  dependency on  $g_d$  and  $v_a$ . Although  $p_{dc}$  is positive the dominant term in this case in (2.16) is the second one because  $g_d$  ranges from 0 to 55 p.u.

This sub-case can be described by the same equations as sub-case 2 i.e. (4.4), which are solved for  $p_{dc} = 1$  p.u. and variable  $g_1$ . Phase currents  $i_a$ ,  $i_b$  and  $i_c$  are depicted in Fig. 4.10 (a), (c) and (e), respectively. These results show that the phase currents tend to extremely high values when  $g_d$  assumes high values and  $v_a$  is in its extremes. If  $v_a$  is close to its nominal value, then the injected currents are decreasing due to the less unbalance at the PCC. Finally, if  $v_a = 1$  p.u. all phase currents equal their nominal value and they are invariant of the value of the damping conductance  $g_d$ .

All angles  $\theta_{i,a}$ ,  $\theta_{i,b}$  and  $\theta_{i,c}$  of the injected phase currents are depicted in Fig. 4.10 (b), (d) and (f), respectively. By using the characterisation equations (4.10) and (4.12) the border mode of the three-phase damping control strategy can be found when operating in rectifier mode. The simulation results show that the border mode occurs when  $v_a$  is far from its nominal values. At high values of the damping conductance, the border mode occurs at values, which are closer to the nominal values of  $v_a$ .

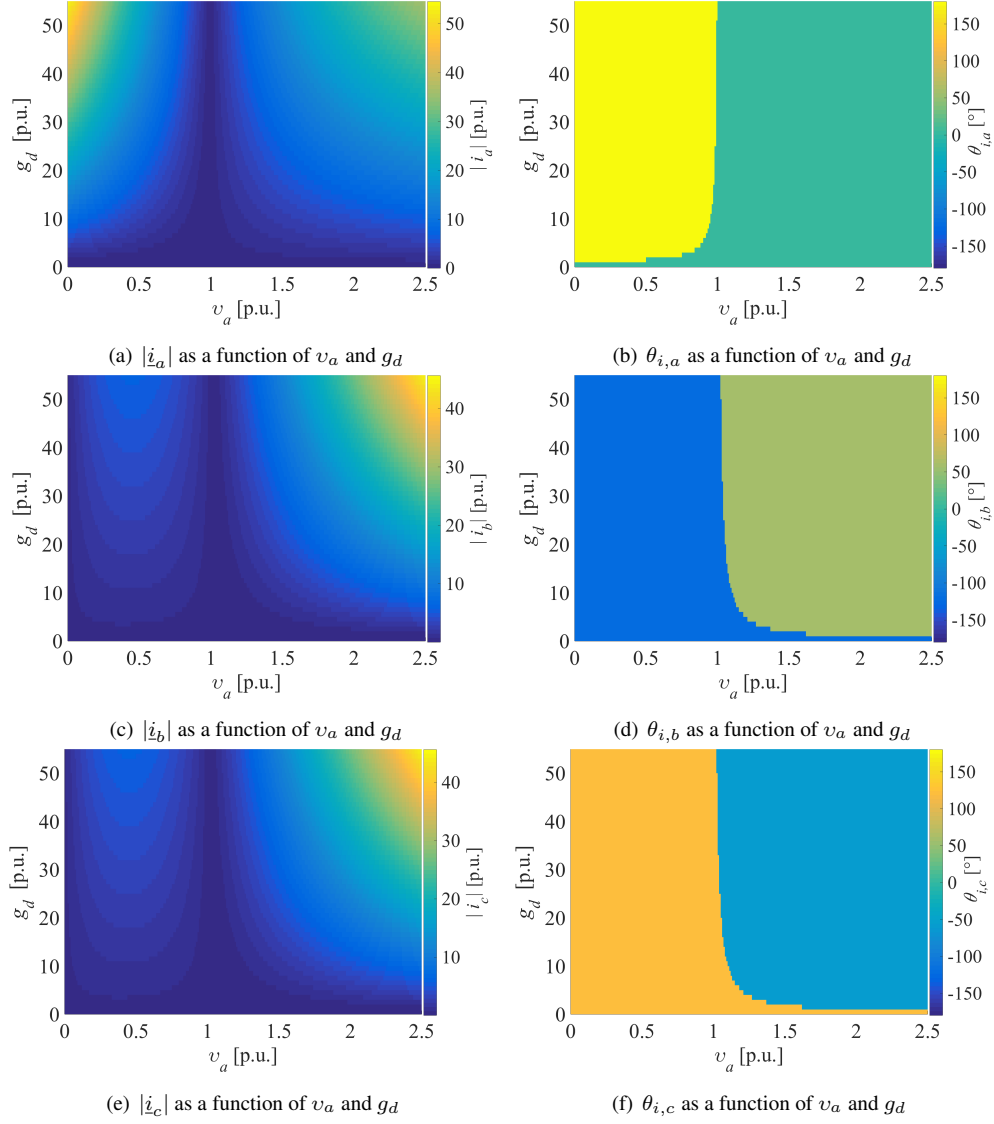


Figure 4.10: Phase currents magnitudes and current angles dependency on the variation of the phase angle  $\theta_a$  and the damping conductance  $g_d$  and nominal input power  $p_{dc} = 1$  p.u.

From the obtained results in sub-case 3, it can be concluded that the three-phase damping control strategy is able to mitigate the voltage unbalance at the PCC by consuming asymmetrical phase currents from the grid while supplying a load that is connected at the dc bus side of the DER. The current magnitudes are strongly dependent on the voltage unbalance and the damping conductance value. This property of the three-phase damping control strategy makes it ex-

tremely suitable for renewable energy applications that also incorporates battery storage systems.

### 4.1.2 Case 2: Phase angle $\theta_a$ variation

In case 1, the voltage unbalance is created by voltage asymmetry between the phase to neutral voltages. Nevertheless, the voltage unbalance is influenced besides by the voltage magnitudes but also by the phase shift between the three phases. This study represents the case where the voltage unbalance at the PCC is caused due to unequal phase angle shifting. Abnormal conditions such as faults and some loads such as inductive and capacitive loads may cause unequal phase angle shifting. The goal of this case study is to examine the behaviour of the three-phase damping control strategy under these conditions and assess its performance in terms of voltage unbalance mitigation. For simplicity, the phase voltages at the PCC are kept at their nominal values and the injected currents are investigated under variable phase angle  $\theta_a$ . Since this is a theoretical study, it can be pushed to limits beyond the practical cases and the interval under investigation for  $\theta_a$  is chosen to be  $\pm\pi$ . Similar to Case 1 (and its sub-cases), Case 2 is subdivided into three sub-cases where no power, nominal input power and nominal consumed power are considered.

#### 4.1.2.1 Sub-case 1: Phase angle $\theta_a$ variation under zero input power

In this sub-case, the behaviour of the three-phase damping control strategy is studied when the voltages at the PCC are kept at their nominal values i.e.  $v_a = v_b = v_c = 1$  p.u. and the input power available from the primary source is  $p_{dc} = 0$  p.u. The variable in this sub-case is the angle of phase  $\theta_a$  while the other two phase angles  $\theta_b = -\frac{2\pi}{3}$  and  $\theta_c = +\frac{2\pi}{3}$  are kept at their nominal values. The power balance under these conditions obeys on (4.1). Since  $p_{dc} = 0$  p.u. then the fundamental input conductance is equal to the second term of (2.16) and it is then calculated as:

$$g_{1_{p_{dc}=0, \theta_a(m)}} = -2g_d \frac{|v_a|^2 + |v_b|^2 + |v_c|^2 - A}{|v_a|^2 + |v_b|^2 + |v_c|^2 + 2A} \quad (4.17)$$

where A is:

$$\begin{aligned} A = & |v_a||v_b| \cos(\theta_a(m) - \theta_b - \frac{2\pi}{3}) \\ & + |v_b||v_c| \cos(\theta_b - \theta_c - \frac{2\pi}{3}) \\ & + |v_c||v_a| \cos(\theta_c - \theta_a(m) - \frac{2\pi}{3}) \end{aligned} \quad (4.18)$$

By using the new value of  $g_{1_{p_{dc}=0, \theta_a(m)}}$  back in the phase currents calculation

(2.15), the former one results in:

$$\begin{aligned}
\dot{i}_a(m) &= \frac{1}{3} \left\{ g_{1p_{dc}=0, \theta_a(m)} \left[ |v_a| e^{j\theta_a(m)} + |v_b| e^{j(\theta_b + \frac{2\pi}{3})} + |v_c| e^{j(\theta_c - \frac{2\pi}{3})} \right] \right. \\
&\quad \left. + g_d \left[ 2|v_a| e^{j\theta_a(m)} - |v_b| e^{j(\theta_b + \frac{2\pi}{3})} - |v_c| e^{j(\theta_c - \frac{2\pi}{3})} \right] \right\} \\
\dot{i}_b(m) &= \frac{1}{3} \left\{ g_{1p_{dc}=0, \theta_a(m)} \left[ |v_b| e^{j\theta_b} + |v_a| e^{j(\theta_a(m) - \frac{2\pi}{3})} + |v_c| e^{j(\theta_c + \frac{2\pi}{3})} \right] \right. \\
&\quad \left. + g_d \left[ 2|v_b| e^{j\theta_b} - |v_a| e^{j(\theta_a(m) - \frac{2\pi}{3})} - |v_c| e^{j(\theta_c + \frac{2\pi}{3})} \right] \right\} \\
\dot{i}_c(m) &= \frac{1}{3} \left\{ g_{1p_{dc}=0, \theta_a(m)} \left[ |v_c| e^{j\theta_c} + |v_a| e^{j(\theta_a(m) + \frac{2\pi}{3})} + |v_b| e^{j(\theta_b - \frac{2\pi}{3})} \right] \right. \\
&\quad \left. + g_d \left[ 2|v_c| e^{j\theta_c} - |v_a| e^{j(\theta_a(m) + \frac{2\pi}{3})} - |v_b| e^{j(\theta_b - \frac{2\pi}{3})} \right] \right\}
\end{aligned} \tag{4.19}$$

Further expansion and solving (4.19) for  $v_a = v_b = v_c = 1$  p.u.  $p_{dc} = 1$  p.u.  $\theta_b = -\frac{2\pi}{3}$  and  $\theta_c = +\frac{2\pi}{3}$  and leaving  $\theta_a$  and  $g_d$  as variables leads to:

$$\begin{aligned}
\dot{i}_a &= \frac{g_d(2 \exp(j\theta_a) - 2)}{3} + \frac{2g_d(2 \cos(\theta_a) - 2)(\exp(j\theta_a) + 2)}{3(4 \cos(\theta_a) + 5)} \\
\dot{i}_b &= \frac{g_d(j\sqrt{3} + 1)(1 + j3 \sin(\theta_a) - \cos(\theta_a))}{8 \cos(\theta_a) + 10} \\
\dot{i}_c &= -\frac{g_d(\sqrt{3} + j)(1 + j3 \sin(\theta_a) - j \cos(\theta_a))}{8 \cos(\theta_a) + 10}
\end{aligned} \tag{4.20}$$

Developing further (4.20) down to sin and cos functions leads to:

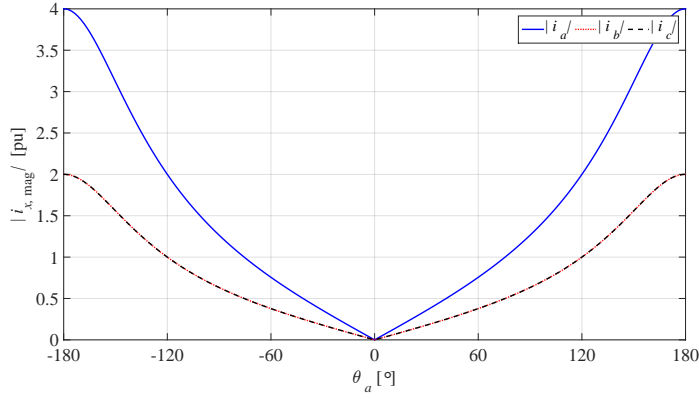
$$\begin{aligned}
\dot{i}_a &= \frac{18g_d \cos(\theta_a)(2 \cos(\theta_a) + 1) - 2g_d}{36 \cos(\theta_a) + 45} \\
&\quad + j \frac{18g_d \sin(\theta_a)(2 \cos(\theta_a) + 1)}{36 \cos(\theta_a) + 45} \\
\dot{i}_b &= \frac{g_d(1 - 3\sqrt{3} \sin(\theta_a) - \cos(\theta_a))}{8 \cos(\theta_a) + 10} \\
&\quad + j \frac{g_d(3 \sin(\theta_a) - \sqrt{3} \cos(\theta_a) + \sqrt{3})}{8 \cos(\theta_a) + 10} \\
\dot{i}_c &= \frac{g_d(3 \sin(\theta_a) - \cos(\theta_a) - \sqrt{3})}{8 \cos(\theta_a) + 10} + \\
&\quad + j \frac{g_d(\sqrt{3} \cos(\theta_a) - 3 \sin(\theta_a) - 1)}{8 \cos(\theta_a) + 10}
\end{aligned} \tag{4.21}$$

where the first fraction of (4.21) is related to the active current and the second fraction to the reactive current exchange. It can be seen that both terms are propor-

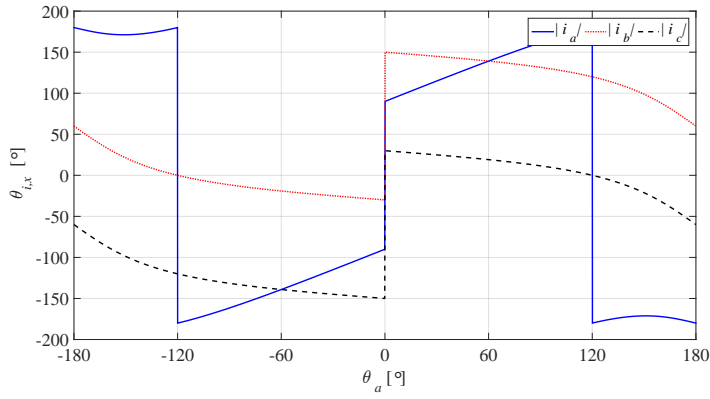
tional to  $g_d$ . From (4.21) it also appears that if  $g_d = 0$  p.u. then there will be no current flow present between the DER and the grid, which implies that the classical positive-sequence control strategy is unable to impact the grid voltages if such conditions are present at the PCC. It is also evident that the damping conductance is equally proportional to both active and reactive responsible terms, which implies that the phase angles in this case do not depend on the damping conductance value. Hence, the damping conductance value in this case is chosen to be  $g_d = 1$  p.u.

Due to the presence of complex numbers in (4.21) the resultant currents will contain both an active and reactive part, despite the fact that only active power is considered in  $g_1$ . The obtained simulation results of the absolute values of the phase currents, phase angles and exchanged active and reactive power are depicted in Fig. 4.11 (a), (b) and (c), respectively. Unlike the previous case, in this case, equation (4.21) leads to complex results and the first derivative of them does not yield any useful results that are clear to be segregated and interpreted individually. However, two regions can be distinguished from Fig. 4.11 (a) and they are  $-\pi < \theta_a < 0$  and  $0 \leq \theta_a \leq \pi$ . Hence, these intervals will be used to describe the behaviour of the three-phase damping control strategy in this sub-case.

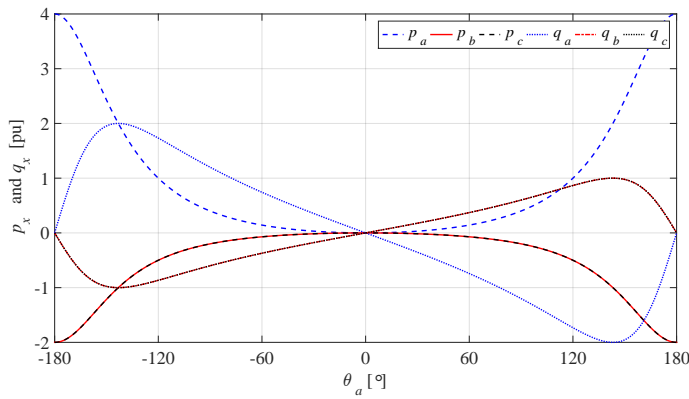
- $-\pi < \theta_a < 0$ : When phase angle  $\theta_a$  is in this range, the magnitudes of the phase currents increase with decreasing  $\theta_a$  where the magnitude of phase current  $i_a$  is the sum of  $i_b$  and  $i_c$  and since phase voltages  $v_b = v_c$ , then  $i_b$  is equal to  $i_c$  as well and this is valid for the entire range of  $\theta_a$ . When  $\theta_a < 0$ , the phase angle  $\theta_{i,a}$  is equal to  $-\frac{\pi}{2}$  with respect to  $\theta_a$ , which means that active and reactive power will be consumed from phase  $a$ , while phase angles  $\theta_{i,b}$  and  $\theta_{i,c}$  are phase shifted at  $180^\circ$  with respect to their phase voltages, hence active power will be injected in these phases. With increasing of  $\theta_a$ ,  $\theta_{i,a}$  decreases further while phase current angles  $\theta_{i,b}$  and  $\theta_{i,c}$  increase. This means that the consumed active and reactive power from phase  $a$  and the injected active and reactive power in phases  $b$  and  $c$  increase as well. The reactive power continues to increase with increasing of  $\theta_a$  up to the point where the active and reactive power become equal, which occurs at  $\theta_a = 143.1^\circ$ . From this point till the end of the interval the reactive power decreases while the active power increases. The reactive power drops down to zero at  $\theta_a = 180^\circ$  while the active power is at its maximum. The same is valid for the active and reactive powers that flow in phases  $b$  and  $c$  with the only difference that the active and reactive powers are being injected.
- $0 \leq \theta_a \leq \pi$ : When  $\theta_a = 0$  the control strategy does not inject any power into the grid and this is considered as the border mode. As in the previous interval ( $-\pi < \theta_a < 0$ ) with increasing the phase angle  $\theta_a$ , the magnitudes of the exchanged currents also increase. Active power is also being consumed from phase  $a$  and injected back into the grid via phases  $b$  and  $c$  but



(a) Phase current magnitudes as a function of  $\theta_a$



(b) Current angles as a function of  $\theta_a$



(c) Active and reactive power as a function of  $\theta_a$

Figure 4.11: Three-phase damping control strategy performance under variable phase angle  $\theta_a$ , zero input power  $p_{dc} = 0$  and damping conductance  $g_d = 1$  p.u.

the reactive power exchange is the opposite i.e. reactive power is injected in phase  $a$  and it is consumed from phases  $b$  and  $c$ .

Unlike the previous Case 1, in this one can be seen that the border mode is invariant to the value of the damping conductance. Furthermore, from (4.21) it can be seen that  $g_d$  is proportional to the active and reactive terms, hence there will be no change in the current angles with increasing  $g_d$ , but there will be a change in magnitudes and the amount of exchanged active and reactive power between the DER and the grid. However, performing additional analysis where  $g_d$  assumes higher values will not reveal anything useful, hence this study will not be conducted.

#### 4.1.2.2 Sub-case 2: Phase angle $\theta_a$ variation under nominal input power

In this sub-case, the behaviour of the three-phase damping control strategy is studied under different values of phase angle  $\theta_a$ , when the input power is nominal  $p_{dc} = -1$  p.u. all three phase voltage magnitudes are equal to their nominal value  $v_a = v_b = v_c = 1$  p.u. and phase angles of phase  $b$  and  $c$  are phase shifted at  $120^\circ$  i.e.  $\theta_b = -\frac{2\pi}{3}$  and  $\theta_c = \frac{2\pi}{3}$ . Solving (4.17), (4.18) and (4.19) for  $\theta_a$ ,  $p_{dc}$  and  $g_d$  yields the following set of equations of the phase currents:

$$\begin{aligned} i_a &= -\frac{(\exp(j\theta_a) + 2)(p_{dc} - 2g_d + 2g_d \exp(j\theta_a))}{4 \cos(\theta_a) + 5} \\ i_b &= -\frac{(j\sqrt{3} + 1)(2p_{dc} - g_d + (g_d + p_{dc}) \cos(\theta_a) - j3g_d \sin(\theta_a) + jp_{dc} \sin(\theta_a))}{8 \cos(\theta_a) + 10} \\ i_c &= \frac{(j\sqrt{3} - 1)(2p_{dc} - g_d + (g_d + p_{dc}) \cos(\theta_a) - j3g_d \sin(\theta_a) + jp_{dc} \sin(\theta_a))}{8 \cos(\theta_a) + 10} \end{aligned} \tag{4.22}$$

By developing further (4.22) to sin and cos functions and grouping it for  $g_d$  and  $p_{dc}$  leads to:

$$\begin{aligned}
\dot{i}_a &= -\frac{p_{dc}(\cos(\theta_a) + 2) + 2g_d(\cos(\theta_a) + \cos(2\theta_a) - 2)}{4\cos(\theta_a) + 5} \\
&\quad -j\frac{p_{dc}\sin(\theta_a) + 2g_d(\sin(2\theta_a) + \sin(\theta_a))}{4\cos(\theta_a) + 5} \\
\dot{i}_b &= -\frac{p_{dc}(\cos(\theta_a) - \sqrt{3}\sin(\theta_a) - 2) + g_d(\cos(\theta_a) + 3\sqrt{3}\sin(\theta_a) - 1)}{8\cos(\theta_a) + 10} \\
&\quad -j\frac{p_{dc}(\sqrt{3}\cos(\theta_a) + \sin(\theta_a) - 2\sqrt{3}) + g_d(2\sqrt{3}\cos(\theta_a) - 3\sin(\theta_a) - \sqrt{3})}{8\cos(\theta_a) + 10} \\
\dot{i}_c &= -\frac{p_{dc}(\cos(\theta_a) - \sqrt{3}\sin(\theta_a) - 2) + g_d(\cos(\theta_a) + 3\sqrt{3}\sin(\theta_a) - 1)}{8\cos(\theta_a) + 10} \\
&\quad +j\frac{p_{dc}(\sqrt{3}\cos(\theta_a) + \sin(\theta_a) - 2\sqrt{3}) + g_d(2\sqrt{3}\cos(\theta_a) - 3\sin(\theta_a) - \sqrt{3})}{8\cos(\theta_a) + 10}
\end{aligned} \tag{4.23}$$

As can be seen from (4.23) the numerator contains sin and cos functions that are proportional to the input power and also to the damping conductance. Therefore, in this sub-case besides the current magnitudes, the current angles will be also affected by  $g_d$  as well as the input power  $p_{dc}$ . Unlike the previous sub-case 1, in this one the damping conductance will have an impact on both: phase current magnitudes and current angles. Due to the complex nature of (4.23) the first derivative of it will not be useful to define different regions for further interpretation. Hence, similar to the previous case two regions will be defined based on the phase angle  $\theta_a$  such as  $-\pi < \theta_a < 0$  and  $0 \leq \theta_a \leq \pi$ .

The simulation results under  $g_d = 0, 1$  and  $5$  p.u. are depicted in Fig. 4.12, Fig. 4.13 and Fig. 4.14, where the exchanged currents, phase angles and exchanged active and reactive power are presented. The performance of the three-phase damping control strategy will be discussed briefly.

When  $g_d = 0$  p.u. is used in (4.23), the three-phase damping control strategy behaves as the positive-sequence control strategy and all phase currents have the same magnitude, as depicted in Fig. 4.12 (a), which is valid for the entire range of the phase angle  $\theta_a$ . At  $\theta_a = 0$  all the phase currents are equal to  $0.333$  p.u., which in fact corresponds to the nominal value of the injected phase currents. The current angles and the active power are at their nominal values and the exchanged reactive power is zero. As can be seen from Fig. 4.12 (b), when  $-\pi \leq \theta_a < 0$  all current angles  $\theta_{i,a}$ ,  $\theta_{i,b}$  and  $\theta_{i,c}$  deviate with  $-30^\circ$  electrical degrees from the nominal value, which corresponds to power injection for phases  $b$  and  $c$  with some reactive component, which is present in the final current values  $\dot{i}_b$  and  $\dot{i}_c$ . However, this is not entirely correct for phase current  $a$ . Although  $\theta_{i,a}$  deviates with the same difference as the other two currents,  $\theta_a$  also changes, hence the injection and consumption regions will be present in this region. This is not clearly visible from

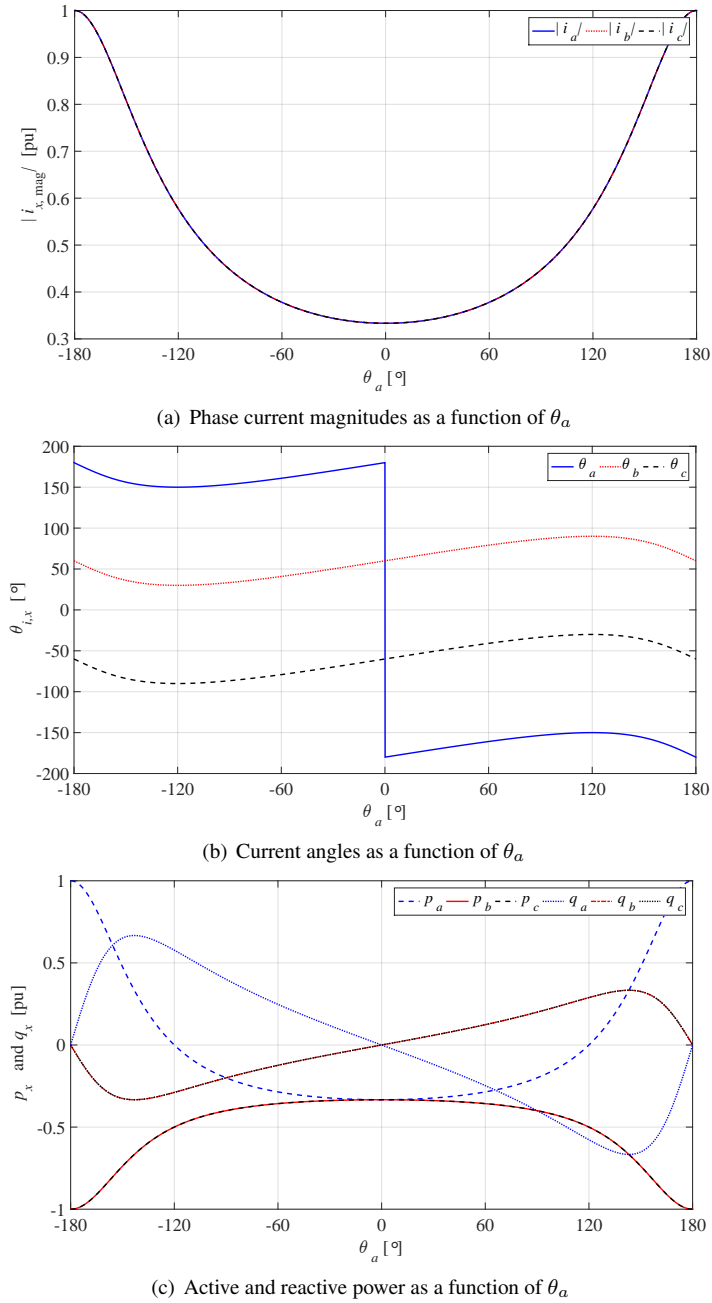
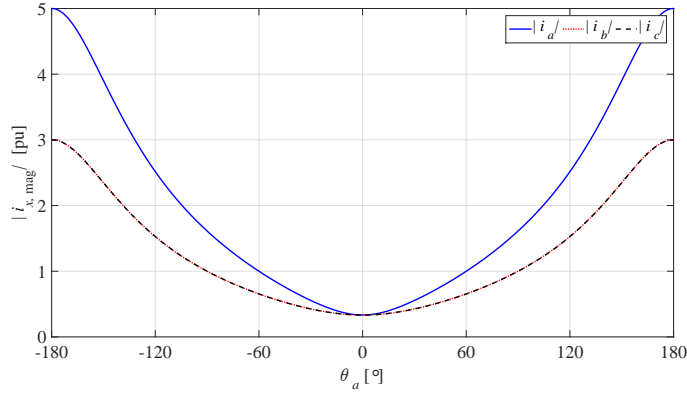
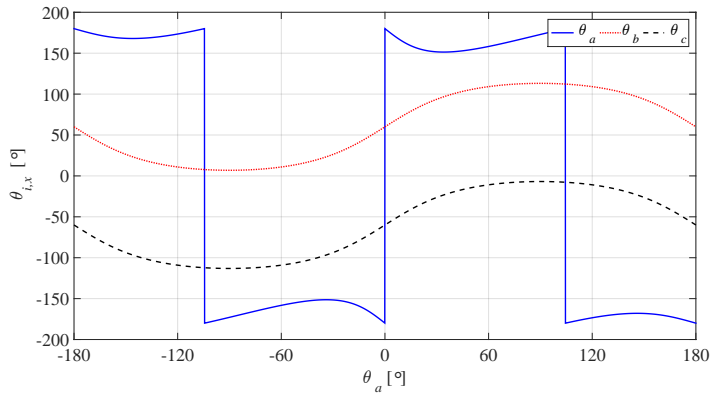


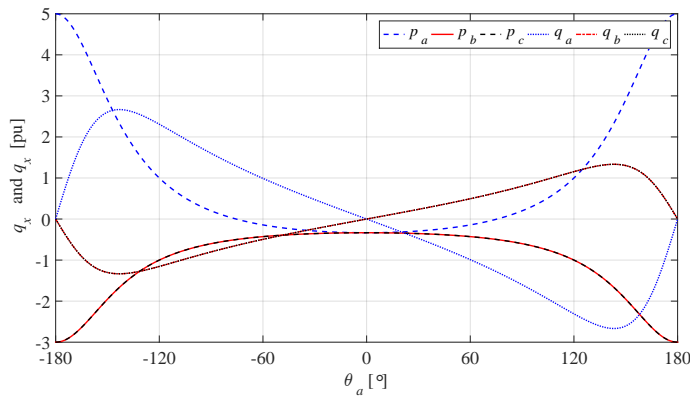
Figure 4.12: Three-phase damping control strategy performance under variable phase angle  $\theta_a$ , nominal input power  $p_{dc} = -1$  p.u. and damping conductance  $g_d = 0$  p.u.



(a) Phase current magnitudes as a function of  $\theta_a$



(b) Current angles as a function of  $\theta_a$



(c) Active and reactive power as a function of  $\theta_a$

Figure 4.13: Three-phase damping control strategy performance under variable phase angle  $\theta_a$ , nominal input power  $p_{dc} = -1$  p.u. and damping conductance  $g_d = 1$  p.u.

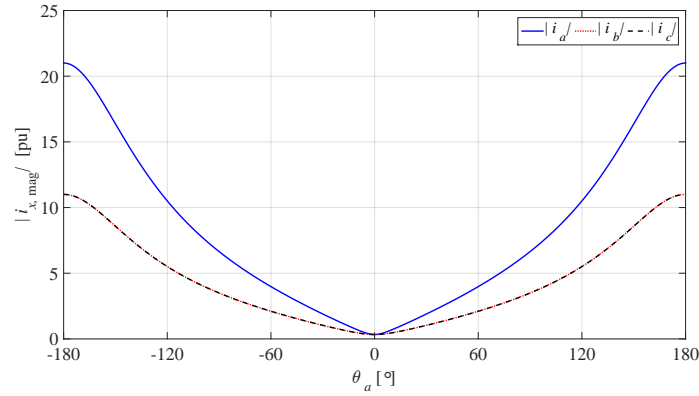
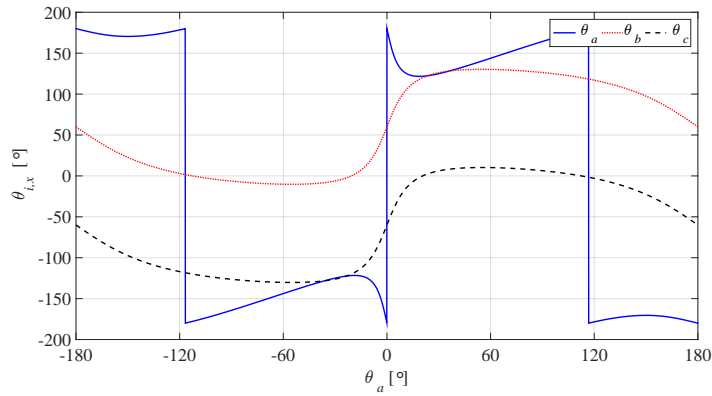
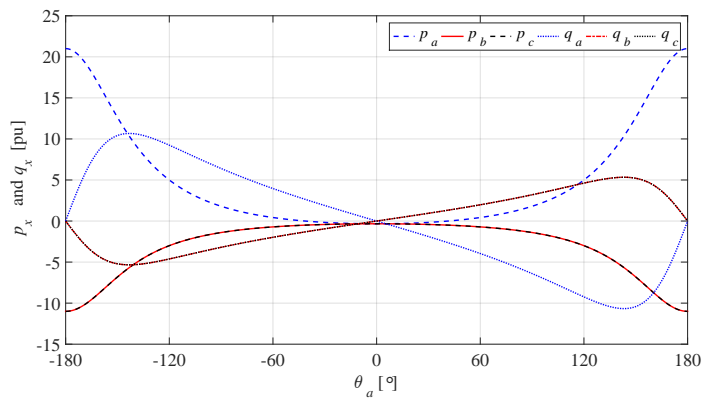
(a) Phase current magnitudes as a function of  $\theta_a$ (b) Current angles as a function of  $\theta_a$ (c) Active and reactive power as a function of  $\theta_a$  variation

Figure 4.14: Three-phase damping control strategy performance under variable phase angle  $\theta_a$ , nominal input power  $p_{dc} = -1 \text{ p.u}$  and damping conductance  $g_d = 5 \text{ p.u}$

(4.23) but it can be observed in Fig. 4.12 (c) where the border mode occurs at  $\theta_a = -120^\circ$  electrical degrees. From Fig. 4.12 (c) it can be also noticed that the positive-sequence control strategy also exchanges both active and reactive power and in this region the reactive power is being consumed from phase  $a$  and reactive power is being injected in phases  $b$  and  $c$ . In region  $0 < \theta_a \leq \pi$  the performance is similar to  $-\pi \leq \theta_a < 0$  with the only difference that the reactive power is being injected in phase  $a$  and consumed from phases  $b$  and  $c$ .

In the following examination, a damping conductance of 1 p.u. is considered. This value is substituted in (4.23) and the simulation results of the exchanged currents, current angles and exchanged active and reactive power are shown in Fig. 4.13 (a), (b) and (c), respectively. It can be noticed that the obtained results in Fig. 4.12 ( $g_d = 1$  p.u.) and in Fig. 4.13 ( $g_d = 1$  p.u.) have identical profiles but they differ in magnitude. In this example as well, the phase currents, angles and active power are equal to their nominal values at  $\theta_a = 0$  i.e. 0.33 p.u. However, when  $-\pi \leq \theta_a < 0$ , the influence of the damping conductance value results in higher current magnitudes, which reach 5 p.u. ( $i_a$ ) and 3 p.u. ( $i_b$  and  $i_c$ ) at the extremes of  $\theta_a$ . From this examination it can be seen that phase angles  $\theta_{i,b}$  and  $\theta_{i,c}$  deviate with approximately  $-50^\circ$ , which will lead to higher reactive power exchange compared to the previously obtained simulation results where  $g_d = 0$  p.u. was considered. The injected active and reactive power are depicted in Fig. 4.13 (c) and indeed in this example the amount of injected reactive power is almost 1 p.u. bigger in comparison with Fig. 4.12. The transition between current injection and consumption turns out to be  $\pm 75.5^\circ$  compared to  $120^\circ$  in the previous example.

The simulation results of the exchanged phase currents when  $g_d = 5$  p.u. is used, are shown in Fig. 4.14 (a). The performance of the three-phase damping control strategy is similar to the example where  $g_d = 1$  p.u. but as it can be seen in Fig. 4.13 (a) and Fig. 4.14 (a), the difference in the magnitude of the exchanged phase currents is higher. The deviation of the current angles is also bigger, which, as anticipated, leads to even bigger amount of active and reactive power exchange. The transition between current injection and consumption turns out to be  $\pm 41.1^\circ$ .

In summary of the above discussion, the damping conductance value has an impact on the current magnitudes and the current angles, which results in additional reactive power exchange. The reactive power has the same profile for all three examples with the only difference that the amount of the exchanged reactive power depends on the  $g_d$  value. From (4.23) it is not obvious where the border mode occurs. However, from the described examples an approximate location of the border mode can be determined, which is between the angle extremum of  $\theta_{i,a}$  and  $\theta_{i,b}$ .

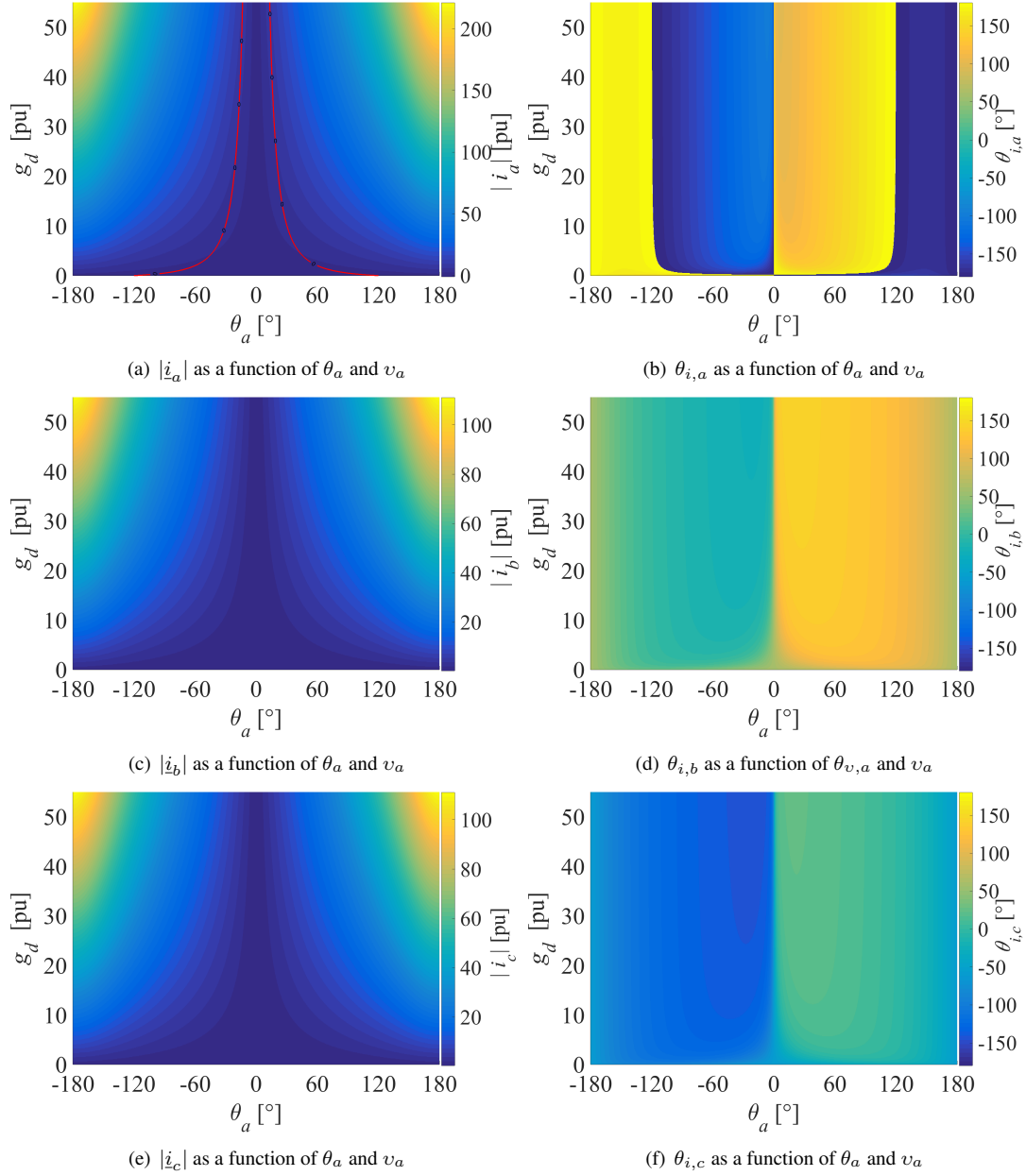


Figure 4.15: Phase currents magnitudes and current angles dependency on the variation of the phase angle  $\theta_a$  and the damping conductance  $g_d$

A last examination of this sub-case, the injected current magnitudes and angles are depending on both damping conductance plus phase angle variation and they vary as follows:  $0 \leq g_d \leq 2.5$  and  $-\pi \leq \theta_a \leq \pi$ . In Fig. 4.15 (a), (c) and (e) the

phase current magnitudes are depicted as a function of  $g_d$  and  $\theta_a$  and as expected the obtained simulation results for the phase currents show that the magnitudes have similar profiles. Furthermore,  $|\dot{i}_a|$  is double in magnitude compared to  $|\dot{i}_b|$  and  $|\dot{i}_c|$ , which was also valid in sub-case 1 (as it is shown in Fig 4.11). Due to the angle deviation of the exchanged currents with respect to  $\theta_a$ , in this sub-case the border mode occurs only in phase  $a$ . To illustrate in a better way where the border mode occurs the former one is highlighted by using a red contour in Fig. 4.15 (a). The control strategy injects active power if the result from (4.23) is multiplied by the corresponding phase voltage falls inside the contour and vice versa. As it can be seen the border mode is highly dependent on the  $g_d$  value and the angle variation  $\theta_a$  and this range, where the control strategy injects currents, becomes narrower at high  $g_d$ .

The angles of the phase currents are depicted in Fig. 4.12 (b), Fig. 4.13 (b) and Fig. 4.14 (b), respectively and also Fig. 4.15 (b), (d) and (f), it can be seen that the deviations from their nominal values are increased from  $\pm 30^\circ$  at  $g_d = 0$  p.u. to  $\pm 50^\circ$  at  $g_d = 1$  p.u. and  $\pm 75^\circ$  at  $g_d = 1$  p.u. Despite these deviations, the profiles of the exchanged active and reactive powers have the same shape for all values of  $g_d$ . They only differ in scale, which later can be used to properly size the power ratings of the power electronic inverter or set maximum limits of  $g_d$ .

#### 4.1.2.3 Sub-case 3: Phase angle $\theta_a$ variation under nominal consumed power

In this sub-case, the behaviour of the three-phase damping control strategy is studied under a variable phase angle  $\theta_a$ , when a load is connected to the dc bus and it consumes nominal power from the grid i.e.  $p_{dc} = 1$  p.u. All three phase voltage magnitudes are equal to their nominal values  $v_a = v_b = v_c = 1$  p.u. and phase angles of phases  $b$  and  $c$  are phase shifted at  $120^\circ$  i.e.  $\theta_b = -\frac{2\pi}{3}$  and  $\theta_c = \frac{2\pi}{3}$ . This sub-case can be described mathematically by using the simplified equations that are used in sub-case 2 (4.23). Without going into too much details only some substantial differences between sub-case 2 and sub-case 3 will be pointed out.

When  $g_d = 0$  p.u. is considered, the positive-sequence control strategy behaves similarly compared to the power injection mode (Case2, sub-case1). All phase currents, angles and active and reactive power exchange are depicted in Fig. 4.16 (a), (b) and (c), respectively. The phase current profile is absolutely the same as in Case2, sub-case1. Since the control strategy operates in a consumption mode, all current angles are in phase with their corresponding phase voltages and this can be seen also in Fig. 4.16 (b). This figure also shows that the maximum deviation of all phase angles is about  $\pm 30^\circ$ , which again corresponds to Case2, sub-case1. Exchanged active and reactive power in the respective regions ( $-\pi \leq \theta_{i,a} < 0$  and  $0 \leq \theta_{i,a} \leq \pi$ ) have opposite signs and profiles in comparison to Case2, sub-case1 but the border mode remains unchanged.

The obtained simulation results of the phase current magnitudes, phase current

angles and exchanged active and reactive power per phase are presented in Fig. 4.16 (a), (b) and (c), respectively. These results are obtained at  $p_{dc} = 1$  p.u. and  $g_d = 1$  p.u. At  $\theta_a = 0^\circ$ , all phase current angles  $\theta_{i,a}$ ,  $\theta_{i,b}$  and  $\theta_{i,c}$  are in phase with respect to their phase voltages. By increasing or decreasing  $\theta_a$ , these angles start deviating from their nominal values. In the extremes of the  $\theta_a$ , the current angles deviate so much that phase  $a$  starts consuming power from the grid whereas current is been injected in the other two phases. At these conditions, the three-phase damping control strategy behaves differently compared to the positive-sequence control strategy (case3, sub-case1). The current angle deviation also results in some reactive power consumption when  $\theta_a < 0$  and reactive power injection when  $\theta_a > 0$ , which is again opposite when compared with case1, sub-case2. The active power is always consumed from phase  $a$ , invariant of the value of  $\theta_a$  (Fig. 4.17 (c)). Phase current angle  $\theta_{i,a}$  is  $0^\circ$  shifted at  $\theta_a = 0^\circ$ , and it also changes with changing  $\theta_a$ . This makes it difficult to define whether the control strategy injects or draws current from phases  $b$  and  $c$  unless the active power is observed (see Fig. 4.17 (c)). The simulation results show that the border mode occurs in phases  $b$  and  $c$  at  $\theta_a = \pm 120^\circ$ , which coincides with the current injection mode of the three-phase damping control strategy examined at  $p_{dc} = -1$  p.u. and  $g_d = 1$  p.u (case 2, sub-case 2).

Similar simulation results are obtained at  $p_{dc} = 1$  p.u. and  $g_d = 5$  p.u. and the exchanged phase currents, their respective current angles and exchanged active and reactive power are presented in Fig. 4.13 (a), (b) and (c). Despite the more rapid change in the current angles, the profiles of the exchanged phase currents, active and reactive power have the same shape as examined in case 2, sub-case 2. They differ in magnitude and border mode. The former one occurs at  $\theta_a = \pm 35^\circ$  while at  $g_d = 1$  p.u. is  $41.1^\circ$  and at  $g_d = 0$  p.u. is  $120^\circ$ .

These simulation results are obtained only for three values of  $g_d$ . In Fig. 4.19 are depicted the obtained simulation results for a wider range of the damping conductance  $0 \leq g_d \leq 55$ . The phase current magnitudes are presented in Fig. 4.19 (a), (c) and (e) and their corresponding angles in Fig. 4.19 (b), (d) and (f), respectively. The exchanged phase currents have the same magnitudes as Fig. 4.15 but their phase angles are different because of the positive  $p_{dc}$  value. The border mode occurs only in phases  $b$  and  $c$  and it is highlighted by using a red contour. The border mode dependency on  $g_d$  is also the same as case 2 sub-case 2.

In this case, the behaviour of the three-phase damping control strategy in the rectifier mode is investigated. The performance is tested under fixed phase voltage magnitudes, consumed power and fixed phase angles  $\theta_b$  and  $\theta_c$ . The variables are phase angle  $\theta_a$  and also  $g_d$ . The results showed that unlike the positive-sequence control strategy, the three-phase damping control strategy is able to mitigate the voltage unbalance under big phase voltage angle variations by exchanging both active and reactive powers. The phase current magnitudes are highly dependent

on  $g_d$  value and they can easily exceed the power ratings of the power electronic inverter when  $g_d$  assumes high values.

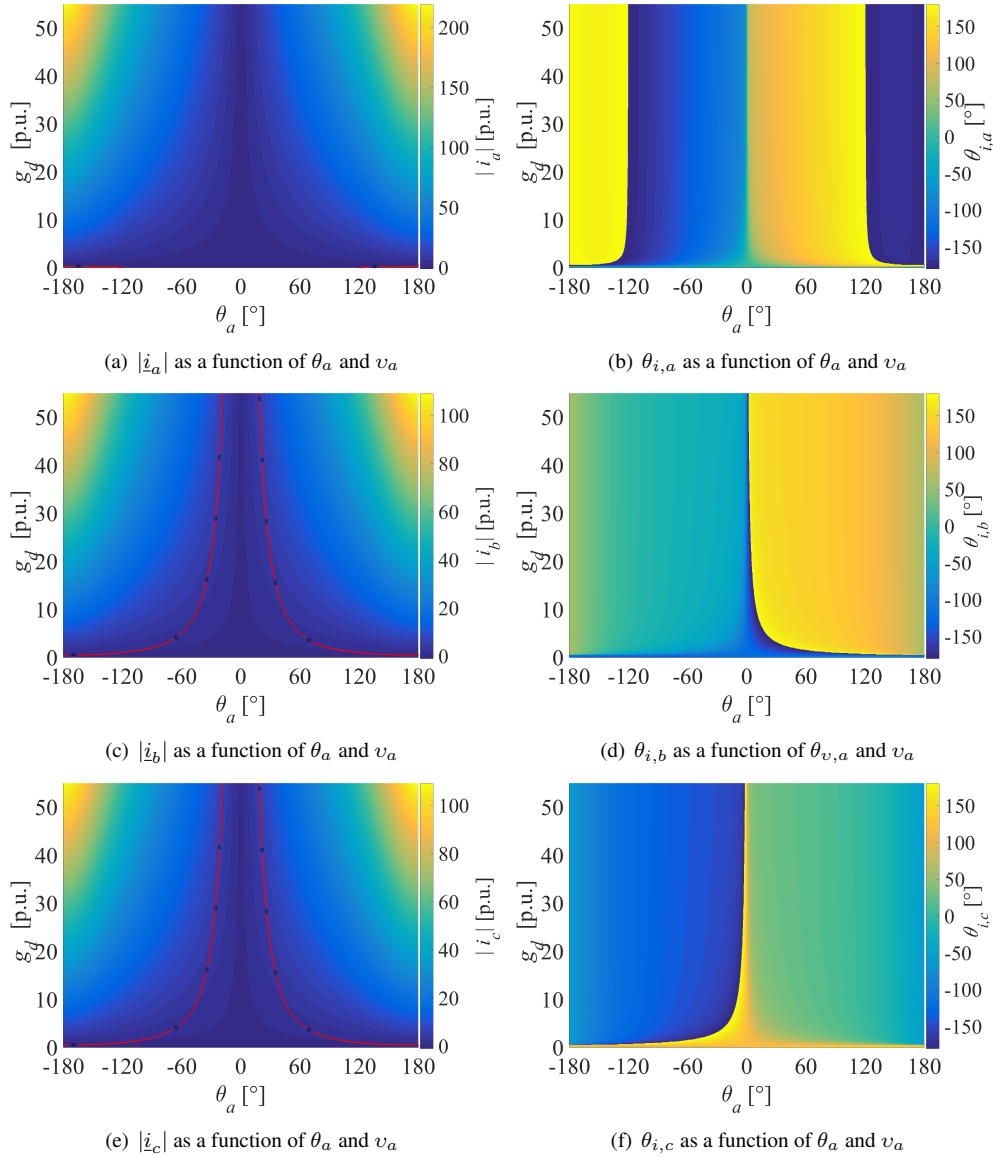


Figure 4.19: Phase currents magnitudes and current angles dependency as a function of the phase angle  $\theta_a$  and the damping conductance  $g_d$  at  $p_{dc} = 1$  p.u.

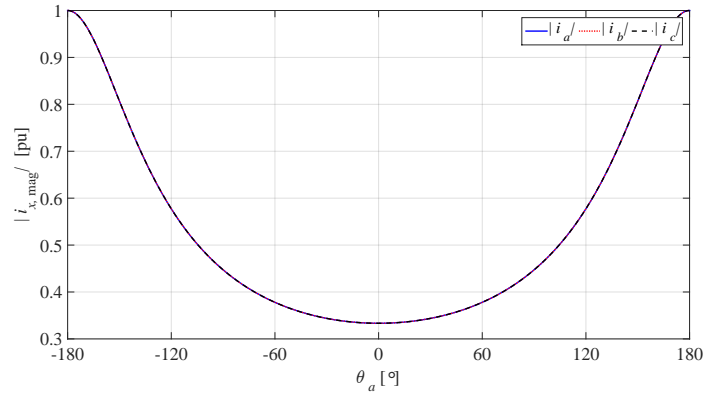
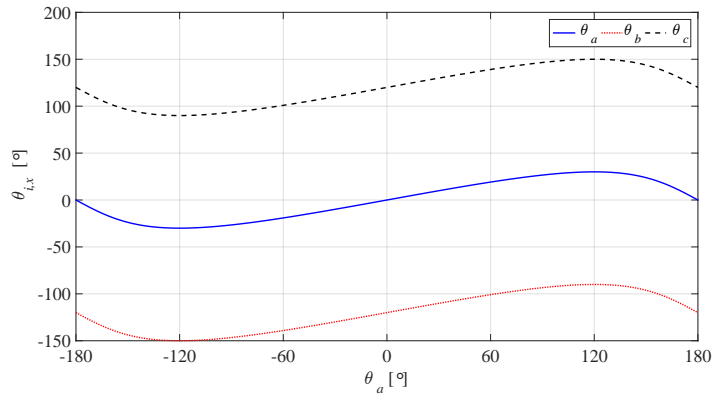
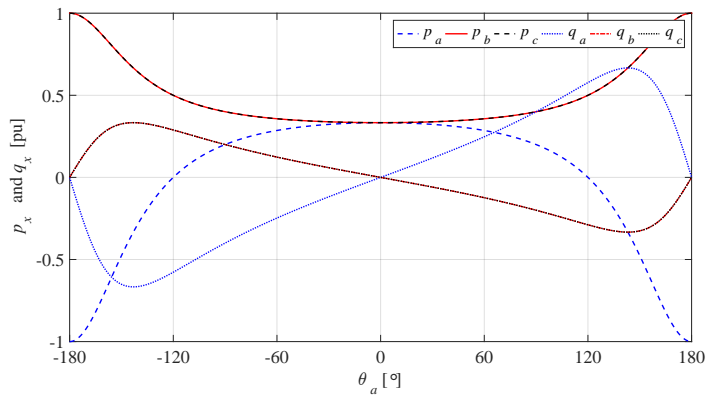
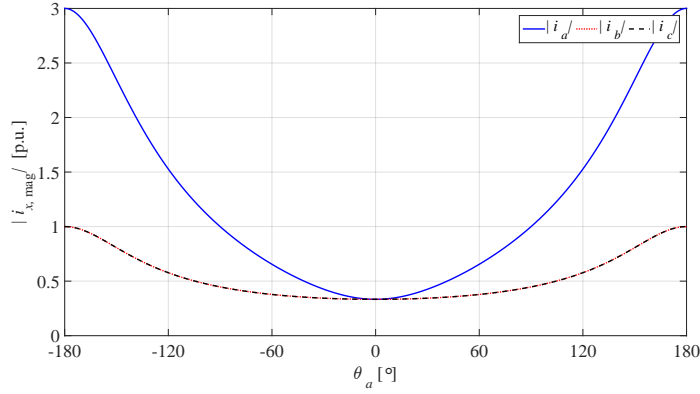
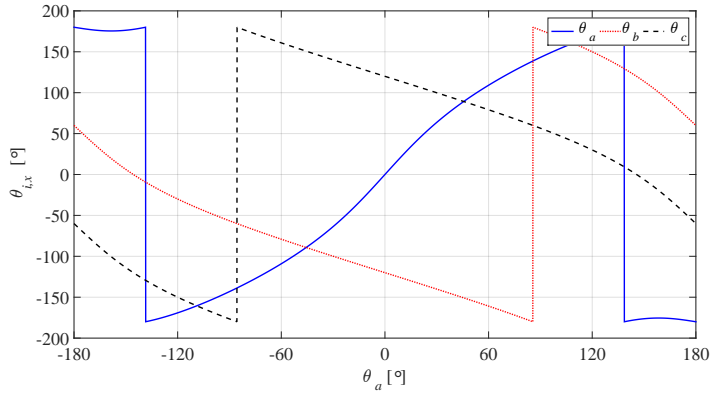
(a) Phase current magnitudes as a function of  $\theta_a$ (b) Current angles as a function of  $\theta_a$ (c) Active and reactive power as a function of  $\theta_a$ 

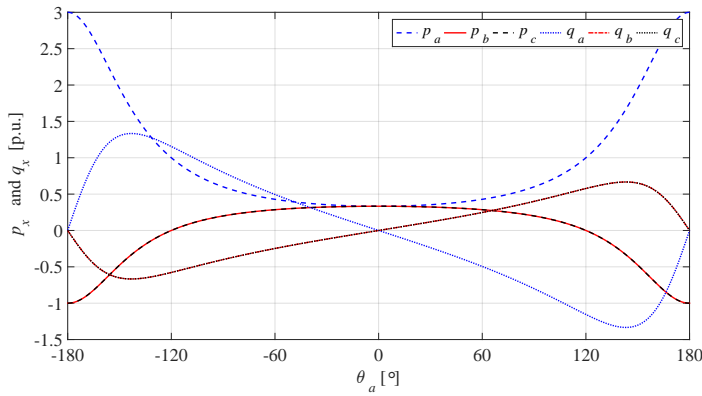
Figure 4.16: Three-phase damping control strategy performance under variable phase angle  $\theta_a$ , nominal input power  $p_{dc} = 1$  p.u. and damping conductance  $g_a = 0$  p.u.



(a) Phase current magnitudes as a function of  $\theta_a$



(b) Current angles as a function of  $\theta_a$



(c) Active and reactive power as a function of  $\theta_a$

Figure 4.17: Three-phase damping control strategy performance under variable phase angle  $\theta_a$ , nominal input power  $p_{dc} = 1$  p.u. and damping conductance  $g_d = 1$  p.u.

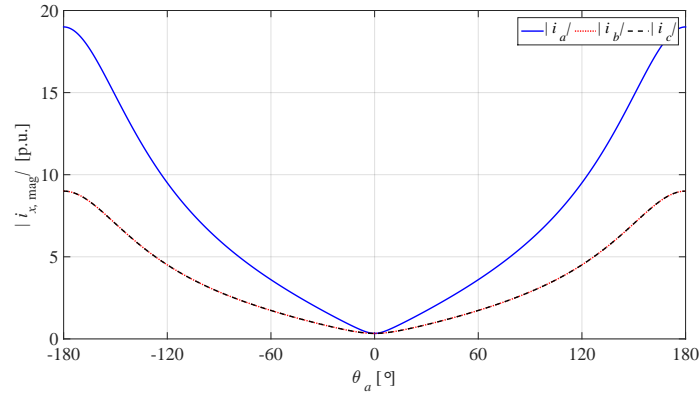
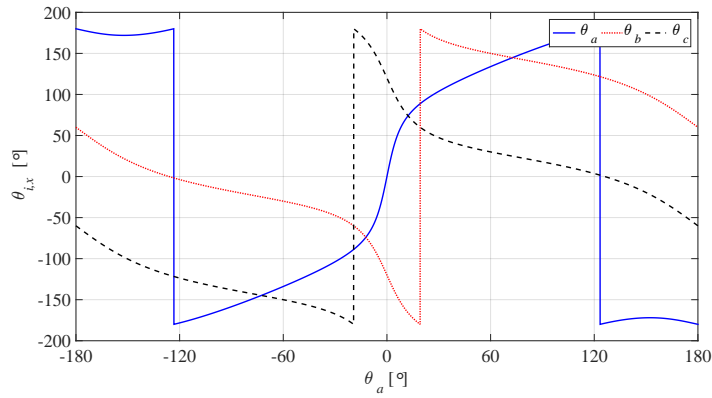
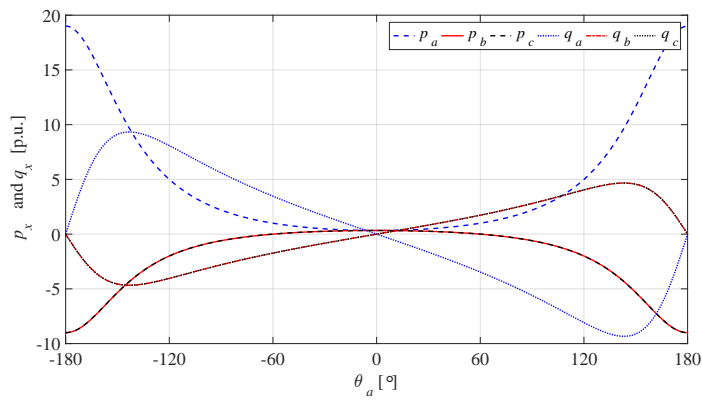
(a) Phase current magnitudes as a function of  $\theta_a$ (b) Current angles as a function of  $\theta_a$ (c) Active and reactive power as a function of  $\theta_a$  variation

Figure 4.18: Three-phase damping control strategy performance under variable phase angle  $\theta_a$ , nominal input power  $p_{dc} = 1$  p.u. and damping conductance  $g_a = 5$  p.u.

### 4.1.3 Case 3: Phase voltage $v_a$ and phase angle $\theta_a$ variation

In this case, the behaviour of the three-phase damping control strategy is investigated at a variable phase voltage  $a$  ( $0 \leq v_a \leq 2.5$ ) and variable phase angle  $\theta_a$  ( $-\pi \leq \theta_a \leq +\pi$ ). The investigation is performed considering different values of the damping conductance  $g_d$ . Phase voltages  $v_b$  and  $v_c$  are equal to their nominal values of 1 p.u. and their corresponding phase angles are equal to  $\theta_b = -\frac{2\pi}{3}$  and  $\theta_c = +\frac{2\pi}{3}$ .

#### 4.1.3.1 Sub-case 1: Phase voltage $v_a$ and phase angle $\theta_a$ variation under zero input power

In this sub-case, the input power is considered to be zero while phase voltage  $v_a$  and phase angle  $\theta_a$  are variables. The rest of the input conditions are as listed above. To perform this analysis, Eq. (2.15) and (2.16) are solved for  $p_{dc}$ ,  $g_d$ ,  $v_a$  and  $\theta_a$  the following equations are obtained:

$$\begin{aligned}
 \dot{i}_a &= \frac{(\exp(j\theta_a) + 2)(-2g_d + 2g_d|v_a|\exp(j\theta_a))}{4\cos(\theta_a) + 5} \\
 \dot{i}_b &= \frac{g_d(|v_a|\exp(j(\theta_a + \frac{2\pi}{3}))) - j\frac{\sqrt{3}}{2} - 1/2}{3} \\
 &+ \frac{(2g_d - 3p_{dc} + 2g_d|v_a|^2 - 4g_d|v_a|\cos(\theta_a))}{3(4|v_a|\cos(\theta_a) + |v_a|^2 + 4)} \\
 &(|v_a|\exp(j(\theta_a + \frac{2\pi}{3}))) + j\sqrt{3} + 1 \tag{4.24} \\
 \dot{i}_c &= -\frac{g_d(|v_a|\exp(j(\theta_a - \frac{2\pi}{3}))) - j\frac{\sqrt{3}}{2} - 1/2}{3} \\
 &+ \frac{(2g_d - 3p_{dc} + 2g_d|v_a|^2 - 4g_d|v_a|\cos(\theta_a))}{3(4|v_a|\cos(\theta_a) + |v_a|^2 + 4)} \\
 &(|v_a|\exp(j(\theta_a - \frac{2\pi}{3}))) + j\sqrt{3} - 1
 \end{aligned}$$

From (4.24) can be seen that when  $p_{dc} = 0$  p.u. all terms in the numerator are proportional to the damping conductance, which is very similar to case 2 sub-case 1 Eq. (4.21). Hence, in this case as well, the damping conductance will have an impact on the current magnitudes but it will not have any influence on the current angles. Therefore, for this analysis the behaviour of the three-phase damping control strategy will be investigated under only one value of the damping conductance which, for simplicity, is chosen to be  $g_d = 1$  p.u.

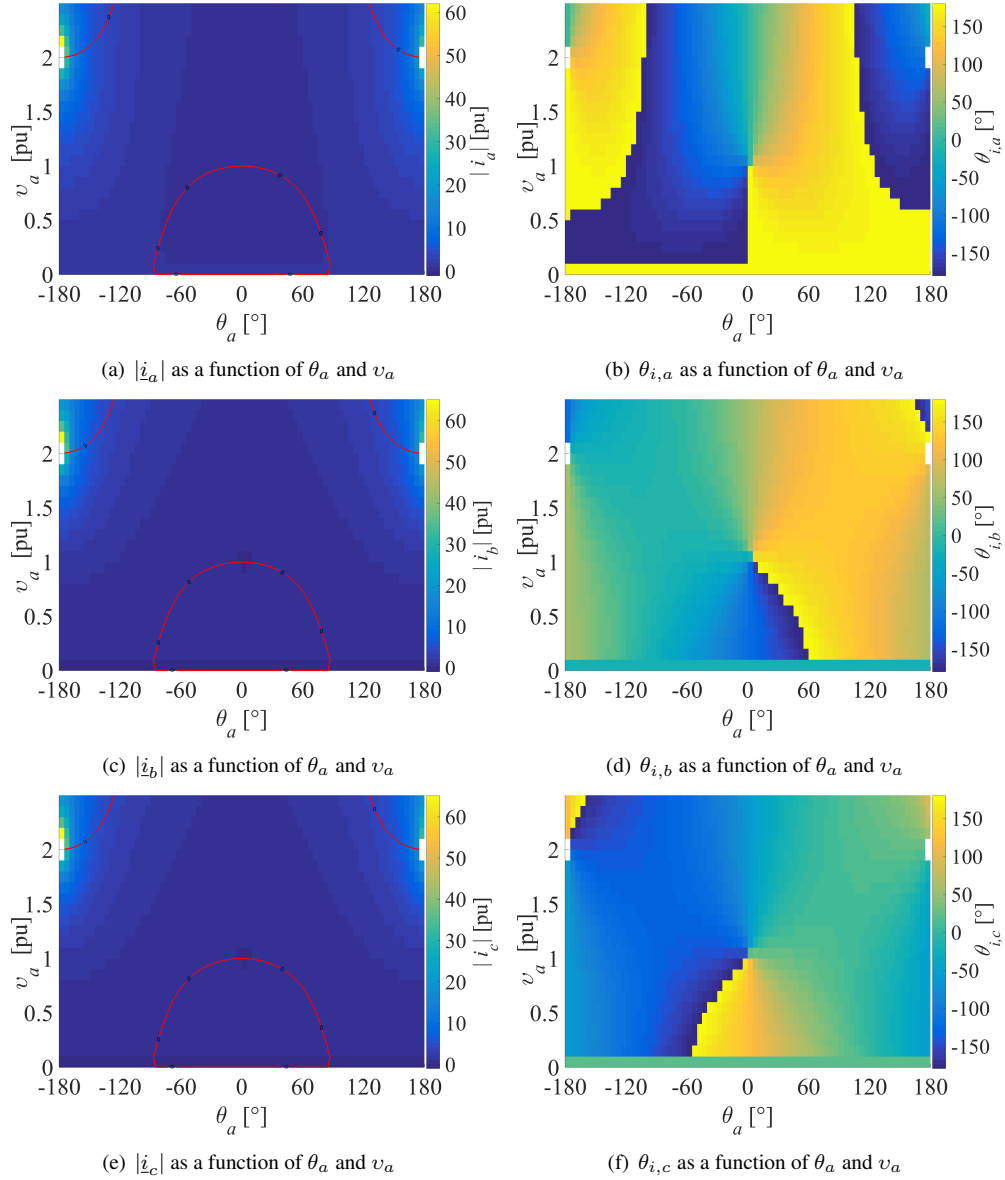


Figure 4.20: Phase currents dependency on the variation of the phase voltage  $v_a$  and the phase angle  $\theta_a$  at zero input power  $p_{dc} = 0$  p.u. and damping conductance  $g_d = 1$  p.u.

The obtained simulation results of the magnitudes of the exchanged currents are presented in Fig 4.20 (a), (c) and (e) and their respective angles (b), (d) and (f). As it can be seen from Fig 4.20, the three phase currents have similar peak magnitudes of 60 p.u. however the current distribution (the darker blue areas) slightly differs for phase  $a$  and  $b$  (c). The border mode where the exchanged real

power is zero, is highlighted by using a contour plot. The control strategy injects active current in phase  $a$  when  $v_a$  and  $\theta_a$  are within the circumference areas and consumes current when  $v_a$  and  $\theta_a$  are out of it. The opposite is valid for phases  $b$  and  $c$ . Since the damping conductance value affects only the current magnitudes, while the current angles remain unchanged, therefore, the border mode will also be invariant to  $g_d$ .

#### 4.1.3.2 Sub-case 2: Phase voltage $v_a$ and phase angle $\theta_a$ variation under nominal input power

In this sub-case, the injected currents by the three-phase damping control strategy are investigated under the same conditions as Case 3 sub-case 1 with the only difference that the input power is considered to be equal to its nominal value i.e.  $p_{dc} = -1$  p.u. From (4.24) it can be seen that when  $p_{dc} = -1$  all terms in the numerator are proportional to both input power and damping conductance, which is very similar to case 2 sub-case 2, Eq. (4.23). Therefore, in this case as well, the damping conductance will have an impact on both: current magnitudes and current angles. Consequently, to conduct this analysis the behaviour of the three-phase damping control strategy will be investigated under two values of the damping conductance. For simplicity one of them is chosen to be  $g_d = 1$ . To illustrate better the behaviour of the three-phase damping control strategy, the other value is expected to be chosen in the extremum of  $g_d$  i.e. 55 pu, however this value will not bring useful information for setting up the practical limits of  $g_d$  on a later stage in this chapter because it will lead to very high magnitudes of the phase currents. Considering this, a smaller value of the damping conductance for the second test will be more suitable and it is chosen to be  $g_d = 10$  p.u.

The obtained simulation results of the magnitudes of the exchanged currents for a damping conductance value of  $g_d = 1$  p.u. are presented in Fig 4.21 (a), (c) and (e) and the results for  $g_d = 10$  p.u. (b), (d) and (f), respectively. The border mode where the exchanged real power is zero, is highlighted by using a contour plot. The control strategy injects active current within the circumference areas and consumes current when  $v_a$  and  $\theta_a$  are out of it. The opposite is valid for phases  $b$  and  $c$ . As it can be seen from Fig 4.20 the three phase currents have similar magnitudes, which resembles the previous example when  $g_d = 1$  p.u. However, the border mode differs and the current distribution (the darker blue areas) are different for the phases  $a$  and  $b$  (c).

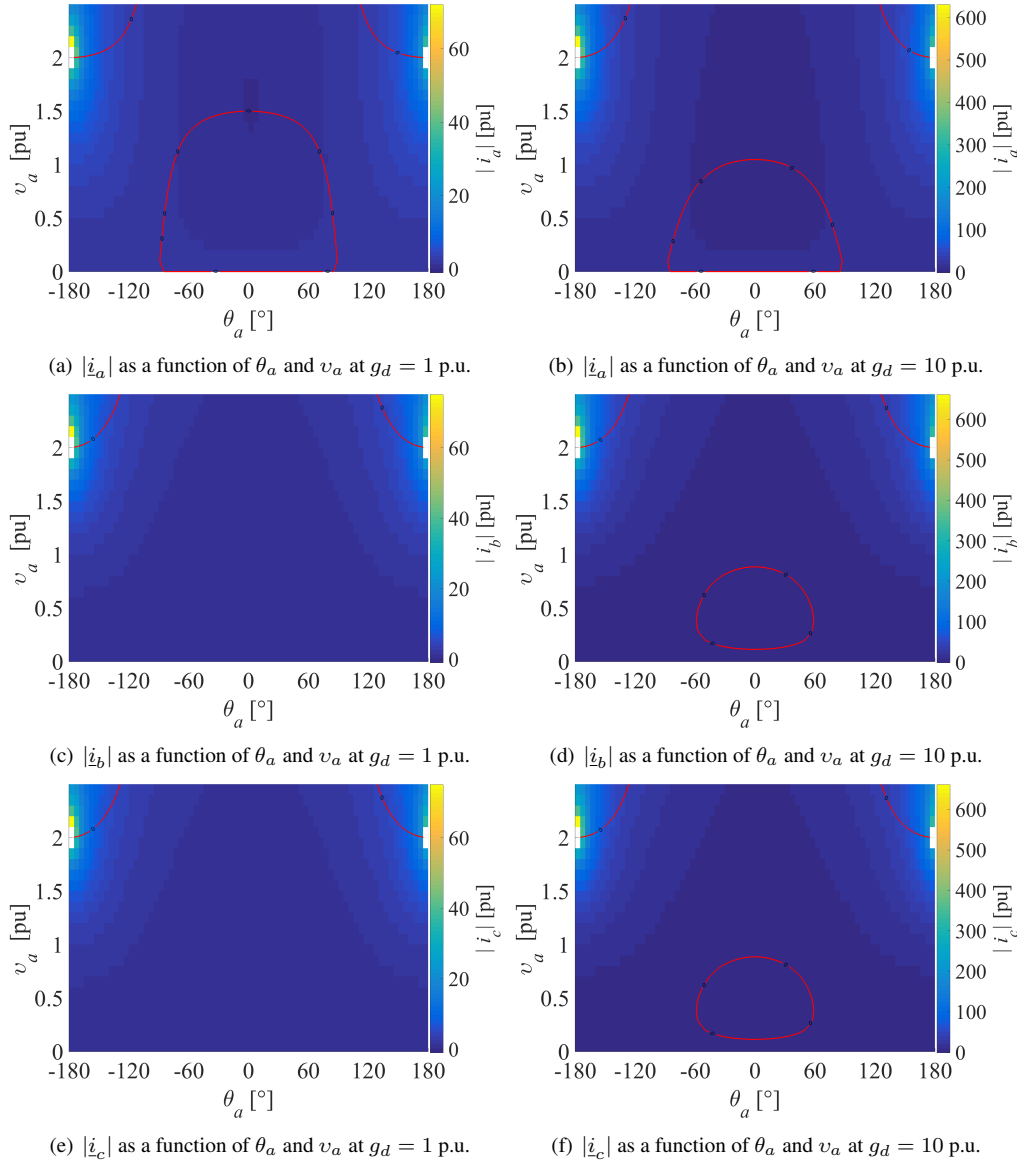


Figure 4.21: Phase currents dependency on the variation of phase voltage  $v_a$ , phase angle  $\theta_a$  at nominal input power  $p_{dc} = -1$  p.u. and damping conductance  $g_d = 1$  p.u. and  $g_d = 10$  p.u.

The simulation results for  $g_d = 10$  p.u. reveal that the current magnitudes are considerably higher and the border mode of phase  $a$  has decreased. Furthermore, at this value of  $g_d$  a border mode appears in phases  $b$  and  $c$ . In these areas the control strategy consumes currents from these phases and injects it back into phase  $a$ . This implies that the damping conductance value has an impact on the border mode and narrows down its area if the the damping conductance assumes high values. Note that, the white areas in the phase current plots that occur at  $v_a = 2$  p.u. and  $\theta_a = \pm 180^\circ$  are due to the fact that the denominator of (4.24) becomes 0, which leads to infinite values of the phase currents. Nevertheless, such conditions are not possible in practice so no further attention will be paid on them.

The phase angles are not presented deliberately, because they will not bring any useful information about the border mode of the phase currents and will increase unnecessarily the volume of this study.

#### 4.1.3.3 Sub-case 3: Phase voltage $v_a$ and phase angle $\theta_a$ variation under nominal consumed power

The examination of the three-phase damping control strategy at variable  $v_a$  and  $\theta_a$  is done in the same manner as Sub-case 2. By using a positive value for the power  $p_{dc} = 1$  p.u. and the same value of the damping conductance  $g_d = 1$  p.u. (or 10 p.u.) back in (4.24) the results presented in Fig. 4.22 are obtained. The results for the exchanged phase currents  $i_a$ ,  $i_b$  and  $i_c$  at  $g_d = 1$  p.u. are presented in Fig. 4.22 (a), (c) and (e) whereas the simulation results for  $g_d = 10$  p.u. are presented in 4.22 (b), (d) and (f).

The border modes of the exchanged phase currents when  $g_d = 1$  p.u. is used are also depicted in all figures. Note that at  $\theta_a = 0^\circ$  the border mode and the magnitude of exchanged currents are the same as the ones obtained in Fig. 4.8. Therefore, if  $v_a$  and  $\theta_a$  are inside the contour, current is being injected in phase  $a$  and if they are outside the contour, then current is being drawn from phase  $a$ . Similarly for phase currents  $i_b$  and  $i_c$  it can be said that if  $v_a$  and  $\theta_a$  are under the contour, phase currents are being drawn from phases  $b$  and  $c$ . The opposite is true if  $v_a$  and  $\theta_a$  are outside the border mode in phases  $b$  and  $c$ . In active rectification regime, the border mode contour is considerably different compared to the border mode in current injection regime. However, this does not deteriorate the damping mitigation properties of the three-phase damping control strategy.

Fig. 4.22 (b), (d) and (f) show the obtained simulation results when a higher value of the damping conductance is considered. These results show that there is a better similarity between the current consumption and current injection modes (Fig. 4.21 (b), (d) and (f)) because the border modes tend to the same voltage values. Therefore, it can be concluded that at higher values of  $g_d$  both modes tend to draw phase currents with similar magnitudes.

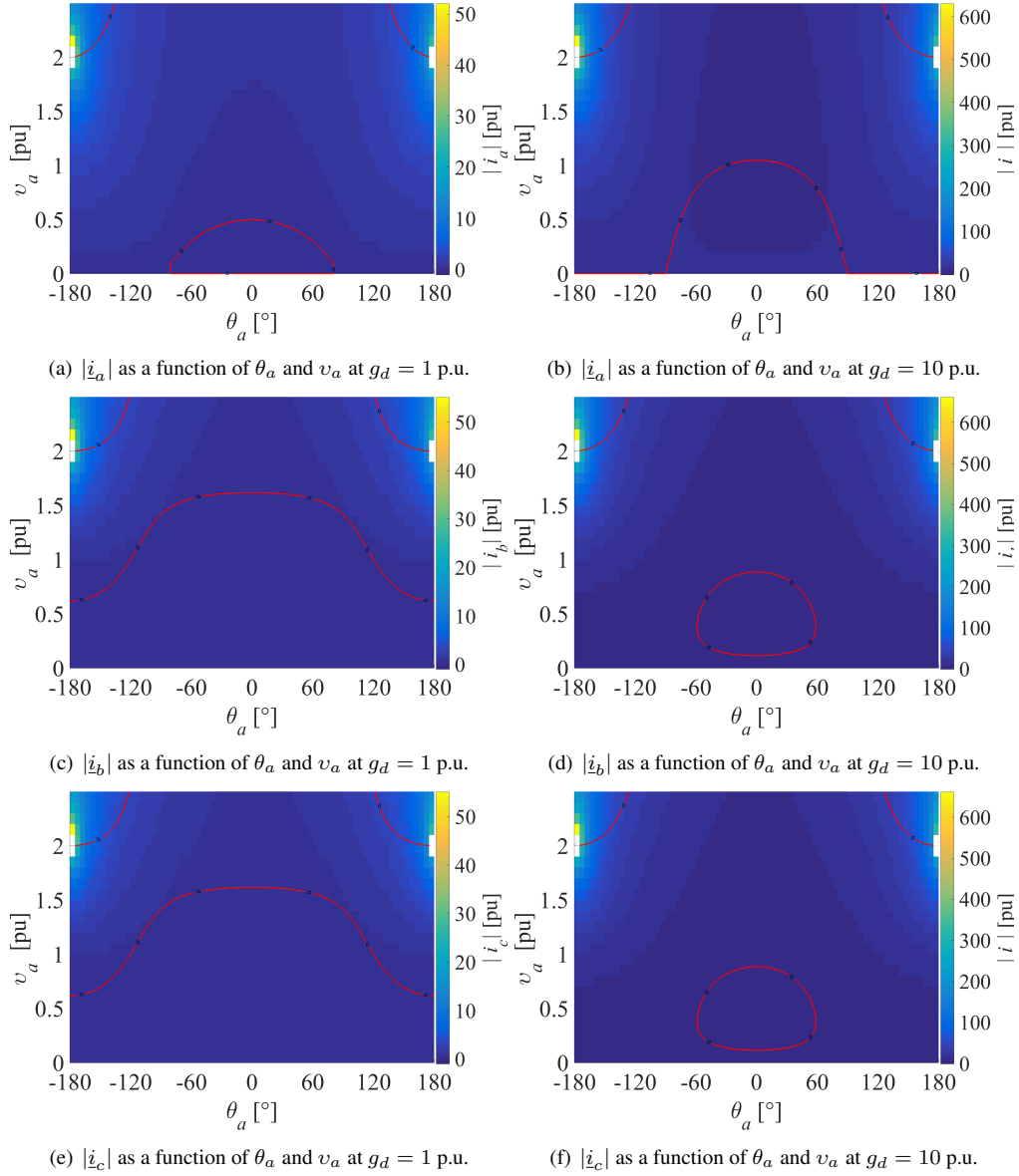


Figure 4.22: Exchanged phase currents as a function of phase voltage  $v_a$ , phase angle  $\theta_a$  at nominal consumed power  $p_{dc} = 1$  p.u. and damping conductance  $g_d = 1$  p.u. and  $g_d = 10$  p.u.

## 4.2 Limits of the damping conductance values based on the current ratings of the power electronic inverter

All examples considered so far were conducted under the assumption that the power electronic inverter of the DER is able to handle infinite power. In practice, all power electronic inverters are designed and dimensioned to some nominal and peak power ratings, which the inverter is able to withstand and operate without a failure. The injected current (power) limits of the inverters are mainly determined by the used power electronic switches, output filters, printed circuit board layout etc. Higher currents than the maximum permitted may cause failure in the power electronic switches or saturate the output inductor filters that will lead to excessive currents, which will damage the power electronic inverter. All off-the-shelf inverters are equipped with protections that will safely disconnect the inverter from the grid in case of abnormal conditions such as overloading. In practice, significant oversizing is economically not viable so appropriate current limits have to be set in order to guarantee safe and reliable operation of the power electronic inverter.

As it was demonstrated above, the three-phase damping control strategy is able to mitigate the voltage unbalance at the point of PCC by injecting higher current in the phase with the lower voltage and lower currents in the phases with the higher voltage. This is also valid when the phase angles deviate from their nominal values but in this case, reactive power is exchanged by the control strategy. Therefore, the voltage unbalance capabilities of the three-phase damping control strategy are directly related to the power ratings of the used power electronic inverter.

The behaviour of the three-phase damping control strategy was studied by its mathematical description and also by means of graphs where the exchanged phase currents magnitude and angles were mapped based on certain variables. This examination showed that the phase current magnitudes depend on the voltage unbalance at the inverter terminals as well as the value of damping conductance. The purpose of this examination was illustrate the behaviour of the three-phase damping control strategy by means of case studies and give an idea of the approximate sizing of the power electronic inverter based on the magnitude of the injected currents. The examination is conducted under balanced and highly unbalanced (voltage magnitudes as well as phase angle deviation) conditions at the inverter terminals.

According to EN50160 [8] the minimum and maximum allowed phase voltages in public LV grids are 0.9 and 1.1 p.u. respectively. However, under abnormal conditions such as voltage dips, the residual voltage might drop down to nearly 0V. The different grid codes in the different countries define the minimum residual voltage at which the inverter must remain connected to the grid for a specific time [51] and provide voltage support during the fault period. This time varies between 80 ms and 150 ms for the different countries and their grid codes. The

exact behaviour of the three-phase damping control strategy and the influence of the damping conductance under voltage dips is studied thoroughly in Chapter 7 of this thesis. Nevertheless, to complete this case study some voltage dips are considered with certain simplifications and assumptions. In [81], the author classifies 7 different types of voltage dips:

- Three-phase fault- Type A
- Single-phase fault -Type B
- phase-to-phase fault - Type C
- phase-to-phase fault - Type D
- Two-phase-to-ground - Type E
- Two-phase-to-ground - Type F
- Two-phase-to-ground - Type G

and they are depicted in Fig. 4.23.

In chapter 7, a detailed literature analysis is conducted regarding the propagation of the voltage dips as well as their residual voltages at the terminals of the sensitive equipment. In practice, not all of the dips present in Fig. 4.23 can be experienced by a load connected at LV network. To reduce the high voltage to medium and low voltage levels, the DSO uses a few step-down transformers. According to [82] the most common MV/LV distribution transformer is Dyg. If a fault occurs at MV network it propagates through at least one distribution transformer. Moreover, a star connected load and delta connected loads may experience a dip of another type. In Table 7.1, the propagation of voltage dips Type B, C and A evolves when propagating through one or more Dyn distribution transformers. These results are found in [81] and used in chapter 7. The results of Table 7.1 are obtained under the assumption that the zero-sequence does not propagate to the terminals of the equipment. This assumption is made because the zero-sequence voltage component does not propagate through the Dy transformer.

In order to have an idea of the injected currents by the three-phase damping control strategy when operating under abnormal conditions the proper voltage dip type must be selected. Voltage dip Type A is a three-phase symmetrical voltage dip and will cause symmetrical current injection by the three-phase damping control strategy. In addition, Table 7.1 shows that this dip type does not change when propagating through the Dy transformers. Therefore, further examination of voltage dip Type A will not be performed. All other voltage dips have the potential to introduce significant voltage unbalance at the PCC depending on the fault type and residual voltages. However, to limit the volume of the study, the dip with the most severe effect on the power quality must be selected.

| Level | 1 ph.-to-gnd   | 2 ph.          | 2ph.-gnd      |
|-------|----------------|----------------|---------------|
| HV    | Type B (33%)   | Type C (33%)   | Type E (25%)  |
| MV    | Type C (20%)   | Type D (20.4%) | Type F (25%)  |
| LV    | Type D (20.4%) | Type C (3.8%)  | Type G (6.1%) |

Table 4.1:  $VUF_2$  of voltage dip propagation in a typical transmission/distribution grid configuration and residual voltage of 50% for star connected load.

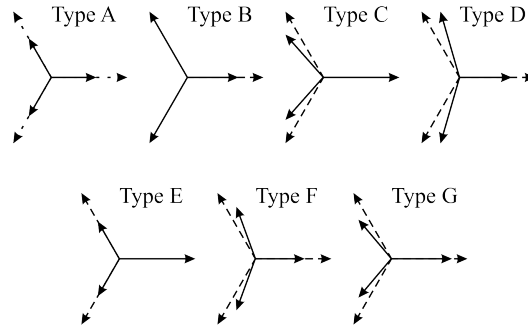


Figure 4.23: Dips classification<sup>1</sup> where - - - represents the nominal phase magnitudes and angles while — represents the residual phase voltages and angles during a voltage dip

By calculating (7.2) to (7.7) for the residual voltages of the voltage dips described in Table 7.1, the resultant negative-sequence voltage unbalance factors are listed in Table 4.1. These results show that at 50% residual voltage, the most severe dip that could occur at the equipment terminals is happening when a voltage dip of type B is present at HV level. It is possible that the residual voltage is lower than 50% but according to (7.2) to (7.7) the trends of the voltage dip propagation and the voltage unbalance factor will be still the same.

Therefore, the results in Table 4.1 allow to conclude that the voltage dip of Type D is among the most severe ones in terms of voltage unbalance. In addition, according to [83,84] this is the most common occurrence (around 40%) of voltage dips in LV grids. Nevertheless, this voltage dip is less severe in terms of voltage unbalance compared to Type B or C voltage dips, which both deliver the same level of  $VUF_2$  for the same residual voltages. To complete these analysis of the power sizing of the inverter, a voltage dip must be selected. Voltage dip of Type C has two variables in it, voltage magnitude and voltage angle, which will unnecessary increase the complexity of the analysis. On the other hand, voltage dip of Type B has only one variable but both voltage dips of Type B and C lead to the same voltage unbalance. In addition, at high values of the damping conductance most of the power will be injected through the one phase when voltage dip Type B is considered, while at Type C, the power is injected through two phases. Consequently, voltage dip Type B will be also examined.

<sup>1</sup>Source [81]

The nominal current that is being injected by the three-phase damping control strategy under balanced conditions at the PCC is 0.333 pu. In this study, the current magnitudes are examined when two different values of  $g_d$  are considered. The line impedances are also considered negligibly small and their influence of the voltage at the PCC can be neglected. An idea of the needed current oversizing of the power electronic inverter, based on the voltage unbalance present at the PCC, can be obtained by mapping the phase currents with contour plots. To achieve that, four inverters with different current ratings are considered:

- Inverter maximum current is 0.333 p.u. - this corresponds to the nominal value of the currents when the three-phase damping control strategy injects only positive-sequence component ( $g_d = 0$  pu).
- Inverter maximum current is 0.433 p.u. - in this case the inverter is oversized with 30%, which allows 30% higher current injection in the phase(s) with the lower voltage.
- Inverter maximum current is 0.666 pu - in this case the inverter is oversized with 100%, which allows 100% higher current injection in the phase(s) with the lower voltage.
- Inverter maximum current is 0.999 p.u. - in this case the inverter is oversized such that all available power can be injected in one phase.

In Chapter 3, the needed oversizing between the positive-sequence and the modified three-phase damping control strategy is calculated to be 22%. To ensure some current reserve, it is assumed that oversizing of 30% will be used. The oversizing of 100% and 200% are used to define some boundary conditions of the injected currents but such oversizings will not be economically viable. All analyses will be performed for the injection and consumption modes of the three-phase damping control strategy. The results of the zero-powered DER will fall within the results of these two modes.

#### **4.2.1 Practical considerations of the damping conductance when DER is subjected to a voltage dip of Type B**

This analysis is performed similarly as §4.1.1.2 and §4.1.1.3, but there are some differences. The range of the residual voltage in phase  $a$  is reduced as well as the value of  $g_d$ . In addition, it is assumed that the fault is occurring at the voltage level of the DER, therefore, the zero-sequence component also plays a role. During faults, the zero-sequence component leads to voltage swells in the non-affected phases. The magnitude of the swell depends on zero-sequence impedance of the feeder and in the literature [81,84] report values between 1.1 and 1.3 p.u. for urban

feeders. Therefore, 1.3 p.u. is assumed to be the phase value of phase voltages  $v_b$  and  $v_c$ .

The obtained results are depicted in Fig. 4.24 where, Fig. 4.24 (a), (c) and (e) are obtained at  $p_{dc} = -1$  p.u. and Fig. 4.24 (b), (d) and (f) at  $p_{dc}g_d = 1$  p.u. One dashed vertical red line is added to highlight the voltage limit 0.85 set by [85]. The border mode is plotted as well and it is presented by a red contour. If  $v_a$  outside the red contour the control strategy injects current into the phase under consideration and vice versa if  $v_a$  is above. The exchanged currents by the different inverter ratings are highlighted by yellow contours. The sequence of the current contours, describing the different oversizing, is from inner to outer contour, which starts from 0.333, 0.433, 0.666 to 0.999 p.u. and it is valid for all figures. In this examination the contour (0.333 p.u.) will be used as a reference and it will not be discussed in details, because the voltage unbalance mitigation requires asymmetrical current injection and in all cases different than  $v_a = v_b = v_c = 1$  p.u.  $p_{dc} = -1$  p.u. and  $\theta_a = \theta_b - \frac{2\pi}{3} = \theta_c + \frac{2\pi}{3}$  the phase currents will deviate from this nominal value. The current magnitudes injected by the different inverters under the above listed conditions are as follows:

- *30% oversizing:*
  - injection mode: From the results presented in Fig. 4.24 (a) the phase current  $|i_a|$  reaches 0.433 p.u. limit at  $v_a = 0.85$  p.u. and  $g_d = 0.4$  p.u. The lower the residual voltage gets, the lower must be the value of the damping conductance. For the considered oversizing limit, at  $v_a = 0$  p.u. the value of  $g_d$  must be lower than 0.1 p.u. As of the other two phases, the high value of the phase voltages leads to a smaller current injection into them and the 0.43 p.u. contour is outside the considered area. Note that current is injected in phase  $a$  in the entire range of  $v_a$  and  $g_d$  while in phases  $b$  and  $c$  current is injected outside the red contour and vice versa.
  - consumption mode: From the results presented in Fig. 4.24 (b) it can be seen that the contour of the 0.433 is wider for the entire range of  $g_d$  compared to the injection mode. At  $v_a = 0.85$  p.u. the value of  $g_d$  can assume values of 2 p.u. and at residual voltage  $v_a = 0$  p.u. the damping conductance is almost 0.6 p.u. Within the contour of 30% oversizing, the border mode is situated. If the values of  $g_d$  and  $v_a$  are outside of the contour, current is drawn from phase  $a$  and vice versa. From Fig. 4.24 (d) and (f) it can be seen that the oversizing of 30% is breached at even lower values of  $g_d$  of about 1.2 p.u. when the residual voltages are relatively high. Therefore, in this mode and 30% oversizing the maximum value of  $g_d$  is determined by the current capacity of the non-affected phases and it should not exceed 1.2 p.u.

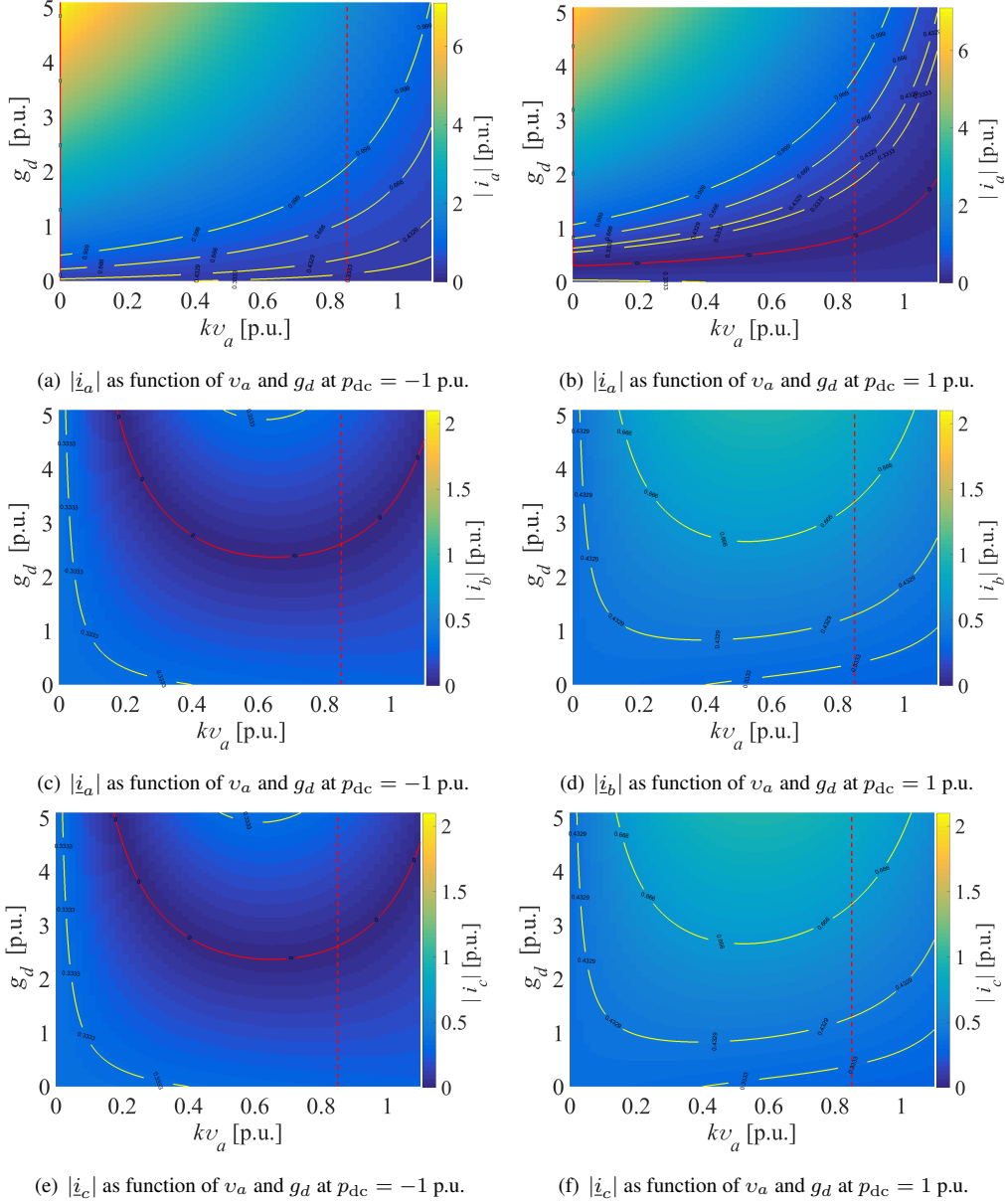


Figure 4.24: Phase currents exchange dependency under Type B voltage dip and  $g_d$  in generation ( $p_{dc} = -1$ ) and consumption ( $p_{dc} = 1$  p.u.)

- 100% oversizing:

- injection mode: From the presented results in Fig. 4.24 (a) the phase current  $|i_a|$  reaches 0.666 p.u. limit at  $v_a = 0.85$  p.u. and  $g_d = 1$

p.u. The trends are similar to the 30% oversizing scenario. For the considered oversizing limit, at  $v_a = 0$  p.u. the value of  $g_d$  must be lower than 0.3 p.u. As of the other two phases, the high value of the phase voltages leads to a smaller current injection into them and the 0.666 p.u. contour is outside the considered area. Note that current is injected in phase  $a$  in the entire range of  $v_a$  and  $g_d$  while in phases  $b$  and  $c$  current is injected outside the red contour and vice versa.

- consumption mode: From the presented results in Fig. 4.24 (b) it can be seen that the contour of the 0.666 is wider for the entire range of  $g_d$  compared to the injection mode. At  $v_a = 0.85$  p.u. the value of  $g_d$  can assume values of 2.7 p.u. and at residual voltage  $v_a = 0$  p.u. the damping conductance is almost 0.8 p.u. Within the contour of 100% oversizing, the border mode is situated. If the values of  $g_d$  and  $v_a$  are outside of the contour, current is drawn from phase  $a$  and vice versa. From Fig. 4.24 (d) and (f) it can be seen that the oversizing of 100% is breached at  $g_d$  values of 3.5 p.u. when the residual voltages are relatively high. Therefore, in this mode and 100% oversizing the maximum value of  $g_d$  is determined by the current capacity of the affected phase and it should not exceed 2.7 p.u.

- *200% oversizing*

- injection mode: From the presented results in Fig. 4.24 (a) the phase current  $|i_a|$  reaches 0.999 p.u. limit at  $v_a = 0.85$  p.u. and  $g_d = 2$  p.u. The trends are similar to the 30% oversizing scenario. For the considered oversizing limit, at  $v_a = 0$  p.u. the value of  $g_d$  must be lower than 0.5 p.u. As of the other two phases, the high value of the phase voltages leads to a smaller current injection into them and the 0.999 p.u. contour is outside the considered area. Note that current is injected in phase  $a$  in the entire range of  $v_a$  and  $g_d$  while in phases  $b$  and  $c$  current is injected outside the red contour and vice versa.
- consumption mode: From the presented results in Fig. 4.24 (b) it can be seen that the contour 0.999 p.u. is wider for the entire range of  $g_d$  compared to the injection mode. At  $v_a = 0.85$  p.u. the value of  $g_d$  can assume values of 3.6 p.u. and at residual voltage  $v_a = 0$  p.u. the damping conductance is almost 1.1 p.u. Within the contour of 200% oversizing, the border mode is situated. If the values of  $g_d$  and  $v_a$  are outside of the contour, current is drawn from phase  $a$  and vice versa. From Fig. 4.24 (d) and (f) it can be seen that the contour of the oversizing of 200% is outside of the range of  $v_a$  and  $g_d$ . Therefore, in this mode and 200% oversizing the maximum value of  $g_d$  is determined by

the current capacity of the affected phase and it should not exceed 3.7 p.u.

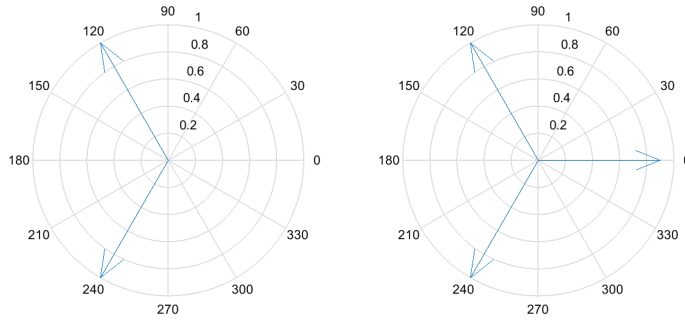
From the presented simulation results it is clear that three-phase damping control strategy requires an oversized power electronic inverter in order to mitigate voltage unbalance or provide fault ride-through capabilities and support the grid voltage. The overizing is fairly proportional to the damping conductance value and the voltage unbalance and it is a compromise between performance and cost.

## 4.2.2 Practical considerations of the damping conductance when DER is subjected to a voltage dip of Type D

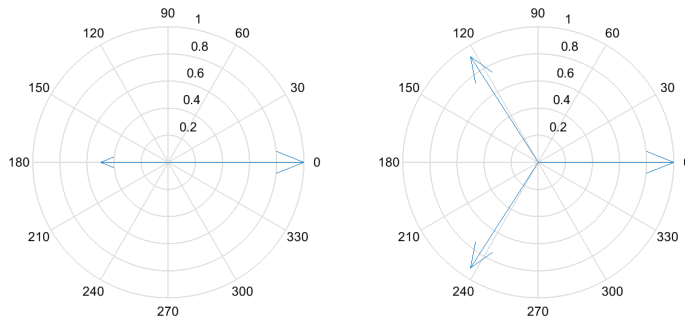
This analysis is performed according to Fig. 7.4, where a voltage dip of Type B occurs at the HV level and the dip propagated through two Dy transformers. The residual voltage  $v_a$  is varying from 0 to 0.9 p.u. The extreme values of the residual voltage  $v_a$  of the voltage dip propagation from HV to LV level are presented in Fig. 4.25. Fig. 4.25 (a), (c) and (e) show the evolution of the voltage dip when the residual voltage is considered to be 0 p.u. while Fig. 4.25 (b), (d) and (f) show the evolution of the dips at residual voltage of 0.9 p.u. These voltage dips are calculated according to (7.2), (7.3) and (7.4).

The reaction of the three-phase damping control strategy as a function of the residual voltage  $kv_a$  and the damping conductance is presented in Fig. 4.26. Fig. 4.26 (a), (c) and (e) show the obtained simulation results of the different phase currents in injection mode while Fig. 4.26 (b), (d) and (f) depict the phase currents in consumption mode. Similarly to Fig. 4.24 the oversizing is marked by using yellow contours while the border mode is denoted by using a red contour. A dashed red line indicates the lower voltage limit set by [9]. The same oversizing ratings are adopted in this case study.

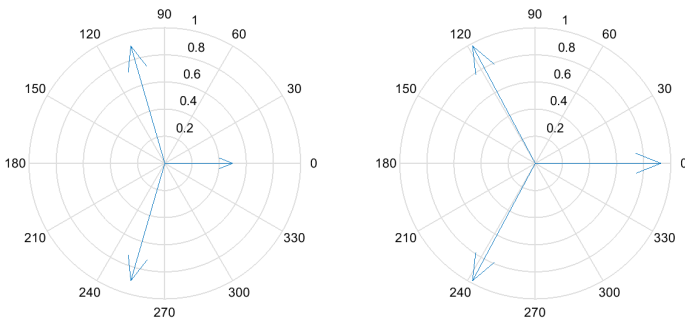
The sequence of the current contours, describing the different oversizing, is from inner to outer contour, which starts from 0.333, 0.433, 0.666 to 0.999 p.u. and it is valid for all figures. In this examination the most inner contour (0.333 p.u.) will be used as a reference and it will not be discussed in detail, because the voltage unbalance mitigation requires asymmetrical current injection and in all cases different than  $v_a = v_b = v_c = 1$  p.u.  $p_{dc} = -1$  p.u. and  $\theta_a = \theta_b - \frac{2\pi}{3} = \theta_c + \frac{2\pi}{3}$  the phase currents will deviate from its nominal value. The current magnitudes injected by the different inverters under the above listed conditions are as follows:



(a) Voltage dip Type B at  $v_a = 0$  p.u. (HV-level) (b) Voltage dip Type B at  $v_a = 0.90$  p.u. (HV-level)



(c) Voltage dip Type C at  $v_a = 0$  p.u. according to (7.3)(MV-level) (d) Voltage dip Type C at  $v_a = 0.90$  p.u. according to (7.3)(MV-level)



(e) Voltage dip Type D at  $v_a = 0$  p.u. according to (7.4)(LV-level) (f) Voltage dip Type D at  $v_a = 0.90$  p.u. according to (7.4)(LV-level)

Figure 4.25: Voltage dip evolution from HV to LV level through two Dy transformers

• 30% oversizing:

- injection mode: From the presented results in Fig. 4.26 (a) the phase current  $|i_a|$  reaches 0.433 p.u. limit at  $v_a = 0.85$  p.u. and  $g_d = 1.5$  p.u. The lower the residual voltage gets, the lower must be the value

of the damping conductance up to the point where  $g_d = 0$  p.u. at  $kv_a = 0.2$  p.u. As of the other two phases, the damping conductance value can be higher near the nominal values of  $v_a$  but at low values of  $|\dot{i}_a|$  breaches the oversizing limit of 30% at  $v_a = 0.25$  p.u. Therefore, 30% oversizing of the power electronic inverter will be insufficient to provide voltage dip mitigation.

- consumption mode: From the presented results in Fig. 4.26 (b) it can be seen that the contour of the 0.433 is wider for the entire range of  $g_d$  compared to the injection mode. At  $v_a = 0.85$  p.u. the value of  $g_d$  is greater than the maximum value of the examined range and at residual voltage  $v_a = 0$  p.u. the damping conductance is almost 2.6 p.u. Within the contour of 30% oversizing, the border mode is situated. If the values of  $g_d$  and  $v_a$  are outside of the contour, current is drawn from phase  $a$  and vice versa. From Fig. 4.26 (d) and (f) it can be seen that the oversizing of 30% is breached at very low values of  $g_d$  of about 2 p.u. when the residual voltages are relatively high and  $g_d$  must be set to zero at  $kv_a = 0.25$  p.u. Therefore, the same conclusions can be drawn as the injection mode.

- *100% oversizing*

- injection mode: From the presented results in Fig. 4.26 (a) the phase current  $|\dot{i}_a|$  reaches 0.666 p.u. limit at  $v_a = 0.85$  p.u. and  $g_d = 5.1$  p.u. The lower the residual voltage gets, the lower must be the value of the damping conductance up to the point where  $g_d = 0.7$  p.u. at  $kv_a = 0$  p.u. As of the other two phases, the damping conductance value can be higher near the nominal values of  $v_a$  but at low values of it  $g_d$  must not exceed 2.7 p.u. In conclusions, 100% oversizing of the power electronic inverter is sufficient to provide some voltage dip mitigation.
- consumption mode: From the presented results in Fig. 4.26 (b) it can be seen that the contour of 0.666 p.u. is wider for the entire range of  $g_d$  compared to the injection mode. At  $v_a = 0.85$  p.u. the value of  $g_d$  is greater than the maximum value of the examined range and at residual voltage  $v_a = 0$  p.u. the damping conductance is almost 3.6 p.u. Within the contour of 100% oversizing, the border mode is situated. If the values of  $g_d$  and  $v_a$  are outside of the contour, current is drawn from phase  $a$  and vice versa. From Fig. 4.26 (d) and (f) it can be seen that the oversizing of 100% is breached at very low values of  $g_d$  of about 2 p.u. when the residual voltages are relatively low. Therefore, the same conclusions as for the injection mode can be drawn here.

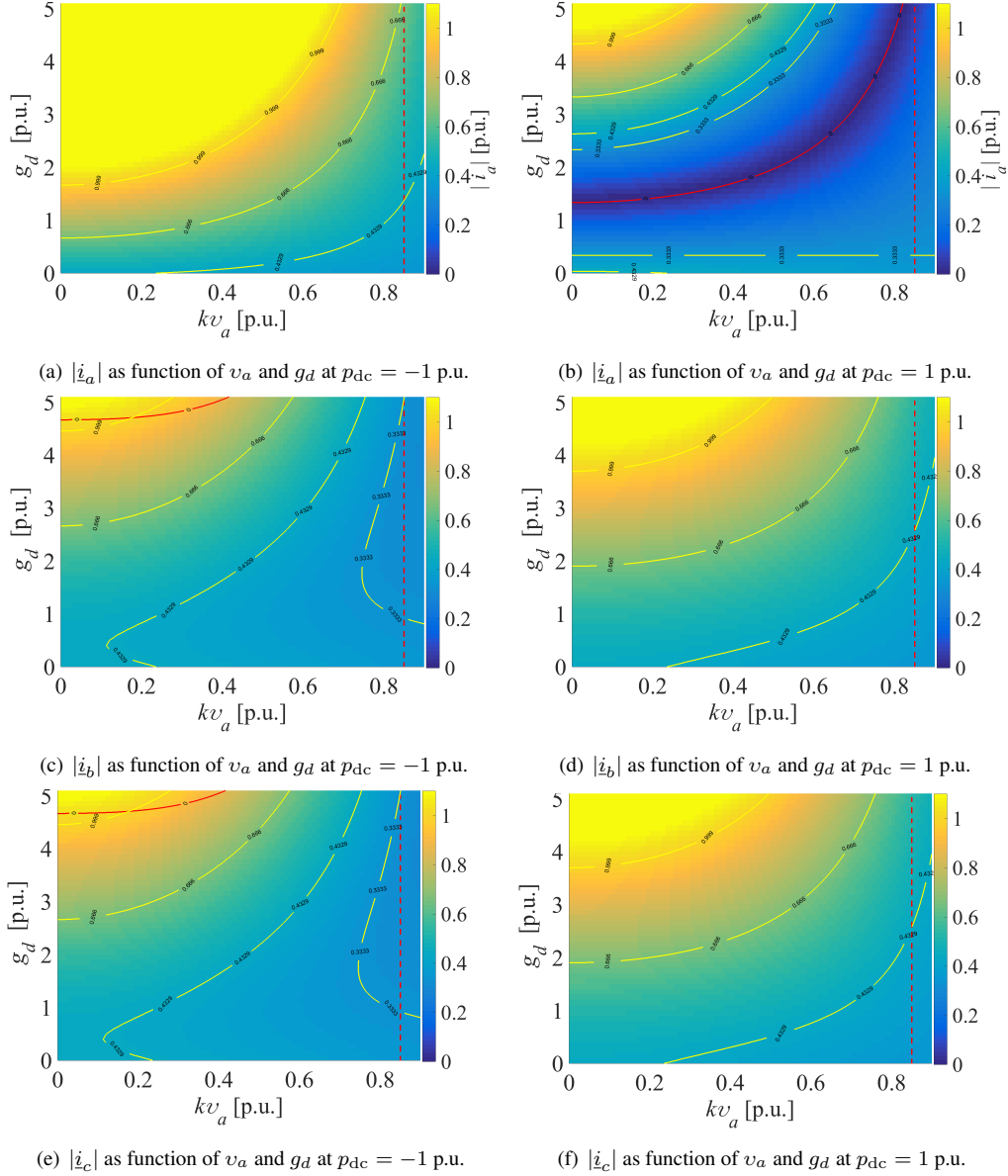


Figure 4.26: Phase currents exchange dependency under Type D voltage dip and  $g_d$  in generation ( $p_{dc} = -1$ ) and consumption ( $p_{dc} = 1$  p.u.)

- 200% oversizing

– injection mode: From the presented results in Fig. 4.26 (a) the phase

current  $|\dot{i}_a|$  reaches 0.999 p.u. limit at  $v_a = 0.85$  p.u. and  $g_d > 5.1$  p.u. The lower the residual voltage gets, the lower must be the value of the damping conductance up to the point where  $g_d = 1.7$  p.u. at  $kv_a = 0$  p.u. As of the other two phases, the damping conductance value can be higher near the nominal values of  $v_a$  but at low values of it  $g_d$  must not exceed 4.5 p.u. In conclusion, 200% oversizing of the power electronic inverter is sufficient to provide some voltage dip mitigation.

- consumption mode: From the presented results in Fig. 4.26 (b) it can be seen that the contour of the 0.999 is wider for the entire range of  $g_d$  compared to the injection mode. At  $v_a = 0.85$  p.u. the value of  $g_d$  is greater than the maximum value of the examined range and at residual voltage  $v_a = 0$  p.u. the damping conductance is almost 4.4 p.u. Within the contour of 200% oversizing, the border mode is situated. If the values of  $g_d$  and  $v_a$  are outside of the contour, current is drawn from phase  $a$  and vice versa. From Fig. 4.26 (d) and (f) it can be seen that the oversizing of 200% is breached at higher values of  $g_d$  of about 3.8 p.u. when the residual voltages are relatively low. Therefore, the same conclusions as for the injection mode can be drawn here.

From the presented simulation results it is clear that three-phase damping control strategy requires an oversized power electronic inverter in order to mitigate voltage unbalance or provide fault ride-through capabilities and support the grid voltage. The oversizing is a compromise between performance and cost.

### 4.2.3 Discussion and future work

If the purpose of DER is to perform only voltage unbalance mitigation, then the value of the damping conductance can be high (10 p.u. or more), which will improve the resistive behaviour of the control strategy and an oversizing between 30% and 100% can be used. If voltage dip mitigation is required then damping conductance must be kept at low levels (1 to 2 p.u.) in order not to exceed the current ratings of the power electronic inverter.

If the three-phase damping control strategy is combined with model-based predictive control, which calculates the rms values of the injected currents as a function of the input power and damping conductance, real time optimisations can be made so that a desired operating condition is achieved. In order to avoid malfunctioning of the DER, in these optimisations, constraints such as input power and inverter power ratings are imposed. Optimisation objectives could be optimal power quality performance, maximum renewable energy harvesting with acceptable power quality performance, grid loss minimisation, etc.

### **4.3 Validation of the discussed case studies in a distribution network by means of simulations on a real LV feeder**

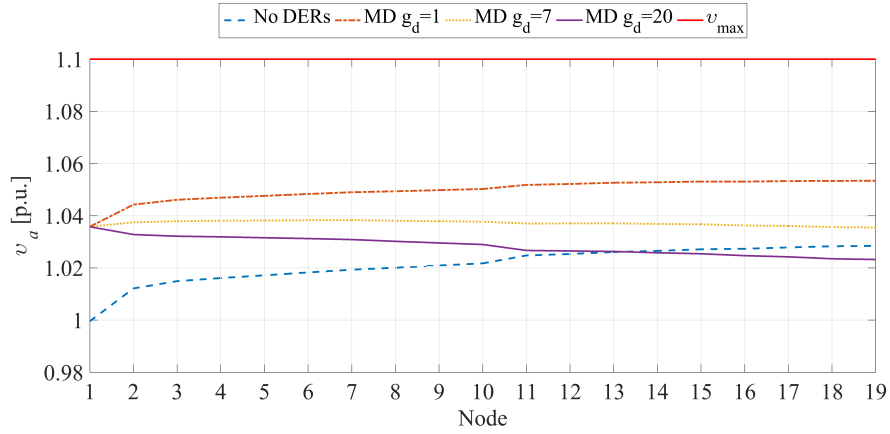
Up to this point, the line impedances in all examples were neglected in order to simplify the case studies and investigate the performance of the three-phase damping control strategy individually. The generation mode of the three-phase damping control strategy is described in details in Chapter 3. Therefore in this section the behaviour of the three-phase damping control strategy at zero dc power and consumption modes are investigated in a typical LV distribution feeder and the impact on the power quality is assessed. In these examinations the voltage unbalance is introduced by loads and the performance of the DER equipped with the modified three-phase damping control strategy is evaluated.

#### **4.3.1 Verification of zero-powered DERs in an LV distribution network by means of simulations**

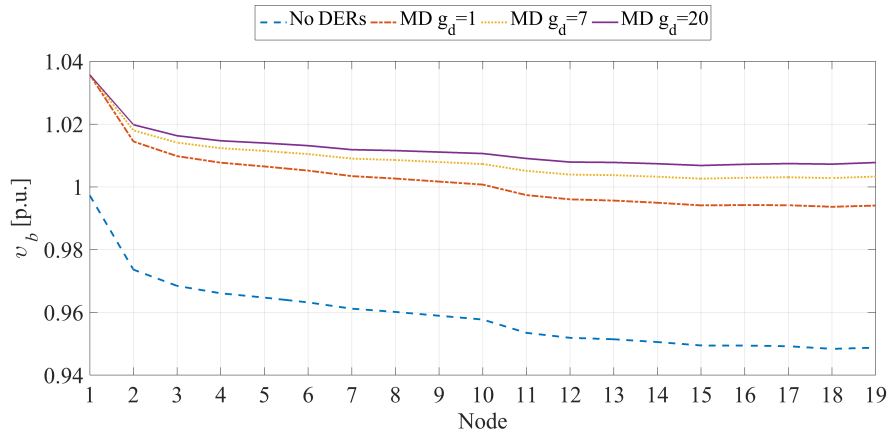
In this section, the performance of the three-phase damping control strategy is examined in the LV feeder presented in § 3.2, Fig. 3.6. The other control strategies such as the positive-sequence and the drooped positive-sequence are excluded from this examination because they are not able to provide any contribution to the voltage profile improvement when no power is provided by the primary source. The control strategies that are able to provide some voltage control by means of reactive power are also not considered because of the same reason. For consistency with the study conducted in Chapter 3, the locations of the DERs and the loads are kept the same as § 3.2. More information about the loads connections and power ratings can be found in Table 3.4 and Table 3.2, respectively.

The simulations are conducted in the same manner as § 3.2 i.e. the initial voltage of the programmable power source is set to 1.04 p.u. and a time domain simulation is used with simulation time of 2 seconds. When the simulations is completed, the results are post-processed and the last readings are used to present the obtained simulation results. To keep consistency with the simulations performed in §3.2, the same values of the damping conductance will be used. In this examination, four different cases are examined:

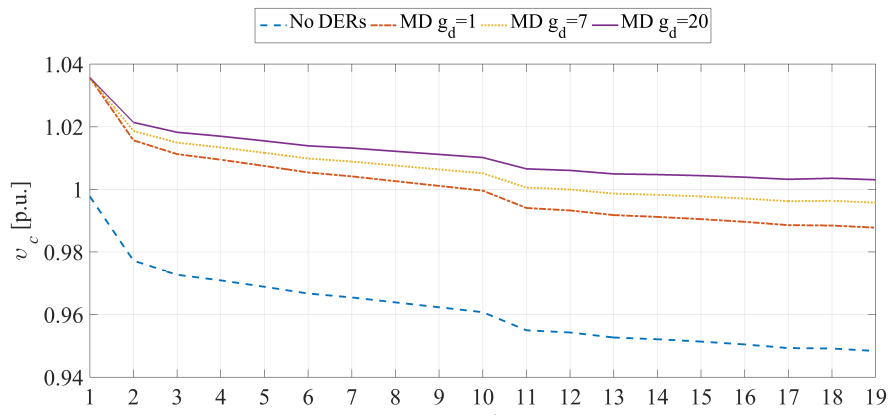
- case (i) where no DERs are connected to the feeder
- case (ii) where all DERs are not supplied with any power from the primary source and the damping conductance is set to 1 p.u.
- case (iii) similar to case (ii) but the damping conductance assumes a value of 7 p.u.



(a) Voltage profile of phase a across the 19 node feeder



(b) Voltage profile of phase b across the 19 node feeder



(c) Voltage profile of phase c across the 19 node feeder

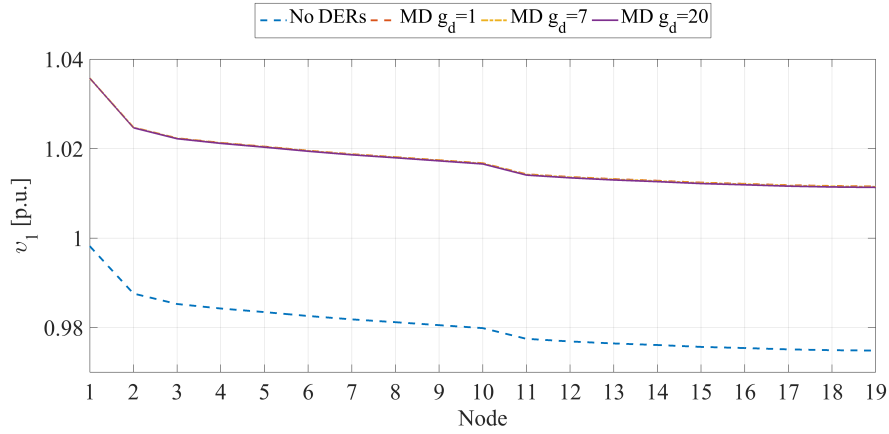
Figure 4.27: Phase voltage results comparison between the four case studies when  $p_{dc} = 0$  p.u. is used

- case (iv) similar to case (ii) but the value of the damping conductance assumes value of 20 p.u.

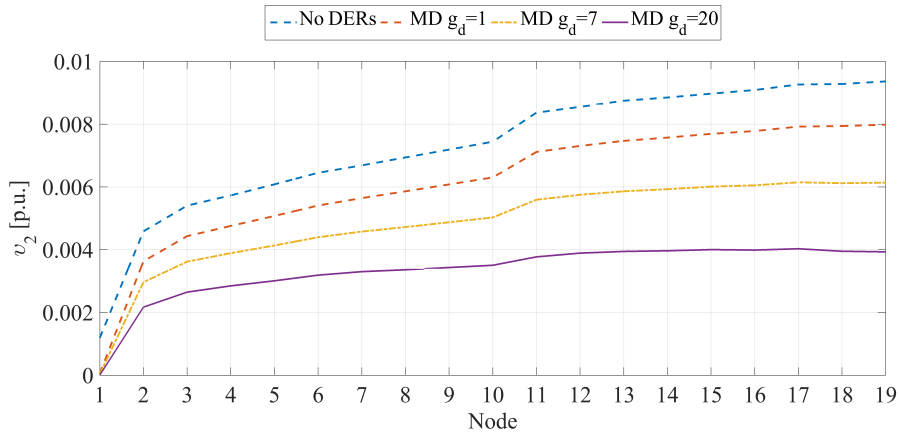
The obtained simulation results of the phase voltages are presented in Fig. 4.27 (a), (b) and (c), respectively. When no DERs are present in the feeder, the voltage profile of phase  $a$  experiences the effect of neutral point shifting because phases  $b$  and  $c$  are the most loaded ones. As a result, at the end of the feeder  $v_a$  is higher compared to the initial setting of 1.04 p.u. while  $v_b$  and  $v_c$  drop with 0.05 p.u. down to almost 0.985 p.u.

By using the modified three-phase damping control strategy in DERs at nodes 11, 18 and 19, the voltage unbalance is mitigated by consuming current from the phase with the higher voltage and it injects it back in the phases with the lower voltages. When an initial value of the damping conductance of 1 p.u. is used, it can be seen already the positive effect of reducing the voltage level in phase  $a$  and increasing the voltages in the most loaded phases  $b$  and  $c$ . The effect is even more prominent when higher values for  $g_d$  are used, which in this example are 7 p.u. and 20 p.u. The negative effect of the neutral point shifting is almost eliminated when  $g_d = 7$  p.u. because the initial value of  $v_a$  at node 1 is almost equal to the one at node 19. At  $g_d = 20$  p.u. phase voltage  $v_a$  experiences a voltage drop compared to node 1 because the DERs consume significant amount of power and inject it back in phases  $b$  and  $c$  to mitigate the voltage unbalance. As a result, the voltage difference between the phases is reduced.

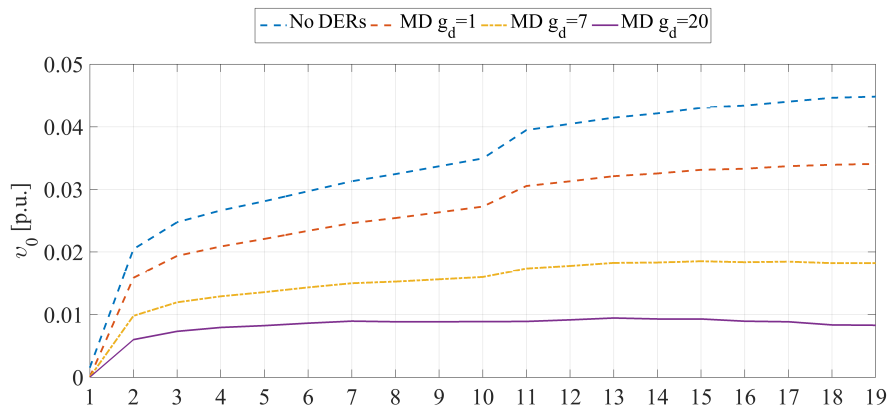
The positive-, negative- and zero-sequence symmetrical components voltages are depicted in Fig. 4.28 (a), (b) and (c), respectively. From the obtained simulation results it can be seen that in all considered cases the positive-sequence component is decreasing across the feeder no matter what value of the damping conductance is used. Since  $p_{dc} = 0$  p.u. the input conductance  $g_1$  has a small value, which determines the positive-sequence term in (4.4) (the first term in the brackets that is multiplied by  $g_1$ ), hence this term has insignificant contribution to the injected currents. On the other hand, the second term (the one multiplied by  $g_d$ ), determines the final exchanged current due to the non-zero value of  $g_d$ . As a matter of fact, this statement is confirmed when observing the negative- and zero-sequence components in Fig. 4.28 (b) and (c). When only loads are considered, the negative- and zero-sequence components have the highest voltage profiles. With introducing the DERs with  $g_d = 1$  p.u. both profiles of  $v_2$  and  $v_0$  are slightly lowered due to the resistive behaviour of the damping control strategy. With increasing the value of the damping conductance the resistive behaviour is improved and the impact over  $v_2$  and  $v_0$  profiles is significant. As a result, both profiles are lowered. The negative-sequence is decreased almost by 50%, whereas the zero-sequence is decreased by 77.7% when compared to case (i).



(a) Positive-sequence voltage profile across the 19 node feeder



(b) Negative-sequence voltage profile across the 19 node feeder



(c) Zero-sequence voltage profile across the 19 node feeder at

Figure 4.28: Symmetrical components voltage comparison between the four case studies when  $p_{dc} = 0$  p.u. is used

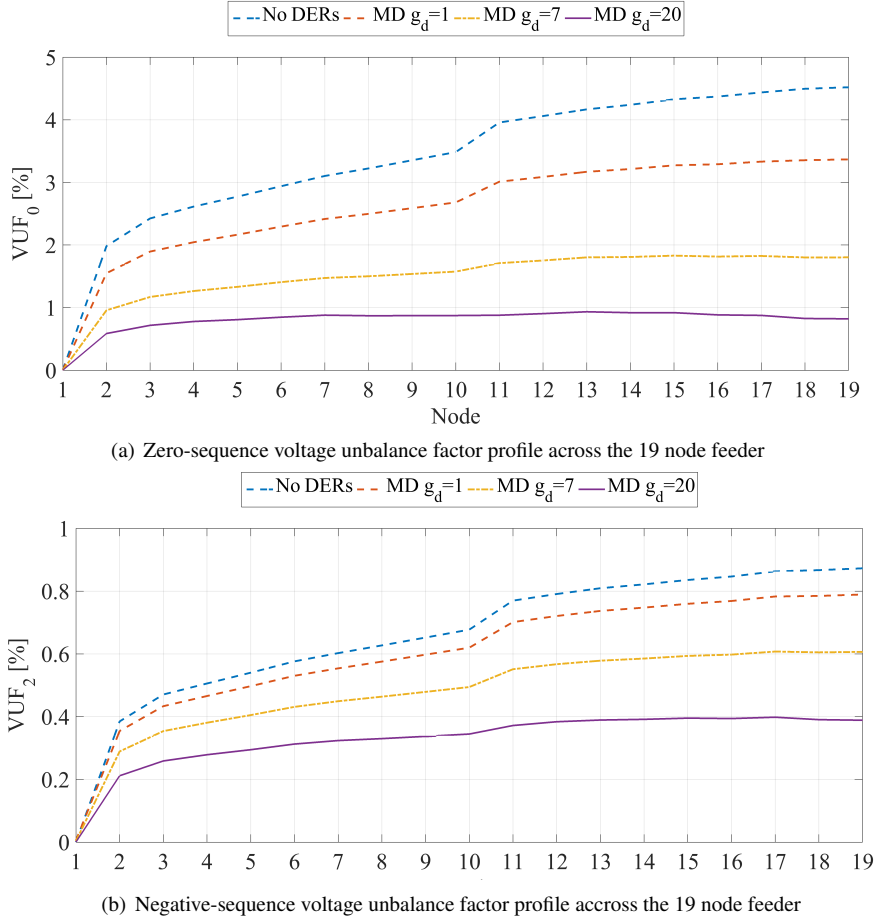


Figure 4.29: Voltage unbalance factors profiles comparison between the four case studies when  $p_{dc} = 0$  p.u. is used

Taking into account that there is no positive-sequence current injection by the DERs, the positive-sequence voltage is reducing towards the end of the feeder, while the zero- and negative-sequence voltage components are increasing due to the asymmetrical loading. Since the voltage unbalance factors are calculated as a ratio of  $\underline{v}_0$  ( $\underline{v}_2$ ) to  $\underline{v}_1$ , then the  $VUF_0$  and  $VUF_2$  are also deteriorated, which can be also seen in Fig. 4.29. Similar to Fig. 4.28, both  $VUF_0$  and  $VUF_2$  are influenced by the modified damping control strategy even though the damping conductance value is set to 1 p.u. By increasing  $g_d$  up to 20 p.u., both voltage unbalance factors are significantly reduced by almost the same factors of 77% for  $VUF_0$  and 50% for  $VUF_2$ .

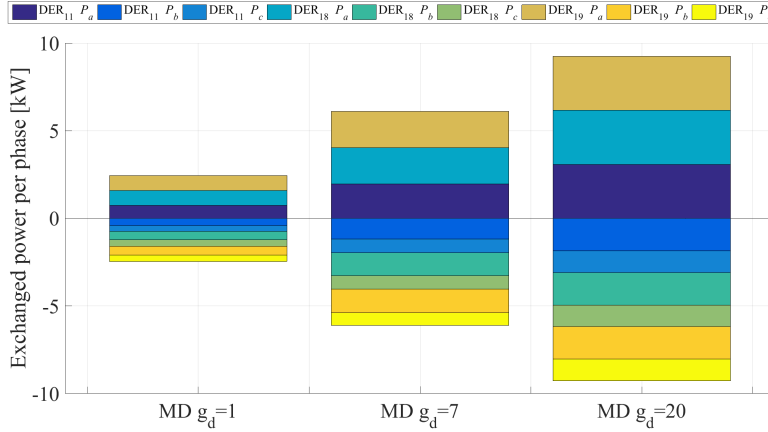


Figure 4.30: Per phase active power injection by the different DERs

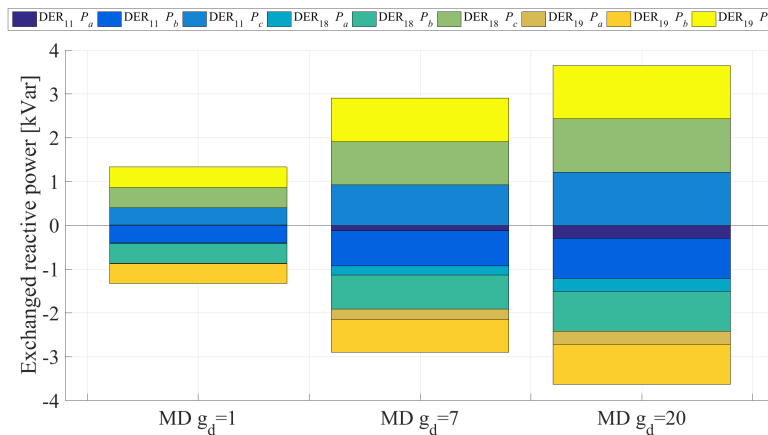


Figure 4.31: Per phase reactive power injection by the different DERs

The beneficial effect of the modified damping control strategy on the voltage profiles is achieved by current consumption from the phase with the higher voltage and current injection in the phases with the lower voltages. Fig. 4.30 shows the segregated power exchange by the different DERs and a segregation by phase power is also done. Since the voltage in phase *a* is the highest, the modified damping control strategy consumes active power from phase *a* and it can be seen that the exchanged power in phase *a* for all DERs is positive, which corresponds to a power consumption in this phase. The consumed currents are injected back in phases *b* and *c* and as it can be seen from Fig. 4.30 the exchanged power for these two phases is negative, which corresponds to a current injection. For this particular

case, the most beneficial effect on the voltage profiles is obtained when  $g_d = 20$  p.u. is used. This beneficial effect is achieved by consuming total active power (by all DERs) from phase  $a$ , which in this example is around 9kW and the sum of the injected powers in phases  $b$  and  $c$  is also 9kW, which indeed corresponds to  $p_{dc} = 0$  pu. Hence, the power balance of the control strategy is met. However, as it was shown in the earlier theoretical studies in this chapter, the voltage unbalance together with the damping conductance lead to reactive power exchange as well. The reactive power exchange is shown in Fig. 4.31 where the three bars represent the modified damping control strategy when three different values of the damping conductance are used. In addition, the bars of the exchanged reactive power are segregated by phase and by DERs. The control strategy consumes reactive power from phase  $a$ , which in combination with the active power consumption helps to improve the voltage profile in this phase. The opposite holds for phases  $b$  and  $c$  where the control strategy injects reactive power, which in combination with the injected active power, helps to increase the voltage profiles and thus the voltage unbalance is reduced.

The total feeder losses for all four cases are depicted in Fig. 4.32 and it can be seen that the total losses when no DERs are present are about 2kW. Since phase  $a$  is unloaded, there is no loss present in it and the losses are distributed over phases  $b$ ,  $c$  and the neutral conductor. When DERs equipped by the modified damping control strategy are introduced the losses are reduced because of the active and reactive power exchange. The more prominent decrease of the losses is present in case (iv) where the damping conductance assumes a value of 20 p.u. Despite the high reactive power exchange between the DERs and the feeder, the total losses are decreased by approximately 44%.

The beneficial effect on the voltage profile is accomplished by exchanging, i.e., consuming and injecting, currents by the modified three-phase damping control strategy. These rms values of the phase currents are listed in Table 4.2 and it appears that the voltage profile can be still improved by exchanging relatively low values of the phase currents.

The initial and calculated values of the damping conductance used by the different DERs are listed in Table. 4.3. When  $g_d = 1$  p.u. the control strategy decreases the voltage profile in phase  $a$  (see Fig. 4.27 (a)) compared to the “No DERs” case but still the voltages at nodes 11, 18 and 19 are higher than  $v_{cdb}$ , which results in higher damping conductance compared with the initial setting of  $g_d$ . If  $g_d$  assumes values of 7 p.u. and 20 p.u. the voltage profile in phase  $a$  is lowered below  $v_{cdb}$  and the damping controller calculates a  $g_d$  value to be equal to the initial one.

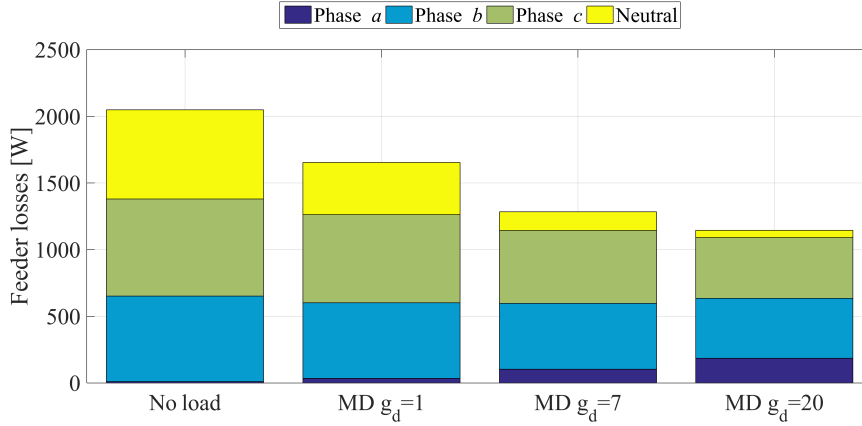


Figure 4.32: Total feeder losses when  $p_{dc} = 0$  p.u. is applied

| DER num         | DER <sub>11</sub> |       |       | DER <sub>18</sub> |       |       | DER <sub>19</sub> |       |       |
|-----------------|-------------------|-------|-------|-------------------|-------|-------|-------------------|-------|-------|
| currents [p.u.] | $i_a$             | $i_b$ | $i_c$ | $i_a$             | $i_b$ | $i_c$ | $i_a$             | $i_b$ | $i_c$ |
| $g_d = 1$ p.u.  | 0.028             | 0.023 | 0.021 | 0.041             | 0.033 | 0.030 | 0.041             | 0.034 | 0.030 |
| $g_d = 7$ p.u.  | 0.076             | 0.057 | 0.049 | 0.10              | 0.076 | 0.062 | 0.01              | 0.077 | 0.061 |
| $g_d = 20$ p.u. | 0.120             | 0.082 | 0.069 | 0.145             | 0.100 | 0.075 | 0.144             | 0.104 | 0.071 |

Table 4.2: Injected phase currents by DER<sub>11</sub>, DER<sub>18</sub> and DER<sub>19</sub>

### 4.3.2 Verification of dc-bus loaded DER on an LV distribution network by means of simulations

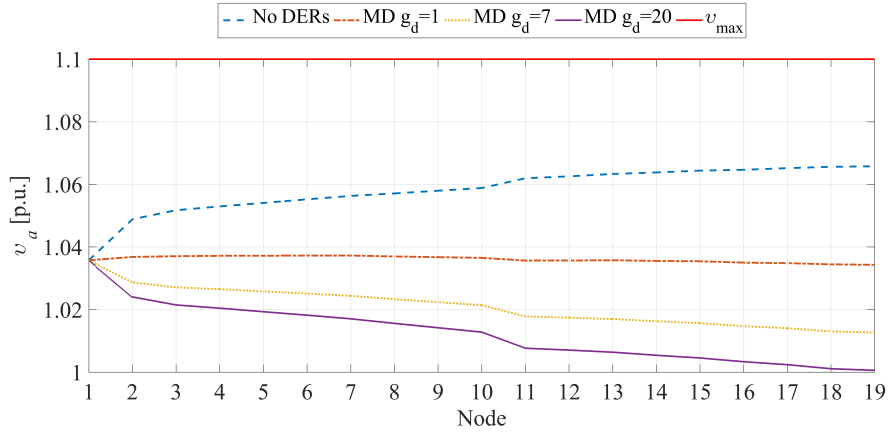
In this study, a load is connected at the dc bus of the DER. The DER in this case will react as an active rectifier driven by the modified three-phase damping control strategy. As it was mentioned above, the load can be a battery storage system that is being used in special conditions to support the grid voltages or other applications such as centralised storage [69], active rectification for charging stations of EV and many more that require three-phase connection and their front end is using a power factor corrector (PFC). Further details about the combination of storage elements and a comparison between the different control strategies is given in Chapter 6. The amount of storage, which is sufficient to reduce the power quality problems such as overvoltages is studied widely in the literature. In [86], the authors have conducted an investigation on the amount of storage that is sufficient to minimise the power drooping periods during peak production. The results of the studied test case in [86], have shown that a storage element with a capacity of 67% of the peak power of the DER is sufficient to reduce the overvoltages that occur in periods with peak generation. Hence, for the following example the dc bus

| DER num         | DER <sub>11</sub> | DER <sub>18</sub> | DER <sub>19</sub> |
|-----------------|-------------------|-------------------|-------------------|
| $g_d = 1$ p.u.  | 1.59              | 1.67              | 1.67              |
| $g_d = 7$ p.u.  | 7                 | 7                 | 7                 |
| $g_d = 20$ p.u. | 20                | 20                | 20                |

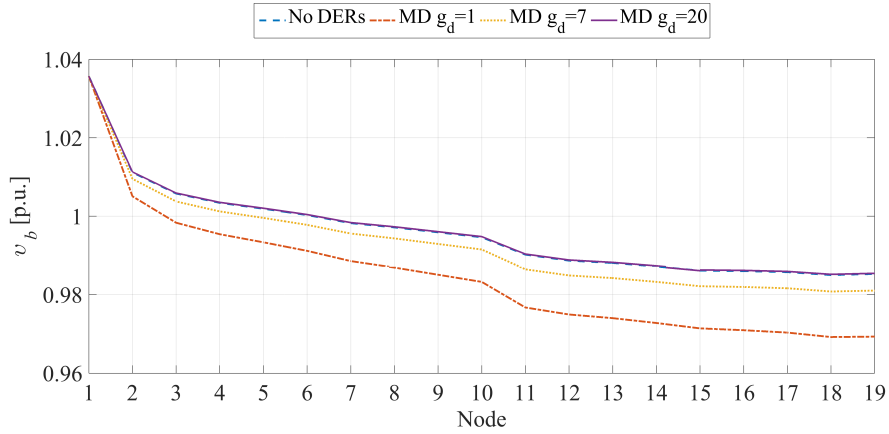
Table 4.3: Initial and calculated values by the damping controllers values of the damping conductance used by DER<sub>11</sub>, DER<sub>18</sub> and DER<sub>19</sub>

storage elements are considered for DER<sub>11</sub>, DER<sub>18</sub> and DER<sub>19</sub> and based on the aforementioned discussion, the capacity is chosen to be 16.75 kWh, 13.4 kWh and 13.4 kWh, respectively. This choice of storage capacity, although arbitrary, will give a basic idea on the performance and capabilities of the modified three-phase damping control strategy. Different values of the storage capacity and its impact on the power quality is studied in details in Chapter 6. For simplicity, it is assumed that the storage system is charged for 1 hour, so the dc bus load power is 13.4 kW, 16.75 kW and 13.4 kW, respectively. The load connections are the same as the ones used in Chapter 3 and they can be seen in Table 3.2.

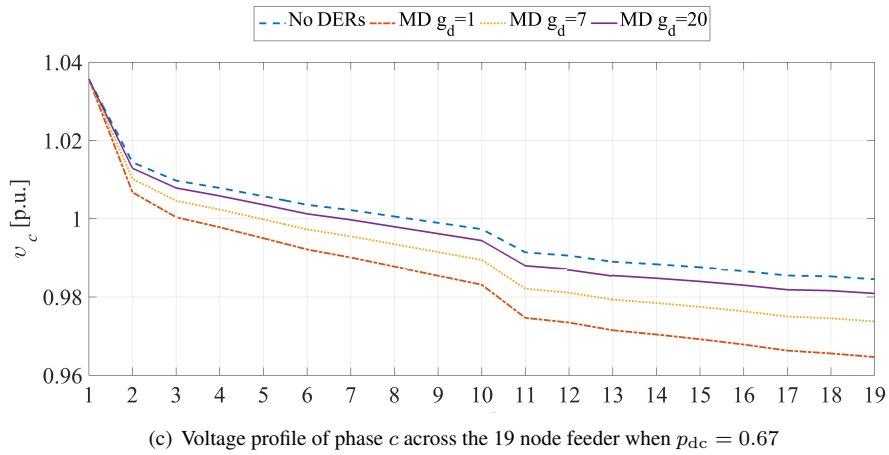
The obtained simulation results of the phase voltages across the feeder are presented in Fig. 4.33. If no DERs are connected, the voltage profiles of all phases experiences neutral point shifting because phase  $a$  is the least loaded one. Since phases  $b$  and  $c$  supply loads, their voltages are decreasing across the feeder. When the modified damping control strategy with  $g_d = 1$  p.u. is used, the voltage profile of phase  $a$  is decreased to the initial voltage of 1.04 p.u. through the entire length of the feeder. The voltage profiles in the other two phases however, are lower compared to the *No DERs* case because additional current is being consumed to supply the dc-bus loads at the dc-buses. With increasing the initial value of the damping conductance to  $g_d = 7$  p.u. the voltage profile in phase  $a$  is additionally lowered because the control strategy consumes even more current from it and the feeder voltage profile is decreasing. The voltage profiles in phases  $b$  and  $c$  are slightly increased compared to the previous case where  $g_d = 1$  p.u. is considered. As of the case where an initial value of the damping conductance of 20 p.u. is used, the voltage profile in phase  $a$  is decreased even more such that the voltage at the end of the feeder is close to 1 p.u. while in the other two phases the voltage profile is more close to the *No DERs* case. The reason for the voltage profile improvement is due to the fact that the higher value of the damping conductance improves the resistive behaviour of the modified damping control strategy, which helps to redistribute the consumed currents such that the DER consumes less current from the phases with the lower voltages higher current from the phase with the higher voltage and thus reduce the voltage unbalance even though power is being consumed from the grid.



(a) Voltage profile of phase a across the 19 node feeder when  $p_{dc} = 0.67$

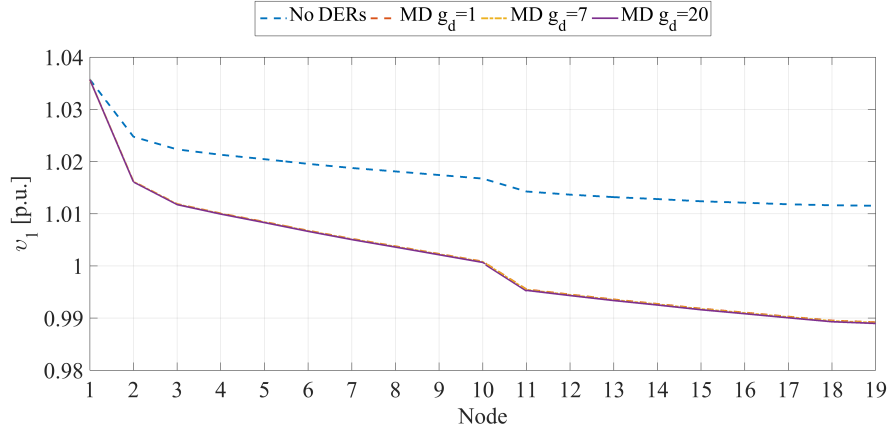


(b) Voltage profile of phase b across the 19 node feeder when  $p_{dc} = 0.67$

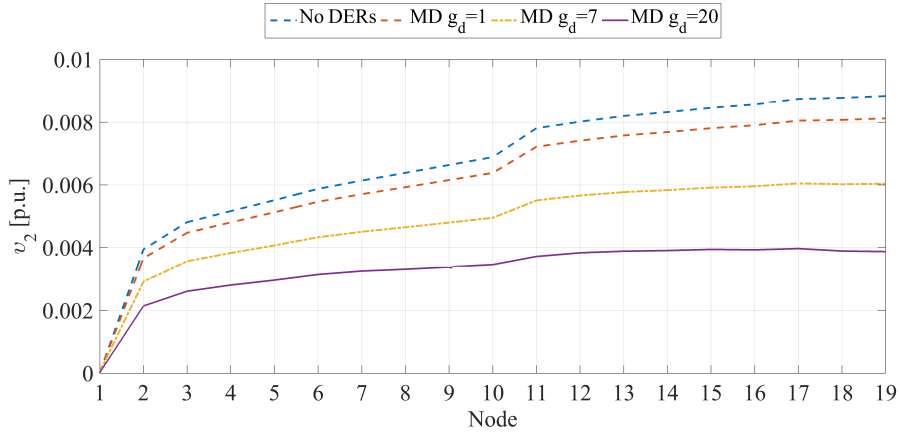


(c) Voltage profile of phase c across the 19 node feeder when  $p_{dc} = 0.67$

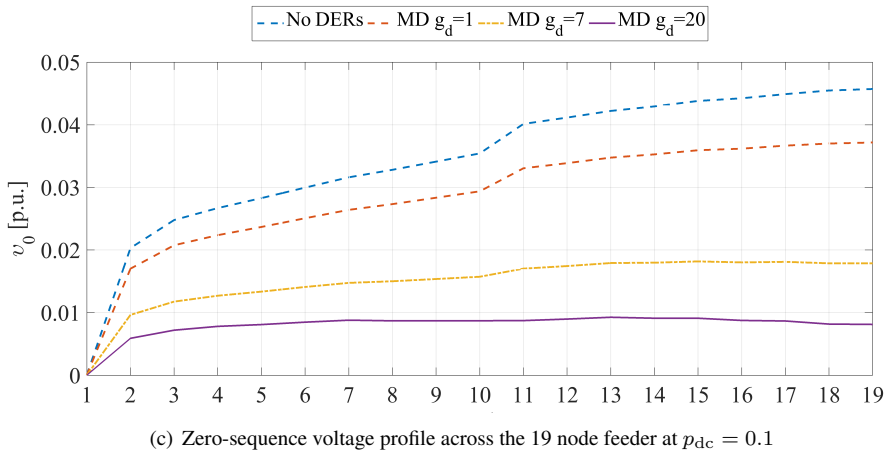
Figure 4.33: Phase voltage results comparison between the four case studies when  $p_{dc} = 0.666$



(a) Positive-sequence voltage profile across the 19 node feeder  $p_{dc} = 0.1$



(b) Negative-sequence voltage profile across the 19 node feeder  $p_{dc} = 0.1$



(c) Zero-sequence voltage profile across the 19 node feeder at  $p_{dc} = 0.1$

Figure 4.34: Symmetrical components voltage comparison between the four case studies when  $p_{dc} = 0.666$

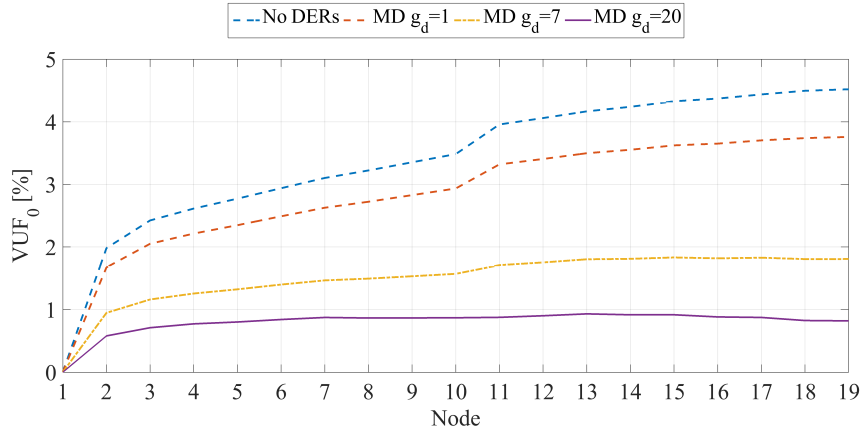
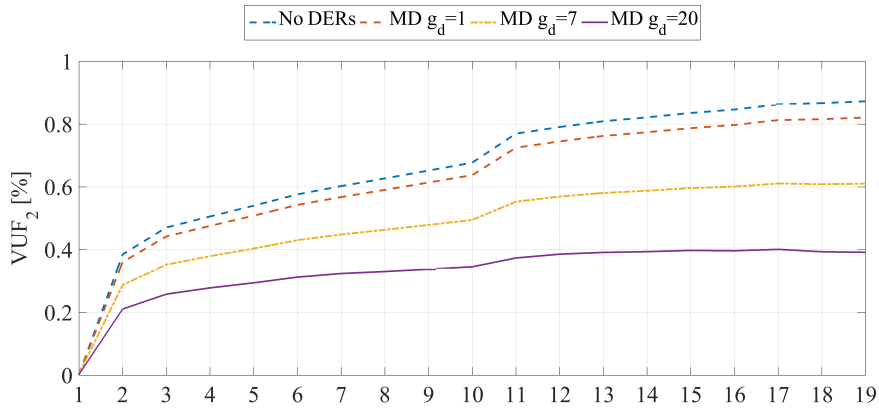
(a) Zero-sequence voltage unbalance factor profile across the 19 node feeder when  $p_{dc} = 0.1$ (b) Negative-sequence voltage unbalance factor profile across the 19 node feeder when  $p_{dc} = 0.67$ 

Figure 4.35: Voltage unbalance factors profiles comparison between the four case studies when  $p_{dc} = 0.666$

The voltage profiles across the feeder of the positive-, negative- and the zero-sequence components are shown in Fig. 4.34 (a), (b) and (c), respectively. Since renewable power injection is not considered, the positive-sequence voltage component is decreasing across the feeder. Due to additional power consumption by the DERs, the positive-sequence component drops even more but remains the same for all different values of  $g_d$ . The negative- and zero-sequence voltage components however, do change when different values of  $g_d$  are used as shown in Fig. 4.34 (b) and (c). As previously demonstrated, a better positive impact is achieved when  $g_d$  assumes higher values where in this case both profiles are lowered significantly. When  $g_d = 20$  p.u. is used, the negative-sequence is decreased by more than 50%,

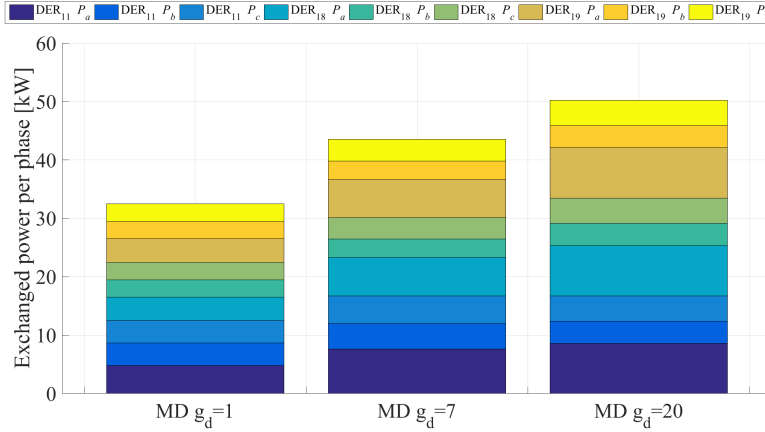


Figure 4.36: Per phase active power injection by the different DERs

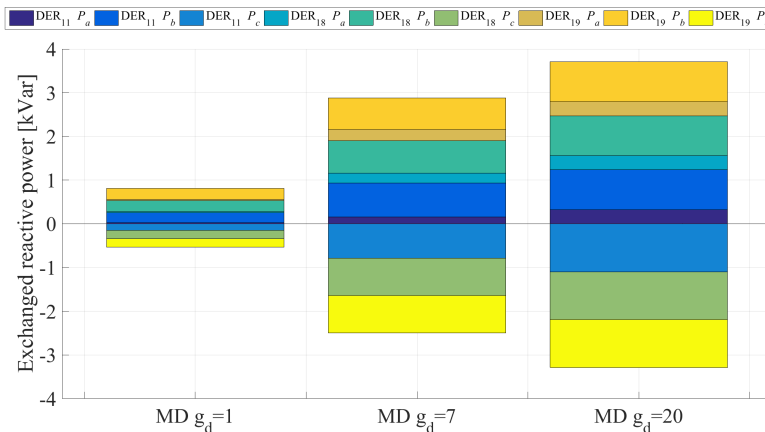


Figure 4.37: Per phase reactive power injection by the different DERs

whereas the zero-sequence is decreased approximately by 77.7%.

Despite the fact that the positive-sequence voltage component is decreased due to the additional consumption from the DERs the voltage unbalance factors  $VUF_0$  and  $VUF_2$  are improved, which can be seen from Fig. 4.35 (a) and (b).

The beneficial influence of the modified damping control strategy on the voltage profiles is achieved by asymmetrical power consumption from the different phases. The consumed power for cases (ii),(iii) and (iv) are depicted in Fig. 4.36 (a) where the consumed power is also segregated by DER and phase. When  $g_d = 1$  p.u. is used it can be seen already that the consumed power from phase  $a$  is slightly higher (for all DERs) compared to phases  $b$  and  $c$ . By increasing the damping con-

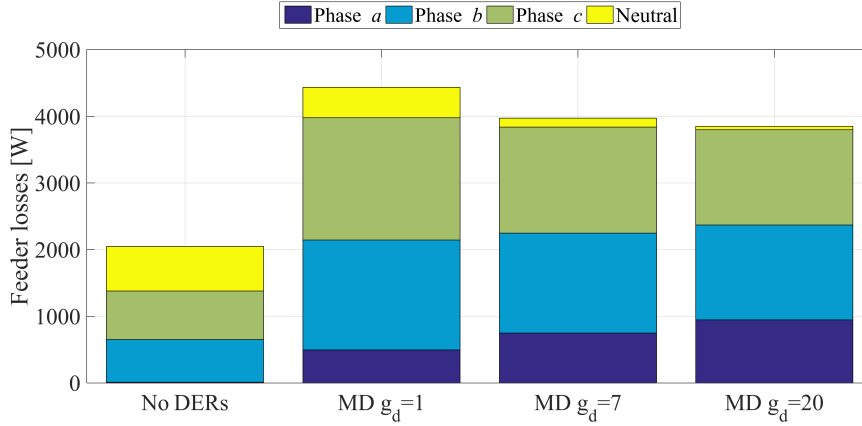


Figure 4.38: Total feeder losses when  $p_{dc} = 0.67$  p.u.

ductance value up to 20 p.u. the difference between the power consumption per phase becomes even more prominent. As it was discussed previously, the damping control strategy exchanges some amount of reactive power with the LV grid, which is depicted in Fig. 4.36 (b). The exchanged reactive power is relatively small at low values of  $g_d$ , which leads to smaller reactive power consumption from phase  $a$ . When the damping conductance is increased up to 7 or 20 p.u. the reactive power exchange increases significantly. Since the voltage profile in phase  $c$  is the lowest the control strategy tries to support the voltage profile by consuming less active power from it but also by injecting reactive power.

The total feeder losses are depicted in Fig. 4.38, where the *No DERs* case leads to total losses of approximately 2 kW but they are distributed over the conductors of phases  $b$ ,  $c$  and the neutral conductor. By introducing the DERs, which use an initial value of  $g_d = 1$  p.u. the losses are more than double due to the additional loading. However, the losses in the neutral conductor are slightly lower. As of the results obtained for  $g_d = 7$  p.u. the neutral conductor losses decrease even more whereas the losses in conductor  $a$  increase. When the initial value of the damping conductance is 20 p.u. the losses are mainly distributed in the phase conductors and almost no losses are present in the neutral conductor, which means that almost no neutral current is drawn from the programmable voltage source (MV/LV transformer). The positive effects of the neutral current minimisation were described earlier in this thesis.

In this particular case, the voltage profile improvement is achieved by consuming asymmetrical currents by the modified three-phase damping control strategy. These rms values of the phase currents are listed in Table 4.4 and it can be seen

| DER num         | DER <sub>11</sub> |       |       | DER <sub>18</sub> |       |       | DER <sub>19</sub> |       |       |
|-----------------|-------------------|-------|-------|-------------------|-------|-------|-------------------|-------|-------|
| currents [p.u.] | $i_a$             | $i_b$ | $i_c$ | $i_a$             | $i_b$ | $i_c$ | $i_a$             | $i_b$ | $i_c$ |
| $g_d = 1$ p.u.  | 0.242             | 0.213 | 0.215 | 0.251             | 0.209 | 0.213 | 0.251             | 0.209 | 0.213 |
| $g_d = 7$ p.u.  | 0.298             | 0.179 | 0.196 | 0.323             | 0.164 | 0.194 | 0.323             | 0.162 | 0.197 |
| $g_d = 20$ p.u. | 0.341             | 0.156 | 0.181 | 0.366             | 0.135 | 0.183 | 0.364             | 0.129 | 0.19  |

Table 4.4: Injected phase currents by DER<sub>11</sub>, DER<sub>18</sub> and DER<sub>19</sub>

| DER num         | DER <sub>11</sub> | DER <sub>18</sub> | DER <sub>19</sub> |
|-----------------|-------------------|-------------------|-------------------|
| $g_d = 1$ p.u.  | 1                 | 1                 | 1                 |
| $g_d = 7$ p.u.  | 7                 | 7                 | 7                 |
| $g_d = 20$ p.u. | 20                | 20                | 20                |

Table 4.5: Initial and calculated damping conductance by the damping controllers of DER<sub>11</sub>, DER<sub>18</sub> and DER<sub>19</sub>

that the neutral current losses are reduced because of the increased consumption by the DERs from phase  $a$ . It can be noted that at  $g_d = 20$  p.u. phase current  $i_a$  exceeds its nominal value, hence oversizing of the power electronic inverter must be considered.

The initial and calculated values of the damping conductance used by the different DERs are listed in Table. 4.3. Since phase voltage  $v_a$  is lower than  $v_{cdb}$  in all examined cases then the calculated damping conductance equals its initial setting.

### 4.3.3 Discussion

The conducted simulations of both modes show that the modified three-phase damping control strategy is able to improve the power quality at the PCC if input power is not present or even when power is being consumed from the grid. The control strategy successfully mitigates the voltage unbalance at the PCC but it is also able to prevent undervoltages caused by the neutral point shifting. On the top of that, the grid efficiency is improved by reducing the feeder losses, despite the additional reactive power exchange by the modified damping control strategy.

## 4.4 Performance assessment of the considered control strategies on annual basis

So far, the modified three-phase damping control strategy showed excellent performance compared to the drooped positive-sequence control strategy when employed in grid injection mode (Chapter 3), zero-powered mode and active rectifier mode in this chapter in §4.3.1 and §4.3.2. Nevertheless, this performance is obtained at a fixed input power, which in all examined cases is considered to be at

maximum. In this section, the overall impact of the described control strategies in Chapter 3 will be investigated on annual basis.

#### 4.4.1 Data of 78 node LV grid

The performance evaluation of the considered control strategies and their combinations are tested by means of simulations on an existing LV grid. The single line diagram of LV grid is shown in Fig. 4.39. This feeder is 78 node LV network located in Suha, Slovenia. The MV/LV transformer of Dyn type has a nominal power of 250 kVA, short circuit voltage of 4% while the no load losses are 325 W and on-load losses are 3250 W, respectively. The primary and secondary nominal voltages are 20 kV and 0.4 kV, respectively. The voltages at the secondary side are set to be 1.05 p.u., which is a typical setting used by the DSO in order to avoid undervoltages to the most distant customers when high loading conditions are present. The three-phase short circuit power at the slack bus is 100 MVA. DER<sub>24</sub>, DER<sub>47</sub> and DER<sub>59</sub> are existing PV systems in the presented LV grid. The rest of the DERs have been added in order to examine the different control strategies when operating at very high penetration level of renewables.

#### 4.4.2 Loads, DERs and irradiation data

The considered LV grid is consisting of 78 nodes and to each node three different loads are connected. All loads are considered to be household loads and they are generated by using the methodology adopted in [87]. Overall, 200 domestic load profiles are generated and grouped in clusters of three, which are connected to each node to a different phase. They are grouped such that the relative deviation between the loads, at any time instance, is minimum. The clusters are connected to the different nodes. By clustering the loads, the difference in the average power at each node is very low, which will help to limit the voltage unbalance below 2%. In this section, all loads are assumed to have PF=0.9 and are modelled as constant power loads. All loads are 15 min-based and the sum of the apparent power of all loads is depicted in Fig. 4.40. The load profiles are generated for one year, which gives in total 35136 values.

In this section, 5 three-phase DERs and 14 single-phase DERs are considered to be connected in the LV grid. The rated active power and phase connections are listed in Table 4.6. The rated power of all DERs is chosen such that overvoltages occur at the feeder if maximum renewable generation is present when the non-drooped classical positive-sequence and single-phase control strategies are employed in all DERs. Thus, no further penetration of other DERs is possible. DERs with rated power above 5 kW are three-phase connected and equipped with active power drooping (unless otherwise specified). All DERs with rated power lower than 5 kW are equipped with variable PF as a function of the injected power. In

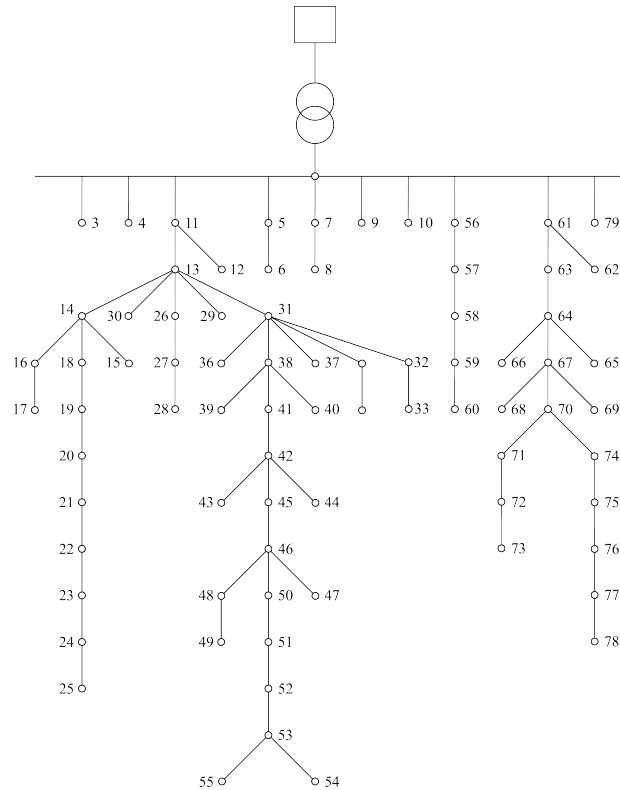


Figure 4.39: Feeder topology used to access the performance the examined control strategies

this particular case, the total installed peak power is 214 kW, which related to the nominal power of the MV/LV transformer gives a penetration level of 85%. Solar irradiation profile based on real measurements is used as an input for all DERs. The normalised solar irradiation profile that is used to perform the power flows is depicted in Fig. 4.41.

A few test cases are examined in order to compare the different results. The cases are defined as follows:

- In the first case *C0*, the grid only consists of loads.
- In the second case *C1*, all DERs inject their maximum power and this case will be used as a reference case to check how much power is been curtailed or drooped.
- In the next case *C2*, the classical hard curtailment is implemented together with voltage control based on reactive power exchange is in all DERs. Single-

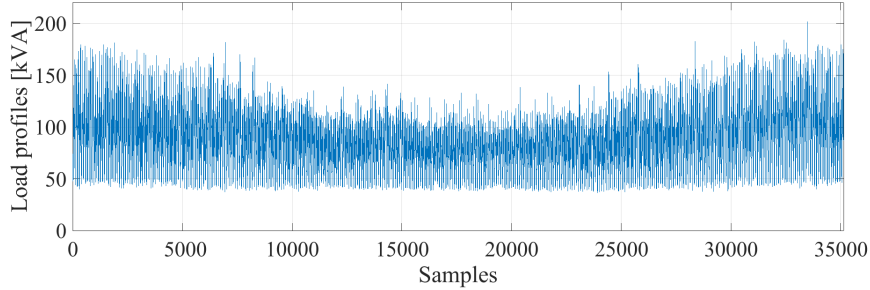


Figure 4.40: Aggregated load profile of all loads

| DERs              | Rated power | DERs              | Rated power | DERs              | Rated power |
|-------------------|-------------|-------------------|-------------|-------------------|-------------|
| DER <sub>24</sub> | 30 kW (Yn)  | DER <sub>13</sub> | 2 kW (an)   | DER <sub>21</sub> | 3 kW (cn)   |
| DER <sub>47</sub> | 44 kW (Yn)  | DER <sub>14</sub> | 2 kW (cn)   | DER <sub>22</sub> | 1 kW (an)   |
| DER <sub>52</sub> | 40 kW (Yn)  | DER <sub>15</sub> | 2 kW (cn)   | DER <sub>23</sub> | 3 kW (an)   |
| DER <sub>59</sub> | 30 kW (Yn)  | DER <sub>17</sub> | 3 kW (an)   | DER <sub>45</sub> | 5 kW (cn)   |
| DER <sub>70</sub> | 30 kW (Yn)  | DER <sub>18</sub> | 2 kW (bn)   | DER <sub>49</sub> | 5 kW (an)   |
| -                 | -           | DER <sub>19</sub> | 2 kW (cn)   | DER <sub>50</sub> | 2 kW (cn)   |
| -                 | -           | DER <sub>20</sub> | 3 kW (bn)   | DER <sub>54</sub> | 3 kW (bn)   |

Table 4.6: Nominal power of DERs

phase control strategy of this type is described in §3.2.2 while the three-phase positive-sequence control strategy is described in §3.2.3. More information about the implementation of the hard curtailment will be given later on in this section.

- The combination of active power drooping together with the positive-sequence control strategy forms case *C3* where only active power is considered to be drooped and injected. This control strategy is described in §3.1.1.
- The drooped three-phase damping control strategy, which mitigates only the negative-sequence voltage components is assigned to case *C4*. The drooped part is described in Chapter 3 by using (3.1). The analytical description of the control strategy will be given later on in this section.
- Cases *C5*, *C6* and *C7* represent the modified three-phase drooped damping control strategy with initial damping conductance values of  $g_d = 3$  p.u.,  $g_d = 10$  p.u. and  $g_d = 50$  p.u. respectively. In order to compare the difference in damping capabilities and power quality performance between test cases *C4* and *C7* the value of  $g_{d2}$  is chosen to be equal to 50 p.u. similarly to case *C7*

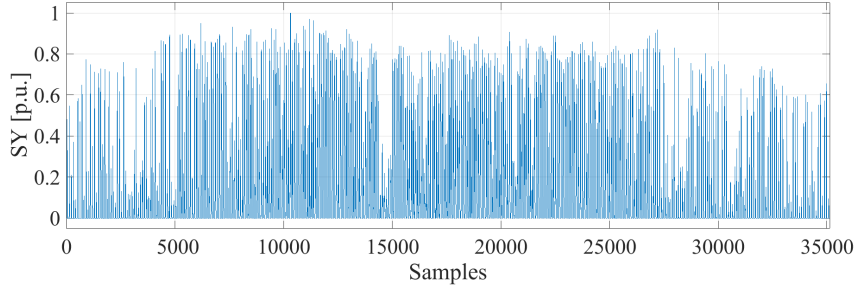


Figure 4.41: Solar irradiation profile used in the simulation model

- In the last case *C8*, the modified three-phase drooped damping control strategy is examined in zero-powered mode as examined previously in this chapter. A value of 50 p.u. is chosen for the damping conductance. Thus a comparison between cases *C7* and *C8* in terms of grid losses minimisation can be made and the effect of the zero-powered mode can be assessed.

#### 4.4.3 Three-phase damping control strategy with segregate negative- and zero-sequence mitigation

Usually the three-phase DERs are connected via a three-phase, three-wire connection and inject only positive-sequence currents. Therefore, by using such a system, only the negative-sequence component can be impacted. In addition, [8] recommends only limits to the negative voltage unbalance factor, which is the ratio of the negative- to positive-sequence voltage components and no recommendation to the zero-sequence components are given whatsoever. In order to make the three-phase damping control strategy compliant to act resistively only to the negative-sequence voltage component, a modification in (2.13) can be made such that only the negative-sequence component is impacted by the three-phase damping control strategy:

$$\begin{bmatrix} \underline{i}_a \\ \underline{i}_b \\ \underline{i}_c \end{bmatrix} = T^{-1} \begin{bmatrix} g_{d0} & 0 & 0 \\ 0 & g_1 & 0 \\ 0 & 0 & g_{d2} \end{bmatrix} T \begin{bmatrix} \underline{v}_a \\ \underline{v}_b \\ \underline{v}_c \end{bmatrix} \quad (4.25)$$

where  $g_{d0}$  and  $g_{d2}$  are the damping conductances that set independently the resistive behaviour towards the zero- and negative-sequence voltage component, respectively. By further developing this equation, the following set of expressions

for the phase currents are obtained:

$$\begin{aligned}
\dot{i}_a &= \frac{1}{3} \left\{ g_{d1} \left[ |v_a| e^{j\theta_a} + |v_b| e^{j(\theta_b + \frac{2\pi}{3})} + |v_c| e^{j(\theta_c - \frac{2\pi}{3})} \right] \right. \\
&\quad + g_{d2} \left[ |v_a| e^{j\theta_a} + |v_b| e^{j(\theta_b - \frac{2\pi}{3})} + |v_c| e^{j(\theta_c + \frac{2\pi}{3})} \right] \\
&\quad \left. + g_{d0} \left[ |v_a| e^{j\theta_a} + |v_b| e^{j\theta_b} + |v_c| e^{j\theta_c} \right] \right\} \\
\dot{i}_b &= \frac{1}{3} \left\{ g_{d1} \left[ |v_b| e^{j\theta_b} + |v_a| e^{j(\theta_a - \frac{2\pi}{3})} + |v_c| e^{j(\theta_c + \frac{2\pi}{3})} \right] \right. \\
&\quad + g_{d2} \left[ |v_b| e^{j\theta_b} + |v_a| e^{j(\theta_a + \frac{2\pi}{3})} + |v_c| e^{j(\theta_c - \frac{2\pi}{3})} \right] \\
&\quad \left. + g_{d0} \left[ |v_a| e^{j\theta_a} + |v_b| e^{j\theta_b} + |v_c| e^{j\theta_c} \right] \right\} \quad (4.26) \\
\dot{i}_c &= \frac{1}{3} \left\{ g_{d1} \left[ |v_c| e^{j\theta_c} + |v_a| e^{j(\theta_a + \frac{2\pi}{3})} + |v_b| e^{j(\theta_b - \frac{2\pi}{3})} \right] \right. \\
&\quad + g_{d2} \left[ |v_c| e^{j\theta_c} + |v_a| e^{j(\theta_a - \frac{2\pi}{3})} + |v_b| e^{j(\theta_b + \frac{2\pi}{3})} \right] \\
&\quad \left. + g_{d0} \left[ |v_a| e^{j\theta_a} + |v_b| e^{j\theta_b} + |v_c| e^{j\theta_c} \right] \right\}
\end{aligned}$$

The calculation of the fundamental input conductance is done by the power balance (2.2) and it gives the following expression:

$$\begin{aligned}
g_1 &= \frac{3 p_{dc}^{\bullet}}{\sum |v_x|^2 + 2 \sum_{x \neq y} |v_x| |v_y| \cos(\theta_x - \theta_y - \frac{2\pi}{3})} + \\
&\quad g_{d2} \frac{\sum |v_x|^2 + \sum_{x \neq y} |v_x| |v_y| \cos(\theta_x - \theta_y + \frac{2\pi}{3})}{\sum |v_x|^2 + 2 \sum_{x \neq y} |v_x| |v_y| \cos(\theta_x - \theta_y - \frac{2\pi}{3})} + \\
&\quad g_{d0} \frac{\sum |v_x|^2 + \sum_{x \neq y} |v_x| |v_y| \cos(\theta_x - \theta_y)}{\sum |v_x|^2 + 2 \sum_{x \neq y} |v_x| |v_y| \cos(\theta_x - \theta_y - \frac{2\pi}{3})} \quad (4.27)
\end{aligned}$$

By setting  $g_{d0} = 0$  p.u. only the negative-sequence component can be impacted by the three-phase damping control strategy.

#### 4.4.4 Description of the Open DSS model

The grid is simulated in a time series manner by using Open DSS that is interfaced with Matlab. The single line diagram of the grid is depicted in Fig. 4.39 and as can be seen there are 78 nodes. The location of the DER, rated power and phase

connection are shown as well. The majority of DER is single-phase connected with rated power between 2 and 5 kWp. Since the physical area of the grid is small, it is assumed that all DERs have the same solar irradiation. The solar irradiation profiles, presented in Fig. 4.41 are used by all DERs. The examined period is one year with a 15 min basis between the samples. As mentioned above, the power of all DERs is chosen such that overvoltages occur at the end of some feeders. The simulation is performed with time series and the corresponding values of the vectors of the solar irradiation and the load profiles are simulated.

Case C2 represent the massively used positive-sequence control strategy with variable PF as function of the active power and hard curtailment. Suppose that at some point nodes 54 to 52 experience overvoltages, then DER<sub>52</sub> and DER<sub>54</sub> will be turned off immediately for that time step and the simulation will move to the next step. This however will result in a large power curtailment, which actually may not happen in practice because of the discretisation of 15 min. In practice, DER<sub>54</sub> will turn off before DER<sub>52</sub> because it is further connected from the MV/LV transformer. This might be sufficient to prevent the overvoltages and it may not be necessary to turn off DER<sub>52</sub> at all. In order to overcome this disadvantage of the time series simulations and prevent false overvoltage tripping, an internal loop is introduced. This internal loop is accessed only if an overvoltage problem occurs. In this loop, the set power is increased gradually to the maximum set point, which will trip the DERs one by one in case of overvoltages and not all at once. Thus a more realistic behaviour of the model is achieved and the curtailed power will not be overestimated.

Cases C3 to C8 use active power drooping as a function of the grid voltages, which requires different approach because Open DSS does not have controllable DER strategies in its library. In [66], a four step approach for implementing active power drooping in Open DSS is proposed. In the first step, the normalised solar irradiation profile is multiplied with the rated power of the DERs as well as the load profiles. Then an asymmetrical power flow is performed in Open DSS. In this step, the DERs do not droop any power, which will result in overvoltages. In the second step, the drooped power is calculated as a function of the grid voltages. Since there is always some voltage unbalance present in the LV grid, the maximum among the phase voltages is chosen to calculate the injected power. In the third step, another power flow is ran with the new values of the drooped power. In the last step, a convergence check is performed based on predefined tolerance. The absolute error between the current values of the phase voltages and the previous values is made. If the result is lower than 0.023V the simulation continues with the next time series. If this is not the case, the simulation repeats step 2. More information about the droop implementation can be found in [71] and the developed simulation model in [66]. In the last reference, the proposed combination of Open DSS and Matlab is also compared with a Matlab & Simulink model. The results show very good

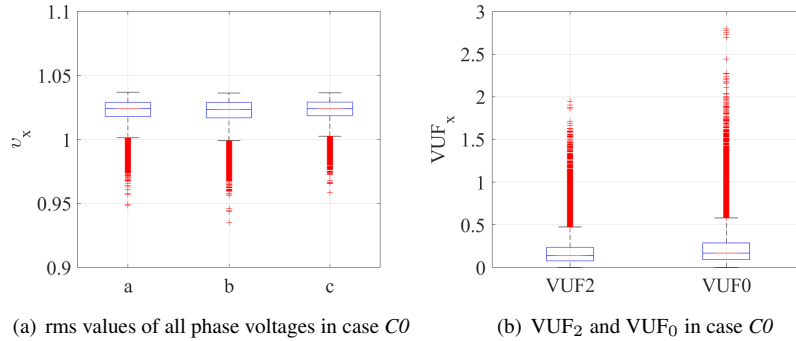


Figure 4.42: Concatenated results of the entire LV grid when case  $C0$  is examined

agreement between the two models.

#### 4.4.5 Simulation results

The total length of the solar and load vectors is 35136 points while the node numbers are 78. This results in a matrix of 78 rows and 35136 columns. In order to avoid unnecessary data and figures, a box plot will be used to represent the obtained simulation results. First, each voltage in matrix is concatenated from  $78 \times 35136$  to  $1 \times 2740608$ . The same is done also for  $VUF_2$  and  $VUF_0$ .

The obtained simulation results of case  $C0$  are depicted in Fig. 4.42. All phase voltages are depicted in Fig. 4.42 (a) and as it can be seen, the mean phase voltages are within the standard limits set by [8]. Furthermore, even the outliers (the red plus signs) do not reach the bottom limit of the standard voltage band. In Fig. 4.42 (b), the negative- and zero-sequence voltage unbalance factors are presented. The simulation results show that the mean value of  $VUF_2$  is lower than 0.2% while the outliers do not exceed 2%. The outliers of  $VUF_0$  reach 2.8%, however, there is no limit of this parameter in the currently acting standard. Based on the obtained simulation results, it can be concluded that the loads are properly distributed feeders grid because there are no power quality problems in the LV.

In Fig. 4.43 (a), the phase voltages are depicted when no control is applied to all DERs whatsoever. Because of the high penetration of level of DERs, severe overvoltages can be observed in all phases, which reach almost 1.17 p.u. The obtained simulation results of case  $C2$  are presented in Fig. 4.43 (b). The mean values and the maximum deviations of the phase voltages are more or less the same as the previous case, however, the maximum values reached by the outliers are limited to 1.105 p.u.

The drooped three-phase positive-sequence control strategy performs active

power drooping as function of the grid voltages and it is able to provide lower and safer rms voltage levels on all phases. Fig. 4.43 (c) shows that the maximum voltage deviations are slightly lower compared to case C2 but the outliers barely reach 1.08 p.u. in phase *b* while in the other two phases the maximum values are lower than 1.07 p.u.

The obtained results of case 4 are presented in Fig. 4.43 (d). In this case, only negative-sequence component mitigation is applied and as it can be seen, the maximum deviation of  $|v_b|$  is slightly wider compared to case C3 and also the maximum outliers are slightly lower in phase *b*.

In Fig. 4.44 (a) to (c), the drooped three-phase damping control strategy is examined with  $g_d$  values of 3, 10 and 50 p.u. The simulation results show that, the mean values of the phase voltages are rather the same for all three cases but the outliers are better equalised when a damping conductance value of 50 p.u. is used.

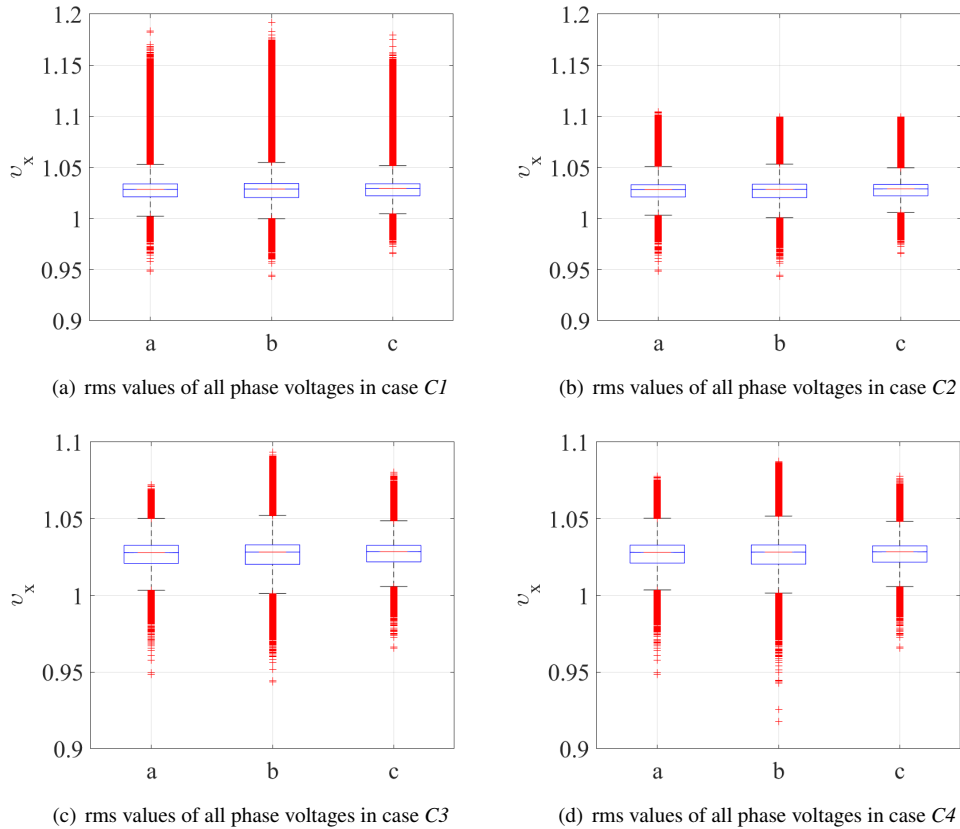


Figure 4.43: Concatenated voltage results of the entire LV grid when cases C1 to C4 are examined

In Fig. 4.44 (d) the zero-power mode of DER is examined. The results show that the outliers are much lower compared to all other cases, which implies that big part of the voltage unbalance is occurring during night times.

The negative- and zero-sequence voltage unbalance factors of cases *C1* to *C4* are depicted in Fig. 4.45 (a), (b), (c) and (d), respectively. Although case *C1* does not consider any control of all DERs and overvoltages are present in all phases,  $VUF_2$  is smaller than 2%, which means the power of the loads and DERs is more or less distributed equally among the three phases.

Since cases *C1* to *C3* do not impact the sequence components, the range of the maximum deviations are  $VUF_2=0.6\%$  and  $VUF_0=0.7\%$ . The outliers of  $VUF_2$  for these cases also do not exceed 2% and the outliers of  $VUF_0$  are all lower than 3%.

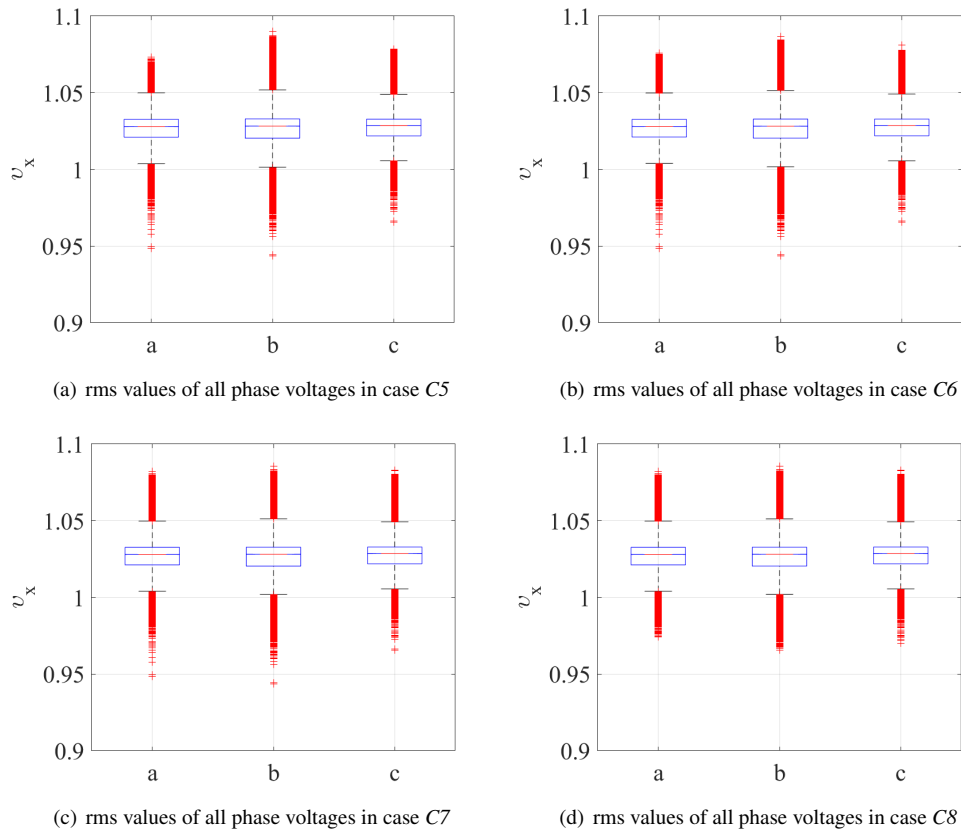


Figure 4.44: Concatenated voltage results of the entire LV grid when cases C5 to C8 are examined

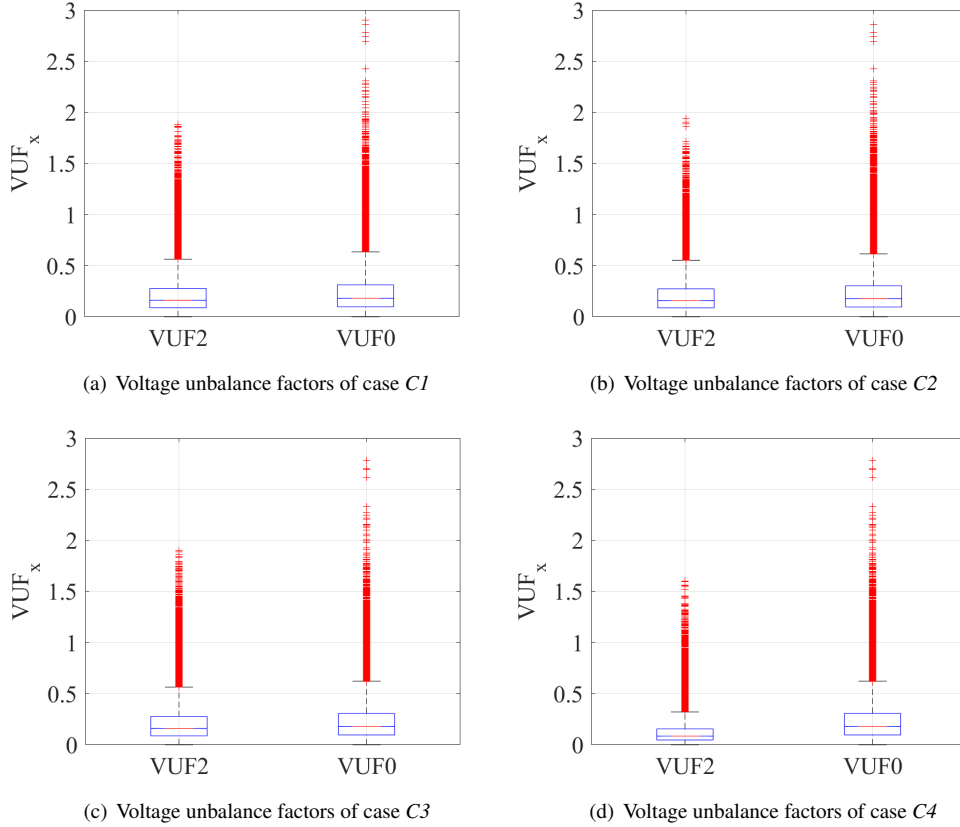


Figure 4.45: Concatenated VUFs results of the entire LV grid when cases C1 to C4 are examined

Case C4 impacts only the negative-sequences and as it can be seen in Fig. 4.45 (d), the mean value of  $VUF_2$  is decreased down to 0.12% while in the previous cases these values were around 0.2%. The maximum deviations of the quartiles are also decreased down to 0.35% while the outliers hardly exceed 1.6%. The obtained simulation results of  $VUF_0$  are the same as the previous cases.

In Fig. 4.46 the obtained simulation results for cases C5 to C8 are depicted. By increasing the damping conductance from 3 p.u. to 50 p.u. in cases C5 to C7, it can be seen that the mean values of both unbalance factors decrease as well as their maximum deviation ranges. The outliers are also decreased and barely exceed 1.8% in all cases.

The obtained simulation results of case C8 for  $VUF_2$  and  $VUF_0$  are depicted in Fig. 4.46 (d). Since in this case the DERs are not shut down during night times, they are constantly improving the power quality in the LV grid. This leads to lower values of the outliers compared to the previous cases, which means that some of the voltage unbalance problems are present in the evenings.

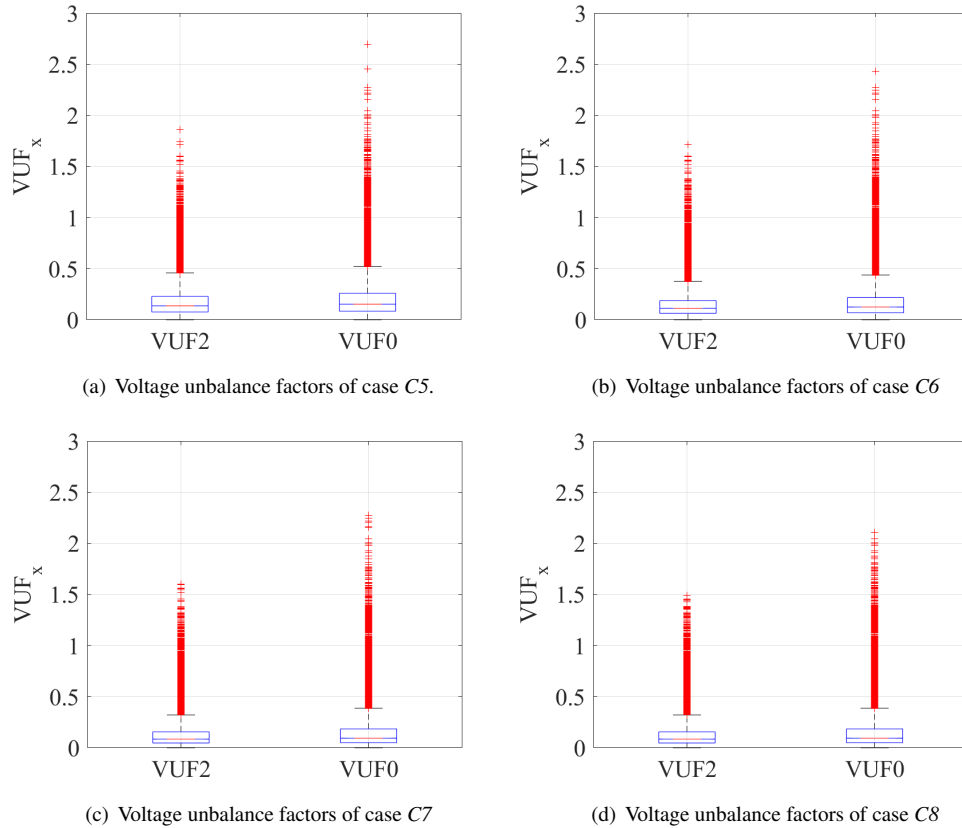


Figure 4.46: Concatenated VUFs results of the entire LV grid when cases C5 to C8 are examined

The total injected energy by all DERs are presented in Fig. 4.47. Case C1 injects all available and no control is applied whatsoever. The total injected power by this case is 248 MWh it will be used as a reference for the other cases. The reactive power voltage support and hard active power curtailment allow Case C2 to inject a total of 218.3 MWh/a. By using different colours, a segregation of the injected energy per DER is presented. In Case C2, some of the single-phase connected DERs are curtailed and also DER<sub>24</sub> and DER<sub>52</sub>. When the three-phase positive-sequence control strategy is used, DER<sub>24</sub> droops slightly more energy compared to case C2, while DER<sub>52</sub> injects almost twice the energy compared with the same case. In addition, none of the single-phase DERs is subjected to hard curtailment. Overall, in case C3 total of 219.5 MWh/a are injected, which is 1.2 MWh/a more compared to case C2.

The negative-sequence voltage component mitigation is assigned to case C4. The annual injected energy by this case is 220 MWh, which is slightly more compared to the previous cases. This control strategy considered an initial value of the

$g_{d2} = 50$  p.u. Although such a high value of the damping conductance is used, the injected energy is lower compared to the modified damping control strategy with initial value of  $g_d = 3$  p.u. (case *C5*). In this case, total of 224.7 MWh/a are injected, which is 2.7 MWh/a more compared to case *C4*.

Cases *C6* and *C7* represent the modified damping control strategy with initial values of the damping conductance 10 and 50 p.u., respectively. The difference between these cases in terms of annual energy exchange is very small - 231.1 MWh and 231.3 MWh, respectively. Despite the fact that cases *C4* and *C7* use the same value of the damping conductance, impacting the zero-sequence component results in less energy drooping.

In this particular LV grid, the difference in produced energy between the reactive power support and the three-phase damping control strategy with  $g_d = 50$  p.u. is 13 MWh/a (231MWh/a-218MWh/a). Overall, this leads to penetration level increase of 5.9%.

Case *C8* considers the modified three-phase damping control strategy to continue operating even though there is no power delivered by the primary source. However, both cases (*C7* and *C8*) deliver the same amount of injected energy because the amount of input energy is the same. There will be a small difference in circulating energy, which will give difference in grid loss reduction.

A common trend in all active power drooping control strategies is that with increasing the damping conductance, the injected energy by DER<sub>24</sub> and DER<sub>52</sub> gradually increases. Almost no energy is drooped by DER<sub>59</sub> and DER<sub>70</sub> because the penetration level of renewables in their feeders is very low and no power quality issues are observed.

The aggregated energy losses in all feeders are presented in Fig. 4.48. Case *C0* considers only loads and it leads to losses of 8.26MWh/a. When DER inject all available power (*C1*) the losses are doubled and reach 16.52 MWh/a. In case *C2*, some active power is curtailed, which reduces the losses to 12.4 MWh/a. The drooped positive-sequence control strategy does not inject any reactive power, which leads to lower losses (10.57MWh/a) compared to *C2*.

In case *C4*, the negative-sequence component mitigation leads to slightly more losses (10.7MWh/a) compared to *C3*. Since both cases do not impact the zero-sequence component, the only reason for the loss increase is the higher energy injection of 1.2 MWh/a compared to case *C3*.

The modified three-phase damping control strategy with  $g_d$  values of 3 p.u., 10 p.u. and 50 p.u. is represented by cases *C5*, *C6* and *C7*, respectively. These cases lead to losses of 9.83 MWh/a, 9.64MWh/a and 9.59 MWh/a, respectively. This is a grid performance improvement between 2.57MWh/a and 2.81 MWh/a compared to case *C3*. Case *C8* delivers the lower grid losses of all cases. This is because it still mitigates the voltage unbalance even though solar irradiation is not present.

In this particular LV grid, the difference in losses between the reactive power

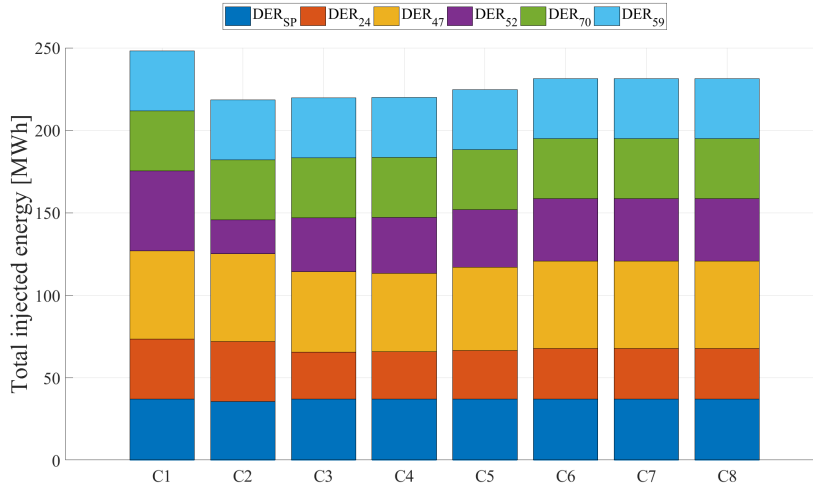


Figure 4.47: Total annual injected power by DERs when different control strategies are applied

support and the three-phase damping control strategy with  $g_d = 50$  p.u. is 2.81 MWh/a (12.4MWh/a-9.59MWh/a). This leads to grid loss minimisation for the DSO of 22.6 %.

From the presented case studies it can be seen that even the drooped positive-sequence control strategy has a better performance compared to the hard active power curtailment with reactive power exchange. In summary, three-phase damping control strategy considered in case C7 droops 16.6 MWh/a compared to the reference case C1 while the currently employed control strategy with reactive power exchange, curtails about 30 MWh/a.

#### 4.4.6 Discussion and future work

From the conducted examination of different cases, it can be seen that the voltage support by means of reactive power is not an effective solution in LV grids with high penetration level of renewables. Besides the bigger amount of curtailed energy, the grid performance is also deteriorated due to the additional reactive power.

The mitigation of the negative-sequence voltage component alone, is not sufficient to increase the penetration level of DERs. The presented results showed too small improvement in energy exchange and grid performance compared to the case where both sequence components are impacted at the same value of the damping conductance ( $g_d = 50$  p.u.). In conclusion, in order to increase the penetration level of DERs and improve the grid performance the zero-sequence component must be mitigated, too.

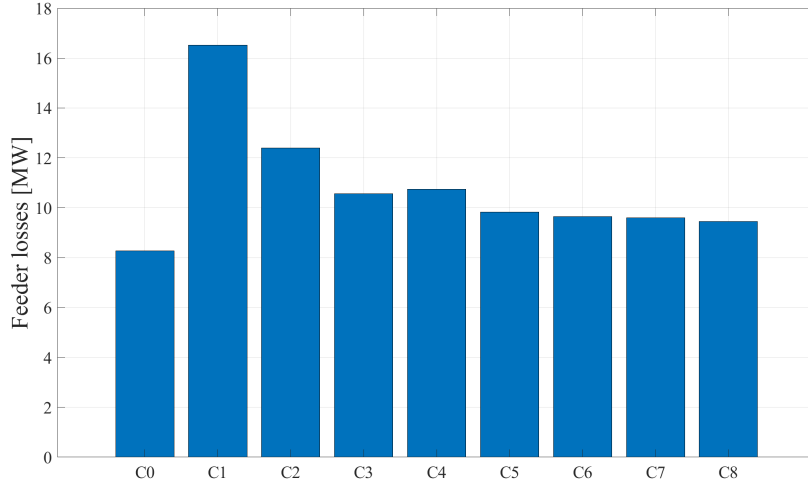


Figure 4.48: Total feeder losses when different control strategies are applied

In order to assess the behaviour of the considered cases in this section, further examinations of different penetration ratios are needed. In addition, the loads and DERs distribution is made such that  $VUF_2$  is always lower than 2%. According to [8], this value must be guaranteed 95% of the time (on a weekly basis), which means higher values of it can occur in practice.

By segregating the damping conductance to  $g_{d0}$  and  $g_{d2}$  gives the opportunity to the three-phase damping control strategy to target the zero- and negative sequence voltage components individually and only if necessary. For instance  $VUF_2$  might be within limits but the zero-sequence component may cause neutral point shifting in the phase voltages. Therefore, only  $g_{d0}$  could be used to solve the power quality problem. In addition, if both conductances are slightly varied the difference in the phase voltages and angles can be used to calculate the sequence impedances of the cable. These measurements can be sent to an MAS to perform some optimisations and send new power set-points to all DERs in order to reach a desired operating state of the network is achieved.

## 4.5 Experimental validation of the conducted theoretical analysis

In this section the experimental validation of the previously discussed three cases is performed. To limit the volume of the experiments, case 1 (§4.1.1) will be validated experimentally together with §4.2 where some limits of the damping

conductance were recommended. To this end, the experimental set-up becomes very similar to the one described in Chapter 3 §3.3. However, to conduct these particular test cases, the set-up is modified according to each case individually. These modifications are only done at the dc-side of the DER so that all three sub-cases ( $p_{dc} = -1$  p.u.  $p_{dc} = 0$  p.u. and  $p_{dc} = 0.66$  p.u.) are experimentally validated on the laboratory set-up.

Although the DER behaves as a current source, for safety reasons, it is connected through a line impedance to the voltage source in order to limit the short-circuit currents in case of faults. In addition, the LV grid is not infinitely strong and there is always some impedance present in the cables. The feeder properties are the same as the ones used in §5.5.2 in, which paragraph more information is given of how the feeder is modelled. The voltages at the PCC and injected currents, together with their respective angles, are measured by using a power analyser PM3000. The upper value of the test voltages will be limited to 1.1 p.u. due to limits imposed by the dc bus voltages of the power electronic inverter. The minimum voltage however, will be limited by the maximum current ratings of the power electronic inverter. Whereas in the theoretical studies conducted in the beginning of this chapter, the inverter efficiency was assumed to be 100% and it also has the abilities to deliver infinite power, in practice however, the inverters always have some losses and they can deliver finite amount of power. In these particular experiments, the inverter efficiency at nominal power is 95% and it can deliver 3 kVA peak power. More data regarding the power electronic inverter properties, used in these experiments can be found below:

$$\begin{array}{llll} I_{\text{ref}} = 10 \text{ A} & I_{\text{nom}} = 3.3 \text{ A} & V_{\text{g,ref}} = 170 \text{ V} & V_{\text{g,nom}} = 110 \text{ V ac} \\ P_{\text{ac}} = 3 \text{ kVA} & V_{\text{dc,ref}} = 600 \text{ V} & V_{\text{dc,nom}} = 400 \text{ V} & P_{\text{dc}} = 1.2 \text{ kW} \\ C_{\text{dc}} = 1000 \mu\text{F} & L_x = 2 \text{ mH} & L_n = 0.666 \text{ mH} & C_x = 5 \mu\text{F} \end{array}$$

where  $I_{\text{ref}}$  is the reference current,  $I_{\text{nom}}$  is the nominal rms current of the inverter,  $V_{\text{g,ref}}$  is the reference grid voltage,  $V_{\text{g,nom}}$  is the rms value of the phase to neutral nominal voltage,  $P_{\text{ac}}$  is the total peak power of the power electronic inverter,  $V_{\text{dc,ref}}$  is the reference dc-bus voltage,  $V_{\text{dc,nom}}$  is the nominal value of the dc-bus voltage,  $P_{\text{dc}}$  is the input power delivered by the programmable dc power supply,  $C_{\text{dc}}$  is the value of the used dc-bus capacitor. The output differential filter is implemented by using an inductance of  $L_x = 2$  mH and  $C_x = 5 \mu\text{F}$ .

The theoretical study in Case 1 sub-case 2 (§4.1.1.2) is conducted at variable phase voltage  $v_a$  and nominal values and angles of the other parameters. Therefore, in order to experimentally validate all sub-cases of Case 1, the programmable ac power source is used to set different values of phase voltage  $v_a$ . In other words, the experiment is designed such that phase voltage  $v_a$  is manually adjusted from

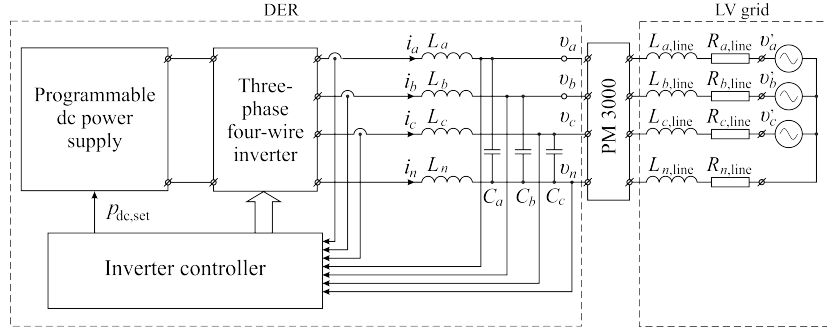


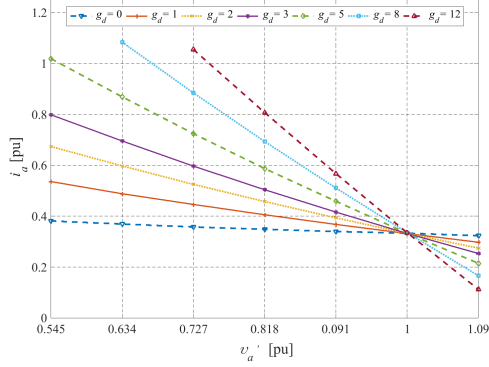
Figure 4.49: Connection of DER in the laboratory experimental set-up

60 V up to 120 V with a step of 10 V by the programmable three-phase voltage source. When these values are converted from absolute into per unit values they result in: 0.545, 0.634, 0.727, 0.818, 0.909, 1 and 1.09 p.u. In addition to the voltage variation, the experiment is also conducted when different values of the damping conductance are used. Seven different values of  $g_d$  are used to study the performance of the three-phase damping control strategy and they are chosen to be 0, 1, 2, 3, 5, 8 and 12 p.u. These conditions are used in the experiments for all sub-cases.

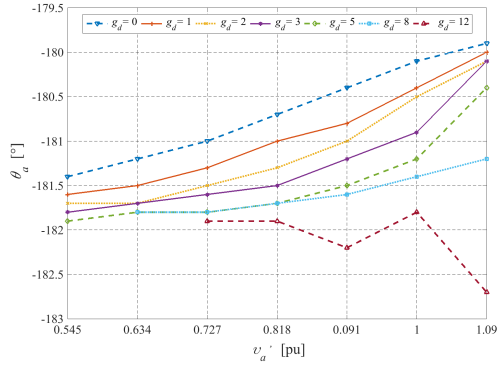
#### 4.5.1 Experimental validation of case 1 sub-case 2

The theoretical study in Case 1 sub-case 2 (§4.1.1.2) is conducted constant input power  $p_{dc} = -1$  p.u. and variable  $v_a$ . The rest of the parameters are kept at their nominal values. As it was mentioned above the experimental set-up is the same to the one used in Chapter 3 but for convenience and clarity, the block diagram of it is presented again in Fig. 4.49. A power analyser is connected between the DER and the feeder, which will allow to accurately measure the rms values of the injected currents and voltages at the PCC and also the current and voltage angles.

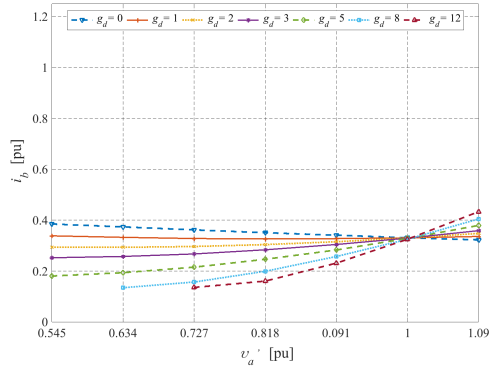
The experimental data obtained for the rms phase currents  $i_a$ ,  $i_b$  and  $i_c$  are presented in Fig. 4.50 (a), (c) and (e) and their phase angles  $\theta_{i,a}$ ,  $\theta_b$  and  $\theta_c$  in Fig. 4.50 (b) (d) and (f), respectively. On the horizontal axis the voltage of the programmable voltage source -  $v_a$  is shown. From the presented results of the measured phase currents it is clear that when the grid is balanced i.e.  $v_a = v_b = v_c = 1$  p.u. all phase currents are equal to their nominal value of 0.333 p.u. as well as their respective phase angles. This is also valid for all 7 values of the damping conductance and similar behaviour is also observed in the theoretical study of this sub-case (Fig. 4.5 and Fig. 4.7).



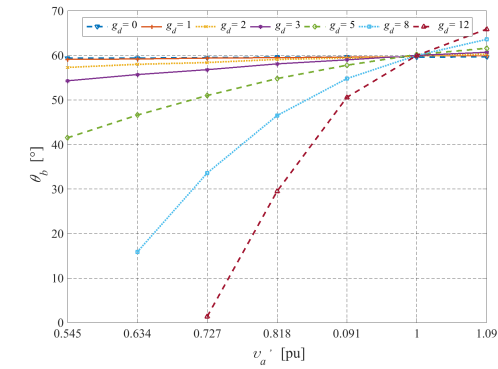
(a)  $i_a$  as a function of  $v_a'$  and  $g_d$  at  $p_{dc} = -1$  p.u.



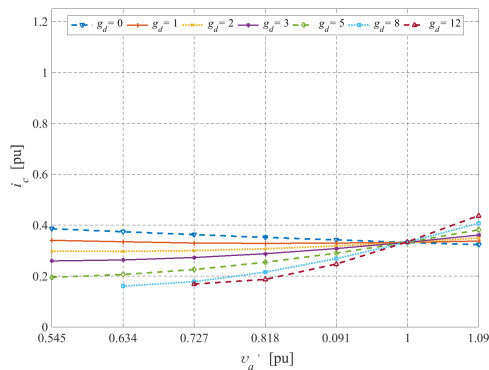
(b)  $\theta_{i,a}$  as a function of  $v_a'$  and  $g_d$  at  $p_{dc} = -1$  p.u.



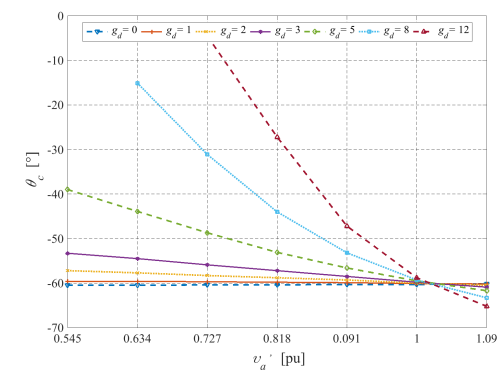
(c)  $i_b$  as a function of  $v_a'$  and  $g_d$  at  $p_{dc} = -1$  p.u.



(d)  $\theta_{i,b}$  as a function of  $v_a'$  and  $g_d$  at  $p_{dc} = -1$  p.u.



(e)  $i_c$  as a function of  $v_a'$  and  $g_d$  at  $p_{dc} = -1$  p.u.



(f)  $\theta_{i,c}$  as a function of  $v_a'$  and  $g_d$  at  $p_{dc} = -1$  p.u.

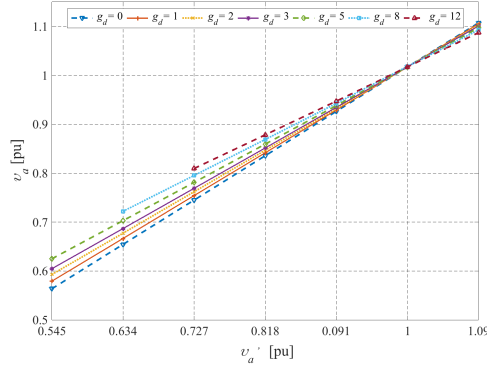
Figure 4.50: Phase currents and angles dependency on the variation of the phase voltage  $v_a'$  at nominal input power  $p_{dc} = -1$  p.u. and different values of the damping conductance  $g_d$

When the positive-sequence control strategy is used ( $g_d = 0$  p.u.) all phase currents are equal to their nominal values. There is a slight increase of the phase currents when  $v_a$  becomes lower but this is because the control strategy is trying to maintain the power balance between the ac and dc sides. The angles of the injected currents slightly deviate with about  $1.5^\circ$  in the investigated voltage range and they are still  $180^\circ$  phase shifted with respect to their phase voltage because the control strategy operates in injection mode.

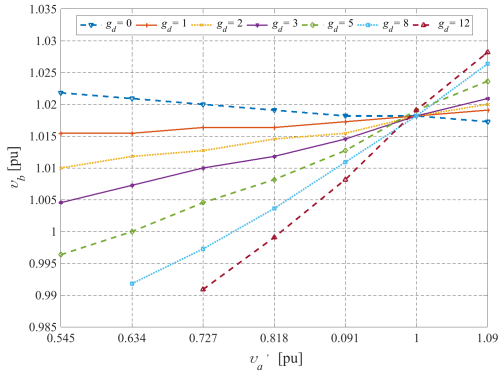
When the value of the damping conductance is increased, the control strategy injects more current in phase  $a$  and less current in phases  $b$  and  $c$ . The trends of the obtained curves of the phase currents do resemble the ones obtained in Fig. 4.5. However, there are some differences when comparing the experimental and theoretical results. For instance in the theoretical study  $i_a$  assume a value of about 0.7 p.u. at  $v_a=0.54$  p.u. while the experimental results show that  $i_a = 0.53$  p.u. In addition, the phase current angles  $\theta_{i,b}$  and  $\theta_{i,c}$  are not exactly  $180^\circ$  phase shifted with respect to their phase voltages, especially at high values of  $g_d$  where this deviation reaches  $60^\circ$  and these two currents are lagging the phase voltages. This misalignment is because of the assumptions needed to simplify the theoretical cases, which were (i) negligible feeder impedance and also (ii) DER efficiency of 100%. In the practical set-up however, there is some feeder impedance and lower efficiency and therefore  $p_{ac} < p_{dc}$ . On top of that, due to the present impedance in the feeder, the voltages at the PCC differ from the ones that are set by the programmable ac voltage source.

Note also that, according to Fig. 4.7 (b), (d) and (f) the border mode of all phases is crossed at  $g_d = 4.1$  p.u. but due to the feeder impedance and inverter efficiency in the experimental set-up this is not achieved even if the damping conductance is equal to 5 p.u., 8 p.u. and even 12 p.u. Despite the fact that the power electronic inverter is significantly oversized (4 times the nominal current) at high values of  $g_d = 8$  and 12 p.u. and low values of  $v_a$ , the injected current  $i_a$  exceeds the maximum current ratings of the inverter and the data for these points are not available.

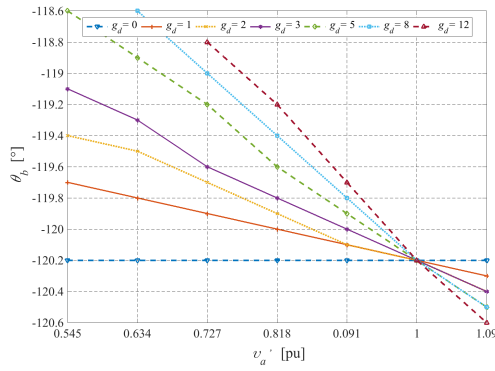
The experimental data obtained for the phase voltages at the PCC versus  $v_a$  and different values of the damping conductance  $g_d$  are presented in Fig. 4.51. On the horizontal axis the voltage of the programmable voltage source  $v_a$  is shown, while on the vertical axis the measured voltage at the PCC is shown. Phase voltages  $v_a$ ,  $v_b$  and  $v_c$  are presented in Fig. 4.51 (a), (b), (c) and phase angles  $\theta_b$  and  $\theta_c$  in Fig. 4.51 (c), (e), respectively. The used power analyser uses phase angle  $\theta_a$  as a reference, which means that it is being considered to be equal to zero all the time therefore, the angle  $\theta_a$  will not be presented in Fig. 4.51 since its value is always  $0^\circ$ .



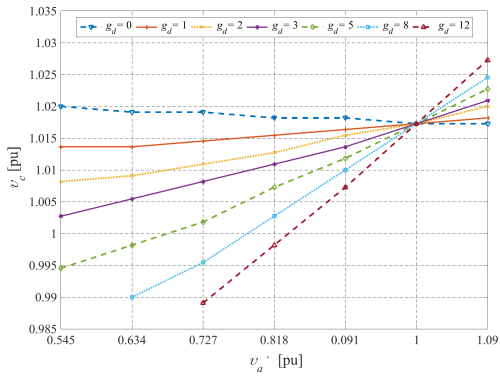
(a)  $v_a$  as a function of  $v_a'$  and  $g_d$  at  $p_{dc} = -1$  pu



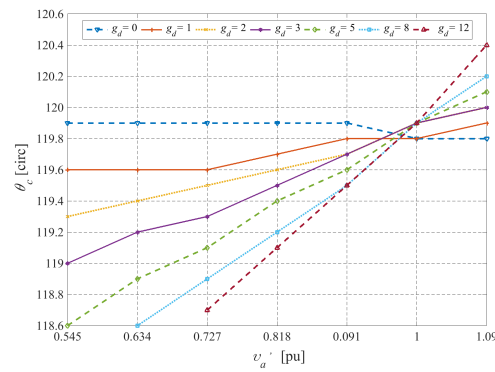
(b)  $v_b$  as a function of  $v_a'$  and  $g_d$  at  $p_{dc} = -1$  pu



(c)  $\theta_b$  as a function of  $v_a'$  and  $g_d$  at  $p_{dc} = -1$  pu



(d)  $v_c$  as a function of  $v_a'$  and  $g_d$  at  $p_{dc} = -1$  pu



(e)  $\theta_c$  as a function of  $v_a'$  and  $g_d$  at  $p_{dc} = -1$  pu

Figure 4.51: Phase voltages and angles dependency on the variation of the phase voltage  $v_a'$  at nominal input power  $p_{dc} = -1$  p.u. and different values of the damping conductance  $g_d$

From the presented results in Fig. 4.51 (a), it can be seen the impact of the different damping conductance values on the voltages at the PCC. In the trivial case when  $v_a = v_b = v_c = 1$  p.u. the actual impact of the PCC voltages it can be seen caused by the DER. In this particular case, the injected currents cause a voltage rise of about 0.0175 p.u. When  $v_a < 1$  due to the symmetrical current injection by the positive-sequence control strategy,  $v_a$  is the lowest one of all (the opposite is valid for phases  $b$  and  $c$ ). When  $g_d$  differs from 0 the advantageous effect of the three-phase damping control strategy on the PCC voltages starts to appear. If the extreme cases are compared ( $g_d = 0$  p.u. and  $g_d = 12$  p.u.) within the standard voltage band of 0.9 p.u. to 1.1 p.u. the difference between them is around 0.02 p.u. and it becomes even more prominent at lower values of  $v_a$  where a difference of 0.066 p.u. at  $v_a = 0.727$  p.u. is observed. When  $v_a > 1$  the behaviour of the three-phase damping control strategy is opposite to the explained above. In addition to these measurements, the zero- and negative-sequence are calculated and the influence of the damping conductance is demonstrated. More information about these measurements can be found in Appendix A, Table A.1.

#### 4.5.2 Experimental validation of case 1 sub-case 1

In the previous experiment, the advantageous performance of the three-phase damping control strategy over the positive-sequence control strategy was demonstrated. This performance is achieved by asymmetrical current injection in the different phases and the power is delivered by the primary source. Considering the fact that the nature of the renewable energy resources is intermittent implies that input power will not be always available at the dc-bus side. In Case 1, sub-case 1 (§4.1.1.1) it was theoretically proven (in §4.3.1 by means of simulations in Matlab&Simulink on a real LV feeder) that the three-phase damping control strategy is able to exchange currents with the grid and still be able to improve the power quality and decrease the grid losses, even though the input power is not present. Hence, it is of great importance to investigate experimentally the performance of the three-phase damping control strategy under these conditions.

In §4.1.1.1 was shown that if  $p_{dc} = 0$  p.u. and  $g_d = 0$  p.u. the three-phase damping control strategy does not exchange any currents with the grid, hence this experiment is not conducted for further investigation. Therefore, in this experiment, the  $g_d$  assumes values 1, 2, 3, 5, 8 and 12 p.u.

The obtained experimental results of the exchanged rms phase currents as a function of  $v_a$  are shown in Fig. 4.52 (a), (c) and (e) and their corresponding angles in Fig. 4.52 (b), (d) and (f). At  $v_a = 1$  p.u. the voltages at the PCC are perfectly balanced and the exchanged currents are very low.

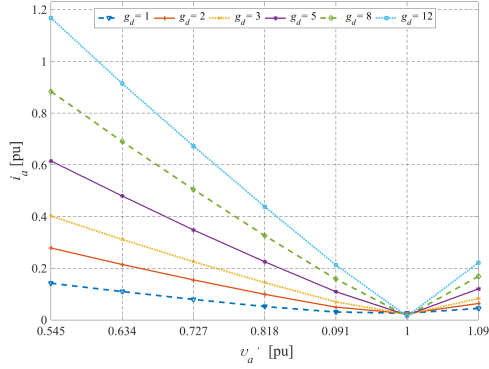
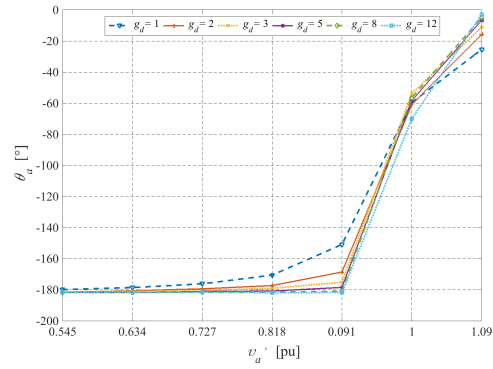
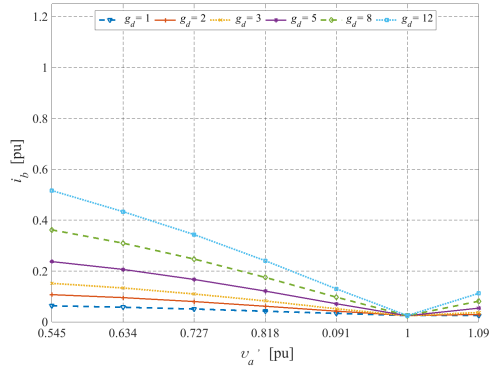
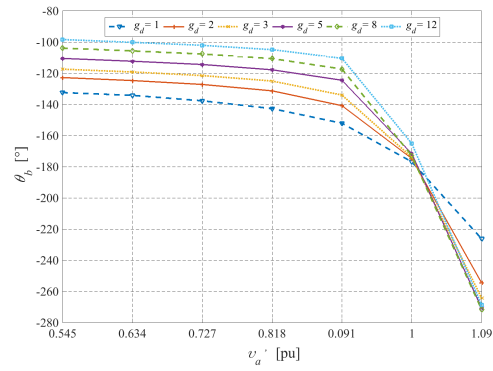
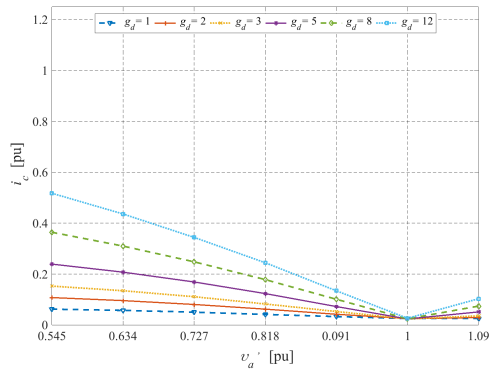
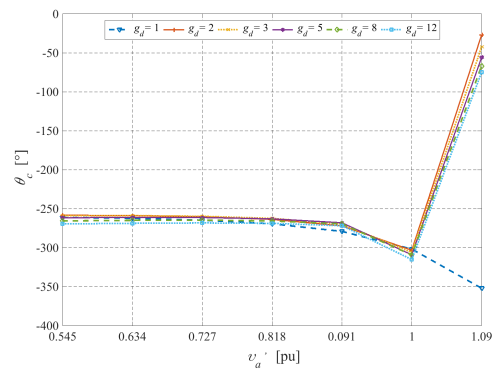
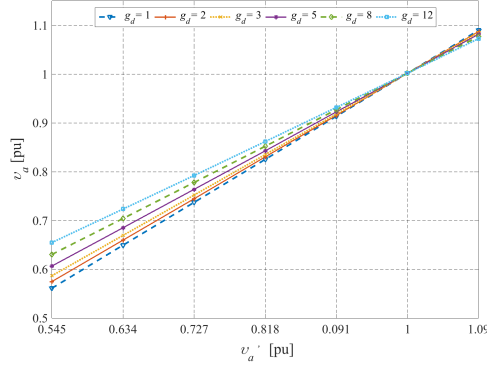
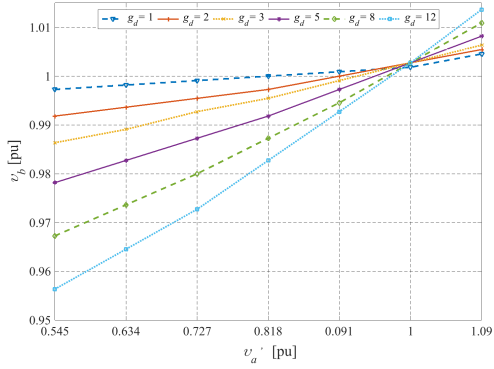
(a)  $i_a$  as a function of  $v_a'$  and  $g_d$  at  $p_{dc} = 0$  p.u.(b)  $\theta_{i,a}$  as a function of  $v_a'$  and  $g_d$  at  $p_{dc} = 0$  p.u.(c)  $i_b$  as a function of  $v_a'$  and  $g_d$  at  $p_{dc} = 0$  p.u.(d)  $\theta_{i,b}$  as a function of  $v_a'$  and  $g_d$  at  $p_{dc} = 0$  p.u.(e)  $i_c$  as a function of  $v_a'$  and  $g_d$  at  $p_{dc} = 0$  p.u.(f)  $\theta_{i,c}$  as a function of  $v_a'$  and  $g_d$  at  $p_{dc} = 0$  p.u.

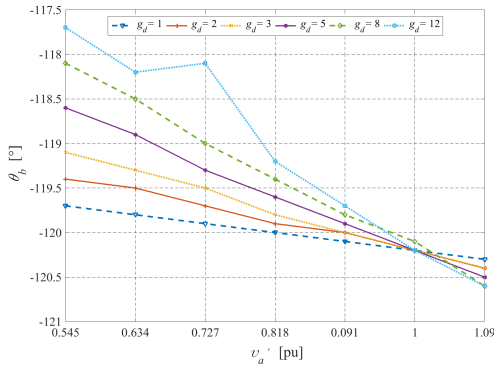
Figure 4.52: Phase currents and angles dependency on the variation of the phase voltage  $v_a'$  at zero input power  $p_{dc} = 0$  p.u. and different values of the damping conductance  $g_d$



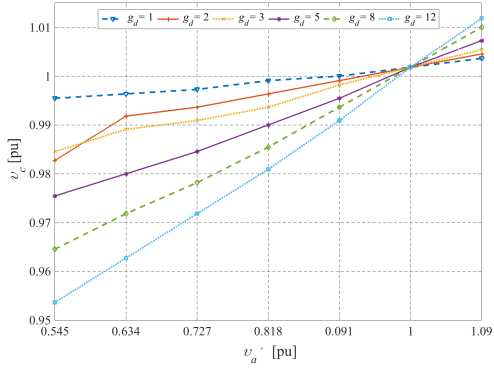
(a)  $v_a$  as a function of  $v_a'$  and  $g_d$  at  $p_{dc} = 0$  p.u.



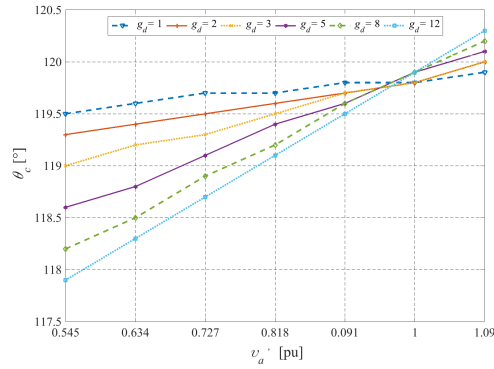
(b)  $v_b$  as a function of  $v_a'$  and  $g_d$  at  $p_{dc} = 0$  p.u.



(c)  $\theta_b$  as a function of  $v_a'$  and  $g_d$  at  $p_{dc} = 0$  p.u.



(d)  $v_c$  as a function of  $v_a'$  and  $g_d$  at  $p_{dc} = 0$  p.u.



(e)  $\theta_c$  as a function of  $v_a'$  and  $g_d$  at  $p_{dc} = 0$  p.u.

Figure 4.53: Phase voltage and angle errors dependency on the variation of the phase voltage  $v_a'$  at zero input power  $p_{dc} = 0$  p.u. and different values of the damping conductance  $g_d$

Theoretically, the phase currents are equal to zero as it was investigated in §4.1.1.1. However, there are some losses in the inverter of the practical set-up. As it can be seen from the obtained results, the phase currents have some small offset and one part of it is to compensate for these inverter losses.

From the theoretical study conducted in §4.1.1.1, Fig. 4.4 (b), (d) and (f) it was also shown that the three-phase damping control strategy has a very prominent border mode at  $v_a = 1$  p.u., which is invariant of the damping conductance value. Comparing the theoretical and measured angles of this operational mode it is obvious that there is a big difference between both results. Ideally, the measured angles should have been  $0^\circ$  or  $180^\circ$  phase shifted with respect to their corresponding voltages. However, this is not present in the measurements. Considering the differential output filter capacitance of  $5\mu\text{F}$  and the reactive current flowing through it, this would explain the phase angle variation between the theory and practice. Furthermore, this reactive current represents the second component of the offset of the exchanged phase current that was mentioned earlier.

Apart from this, it can be observed that the injected current in phase  $a$  fairly resembles trends obtained in the theoretical results presented in Fig. 4.2 and Fig. 4.3. When  $v_a < 1$ , phase current  $i_a$  is being injected into the grid because  $\theta_{i,a}$  tends to  $180^\circ$ . Phase currents  $i_b$  and  $i_c$  are being consumed from the grid because their angles are in phase with the corresponding voltage angles. It can be noted that in practice, the current angles  $\theta_{i,b}$  and  $\theta_{i,c}$  are not exactly in phase with  $v_b$  and  $v_c$ . The opposite can be stated when  $v_a > 1$ .

The measured voltages and their voltage angles are shown in Fig. 4.53 (a), (b) and (d). Similar to § 4.5.1 only the angles of phases  $b$  and  $c$  are depicted. At  $p_{dc} = 0$  p.u. condition, the current oversizing of the inverter is sufficient to cover the entire range of  $v_a$  for all values of the damping conductance, which allows for a complete set of measurements. When  $v_a < 1$  p.u. the control strategy consumes currents from phases  $b$  and  $c$  and injects it back into phase  $a$  thus providing support to  $v_a$  at the PCC. In the standard voltage range, the control strategy is able to increase  $v_a$  from 0.91 to 0.93 p.u. when  $g_d$  of 1 and 12 p.u. is applied. The beneficial effect of the voltage unbalance mitigation is even more prominent at the extreme values of  $v_a$  where  $v_a$  is increased from 0.56 p.u. to 0.65 p.u. for the same values of the damping conductance (1 to 12 p.u.). The current consumption from phases  $b$  and  $c$  leads to significant voltage drop of 0.06 p.u., which is present in both phases. Nevertheless, these voltages are still within standard limits so a power quality issue is not present. The opposite is valid when  $v_a > 1$  p.u. The control strategy consumes current from phase  $a$  and injects it back into phases  $b$  and  $c$ , which causes voltage drop in phase  $a$ . At the upper extreme value of  $v_a$ , phase voltage is decreased down to 1.073 p.u. at  $g_d = 12$  p.u. More information about zero- and negative-sequence voltage unbalance factors is listed in Table A.2.

The obtained experimental results confirm that the three-phase damping con-

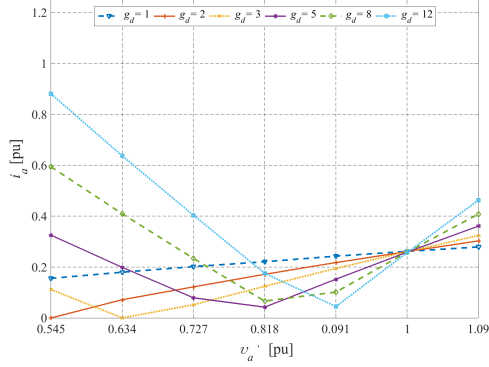
control strategy is able to improve the voltage profile despite the fact that the power from the primary source is not present. Hence, if the three-phase damping control strategy is used in PV applications it could be employed to mitigate the voltage unbalance during night time and also in days with very little solar irradiation like cloudy days and winter time.

### 4.5.3 Experimental validation of case 1 sub-case 3

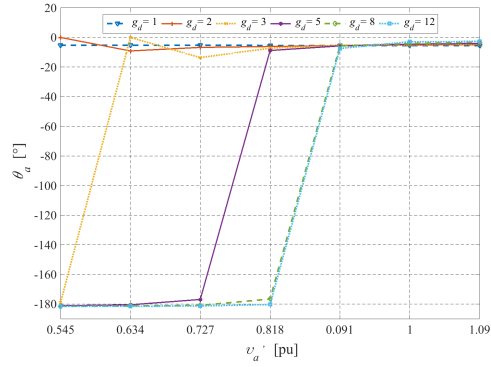
In this paragraph, an experimental validation of case 1 sub-case 3 is conducted. This sub-case represents a functionality of the three-phase damping control strategy where the dc-bus is loaded and the DER consumes current from the grid in order to satisfy the demand of the dc load. For the sake of validation of this functionality, the dc-bus of the experimental set-up is loaded with a variable electronic load. In §4.3.2 a load of 66% of the nominal power was used to demonstrate the excellent property of the three-phase damping control strategy to mitigate the voltage unbalance in a real LV feeder. Therefore, this load value will be also used to validate experimentally the performance of the control strategy on this set-up.

The rms measurements of the phase currents are depicted in Fig. 4.54 (a), (c), (e) and their corresponding angles in Fig. 4.54 (b), (d), (f). The experiments are conducted for six values of the damping conductance  $g_d = 1, 2, 3, 5, 8$  and  $12$  p.u. The trivial case of the positive-sequence control strategy is not conducted because the outcome of this experiment will not lead to any power quality improvement. In this mode the control strategy operates as an active rectifier and when  $v_a < 1$  p.u. the control strategy consumes currents from all phases if damping conductance values of 1 and 2 p.u. are considered. However, if  $g_d = 3$  p.u. phase current  $i_a$  changes from current consumption mode to current injection mode. The border mode where  $i_a = 0$  p.u. occurs is between  $0.545v_a < 0.635$ , which can be also seen from the change of  $\theta_{i,a}$  depicted in Fig. 4.54 (b). By increasing the damping conductance value, the border mode occurrence shifts to higher values of  $v_a$ , which is more or less with an agreement to the theoretical study conducted in §4.1.1.3.

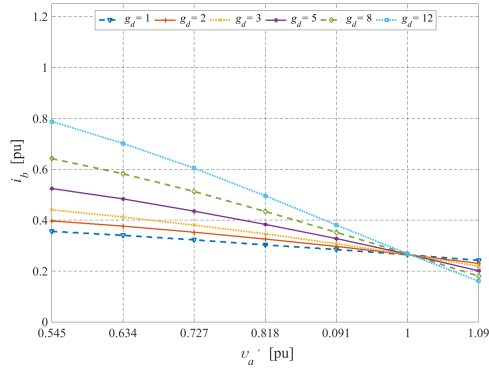
The rms values of the voltages at PCC, measured by the power analyser, are depicted in Fig. 4.55. At  $v_a = v_b = v_c = 1$  p.u. the actual impact on the grid voltage levels can be seen. In this particular case, the grid voltages are decreased by 0.01 p.u. in all phases when  $p_{dc} = 0.66$  p.u. The interpretation of these results is similar to the one given in the previous experiments. The only difference is the slightly lower voltage levels in phases  $b$  and  $c$  at PCC due to the loading of the feeder. The beneficial effect of the voltage unbalance mitigation can be seen in Table A.3 where the data about the zero- and negative-sequence unbalance factors are listed.



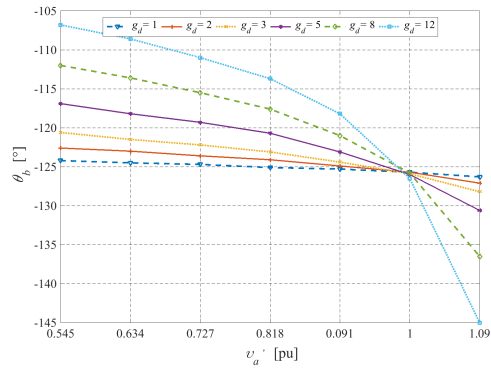
(a)  $i_a$  as a function of  $v_a'$  and  $g_d$  at  $p_{dc} = 0.66$  p.u.



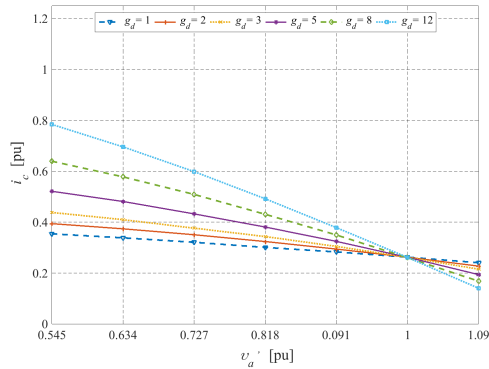
(b)  $\theta_{i,a}$  as a function of  $v_a'$  and  $g_d$  at  $p_{dc} = 0.66$  p.u.



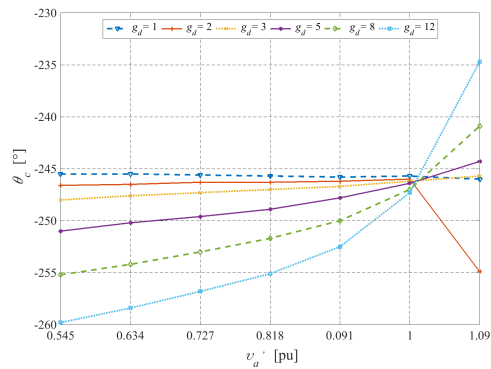
(c)  $i_b$  as a function of  $v_a'$  and  $g_d$  at  $p_{dc} = 0.66$  p.u.



(d)  $\theta_{i,b}$  as a function of  $v_a'$  and  $g_d$  at  $p_{dc} = 0.66$  p.u.

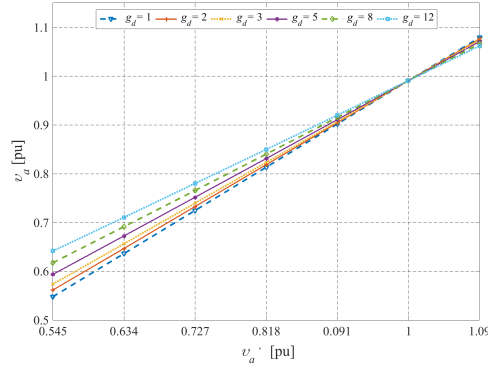


(e)  $i_c$  as a function of  $v_a'$  and  $g_d$  at  $p_{dc} = 0.66$  p.u.

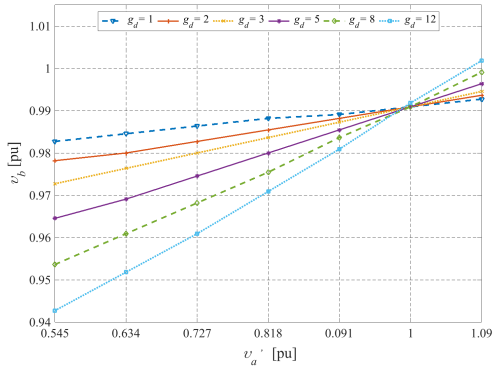


(f)  $\theta_{i,c}$  as a function of  $v_a'$  and  $g_d$  at  $p_{dc} = 0.66$  p.u.

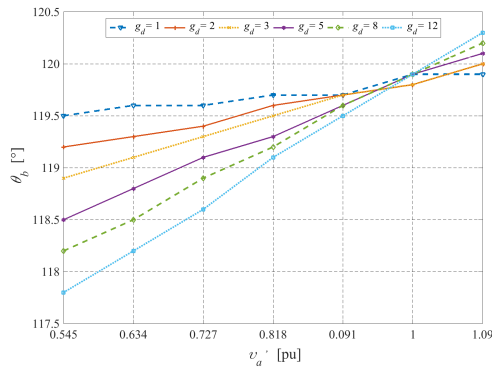
Figure 4.54: Phase currents and angles dependency on the variation of the phase voltage  $v_a'$  at consumed power  $p_{dc} = 0.66$  p.u. and different values of the damping conductance  $g_d$



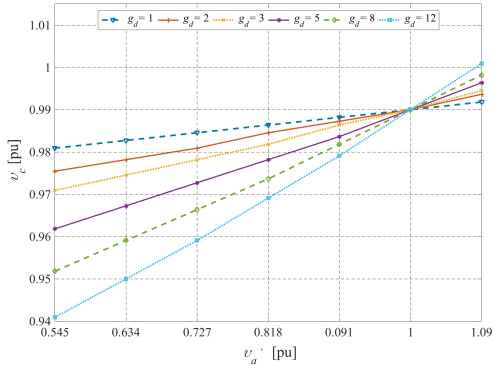
(a)  $v_a$  as a function of  $v_a'$  and  $g_d$  at  $p_{dc} = 0.66$  p.u.



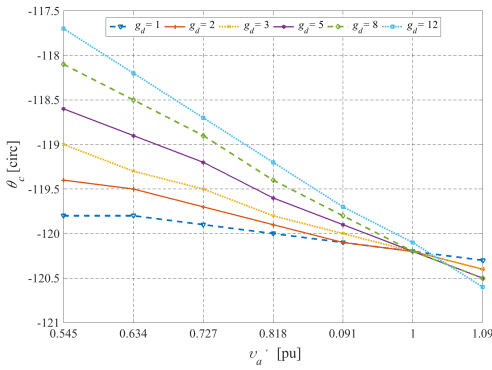
(b)  $v_b$  as a function of  $v_a'$  and  $g_d$  at  $p_{dc} = 0.66$  p.u.



(c)  $\theta_b$  as a function of  $v_a'$  and  $g_d$  at  $p_{dc} = 0.66$  p.u.



(d)  $v_c$  as a function of  $v_a'$  and  $g_d$  at  $p_{dc} = 0.66$  p.u.



(e)  $\theta_c$  as a function of  $v_a'$  and  $g_d$  at  $p_{dc} = 0.66$  p.u.

Figure 4.55: Phase voltages and angles dependency on the variation of the phase voltage  $v_a$  at zero consumed power  $p_{dc} = 0.66$  p.u. and different values of the damping conductance  $g_d$

#### 4.5.4 Discussion

Due to the fact that an impedance is present in the experimental set-up, the voltages at the PCC differ from the ones that are set by the programmable ac voltage source. This leads to slightly different results between the theoretical and practical examinations. Nevertheless, due to the presence of feeder impedance, the experimental result trends more or less resemble the theoretical ones. In practice, DERs that are closer to the distribution transformer will inject current through a lower feeder impedance and their behaviour will resemble closely the theoretical one, while the DERs connected further in the feeder will resemble the behaviour obtained by the experimental results.

#### 4.6 Future work

The three-phase damping control strategy has the potential to perform also active power balancing by consuming power from the phases with the highest voltage and injecting it back into the phases with the lower voltage levels. Nevertheless, some DSOs do not like reverse power flows of this kind in their grids because of the complex energy flow, which makes their assessment of the grid losses less accurate. For these reasons, the three-phase damping control strategy can be implemented such that the reverse power flow is prohibited. By solving the characterisation equation of (2.15) the border mode can be found for the given input power (measured input power) an optimum value of the damping conductance can be calculated. Furthermore, if reverse power flow is not prohibited, the power ratings of the inverter also play a role in the voltage unbalance mitigation and great attention must be paid on this matter. In order to avoid reverse power flows or constrain the injected currents within some boundaries an MPC or other techniques can be used. This is an interesting topic for future work to enhance even more the capabilities of the damping control strategy to improve the power quality and in the same time to use the power electronic inverter at its maximum power ratings.

#### 4.7 Conclusions

In this chapter, a comparison between the classical positive-sequence and the three-phase damping control strategy was made. Theoretical case studies are used to illustrate the performance of the control strategies where some limits of the damping conductance are defined based on the voltage unbalance level and the power ratings of the power electronic inverter. As mentioned earlier, the beneficial effect on the voltages at the PCC is because of the resistive behaviour of the control strategy towards the zero- and negative-sequence components, which is set by the value of the damping conductance. From the investigated case studies -theoretical

and experimental - it can be concluded that the damping conductance value can assume low values if the control strategy is required to provide fault-ride through capabilities, which are typically 1 to 2 p.u. without significant oversizing of the power electronic inverter. If the control strategy is used only for voltage unbalance mitigation, then the damping conductance value can be increased from 2 to 20 p.u. again without severe oversizing of the inverter.

In addition to the above mentioned conclusions, the three-phase damping control strategy is also examined in a realistic LV grid and the results showed that the system performance can be still greatly improved when there is no power from the primary source and if the control strategy is used to supply a load. The theoretical and experimental comparison between the positive-sequence and the three-phase damping control strategy highlights a few positive features in favour of the later one. The three-phase damping control strategy is able to mitigate the voltage unbalance in current injection, zero-power and consumption mode. With the much increased flexibility, new opportunities are open to incorporate such intelligent control algorithms to improve power quality issues in LV grids. Furthermore, this allows to mitigate the need of the DSO to install dedicated devices to improve the power quality (DSTATCOM, APF, DVR, etc.) in LV and MV grids because the modified three-phase damping control strategy can be utilised by the DERs and the power quality problems could be solved at the points where they are present.



# 5

## Practical implementation of the three-phase modified damping control strategy

In this chapter, some guidelines are given regarding the practical implementation of the modified three-phase damping control strategy. Recommendations are provided for the proper sampling as well as stabilisation techniques for the split dc-link capacitors. A model of the three-phase DER is built in Matlab & Simulink environment and the transient behaviour of the local control is briefly examined. In addition, the model is examined for different values of the damping conductance as well as phase voltage  $v_a$  and its accuracy is assessed. Finally, some results are presented from a field trial conducted in the frame work of project INCREASE in Graz, Austria, where the the positive-sequence and the three-phase damping control strategies are compared in a real LV grid.

### 5.1 Three-phase damping control strategy

The modified three-phase damping control strategy is able to mitigate the voltage unbalance at the PCC because of its resistive behaviour towards the zero- and negative-sequence components. In order to influence the zero-sequence component the three-phase damping control strategy is interfaced with the grid by means of a three-phase, four-wire VSI. A simplified connection diagram of the damping

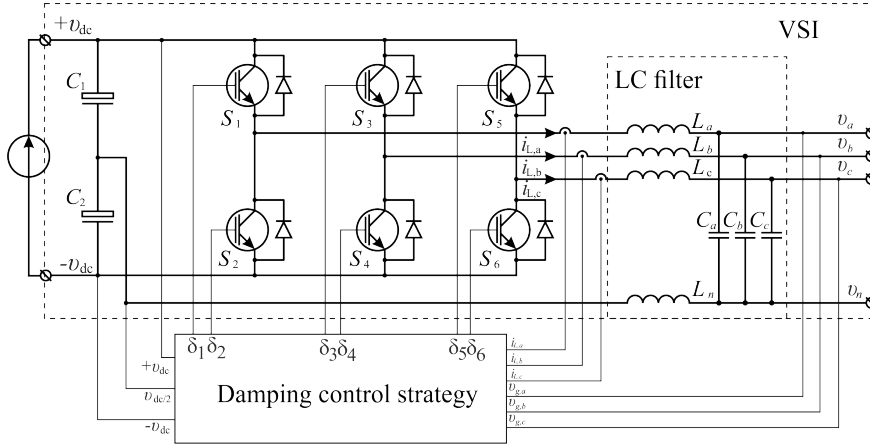


Figure 5.1: Simplified connection diagram of the damping control strategy

control strategy is depicted in Fig. 5.1. The set-up consists of a power supply, a VSI and a controller. The power supply is configured as a controllable current source, which is used to supply the dc-bus of the VSI. The phase currents are injected by the three legs of the power electronic inverter and an LC filter is used to filter out the high frequency component. More information about the fourth wire of VSI is given later in this chapter. The necessary measurements required by the damping control strategy for its proper operation are the dc-bus voltages, inductor currents and phase voltages. Based on these measurements the three-phase damping control strategy generates driving signals  $\delta_1$  to  $\delta_6$ , which drive the power electronic switches accordingly.

A detailed overview of the three-phase damping control strategy blocks is presented in Fig. 5.2. The dc-bus controller ensures the power balance between the dc and ac side of the VSI and the output of which is the fundamental input conductance  $g_1$ , which also participates in the reference current calculation. The phase voltages are passed to a phase locked loop (PLL), which accurately extracts the voltage angle and rms value for the respective phase. The local control is implemented by the damping and droop controllers that set the damping conductance and output power value based on the rms value of the highest among the phase voltages. All these signals (except the signal coming from the droop controller) are passed to the reference current former block where the reference currents are calculated according to the local measurements. Then the reference currents are subtracted from the measured values and the errors are fed to three PI controllers, which outputs are passed to a PWM generator. Thus the driving signals for the power electronic switches are generated.

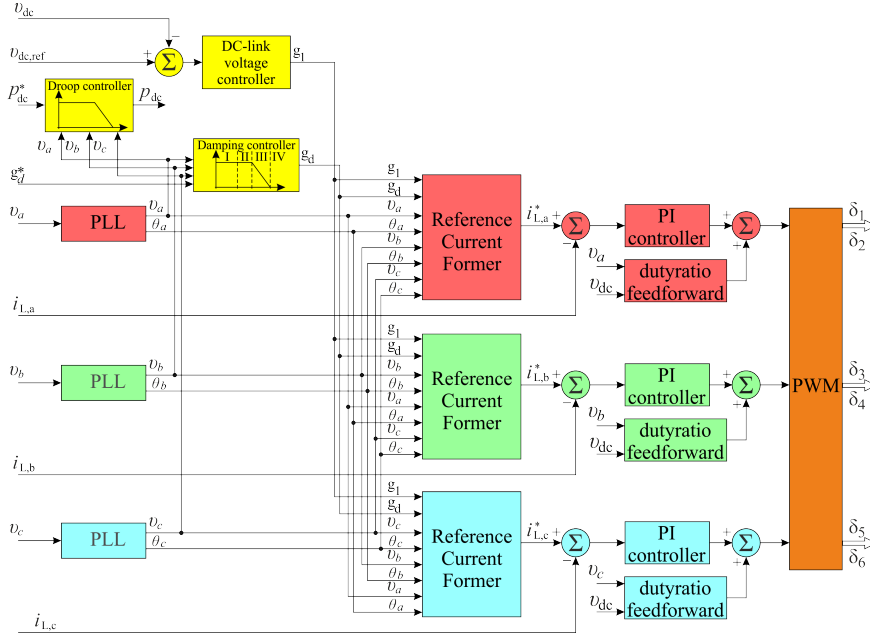


Figure 5.2: Block diagram of the modified three-phase damping control strategy

## 5.2 Sampling of the different variables

In this section, the signals used to calculate the reference currents and their appropriate sampling is discussed. The minimum sampling frequency of the variables according to Nyquist-Shannon theorem should be at least twice as high as the fundamental frequency [88]. Nevertheless, such a sampling frequency will not be sufficient to generate reference currents with low THD. Values of at least 10 (or higher) times the fundamental frequency are recommended [89]. During turn on and off of the power electronic switches, some high  $dV/dt$  voltage transients are present, which can pollute the measurements. To avoid this, the choice of sampling frequency is often the same or a multiple of the switching frequency and the sampling itself is performed after the on-off transients have decayed. If the switching frequency coincides with the sampling frequency, the choice of the former one is a compromise between switching losses and resolution. In this chapter, a switching frequency of 20kHz is chosen, which gives sufficient data to generate reference currents with low THD.

Furthermore, to ensure a smooth operation of the DER equipped with the three-phase damping control strategy each parameter used by the current reference block (see Fig.5.2) must be used in the correct instance. Improper sampling of these signals may lead to excessive distortions of the reference current, thus the phase

current will be polluted as well. Hence, the correct sampling of the variables is of great importance for the reliable operation of the control strategy. To form the reference currents (2.15) is rewritten as (5.1) with instantaneous values, which are used to calculate the reference currents as shown below:

$$\begin{aligned}
 i_{a,\text{ref}}(t) &= \frac{1}{3} \left\{ g_1 [v_a \sin(A) + v_b \sin(B) + v_c \sin(C)] \right. \\
 &\quad \left. + g_d [2v_a \sin(A) - v_b \sin(B) - v_c \sin(C)] \right\} \\
 i_{b,\text{ref}}(t) &= \frac{1}{3} \left\{ g_1 [v_b \sin(D) + v_a \sin(E) + v_c \sin(F)] \right. \\
 &\quad \left. + g_d [2v_b \sin(D) - v_a \sin(E) - v_c \sin(F)] \right\} \\
 i_{c,\text{ref}}(t) &= \frac{1}{3} \left\{ g_1 [v_c \sin(G) + v_a \sin(H) + v_b \sin(I)] \right. \\
 &\quad \left. + g_d [2v_c \sin(G) - v_a \sin(H) - v_b \sin(I)] \right\}
 \end{aligned} \tag{5.1}$$

where:

$$\begin{aligned}
 A &= \omega t + \theta_a, & B &= \omega t + \theta_b + \frac{2\pi}{3}, & C &= \omega t + \theta_c - \frac{2\pi}{3} \\
 D &= \omega t + \theta_b, & E &= \omega t + \theta_a - \frac{2\pi}{3}, & F &= \omega t + \theta_c + \frac{2\pi}{3} \\
 G &= \omega t + \theta_c, & H &= \omega t + \theta_a + \frac{2\pi}{3}, & I &= \omega t + \theta_b - \frac{2\pi}{3}
 \end{aligned}$$

where in practice, the fundamental input conductance  $g_1$  is calculated by the dc-bus controller, the damping conductance  $g_d$  is calculated by the damping controller and the rms values of the phase voltages are obtained by using a PLL and an rms algorithm.

### 5.3 Phase angle and voltage magnitude extraction

According to [14] the total harmonic distortion of the injected current by a DER must be limited to 5% when nominal current is injected. Taking into account also

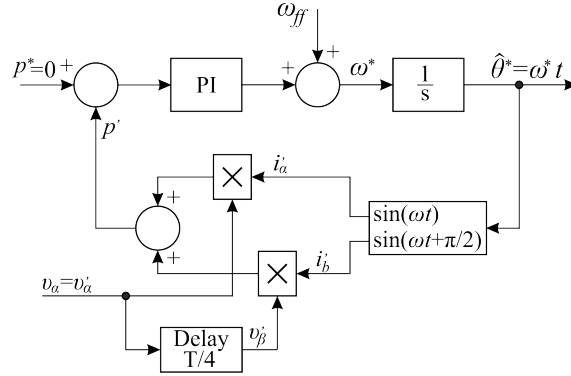


Figure 5.3: Structure of the T/4 based PLL

the voltage variation of  $\pm 10\%$  and the frequency variation of  $\pm 1\%$  [8], the synchronisation unit must then be accurate, reliable and also fast tracking to be able to comply with the above listed requirements [90]. In general, there are two major methods for grid synchronisation: phase locked loop (PLL) and non-PLL-based ones. The non-PLL methods include Fourier analysis and Inducverters but these methods are not so commonly used in practice [90]. The PLL-based ones are more used in practice. In this group, the PLL methods can be classified as: T/4 delay, Inverse Park's transformation, Enhanced PLL, Robust PLL and second order generalised integrator (SOGI) type [90, 91]. In literature, there are also other PLL algorithms, which are combinations of the above mentioned ones but they have increased complexity, which makes them less attractive for practical implementation.

Some of the above listed PLL types are three-phase ones and their output is the positive-sequence angle of the three-phase voltages. In order to operate accordingly, the three-phase damping control strategy requires the phase angle and voltage values of each phase individually, which implies that a single-phase PLL unit will be more appropriate. Among the listed ones the T/4 PLL provides excellent tracking and dynamic response in case of disturbances [41, 92]. In [93], the authors have proposed a T/4 topology, which is depicted in Fig. 5.3 and uses a modified p-q method to extract the phase angle. The operation principal of this PLL can be described mathematically by introducing the Clark transformation of the input voltage  $v_\alpha$  and the delayed orthogonal voltage  $v_\beta$ :

$$\begin{aligned} v'_\alpha(t) &= v_\alpha(t) \\ v'_\beta(t) &= v_\alpha(t - \frac{\pi}{2\omega}) \end{aligned} \tag{5.2}$$

$$\begin{aligned} i'_\alpha(t) &= i_\alpha(t) \\ i'_\beta(t) &= i_\alpha(t - \frac{\pi}{2\omega}) \end{aligned} \quad (5.3)$$

The instantaneous active power  $p(t)$  of a two-phase system and the fictitious instantaneous power  $p'(t)$  are given by:

$$p(t) = v_\alpha(t) i_\alpha(t) + v_\beta(t) i_\beta(t) = \bar{p}(t) + \tilde{p}(t) \quad (5.4)$$

$$p'(t) = v'_\alpha(t) i'_\alpha(t) + v'_\beta(t) i'_\beta(t) = \bar{p}'(t) + \tilde{p}'(t) \quad (5.5)$$

where the two-phase input voltages  $v'_\alpha$  and  $v'_\beta$  are:

$$\begin{aligned} v'_\alpha(t) = v_x(t) &= \sqrt{2} V_{\text{rms}} \sin(\omega t) = |v_x| \sin(\omega t) \\ v'_\beta(t) &= |v_x| \sin(\omega t - \frac{\pi}{2}) \end{aligned} \quad (5.6)$$

where  $v_x(t)$  is the input phase voltage,  $V_{\text{rms}}$  is the rms value of the respective phase voltage and  $|v_x|$  is the amplitude of the respective phase voltage.

In a similar way the fictitious currents  $i'_\alpha$  and  $i'_\beta$  are expressed as:

$$\begin{aligned} i'_\alpha(t) &= \sin(\theta^*) \\ i'_\beta(t) &= \sin(\theta^* - \frac{\pi}{2}) = -\cos(\theta^*) \end{aligned} \quad (5.7)$$

where  $\theta^*$  is the output angle of the PLL. Then the fictitious instantaneous power is:

$$\begin{aligned} p'(t) &= |v| \sin(\omega t) \sin(\theta^*) + |v| \sin(\omega t - \frac{\pi}{2}) \sin(\theta^* - \frac{\pi}{2}) \\ &= |v| \cos(\omega t - \theta^*) \end{aligned} \quad (5.8)$$

The dc component in  $p'(t)$  is eliminated only when currents  $p'_\alpha(t)$  and  $p'_\beta(t)$  are orthogonal. In this way, the following equation for the voltage angle can be obtained:

$$\theta^* = \omega' t + \frac{\pi}{2} = \theta' + \frac{\pi}{2} \quad (5.9)$$

By substituting (5.9) in to (5.8) yields to:

$$p'(t) = |v| \cos(\omega t - \theta' - \frac{\pi}{2}) = |v| \sin(\omega t - \theta') \quad (5.10)$$

where it can be seen that the fictitious instantaneous power  $p'(t) = 0$  when the grid frequency is equal to the PLL frequency. The absolute error between the phase angle and calculated angle is then:

$$\Delta\theta = \theta - \theta' \quad (5.11)$$

The presented structure in Fig. 5.3 of the PLL is implemented in Matlab & Simulink where the proportional and integral part of the PI controller are tuned manually in order to obtain satisfying response and tracking. The final parameters obtained for the proportional and integral parts are  $P=5000 \text{ rad/sec}$  and  $I=120 \text{ rad/sec}^2$ .

$$PI_{PLL}(s) = \frac{120s - 5000}{s} \quad (5.12)$$

This structure is implemented in Laplace domain, however a digital system requires a discretisation. Then (5.12) is transferred to a discrete system in z-domain by using a bilinear transformation:

$$s = \frac{2}{T_s} \frac{z - 1}{z + 1} \quad (5.13)$$

where  $T_s$  is the discretisation interval. The final transfer function in z-domain of the PI controller becomes:

$$PI_{PLL}(z) = 120 \frac{z - 0.9999}{z - 1} \quad (5.14)$$

The performance of the PLL model is tested in Simulink and the simulation results are depicted in Fig. 5.4. The input signal is the normalised grid voltage with amplitude of 1 V. The phase voltage and the output signal of the PLL are depicted in Fig. 5.4 (a) and the obtained phase angle is shown in Fig. 5.4 (b). The relative error between the phase voltage and PLL signal is depicted in Fig. 5.4 (c). As it can be seen, with the currently used PI settings, the PLL is able lock to the input voltage within 1 to 2 cycles when started without using initial condition values into its blocks. Furthermore, the input voltage is subjected to a phase jump  $+\frac{\sqrt{2}\pi}{2}$  at 150 ms. The angle is chosen based on the discussion in Chapter 4 §4.2. From the conducted simulation it can be seen that the PLL model requires again 1 to 2 cycles to lock back to the input voltage, which is an excellent indicator for a fast tracking system.

The advantages of this PLL structure are low complexity and fast response if the signal is subjected to a phase jump under fault conditions. This PLL has two disadvantages, which are: unable to operate well at frequencies that are not multiples of  $t/4$  [91] and due to the fact that the PLL does not have a low pass filter, higher order harmonic will penetrate through it and pollute the output signal, thus the reference currents are going to be polluted as well. Hence, this makes this PLL inappropriate for real LV grids application. However, in a controllable environment, such as laboratory environment, where frequency is rather fixed and the distortion levels are rather low, this PLL is useful and preferred because of its simplicity.

For commercial implementation, more durable and reliable PLL structures are proposed in [94–97], where the authors have tested them under different types of

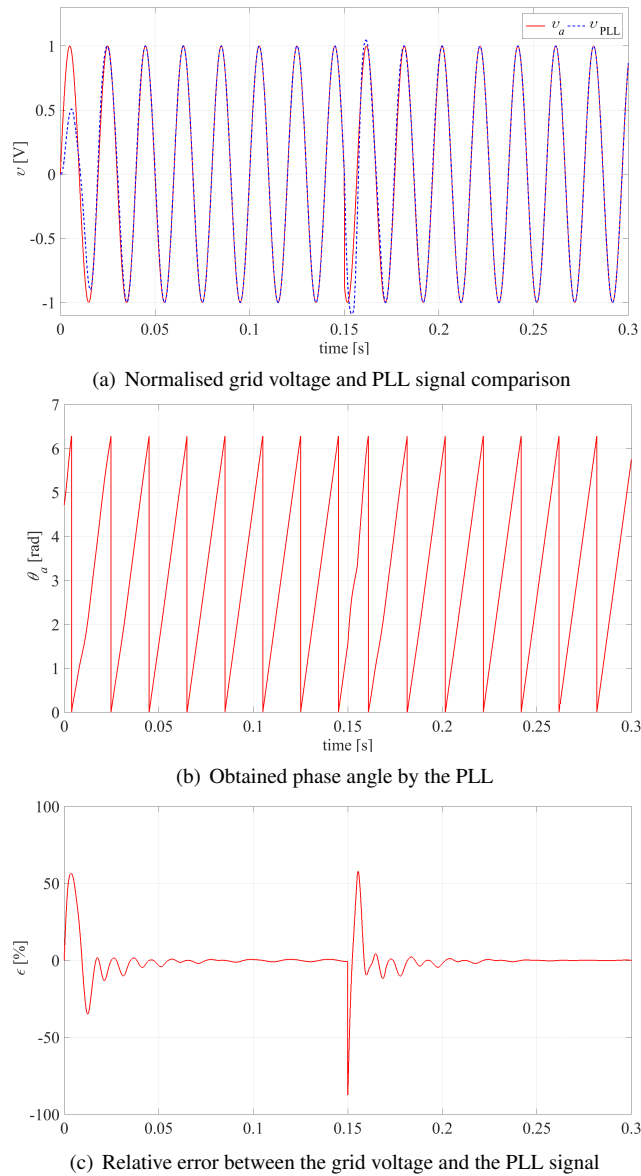


Figure 5.4: Simulation results of the the T/4 PLL

faults and distorted grid voltage conditions. The results of these studies showed that the compared PLLs are able to lock with the grid voltage within 20 ms to 30 ms (1 to 1.5 cycles) after the moment of fault occurrence, which makes them perfectly suitable DER applications. However, these types of PLL are more complex and

difficult to design, which makes them less attractive in research implementations.

### 5.3.1 Sampling of phase voltages $v_a$ , $v_b$ and $v_c$

Accurate rms voltage measurements are very important for the proper functioning of the local control. Due to the intermittent nature of the renewables, connection and disconnection of loads, etc. the grid voltages always deviate from their nominal value. As it was discussed earlier, the PLL extracts the phase angle from the grid voltage but the rms value of the phase voltages is also needed in (5.1). The rms value of a continuous signal is calculated by the following equation:

$$v_{\text{rms}} = \sqrt{\frac{1}{T} \int_0^T v(t)^2 dt} \quad (5.15)$$

where the  $T$  is the period under observation. In a discrete form (5.15) is written as:

$$v_{\text{rms}} = \sqrt{\frac{\sum_{n=1}^m v(n)^2}{m}} \quad (5.16)$$

where,  $n$  is the current sample of the variable and  $m$  are the total samples of the variable. The disadvantage of this implementation is that the final value is delivered at the end of the examined period i.e. 20 ms and if  $v_a$  experiences some variations, they will result in a sudden change of the rms value. If (5.16) is used directly in (5.1) it will result in reference current distortion due to the sudden changes introduced by (5.16). Therefore, a more appropriate approach is to use rolling rms calculation:

$$v_{\text{rms}}(n) = \sqrt{\frac{\sum_{k=n-m+1}^n v(k)^2}{m}} \quad (5.17)$$

where the rms value is calculated by the sampling frequency and later processed accordingly when needed in (5.1). Since the T/4 PLL requires a buffer to provide some delay, then this buffer becomes very useful for the rms voltage calculation as well.

To use the rms voltage measurements in the correct time instances a zero-crossing of the respective phase voltage can be applied. Nevertheless, the disadvantage of this principle is the accurate extraction of the zero-crossing, which could be deteriorated when the input signal contains high frequency noise. As it was mentioned above in a controlled environment, the selected PLL provides a clean output signal, which is always synchronised with the respective phase voltage, hence this signal can be used to detect successfully the zero-crossing of the

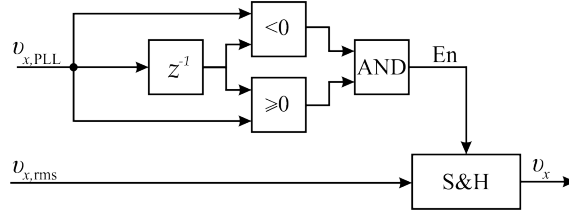


Figure 5.5: Zero-crossing detection of the PLL voltage used for sampling and hold of the rms value of the phase voltages

phase voltage. The zero-crossing scheme used in the practical implementation of the modified three-phase damping control strategy is depicted in Fig. 5.5. The instantaneous PLL signal and one previous sample of it are compared. Then a comparison to 0 is done between them and the scheme generates enable signals with a width of one switching cycle to a sample & hold block that updates the measured voltage. Thus the measured voltage is stable for the next 10 ms ensuring constant value of the phase voltage and thus an undistorted reference currents can be generated.

### 5.3.2 Sampling of $g_1$

The dc-bus controller plays a crucial role as a part of the VSI. Its purpose is to ensure the power balance between the dc and ac side of VSI and also to provide sufficient voltage margin between the dc-bus voltage and the peak value of the grid voltage. The output signal of this controller is used to determine the values of the reference currents. In general, there are two methods to control power balance between the ac and dc side of a VSI: instantaneous and average power control. The instantaneous power control method uses the fundamental current component to control and compensate for the grid voltage disturbances. In a similar way the APFs are controlled as studied in [98]. However, regulating the instantaneous power leads to non-sinusoidal current injection if the grid voltage is distorted because the instantaneous power must be kept constant. Hence, if the objective is to provide high power quality of the injected currents then instantaneous power control should not be used.

The other method to ensure the power balance is the average power control method, which is able to provide higher quality sinusoidal output current by controlling the average power flow. The role of the dc-bus controller is to generate output current references by filtering out higher harmonic content from the power spectrum. Taking into account that in most of the times the power control transient response time is in order of 100 ms, these controllers provide a slowly changing current reference to ensure high quality of the injected currents [98]. When these

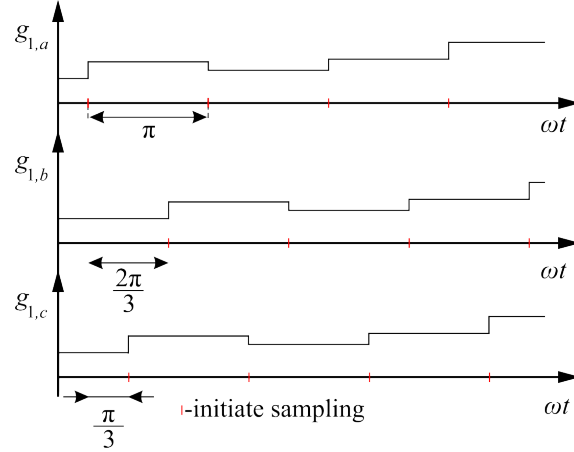


Figure 5.6: Input conductance sampling method<sup>1</sup>

controllers are employed in control strategies that inject positive-sequence currents the dc-bus voltage does not contain any voltage ripples because the instantaneous sum of the injected phase currents is zero. The three-phase damping control strategy, however, injects asymmetrical currents to mitigate the voltage unbalance at the PCC, which means that the sum of the instantaneous values of the injected currents is no longer zero. This results in voltage ripple at the dc-bus, which happens to be the second harmonic of the grid frequency [45, 99].

Therefore, it is of great importance for the dc-bus controller to compare the accurately measured value with the reference voltage, otherwise the voltage ripples will deteriorate the performance of the dc-bus controller and these higher order components of the dc voltage will be super imposed to the injected currents and thus it will introduce unwanted distortion to the system, which may also lead to a power balance mismatch [100].

Many techniques are proposed in the literature to avoid this problem. For instance, a low pass filter can be used to filter out the ac ripple of the dc-bus voltage but this solution deteriorates the dynamic response of the dc-bus controller. Furthermore, in case of using a split dc-link VSI and asymmetrical current injection, the capacitor voltages contain besides 100 Hz but also 50 Hz ripple. This implies that the cut off frequency should be lower than 50 Hz, which will deteriorate the system dynamics even more.

In [100–102], it is proposed that the dc-bus controller to be sampled with 100 Hz frequency as shown in Fig. 5.6 which, coincides with the zero-crossing of  $v_a$ . Thus the fundamental input conductance  $g_1 = g_{1,a}$  is synchronised with  $v_a$  and it is used to form the reference current  $i_{a,ref}$ . Reference currents  $i_{b,ref}$  and  $i_{c,ref}$

<sup>1</sup>Source [101] and [102]

use input conductances  $g_{1,b}$  and  $g_{1,c}$ , which are the same as  $g_1$  but sampled with the zero-crossing of  $v_b$  and  $v_c$ , respectively. However, this approach works well if all phase voltages are equal or phase voltage  $v_a$  is the lowest one of all. In these two conditions the three-phase damping control strategy will inject larger current in phase  $a$  and the zero-crossing of the ac component of the dc-bus voltage will coincide with the zero-crossing of  $v_a$ . This principle has two disadvantages such that the dc-bus controller will not operate well when phase voltages  $v_b$  or  $v_c$  is the lowest (or both) and when reactive currents are injected. As shown in Chapter 4 the three-phase damping control strategy tends to exchange also reactive currents when the damping conductance assumes high values. Consequently, if one of the upper conditions is present the dc bus ripple will not coincide with the zero-crossing of  $v_a$  and the input conductance  $g_1$  will not be calculated accurately.

The authors in [103], propose a dc value extraction technique without deteriorating the dynamic response of the dc-bus controller, which makes the dc-bus controller invariant to the ac ripple. Nevertheless, the system is complex, requires significant computation effort and difficult to implement in practice. In [17], a solution is proposed that uses a notch filter tuned at twice the grid frequency (100 Hz) to ensure voltage ripple reduction when asymmetrical phase currents are injected. Thus, only the 100 Hz ripple is filtered out and the dynamic response is not deteriorated that much compared to the low-pass filter solution. The attenuation of the ac component at dc-bus level makes the dc-bus controller less vulnerable to the zero-crossing of the fore mentioned one and the principle depicted in Fig. 5.6 can be successfully used in the practical implementation of the control strategy.

### 5.3.3 Sampling of the damping conductance $g_d$

Sampling of the damping conductance is performed in a similar manner as the fundamental input conductance. As it was discussed in §3.1.2 the modified damping control strategy changes the value of the damping conductance depending of the rms values of the grid voltages. This is done by using a damping controller in which (3.4) is implemented. The calculated value is then passed to the input of the zero-crossing detector depicted in Fig. 5.5. Three zero-crossing detectors are used for each phase voltage and the sampled value of  $g_d$  is then used in (5.1).

### 5.3.4 Midpoint stabilisation

All control strategies that are able to impact the zero-sequence voltage component, are interfaced to the grid via a three-phase, four-wire VSI. To ensure a reliable operation of the VSI, the neutral point must be maintained as stable as possible. The neutral in these VSIs is formed via additional hardware such as capacitors, inductors, semiconductor switches or a combination of the above. However, the average value of the neutral current in most of the time is not zero. Therefore, the

neutral point drifts from its original value. The main sources for the neutral point drifting are:

- during transients of the grid voltages and injected currents
- neutral currents
- common mode currents
- capacitor value tolerances
- temperature drift of the capacitor parameters
- conditioning circuit offset (also temperature dependent)
- other perturbations

As a result, an increase of the harmonic distortion of the injected currents, possible dc component injection and malfunction of the inverter will occur. Consequently, keeping the midpoint stable is of great importance for these inverters. For multi-level neutral point clamped inverters, solutions based on space vector modulation are proposed in literature [104–106]. The advantage of these modulation techniques is that no additional hardware is required. Despite their complex control, these inverters have many advantages when used in MV applications such as improved efficiency, high power ratings, lower voltage stress on the semiconductor switches, etc. Unfortunately, they are not that attractive when used in LV applications because their performance is similar to the classical topologies and the added value of the advanced power electronic topology is difficult to be justified in terms of cost and complexity.

On the other hand, the two-level neutral point clamped inverter topologies are less complex but maintaining the midpoint potential requires additional hardware. Many solutions are suggested in the literature that are based on additional circuitry, which is specially dedicated to maintain the voltage equilibrium of the capacitor voltages [107–111]. In Fig. 5.7 (a), one of the most basic topologies is depicted where the neutral point is formed by controlling the switches  $S_7$ ,  $S_8$ . The disadvantage of this topology is the high common mode current due to the parasitic capacitance of the dc bus and the neutral. In Fig. 5.7 (b), a topology is presented that forms the neutral by using a half-bridge converter in which the disadvantage of the previous one is not present. This topology forms the neutral by driving  $S_7$  and  $S_8$  with the needed duty ratio to overcome or even to cancel out the disturbance. The advantage of these topologies is that the neutral current can be controlled individually by the fourth leg and also, neutral current harmonics can be injected to reduce the excessive neutral current harmonics in the LV grids [112]. The disadvantages of both topologies are the additional power-electronic leg and also its control.

Therefore, it is better to keep the control complexity and the inverter topology as little as possible. Consequently, the additional switches and complex modulation strategy can be avoided. Therefore, the topology depicted in Fig. 5.7 (c) is preferred due to its simplicity because the neutral point is formed by using only two capacitors. Many solutions based on sinusoidal PWM for capacitor voltage balancing are proposed in the literature [113–115], which all have the same conceptual approach i.e. they are based on offsetting the reference currents. However, some of the approaches are difficult and complex to implement in practice. In this subsection, the topology shown in Fig. 5.7 (c) is used and two software solutions that are able to maintain the voltage potential of  $C_1$  and  $C_2$  equal are proposed. The first solution uses a split dc-link controller i.e. each capacitor is monitored by a controller and the second solution is based on reference current offsetting. The three-phase damping control strategy is used to validate experimentally the proposed control algorithms for maintaining the midpoint potential. In order to mitigate the voltage unbalance, the three-phase damping control strategy injects more current in the phase with the lowest voltage and less currents in the phases with the highest voltage. This results in high neutral current that can further shift the midpoint potential and it can be used to validate the proposed algorithms.

The three-phase damping control strategy is interfaced to the grid as shown in Fig. 5.1 and the block diagram of the three-phase damping control strategy is depicted in Fig. 5.2. The power balance is maintained by the dc-bus voltage controller and its output signal  $g_1$  is the fundamental input conductance. All phase voltages  $v_a(t)$ ,  $v_b(t)$  and  $v_c(t)$  are normalised and passed to a phase locked loop (PLL), which extracts the phase voltage magnitude and the phase angle  $v_a$ ,  $\theta_a$ ,  $v_b$ ,  $\theta_b$ ,  $v_c$  and  $\theta_c$ . The damping conductance  $g_d$  sets the resistive behaviour of the inverter [68, 79] and in this case will be used to inject phase currents with different rms values.

These signals are used for the calculation of the reference currents  $i_a$ ,  $i_b$  and  $i_c$  in the reference current former blocks. The calculated reference currents are added to the measured currents  $i_{L,a}$ ,  $i_{L,b}$  and  $i_{L,c}$  and PI controllers calculate the needed action to zero the error between the reference and measured value. Since the PI controller has a poor performance in tracking first order reference signals its output is added to a duty-ratio feed-forward block [116]. The output of this block is used to generate the driving signals for the semiconductor switches. The dc-bus controller is sampled with 100 Hz sampling frequency while the current controller is sampled with 20 kHz. The power balance between the ac and dc side can be written as:

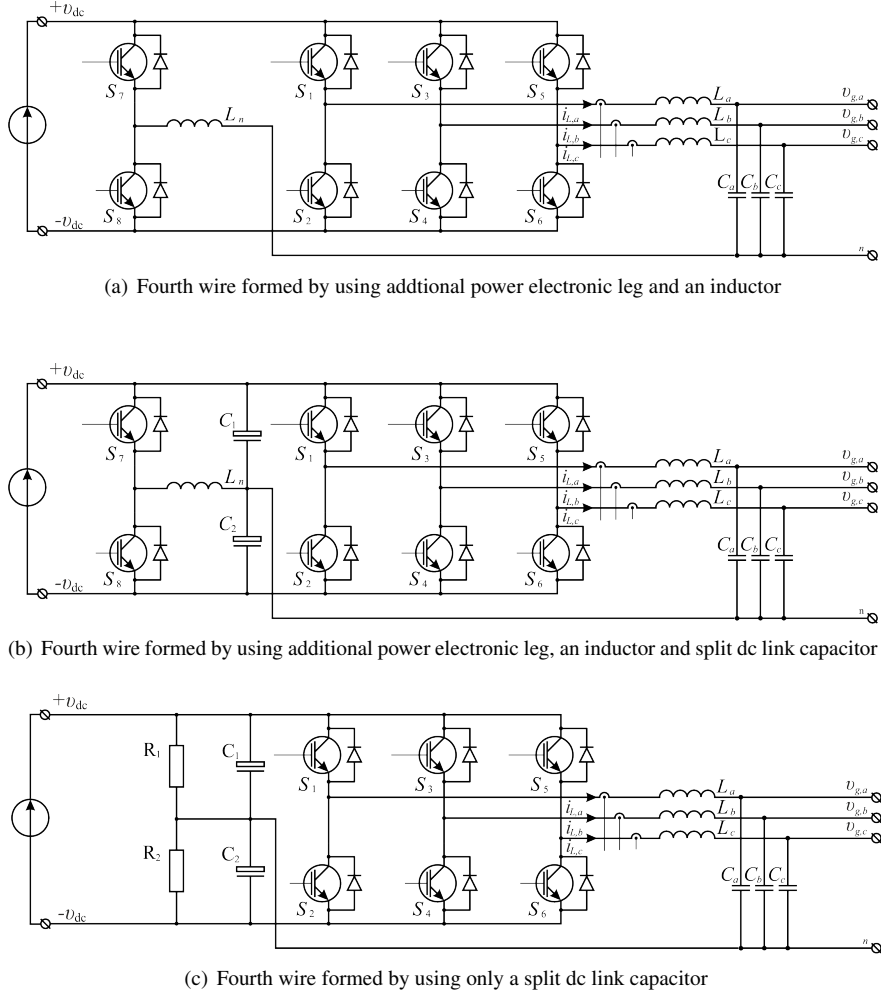


Figure 5.7: Different fourth leg topologies used in practice to form the neutral

$$\begin{aligned}
 p_1(t) = & v_a(t)i_{L,a}(t) - \frac{L_a + L_n}{2} \frac{d(i_{L,a}(t))^2}{dt} \\
 & + v_b(t)i_{L,b}(t) - \frac{L_b + L_n}{2} \frac{d(i_{L,b}(t))^2}{dt} \\
 & + v_c(t)i_{L,c}(t) - \frac{L_c + L_n}{2} \frac{d(i_{L,c}(t))^2}{dt}
 \end{aligned} \tag{5.18}$$

where,  $p_1(t)$  is the power of the fundamental component,  $v_x$  and  $i_{L,x}$  are the respective phase voltages and currents,  $L_x$  and  $L_n$  are the differential filter induc-

tances for the corresponding phase and neutral inductor, respectively. By replacing the phase currents with the corresponding input conductance  $g_x(t)$ , then the power balance equation can be written as:

$$\begin{aligned}
p_1(t) &= g_a(t)v_a(t)^2 - \frac{L_a + L_n}{2} \frac{d(g_a(t)(v_a(t))^2)}{dt} \\
&+ g_b(t)v_b(t)^2 - \frac{L_b + L_n}{2} \frac{d(g_b(t)(v_b(t))^2)}{dt} \\
&+ g_c(t)v_c(t)^2 - \frac{L_c + L_n}{2} \frac{d(g_c(t)(v_c(t))^2)}{dt} \\
&= \eta p_{dc}(t) - \eta \frac{C_{dc}}{2} \frac{d(v_{dc}(t))^2}{dt}
\end{aligned} \tag{5.19}$$

where  $\eta$  is the efficiency of the power electronic inverter,  $C_{dc}$  is the dc-bus capacitor value and  $v_{dc}(t)$  is the instantaneous value of the dc-bus voltage. By knowing that the representation of a control variable can be expressed by the large-signal ( $X$ ) and small-signal perturbations  $\hat{x}$  as:

$$x = X + \hat{x} \tag{5.20}$$

and with phase voltage equal to:

$$V_x = \sqrt{2}V_{rms} \sin(\omega t + \theta_x) \tag{5.21}$$

the small signal model can now be obtained after substituting (5.20) and (5.21) in (5.19) and simplifying it to (5.22):

$$g_{tot}(t)V_{rms}^2 - (L_x + L_n)GV_{rms}^2 = \eta \hat{p}_{dc}(t) - \eta C_{dc} \frac{dV_{dc} \hat{v}_{dc}}{dt} \tag{5.22}$$

Eq. (5.22) can be expressed in the Laplace domain as follows:

$$\hat{v}_{dc}(s) = \hat{p}_{dc}(s) \frac{1}{\eta V_{dc} C_{dc}} + \hat{g}_{tot}(s) \frac{3V_{rms}(sL_f G_{tot})}{\eta V_{dc} C_{dc}} \tag{5.23}$$

and then further simplified to:

$$\frac{\hat{v}_{dc}(s)}{\hat{g}_{tot}(s)} = \frac{1}{\eta \tau} \frac{-1}{s} \tag{5.24}$$

where  $\hat{g}_{tot} = \hat{g}_a + \hat{g}_b + \hat{g}_c$  is the total input conductance and  $\tau = \frac{\eta V_{dc} C_{dc}}{3V_{rms}}$ . The open loop transfer function in the z-domain becomes:

$$G(z) = \frac{T}{2\tau} \frac{z+1}{z(z-1)} \tag{5.25}$$

The sampling time of this PI controller is 10ms and it calculates its new output value at every zero-crossing of phase  $a$ .

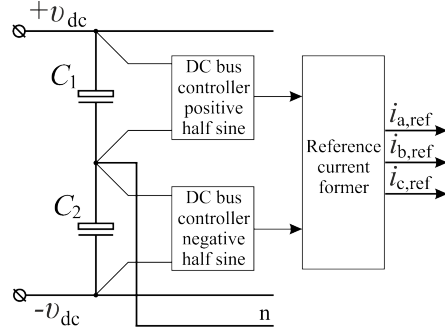


Figure 5.8: Block diagram of the split dc-bus controller - concept

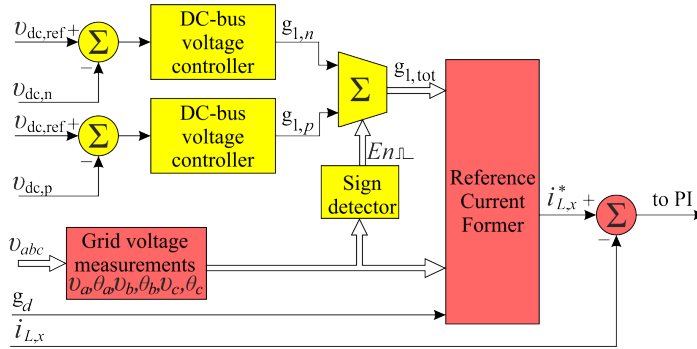


Figure 5.9: Block diagram of the split dc-bus controller concept for midpoint stabilisation

### 5.3.4.1 Midpoint stabilisation by using a split dc controller

The first solution is depicted in Fig. 5.8 and it uses two identical dc-bus controllers to maintain the equilibrium between  $v_{C1}$  and  $v_{C2}$ . A detailed block diagram of this algorithm is shown in Fig. 5.9. The output signals of the dc-bus controllers are  $g_{1,n}$  and  $g_{1,p}$  where the first one is used to determine the negative half-sine and the other the positive half-sine of the reference currents. The output of the two controllers is passed to a multiplexer that switches between  $g_{1,n}$  and  $g_{1,p}$  depending on the output of the sign detector. A sign detector block switches its output state based on the zero-crossing of the synchronised PLL signal for the respective phase and it drives a multiplexer according to the algorithm presented in Fig. 5.6.

The total input conductance  $g_{1,tot}$ , together with the other signals (voltage magnitudes and phase angles) are used to calculate the magnitude of the reference currents. Index  $x$  represents the respective reference phase current. The rest of the control algorithm is the same as shown in Fig. 5.2. From (5.18) and (5.23) it can be seen that the power balance depends on the rms value of the grid voltage  $V_{rms}$ . Therefore, the open loop transfer function for each controller will be the same as

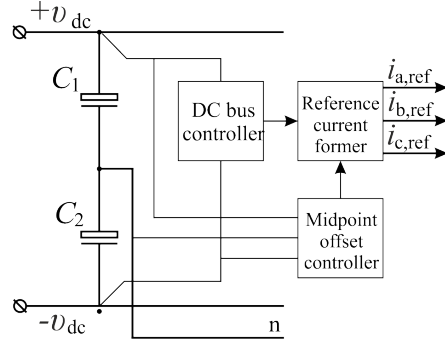


Figure 5.10: Midpoint stabilisation by offsetting the reference currents - concept

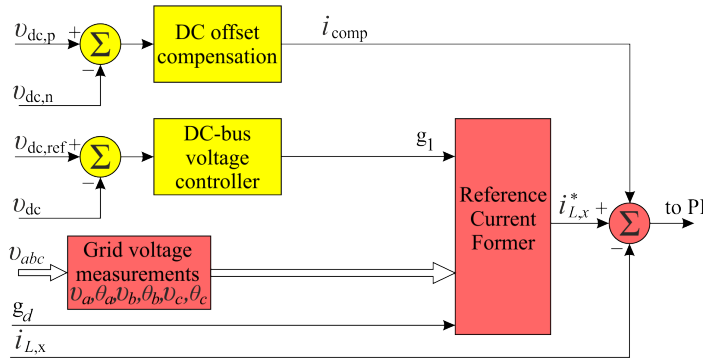


Figure 5.11: Block diagram of midpoint stabilisation by offsetting the reference currents

(5.24) and (5.25).

### 5.3.4.2 Reference current offset

The second solution, is proposed in Fig. 5.10 and a simplified block diagram shown is in Fig. 5.11. This algorithm uses only one dc-bus voltage controller to ensure the power balance between dc and ac side and a second controller that maintains the difference between  $v_{C1}$  and  $v_{C2}$  to be zero. If for example  $v_{C1} > v_{C2}$ , then the midpoint offset controller will add a small positive offset to all reference currents and the voltage difference will be restored to zero.

The mathematical expression can be written as:

$$i_{\text{comp}} = 4C_{\text{dc}} \frac{dv_{\text{dc}}}{dt} \tag{5.26}$$

where  $i_{\text{comp}}$  is the needed offset current. Then taking into account the difference

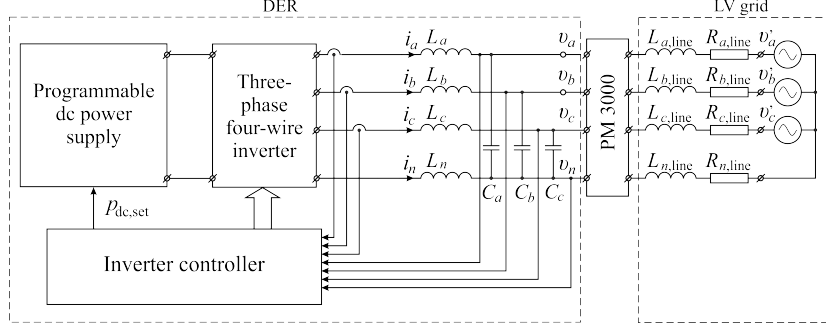


Figure 5.12: Test set-up used to validate the midpoint stabilisation algorithms

between the capacitor voltages  $\Delta v_{dc} = v_{C_1} - v_{C_2}$  yields to:

$$\frac{d\Delta v_{dc}}{dt} = -2 \frac{dv_{dc}}{dt} \quad (5.27)$$

The open loop transfer function can now be derived as:

$$\frac{\Delta v_{dc}}{i_{comp}} = -3 \frac{I_{ref}}{2sC_{dc}V_{dc,ref}} = \frac{-1}{\tau s} \quad (5.28)$$

This leads to the same transfer function as (5.24) but the time constant is different as well as the sampling frequency, which is 20kHz.

| Parameter   | Value                       |
|---|-----------------------------|
| $v_a, v_b$ and $v_c$                                    | 100 V, 110 V, 110 V (50 Hz) |
| $Z_{a,line}, Z_{b,line}, Z_{c,line}$ , and $Z_{n,line}$ | (0.470+j0.201)              |
| Power analyser  | PM3000                      |
| $C_a, C_b$ and $C_c$                                    | 5 $\mu$ F                   |
| $L_a, L_b$ and $L_c$                                    | 2 mH                        |
| $L_n$   | 0.666 mH                    |
| Three-phase inverter                                    | 1.8 kVA                     |
| $C_1$ and $C_2$   | 2000 $\mu$ F                |
| $v_{dc,p}+v_{dc,n}$                                     | 400 V                       |
| Switching frequency                                     | 20 kHz                      |
| Current base value                                      | 7.5 A                       |
| Phase voltage base value                                | 225 V                       |
| dc-bus voltage base value                               | 200 V                       |

Table 5.1: Test set-up parameters

| Controller                      | parameter      |
|---------------------------------|----------------|
| <i>Split dc-bus controller</i>  |                |
| dc-bus controller 1             | P=3.48, I=0.95 |
| dc-bus controller 2             | P=3.48, I=0.95 |
| <i>Reference current offset</i> |                |
| dc-bus controller 1             | P=7.48, I=0.96 |
| Offset controller               | P=1.07, I=0.91 |

Table 5.2: Settings of the dc-bus PI controllers

### 5.3.4.3 Experimental validation

The experimental validation of the proposed control algorithms for midpoint balancing is performed on the set-up presented in Fig. 5.12. The three-phase four-wire inverter is connected to a three-phase programmable voltage source via a power analyser and a line impedance. More information about the set-up parameters can be found in Table 5.1. The programmable voltage source is able to deliver asymmetrical voltages, which forces the three-phase damping control strategy to inject asymmetrical currents. The proportional and integral coefficients used for the PI controllers used in the set-up are listed in Table 5.2.

The measured waveforms of the phase voltages and the dc-bus voltages at the inverter terminals are shown in Fig. 5.13. As it can be seen the positive and negative dc-bus voltages are relatively smooth despite the injected asymmetrical currents, which are depicted in Fig. 5.14. This implies that the 100Hz component at the dc level does not introduce any additional error concerning the correctness of the dc-bus controller sampling. Note that the spikes in the phase currents are due to oscilloscope aliasing problems. The asymmetrical current injection leads to a neutral current with rms value of 2 A. Both algorithms for midpoint stabilisation are tested on the same set-up under the same conditions and the measured waveforms of the voltages and the currents are identical when both algorithms are compared. In Fig. 5.15, the waveforms of the input conductance signals  $g_{1,tot}$  are presented, when two dc-bus controllers are used. The three signals  $g_a$ ,  $g_b$  and  $g_c$  represent the assembled signal after summing up signals  $g_{1,n} + g_{1,p}$  and updated when a zero-crossing occurs of the respective phase voltage as explained in §5.3.2.

Waveforms of the input conductance  $g_1$  and the compensating current  $i_{comp}$ , needed for the reference current offset, are depicted in Fig. 5.16. For a better visualisation, the compensating current is multiplied by a factor of 100. Since both algorithms react in the order (lower than 0.1 s) the controllers will react adequately towards changes of the power from the primary source, which is usually in the order of seconds. From the obtained experimental measurements listed in Table 5.3, it can be seen that the rms values of the phase voltages, phase currents, neutral current and the power factors are almost equal when comparing the two algorithms.

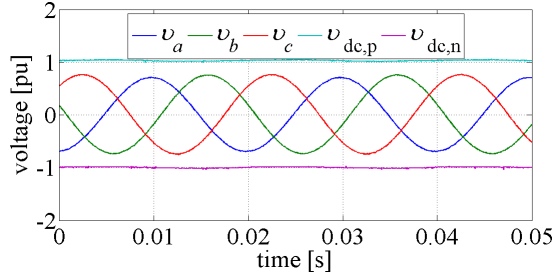


Figure 5.13: Phase voltages and dc-bus voltages at the inverter terminals

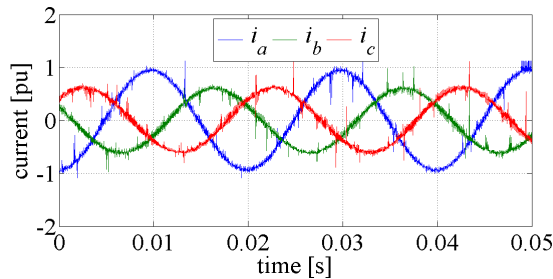


Figure 5.14: Injected phase currents by the DER

Although the reference current offset algorithm injects a slightly higher neutral current the performance of both algorithms is very similar.

The harmonic content of the injected currents is also similar. The results from Table 5.3 show that the THD is slightly better when the split dc-bus controller is used but overall both algorithms manage to keep the THD below 5% as required by the standard IEC 61000-3-2 [117]. The main difference between the proposed algorithms is that the split dc-bus injects a slightly higher magnitude of even harmonics but overall the performance of both algorithms is very similar. Both algorithms are studied up to the 5<sup>th</sup> harmonic because the higher order current harmonics are very low in magnitude and therefore, they have insignificant contribution to the THD of the injected currents. In Table 5.3, the IEC 61000-3-2 limit values for harmonic currents [117] are compared to the measured values and it was found out to be lower in order of magnitude. The last comparison is related to the injection of a dc current. According to [117] the injection of the dc current must be limited to 1% of the nominal current of the inverter. The nominal inverter current is 5.1A (in case of balanced conditions) and the absolute value of the dc current injection from both algorithms does not exceed 40mA, which is an excellent key performance indicator.

| Parameter                             | Split dc-bus controller |       |       | Reference current offset |       |       | Std      |
|---------------------------------------|-------------------------|-------|-------|--------------------------|-------|-------|----------|
|                                       |                         |       |       |                          |       |       |          |
| Vrms [V]                              | 104.5                   | 112.0 | 111.8 | 104.5                    | 112.0 | 111.8 | -        |
| PF                                    | 0.999                   | 0.997 | 0.997 | 0.999                    | 0.997 | 0.996 | -        |
| Irms [A]                              | 6.95                    | 4.381 | 4.483 | 6.948                    | 4.387 | 4.474 | -        |
| THD[%]                                | 1.6                     | 2.5   | 2.7   | 2.6                      | 2.6   | 3.1   | 5        |
| H1 [A]                                | 6.952                   | 4.391 | 4.477 | 6.943                    | 4.389 | 4.469 | 16.0     |
| H2 [A]                                | 0.100                   | 0.071 | 0.086 | 0.096                    | 0.070 | 0.084 | 1.08     |
| H3 [A]                                | 0.01                    | 0.011 | 0.01  | 0.012                    | 0.014 | 0.014 | 2.3      |
| H4 [A]                                | 0.006                   | 0.007 | 0.006 | 0.003                    | 0.001 | 0.001 | 0.43     |
| H5 [A]                                | 0.012                   | 0.009 | 0.007 | 0.011                    | 0.012 | 0.012 | 1.14     |
| In [A]                                | 2.018                   |       |       | 2.043                    |       |       |          |
| Idc [A]                               | -0.04                   | 0.02  | 0.02  | -0.02                    | 0.02  | 0.01  | 0.01Inom |
| Standard values set by *IEC 61000-3-2 |                         |       |       |                          |       |       |          |

Table 5.3: Obtained measurements under unbalanced current injection

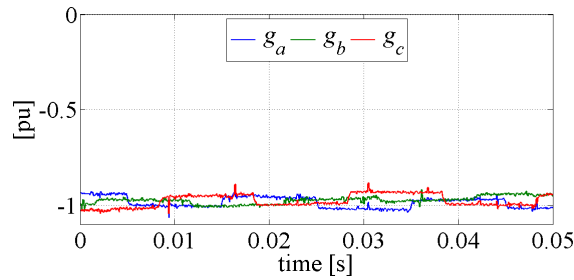


Figure 5.15: The input conductance when two dc-bus controllers are used

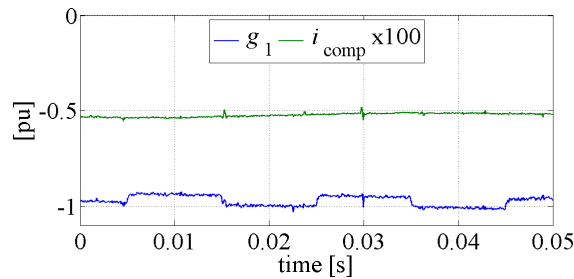


Figure 5.16: Input conductance and compensation current waveforms when reference current offset is used

### 5.3.5 Discussion

Two different control algorithms for stabilising the midpoint voltage of a three-phases, four-wire inverter with a split dc-bus capacitor are proposed. Both algo-

rithms were analysed and the performance then validated against the same conditions in a controllable experimental environment. It was found that both algorithms are able to maintain the midpoint potential stable while the quality of the injected currents is kept within the limits set by IEC 61000-3-2 [117], thus both algorithms are suitable for embedding in renewable energy applications.

### 5.3.6 Current controller

The small signal model of the current controller used in the present simulation model is described in [18, 41] where the author proposes a methodology for calculating discrete PI controllers. The methodology takes into account the discretisation of the ADC, PWM delay and the sampling times of the PI controller and the algorithm is also experimentally validated. By using the algorithm provided in [18, 41] for tuning the current PI controller the proportional and integral part are obtained as 0.4 and 0.93 respectively. This gives a phase margin of  $65^\circ$  at 1.2 kHz, which is sufficient to track zero order signals with relatively small steady-state error.

### 5.3.7 Duty ratio feed-forward

From the Laplace perspective the sinusoidal signal is a first order signal and from the control theory is known that the controller must be one order higher with respect to the reference signal and only then the controller will be able to track the reference current with zero steady-state error. Since the PI controller is a first order controller, it will track the first order reference signal with some steady-state error. A second order controller that can be used is the proportional resonant controller. It has zero gain and closed loop system for the resonant frequency on which it is tuned, thus it is able to track the reference without any steady-state error. However, when the grid frequency varies within some limits set by [8], the closed loop gain will be less than 0 and some steady-state error will occur. Furthermore, the PR controllers are rather slow in comparison with the classical PI controller but the dynamic performance of the system will deteriorate. Higher order controllers such as predictive, dead-beat and fuzzy logic controllers could be used in such applications as described in [118–120] but designing a controller of higher order is a complex and difficult endeavour. In [116], a duty-ratio feed-forward control with a combination with a PI controller for power factor correctors is proposed, which can be used also for DERs as demonstrated in [46, 54, 121] and later in [18]. The effect of duty-ratio feed forward on the inverter behaviour can be explained by considering the small signal equation of the phase currents obtained in [41]:

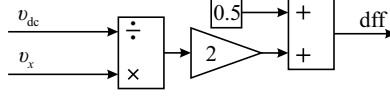


Figure 5.17: Block diagram of the used duty-ratio feed-forward

$$\begin{aligned}
 i_{L,a}(s) &= \frac{1}{s L_f} \hat{v}_a(s) + \frac{V_{dc}}{s L_f} D_a(s) + \frac{(2 D_a - 1)}{2 s L_f} \hat{v}_{dc}(s) \\
 i_{L,b}(s) &= \frac{1}{s L_f} \hat{v}_b(s) + \frac{V_{dc}}{s L_f} D_b(s) + \frac{(2 D_b - 1)}{2 s L_f} \hat{v}_{dc}(s) \\
 i_{L,c}(s) &= \frac{1}{s L_f} \hat{v}_c(s) + \frac{V_{dc}}{s L_f} D_c(s) + \frac{(2 D_c - 1)}{2 s L_f} \hat{v}_{dc}(s)
 \end{aligned} \tag{5.29}$$

where,  $i_{L,a}(s)$  and  $\hat{v}_a(s)$  are the Laplace form of the phase current and voltage,  $L_f$  is the output inductor value,  $V_{dc}$  is the value of the dc bus voltage and  $D_x$  is the duty ratio of the respective phase. Further simplification by eliminating the large signal values leads to:

$$\begin{aligned}
 \frac{i_{L,a}(s)}{\hat{\delta}_a(s)} &= \frac{V_{dc}}{s L_f} \\
 \frac{i_{L,b}(s)}{\hat{\delta}_b(s)} &= \frac{V_{dc}}{s L_f} \\
 \frac{i_{L,c}(s)}{\hat{\delta}_c(s)} &= \frac{V_{dc}}{s L_f}
 \end{aligned} \tag{5.30}$$

These equations show that the injected phase currents are dependent not only on the control variable but also on the grid voltage and the dc-bus voltage. The last two are uncontrollable and the current PI controller considers them as disturbances, which has to compensate for it. By using the duty-ratio feed-forward these disturbances are cancelled out. Thus, the current controller does not have to compensate the first order grid voltage, which results in an improved current reference tracking.

In Fig. 5.17 the duty ratio feed forward structure is depicted, which is used in this thesis. The phase voltages are normalised and divided to the normalised total dc-bus voltage. Since the purpose of the duty-ratio feed-forward is to help the PI controller reducing the influence of the dc bus voltage, the used dc voltage in this block is not filtered by the notch filter.

## 5.4 Simulation results of the obtained model

By combining all different blocks from Fig. 5.2 a simulation model is built in Matlab & Simulink by using the toolbox Simscape/SimPowerSystems. This toolbox is able to simulate unbalanced power flows in distribution grids (MV and/or LV grids) in time domain or phasor modes. The developed model is built in the time domain in order to investigate the transient behaviour DER when the different controls are applied. This toolbox uses piecewise linear approximations, which are very suitable for transient and harmonic analysis and require relatively small time per simulation. However, it has a limitation concerning the full modelling of a power electronics VSI, which is the inability to simulate the switching losses of the power electronic switches. More detailed assessment of the model losses can be obtained by using SPICE based softwares such as PSpice (Cadance) and SimElectronics (Matlab). To model accurately the switching losses a simulation time step of about 1 to 5 ns is required, which will result in a cumbersome simulation model, which will make it less attractive for practical use. Despite the inability to accurately simulate the switching losses, the toolbox SimPowerSystems is used to further investigate the built model.

### 5.4.1 Case studies

The design of the control loops and tuning the used PI controllers do not fall in the scope of this work. Nevertheless, the performance of the built model is demonstrated by means of three case studies, which cover the three operational modes of the modified three-phase damping control strategy. To do so, some assumptions for the response time of the used controllers are done.

The DERs and more particularly the local control have two signals that are controlled based on the grid voltages the active power is computed by the droop controller and the damping conductance, which is computed by the damping controller. In addition, there are the phase current PI controller as well as the dc-bus PI controller. To ensure stability in this multi-feedback multi-input multi-output system, the time response of the controllers must be built in ascending order with certain response time as advised in the fundamentals of the control theory. Only then the system can be simplified to single-input single-output system and then properly modelled.

The used controllers in this control strategy are current (PI) controllers, dc-bus controllers (PI), droop controller (P) and damping controller (P). The PI current controllers and the PI dc-bus controllers are thoroughly tested in [41] and the obtained results are going to be used in this work. The response times for the current controllers are about 0.5 ms while the response time of the dc-bus controller is obtained to be 0.1 s. In practice, the overvoltages are more dangerous compared to the voltage unbalance, therefore, priority is given to the droop controller over the

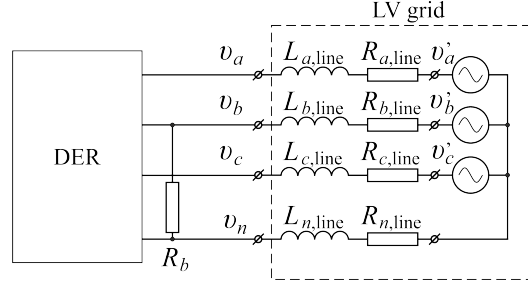


Figure 5.18: Connection diagram of the DER used to investigate the performance of the local control under unbalanced voltages and different input power

damping controller. All rms phase voltage measurements require a measurement time between 10 ms and 20 ms to be updated. This implies that the speed of the droop controller is limited by the speed of the rms voltage measurements. Since the response time of the dc-bus PI controller is 0.1 s, a response time of 20 ms is a sufficient condition to simplify the multi-feedback system to single-feedback system. Hence, the ascending order becomes: current control, droop control and dc-bus controllers. The reason why the damping controller is not included in the this order is because in practice, the damping conductance is not used to calculate the fundamental input conductance.

The damping conductance participates only in the calculation of the reference currents and their PI controller has the fastest response time of all. Therefore, the theoretical speed of this controller could be the speed of the current PI controller. Nevertheless, the output of this controller is also based on the rms vales of the phase voltage measurements and since the priority is given to the droop controller, the damping controller must have a response time greater than 0.1 s. It is important to state that unlike the phase currents, voltages and dc-bus voltages, the damping conductance is a non-measurable parameter, which cannot be fed back into a closed loop system. This is why the damping controller can be only proportional one. In order to slow it down to the desired response time a low pass filter with a cut-off frequency of 10 Hz is used.

The simulation model is connected to a three-phase voltage source through a line impedance as described later on in §5.5.1. The goal of the presented case studies is to give a basic performance evaluation of the droop and damping controllers and their influence on the transient behaviour of the VSI by simulating different scenarios when subjected step responses of the input power. These analyses will show whether or not the time response of the different controllers is correct.

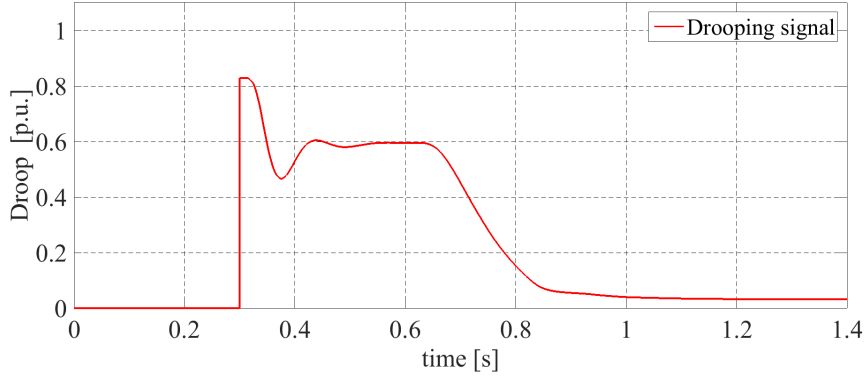
### 5.4.2 Case study 1

In the first case study, the voltage source, which is supplying phase  $a$  is set to  $|v'_a| = 1.07$  p.u. while the other two phase voltages are kept at their nominal values  $|v_b| = |v_c| = 1$  p.u. Additional unbalance is introduced at the PCC by loading phase  $b$  with a resistive load of  $15\Omega$  as shown in Fig. 5.18. All parameters of the DER can be seen in Fig. 4.49. This combination of voltage settings and loading, results in some voltage unbalance and neutral point shifting at the PCC, which will force the damping control strategy to inject asymmetrical currents. Furthermore, the modified damping control strategy will operate in the drooping region because the grid voltage is greater than  $v_{cpb} = 1.06$  p.u. (see Fig. 3.2). The total simulation time is 1.4 s where from time interval 0 to 0.3 s the local control is disabled. So despite that  $v_a > v_{cpb}$  the DER injects all available power. At time instance 0.3 s, the droop controller is activated and since the  $g_d = 0$  p.u. only positive-sequence current is being injected. Finally, at time instance 0.6 s the damping controller is enabled and the damping conductance is ramped up to its nominal value for 0.2 s. Thus the full local control is enabled.

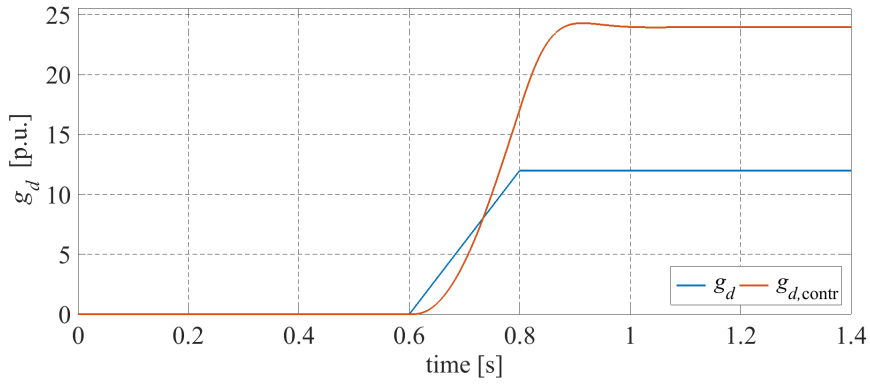
Fig. 5.19 (a) and (b) show the signals of the local control composed by the damping controller signal and the droop signal. The later one is passed to the programmable dc power supply to set the value of the injected power. The injected rms phase currents and three-phase voltages at the inverter terminals are depicted in Fig. 5.19 (c) and Fig. 5.20 (a) respectively, followed by the positive and negative dc-bus voltages presented in Fig. 5.20 (b) and the zero- and negative-sequence unbalance factors presented in Fig. 5.20 (c).

Fig. 5.20 (b) shows that during the first interval between 0 and 0.3 s the dc-bus controller settles down and reaches a steady-state operation, hence the VSI. Note that appropriate initial conditions for the dc-bus capacitors are set in order to avoid severe transients. In this interval, the droop controller is turned off as well as the damping controller, thus the VSI injects its nominal power. As it can be seen from Fig. 5.20 (a) these conditions lead to an rms voltage value of 1.092 p.u. in phase  $a$ , which is close to the maximum allowed. Since in this interval only positive-sequence current is injected the difference between the rms values of the phase voltages is considerable, which also leads to high values of  $VUF_0$  and  $VUF_2$ . Note that dc-bus voltage ripples are not present in the positive and negative dc-bus voltages because only positive-sequence current is injected.

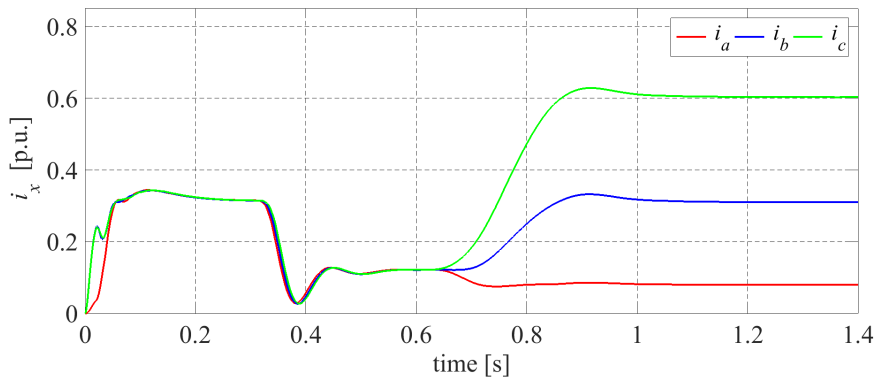
At time instance  $t=0.3$  s the droop controller is enabled and immediately sends a signal to the controllable power supply to reduce its output power with 80% because  $|v_a| \geq v_{cpb}$ . The dc-bus controller needs another 0.3 s to reach steady-state regime and the droop signal is finally settled at 60% whereas the phase voltage  $|v_a|$  is decreased down to a lower (more safer) level of 1.075 p.u. Despite this transient in the power, the injected rms phase currents are still equal and the same can be stated for the positive and negative dc-bus voltages. Note that the positive and



(a) Profile of the drooping signal

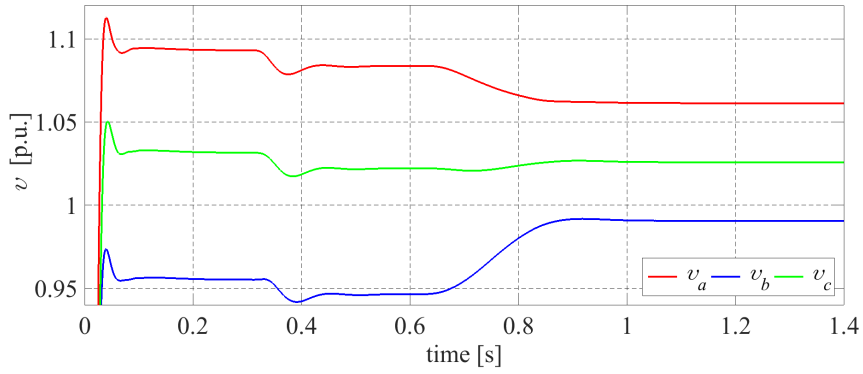


(b) Damping conductance profile

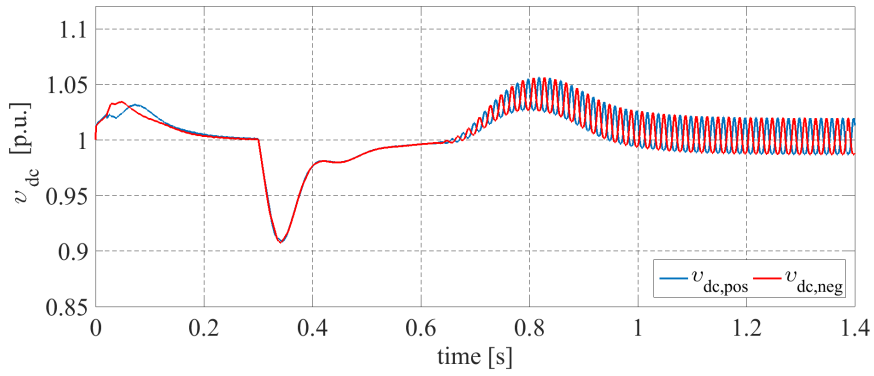


(c) Injected rms currents by the DER

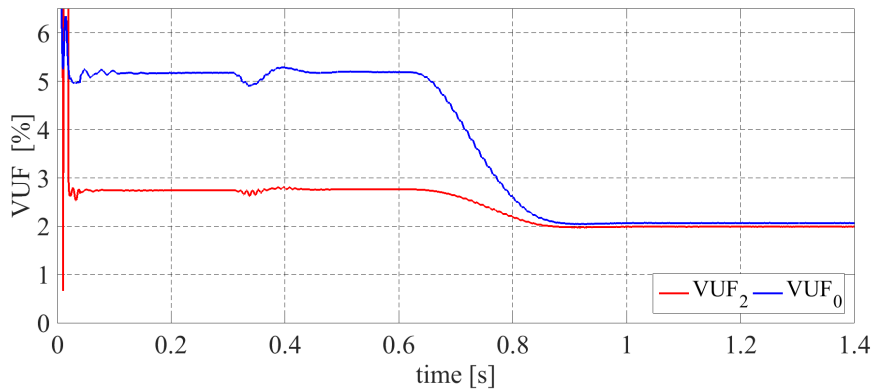
Figure 5.19: DER reaction when  $g_d$  is set from 0 to 12 p.u.



(a) rms voltages at the inverter terminals



(b) Voltages across the dc-bus capacitors



(c) Voltage unbalance factors  $VUF_0$  and  $VUF_2$

Figure 5.20: DER reaction when  $g_d$  is set from 0 to 12 p.u.

negative dc-bus voltages are measured with respect to the midpoint of the dc-bus capacitors,

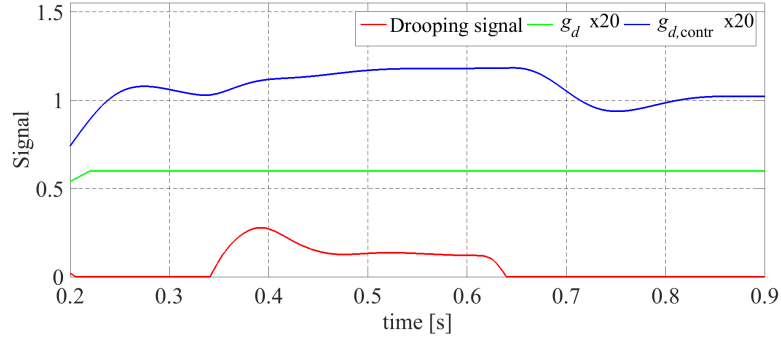
At time instance 0.6 s the damping conductance is ramped up to its nominal value and it reaches its maximum at time instance 0.8 s. By using (3.5), the damping controller calculates  $g_{d,\text{contr}}$  to be almost 24 p.u. (this value is used in the final equation to calculate the reference currents (5.1)). With the activation of the damping controller, the injected phase current  $i_a$  is reduced, thus phase voltage  $v_a$  is decreased further, which leads to decreasing the drooped power down to about 5%. As expected, since the injected currents in this interval are not equal, ac-ripples appear in the dc-bus voltages. However, with the sampling and filtering techniques described earlier, the model becomes less susceptible to these ripples and the performance of the model is not deteriorated. This figure shows also that both capacitor voltages have very similar profile during transients, which demonstrates the effectiveness of the split dc-bus controller approach presented earlier. Finally, the zero- and negative-sequence voltage unbalance factors are presented in Fig. 5.20. During the first and second time intervals both voltage unbalance factors remain unchanged till the moment when the  $g_d$  starts increasing and eventually reaches 24 p.u. where the  $VUF_0$  and  $VUF_2$  are decreased to their minimum.

Note that the initial transients in the phase current and voltages as well as the voltage unbalance factors are due to the nature of the rms measurements themselves. The used measurement blocks require at least one grid cycle to obtain accurate measurements.

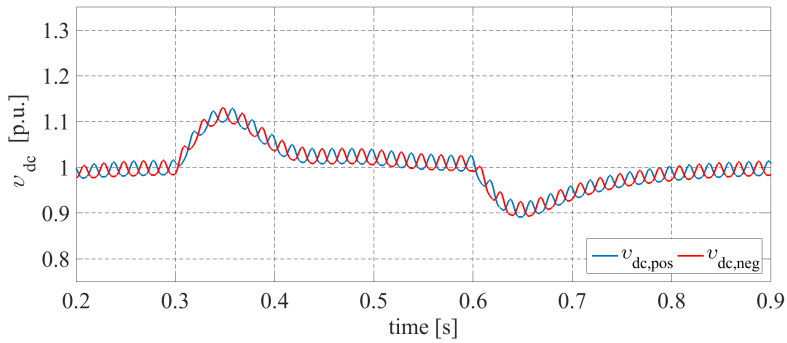
### 5.4.3 Case study 2

In this case study, the VSI is subjected to a step power jump from 0 to  $-1$  p.u. at time 0.3 s and then from  $-1$  p.u. to 0 p.u. at time 0.6 s till the end. The grid parameters are the same as the previous case study. The droop controller is enabled from the beginning of the simulation while the damping conductance is ramped to its nominal value from time 0 s to 0.2 s, which means that the local control will be fully enabled during the power transient. The purpose of this case study is to demonstrate the transient behaviour of the VSI when the local control is active and the power from the primary source is supplied with a step from 0 to  $-1$  p.u. This example resembles a cloud shading of a PV system and it is of interest to observe the reaction of the full local control under such conditions.

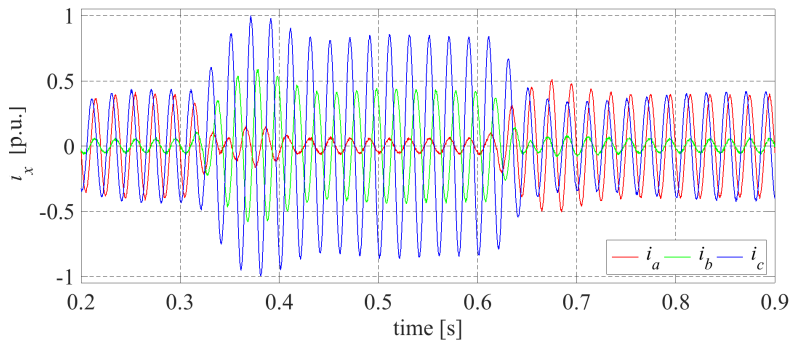
The signals of the droop and damping controllers are shown in Fig. 5.21 (a). The damping conductance is ramped up and it reaches its nominal value of 12 p.u. a little bit after 0.2 s. A value of almost 20 p.u. is computed by the damping controller before time instance 0.3 s. Note that for the time interval 0 to 0.3 s the dc power is zero and also the damping conductance is high. Consequently, none of the phase voltages is higher than  $v_{\text{cpb}}$  and the output signal of the droop controller



(a) Drooping and damping conductance signals



(b) Voltages across the dc-bus capacitors



(c) Currents exchanged by the DER

Figure 5.21: DER reaction when the input power changes from 0 to  $-1$  p.u. and back to 0 p.u. are applied and the full local control is enabled

is 0. Both positive and negative dc bus voltages are depicted in Fig. 5.21 (b) and as it can be seen they are equal and have the same ac ripples and transient trends.

All phase currents are shown in Fig. 5.21 (c). Since there is not any dc power delivered by the power supply, voltage unbalance is present at the inverter ter-

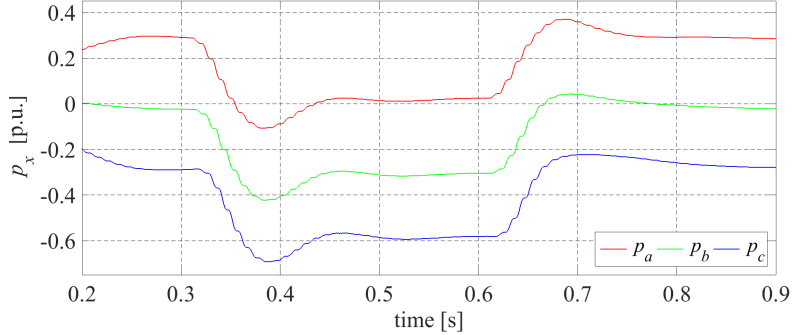
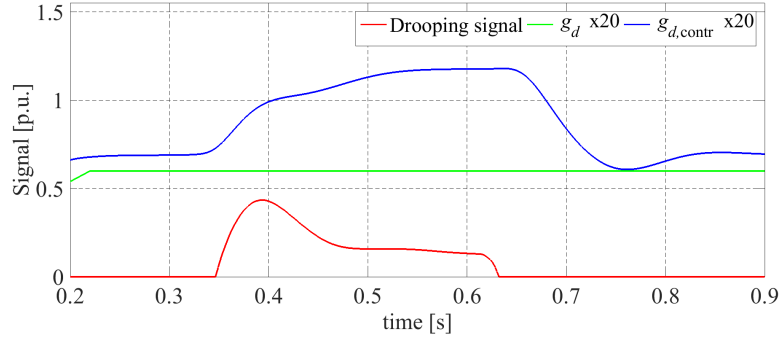


Figure 5.22: Exchanged active power by the DER when the input power changes from 0 to  $-1$  p.u. and back to 0 p.u. are applied and the full local control is enabled

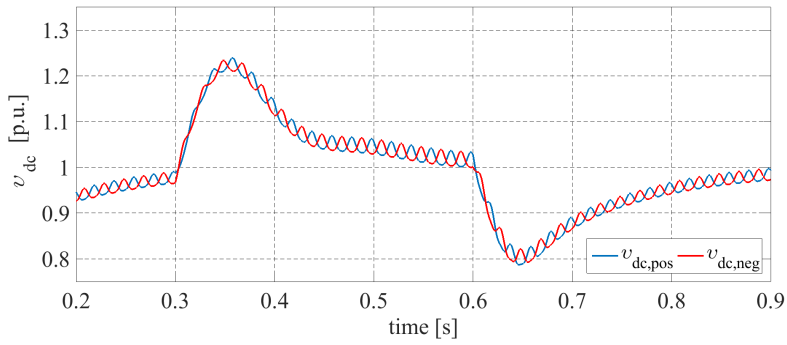
minals and the damping conductance is about 20 p.u. then current is being drawn from phase  $a$  because it is the phase with the highest rms voltage among all phases. Phase  $c$  is the most loaded one and it has the lower rms voltage and current is being injected by the DER into it while very little current is being injected into phase  $b$ . Fig. 5.22 depicts the exchanged active power by the DER and as it can be seen in the end of the transient, the sum of all powers is close to zero because  $p_{dc} = 0$  p.u.

At time instance 0.3 s the input power is set to  $-1$  p.u. and the injected power rises the grid voltage  $|v_a|$ , which activates the droop controller. The later one settles down at 0.45 s to a value of 0.12 p.u. while the damping controller needs more time to settle down at 0.55 s to a value of about 23 p.u. The dc bus controllers need almost the same time to settle down as the droop controller and both dc-bus voltages experience an overshoot of nearly 10%, which is acceptable performance from control point of view. The high value of the damping conductance forces the control strategy to exchange all dc power with phases  $c$  and  $b$  while there is still some active power that is being drawn from phase  $a$ .

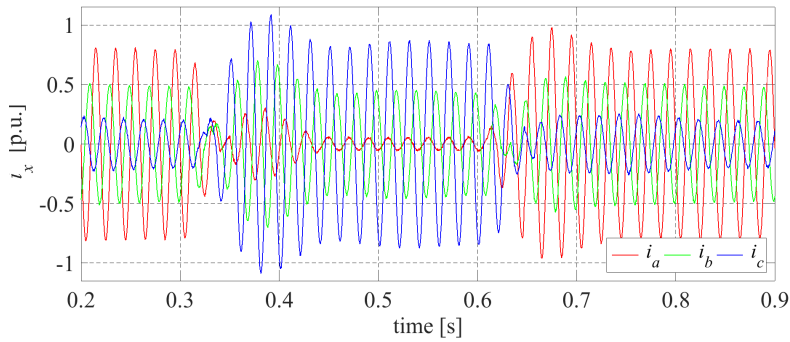
At time instance 0.6 s the transient of  $p_{dc} = -1$  to  $p_{dc} = 0$  p.u. occurs. The lack of dc bus power forces the grid voltages to drop below  $v_{cpb}$  and the droop controller is disabled at time 0.65 s while the slower damping controller settles down at 0.85 s. The overshoot of the capacitor voltages is again close to 10% and the same overshoot is present in the phase currents. In summary, the same settling times of the dc-bus controllers are the same when the input power is changed from  $-1$  p.u. to 0 p.u.



(a) Damping conductance profile



(b) Voltages across the dc-bus capacitors



(c) Currents injected by the DER

Figure 5.23: DER reaction when the input power changes from 1 to -1 p.u. and back to 1 p.u. when the full local control is enabled

### 5.4.4 Case study 3

This case study represents the case when the input power is changed from -1 p.u (consumption) to 1 p.u (injection) and vice versa. The conditions are the same as

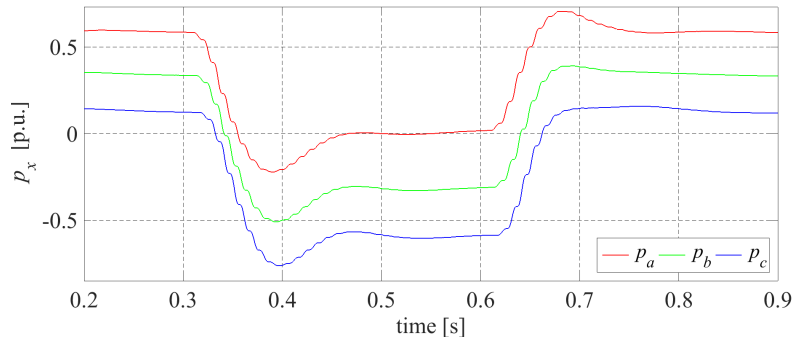


Figure 5.24: Exchanged active power by the DER when the input power changes from 1 to  $-1$  p.u. and back to 1 p.u. are applied and the full local control is enabled

in Case study 2 i.e. time intervals and grid voltages and the obtained simulation results are depicted in Fig. 5.23 and Fig. 5.24. Without loss of generality it will be just pointed out that the overshoot in the dc-bus voltages is increased up to 20% during the transient intervals.

#### 5.4.5 Discussion

From the presented test cases it can be seen that the system response is stable and it is able to operate reliably, despite the complexity of the system, which involves two additional controllers i.e. droop and damping controllers. The assigned priority of the different controllers does not influence the stability of the DER. Furthermore, it can be also seen from all case studies that the proposed split dc-bus controller topology ensures almost identical voltage profiles across the dc-bus capacitors even during severe power changes.

### 5.5 Experimental validation of the modified three-phase damping control strategy in a laboratory environment

In this paragraph, the LV feeder of the laboratory set-up is modelled in Matlab & Simulink and a comparison is made between the measured and simulated results. Once the accuracy of the feeder model is known, the full DER model is included and a comparison is made between the obtained results from the built simulation model and experimental set-up under the three operation modes of the three-phase damping control strategy.

| Parameter                                  | Value                       |
|--|-----------------------------|
| nominal phase voltage $v_a, v_b$ and $v_c$ | 110 V, 110 V, 110 V (50 Hz) |
| nominal phase current                      | 3.63 A (at $g_d = 0$ p.u.)  |
| maximum phase current                      | 12 A                        |
| $C_a, C_b$ and $C_c$                       | 5 $\mu$ F                   |
| $L_a, L_b$ and $L_c$                       | 2 mH                        |
| $L_n$                                      | 0.666 mH                    |
| Three-phase nominal inverter               | 1.2 kVA                     |
| Three-phase peak inverter                  | 4 kVA                       |
| $C_1$ and $C_2$                            | 2000 $\mu$ F                |
| $v_{dc,p} + v_{dc,n}$                      | 400 V                       |
| Switching frequency                        | 20 kHz                      |
| Current base value                         | 7.5 A                       |
| Phase voltage base value                   | 225 V                       |
| dc-bus voltage base value                  | 200 V                       |

Table 5.4: Prototype parameters

### 5.5.1 Laboratory test

The connection diagram of the set-up used to test the proposed control strategies is depicted in Fig. 5.1. The set-up consists of an LV grid, a power analyser PM 3000 and DER. The LV grid is implemented by using a programmable three-phase voltage source and a copper cable with a length of 30 m and a cross section of 2.5 mm<sup>2</sup>. More information about the LV grid properties is given in §5.5.2. The DER is connected to the grid via a power analyser, which is used to accurately measure the data of interest and later compare them with the obtained simulation results. The power electronic inverter is implemented by using IGBT switches and amorphous steel-based differential inductors. The developed inverter prototype is depicted in Fig. B.1 and its parameters are listed Table 5.4. The modified control strategy is implemented on a digital signal processor (DSP) TMS320F28335 of Texas Instruments. A detailed block diagram and a picture of the developed control board can be found in Appendix B.

The theoretical study in Chapter 4 revealed that if the damping conductance  $g_d$  assumes high values then the phase currents can reach very high values as well, thus their nominal value can be exceeded several times. The significant current over-sizing (almost 4 times) in the developed inverter will allow to investigate the influence of  $g_d$  in a wider range, which is also feasible in a laboratory set-up.

### 5.5.2 Feeder modelling in Matlab & Simulink

Since the set-up consists of multiple components, a better approach to assess the accuracy of the built model can be obtained by splitting the model in different parts and examine independently their accuracy and different errors. First, an assessment of the LV grid is conducted and second, a total assessment of the complete model is performed.

In order to examine the LV grid behaviour, a time domain Simulink model is built. The cable properties are measured by using a precise RLC meter -Hammeg 8118. For that particular feeder a resistance  $R = 0.470\Omega$  and inductance  $L=640\mu\text{H}$  are measured, which yields to  $R/X$  ratio of 2.3, which is within the range of 2 to 10 (typical ratios for the LV networks). To accurately simulate the cable properties, the full impedance matrix must be used in the model. By measuring the mutual inductance, the impedance matrix is constructed and the data are listed in Table 5.5. In this particular case, the cable is not an underground cable and the non-diagonal terms are only reactive and equal to each other. In case of an underground cable, the influence of the ground and injected eddy currents in it makes these non-diagonal terms not equal to each other. This is especially valid for unbalance of LV grids, which are considered in this thesis. Hence, the ground effect must be taken into account if a real LV feeder is modelled [64, 65, 71]. The programmable three-phase voltage source is based on analogue voltage amplifiers with a feedback, which ensures very low internal impedance and stable output. Hence, in the simulation model the three-phase programmable supply is represented by three ideal sinusoidal voltage sources.

Three different tests are performed in order to assess the accuracy of the LV grid model in Simulink. The first one is (i) balanced loading test, followed by (ii) unbalanced loading - loads connected the phases  $a$  and  $c$ , and in the final test (iii) only one phase ( $a$ ) is loaded. The tests are conducted by using loads with unity power factor and resistance of  $25\ \Omega$ . The connection diagram of the set-up is depicted in Fig. 5.25. The three voltages of the programmable power source are measured and also inserted in the Simulink model. The obtained measurements by the power analyser and the simulation results obtained by the time domain Simulink model are listed in Table 5.6. For the evaluation of the model, the relative error is used to quantify the model accuracy.

The relative error of the obtained experimental and simulation results is calcu-

|                  |                  |                  |                  |
|------------------|------------------|------------------|------------------|
| $0.470 + j0.201$ | $j0.173$         | $j0.173$         | $j0.173$         |
| $j0.173$         | $0.470 + j0.201$ | $j0.173$         | $j0.173$         |
| $j0.173$         | $j0.173$         | $0.470 + j0.201$ | $j0.173$         |
| $j0.173$         | $j0.173$         | $j0.173$         | $0.470 + j0.201$ |

Table 5.5: Full cable impedance matrix

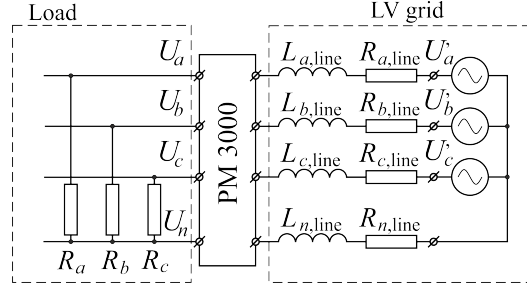


Figure 5.25: LV feeder measurements

| Initial voltage values   | $U_a$         | $U_b$         | $U_c$         |
|--|---------------|---------------|---------------|
|  | 110.1         | 110.4         | 110.4         |
| Balanced loading conditions $R_a=25.0 \Omega$ , $R_b=25.0 \Omega$ and $R_c=25.1 \Omega$    |               |               |               |
| Measurements values [V]  | 108.1         | 108.2         | 108.3         |
| Simulation values [V]  | 108.06        | 108.35        | 108.37        |
| Relative error $\delta$ [%]  | <b>0.037</b>  | <b>0.1386</b> | <b>0.064</b>  |
| Unbalanced load conditions $R_a=25.0 \Omega$ , $R_b=\infty \Omega$ and $R_c=25.1 \Omega$   |               |               |               |
| Measurements values [V]  | 107.1         | 112.4         | 107.4         |
| Simulation values [V]  | 107.21        | 112.35        | 107.32        |
| Relative error $\delta$ [%]  | <b>0.1027</b> | <b>0.0444</b> | <b>0.0744</b> |
| Unbalanced load conditions $R_a=25.0 \Omega$ , $R_b=\infty \Omega$ and $R_c=\infty \Omega$ |               |               |               |
| Measurements values [V]  | 106           | 111.4         | 111.4         |
| Simulation values [V]  | 106.1         | 111.5         | 111.3         |
| Relative error $\delta$ [%]  | <b>0.0943</b> | <b>0.0898</b> | <b>0.0897</b> |

Table 5.6: Comparison between the obtained simulation and measured values of the test set-up feeder and power supply

lated by using:

$$\delta = \left| \frac{U_m - U_s}{U_m} \right| \times 100\% \quad (5.31)$$

where  $U_m$  is the measured value and  $U_s$  is the simulated one. The relative error is also listed in Table 5.6 and it can be seen that it is very small (less than 0.14%) under balanced and unbalanced loading, hence the LV grid is modelled accurately and the influence of the LV grid can be neglected in the final results when DER model accuracy is assessed.

### 5.5.3 Experimental verification of the three-phase damping control strategy

In Chapter 4, a detailed theoretical analysis of the three-phase damping control strategy was conducted and the injected phase currents (magnitudes and angles) were examined at different phase voltage values. The tests were conducted under zero, nominal input and nominal consumed power and also under variety of unbalanced conditions such as phase voltage and angle deviation. In this paragraph, the conducted experiments in Chapter 4 are simulated in the assembled time domain Simulink model and the obtained data are compared. In Chapter 4, the voltage variation in phase  $a$  is chosen to vary from 0 to 2.5 p.u. to examine the theoretical behaviour of the three-phase damping control strategy. However, in practice such a wide range is difficult to cover by the power electronic inverter due to hardware and grid standard limitations. When practically examined, a more suitable value for the upper limit of the voltage range can be selected such as the maximum value of the grid voltage (or close to it). The lower value however, depends on the maximum current ratings of the power electronic inverter, as well as the damping conductance value.

The conducted experiments in § 4.5.2, §4.5.1 and § 4.5.3 are performed for 7 different values of phase voltage  $v_a$ : 0.545, 0.634, 0.727, 0.818, 0.909, 1 and 1.09 p.u. The experiments are also conducted for 7 different values of the damping conductance  $g_d$ : 0, 1, 2, 3, 5, 8 and 12 p.u. In addition, they are repeated for all three cases (operation modes) such as (i) zero input power, (ii) nominal input power and (iii) 0.66 p.u. consumed power.

The simulation model is ran in a for loop for all cases with the conditions listed above. All variables of interest are saved in individual workspaces in Matlab. When the for loop is finished, the variables of interest are loaded back into the workspace and post processed. By using fast Fourier transformation (FFT), the magnitudes and the angles are extracted from these variables.

The biggest part of the losses in a power electronic inverter is in the semiconductor switches and differential output filters. The semiconductor switches have two major type of losses: conduction losses and switching losses (the reverse recovery losses are assumed to be part of the switching losses). The last ones cannot be modelled due to the imposed limitations of the used toolbox. Since switches as IGBT are used, the conduction losses are also nonlinear and they are dependent on the temperature and the current flowing through the switches, but an assumption of the voltage drop across them can be made based on the output rms current of the inverter. The differential filter losses are more complex and can be split into losses in the windings and the magnetic core. The losses in the windings include conduction (ohmic) losses for the fundamental component, eddy currents losses - proximity effects and transverse fields, while the core losses are due to the hysteresis of the soft magnetic material and bulk currents. From the above

listed components, only the conduction losses of the fundamental can be used in the model. The rest of the losses are also very difficult to be included and modelled accurately in Simulink. In summary, only the voltage drop of the used semiconductor IGBT (IXYS) switches is used and for the rated current of 3.3 A this drop is about 0.8 V. Only the ohmic losses of the differential output filters are taken into account in the built simulation model. The ohmic resistance at 50 Hz is measured by using RLC meter Hammeg 8118 and a value of 24 m $\Omega$  is obtained. In the simulation model, the output differential inductor is replaced by an RL equivalent circuit where R=0.024  $\Omega$  and L= 0.002 H.

### 5.5.3.1 Model accuracy assessment at variable phase voltage $v_a$ and zero input power

In §4.1.1.1 the theoretical behaviour of the three-phase damping control strategy under zero input power was studied. The results showed that the control strategy is still able to mitigate the voltage unbalance at the PCC by consuming current from phase  $a$  and injecting it back in phases  $b$  and  $c$ . This mode of operation was also experimentally verified in Chapter 4 §4.5.2. This valuable property of the three-phase damping control strategy makes it very suitable for power quality improvement and such a behaviour resembles the one of the active power filters [122–124] and UPFCs [125].

In this section, the developed Simulink model of the three-phase damping control strategy is compared with the measurements presented in Chapter 4 §4.5.2. The DER is connected as shown in Fig. 5.12 but the programmable dc source does not deliver any power to the dc side. The obtained results from the simulation model and the experimental ones are expressed by using the relative and absolute errors. The relative error is used to quantify the accuracy of the built simulation model and it is calculated by using (5.31).

The voltage levels at the PCC are dependent on the exchanged current between the DER and the grid (feeder impedance). Hence, first the exchanged currents will be examined and afterwards the voltages at the PCC. The relative errors between the measured phase currents and the ones obtained by the simulation model are depicted in Fig. 5.26. Based on the measured difference between input and injected active power is calculated that the inverter prototype has about 50 W of no-load losses while the simulation model is implemented by considering only the conduction losses at full load. This difference results in a rather big relative and absolute errors for the injected currents and their respective angles at nominal value of the phase voltage  $v'_a$ . From Fig. 5.26 it appears that these relative errors within the standard voltage range of  $v'_a$  are about 30% for  $i_a$  and about 20% for currents  $i_b$  and  $i_c$ . The relative error of the exchanged phase currents  $i_b$  and  $i_c$  remains above 10% at the upper limit of  $v'_a$  while  $\delta_{i,a}$  is between 6% and 15%. Note that these errors are different for the different values of  $g_d$ . Nevertheless, the

obtained results do not show a straightforward relation between the error and the value of  $g_d$ . At the lower limit of  $v'_a$  the  $\delta_{i,a}$  is below 5% while for the other two phase currents this error is in between 10% and 20%. These trends in the error values remain more or less unchanged for the values of  $v'_a$  that are lower than  $v_{g,\min}$ . Because of the inability of the toolbox SimPowerSystems to model accurately the switching losses, magnetic component losses and the non-linear conduction losses in the IGBT, the accuracy of the model is between 5% and 25% for the different phases. Further research could be conducted on improving the accuracy of the simulation model by introducing a look-up table in which the efficiency of the VSI is mapped. However, due to the asymmetrical current injection the different power electronic legs operate in different points of the efficiency curve, therefore the look-up table should be used by each leg independently, which will increase the complexity of the model.

The angle measurements of the phase currents from the practical set-up are provided by the power analyser, which uses  $v_a$  as a reference and  $\theta_a = 0^\circ$  for all measurements. Since that zero will appear in the denominator of (5.31) it will give an infinite error and the model accuracy cannot be quantified correctly. Hence, the absolute error is used as a quantifier instead of the relative one and the former one is calculated as:

$$\epsilon = \theta_{m,x} - \theta_{s,x} \quad (5.32)$$

where  $\theta_{m,x}$  is the measured angle and  $\theta_{s,x}$  is the angle obtained from the simulation model.

All absolute errors  $\epsilon_{\theta,i,a}$ ,  $\epsilon_{\theta,i,b}$  and  $\epsilon_{\theta,i,c}$  of the phase currents are depicted in Fig. 5.26 (b), (d) and (f), respectively. Within the standard voltage band range, the obtained results show that the relative errors of the phase angles is about  $30^\circ$  to  $-10^\circ$  for  $\epsilon_{\theta,i,a}$ ,  $-5$  to  $33^\circ$  for  $\epsilon_{\theta,i,b}$  and  $-15$  to  $25^\circ$  for  $\epsilon_{\theta,i,c}$ . These errors are rather high and the reason for this deviation is again the poor efficiency modelling of the chosen toolbox.

The obtained results of the relative errors  $\delta_{v,a}$ ,  $\delta_{v,b}$  and  $\delta_{v,c}$  for the phase voltages  $v_a$ ,  $v_b$  and  $v_c$  are shown in Fig. 5.27 (a), (c) and (e). The results show that the relative error is small when  $v_a$  is close to its nominal values. Considering the values of  $0.91 < v_a < 1.09$  within the standard voltage band voltage of 0.9 to 1.1 p.u. the relative errors for all phase voltages are still small and do not exceed 0.2% for all values of the damping conductance. At  $g_d$  values equal to 1 p.u. the relative error remains rather small for the entire voltage range of  $v_a$ . Within the standard band of the  $v'_a$  the exchanged currents between the DER and the grid are very small. According to Fig. 4.52 (c) and (e) the consumed currents do not exceed 0.1 p.u.

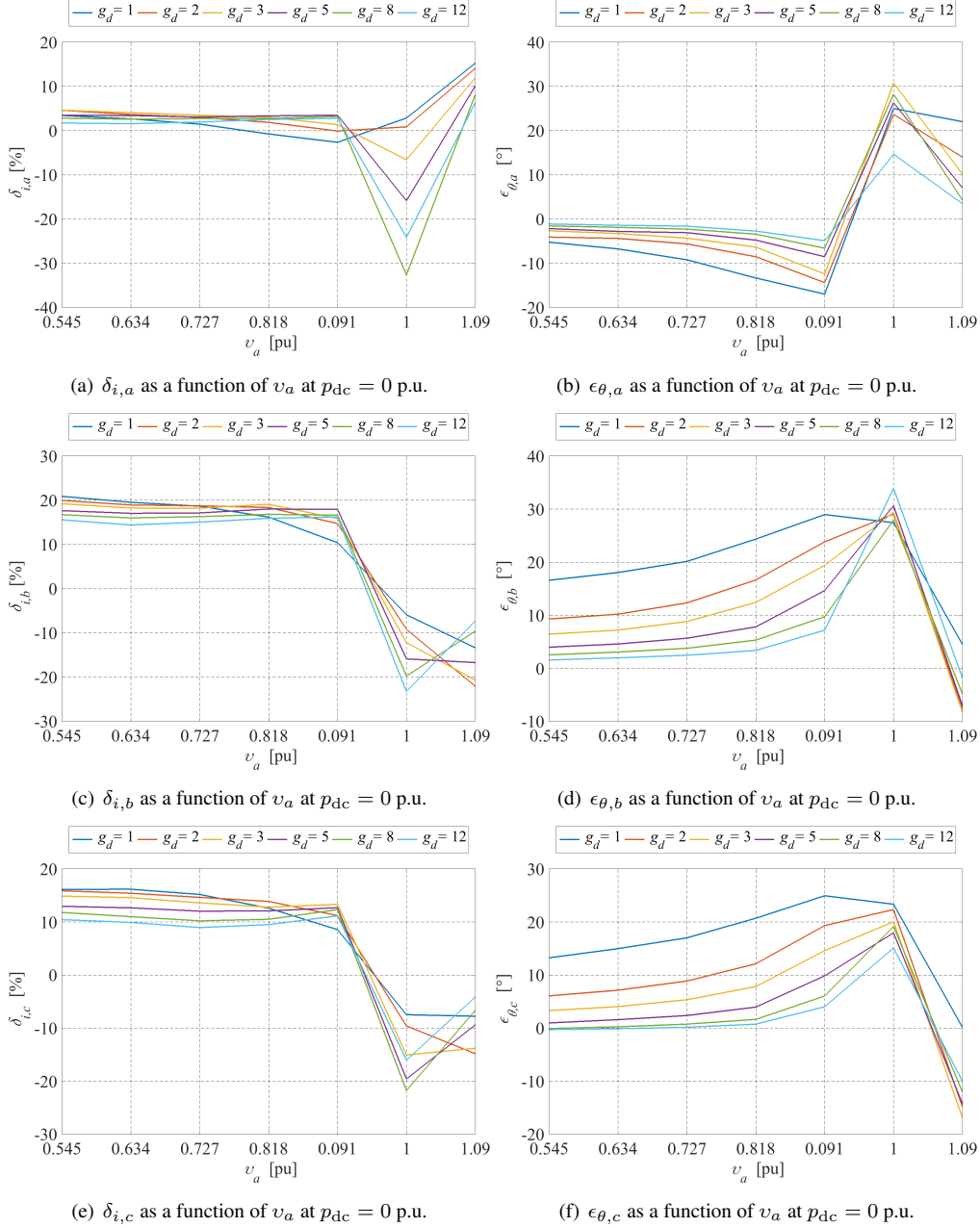


Figure 5.26: Phase currents and angle errors dependency on the variation of the phase voltage  $v_a$  at zero input power  $p_{dc} = 0$  p.u. and different values of the damping conductance  $g_d$

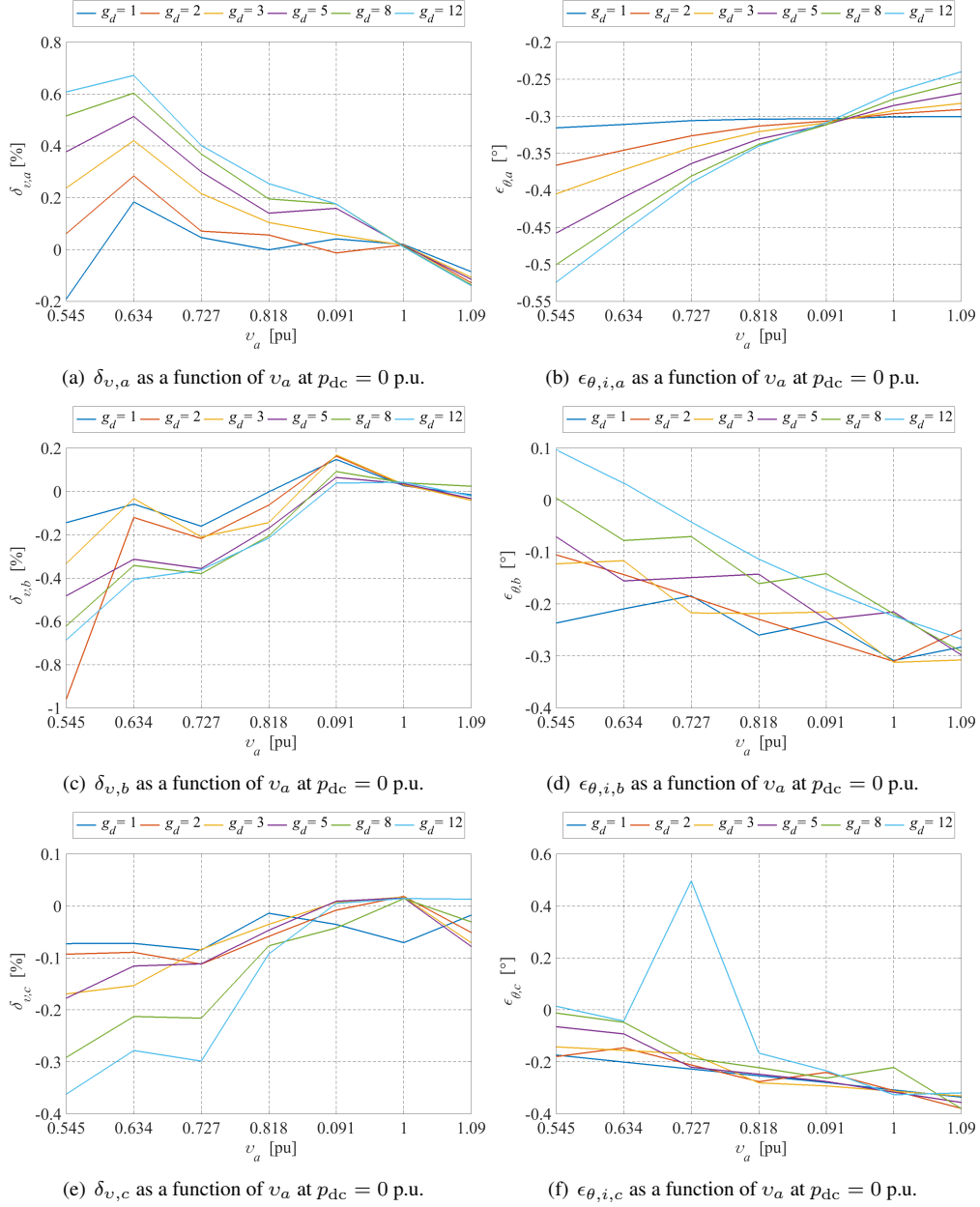


Figure 5.27: Phase voltage and angle errors dependency on the variation of the phase voltage  $v_a$  at zero input power  $p_{dc} = 0$  p.u. and different values of the damping conductance  $g_d$

The voltages at the PCC are dependent on the feeder impedance and the injected currents. Since the later ones are low, the relative error is also low. When  $g_d$  increases however, the relative error ( $\delta_{v,b}$ ) increases and it becomes 1% when the  $v_a = 0.545$  p.u. at  $g_d = 12$  p.u. It is obvious that with increasing the value of the damping conductance decreasing the phase voltage  $v_a$  the model accuracy is slightly deteriorated. This deterioration is due to the assumptions of the losses modelling of the VSI as explained earlier.

The calculated absolute errors  $\epsilon_{\theta,a}$ ,  $\epsilon_{\theta,b}$  and  $\epsilon_{\theta,c}$  for the different phase angles  $\theta_a$ ,  $\theta_b$  and  $\theta_c$  are depicted in Fig. 5.27 (b), (d) and (f). Similar to the relative error of the phase currents, here as well, the absolute error is very small at nominal values of the  $v_a$  and it starts increasing when  $v_a$  is deviating from its nominal value. At low values of  $g_d$  the absolute error remains rather low - less than  $0.3^\circ$  change for the entire range of  $v_a$  and it increases up to  $0.55^\circ$  with increasing the damping conductance value.

### 5.5.3.2 Model accuracy assessment at variable phase voltage $v_a$ and nominal input power

In §4.1.1.2, the three-phase damping control strategy is studied analytically under nominal input power and variable voltage in phase and in Chapter 4 paragraph §4.5.3 experimental data are obtained that cover part of the theoretical study. In this paragraph, the developed simulation model is examined in a similar voltage variation range and the obtained simulation results are compared with the experimental ones. In Fig. 5.28 (a), (c) and (e), the calculated relative errors of the exchanged phase currents are presented. From these results it can be seen that the relative error  $\delta_{i,a}$  is between  $-1.5\%$  and  $3.5\%$  and between 0 and  $2.5\%$  in phases  $b$  and  $c$  and this is valid for all values of the damping conductance. By decreasing phase voltage  $v'_a$  the all relative errors are very low at  $g_d = 0$  p.u. and start increasing when higher values of  $g_d$  are used. Nevertheless, this increase does not exceed an absolute value of 5% in all three phases, which can be considered as a satisfactory performance of the developed model.

Unlike the previously considered study case, the accuracy of this one is better because the power electronic inverter operates at much more favourable conditions. In addition, this accuracy is achieved by completely neglecting the switching losses, magnetic core losses and eddy currents losses of the differential inductors, which simplifies the model significantly. A better accuracy can be achieved if the model is improved further by considering these losses. However, the complexity of the model will become bigger and more simulation time will be needed to execute the simulations.

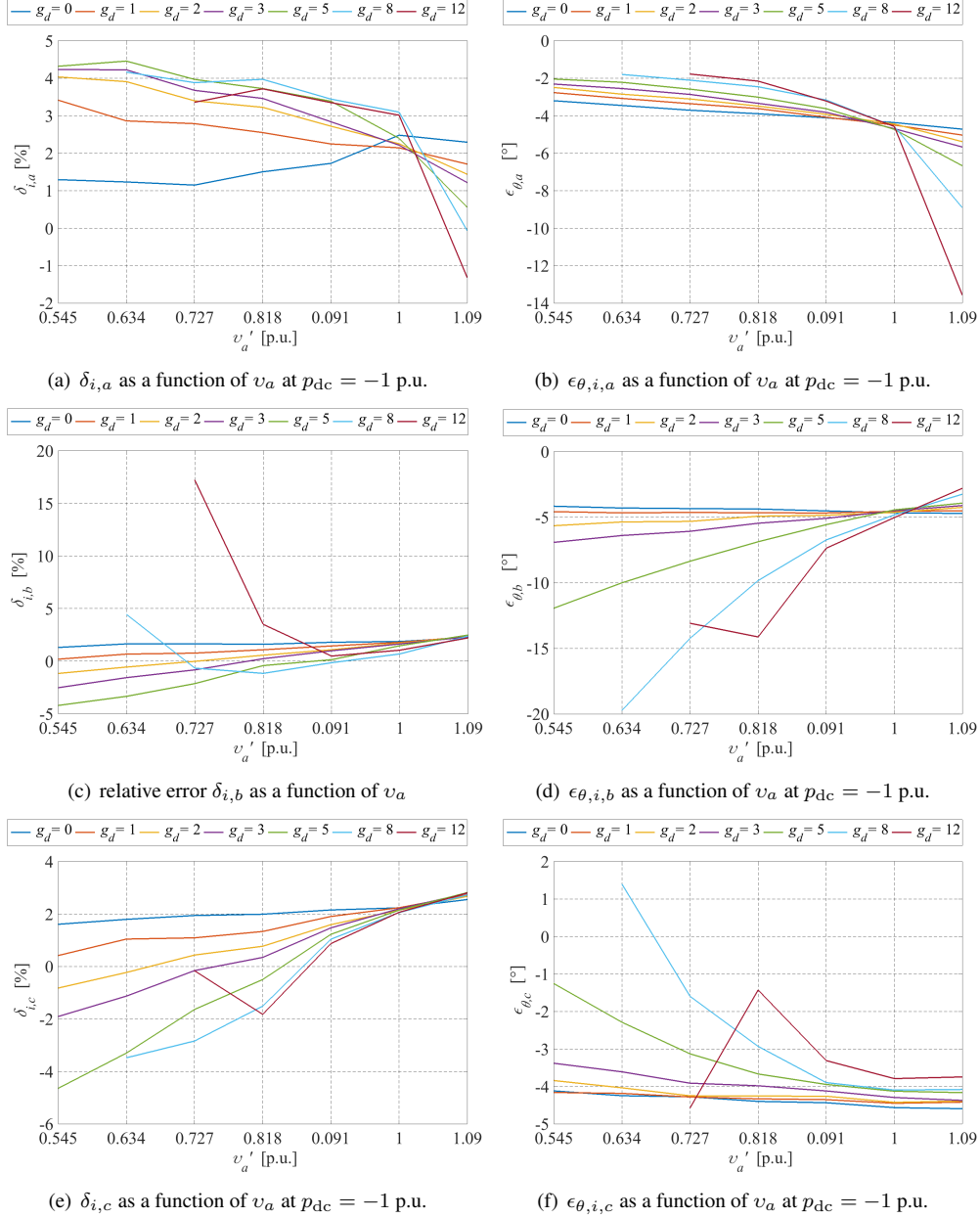


Figure 5.28: Phase currents and angle errors dependency on the variation of the phase voltage  $v_a$  at nominal input power  $p_{dc} = -1$  p.u. and different values of the damping conductance  $g_d$

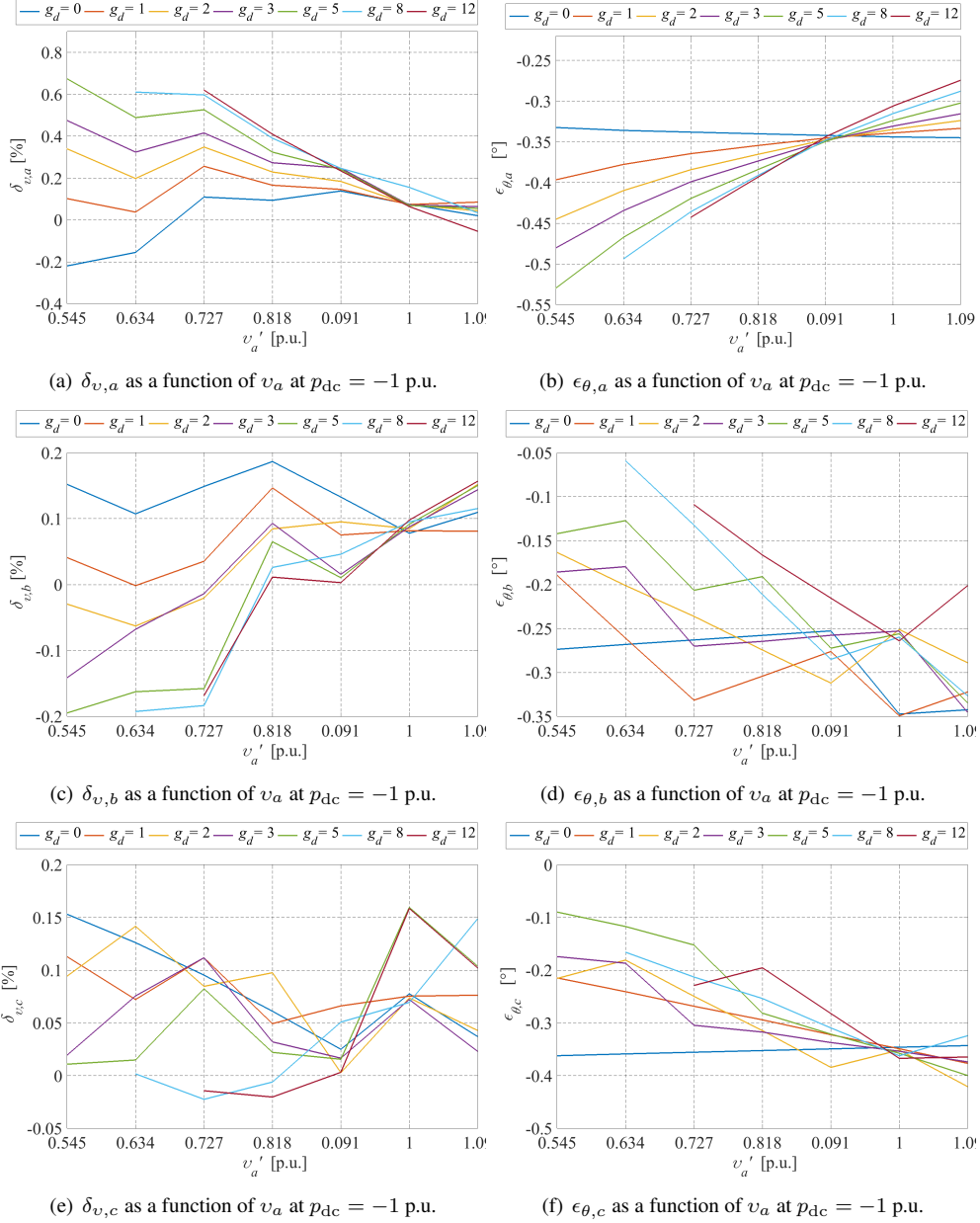


Figure 5.29: Phase voltages and angle errors dependency on the variation of the phase voltage  $v_a$  at nominal input power  $p_{dc} = -1$  p.u. and different values of the damping conductance  $g_d$

It is also important to note that the experiments for  $g_d = 8$  and 12 p.u. are conducted down to  $v_a = 0.634$  and 0.727 p.u. respectively. Further decrease of  $v_a$  creates significant voltage unbalance, which forces the three-phase damping control strategy to inject currents close to the maximum allowed and experimental data for these points are not obtained due to current limitations of the power electronic switches and differential inductors. In the simulation model, the phase angles are extracted from the phase voltages by using FFT. Then the absolute errors between the measured (Fig. 4.50) and extracted angles are computed and the obtained calculation results are depicted in Fig. 5.28 (b), (d) and (f). These results show that within the standard voltage band the absolute error  $\epsilon_{\theta,i,a}$  does not exceed  $7^\circ$  whereas the absolute errors in the other two phases do not exceed  $5^\circ$ . As of the entire range of  $v'_a$  and  $g_d$  the absolute errors are still rather small and  $\epsilon_{\theta,i,b}$  does not exceed  $10^\circ$  while the absolute errors  $\epsilon_{\theta,i,a}$  and  $\epsilon_{\theta,i,c}$  are below  $5^\circ$ .

The relative errors of the phase voltages and angles are presented in Fig. 5.29. From these obtained results it can be seen that within the standard voltage band, the relative errors are rather small and they do not exceed 0.3%. As of the entire range of  $v'_a$  and  $g_d$ , the relative error  $\delta_{i,a}$  is kept below 0.8% at the lowest value  $v'_a$  and the highest of  $g_d$ . The obtained relative errors under the entire investigated voltage range of phases  $b$  and  $c$  show that the maximum relative error does not exceed 0.2%.

All absolute errors of the voltage phase angles are depicted in Fig. 5.29 (b), (d) and (f). From the presented results of the calculated absolute error it can be seen that the maximum deviation hardly exceeds  $0.55^\circ$  for all phases. From the presented relative and absolute errors of the phase currents and voltages, it can be concluded the built model provides sufficient accuracy and it can be used to obtain preliminary results for real LV grids.

### 5.5.3.3 Model accuracy assessment at variable phase voltage $v_a$ and 66% consumed power

In this mode, power is consumed from the grid and the DER is used to supply a load such as a BESS or the control strategy can be used as an active rectifier to supply a load as studied in [80]. All experimental data are presented in §4.1.1.3. The obtained relative errors of the exchanged phase currents are depicted in Fig. 5.30 (a), (c) and (f) whereas the absolute error of the current angles are depicted in Fig. 5.30 (b), (d) and (e).

From the obtained results of the relative errors it can be seen that,  $\delta_{i,a}$ ,  $\delta_{i,b}$  and  $\delta_{i,c}$  are rather low within the range of  $1.0 \leq v'_a \leq 1.09$ . In the lower band of the standard voltage the relative errors are also small, except for values  $g_d = 5$  p.u. to  $g_d = 12$  p.u. At these values of  $g_d$ , the damping control strategy enters in a mixed mode of operation where  $i_a$  is close to its border mode. Since the exchanged power is close to 0 p.u. the efficiency is very poor and the accuracy of the model

is deteriorated. This also leads to an increased absolute error  $\epsilon_{\theta,i,a}$ .

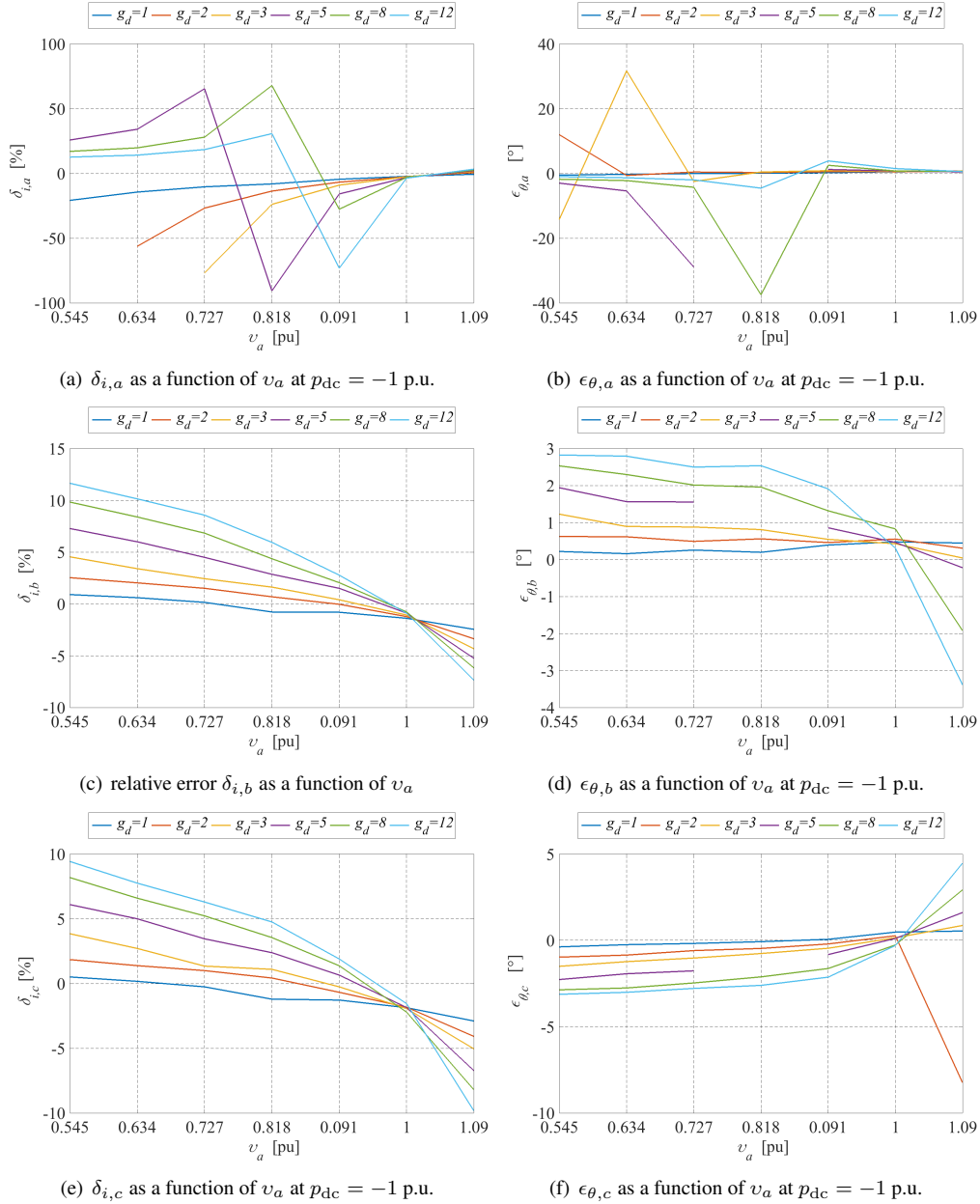


Figure 5.30: Phase currents and angle errors dependency on the variation of the phase voltage  $v_a$  at nominal input power  $p_{dc} = 0.66$  p.u. and different values of the damping conductance  $g_d$

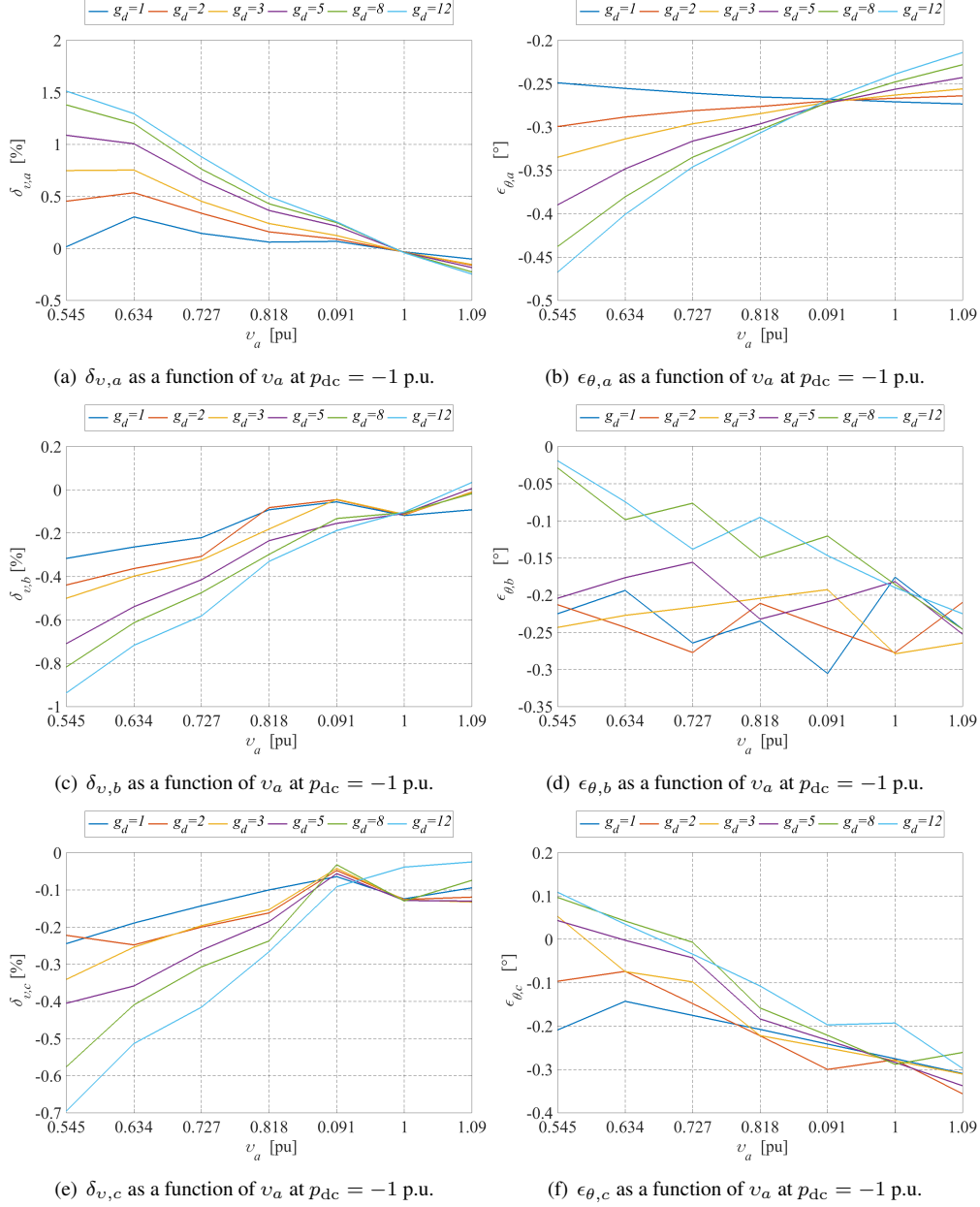


Figure 5.31: Phase voltages and angle errors dependency on the variation of the phase voltage  $v_a$  at nominal input power  $p_{dc} = 0.66$  p.u. and different values of the damping conductance  $g_d$

The relative errors  $\delta_{i,b}$  and  $\delta_{i,c}$  of the other two phase currents are between  $-10$  to  $2.5\%$  within the standard voltage range for all  $g_d$  values and between  $0.5\%$  to

12% for the extreme values of  $v'_a$  and  $g_d$ . The absolute errors of the phase angles are also between  $-4^\circ$  and  $5^\circ$  for all phases.

Despite the lower accuracy of the model, the relative errors of the phase voltages remain very low because the exchanged currents are lower as well. Within the standard range, all absolute values of the relative errors do not exceed 0.3%. As for the extremes values of  $v'_a$  and  $g_d$  the overall accuracy of the model is about 1.5%. All absolute errors  $\epsilon_{\theta,a}$ ,  $\epsilon_{\theta,b}$  and  $\epsilon_{\theta,c}$  are also very low and they barely exceed  $0.5^\circ$  for the full range of  $v'_a$  and  $g_d$  under consideration.

#### 5.5.4 Discussion

The difference between the experiments and simulations are very small when the DER injects its nominal power despite the fact that only the conduction losses are considered in the model. However, when the input power is lower than the nominal or even zero, the efficiency is deteriorated. As mentioned earlier, the reason for this deterioration is because of the limitations of the used toolbox to simulate losses in magnetic components and switching losses. An improvement of the model could be implemented by measuring the efficiency of the set-up and insert it in the simulation model by using a look-up table but this will increase the complexity of the model as well as the simulation time. On top of this, the three-phase damping control strategy injects asymmetrical currents to mitigate the voltage unbalance, which will lead to different operation points in the efficiency curve for the different legs. Hence, the model complexity will be further increased.

Future work on this topic could be implementing the look-up tables into numerical phasor simulations where the computation time for complex grids can be in order of 0.1s or lower [126]. Increasing the complexity of the phasor models by adding these tables will not increase the simulation time that drastically compared to the time domain models. However, the time domain models have their advantages when the stability of the different controllers is concerned and when a control strategy has to be developed and tested. Consequently, despite the above assumptions regarding the losses, the accuracy of the model within the standard voltage range provides a good accuracy of the injected currents and the relative errors are within 5 to 6% range which makes the model appropriate for preliminary analyses in simple case studies.

### 5.6 Conducted field trial in Graz, Austria

The three-phase damping control strategy is tested on a field trial in Graz, Austria within the frame work of project INCREASE [60]. The built installation of the field trial network is presented in Fig. 5.32. The network is located at the 10<sup>th</sup> floor of the building of Energienetze Steiermark. PV panels are installed on the

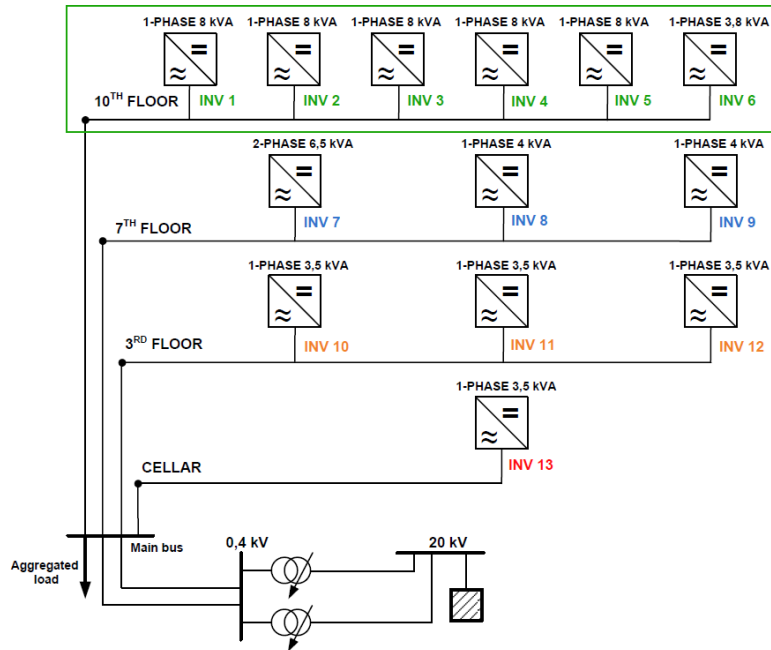


Figure 5.32: Connection diagram of the original set up used to test the three-phase damping control strategy in a real LV grid

facade and roof. The inverters that are located at the ground, 3<sup>rd</sup> and 7<sup>th</sup> floors are connected only to the facade PV panels but they are not part of the field trial. The installed rooftop PVs have a peak power of 47kWp and they are connected to 5 inverters with a peak power of 8 kVA and one inverter of 3.8 kVA. All inverters are classical ones and manufactured by SMA. The inverters located on the 10<sup>th</sup> floor are shown in Fig. 5.33 and highlighted by a green rectangle. In this configuration, the inverters are connected to the grid such that the injected currents are distributed almost equally among the three-phases.

In order to influence the zero-sequence component, the three-phase damping control strategy requires a four-wire power electronic inverter. Since the developed inverter prototype is not certified, it is not allowed to be connected to the distribution grid. Unfortunately three-phase four-wire inverters are not available on the market for PV applications, which makes the integration of the three-phase damping control strategy even more difficult. Even if such inverters were available on the market, the firmware would not be available to do any modifications on it. In [18], three single-phase inverters were connected to a common dc bus where each inverter is driven by a single phase damping control strategy. In [68],



Figure 5.33: PV inverters, available at the 10<sup>th</sup> floor of the field trial building

a comparison is conducted between the three-phase damping and the three single-phase damping topology and the results showed that both control strategies have similar performance towards the zero- and negative-sequence components. Therefore, a similar solution can be used for the experimental field trial validation of the three-phase damping control strategy.

Connecting a three single-phase inverter to a common dc-bus however cannot be implemented by using standard inverters because a line-to-line short circuit will appear through the free-wheeling diodes of the power electronic inverter. To avoid this, the dc-bus must be isolated galvanically from the ac side. Another challenge is the implementation of the three-phase damping control strategy such that the inverters are controlled accordingly.

In Fig. 5.34 the field trial connection diagram is presented. All classical inverters (surrounded by a purple dashed rectangle) are reconnected such that the available PV power is half of the total installed i.e. 23.5 kWp and the outputs are connected to phase *a*. In this way some artificial voltage unbalance conditions are created. The six additionally installed inverters, called INCREASE inverters, are manufactured by ILPRA (Inverter manufacturer also part of the INCREASE consortium). They are split in 2 groups, where each group consists of three single-phase inverters and one controller. The other half of the PV power is again split in two and connected to each inverter group. The nominal power of each of the inverters is 5 kVA. The firmware of the inverters is modified such that the inverters are able to send the measured grid voltages at the inverter terminals, the available dc-bus power and the injected currents via Ethernet to the controller. The controllers, which are also manufactured by ILPRA, calculate the fundamental input conductance by using a simplified equation where the phase angles are not included:

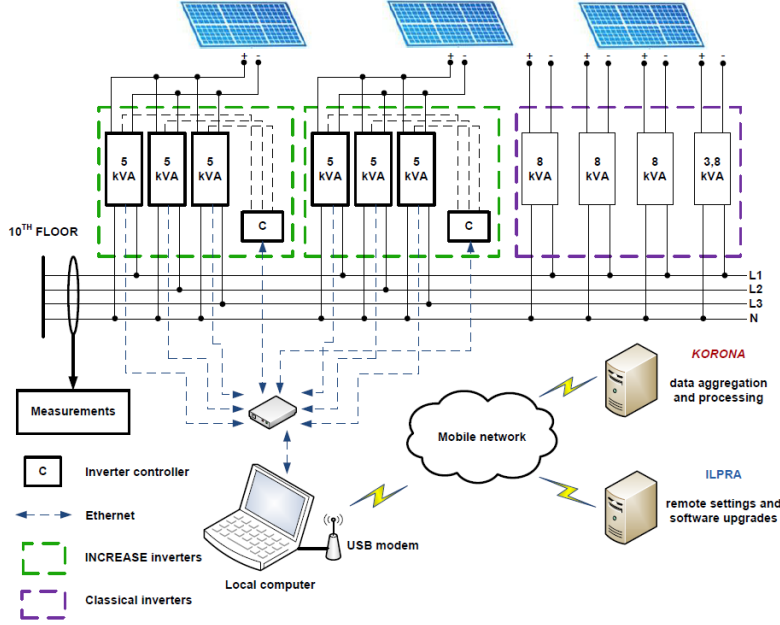


Figure 5.34: Connection diagram of the field set-up where the three-phase damping control strategy is implemented by using three single-phase inverters

$$g_1 = \frac{3 p_{dc}}{|\underline{v}_a|^2 + |\underline{v}_b|^2 + |\underline{v}_c|^2 + 2(|\underline{v}_a||\underline{v}_b| + |\underline{v}_b||\underline{v}_c| + |\underline{v}_c||\underline{v}_a|)} - 2g_d \frac{|\underline{v}_a|^2 + |\underline{v}_b|^2 + |\underline{v}_c|^2 - (|\underline{v}_a||\underline{v}_b| + |\underline{v}_b||\underline{v}_c| + |\underline{v}_c||\underline{v}_a|)}{|\underline{v}_a|^2 + |\underline{v}_b|^2 + |\underline{v}_c|^2 + 2(|\underline{v}_a||\underline{v}_b| + |\underline{v}_b||\underline{v}_c| + |\underline{v}_c||\underline{v}_a|)} \quad (5.33)$$

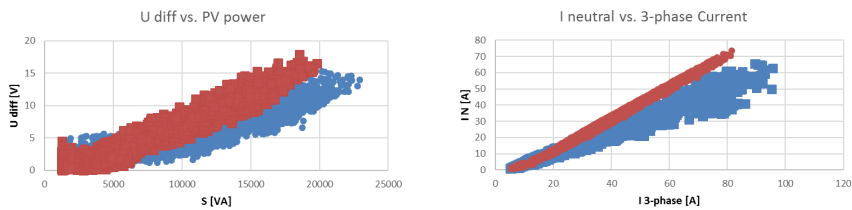
where in this equation, the  $v_x$  is the rms value of the respective phase voltage. Then the fundamental input conductance together with the measured voltages is used to calculate the reference currents again with a simplified equation:

$$\begin{aligned} \dot{i}_a &= \frac{1}{3} \{g_1(|\underline{v}_a| + |\underline{v}_b| + |\underline{v}_c|) + g_d(2|\underline{v}_a| - |\underline{v}_b| - |\underline{v}_c|)\} e^{j(\theta_a)} \\ \dot{i}_b &= \frac{1}{3} \{g_1(|\underline{v}_a| + |\underline{v}_b| + |\underline{v}_c|) + g_d(2|\underline{v}_b| - |\underline{v}_a| - |\underline{v}_c|)\} e^{j(\theta_b)} \\ \dot{i}_c &= \frac{1}{3} \{g_1(|\underline{v}_a| + |\underline{v}_b| + |\underline{v}_c|) + g_d(2|\underline{v}_c| - |\underline{v}_a| - |\underline{v}_b|)\} e^{j(\theta_c)} \end{aligned} \quad (5.34)$$

The calculated reference currents are sent back to the corresponding inverter. In this way, a close representation of the three-phase four-wire inverter is created.



Figure 5.35: Connection diagram of the field set-up where the three-phase damping control strategy is implemented by using three single-phase inverters



(a) Relationship between the phase-voltage deviation from the nominal value and the injected power when positive-sequence (red) or three-phase damping (blue) control strategy is used

(b) Relationship between the neutral and phase currents injection when positive-sequence (red) or three-phase damping (blue) control strategy is used where  $\circ$  positive sequence,  $\square$  three-phase damping control strategy

Figure 5.36: Comparison between the positive-sequence and three-phase damping control strategy obtained by the field trial

The necessity of simplification of (5.33) and (5.34) is because of the communication rate limits between the inverters and controllers. In this particular case, the sampling time of the controllers is 0.5 s.

The controller is also able to communicate with a computer. The later one is used to store the necessary data such as phase voltages, phase currents and injected power. The collected data were later processed by KORONA (a company, which is part of the INCREASE consortium) and ILPRA.

The field trial is conducted from the beginning of August 2016 till end of October 2016. Two control strategies are compared in this field experiment i.e. positive-sequence and three-phase damping control strategy. The goal of the field trial is to access the performance of the classical positive-sequence and the three-phase damping control strategy. The damping conductance value of the three-phase damping control strategy is chosen experimentally so that the maximum injected phase currents do not exceed the current limits of the single-phase inverters. In this particular case the maximum value of the damping conductance is 5 p.u.

The obtained measurements results regarding the deviation of the phase voltages from their nominal values versus the injected renewable power are depicted in Fig. 5.36 (a). In this figure, the positive-sequence control strategy is indicated with a red square marker and the damping control strategy with a blue circle marker. The results show that the deviation between phase voltages is less than 5 V when the three-phase damping control strategy is used. The total injected renewable power is also increased up to 22.5 kVA compared to the positive-sequence, which is able to inject only 20 kVA.

In Fig. 5.36 (b) is shown the relationship between the neutral current and the sum of the phase currents. As can be seen from the presented measurements results, the neutral current is decreased with approximately 10 A, which is the reason for a beneficial effect over the reduced voltage deviation presented in Fig. 5.36 (a). Note that in both measurements (voltage and current) the three-phase damping control strategy has a more wider range of the data deviation. For instance in Fig. 5.36 (b) the positive-sequence control strategy results in more narrower line while the three-phase damping control strategy results in a more disperse curve. This disperse effect is because of the fact that the three-phase damping control strategy forms the reference currents based on the voltages at the inverter terminals while the positive sequence makes an average of the phase voltages.

From the obtained measurements of the field trial it can be concluded that the three-phase damping control strategy is able to mitigate the voltage unbalance in real LV grids while maximising the drooped renewable energy and most importantly the power quality of the grid voltages at the PCC is improved.

## 5.7 Conclusions

In this chapter, practical guide lines regarding the implementation of the modified three-phase damping control strategy are given. Proper sampling of the measured signals as well as the stabilisation of the split dc-link capacitor voltages are examined. The chosen stabilisation of the capacitor voltages showed very good performance for stabilising the voltages as well as delivering very little THD into the exchanged currents and dc current injection.

The response order of the different controllers is also tested by enabling the droop and damping controllers during maximum generation. The same tests are performed also for the input power transient and the results showed that the proposed response order of the controllers does not lead to excessive overshoots or undershoots in the injected currents and also power oscillations are not present. During the transients both capacitor voltages were experiencing very similar transient profiles, which confirms that the voltage stabilisation will guarantee equal voltages during power changes and disturbances.

A simulation model in Matlab & Simulink is also built in this chapter and its accuracy is assessed based on the measurements conducted in Chapter 4. The results showed that the injected currents by the control strategy have a good accuracy of about 5% when nominal input power is considered. This accuracy decreases to 20% when the input power decreases and the reason for it is identified to be the inability of the chosen toolbox to model the switching losses of the power electronic switches and hysteresis losses in the magnetic components. Nevertheless, the built model provides sufficient performance to allow for conducting transient analysis and stability assessment.

Finally, the three-phase damping control strategy and the positive-sequence control strategies are experimentally tested on a field-trial in Austria and the results showed that the three-phase damping control strategy is able to mitigate the voltage unbalance and prevent overvoltages in three-phase low-voltage grids as well as reduce the neutral current. This makes the modified three-phase damping control very suitable for integration onto DERs in areas with high penetration of renewable energy and power quality issues.



# 6

## Incorporation of battery storage in DERs

The increased utilisation of DER in low voltage grids leads to power quality problems such as overvoltages and voltage unbalance. This poses challenges to the distribution system operators to maintain the power quality in their grids. To overcome these issues, energy storage systems could be integrated together with the DER and the stored energy could be used when needed to better improve power quality and reduction of grid losses. However, integrating an energy storage system introduces additional cost, therefore, determining the right capacity is of essence. In this chapter, an energy storage system is combined with the classical positive-sequence control strategy and the three-phase damping control strategy. The three-phase damping control strategy is able to mitigate the voltage unbalance by emulating a resistive behaviour towards the zero- and negative-sequence voltage components. This resistive behaviour can be set on different values such that the desired voltage unbalance mitigation is achieved. Hence, the three-phase damping control strategy, equipped with the energy storage system is investigated under different values of the resistive behaviour. Both control strategies are investigated under the same conditions and the impact of the different capacities of the energy storage systems is investigated.

## 6.1 Introduction

Nowadays, the share of the DER in the distribution grids is growing continuously because of environmental and economical concerns. The decreasing prices of the PV panels accelerates the penetration of DER even more compared to previous years [127]. Therefore, the DSOs face power quality challenges such as overvoltages. Due to the single-phase DER and asymmetrical loading the voltage unbalance additionally decreases the hosting capacity of the LV feeders [128].

To overcome these issues, the DSO could reinforce the LV grids in which the problems occur but this is an incredibly expensive solution. Installing dedicated equipment such as DSTATCOM and DVR are mostly used at MV level and usually they are installed in the vicinity of the LV networks with high penetration of DER. If power quality issues appear in another LV grid which is part of the same MV network but more distant from the dedicated equipment, then the last one should be relocated or a new one must be installed which is associated with additional costs [129]. On-load tap changers (OLTC) are very efficient devices for overvoltage mitigation. However, the voltage unbalance still remains as an issue. In literature, many research is carried out regarding voltage control by means of reactive power provided by DER themselves. Control strategies such as variable power factor (PF), fixed power factor (FPF) and volt/var control are have been developed and examined [130]. Nevertheless, the reactive power is very effective in MV networks but very inefficient in LV grids due to the high  $R/X$  ratios as demonstrated in [71].

Active power drooping can be used to prevent overvoltages but eventually leads to a significant losses of renewable energy and cost for the prosumer which will extend the payback period. The rapid development of battery energy storage systems (BESS) in the recent years has led to new opportunities to solve the technical and economic challenges of increasing the penetration level of renewables and decrease the CO<sub>2</sub> emissions even more compared to the targets set for 2020 [131]. To reduce the curtailed active power, BESS can be incorporated in the DER. BESSs have great potential to help with the power quality improvement in many aspects such as peak shaving, overvoltage mitigation and voltage unbalance mitigation [132–136]. BESS can have a significant advantageous impact in areas with high penetration of renewables [137, 138]. Furthermore, they can contribute to the load shifting caused by electric vehicles and plug-in electric vehicles [139]. In [140], an examination is carried out on a BESS connected at MV level and the results show that the reactive power control in combination with the active power curtailment is more economically viable compared to a BESS solution. As mentioned above however, LV grids have higher  $R/X$  ratio and the reactive power control is an ineffective solution for voltage control in these grids. In [127], different types of battery storage elements are examined and the findings reveal that the Li-Ion batteries can be a costeffective solution for improving the power qual-

ity by mitigating overvoltages during peak generation times. In [141], the authors have investigated the *Tesla PowerWall 2.0* and the findings of the paper show that this BESS can be a profitable investment. The authors in [142] have investigated BESSs with different capacities starting from 5 kWh to 25 kWh and according to this reference and studied scenarios these BESS can bring a profit to the prosumer between 200 to 350 euro per year. The authors in [143] report that the Tesla PowerWall 1.0 and 2.0 can be used for peer-to-peer energy supply and the price per kWh is around 0.075 € and 0.069 €, respectively. Therefore, the integration of BESS has the potential to become a very attractive solution for overvoltage mitigation in LV grids.

However, very often the integration of BESS is associated only with overvoltages while the voltage unbalance is completely neglected. Power quality issues such as overvoltages and voltage unbalance in areas with high penetration of renewables are examined in detail in [68]. In this study, the authors use the three-phase damping control strategy to mitigate the voltage unbalance and a droop controller to prevent overvoltages. The results revealed that this combination is able to increase the penetration of DER in LV grids, however some active power is drooped in order to keep the phase voltages within limits. Therefore, the objective of this chapter is to investigate the impact of energy storage on the voltage profiles, power quality and also investigate the grid performance, when the classical positive-sequence and the three-phase damping control strategies are used.

## 6.2 Control strategies description

### 6.2.1 Active power drooping

During periods of peak generation in combination with low loading levels, some feeders may suffer from overvoltages and voltage unbalance problems. Consequently, some of the DER must be turned off, which is known as hard active power curtailment. Eventually, this leads to loss of renewable energy and financial loss for the prosumer. An appropriate solution for this problem is the active power drooping. This solution also curtails active power but it does not disconnect the DER entirely. The active power curtailment, in combination with the positive-sequence and the three-phase damping control strategies, is implemented in [68] and it relies on local measurements such as voltages and currents at the inverter terminals. Thus the necessity of communication between the different DER that are connected in the same network could be avoided. Based on these measurements, an appropriate active power curtailment is applied such that the DER is still connected to the grid and renewable energy is being injected into it, but most importantly, the power quality is not deteriorated. Some of the outcomes of the project INCREASE [59] are published in [126] and the results revealed that the soft ac-

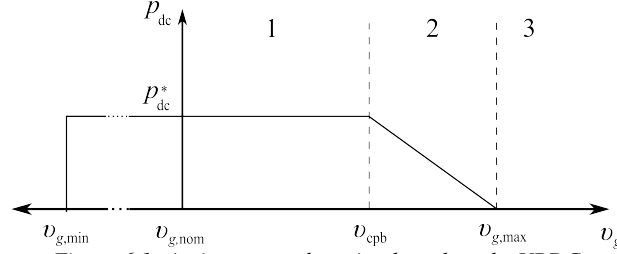


Figure 6.1: Active power drooping based on the VBDC

tive power curtailment is able to increase the energy yield with 50% compared to the hard active power curtailment. Therefore, in order to prevent overvoltages and maximise the renewable energy penetration, without introducing a secondary level control such as coordinated and multi-agent systems, the active power drooping is a preferable solution due to its simplicity, effectiveness and reliability.

This droop controller measures the rms values of the grid voltages and uses the maximum one among the three-phase voltages and this value is used on the  $x$  axis of the droop function as explained in Chapter 3. For more clarity, the active power drooping is shown in Fig. 6.1. If  $|\underline{v}_g|$  is in region 1, the droop controller allows the DER to inject all available power provided by the primary source. The first region ranges from the nominal grid voltage  $v_{g,nom}$  to the constant power band voltage  $v_{cpb}$ . Region 2, ranges from  $v_{cpb}$  to the maximum allowable grid voltage  $v_{g,max}$  and droops the injected active power in a linear way. If the grid voltage is above  $v_{g,max}$  then the DER is being disconnected from the grid and all renewable power is curtailed. The droop controller can be described mathematically by the following piecewise linear function:

$$p_{dc} = \begin{cases} 0, & \text{if } |\underline{v}_g| < v_{g,min} \\ p_{dc}^*, & \text{if } |\underline{v}_g| \leq v_{cpb} \\ p_{dc}^* \left(1 - \frac{|\underline{v}_g| - v_{cpb}}{v_{g,max} - v_{cpb}}\right), & \text{if } v_{cpb} < |\underline{v}_g| \leq v_{g,max} \\ 0, & \text{if } |\underline{v}_g| > v_{g,max} \end{cases} \quad (6.1)$$

To comply with EN50160 [8], parameters  $v_{g,min}$  and  $v_{g,max}$  are usually set to 0.9 and 1.1 p.u. respectively. The conditioning algorithm that ensures maximum power harvesting called a maximum power point tracking algorithm is also neglected because it is out of the scope of this work.

## 6.2.2 Controller for the battery energy storage system

The BESS controller is an important part of the DER and it has an impact of the overall performance of the total system. Some of the most important aspects of this controller are to maintain the storage elements in good condition, control the state-

of-charge and also source or sink power when requested by DER. The requested power by DER occurs when some specific circumstances are present. In literature, there are different control strategies developed for BESS based on different parameters. In [142, 144], two BESS strategies are proposed where the decision of storing or sourcing the energy is based on the available power from the primary source meaning that above a certain value of the peak power, BESS is charged and vice versa if the power is below a certain value. The drawback of this solution is overusing the BESS in times even when the grid voltages are within limits. In [145], a control strategy for BESS is proposed that is based on the grid voltage measurements and the battery is charged based on a certain voltage threshold. However, the voltage threshold when BESS is charging and discharging is chosen to be 1.00 p.u. which is very low and also a three-phase balanced grid is examined. Nevertheless, the three-phase four-wire LV feeders are unbalanced by nature due to asymmetrical loading by single-phase customers and also single-phase DER. This implies that a controller based on the power of the primary source would be more suitable. Nonetheless, as mentioned above these types of control are less effective. In [68], a droop controller is examined under unbalanced conditions and the results show that a better practice is to use the maximum rms value among the phase voltages and use this value to calculate the necessary active power drooping. Hence, in this chapter the same practice is adopted for the BESS controller. The battery controller checks whether or not the BESS is able to source or sink the calculated power and this procedure is executed in three major steps. In the first step, the requested battery power is calculated, then the battery power output is calculated based on the requested power and the maximum allowed by BESS. Finally, the SOC is calculated and the requested power is been sourced or sunk to the DER by taking into account the remaining energy in the battery.

As mentioned above, the droop controller relies on local measurements to droop the necessary active power and thus it prevents overvoltages. The same principle is adopted for the BESS controller in this chapter. Hence, the requested power by the BESS starts with the measurements of the grid voltages which is the first step (i) of the entire procedure. The process can be described with the following linear piecewise function:

$$P_{\text{BAT},r} = \begin{cases} P_{\text{BAT},\text{max}}, & \text{if } |v_g| < v_{g,\text{min}} \\ P_{\text{BAT},\text{max}} \left( \frac{v_{\text{bh},1} - |v_g|}{v_{\text{bh},1} - v_{g,\text{min}}} \right), & \text{if } v_{g,\text{min}} \leq |v_g| \leq v_{\text{bh},1} \\ 0 & \text{if } v_{\text{bh},1} \leq |v_g| \leq v_{\text{bh},2} \\ -P_{\text{dc}}, & \text{if } v_{\text{bh},2} \leq |v_g| \leq v_{\text{max}} \\ -P_{\text{BAT},\text{max}}, & \text{if } |v_g| > v_{g,\text{max}} \end{cases} \quad (6.2)$$

If  $|v_g|$  is lower than the minimum grid voltage  $v_{g,\text{min}}$  the calculated battery output is equal to the maximum battery power ( $P_{\text{BAT},\text{max}}$ ) that BESS is able to deliver

(source). If the grid voltage is between  $v_{g,\min}$  and the lower threshold of the discharge range  $v_{bh,1}$ , the calculated power is within the linear zone of the discharge region. The battery power output is 0 when the grid voltage is within the lower ( $v_{bh,1}$ ) and upper ( $v_{bh,2}$ ) thresholds of the BESS controller. When  $|\underline{v}_g|$  is greater than  $v_{bh,2}$  and lower than the maximum grid voltage  $v_{g,\max}$ , the droop controller is activated and the drooped power is used to charge the battery. In this case study,  $v_{bh,2}$  is chosen to be equal to  $v_{cpb}$ . Since in this region the battery is charged, then the sign of the battery output power becomes negative. In the last region,  $|\underline{v}_g|$  is greater than  $v_{g,\max}$  and therefore, all the energy available from the primary source is being drooped. Hence, the battery output power is negative and equals to the maximum battery power ( $p_{BAT,\max}$ ) that is allowed to charge the BESS.

In the second stage (ii) of the BESS controller, the battery power output is calculated based on the requested power, the maximum allowed power by the BESS and also the nominal power of the DER:

$$p_{BAT,o} = \begin{cases} \min(p_{dc} - p_{dc}^{\bullet}, p_{BAT,r}) & \text{if } p_{BAT,r} + p_{dc}^{\bullet} > p_{dc} \text{ and } p_{BAT,r} > 0 \\ p_{BAT,r} & \text{if } p_{BAT,r} + p_{dc}^{\bullet} < p_{dc} \text{ and } p_{BAT,r} > 0 \\ \max(-p_{BAT,\max}, p_{BAT,r}, -p_{dc}^{\bullet}) & \text{if } p_{BAT,r} < 0 \end{cases} \quad (6.3)$$

If the battery power request  $p_{BAT,o}$  is positive, then a check is done if the sum of  $p_{BAT,r}$  plus the available power  $p_{dc}^{\bullet}$  is greater than the nominal power  $p_{dc}$ . If this statement is true, then the minimum between the remainder to the nominal power and the  $p_{BAT,r}$  is selected. When the sum of the available power  $p_{dc}^{\bullet}$  and  $p_{BAT,r}$  is lower than  $p_{dc}$ , then the battery power output is equal to the requested power  $p_{BAT,r}$ . These two checks are performed when power is being injected into the BESS. In case of power sourcing from BESS to DER, a check is performed between the maximum charging power of BESS, the requested power  $p_{BAT,r}$  and the available power at the dc side. The checks are performed in order to deal with the constraints imposed by the power ratings of the power electronic converter and inverter embedded in BESS and DER, respectively.

In the final stage (iii), the exchanged power  $p_{BAT}$  of the BESS and the DER is calculated, based on the SOC and requested battery output power:

$$p_{BAT} = \begin{cases} \max(p_{BAT,o}, -p_{BAT,\max}) & \text{if } SOC - p_{BAT,o}\eta\frac{\Delta t}{C_{BAT}} < 1.0 \\ (1 - SOC_{i-1}) * \frac{C_{BAT}}{\Delta} & \text{if } SOC - p_{BAT,o}\eta\frac{\Delta t}{C_{BAT}} \geq 1.0 \\ \min((p_{dc} - p_{dc}^{\bullet}), p_{BAT,o}) & \text{if } p_{BAT,o} + p_{dc}^{\bullet} > p_{dc} \text{ and } p_{BAT,o} > 0 \\ p_{BAT,o} & \text{if } p_{BAT,o} + p_{dc}^{\bullet} < p_{dc} \text{ and } p_{BAT,o} > 0 \end{cases} \quad (6.4)$$

where  $\eta$  is the charge and discharge efficiency of the BESS,  $C_{BAT}$  is the capacity of BESS,  $\Delta t$  is the time between the samples of BESS controller or the time

between the load and solar profile measurements which is 15 min.  $SOC_{i-1}$  is the previous state of the SOC. The SOC is calculated as follows:

$$SOC_{i+1} = SOC_i + \int_0^{\Delta t} (P_{BAT} \cdot \eta) dt \quad (6.5)$$

In this stage, the SOC is checked and the battery controller ensures that the minimum and maximum battery charge is in between 20% and 100%. Furthermore, if  $P_{BAT}$  is positive, the storage will only be discharged until 80% or 50% depth of discharge (DoD), whether it is morning or afternoon, respectively. This distinction is made to ensure that in the evening enough energy remains in BESS that can be used during the morning peak load. Therefore, the initial condition of the SOC at midnight is 50%.

Finally, the used curves of the droop and BESS controller are depicted in Fig. 6.2 (a) and (b), respectively. When  $|\underline{v}_g|$  is greater than  $v_{g,nom}$ , the used droop controller behaves as the one shown in Fig. 6.1 and described by (6.1). Region 1' and 2' are active if the grid voltage is lower than  $v_{g,nom}$  and  $v_{g,min}$ , respectively. In these region, the control strategy tries to support the grid voltage by consuming energy from BESS plus the primary source and injecting it into the grid. Note that in the first quadrant, the droop takes into account the maximum among the phase voltages to prevent overvoltages in any phase, while in quadrant IV the droop is driven by the minimum of the phase voltages to prevent undervoltages. This controller is then described by using the following linear piecewise function:

$$p_{dc} = \begin{cases} p_{dc}^{\bullet} + P_{BAT}, & \text{if } |v_g| \leq v_{bh,1} \\ p_{dc}^{\bullet}, & \text{if } v_{bh,1} < |v_g| \leq v_{cpb} \\ p_{dc}^{\bullet} \left(1 - \frac{|v_g| - v_{cpb}}{v_{g,max} - v_{cpb}}\right), & \text{if } v_{cpb} < |v_g| \leq v_{g,max} \\ 0, & \text{if } |v_g| > v_{g,max} \end{cases} \quad (6.6)$$

In [140], the drooping point value (in this chapter called constant power power band) is chosen to be 1.04 p.u. and maximum active power curtailment is applied when the grid voltage is above 1.05 p.u. These values will almost lead to a constant active power curtailment considering the fact that the initial settings of the MV/LV transformers are set to similar levels. In [68], a value for  $v_{cpb}$  of 1.06 p.u. is investigated and obtained results showed that such a value is more suitable if used in droop curves when DER are equipped with the positive-sequence control strategy and a droop controller.

The BESS controller is depicted in Fig. 6.2 (b). In region 1 the grid voltage  $|\underline{v}_g|$  is lower than  $v_{g,min}$  and maximum battery power is requested. Region 2 is active if the grid voltage  $|\underline{v}_g|$  is between  $v_{g,min}$  and  $v_{bh,1}$ . In this region, power is also been requested from BESS but it is associated with the grid voltage  $|\underline{v}_g|$  and as can be seen from (6.2) a positive power is been requested from BESS. Region 3 ranges from  $v_{bh,1}$  to  $v_{bh,2}$  and zero power is requested if  $|\underline{v}_g|$  falls within

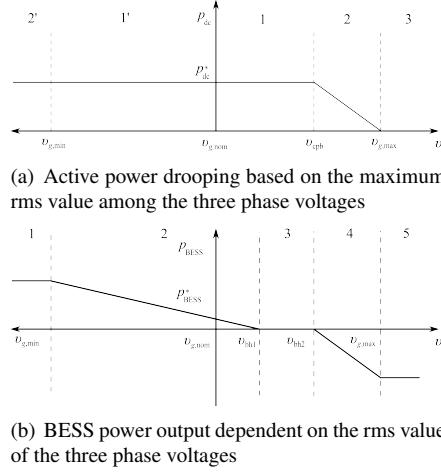


Figure 6.2: Active power droop controller and BESS controller used for the integration in the examined control strategies

this interval. As can be seen from (6.2) a negative power will be requested if the grid voltage is in region 4. Droop parameter  $v_{bh,2}$  is chosen to be equal to  $v_{cpb}$  thus the BESS is charged only when active power is drooped to prevent overvoltages. Finally, maximum power is been consumed by BESS if the grid voltage is above  $v_{g,max}$ . Note that this controller takes into account the maximum among the three-phase voltages when BESS is charged to prevent overvoltages and to prevent undervoltages the minimum rms voltage value is chosen if the BESS is discharged.

To improve the grid efficiency, the droop and BESS controller parameters could be set to different values depending on the grid properties. Moreover, a secondary layer of control could use forecasts to adjust these values and thus further improve the grid performance. However, this requires a secondary level of control that sets these parameters for the different DER individually which is not the scope of this work.

### 6.2.3 Positive-sequence control strategy

The most common practice for controlling three-phase inverter-connected DER to the distribution grid is done by exchanging only positive-sequence current. This comes from the fact that most of the three-phase angle detection techniques are based on phase locked loop (PLL) algorithms using a synchronous reference frame [45]. In other words the three-phase PLLs use a coordinate transformation from  $abc$  to  $dq$  [46] and, therefore, the output signals of these PLLs have phase angles corresponding to the positive-sequence component of the grid voltage [46, 49, 146, 147]. An analytical model of the positive-sequence control strategy can then be

obtained as:

$$\begin{aligned}
 \underline{i}_a &= \frac{1}{3} \left\{ g_1 \left[ |\underline{v}_a| e^{j\theta_a} + |\underline{v}_b| e^{j(\theta_b + \frac{2\pi}{3})} + |\underline{v}_c| e^{j(\theta_c - \frac{2\pi}{3})} \right] \right\} \\
 \underline{i}_b &= \frac{1}{3} \left\{ g_1 \left[ |\underline{v}_b| e^{j\theta_b} + |\underline{v}_a| e^{j(\theta_a - \frac{2\pi}{3})} + |\underline{v}_c| e^{j(\theta_c + \frac{2\pi}{3})} \right] \right\} \\
 \underline{i}_c &= \frac{1}{3} \left\{ g_1 \left[ |\underline{v}_c| e^{j\theta_c} + |\underline{v}_a| e^{j(\theta_a + \frac{2\pi}{3})} + |\underline{v}_b| e^{j(\theta_b - \frac{2\pi}{3})} \right] \right\}
 \end{aligned} \tag{6.7}$$

where  $v_x$  and  $\theta_x$  are the respective phase voltages and angles and  $g_1$  is the fundamental input conductance of the inverter. The later ensures the power balance between the ac and the dc side and it is calculated by using the following equation:

$$g_1 = \frac{3 p_{dc}^{\bullet}}{\sum |v_x|^2 + 2 \sum_{x \neq y} |v_x| |v_y| \cos(\theta_x - \theta_y - \frac{2\pi}{3})} \tag{6.8}$$

Additional information about the fundamental conductance and its mathematical extraction can be found in [68, 71].

## 6.2.4 Three-phase damping control strategy

The second most common problem in areas with high penetration of renewable energy resources is the voltage unbalance in three-phase LV grids. Usually the three-phase DERs are connected via a three-phase three-wire connection and inject only positive-sequence currents. Even if these DERs would have been equipped with voltage unbalance mitigation control strategies, then they would have been able to impact only the negative-sequence component due to the three-wire interface. Furthermore, [8] recommends only limits to the negative voltage unbalance factor which is the ratio of the negative to positive-sequence components. Nevertheless, the zero-sequence component has a huge impact on the penetration of DER, especially when asymmetrical loading and current injection are involved. The three-phase damping control strategy studied in [18, 68, 69] is able to successfully mitigate the voltage unbalance at the point of common coupling (PCC). The idea behind the three-phase damping control strategy is as follows: the desired reaction of the three-phase damping control strategy is to behave resistively towards the zero- and negative-sequence voltage components in LV networks [18] [41, 148]. The injected currents by the damping control strategy can be described mathematically by the following set of equations:

$$\begin{aligned}
\dot{i}_a &= \frac{1}{3} \left\{ g_1 \left[ |\underline{v}_a| e^{j\theta_a} + |\underline{v}_b| e^{j(\theta_b + \frac{2\pi}{3})} + |\underline{v}_c| e^{j(\theta_c - \frac{2\pi}{3})} \right] + \right. \\
&\quad \left. g_d \left[ 2|\underline{v}_a| e^{j\theta_a} - |\underline{v}_b| e^{j(\theta_b + \frac{2\pi}{3})} - |\underline{v}_c| e^{j(\theta_c - \frac{2\pi}{3})} \right] \right\} \\
\dot{i}_b &= \frac{1}{3} \left\{ g_1 \left[ |\underline{v}_b| e^{j\theta_b} + |\underline{v}_a| e^{j(\theta_a - \frac{2\pi}{3})} + |\underline{v}_c| e^{j(\theta_c + \frac{2\pi}{3})} \right] + \right. \\
&\quad \left. g_d \left[ 2|\underline{v}_b| e^{j\theta_b} - |\underline{v}_a| e^{j(\theta_a - \frac{2\pi}{3})} - |\underline{v}_c| e^{j(\theta_c + \frac{2\pi}{3})} \right] \right\} \quad (6.9) \\
\dot{i}_c &= \frac{1}{3} \left\{ g_1 \left[ |\underline{v}_c| e^{j\theta_c} + |\underline{v}_a| e^{j(\theta_a + \frac{2\pi}{3})} + |\underline{v}_b| e^{j(\theta_b - \frac{2\pi}{3})} \right] + \right. \\
&\quad \left. g_d \left[ 2|\underline{v}_c| e^{j\theta_c} - |\underline{v}_a| e^{j(\theta_a + \frac{2\pi}{3})} - |\underline{v}_b| e^{j(\theta_b - \frac{2\pi}{3})} \right] \right\}
\end{aligned}$$

where  $g_d$  is the fundamental damping conductance of the inverter which has an opposite sign of  $g_1$  in case of power injection to the grid. The terms related to  $g_1$  can be interpreted as the steady-state value of the fundamental component of the injected current. These terms are adapted by the dc bus-voltage controller in order to balance the power exchanged with the grid. Since the bus voltage controller is slow,  $g_1$  is slowly varying. The terms related to  $g_d$  emulate the resistive behaviour towards the zero- and negative-sequence voltage components. More information about the derivation of the three-phase damping control strategy can be found in [68]

In practice, the power balance between the dc side and the utility grid is maintained by using a dc-bus controller, the output of which is the fundamental conductance  $g_1$  of the voltage source inverter (VSI) [36]. In order to incorporate the input conductance into a simulation model, the following equation for the power balance can be used:

$$\begin{aligned}
g_1 &= \frac{3 p_{dc}^{\bullet}}{\sum |\underline{v}_x|^2 + 2 \sum_{x \neq y} |\underline{v}_x| |\underline{v}_y| \cos(\theta_x - \theta_y - \frac{2\pi}{3})} \\
&\quad - 2g_d \frac{\sum |\underline{v}_x|^2 - \sum_{x \neq y} |\underline{v}_x| |\underline{v}_y| \cos(\theta_x - \theta_y - \frac{2\pi}{3})}{\sum |\underline{v}_x|^2 + 2 \sum_{x \neq y} |\underline{v}_x| |\underline{v}_y| \cos(\theta_x - \theta_y - \frac{2\pi}{3})} \quad (6.10)
\end{aligned}$$

The term of the positive-sequence fraction describes the exchanged active power with the grid and the term determined by the second fraction compensates also for the power of the zero-sequence and the negative-sequence components [18]. This control strategy mitigates the voltage unbalance by injecting higher currents in the phase with lower voltage and lower current in the phase with higher voltage and

the damping capabilities of this control strategy are determined by the damping conductance  $g_d$  which can be calculated by using the nominal ratings of the DER:

$$G_d = \frac{P_{\text{DCnom}}}{V_{\text{nom}}^2} \quad (6.11)$$

where  $P_{\text{DCnom}}$  is the nominal power of the inverter and  $V_{\text{nom}}$  is the nominal grid voltage. In a p.u. system the damping conductance is expressed as:

$$g_d = \frac{P_{\text{nom}}/P_{\text{DCbase}}}{V_{\text{nom}}^2/V_{\text{base}}^2} \quad (6.12)$$

where  $P_{\text{base}}$  is the base power of the power electronic inverter and  $V_{\text{base}}$  is the base value of the grid voltage. From (6.9) it can be seen that the value of the damping conductance plays an important role in the resistive behaviour towards the zero- and the negative-sequence voltage components. In [18, 41, 46, 54–56], the authors have used a fixed value of the damping conductance and it was chosen to be 1 p.u. Therefore, further investigation of the value of this parameter can be made in order to improve the performance of the three-phase damping control strategy. More information about the detailed description of the three-phase damping control strategy can be found in [68, 79] and also in Chapter 3.

## 6.3 Simulation results

### 6.3.1 Model description

#### 6.3.1.1 Grid data

The incorporation of a storage system into the three-phase damping control strategy is tested by means of simulations on an existing feeder which is shown in Fig. 6.3. This feeder is a small part of an 78 node LV network located in Suha, Slovenia. The MV/LV transformer of Dyn5 type and it has a nominal power of 250 kVA, short circuit voltage of 4% while the no load losses are 325 W and 3250 W, respectively. The primary and secondary nominal voltages are 20 kV and 0.4 kV, respectively. The voltages at the secondary side are set to be 1.04 p.u. which is a typical setting used by the DSO in order to avoid undervoltages to the most remote customers when high loading conditions are present. The zero- and positive-sequence impedances of the cables in the feeder as well as their lengths are listed in Table 6.1.

#### 6.3.1.2 DER, BESS and load data

In this chapter, four DERs are considered to be connected to the LV feeder and their nominal powers are as listed in Table 6.2. The rated power of all DER is

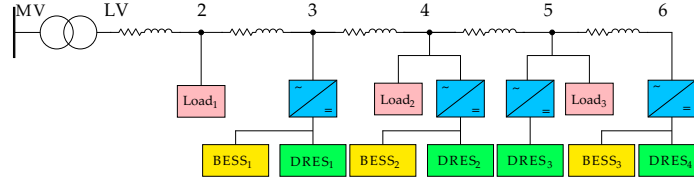


Figure 6.3: Feeder topology used to access the performance the examined control strategies

| LINE  | $R_1$ ( $\Omega/\text{km}$ ) | $X_1$ ( $\Omega/\text{km}$ ) | $C_1$ (nF/km) | $R_0$ ( $\Omega/\text{km}$ ) | $X_0$ ( $\Omega/\text{km}$ ) | Length (km) |
|-------|------------------------------|------------------------------|---------------|------------------------------|------------------------------|-------------|
| LV-2  | 0.456                        | 0.088                        | 250           | 4                            | 0.0877                       | 0.057       |
| 2 - 3 | 0.468                        | 0.085                        | 250           | 4                            | 0.0851                       | 0.094       |
| 3 - 4 | 0.48                         | 0.08                         | 250           | 4                            | 0.08                         | 0.025       |
| 4 - 5 | 0.462                        | 0.083                        | 250           | 4                            | 0.0833                       | 0.132       |
| 5 - 6 | 0.924                        | 0.076                        | 200           | 4                            | 0.0758                       | 0.066       |

Table 6.1: Properties of the LV feeder.

chosen such that overvoltages occur at the feeder if maximum renewable generation is present and the classical positive-sequence control strategy is employed in all DER. Thus, no further penetration of other DERs is possible. All DERs are chosen to have the same power ratings. This decision, although arbitrary will help to better illustrate and assess the effect of the power drooping and BESS impact on the total renewable energy loss. DERs with rated power above 5 kW are three-phase connected and equipped with active power drooping and BESS. One of the test cases is formed when the classical positive-sequence control strategy is equipped in all three-phase DERs and this test case is used as reference one.

A BESS with 25 % of the peak power of the DER is proposed in [149], however, this capacity is too small when high penetration of renewables is present. In [86], a small BESS is incorporated in single-phase residential PV installations in an LV grid of 30 nodes. By using synthetic load and irradiation profiles, a probability study is performed to estimate the occurrence of overvoltages. The results showed that a capacity of about 4/5 the peak power is needed to overcome the overvoltages. A large network is studied in [150] and it consists of 52 customers and each one of them has installed 5.2 kWp PV installation. All PV installations are connected via three-phase inverters and the authors consider the grid to be balanced. However, the results of the conducted examinations showed that the capacity of BESS, needed to prevent overvoltages in a grid with 50% penetration of renewables, should be equal to the peak power of the PV system and almost 5 times capacity is needed if 100 % renewable penetration is present.

In addition, the positive-sequence control and the three-phase damping control strategies are tested without a BESS which forms the reference case  $C0$ . As of the storage, two different storage capacities are examined as listed in Table 6.2. Case

| DER                     | Rated Active Power | Case 0 capacity/power | Case 1 capacity/power | Case 2 capacity/power |
|-------------------------|--------------------|-----------------------|-----------------------|-----------------------|
| Node 2 DER <sub>1</sub> | 20 kW (Y)          | 0 kWh/ 0 kW           | 7 kWh/3.3 kW (0.35)*  | 14 kWh/5 kW (0.70)*   |
| Node 4 DER <sub>2</sub> | 20 kW (Y)          | 0 kWh/ 0 kW           | 7 kWh/3.3 kW (0.35)*  | 14 kWh/5 kW (0.70)*   |
| Node 5 DER <sub>3</sub> | 5 kW/bn            | -                     | -                     | -                     |
| Node 6 DER <sub>4</sub> | 20 kW(Y)           | 0 kWh/ 0 kW           | 7 kWh/3.3 kW (0.35)*  | 14 kWh/5 kW (0.70)*   |

\* ratio between the capacity of BESS and the nominal power ratings of the DER

Table 6.2: Nominal power of DER and storage capacity

|                | $g_d = 0$ p.u. | $g_d = 5$ p.u. | $g_d = 10$ p.u. | $g_d = 20$ p.u. | $g_d = 40$ p.u. |
|----------------|----------------|----------------|-----------------|-----------------|-----------------|
| Case 0 (APD)   | C0S1           | C0S2           | C0S3            | C0S4            | C0S5            |
| Case 1 - 7kWh  | C1S1           | C1S2           | C1S3            | C1S4            | C1S5            |
| Case 2 - 14kWh | C2S1           | C2S2           | C2S3            | C2S4            | C2S5            |

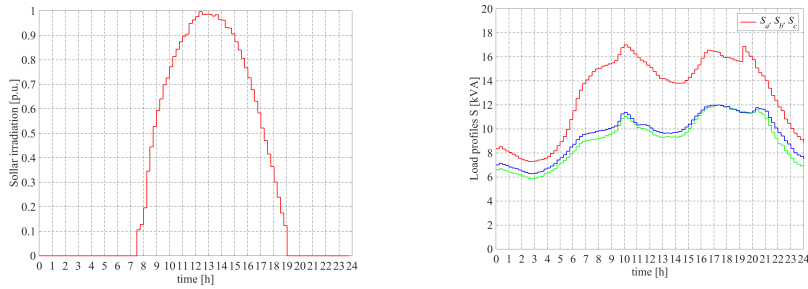
Table 6.3: Examined test cases

study C1 (i) is defined when *Tesla PowerWall 1.0 DC* is used which has the ability to source and sink 3.3 kW and it has a maximum capacity of 7 kWh. Case study C2 (ii) uses one *TeslaWall 2.0 DC* system. Their specifications are given in [151], and they show that these systems have a round trip efficiency of 91%. These capacity values give ratios of 0.3 to 0.7 with respect to the rated power of the DERs which is within the range of the values suggested in [86,150]. The positive-sequence control strategy forms the sub-case (S1). Eq. (6.9) shows that the resistive behaviour of the three-phase damping control strategy is dependent on the damping conductance  $g_d$ . Hence, four different values of the damping conductance  $g_d = 5$ ,  $g_d = 10$ ,  $g_d = 20$  and  $g_d = 40$  p.u. are further investigated which form four additional sub cases S2, S3, S4 and S5, respectively. Analytically speaking, the three-phase damping control strategy is a special case of the positive-sequence control strategy i.e. if  $g_d = 0$  p.u. the damping control strategy becomes the positive-sequence control strategy. Therefore, later in the chapter  $g_d = 0$  p.u. will be used to refer to the positive-sequence control strategy. Finally, the formed cases and sub-cases are compared to a case where the DER are not equipped with storage. Thus the performance of the three-phase damping control strategy and the BESS can be assessed individually. In summary, all test cases are presented in Table 6.3. Note that active power drooping is incorporated into all cases and sub-cases whether or not storage is considered.

The aggregated load profiles that are measured at the terminals of the MV/LV transformer as well as the solar irradiation profile are depicted in Fig. 6.4. Both load and irradiation profiles are measured on a 15 min. basis. The apparent power measured at the beginning of the feeder is distributed over the PQ loads based on their power ratings and an asymmetrical load flow simulation is ran for each time slot.

| Load              | Rated Active power | Rated reactive power |
|-------------------|--------------------|----------------------|
| Node 3 Load 1 (Y) | 4.5/2.7/2.7 kW     | 2.17/1.3/1.3 kvar    |
| Node 4 Load 2 (Y) | 3.6/3.6/3.6 kW     | 1.74/1.74/1.74 kvar  |
| Node 6 Load 3 (Y) | 5.4/3.6/3.6 kW     | 2.61/1.74/1.74kvar   |

Table 6.4: Nominal power of the loads and type of connection



(a) Solar irradiation profile used in the simulation model (b) Load profiles of the different phases measured at the beginning of the feeder

Figure 6.4: Solar irradiation and load profiles used in the simulation model

### 6.3.1.3 Short description of the Simulink model

The data of the solar irradiation and load profiles are depicted in Fig. 6.4 (a) and (b), respectively. The load profiles are obtained when no DERs are connected. These data are put in the simulation model as described in [66]. The simulation model that uses Matlab & Simulink in [126] is a time domain one which is able to solve asymmetrical power flows and it is used to perform the time series simulations in this chapter. Since the model is a time-domain-based one, the duration of one simulation can vary between 10 to 20 min. Therefore, reducing the simulation time is very important to speed the developed model up. A simulation is ran and when a steady-state regime is achieved, the simulation is stopped automatically and the data are stored in the workspace of Matlab.

### 6.3.1.4 Integration of BESS into DER

The energy storage unit is considered as a black box which is connected to the dc bus of the DER as shown in Fig. 6.5. It is characterised only by the listed capacity and round trip efficiency while the behaviour of the power electronic dc-dc converter is neglected. This assumption significantly simplifies the simulation model and the exchanged power with the dc-bus is calculated by using (6.4). These assumptions, although arbitrary, do not deteriorate the accurate representation of

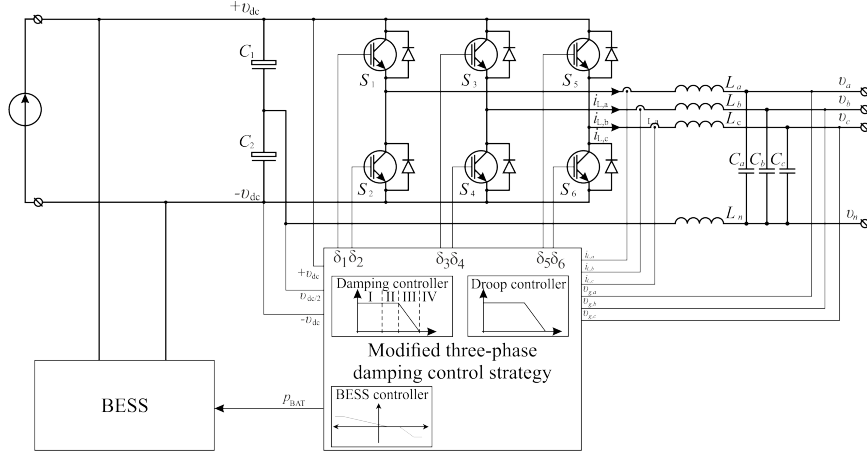


Figure 6.5: Integration of BESS into the DER

the obtained simulation results.

The droop parameters are chosen to be  $v_{g,\min} = 0.9$  p.u.  $v_{g,\max} = 1.1$  p.u.  $v_{cpb} = 1.06$  p.u. The BESS controller is designed to draw power only if active power drooping is applied therefore, the upper BESS threshold  $v_{bh,2}$  is set to be equal to  $v_{cpb}$ . In practice, areas with high penetration of DER usually do not suffer from severe undervoltage problems hence, the lower threshold  $v_{cpb}$  of the BESS controller is set to 1.04 p.u. Zero power is requested from BESS if the grid voltage is within the range of  $v_{bh,1} < v_g \leq v_{bh,2}$ .

### 6.3.2 Simulation results

The measured unbalanced load profiles show that phases  $b$  and  $c$  are the least loaded ones. Taking into account that an additional single-phase DER is connected at node 5 then the highest phase voltage among all will be the one of phase  $b$ . Hence, during high solar irradiation levels, the droop and BESS controllers will be mainly driven by the rms values of  $|v_b|$  because this phase has the highest voltage. The considered scenario of testing the presented grid configuration i.e. DER, solar irradiation and load profiles, does not lead to undervoltages so neither the droop nor the BESS controllers are operating in the undervoltage region. Hence, in this particular case, only phase voltage  $v_b$  is of interest for the further analysis of integrating BESS into the DER. Fig. 6.6 (a) to (g) show the obtained simulation results for phase voltage profile  $v_b$  across the feeder for an entire day when different controls strategies and BESS sizes are applied. The abbreviation SB stands for “slack bus” which is at the medium voltage side and LV stands for low voltage side which is after the distribution transformer. Fig. 6.6 (a) represents the case when no control is applied and it can be clearly seen that there are times when

overvoltages occur in the end of feeder when high solar irradiation is present. The overvoltages occur at node 4 to 6 and in practice, DER<sub>2</sub> and DER<sub>4</sub> would have been disconnected from the grid due to the embedded overvoltage on-off control algorithm. At a closer look at the obtained simulation results, it can be seen that DER<sub>2</sub> would have been disconnected around 13h00. Due to the unbalanced loading and the neutral point shifting effect, studied in [15], DER<sub>3</sub> and DER<sub>4</sub> are subjected to overvoltages almost at the beginning and end of the solar irradiation profile which eventually would lead to incredible loss of renewable energy due to hard curtailment.

The simulation results of case *COS0* are presented in Fig. 6.6 (b) where the positive-sequence control strategy with active power drooping is investigated. In this case (and all other that follow), active power drooping is incorporated and it can be seen that phase voltage  $v_b$  does not exceed 1.1 p.u. during the peak generation periods. To limit the amount of the presented data, only the extreme cases ( $g_d = 0$  and 40 p.u. as well as storage of 7kWh and 14 kWh) will be considered for further interpretation. In Fig. 6.6 (c) the simulation results of the three-phase damping control strategy are presented where the damping conductance is  $g_d = 40$  p.u. and active power drooping is applied (*COS5*). Since active power drooping is used in this case, there are no overvoltages that are present at the far end of the feeder. Furthermore, because of the voltage unbalance mitigation properties of this control strategy, higher currents are being injected in the other two phases and lower current into phase  $b$ . Consequently, the yellow colour in Fig. 6.6 (c) is less intensive which means that  $v_b$  is closer to its nominal value at the end of the feeder.

The simulation results, obtained when case *CIS1* is used in all DERS, are presented in Fig. 6.6 (d). Since active power drooping and BESS of 7kWh are incorporated in all DERS, overvoltages are prevented across the feeder. Despite the BESS, the yellow density of Fig. 6.6 (d) resembles very much the one of (b). If case *CIS5* is considered, the high value of the damping conductance helps with improving the resistive behaviour and the voltage profile of  $v_b$  and the later one has significantly lower voltages as shown in Fig. 6.6 (e).

The obtained simulation results of BESS with capacity of 14 kWh and positive-sequence control strategy are shown in Fig. 6.6 (f). As anticipated, overvoltages are not present across the feeder for the entire day because of the droop controller. The intensity of the yellow colour slightly differs from cases *COS1* and *CIS1* where a small difference in the morning and evening hours can be seen. Nevertheless, the similarity between *COS1*, *CIS1* and *C2S1* is very high which implies that even if a BESS with is doubled capacity is used, the voltage profile of  $v_b$  will be rather the same if the positive-sequence control strategy is used. When case *C2S5* is considered, the high damping conductance value in combination with a BESS with storage capacity of 14kWh helps to maintain even lower voltage levels in phase  $b$ .

The simulation results of this case are presented in Fig. 6.6 (g). In this case, there is a small difference in the yellow density around the noon hours but overall the colour map and density is quite similar to cases *COS5* and *CIS5*. A detailed description of the amount of the drooped power and the SOC are given in the next paragraphs.

### 6.3.2.1 BESS controller operating principle

The operation of the used BESS controller can be seen in Fig. 6.7 (a) to (m). In this figure, the different inflection points of the SOC curves are examined. Note that the interpretation of the results is focused on the charging and discharging points of the curves. In addition, the performance of the BESS is examined when used in the positive-sequence and the three-phase damping ( $g_d = 20$  p.u.) control strategies and the point under consideration plus the previous point are used to explain the controller actions. All SOC curves of the BESS controller are depicted in Fig. 6.7 (a).

The BESS controllers are enabled in the beginning of the morning peak loading and at point  $t_0$  the voltage in phase  $v_a$  is the lowest among the phases and low enough to trigger all BESS controllers to draw power from the batteries. Voltage profiles of  $v_a$  of both examined control strategies are shown in Fig. 6.7, (b) where by using a solid line are shown the results at  $t_0$  and a dashed line is used to depict the results at point  $t_0+1$ . As it can be seen from these two samples, the phase voltages for the positive-sequence and the damping control strategies are quite close to each other. Hence, the voltage unbalance is not dominant yet. From  $t_0$  till  $t_1$ , all BESS are being depleted since all phase voltages are lower than  $v_{bh,1}$ .

The minimum of the SOC curve of BESS<sub>3</sub>, when storage is combined with the positive-sequence control strategy, is located at time instance  $t_1$ . At time instance  $t_1+1$  the solar irradiation is high enough to rise the phase voltage  $v_b$  above  $v_{cpb}$  at node 6 and DER<sub>4</sub> starts to droop power. According to (6.2) and (6.6) all drooped power is redirected to charge the BESS<sub>3</sub>. The voltage profiles of phase voltages  $v_b$  are depicted in Fig. 6.7 (c). The phase voltage  $v_b$  is lower than  $v_{bh,1}$  for almost 2h 45min and BESS<sub>3</sub> is depleted down to 0.3 p.u. It is important to note that the three-phase damping control strategy mitigates the voltage unbalance very well and for this time instance, the voltage profile is kept within  $v_{bh,1}$  and  $v_{cpb}$  which does not activate the droop nor the BESS controllers. The interpretation of the simulation results for time instances  $t_2$ ,  $t_2+1$ ,  $t_3$  and  $t_3+1$  is similar to time instance  $t_1$  with the only difference that DER<sub>2</sub> and DER<sub>1</sub> start drooping active power at  $t_2+1$  and  $t_3+1$ , respectively. The voltage profiles of phase voltage  $v_b$  are shown in Fig. 6.7 (d) and (e), respectively. Note that the BESS controllers of the DERS, which are equipped with the three-phase damping control strategy are still not activated because all phase voltages are lower than  $v_{bh,1}$ .

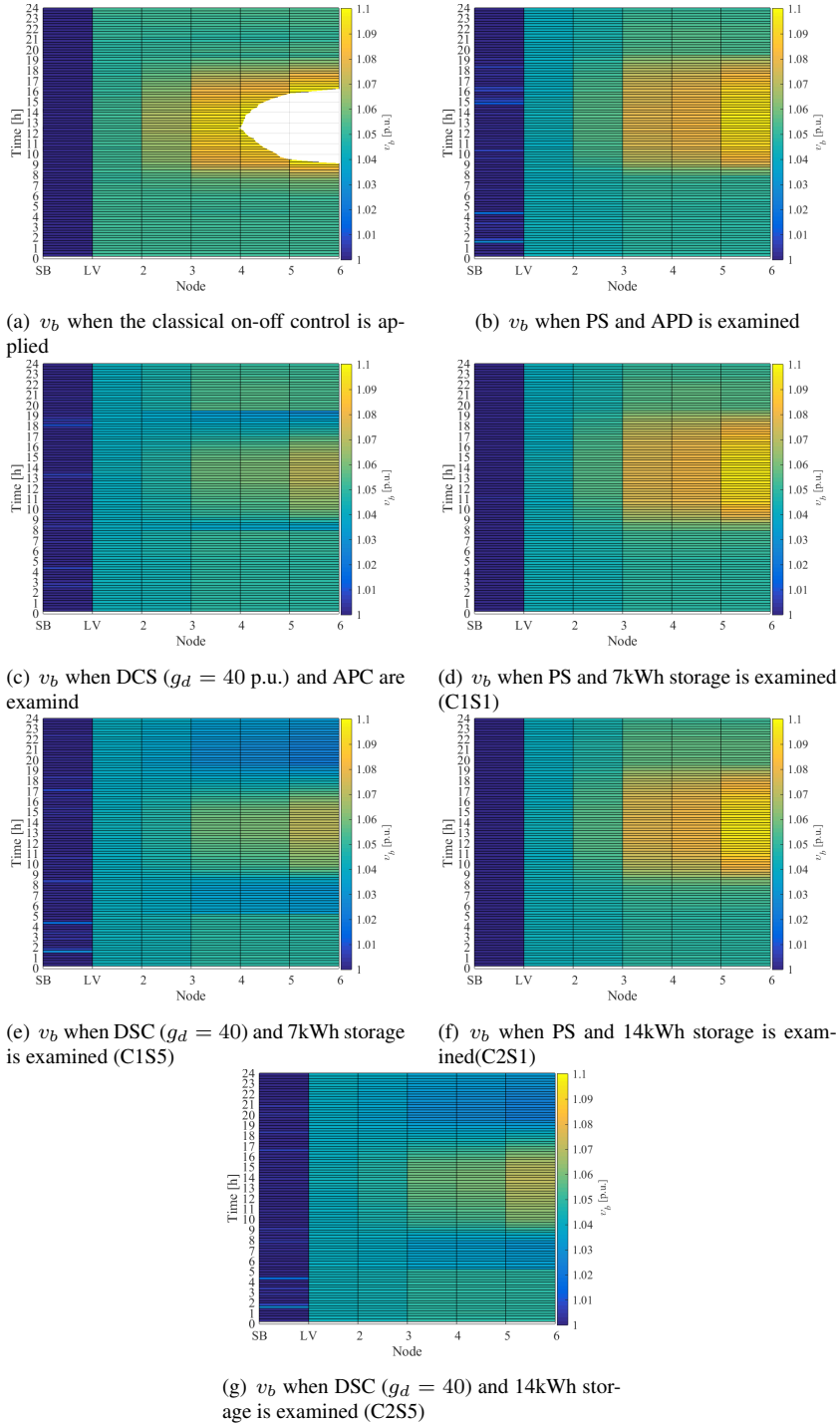
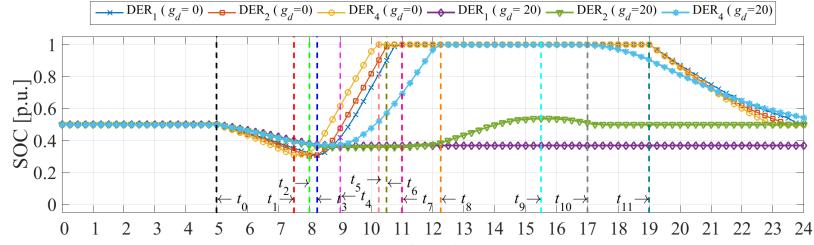


Figure 6.6: Voltage profile of phase b during an entire day when the positive-sequence and three-phase damping (under two values of  $g_d$ ) control strategies and storage capacities are examined



(a) SOC curves when positive-sequence and damping control strategies are examined

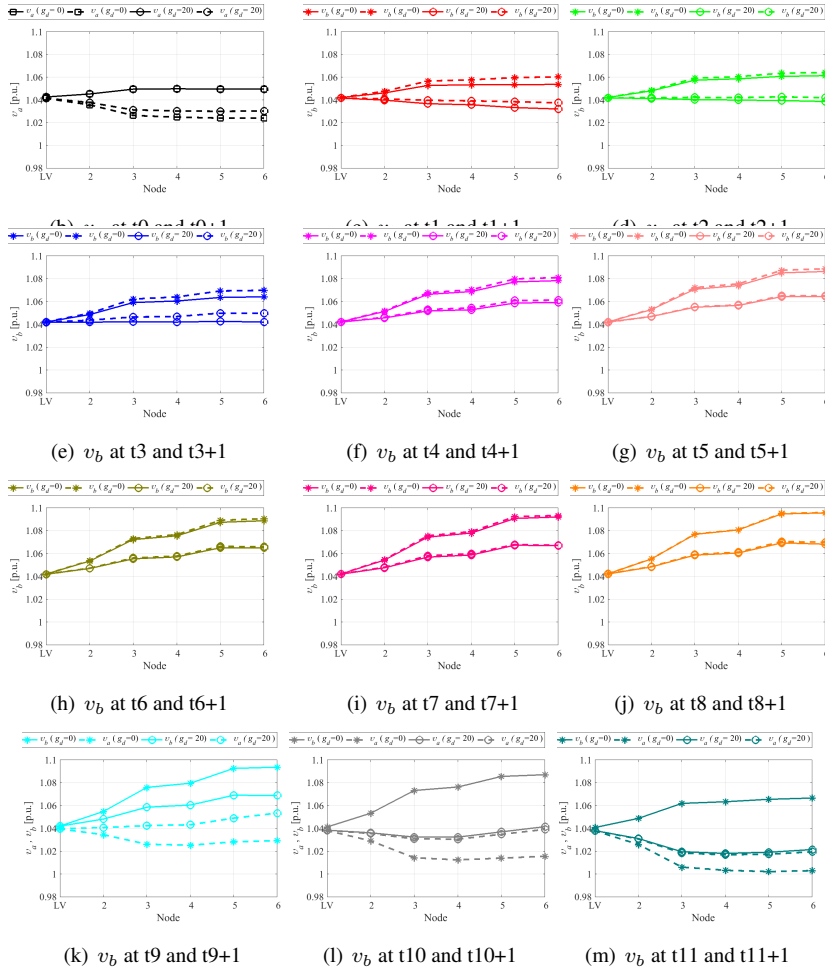


Figure 6.7: Reaction of the BESS controllers when positive-sequence ( $g_d = 0$ ) p.u. and three-phase damping control ( $g_d = 20$ ) p.u. strategies are examined at different time instances

The positive-sequence control strategy droops considerable amount of power which results in fully charged BESS for DER<sub>1</sub>, DER<sub>2</sub> and DER<sub>4</sub> at time instances t7, t6 and t5, respectively. This means that all BESS are fully charged in about 2h45min and the rest of the drooped renewable energy is being lost. The voltage profiles of phase voltage  $v_b$  for time instances t5, t6 and t7 are depicted in Fig. 6.7 (g), (h) and (i), respectively.

Unlike the positive-sequence control strategy, the three-phase damping control strategy starts drooping power way later during the day due its voltage unbalance mitigation abilities. The inflection point of SOC<sub>3</sub> occurs at time instance t5 and at t5+1 starts the active power drooping. The three-phase damping control strategy is able to provide some support to the grid voltages by depleting BESS<sub>3</sub> until 9h00 which is 1h30min more compared to the positive-sequence control strategy (for DER<sub>4</sub>) but this does not necessarily means that BESS is depleted deeper. Because of the balancing abilities of the three-phase damping control strategy the lowest phase voltage is supported, allowing the BESS<sub>3</sub> controller to exchange smaller quantities of power but for a longer period. Furthermore, BESS<sub>3</sub> is discharged down to about 0.37 p.u. whereas the positive-sequence discharges the BESS to a deeper level for a shorter amount of time. At time instance t8 BESS<sub>3</sub> is fully charged which is 2h00 later compared to DER<sub>4</sub> equipped with the positive-sequence control strategy which means less renewable energy is going to be lost. In addition, at this time instance, the minimum of SOC<sub>2</sub> occurs and at t8+1 phase voltage  $v_b$  is greater than  $v_{cpb}$  (see Fig. 6.7 (j)). Hence, DER<sub>2</sub> enters in the drooping region but it is remarkable to point out that this happens with a delay of about 4h15min compared to the DER<sub>2</sub> which is equipped with the positive-sequence control strategy (point t2).

When the three-phase damping control strategy is used, BESS<sub>2</sub> is not even fully charged and the maximum of SOC<sub>2</sub> occurs at time instance t9 and the voltage profiles of phase voltage  $v_b$  are depicted in Fig. 6.7 (k). BESS<sub>2</sub> starts to be discharged at time instance t9+1 and being discharged and this controller is been driven by phase voltage  $v_a$  since it is the lowest one among the phase voltages. At this time instance it can be seen the superior performance of the three-phase damping control strategy over the positive-sequence control strategy. The voltage level at node 4 is 1.08 p.u. for the positive-sequence and 1.06 p.u. for the damping control strategy which means that the former one still droops renewable energy while the later one is about to exit the drooping region in the next time instance.

It is also important to point out that the three-phase damping control strategy (with  $g_d = 20$  p.u.) is able to maintain the voltage levels at node 4 below  $v_{cpb}$  so that BESS<sub>1</sub> is never been charged. Hence, when the three-phase damping control strategy is used, the size of the storage in DER that are closer to the MV/LV transformer can be reduced or completely eliminated. The discharge times of the different BESS will be discussed later on, where all cases and sub-cases are exam-

ined individually.

The voltage unbalance mitigation abilities of the three-phase damping control strategy allow for less drooped power. This statement is confirmed by the simulation results obtained for time instances  $t_{10}$  and  $t_{10}+1$  where  $DER_4$  exits the drooping region and  $BESS_3$  starts sourcing power. The voltage profiles of phase voltage  $v_a$  and  $v_b$  are shown in Fig. 6.7 (l). As of the positive-sequence control strategy, it is still in the drooping region until time instance  $t_{11}$  where all  $DER_4$  exit the drooping region and this condition is sufficient to trigger  $BESS_2$  and  $BESS_3$  to start sourcing power from the battery. The voltage profiles of phase voltage  $v_a$  and  $v_b$  are shown in Fig. 6.7 (k).

### 6.3.2.2 Performance assessment of the different cases and sub-cases

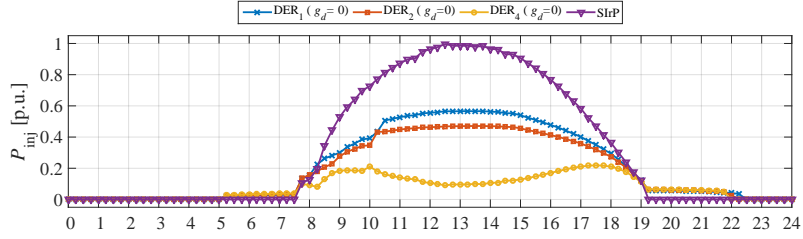
The injected active power by DER of case *CIS1* and their SOC curves of the incorporated BESSs are depicted in Fig. 6.8 (a) and (b), respectively. A solar irradiation curve is used as a reference in Fig. 6.8 (a) to be compared with the injected power curves during the day. The BESS controllers are enabled at 5h00 and it is driven by the rms value of phase voltage  $v_a$  which is lower compared to  $v_{bh,1}$ . From this time instance power is been requested from all BESS so that part of the local demand is covered by the storage. This state remains until 7h30 for  $DER_4$  and 8h15 for  $DER_1$  and  $DER_2$ . At the end of the discharging period, all BESSs are depleted almost to 25 %. When the positive-sequence control strategy is used, the injected power by  $DER_4$  forces the phase voltage to breach the drooping threshold and the droop controller of  $DER_4$  is activated at 7h45.  $DER_2$  and  $DER_1$  start the active power drooping at 8h30. Eventually, the amount of the drooped energy is so great that all BESSs are charged very quickly:  $BESS_3$  is fully charged at 9h45 while  $DER_2$  and  $DER_1$  are charged at 10h00 and 10h15, respectively. From these points on, all DERS equipped with the positive-sequence control strategy droop renewable energy. This will eventually result in enormous losses of renewable energy and it will postpone the revenue of the prosumers despite the fact that storage is incorporated in all DERS. The discharging moment of all BESSs occurs at 19h00 which is a bit after the peak loading and the installed storage is able to cover the rest of the peak load till 22h00 for  $DER_4$  to 22h30 for  $DER_1$ .

The obtained simulation results for the three-phase damping control strategy when  $g_d = 5$  p.u. and 10 p.u. are used, can be seen in Fig. 6.8. The injected active power is depicted in Fig. 6.8 (c) whereas SOC curves are shown in Fig. 6.8 (d). Because of its voltage unbalance mitigation abilities, all of the phase voltages are kept below the drooping threshold  $v_{cpb}$  for a longer time compared to the positive-sequence control strategy. In these figures it can be seen that  $DER_4$  enters the drooping region at 8h30 (when  $g_d = 5$  p.u.) and 8h45 (when  $g_d = 10$  p.u.) which is about 1h later compared to the positive sequence strategy. It takes 1h for  $BESS_3$  to be fully charged at 10h30 (*CIS2*) and 10h45 (*CIS3*). The charge

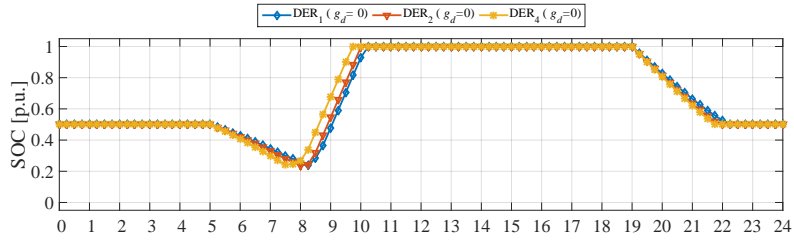
rate is similar to *C1S1* but at least it is postponed with about an hour before  $DER_4$  starts drooping energy. As of  $DER_2$  and  $DER_1$  the higher values of the damping conductance help to increase the voltage levels at their node connections and they enter the drooping region much later compared to the positive-sequence control strategy. On top of that, the charging rate is also slower which allows  $DER_2$  and  $DER_1$  to droop even less renewable energy for the examined period. Unlike the positive-sequence control strategy, the three-phase damping control strategy starts using the stored energy in BESS much earlier which is closer to the start of the peak loading of the feeder. Eventually, all BESSs are depleted between 20h30 and 21h30 which is a bit earlier compared to case *COS1* but the BESS is drained for a longer time period therefore, the local demand is supported for a longer period.

The remarkable performance of the three-phase damping control strategy is accomplished when the damping conductance assumes higher values such as 20 p.u. and 40 p.u. The exchanged power and the SOC curves can be seen in Fig. 6.9 (a) and (b), respectively.  $DER_4$  starts drooping power much later and it charges its BESS for considerably longer time compared to the previous sub-cases. It is important to point out that BESS<sub>2</sub> of  $DER_2$  at  $g_d = 20$  p.u. is not charged to its full capacity which means all drooped power is stored in BESS<sub>2</sub> while BESS<sub>1</sub> is not even been charged because the rms voltage levels at node 4 are always below  $v_{cpb}$  value and there is not any dropped power. The superior performance of the three-phase damping control strategy is even more prominent when  $g_d = 40$  p.u. where  $DER_2$  and  $DER_1$  do not droop any power and also their BESS remain uncharged for the rest of the examined period.

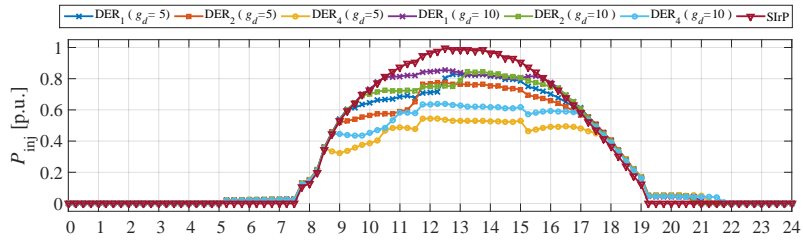
The curves of the injected power and SOC when the positive-sequence control strategy with BESSs size of 14 kWh (*C2S1*) are presented in Fig. 6.10 (a) and (b), respectively. Power is been requested from all BESSs from 5h00 to cover the morning load peak and since the requested power is as a function of the sourcing power, the injected power by all DERS is almost as twice bigger compared to the smaller storage of 7 kWh. Despite the higher power request, the BESSs are not discharged deeper. On the contrary, they were discharged less because the higher injected power increases the voltage levels in phase *a* and thus the BESS controller requests less power from the storage. In this particular case, none of the BESSs are discharged below 0.3 p.u. while *C1S1* has led to a discharge of 0.27 p.u. The bigger capacity also results in a slower charge rate and all BESSs are fully charged in about 2h. Nevertheless, all BESSs are full before 10h45 and from this point on till 19h00 renewable energy is been curtailed. After 19h00 all BESSs controllers are driven by the rms value of  $v_a$  and the local demand is supported by the storage. The double capacity is able to provide energy almost till 23h45 but this energy comes after the peak load demand.



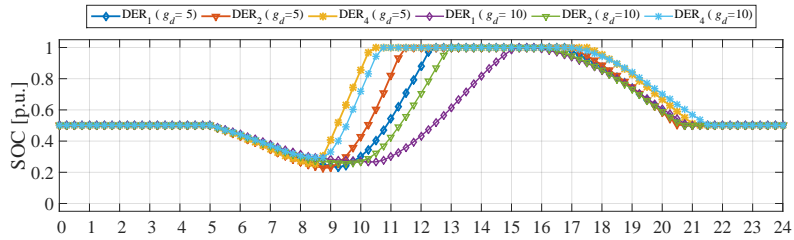
(a) Injected power when the positive-sequence control strategy is examined



(b) SOC of all BESS when the positive-sequence control strategy is examined



(c) Injected power when the damping control strategy with  $g_d = 5$  and  $10$  p.u. are examined



(d) SOC of all BESS when the damping control strategy with  $g_d = 5$  and  $10$  p.u. are examined

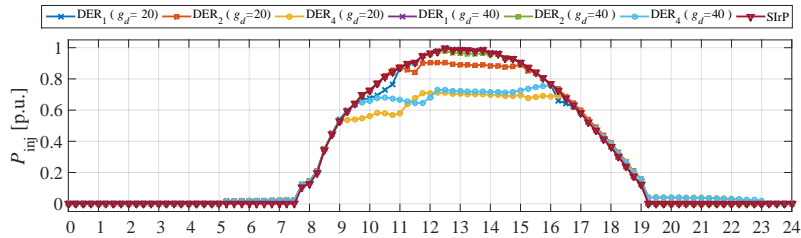
Figure 6.8: Injected power and SOC of all DER when the positive-sequence and the three-phase damping control strategies are examined (C1S1, C1S2 and C1S3)

The simulation results of the power and SOC curves obtained by using the three-phase damping control strategy are shown in Fig. 6.10. This examination is conducted for two values of the damping conductance namely  $g_d = 5$  p.u. and  $g_d = 10$  p.u. which correspond to case studies C2S2 and C2S3. Similar to cases C1S2 and C1S3 by using the three-phase damping control strategy, it results in a

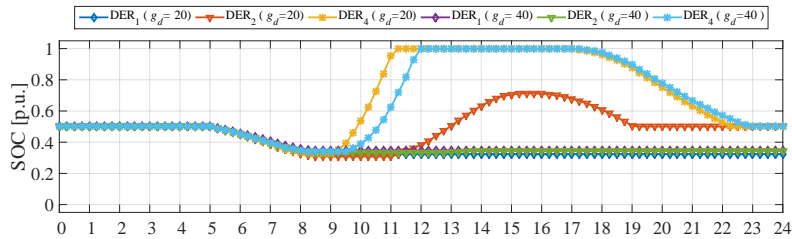
slight delay in the power drooping and also the full charging of BESS<sub>3</sub>. However, because of the bigger storage capacity, the saturation time of the BESSs is lower in comparison to *CIS2* and *CIS3* which eventually leads to less losses of renewable energy. The local demand is supported from about 16h30 till 23h15 which more or less fits in the peak loading of the feeder and thus less energy is exported to the MV network.

Finally, the results of case studies *C2S4* and *C2S5* are depicted in Fig. 6.11. As it can be seen from the obtained results, the similarity of case studies *CIS4* and *CIS5* is very close with cases *C2S4* and *C2S5*. There some differences in the saturation times of BESS<sub>3</sub> and also the peak charging of BESS<sub>2</sub> (at  $g_d = 20$  p.u.) is slightly lower.

In [72–74], the authors investigated ancillary services such as reactive power support, harmonic mitigation, voltage unbalance, etc. that DERs could provide to the DSO. From the conducted examinations it can be clearly seen that the three-phase damping control strategy has a great potential to provide ancillary services such as voltage control, voltage unbalance mitigation. In addition, DERs and BESS controllers could also be a part of a multi-agent system where the different thresholds are adapted based on some parameters and input data such as optimisations and forecasts to improve system performance and use the storage in a more adaptive way which is an interesting topic for future work.



(a) Injected power when the damping control strategy with  $g_d = 20$  p.u. and  $g_d = 40$  p.u. are examined



(b) State of charge of all BESS when the damping control strategy with  $g_d = 20$  p.u. and  $g_d = 40$  p.u. are examined

Figure 6.9: Injected power and SOC of all DER when the the three-phase damping control strategy is examined (*CIS4* and *CIS5*)

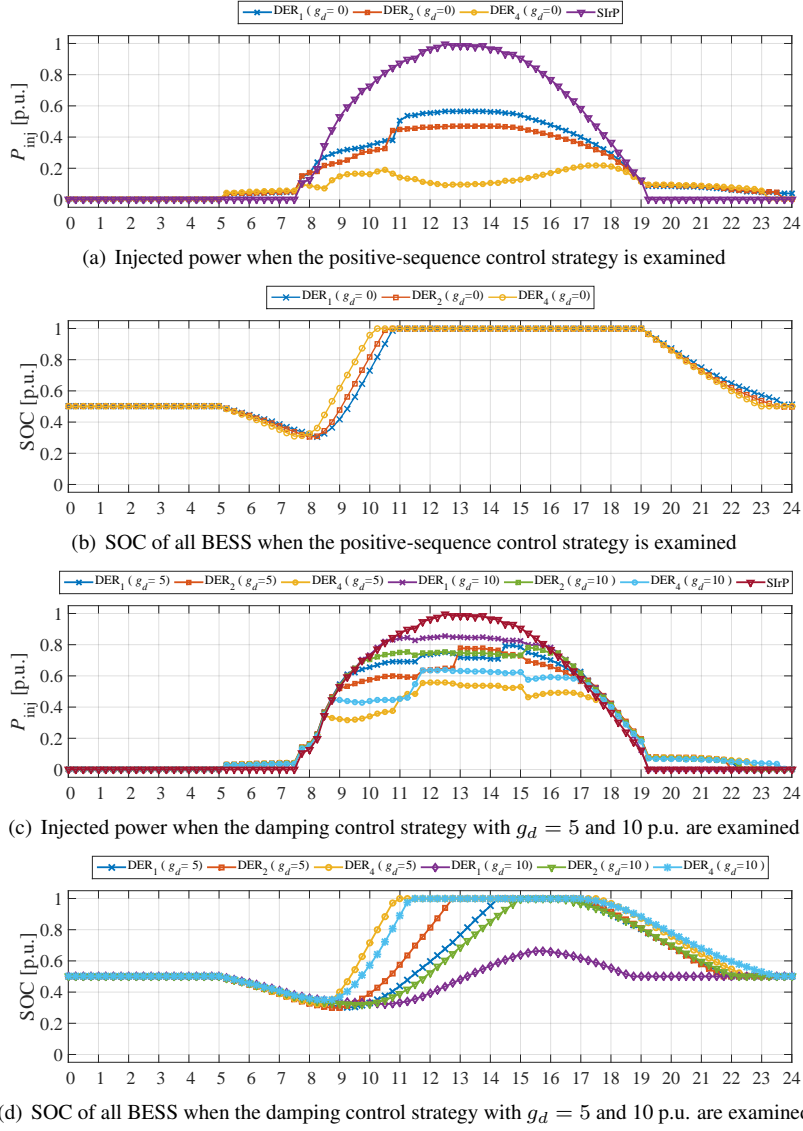
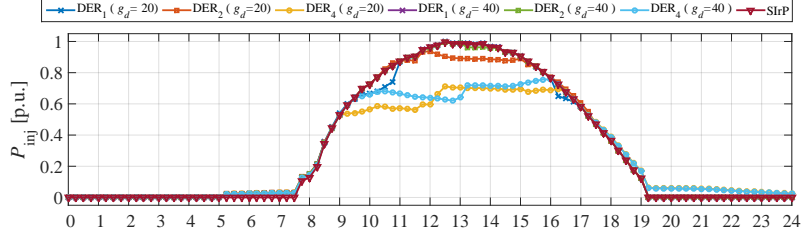
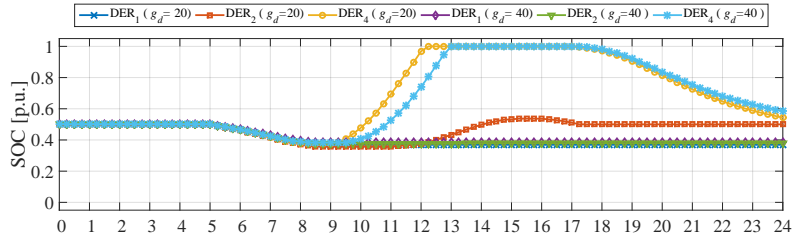


Figure 6.10: Injected power and SOC of all DER when the positive-sequence and the three-phase damping control strategies are examined (C2IS1, C2S2 and C2S3)

Fig. 6.12 shows the energy losses for the investigated period due to active power drooping when the different control strategies are examined. The first five bars represent cases *COS1-COS5* where only a droop controller is incorporated and the simulation results show that the positive-sequence control strategy droops about 249kWh of energy for the investigated period while the theoretical power in-



(a) Injected power when the damping control strategy with  $g_d = 20$  p.u. and  $g_d = 40$  p.u. are examined



(b) State of charge of all BESS when the damping control strategy with  $g_d = 20$  p.u. and  $g_d = 40$  p.u. are examined

Figure 6.11: Injected power and SOC of all DER when the three-phase damping control strategy is examined (CIS4 and CIS5)

jection of all DERs is 472 kWh which is a significant loss of renewable energy. If the drooped damping control strategy is used (COS2), then the total drooped power drops down to 99 kWh which is a bit better compared to COS1. If the three-phase damping control strategy with  $g_d = 10$ ,  $g_d = 20$  p.u. and  $g_d = 40$  p.u. are used (COS3, COS4 and COS5) then the total energy loss is 62 kWh, 36 kWh and 23 kWh, respectively. As anticipated, in COS1 the major energy loss is due to drooping and it comes from DER<sub>4</sub> because it is located at the end of the feeder and usually those DERs suffer the most losses. Less energy is drooped by DER<sub>2</sub> and DER<sub>1</sub> because they are closer to the MV/LV transformer. The same trend is kept in cases COS2 and COS3. It is interesting to point out that in COS4 the drooped power of DER<sub>1</sub> is almost negligible while power drooping is entirely prevented of DER<sub>1</sub> and DER<sub>2</sub> in COS5.

The energy loss when storage of 7kWh is incorporated (cases CIS1 to CIS5) into the DERs are also depicted in Fig. 6.12. As expected, the positive-sequence control strategy has very high energy loss (234 kWh) which is the highest among the CI cases but slightly lower compared to COS1. Therefore, the added value of the storage to the positive-sequence control strategy is only about 15 kWh, which is rather insignificant. Case CIS2 has 84 kWh compared to 99 kWh of case COS2. The performance of the three-phase damping control strategy with  $g_d = 10$  p.u.

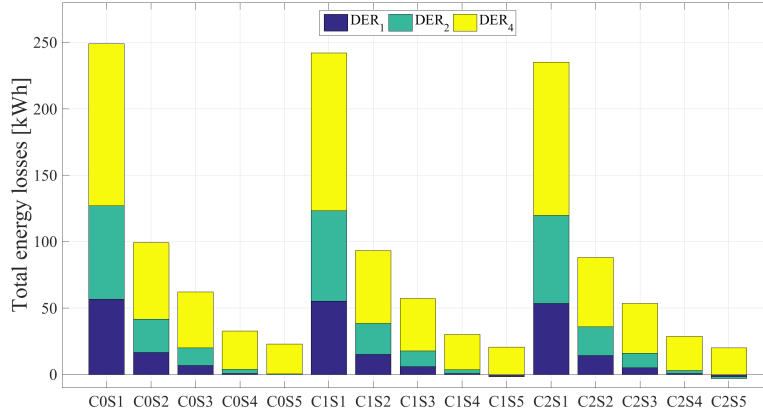


Figure 6.12: Total losses of renewable energy due to drooping of active power of all DER when different test cases are studied

leads to energy loss of only 48 kWh compared to 62 kWh of case *COS3* where the majority of the losses comes from DER<sub>2</sub> and DER<sub>4</sub>. Case *CIS4* the resistive behaviour is able to balance the grid voltages up to the point where DER<sub>1</sub> does not droop any power. Since its BESS is depleted to some level in the morning and it is not charged in the afternoon, it results in a negative energy value in the total losses. The actual energy losses come from DER<sub>2</sub> and DER<sub>4</sub> and total sum is about 29 kWh. As it can be seen from Fig. 6.9, when  $g_d = 40$  p.u. is considered BESS<sub>1</sub> and BESS<sub>2</sub> are not charged which means that DER<sub>1</sub> and DER<sub>2</sub> inject all renewable energy. This also results in a negative value for the losses because of the discharged energy in the morning. The real losses are due to DER<sub>4</sub> and in this particular sub-case they are 18kWh for the considered period.

The energy loss when storage with a capacity of 14kWh are shown in Fig. 6.12 as cases *C2S1* to *C2S4*. As expected the positive-sequence control strategy leads to the highest energy loss of 222 kWh. The damping control strategy leads to less renewable energy drooping - *C2S2* - 72 kWh, *C2S3* - 41 kWh *C2S4* - 21 kWh and *C2S5* - 14 kWh. It is also important to highlight that in sub-case *C2S3* the majority of the energy losses is in DER<sub>4</sub> while in sub-cases *C2S4* - 21 kWh and *C2S5* these losses are only due to DER<sub>4</sub>.

In summary, all DERs that are equipped with the three-phase damping control strategy are able to sink and source power for a longer time period compared to the positive-sequence control strategy. In addition, the positive-sequence control strategy depletes BESS slightly deeper compared to the three-phase damping control strategy which will result in a shorter life time of the battery storage. Despite the high damping conductance values, DER<sub>4</sub> is always drooping some power.

|                | $g_d = 0$ p.u. | $g_d = 5$ p.u. | $g_d = 10$ p.u. | $g_d = 20$ p.u. | $g_d = 40$ p.u. |
|----------------|----------------|----------------|-----------------|-----------------|-----------------|
| $I_{\max}$ [A] | 32             | 38             | 42              | 45              | 47              |

Table 6.5: Maximum current ratings of the power electronic inverters as a function of the damping conductance and storage

The achieved superior performance of the three-phase damping control strategy is achieved by injecting higher current in the phase with the lowest voltage and lower currents in the phases with the highest voltages. Consequently, some oversizing of the power electronic inverter is needed in order to perform the voltage unbalance mitigation. The positive-sequence control strategy needs an inverter with a nominal phase current of about 32 A while the three-phase damping control strategy with  $g_d = 40$  p.u. needs an inverter with output nominal of 47 A which is 50 % oversizing and it would be slightly more expensive. The maximum rms values of the phase currents at different values of  $g_d$  are listed in Table 6.5 which is valid for all cases. In summary, the BESS has a positive impact when incorporated with the three-phase damping control strategy but the effect of energy storage becomes less prominent with the increase of the damping conductance. Providing flexibility by using storage could be another stream of revenue to the prosumers but in the end it is a trade off between oversizing the power electronic inverter and choosing the correct storage capacity for BESS.

DERs are well known with increasing the grid efficiency because some part of the produced energy is consumed locally. However, in the areas with increased penetration of DER some reverse power flow is present because of the excess of energy which is injected back into the MV network. Including BESS in DER

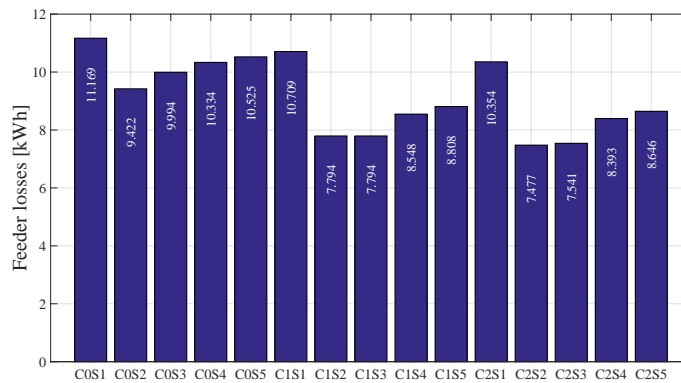


Figure 6.13: Feeder topology used to access the performance the examined control strategies

improves further the system performance because the local demand can be satisfied in times when renewable energy is not present. To assess the added value of the storage to the positive-sequence and the three-phase damping control strategies, the obtained results are compared to the reference cases (*COS1-COS4*) where only active power drooping is applied.

The grid losses of the feeder of all cases are depicted in Fig. 6.13. The positive-sequence cases droops more power compared to the other cases which means less current is flowing through feeder and the local demand is satisfied by both the grid and the DER. Considering the fact that the positive-sequence control strategy is not able to mitigate the voltage unbalance this leads to higher feeder losses. In all cases where the damping conductance assumes values of 5 and 10 p.u. lead to the most decrease of feeder losses because of the balancing abilities of the damping control strategy despite the less drooped losses. However, when the damping conductance assumes a value of 20 p.u. and 40 p.u. all cases show an increase in the feeder losses. The loss increase is due to the fact that more energy is circulating in the feeder and some part of it is exported to the MV grid. Nevertheless, it is important to note that the losses are still lower compared to cases of the positive-sequence control strategy.

The second row of Table C.1 shows the needed power ratings of the power electronic inverter at different damping conductance values. In the same table also the prices of commercially available SMA inverters are listed. If  $g_d$  assumes values of 0 the inverter costs 2769 euro whereas for  $g_d = 5$  p.u. the next more powerful inverter should be selected in order to meet the required power ratings. This inverter costs 2799 euro which is only 40 euro difference compared to the positive-sequence control strategy. For damping conductance values of 10, 20 and 40 p.u. an inverter is selected which has nominal power of 30 kVA and its price is 3593.6 euro which is around 839 euro more expensive compared to SMA *Tripower Sunny 20000TL-30* and 799 euro more expensive compared to SMA *Tripower Sunny 25000TL-30*. Prices of *TeslaWall 1.0* and *TeslaWall 2.0* are also listed in the same table as well as the total system prices depending on the selected storage capacity. From the obtained simulation results in Figure 6.12 it can be seen that if damping conductances of 20 to 40 p.u. are used active power drooping does not occur. Therefore, the necessity of BESS can be avoided if the prosumer pays extra 839 euro. Nevertheless, this is applicable only to prosumers that are close to the distribution transformer. Prosumers that are located farther located farther from the distribution transformer, active power drooping is inevitable during peak generation. Hence, investing in a BESS and larger inverter seems to be the most appropriate solution so that the loss or renewable energy is kept as low as possible.

## 6.4 Discussion

In this chapter, the combination of BESS with the positive-sequence and the three-phase damping control strategies was examined. The simulation results showed that in unbalanced LV grids, the positive-sequence control strategy performs very poorly and droops incredible amount of renewable energy when equipped with a droop controller no matter what capacity of BESS is used. On the other hand, three-phase damping control strategy is able to mitigate the voltage unbalance and by doing so droops less renewable energy. When storage is incorporated in it, the drooped power is further decreased. From the conducted examinations, it can be seen that the value of the damping conductance have incredible impact on the drooped energy which can be used to decrease the capacity of BESS. Furthermore, voltage unbalance mitigation together with the storage helps to reduce the feeder losses which is beneficial for the distribution system performance.

The superior performance of the three-phase damping control strategy, especially with high values of the damping conductance, compared the positive-sequence control strategy is achieved by oversizing the power electronic inverter which is associated with additional cost. In the end it is a trade off between the inverter sizing and the BESS capacity. However, the combination of both have the potential for the prosumer to provide more ancillary services and flexibility to the grid which is an additional stream of revenue that can help for the total system to pay it self sooner.

## 6.5 Centralised energy storage by using voltage unbalance mitigation control strategies to improve the power quality

Nowadays, the share of the RES in LV grids is constantly growing because of the decreasing prices of the photovoltaic panels and power electronic components. This imposes new challenges to the DSO to maintain the power quality in their grids. The increased penetration level of RES causes reverse power flows in times when low loading and high generation are present which leads to overvoltages especially at the end of the LV feeders. Furthermore, the second power quality problem in LV grids is the voltage unbalance caused by the single-phase loads and RES which imposes an additional challenge to the DSO.

There are several solutions that the DSO could use to prevent the above listed power quality issues. On the grid level, the DSO could reinforce the grid by replacing the existing cables with ones with a larger cross section and installing OLTC on the medium to low voltage transformers. Nevertheless, this is a very costly solution and such measures are taken only when necessary. Another possibility is

to install dedicated devices for power quality improvement such as DSTATCOM or DVR but these devices are usually installed at MV level in the vicinity of the affected feeders. If more distant feeders start suffering from overvoltages in the future, another device must be installed in the same MV network. Hence, installing such devices is a short term solution.

Control strategies for voltage control based on reactive power are widely used in RES. However, the reactive power introduces additional losses and also has a limited impact on the voltage levels due to the high R/X ratio of the LV feeders. Active power curtailment is been studied in [68] and the results show that this solution in combination with the three-phase damping control strategy, which is able to perform voltage unbalance mutation, is very promising for areas with high penetration of RES, because it droops less energy compared to other control strategies. Nevertheless, there is a loss of renewable energy when drooping is involved. To overcome this loss, battery storage can be included on domestic level as studied in [133, 135] or centralised storage in [127]. These studies, showed promising results in reducing the overvoltages and improve energy harvesting. In [140], the economical aspects are examined and the results reveal that this solution can be economically viable because of the decreasing prices of the batteries.

In this chapter, a solution for battery energy storage systems (BESS) is proposed that combines the beneficial effect of the drooped three-phase damping control strategy and battery storage elements. The proposed solution is used for central storage systems and usually these systems are connected at the end of the LV feeder where the overvoltages and voltage unbalances are more prominent.

## **6.6 Comparison between positive-sequence and damping control strategies**

In this section, the performance of the positive-sequence and the three-phase damping control strategies are compared when employed in centralised BESS. The positive-sequence and the three-phase damping control strategies are described in §6.2.3 and §6.2.4 of this chapter, respectively.

### **6.6.1 Droop controller**

The control strategies described above, can be combined with a droop controller as described in [68]. In the same source, the behaviour of the positive-sequence and the three-phase damping control strategies with incorporated droop controller is studied and the obtained results showed that the drooped positive-sequence control strategy curtails more renewable energy compared to the drooped three-phase damping control strategy. However, the study considers only RESs and it is limited

to overvoltages, while the undervoltages are neglected. In this chapter, a fully controllable centralised storage device is considered. Therefore the droop controller must be more sophisticated so besides the overvoltages, the undervoltages are also taken into account.

The proposed droop controller is presented in Fig. 6.14 where two modes of the centralised BESS unit can be distinguished such as discharging mode and charging mode. The discharging mode is activated depending on certain circumstances and the energy stored in BESS is been transferred to the grid to provide voltage support. In the charging mode, energy is been consumed from the grid to reduce overvoltages and also stored in BESS to be used later.

When the centralised storage is operating in charging mode its objective is to charge BESS, while not deteriorating the power quality. This mode is used when the grid voltage is close to overvoltages that are caused by other RES units. As can be seen in Fig. 6.14 the droop controller operates in 6 regions. If the maximum rms value among the three phase voltages is within the lower ( $v_{cpb1}$ ) and upper limits ( $v_{cpb2}$ ) of the constant power band (regions 1' and 1), the droop controller allows the BESS to inject all requested power storage elements. The requested power can be set by a secondary control system or by internal signal calculated by a BESS controller, however they are out of the scope of this work. In this chapter, only the droop and damping controllers are considered. In case of higher voltages than  $v_{cpb2}$  (region 2), the droop controller is activated and more power is being consumed from the grid in order to prevent overvoltages and if the grid voltage is above the maximum allowed by [8], the droop controller consumes almost twice the nominal power of the power electronic inverter. This means that a significant oversizing of the power electronic inverter is needed. However, the cost of the power electronic equipment is constantly decreasing which makes the proposed solution still attractive for practical implementation. In case of voltages lower than  $v_{cpb1}$  (region 2'), the droop controllers decreases the consumed active power and in case of undervoltages (region 3') the power consumption is decreased down to 0. In charging mode, the requested power in p.u. values from BESS can be written by the following piecewise equation:

$$p_{dc}^{\bullet} = \begin{cases} 0, & \text{if } |v_g| \leq v_{g,\min} \\ -p_{dc} \left( 1 - \frac{v_{cpb1} - |v_g|}{v_{cpb1} - v_{g,\min}} \right), & \text{if } v_{g,\min} < |v_g| \leq v_{cpb1} \\ -p_{dc}, & \text{if } v_{cpb1} < |v_g| < v_{cpb2} \\ -p_{dc} \left( 1 + \frac{|v_g| - v_{cpb2}}{v_{g,\max} - v_{cpb2}} \right), & \text{if } v_{cpb2} \leq |v_g| < v_{g,\max} \\ 2, & \text{if } |v_g| \geq v_{g,\max} \end{cases} \quad (6.13)$$

where  $p_{dc}^{\bullet}$  is the calculated power of the droop controller,  $p_{dc}$  is the requested power by the energy storage element,  $v_{g,\min}$  and  $v_{g,\max}$  are the minimum and maximum rms grid voltages set by [8],  $v_{cpb1}$  and  $v_{cpb2}$  are the lower and higher

thresholds of the constant power band region. Note that since power is being injected into the BESS, the calculated power by the droop controller has a negative sign.

The behaviour of the droop controller when operating in discharging mode is very similar to the charging mode but the power has a positive sign. When the maximum among the phase voltages is within the range of regions 1' and 1 all requested power is injected into the grid. If the grid voltage is higher than the constant power band voltage ( $v_{cpb2}$ ), the active power is reduced in order to prevent further increase of the phase voltages. In case of overvoltages, BESS is completely disconnected from the grid. When the phase voltages are lower than  $v_{cpb1}$ , the voltage level is close to undervoltages and in order for the BESS to support the grid voltages, the injected active power is increased and finally if the grid voltage experiences undervoltages, the active power is set to be twice the nominal power of the power electronic inverter. In discharging mode, the requested power in p.u. values from BESS can be written as follows:

$$p_{dc}^{\bullet} = \begin{cases} 2, & \text{if } |v_g| \leq v_{g,\min} \\ p_{dc} \left( 1 + \frac{v_{cpb1} - |v_g|}{v_{cpb1} - v_{g,\min}} \right), & \text{if } v_{g,\min} < |v_g| \leq v_{cpb1} \\ p_{dc}, & \text{if } v_{cpb1} < |v_g| < v_{cpb2} \\ p_{dc} \left( 1 - \frac{|v_g| - v_{cpb2}}{v_{g,\max} - v_{cpb2}} \right), & \text{if } v_{cpb2} \leq |v_g| < v_{g,\max} \\ 0, & \text{if } |v_g| \geq v_{g,\max} \end{cases} \quad (6.14)$$

Since the droop controller used in [68] does not consider undervoltages, the maximum among the phase voltage is used on the  $x$  axis. However, when undervoltages are considered, then the minimum voltage among the phases must also be taken into account. A check on the maximum and minimum voltages is performed and if the maximum is lower than  $v_{cpb2}$  then the droop controller uses the minimum phase voltage value for the droop controller. Thus the priority is given to the overvoltages because they are more dangerous compared to undervoltages.

## 6.6.2 Damping controller

The beneficial effect of resistive behaviour of the three-phase damping control strategy towards the zero- and negative-sequence voltage components is entirely determined by the value of the damping conductance  $g_d$  which is calculated by (6.12). In [18, 79], the behaviour of the three-phase damping control strategy is examined under a fixed value of the damping conductance which is chosen to be 1 p.u. This parameter is calculated based to the value of the grid voltages in [68] and thus the damping conductance is adapted actively only when needed. Nevertheless, the curves of the proposed damping controller in [68] do not consider any undervoltages. In this chapter, the proposed curves of the damping controller

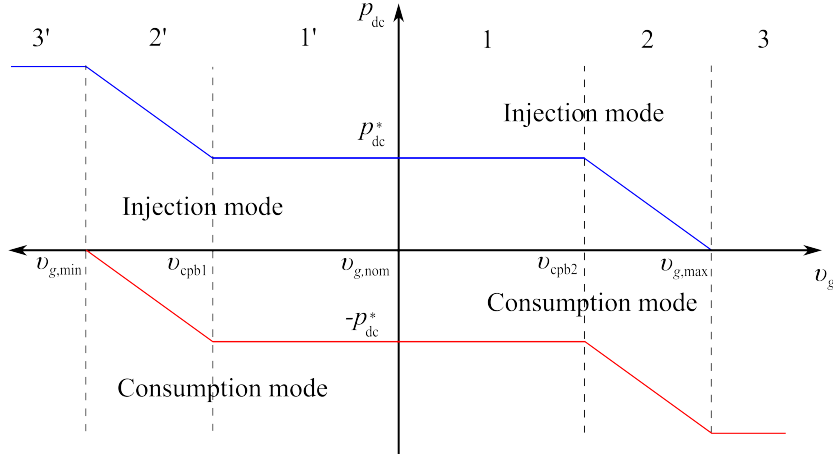


Figure 6.14: Full cycle of the droop controller when charging (—) and discharging the BESS (—)

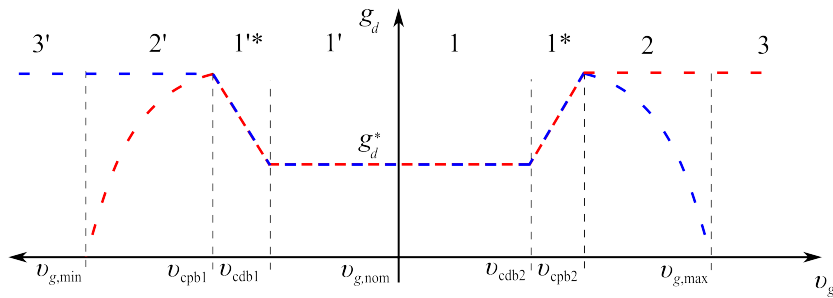


Figure 6.15: Full cycle of the damping controller when charges (---) and discharges the BESS (---)

include the undervoltages for both charging and discharging modes and they are depicted in Fig. 6.15. Note that the droop and damping controllers operate simultaneously. Unlike the requested power which changes signs whether used in charging mode or discharging mode, the damping conductance is positive in both modes.

If the rms value of the grid voltage is within the constant damping band  $v_{cdb1} < |v_g| < v_{cdb2}$  (regions 1' and 1), the damping conductance remains as it is set initially. If the grid voltage is within regions 1'\* and 1\* the damping controller is activated and increases the damping conductance in function of the grid voltage. Thus in case of voltage unbalance, the three-phase damping control strategy will try to mitigate the voltage unbalance better and eventually will prevent the BESS to enter in the drooping regions. Up to this point, the reaction of the damping controller is the same for both modes. The  $g_d$  value is kept constant and at its

maximum in regions 2 and 3 when the control strategy is used in charging mode. In this way, the control strategy will load more the phase with the higher voltage and it will load less the phases with the lower voltages. In combination of the increased power consumption of the droop controller, the overvoltages and voltage unbalances will be better mitigated. When operating in discharging mode, the active power is also drooped as well as the damping conductance up to the point where the grid voltage reaches 1.1 p.u. To make the system compatible to [8], beyond this point,  $g_d$  and  $p_{dc}^*$  assume a value of 0. The opposite can be stated when the damping controller operates in regions 2' and 3'. The piecewise equation that describes the damping controller can be expressed as:

$$g_d^* = \begin{cases} 0, & \text{if } |v_g| \leq v_{g,\min} \\ g_d \left(1 - \frac{v_{cpb1} - |v_g|}{v_{cpb1} - v_{g,\min}}\right) \left(1 + \frac{v_{cdb1} - |v_g|}{v_{cdb1} - v_{cpb1}}\right), & \text{if } v_{g,\min} < |v_g| \leq v_{cpb1} \\ g_d \left(1 + \frac{v_{cdb1} - |v_g|}{v_{cdb1} - v_{cpb1}}\right), & \text{if } v_{cpb1} < |v_g| \leq v_{cdb1} \\ g_d, & \text{if } v_{cdb1} < |v_g| < v_{cdb2} \\ g_d \left(1 + \frac{|v_g| - v_{cdb2}}{v_{cpb2} - v_{cdb2}}\right), & \text{if } v_{cdb2} \leq |v_g| < v_{cpb2} \\ 2, & \text{if } v_{cpb2} < |v_g| < v_{\max} \\ 2, & \text{if } |v_g| \geq v_{g,\max} \end{cases} \quad (6.15)$$

where  $v_{cdb1}$  and  $v_{cdb2}$  are the lower and upper thresholds of the constant damping band region. In charging mode, the damping conductance is calculated as follows:

$$g_d^* = \begin{cases} 2, & \text{if } |v_g| \leq v_{g,\min} \\ 2, & \text{if } v_{g,\min} < |v_g| \leq v_{cpb1} \\ g_d \left(1 + \frac{v_{cdb1} - |v_g|}{v_{cdb1} - v_{cpb1}}\right), & \text{if } v_{cpb1} < |v_g| \leq v_{cdb1} \\ g_d, & \text{if } v_{cdb1} < |v_g| < v_{cdb2} \\ g_d \left(1 + \frac{|v_g| - v_{cdb2}}{v_{cpb2} - v_{cdb2}}\right), & \text{if } v_{cdb2} \leq |v_g| < v_{cpb2} \\ g_d \left(1 - \frac{|v_g| - v_{cpb1}}{v_{\max} - v_{cpb1}}\right) \left(1 + \frac{|v_g| - v_{cdb2}}{v_{\max} - v_{cpb2}}\right), & \text{if } v_{cpb2} < |v_g| \leq v_{\max} \\ 0, & \text{if } |v_g| \geq v_{g,\max} \end{cases} \quad (6.16)$$

In regions 2, 2', 3 and 3' the damping conductance value is calculated by substituting (6.14) and (6.13) into (6.12), while in regions 1' and 1 the damping conductance value is calculated only by using (6.12) and this is valid for both modes.

### 6.6.3 Practical implementation

In order to react on the zero-sequence voltage component, the three-phase damping control strategy requires a three-phase four-wire inverter. The inverter topology uses a split dc-bus capacitor to form the neutral connection as shown in Fig. 6.16. The voltage equilibrium is maintained by using two dc-bus controllers for each capacitor  $C_1$  and  $C_2$  as implemented in [148]. The power electronic switches

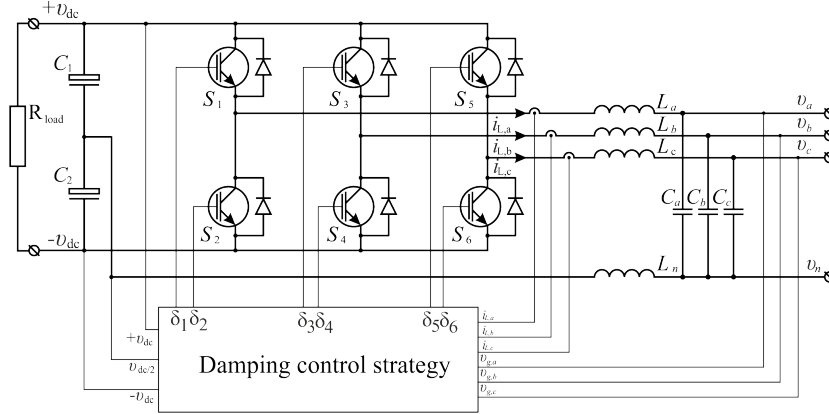


Figure 6.16: Three-phase four-wire inverter used by the three-phase damping control strategy

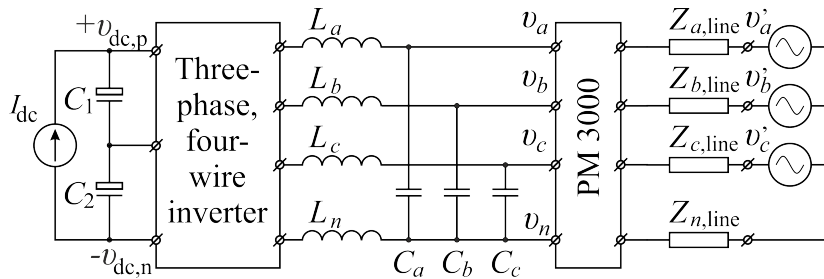


Figure 6.17: Connection diagram of the experimental set-up

are driven by a digital signal processor TMS320F28335 in which the three-phase positive-sequence and damping control strategies are implemented. More details about the practical implementation of the three-phase damping control strategy can be found in [79, 148] as well as in Chapter 5 of this dissertation.

## 6.7 Experimental results

The experimental validation of the proposed BESS control is performed by using a set-up that is presented in Fig. 6.17. The three-phase four-wire bidirectional inverter is connected to a three-phase programmable four quadrant voltage source Spitzenberger & Spies via a power analyser and a cable. To emulate the discharge mode of the system, a dc power supply Sorensen SGI 600/17 is connected to the dc bus. A communication interface between the power supply and the DSP is established and it is used to send different set points regarding the sourced current. The charging mode is emulated by connecting an electronic load Electro Auto-

| Parameter  | Value                       |
|--|-----------------------------|
| $V_a', V_b',$ and $V_c'$                               | 117 V, 106 V, 106 V (50 Hz) |
| $Z_{a,line}, Z_{b,line}, Z_{c,line},$ and $Z_{n,line}$ | (0.470+j0.201)              |
| Power analyser   | PM3000                      |
| $C_a, C_b$ and $C_c$                                   | 5 $\mu$ F                   |
| $L_a, L_b$ and $L_c$                                   | 2 mH                        |
| $L_n$  | 0.666 mH                    |
| Nominal injected/load power                            | 620 W                       |
| $C_1$ and $C_2$  | 2000 $\mu$ F                |
| $V_{dc,p}+V_{dc,n}$                                    | 400 V                       |
| Switching frequency                                    | 20 kHz                      |
| Current base value                                     | 7.5 A                       |
| Phase voltage base value                               | 225 V                       |
| dc-bus voltage base value                              | 200 V                       |

Table 6.6: Test set-up parameters

matic EA-EL-9400 to the dc bus and again a communication channel is used to send the different set points of the drawn current by the control strategies. Additional information about the set-up parameters can be found in Table 6.6. The programmable voltage source is able to deliver asymmetrical voltages  $V_a', V_b'$  and  $V_c'$  which will force the three-phase damping control strategy to draw or inject asymmetrical phase currents. The control strategies are implemented in the p.u. system because the transition from power flow simulation platforms to practical implementation is done in a more easy way. However, the experimental results are presented in absolute values which will give more useful information about the exchanged currents by the different control strategies and also the performance assessment can be done easily.

Both modes are tested in regions 2 and 2' where active power and the damping conductance are dependent on the grid voltages. The discharge mode however is tested only in region 3' where the power is twice the nominal one, while in region 3 the injected power is 0. The opposite can be stated when the charge mode is examined. Values based on the power quality standard EN50160 [8] are used for  $v_{g,min}=0.9$  p.u. (99 V) and  $v_{g,max}=1.1$  p.u. (121 V), while the droop controller uses 0.94 p.u. (103.3 V) for  $v_{cpb1}$  and 1.06 p.u. (116.6 V) for  $v_{cpb2}$ . The constant damping band values for  $v_{cdb1}$  and  $v_{cdb2}$  are 0.96 p.u. (105.6 V) and 1.04 p.u. (114.4 V), respectively.

The instantaneous phase voltages at the inverter terminals are measured by using an oscilloscope and a Matlab script to depict the measurements which are shown in Fig. 6.18. The control strategies are set-up to operate in discharge mode, hence current is being injected into the grid. Initial values of the programmable voltage source are chosen to be  $\underline{V}_a'=117.1 \text{ V } \angle 0^\circ$  (1.065 p.u.),  $\underline{V}_b'=110.3 \text{ V } \angle 120.2^\circ$

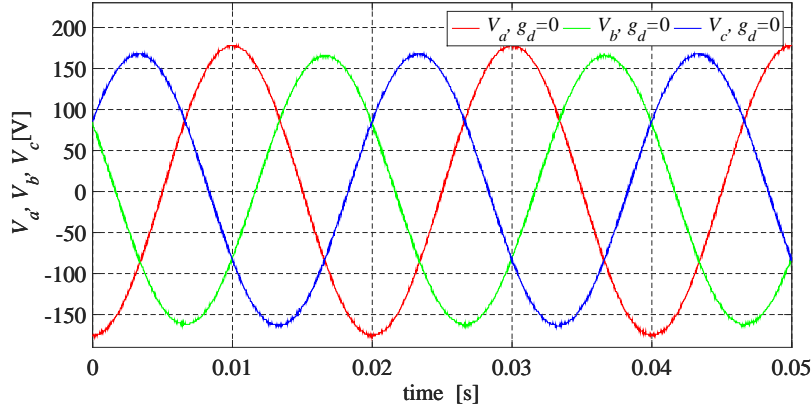


Figure 6.18: Phase voltages measured at the inverter terminals when the damping conductance value is 0 p.u.

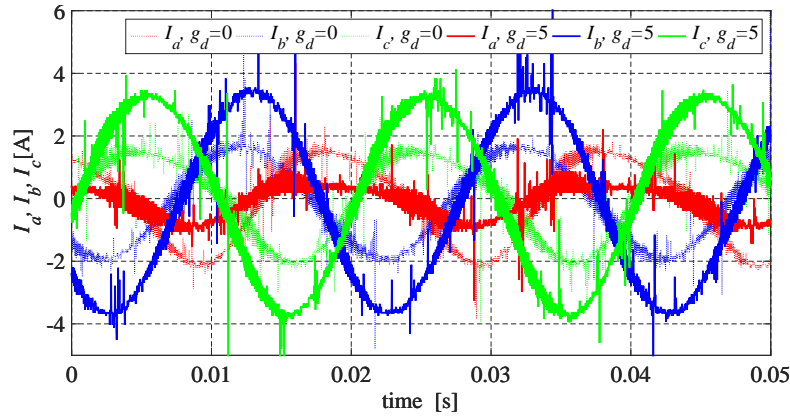


Figure 6.19: Phase currents injected by the three-phase damping control strategy when operating in discharge mode under two initial values of the  $g_d = 0$  and 5 p.u. Note that the high frequency noise is due to the measurements.

and  $\underline{V}'_c = 110.2 \text{ V} \angle 240.2^\circ$ . These settings, force the control strategy to operate in the drooping zone and since this is no load voltage, the eventual value will be higher when current injection is present. In Fig. 6.19 the phase currents are presented when the initial value of damping conductance  $g_d = 0$  p.u. and 5 p.u. are applied. When  $g_d = 0$  p.u. this corresponds to the positive-sequence control strategy thus, only positive-sequence current is been injected to the grid. Therefore, the zero- and negative-sequence remain intact. On the other hand, when the  $g_d = 5$  p.u. the drawn phase currents are not equal in magnitude any more. The damping control strategy injects higher currents in phases  $b$  and  $c$  where the phase voltages are the lowest and injects lower current in phase  $a$ . Thus, the voltage unbalance at the PCC is mitigated.

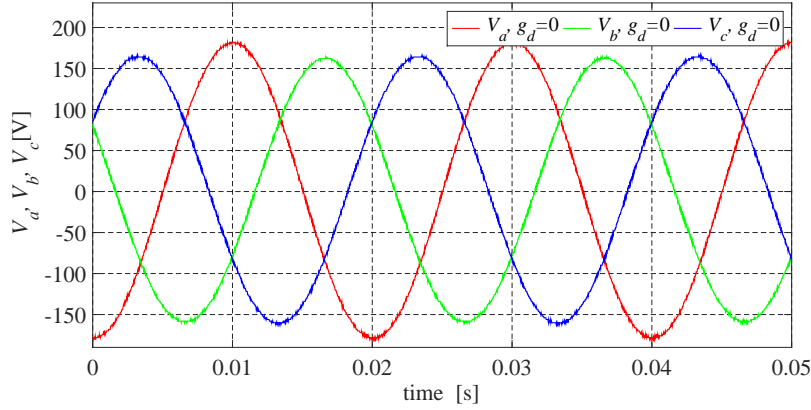


Figure 6.20: Phase voltages measured at the inverter terminals in charging mode when the damping conductance value is 0 p.u.

The experimental results of the measured injected power, damping conductance, voltages and currents when discharge mode is used are listed in Table 6.9 and Table 6.10, respectively. In the first column, the requested power is listed, while in the second one the injected power is presented. When the positive-sequence control strategy ( $g_d = 0$  p.u.) operates in region 2, the drooped power is the highest of all because the maximum grid voltage is close to overvoltages. In the third and fourth columns, the initial and the calculated damping conductances are presented respectively. At these points, the maximum value of  $|\underline{V}_a|$  is around the constant power band value ( $v_{cpb2}$ ) and also the damping conductance is higher at this point. This improves the resistive behaviour of the damping control strategy and in the last examined case, where initial value of 5 p.u. is used, the control strategy is able to deliver almost the nominal power to the grid. This is accomplished because only 0.4 A are injected in phase  $a$ , while in the other two phases the current is almost 2.3 A which means that the BESS will be depleted in a bigger time interval.

The second case study is performed when the discharge mode is examined in region 2' and as can be seen from the obtained results, in order for the positive-sequence control strategy to support the grid voltage the requested power from the source is 125%. Slightly lower requested power is measured when the three-phase damping control strategy with  $g_d = 1$  p.u. is used. In this region, the damping conductance is twice the initial value but this still does not improve enough the resistive behaviour. When initial values of 3 and 5 p.u. are used, the resistive behaviour is improved enough and the operation point of the control strategy is moved from region 2' to 1' where nominal power is injected into the grid. In the last test, the voltage settings force the positive-sequence control strategy to operate in region 3' where 200% power is requested. A remarkable performance

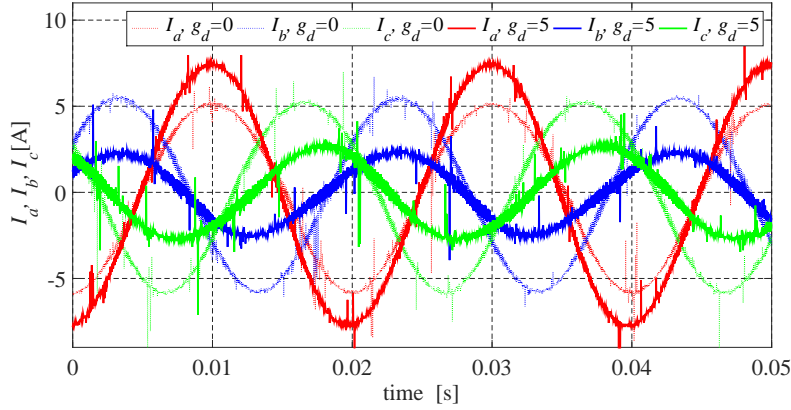


Figure 6.21: Phase currents drawn by the three-phase damping control strategy when operating in charging mode under two values of the  $g_d = 0$  and  $5$  p.u.

of the three-phase damping control strategy can be seen when higher values of the damping conductance are used. This moves the operation point from region 3' to 2' and thus less power is requested from the source (battery) to provide grid voltage support which is again beneficial for the slower depleting of the BESS.

The instantaneous voltages and currents of both positive-sequence and damping control strategies are depicted in Fig. 6.20 and Fig. 6.21, respectively. The positive-sequence control strategy draws phase currents with approximately the same amplitude, while the damping control strategy draws more current from phase  $a$  where the phase voltage is the highest compared to phases  $b$  and  $c$  and draws lower currents from phases  $b$  and  $c$ . Thus, in charge mode the voltage unbalance at the PCC is mitigated.

The experimental data obtained for the charge mode are listed in Table 6.7 and Table 6.8. The initial voltage of the first test in charging mode is  $|V_a| = 123.2$  V and when the feeder is loaded this voltage drops down to 120.9 V which is still very high. The droop controller forces the positive-sequence control strategy to draw twice the nominal power in order to prevent overvoltages. In this region, the value of the damping conductance is twice the initial value which helps the damping control strategy to decrease  $|V_a|$  to 118.8 V which leads to a power request from the grid of 148% which is 50% less compared to the positive-sequence control strategy.

In region 2, the positive-sequence control strategy requires 133%, while the three-phase damping control strategy with high damping conductance is able to load phase  $a$  up to the point where the operating point is pushed from region 2 to 1 where nominal power is requested from the grid. In the last test, region 3' is examined. The grid voltage is very low and the droop controller allows the positive-sequence control strategy to request only 60% power from the grid, oth-

erwise undervoltages will occur. The three-phase damping control strategy is able to extract 90% because it draws less current from phase  $a$  where the voltage is the lowest and thus the BESS will be charged in a shorter time.

From (6.9) it can be seen that besides the current magnitudes, the phase currents will also have a change in the phase angles which is also dependent on the  $g_d$  value. The experimental results show that the phase currents experience some small change in the phase angles which leads to some reactive power flow. Despite the non unity power factor, the damping control strategy is based on the symmetrical component theory and this reactive power flow helps to reduce the voltage unbalance in a natural way without causing additional feeder losses.

| $P_{dc}$   | $P_{dc}^*$ | $g_d$ | $g_d^*$ | $V_a$                    | $V_b$                        | $V_c$                        |
|------------|------------|-------|---------|--------------------------|------------------------------|------------------------------|
| 100.0 (3)  | 197.1      | 0.0   | 0.0     | 120.9 V $\angle 0^\circ$ | 108.5 V $\angle 120.2^\circ$ | 108.4 V $\angle 240.2^\circ$ |
| 100.0 (3)  | 184.3      | 1.0   | 2.0     | 120.3 V $\angle 0^\circ$ | 109.0 V $\angle 120.4^\circ$ | 108.9 V $\angle 240.1^\circ$ |
| 100.0 (3)  | 164.1      | 3.0   | 5.99    | 119.4 V $\angle 0^\circ$ | 109.7 V $\angle 120.6^\circ$ | 109.6 V $\angle 240.0^\circ$ |
| 100.0 (3)  | 149.3      | 5.0   | 9.99    | 118.8 V $\angle 0^\circ$ | 110.2 V $\angle 120.7^\circ$ | 110.1 V $\angle 239.8^\circ$ |
| 100.0 (2)  | 133.1      | 0.0   | 0.0     | 118.0 V $\angle 0^\circ$ | 109.0 V $\angle 120.2^\circ$ | 109.0 V $\angle 240.1^\circ$ |
| 100.0 (2)  | 121.1      | 1.0   | 2.0     | 117.5 V $\angle 0^\circ$ | 109.4 V $\angle 120.4^\circ$ | 109.3 V $\angle 240.2^\circ$ |
| 100.0 (2)  | 108.2      | 3.0   | 5.99    | 116.9 V $\angle 0^\circ$ | 109.9 V $\angle 120.5^\circ$ | 109.6 V $\angle 240.4^\circ$ |
| 100.0 (2)  | 100.0      | 5.0   | 9.71    | 116.5 V $\angle 0^\circ$ | 110.2 V $\angle 120.5^\circ$ | 110.1 V $\angle 240.4^\circ$ |
| 100.0 (2') | 60         | 0.0   | 0.0     | 101.5 V $\angle 0^\circ$ | 109.7 V $\angle 120.2^\circ$ | 109.6 V $\angle 240.1^\circ$ |
| 100.0 (2') | 68.3       | 1.0   | 1.68    | 101.9 V $\angle 0^\circ$ | 109.4 V $\angle 120.1^\circ$ | 109.3 V $\angle 243.3^\circ$ |
| 100.0 (2') | 82.5       | 3.0   | 5.80    | 102.5 V $\angle 0^\circ$ | 109.0 V $\angle 119.9^\circ$ | 108.8 V $\angle 240.4^\circ$ |
| 100.0 (2') | 90.3       | 5.0   | 9.90    | 102.9 V $\angle 0^\circ$ | 108.6 V $\angle 119.8^\circ$ | 108.4 V $\angle 240.5^\circ$ |

(x) No load voltages, measured at the inverter terminals - (3)  $V'_a=123.2$  V  $\angle 0^\circ$ ,  $V'_b=110.3$  V  $\angle 120.2^\circ$ ,  $V'_c=110.2$  V  $\angle 240.2^\circ$ , (2)  $V'_a=119.2$  V  $\angle 0^\circ$ ,  $V'_b=110.3$  V  $\angle 120.2^\circ$ ,  $V'_c=110.2$  V  $\angle 240.2^\circ$ , (2')  $V'_a=102.1$  V  $\angle 0^\circ$ ,  $V'_b=110.3$  V  $\angle 120.2^\circ$ ,  $V'_c=110.2$  V  $\angle 240.2^\circ$ ,

Table 6.7: Voltages measured at the inverter terminals when operating in charge mode

| $P_{dc}$   | $P_{dc}^*$ | $g_d$ | $g_d^*$ | $I_a$                        | $I_b$                         | $I_c$                         |
|------------|------------|-------|---------|------------------------------|-------------------------------|-------------------------------|
| 100.0 (3)  | 197.1      | 0.0   | 0.0     | 3.696 A $\angle -4.9^\circ$  | 3.724 A $\angle -124.7^\circ$ | 3.712 A $\angle -244.7^\circ$ |
| 100.0 (3)  | 184.3      | 1.0   | 2.0     | 4.053 A $\angle -4.3^\circ$  | 3.147 A $\angle -125.8^\circ$ | 3.130 A $\angle -244.9^\circ$ |
| 100.0 (3)  | 164.1      | 3.0   | 5.99    | 4.613 A $\angle -3.5^\circ$  | 2.277 A $\angle -131.7^\circ$ | 2.215 A $\angle -242.4^\circ$ |
| 100.0 (3)  | 149.3      | 5.0   | 9.99    | 5.122 A $\angle -2.5^\circ$  | 1.729 A $\angle -143.8^\circ$ | 2.307 A $\angle -235.2^\circ$ |
| 100.0 (2)  | 133.1      | 0.0   | 0.0     | 2.491 A $\angle -6.0^\circ$  | 2.512 A $\angle -125.7^\circ$ | 2.503 A $\angle -245.8^\circ$ |
| 100.0 (2)  | 121.1      | 1.0   | 2.0     | 2.776 A $\angle -5.2^\circ$  | 2.131 A $\angle -127.2^\circ$ | 2.114 A $\angle -246.4^\circ$ |
| 100.0 (2)  | 108.2      | 3.0   | 5.99    | 3.195 A $\angle -4.0^\circ$  | 1.527 A $\angle -134.0^\circ$ | 1.462 A $\angle -244.6^\circ$ |
| 100.0 (2)  | 100.0      | 5.0   | 9.71    | 3.503 A $\angle -3.0^\circ$  | 1.216 A $\angle -146.2^\circ$ | 1.042 A $\angle -238.2^\circ$ |
| 100.0 (2') | 60         | 0.0   | 0.0     | 1.250 A $\angle -8.9^\circ$  | 1.249 A $\angle -129.1^\circ$ | 1.237 A $\angle -249.4^\circ$ |
| 100.0 (2') | 68.3       | 1.0   | 1.68    | 1.014 A $\angle -9.0^\circ$  | 1.583 A $\angle -127.1^\circ$ | 1.561 A $\angle -249.1^\circ$ |
| 100.0 (2') | 82.5       | 3.0   | 5.80    | 0.632 A $\angle -11.4^\circ$ | 2.198 A $\angle -123.4^\circ$ | 2.174 A $\angle -250.8^\circ$ |
| 100.0 (2') | 90.3       | 5.0   | 9.90    | 0.253 A $\angle -13.6^\circ$ | 2.650 A $\angle -120.1^\circ$ | 2.603 A $\angle -253.2^\circ$ |

(x) No load voltages, measured at the inverter terminals - (3)  $V'_a=123.2$  V  $\angle 0^\circ$ ,  $V'_b=110.3$  V  $\angle 120.2^\circ$ ,  $V'_c=110.2$  V  $\angle 240.2^\circ$ , (2)  $V'_a=119.2$  V  $\angle 0^\circ$ ,  $V'_b=110.3$  V  $\angle 120.2^\circ$ ,  $V'_c=110.2$  V  $\angle 240.2^\circ$ , (2')  $V'_a=102.1$  V  $\angle 0^\circ$ ,  $V'_b=110.3$  V  $\angle 120.2^\circ$ ,  $V'_c=110.2$  V  $\angle 240.2^\circ$ ,

Table 6.8: Currents measured at the inverter terminals when operating in charge mode

| $p_{dc}$ [%] | $p_{dc}^*$ [%] | $g_d$ | $g_d^*$ | $\underline{V}_a$         | $\underline{V}_b$            | $\underline{V}_c$            |
|--------------|----------------|-------|---------|---------------------------|------------------------------|------------------------------|
| 100.0 (2)    | 69.7           | 0.0   | 0.0     | 117.7 V $\angle 0^\circ$  | 110.9 V $\angle 120.2^\circ$ | 110.8 V $\angle 240.2^\circ$ |
| 100.0 (2)    | 78.7           | 1.0   | 1.91    | 117.4 V $\angle 0^\circ$  | 111.2 V $\angle 120.3^\circ$ | 111.0 V $\angle 240.1^\circ$ |
| 100.0 (2)    | 89.9           | 3.0   | 5.94    | 116.9 V $\angle 0^\circ$  | 111.6 V $\angle 120.4^\circ$ | 111.4 V $\angle 239.9^\circ$ |
| 100.0 (2)    | 97.4           | 5.0   | 9.99    | 116.6 V $\angle 0^\circ$  | 111.9 V $\angle 120.5^\circ$ | 111.7 V $\angle 239.8^\circ$ |
| 100.0 (2')   | 125.0          | 0.0   | 0.0     | 102.2 V $\angle 0^\circ$  | 111.4 V $\angle 120.2^\circ$ | 111.3 V $\angle 240.1^\circ$ |
| 100.0 (2')   | 113.4          | 1.0   | 2.0     | 102.64 V $\angle 0^\circ$ | 111.1 V $\angle 120.1^\circ$ | 110.9 V $\angle 240.2^\circ$ |
| 100.0 (2')   | 100.0          | 3.0   | 5.84    | 103.3 V $\angle 0^\circ$  | 110.6 V $\angle 119.9^\circ$ | 110.4 V $\angle 240.4^\circ$ |
| 100.0 (2')   | 100.0          | 5.0   | 8.75    | 103.7 V $\angle 0^\circ$  | 110.4 V $\angle 119.8^\circ$ | 110.2 V $\angle 240.4^\circ$ |
| 100.0 (3')   | 200.0          | 0.0   | 0.0     | 98.83 V $\angle 0^\circ$  | 112.1 V $\angle 120.2^\circ$ | 112.0 V $\angle 240.1^\circ$ |
| 100.0 (3')   | 185.0          | 1.0   | 2.00    | 99.52 V $\angle 0^\circ$  | 111.6 V $\angle 120.0^\circ$ | 111.4 V $\angle 243.3^\circ$ |
| 100.0 (3')   | 162.2          | 3.0   | 6.00    | 100.5 V $\angle 0^\circ$  | 110.9 V $\angle 119.7^\circ$ | 110.7 V $\angle 240.5^\circ$ |
| 100.0 (3')   | 146.0          | 5.0   | 10.0    | 101.1 V $\angle 0^\circ$  | 110.3 V $\angle 119.6^\circ$ | 110.1 V $\angle 240.6^\circ$ |

(x) No load voltages, measured at the inverter terminals - (2)  $\underline{V}'_a=117.1$  V  $\angle 0^\circ$ ,  $\underline{V}'_b=110.3$  V  $\angle 120.2^\circ$ ,  $\underline{V}'_c=110.2$  V  $\angle 240.2^\circ$ , (2')  $\underline{V}'_a=101.5$  V  $\angle 0^\circ$ ,  $\underline{V}'_b=110.3$  V  $\angle 120.2^\circ$ ,  $\underline{V}'_c=110.2$  V  $\angle 240.2^\circ$ , (3')  $\underline{V}'_a=97.1$  V  $\angle 0^\circ$ ,  $\underline{V}'_b=110.3$  V  $\angle 120.2^\circ$ ,  $\underline{V}'_c=110.2$  V  $\angle 240.2^\circ$ ,

Table 6.9: Voltages measured at the inverter terminals when operating in discharge mode

| $p_{dc}$ [%] | $p_{dc}^*$ [%] | $g_d$ | $g_d^*$ | $\underline{I}_a$             | $\underline{I}_b$             | $\underline{I}_c$            |
|--------------|----------------|-------|---------|-------------------------------|-------------------------------|------------------------------|
| 100.0 (2)    | 69.7           | 0.0   | 0.0     | 1.206 A $\angle -175.5^\circ$ | 1.175 A $\angle -296.2^\circ$ | 1.191 A $\angle -56.1^\circ$ |
| 100.0 (2)    | 78.7           | 1.0   | 1.91    | 1.006 A $\angle -175.5^\circ$ | 1.458 A $\angle -296.6^\circ$ | 1.476 A $\angle -57.5^\circ$ |
| 100.0 (2)    | 89.9           | 3.0   | 5.94    | 0.668 A $\angle -176.7^\circ$ | 1.925 A $\angle -294.5^\circ$ | 1.954 A $\angle -60.7^\circ$ |
| 100.0 (2)    | 97.4           | 5.0   | 9.99    | 0.396 A $\angle -175.2^\circ$ | 2.283 A $\angle -292.7^\circ$ | 2.307 A $\angle -63.3^\circ$ |
| 100.0 (2')   | 125.0          | 0.0   | 0.0     | 2.176 A $\angle -179.2^\circ$ | 2.177 A $\angle -299.2^\circ$ | 2.192 A $\angle -59.0^\circ$ |
| 100.0 (2')   | 113.4          | 1.0   | 2.0     | 2.446 A $\angle -180.2^\circ$ | 1.741 A $\angle -298.9^\circ$ | 1.771 A $\angle -56.8^\circ$ |
| 100.0 (2')   | 100.0          | 3.0   | 5.84    | 2.934 A $\angle -181.0^\circ$ | 1.152 A $\angle -303.1^\circ$ | 1.250 A $\angle -47.5^\circ$ |
| 100.0 (2')   | 100.0          | 5.0   | 8.75    | 3.367 A $\angle -181.3^\circ$ | 0.937 A $\angle -311.1^\circ$ | 1.106 A $\angle -38.0^\circ$ |
| 100.0 (3')   | 200.0          | 0.0   | 0.0     | 3.518 A $\angle -180.6^\circ$ | 3.529 A $\angle -300.5^\circ$ | 3.543 A $\angle -60.4^\circ$ |
| 100.0 (3')   | 185.0          | 1.0   | 2.00    | 3.959 A $\angle -181.0^\circ$ | 2.937 A $\angle -300.7^\circ$ | 2.976 A $\angle -58.9^\circ$ |
| 100.0 (3')   | 162.2          | 3.0   | 6.00    | 4.656 A $\angle -181.6^\circ$ | 2.023 A $\angle -304.9^\circ$ | 2.120 A $\angle -51.7^\circ$ |
| 100.0 (3')   | 146.0          | 5.0   | 10.0    | 5.165 A $\angle -181.7^\circ$ | 1.360 A $\angle -316.6^\circ$ | 1.560 A $\angle -37.8^\circ$ |

(x) No load voltages, measured at the inverter terminals - (2)  $\underline{V}'_a=117.1$  V  $\angle 0^\circ$ ,  $\underline{V}'_b=110.3$  V  $\angle 120.2^\circ$ ,  $\underline{V}'_c=110.2$  V  $\angle 240.2^\circ$ , (2')  $\underline{V}'_a=101.5$  V  $\angle 0^\circ$ ,  $\underline{V}'_b=110.3$  V  $\angle 120.2^\circ$ ,  $\underline{V}'_c=110.2$  V  $\angle 240.2^\circ$ , (3')  $\underline{V}'_a=97.1$  V  $\angle 0^\circ$ ,  $\underline{V}'_b=110.3$  V  $\angle 120.2^\circ$ ,  $\underline{V}'_c=110.2$  V  $\angle 240.2^\circ$ ,

Table 6.10: Currents measured at the inverter terminals when operating in discharge mode

## 6.8 Discussion

In this section, the positive-sequence and the three-phase damping control strategy are examined when used in centralised battery storage applications. The obtained experimental results showed that the three-phase damping control strategy has superior performance in terms of mitigating the voltage unbalance and overvoltages compared to the positive-sequence control strategy. Furthermore, the three-phase damping control strategy is able to solve the overvoltages and voltage unbalances by exchanging (consuming or injecting) less currents compared to the positive-sequence control strategy which is beneficial for the BESS and also grid performance.

## 6.9 Conclusions

In this chapter, the combination of BESS with the positive-sequence and the three-phase damping control strategies were examined in two different applications: decentralised and centralised BESS. The decentralised BESS is examined on a LV feeder with the objective to improve the power quality. The employed BESS algorithm relies entirely on the local measurements to charge and discharge the storage. Similarly, the centralised storage is build. From the conducted simulation results for the decentralised and experimental results of the centralised storage, it can be seen that the in unbalanced grids, the three-phase damping control strategy is able to improve the power quality with a lower size of the BESS compared with the positive-sequence control strategy. In addition, the experiments are conducted at different values of the damping conductance and the obtained results show that the higher the damping conductance, the lower BESS capacity is needed to improve the power quality as well as the grid performance by reducing the feeder losses.

The superior performance of the three-phase damping control strategy, especially with high values of the damping conductance, compared the positive-sequence control strategy is achieved by oversizing the power electronic inverter with 50% at  $g_d = 40$  p.u. which is associated with additional cost of 799 euro. In the end, it is a trade off between the inverter sizing and the BESS capacity. However, the combination of both have the potential for the prosumer to provide more ancillary services and flexibility to the grid which is an additional stream of revenue that can help for the total system to pay it self sooner.



# 7

## Voltage dip mitigation capabilities of the three-phase damping control strategy

Because of the increasing penetration of distributed generation (DG) units, distribution system operators are faced with significant challenges such as voltage and congestion problems. This has led to continuously evolving grid interconnection requirements for DG. One of these requirements is voltage support by DG units during voltage dips. In this chapter, the grid support, in case of voltage dips, by two three-phase control strategies is investigated. One of the controllers is the positive-sequence control strategy and the second is the three-phase damping control strategy, which emulates a resistive behaviour towards the negative- and zero-sequence voltage components and has originally been developed for mitigating voltage unbalance in three-phase systems. First, the behaviour of both control strategies under voltage dips is analytically studied showing that the damping control strategy provides voltage support by injecting higher currents in the phase(s) where the fault is presented. Second, the positive effect on the residual grid voltage is validated by means of simulation and experimental results.

## 7.1 Introduction

In literature, voltage dips are considered to be one of the most important aspects of power quality issues in distribution networks [81]. Voltage dip is a drop of the rms value(s) of the grid voltage(s) due to a fault on the feeder levels, which may occur at high voltage (HV), MV or LV level. It may also be caused by energising a transformer or starting up a directly fed induction machine etc. Because of their unpredicted nature, voltage dips can be a very challenging phenomenon. Such an event can lead to the tripping of sensitive loads or if the protection means do not trip, they can be harmful to the loads. Induction machines can have problems with torque ripples and difficulties with the re-acceleration when subjected to voltage dips [152]. When a voltage dip is present in the supply voltage, the adjustable speed-drives might completely turn off the induction motor due to triggering of over-current and/or under-voltage protections [153–155]. Besides the loads, the voltage dips can be dangerous for the transformers in the distribution grid as well. In [156], the authors investigate the voltage recovery of these transformers after a voltage dip and the study shows that LV transformers can saturate, leading to an increase of the total harmonic distortion of the voltage or tripping of the protection circuits. In general, the effect of the dip on the sensitive loads depends on the severity of the dip but also to the voltage dip immunity of the sensitive equipment. Power electronics based equipment such as PV and wind turbine inverters, as well as electronic equipment, sensors relays, etc., are especially susceptible to voltage dips and swells [157]. Adverse effects on the sensitive equipment can vary from a temporary loss of malfunction to severe damage.

Industry that involves assembly lines and electric drives are particularly susceptible to voltage dips due to the fact that several motors are joined together in the entire production process. The influence of the production faults is studied in [158] and if one of the electric motor is affected due to a voltage dip, then the production process may stop. In 2006 European Citizens' initiative started a power quality survey in 2006 and released a report two years later - ECI PQ Survey 2008 [159]. The main objective of this survey is to investigate the problems in the industry and services sectors caused by power quality issues. One of the aspects of the report is the financial cost for the industry in EU-25 and some of the results regarding these losses are presented in Fig. 7.1. The survey includes power quality aspects in five categories. Category one includes dips and short interruptions. Category two considers long interruptions while category three covers harmonics. Surges and transients are considered in category four and finally flickers, voltage unbalance earthing and electromagnetic compatibility are covered by category five. According to this figure, the voltage dips are the main contributor for financial losses of total 85.5 billion euro, which makes voltage dip mitigation an important power quality issue that must be addressed.

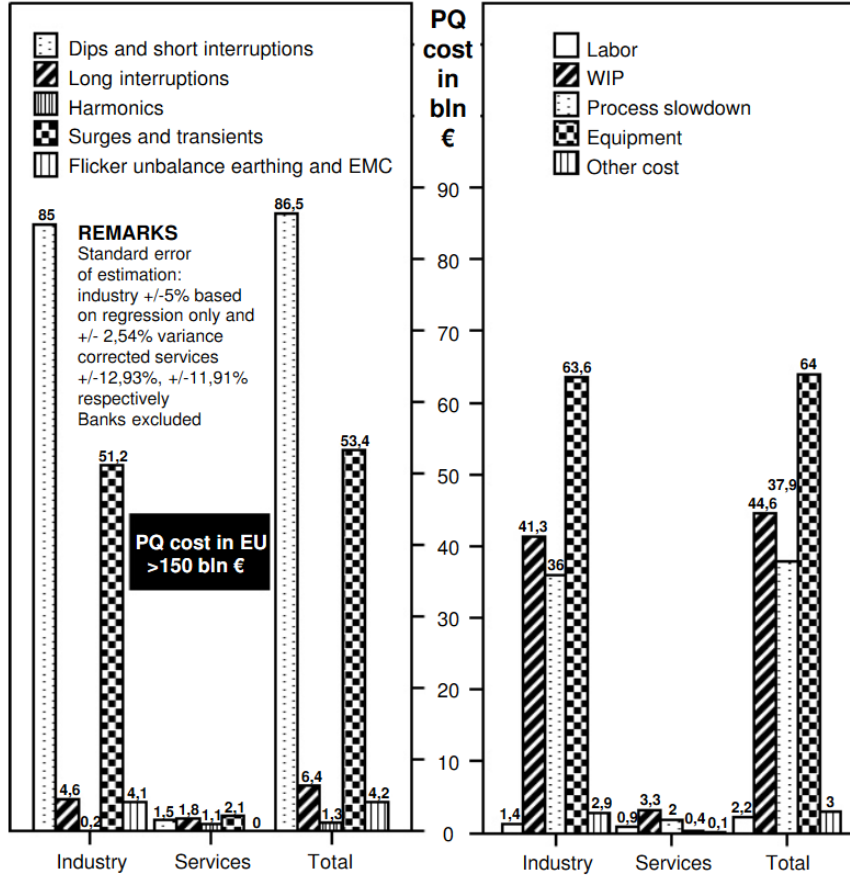


Figure 7.1: Financial losses due to power quality issues<sup>1</sup>

When [159] is released in 2008, despite its comprehensiveness and thorough content, which is giving enough recommendations for improving the power quality issues caused by voltage dips, the research on this topic still continues. Since then, many other research articles have been published on this topic. The databases of Web of Science are checked with key words *voltage sag* and *voltage dips*. The results of all available research articles are depicted in Fig. 7.2 and it can be clearly seen that the interest towards voltage dips continues to be an interesting topic and still draws the attention of the researchers.

<sup>1</sup>Source [159]

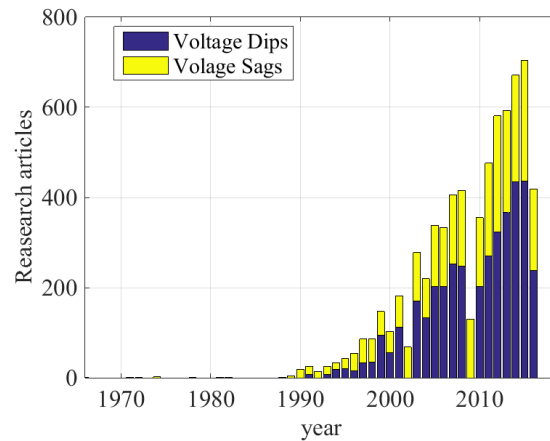


Figure 7.2: Research articles about voltage dips found in Web of Science database with key words "voltage dips" and "voltage sags"

## 7.2 Voltage dip characterisation

As mentioned earlier, the voltage dip is caused by a fault on the transmission grid. This fault can be caused by a customer, energising large transformers, starting a large induction machines etc. These faults can be single-phase, two- or three-phase, which lead to excessive short circuit currents that are consumed from the source. The residual voltage at the faulty phase(s) will be determined by the short circuit impedance and the short circuit current. The voltages in the other phase(s) may or may not change depending on the grid impedance, grid configuration, severity of the dip and also the type of the voltage dip. According to [8] the definition of voltage dip is:

*"A sudden reduction of the supply voltage to a value between 90% and 1% of the declared voltage  $U_{nom}$  followed by a voltage recovery after a short period of time. Conventionally the duration of a voltage dip is between 10 ms and 1 minute. The depth of a voltage dip is defined as the difference between the minimum rms voltage during the voltage dip and the declared voltage. Voltage changes, which do not reduce the supply voltage to less than 90% of the declared voltage  $U_{nom}$  are not considered to be dips."*

In [81], voltage dips are classified in three categories: Type I, Type II and Type III. The first category contains only one voltage dip type called Type A and it is basically a fault between all three phases. Category Type II contains three different voltage dip type: Type B - single-phase to ground fault, Type C - phase-to-phase

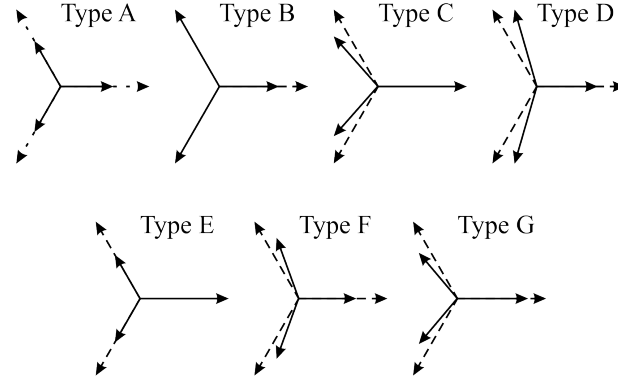


Figure 7.3: Dips classification<sup>2</sup> where - - - represents the nominal phase magnitudes and angles while — represents the residual phase voltages and angles during a voltage dip

fault with a phase jump in the faulty phases and Type D - single-phase-to-ground with a phase jump in phases *b* and *c*. Note that in the given examples the fault is present in phase *a* for dip types B, D, F and G as well as phase *b* and *c* for types C and F. In practice, the faulty phases may be different but reaction of the three-phase system is the same. The last category is Type III and it is also consisted of three voltage dip types: Type E, Type F and Type G. All three types of voltage dips in the last category are phase-to-phase faults but phase jump might or might not be present at the equipment terminals depending on the grid configuration and the load connection. The voltage dips are examined briefly in Chapter 4 where the limits of  $g_d$  are examined. For convenience, the same figure is used in this chapter where all 7 types of voltage dips are depicted in Fig. 7.3 where the dashed vectors represent the nominal rms values of and angles of the phase vectors. The solid lines show the actual voltages under different dips.

In [81], a mathematical description of all 7 types of voltage dips is given and for more clarity this description is shown below:

- Type A - three-phase balanced voltage dip:

$$\begin{aligned}
 \underline{v}_a &= \underline{v} \\
 \underline{v}_b &= -\frac{1}{2}\underline{v} - \frac{1}{2}j\sqrt{3} \\
 \underline{v}_c &= -\frac{1}{2}\underline{v} + \frac{1}{2}j\sqrt{3}
 \end{aligned}
 \tag{7.1}$$

where  $\underline{v}$  denotes the rms value of the residual voltage in the respective phase and if the dip is phase-to-phase then it is interpreted as the residual line-to-line voltage.

<sup>2</sup>Source [81]

- Type B - phase-to-neutral fault:

$$\begin{aligned}\underline{v}_a &= \underline{v} \\ \underline{v}_b &= -\frac{1}{2} - \frac{1}{2}j\sqrt{3} \\ \underline{v}_c &= -\frac{1}{2} + \frac{1}{2}j\sqrt{3}\end{aligned}\quad (7.2)$$

- Type C - phase-to-neutral voltage dip with a phase jump:

$$\begin{aligned}\underline{v}_a &= 1 \\ \underline{v}_b &= -\frac{1}{2} - \frac{1}{2}j\underline{v}\sqrt{3} \\ \underline{v}_c &= -\frac{1}{2} + \frac{1}{2}j\underline{v}\sqrt{3}\end{aligned}\quad (7.3)$$

- Type D - phase-to-phase voltage dip with a phase jump:

$$\begin{aligned}\underline{v}_a &= \underline{v} \\ \underline{v}_b &= -\frac{1}{2}\underline{v} - \frac{1}{2}j\sqrt{3} \\ \underline{v}_c &= -\frac{1}{2}\underline{v} + \frac{1}{2}j\sqrt{3}\end{aligned}\quad (7.4)$$

- Type E two-phase to ground:

$$\begin{aligned}\underline{v}_a &= 1 \\ \underline{v}_b &= -\frac{1}{2}\underline{v} - \frac{1}{2}j\underline{v}\sqrt{3} \\ \underline{v}_c &= -\frac{1}{2}\underline{v} + \frac{1}{2}j\underline{v}\sqrt{3}\end{aligned}\quad (7.5)$$

- Type F- two-phase to ground:

$$\begin{aligned}\underline{v}_a &= \underline{v} \\ \underline{v}_b &= -\frac{1}{3}j\sqrt{3} - \frac{1}{2}\underline{v} - \frac{1}{6}j\underline{v}\sqrt{3} \\ \underline{v}_c &= +\frac{1}{3}j\sqrt{3} - \frac{1}{2}\underline{v} + \frac{1}{6}j\underline{v}\sqrt{3}\end{aligned}\quad (7.6)$$

- Type G - two-phase to ground

$$\begin{aligned}\underline{v}_a &= \frac{2}{3} + -\frac{1}{3}\underline{v} \\ \underline{v}_b &= -\frac{1}{3} - \frac{1}{6}\underline{v} - \frac{1}{2}j\underline{v}\sqrt{3} \\ \underline{v}_c &= -\frac{1}{3} - \frac{1}{6}\underline{v} + \frac{1}{2}j\underline{v}\sqrt{3}\end{aligned}\quad (7.7)$$

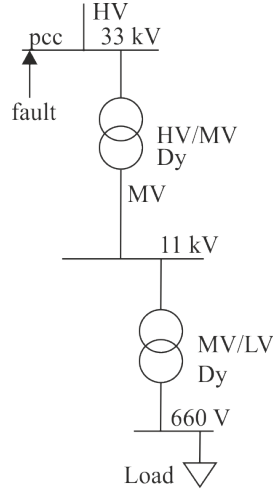


Figure 7.4: Grid topology used to demonstrate the propagation of the different types of voltage dips through the electrical grid<sup>3</sup>

| Level | 1 ph. to gnd | 2 ph.        | 2ph.-gnd     | 3 ph.        |
|-------|--------------|--------------|--------------|--------------|
| HV    | Type B (50%) | Type C (50%) | Type E (50%) | Type A (50%) |
| MV    | Type C (67%) | Type D (50%) | Type F (50%) | Type A (50%) |
| LV    | Type D (67%) | Type C (50%) | Type G (50%) | Type A (50%) |

Table 7.1: Voltage dip propagation in a typical transmission/distribution grid configuration and residual voltage of 50% for star connected load.

A voltage dip experienced by a load connected at LV level can occur at HV, MV or LV level. However, a voltage dip at MV level may not be the same at LV level because of the primary/secondary winding configuration of the MV/LV transformer or the load connection. The typical configuration of the step-down transformer from HV to MV is the  $\Delta$ -Y connection. The same is valid for the distribution transformer that reduces the voltage from MV to LV levels but in most of the cases the star centre is earthed via an earthing system. In [81], the authors have given an example of how the different dips evolve while propagating through the different layers of the transmission and distribution grid as well as the transformers. The grid topology is presented in Fig. 7.4 and data are summarised in Table 7.1.

Fig. 7.4 shows that the fault occurs at HV level and it propagates through two  $\Delta$ -Y transformers to the load. The residual voltage of the fault is 50% and for instance Type B voltage dip propagates to MV level and it transforms into Type C and finally propagates through the MV/LV transformer and the star connected

<sup>3</sup>Source [81]

load experiences a voltage dip of Type D. Note that Type C and Type D have the same residual voltage of 67% regardless of the residual voltage of 50%, which occurs at the fault side. Similarly the 2 phase-to-phase and 2 phase-to-ground can be interpreted however, the residual voltage remains the same through all voltage levels. Of all voltage dips, only Type A does not change its type and residual voltage while propagating to the load. Except voltage dip Type A, all other types experience a transformation if the primary/secondary configuration is different.

Voltage dip Type A will not be considered further in this work because it does not introduce any voltage unbalance at DER level so that the later one cannot mitigate the dip by redistributing the currents through the different phases. Voltage dip Type E is a two-phase-to-ground but the reaction of the control strategy will be similar to Type B. The rest of the voltage dips introduce phase jump at the DER terminals, which is more challenging for the control strategy to overcome and mitigate these dips. The phase jumps at HV level, highly depends on the distance of the fault from the source, feeder properties etc. To calculate the phase jump can be a challenging task. In order to investigate the behaviour of the examined control strategies, a single-phase-to-ground can be used. Voltage dip Type B is characterised only by the residual voltages in the faulty phases. Since this voltage dip evolves into type D at the load terminals and the former one is characterised by residual voltage and phase jump, then this phase jump can be easily calculated by using equations (7.1) to (7.7). Table 4.1 shows that the voltage dip of Type D creates the highest voltage unbalance at LV level compared to the voltage dip Type C and Type G. Therefore, to limit the amount of case studies in this chapter, only voltage dip Type B and Type D will be selected to examine the behaviour of the positive-sequence and three-phase damping control strategy.

### 7.2.1 Immunity curve of equipment

As mentioned in the previous section, voltage dips have different residual voltages, duration and phase shift. Some equipment have different voltage dip immunity dependent on the voltage dip properties. The most susceptible categories of equipment to voltage dips are considered to be personal computers, adjustable speed drives, other equipment supplied by a single-phase rectifier, direct-connected induction machines etc. To assess the voltage dip immunity abilities of a particular equipment extensive tests are required. The tolerances of the immunity curve for a particular equipment can be obtained when the device is tested under different residual voltages, durations and dip types. The negative impact of the voltage dips on the sensitive equipment are:

- Contactors - during voltage dips, the residual voltages might not be able to keep the magnetic flux high enough and the spring opens the contact leading to disconnection of the load from the grid despite the fact that the load might

have high voltage dip immunity. In many sources [160–163], the contactors are identified as one of the weakest spot in the processing industry.

- Direct on-line inductor machines - these machines might have difficulties re-accelerating after fault clear [164]. Furthermore, the post fault current may exceed the start up current leading to lower levels of the post fault voltages and difficult to recover the grid voltages.
- Adjustable speed drives (ASD) - In [164, 165], a comprehensive study is conducted on immunity of the adjustable speed drives with and without active front end under balanced and unbalanced voltage dips. Under balanced voltage dips the immunity curves are determined by the undervoltage protection of the ASD. The time that the ASD will experience undervoltage at the dc-bus, and therefore trip off the drive, is determined by the dc bus capacitance and the loading conditions of the ASD. Under unbalanced voltage dips, the power is transposed by the phases with the highest residual voltage. If the drawn current from these phases becomes too high, then an overcurrent protection trips and turns off the ASD.
- Programmable Logic Controllers (PLC) are used to control industrial processes. If the residual voltage is outside of its immunity curve tolerances the PLC might shut down and restart when the grid voltage is restored [163, 164]. This will result in process tripping or unsafe process conditions. In [164], a comprehensive research is conducted on PLCs and the voltage dips impact on their peripheral devices. The results show that the restart of the PLC in the automated processes is one of the major problems that leads to a production stop.
- Industrial computers and IT equipment - they are usually fed by single-phase rectifiers and both cases: without power factor corrector and with PFC. The power electronic part of their power supply unit makes them very susceptible to voltage dips [163] and in particular the voltage dip may cause excessive inrush currents that charge the dc link capacitors and thus damage the semiconductor diodes [164].

To help the manufacturers of electronic and electrical equipment with the voltage dip ride-through, standards are required to set boundaries for the voltage dip immunity. Different standards that the equipment must comply with are applied depending on the country. Standard IEC 61000-4-11 [85] is used for equipment that draws less than 16 A and IEC 61000-4-34 [166] is used for equipment above 16 A. These two standards prescribe limits for three types of equipment:

- It applies to protected power supplies with compatibility levels lower than public network level. It is applicable to very disturbance sensitive equipment

| Classes | Tests levels and duration for voltage dips   |                      |                         |                         |                          |
|---------|--|----------------------|-------------------------|-------------------------|--------------------------|
| Class 1 | Cycle-by-cycle according to the manufacturer |                      |                         |                         |                          |
| Class 2 | 0% during<br>1/2 cycle                       | 0% during<br>1 cycle | 70% during 25 cycles    |                         |                          |
| Class 3 | 0% during<br>1/2 cycle                       | 0% during<br>1 cycle | 40% during<br>10 cycles | 70% during<br>25 cycles | 80% during<br>250 cycles |

Table 7.2: Standard test residual voltage levels according to IEC 61000-4-11 and IEC 61000-4-34.

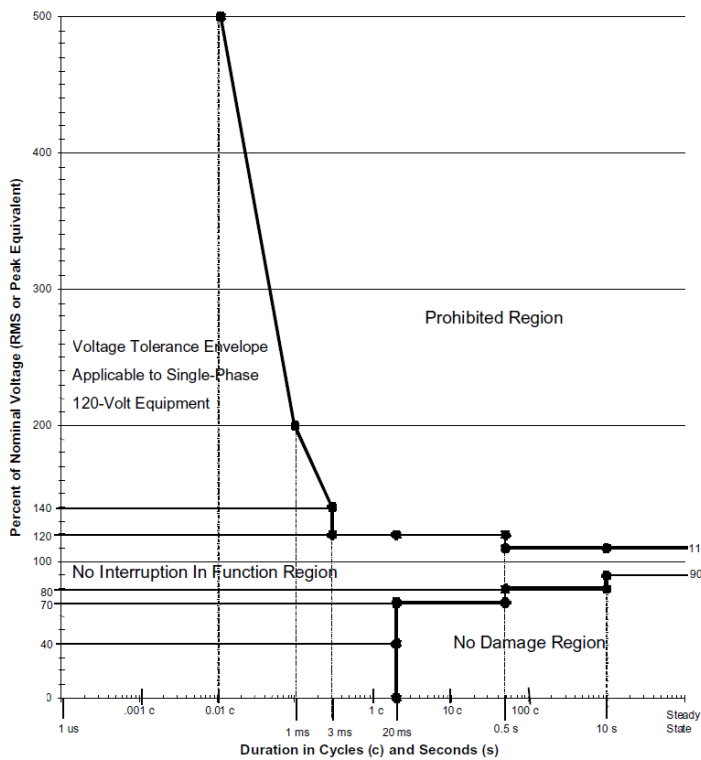


Figure 7.5: Immunity curves of computer equipment set by different standards <sup>4</sup>

in terms of supply voltage: instrumentation in laboratories, automation and protection equipment, computers and servers carrying out critical work load.

- It applies to point of common coupling for consumers system and in-plant point of common coupling in the industrial environment in general
- It applies to in-plant common coupling points in industrial environment.

<sup>4</sup>Sources [163, 167]

The different residual voltages and duration of the voltage dips that the equipment must ride-through are listed in Table 7.2. The impact on sensitive equipment depends on the severity of the voltage dip in terms of magnitude and duration [81, 168, 169].

One of the most common standard and also the most cited one is Information Technology Industry Council (ITIC) [167], which is an updated and improved version of the Computer Business Equipment Manufacturers Association curve (CBEMA) [167]. The ITIC and CBEMA curves are depicted in Fig. 7.5 and they describe the tolerable input voltage range (voltage dip immunity) for which the computer equipment must remain operational. This curve defines the voltage dip immunity range by a upper and lower boundaries. Outside these ranges, the operation of the equipment is considered as unsafe operational area. SEMI (F47-0706) [170] is another standard that is used by the semiconductor industry. However, SEMI is more focused on voltage dips by setting different time intervals and different severity of the voltage dip, while CBEMA and ITIC describe a safety operational range. In addition, some equipment can be complied with ITIC or CBEMA but it does not comply with SEMI and vice versa.

## 7.2.2 Short overview existing technologies for voltage dip mitigation

A lot of research is carried out regarding the mitigation of voltage dips. Some of the most used solutions on TSO and DSO levels are static compensators (STATCOM) which are connected at TSO level, distribution static compensators (DSTATCOM), which are connected at DSO level. Another dedicated device that mitigates the voltage dips in the DVR and it can be connected at DSO, utility or facility level. According to [171], DVR are mainly used on utility and facility level while on machine or group of machines level the possibilities are uninterruptable power supplies, flywheels, dynamic dip corrector etc.

STATCOM and DSTATCOM devices are used to improve the power quality in HV and MV grids. The difference between the STATCOM and DSTATCOM is mainly in the power ratings. These devices are able to provide voltage control, voltage unbalance and harmonic mitigation and usually they consume power from the grid to impact the power quality problems [172–174]. Reference [175], investigates the economic benefit of a DSTATCOM with different power ratings and different penetration levels of PV plants in a medium voltage feeder. At prices of 60 euro per kVA and OPEX of 0.5%, the DSTATCOM have the potential to be a promising solution in MV grids. Nevertheless, as mentioned in Chapter 6, they require additional installation and operational cost, which ultimately leads to higher costs for the TSO and DSO.

DVRs are power electronic based devices that can be connected in series, shunt

or combined configuration. The most used configurations are the series and combined combinations [176]. In the series configuration the DVR is connected to the distribution grid through transformers. Their primary windings are connected in series to the feeder while the secondary windings are connected to the power electronic inverter. In many DVR applications the power electronic part is implemented by using a three-phase three-wire inverter but regardless of the power electronic configuration, all DVRs require significant amount of energy storage element or they draw power from the distribution grid [177]. Usually these devices are installed on feeders with power quality problems or in the vicinity of the sensitive loads [168, 177]. The DVRs can be used for harmonic and voltage unbalance mitigations as well [178]. Despite these valuable qualities of this device its cost and maintenance are significant. Reference [171] reports typical prices cost of 300 euro/kVA for 2 to 10 MVA system and installation cost between 600 000 to 3 000 000 euro with annual maintenance cost of 5% of the initial cost.

Uninterruptable power supplies (UPS) are devices that guarantee constant supply to their loads and they are three types (i) on-line, (ii) off-line and (9) combined. The on-line UPS are used for not that critical loads and when there is a problem with the grid voltages they switch internally to BESS and thus provide a power supply to the load. The off-line UPSs are connected to the grid but the load is decoupled from the grid via a back to back converter. A BESS is used as the storage element to supply the load in case of black out of the grid or other issues. In [171], prices of 500 euro per kVA are reported for systems between 10 to 300 kVA, which are used to supply production chains where synchronisation between the different process is crucial. The same reference also reports that the OPEX for these systems could reach 15% of the installation cost. This high OPEX is mainly driven by the prices of the battery energy storage and its replacement.

On the other hand, the amount of DERs connected to distribution networks increases due to environmental issues and liberalisation of the electricity markets [179]. This has led to a growing share of grid-connected DER systems, where most of them are inverter-connected. Despite the growing number of DERs, their contribution of delivered power to the utility grid often remains small compared with the injected power from the large central power plants [179]. In [180] and [181], it is suggested that the DERs connected to LV grids must support the voltage profile by means of injecting reactive power during faults. Due to the high R/X value of LV grids, the effect of reactive power on the grid voltage in LV grids is low, hence, this is not very effective.

Until recently, operators immediately disconnected the DERs during grid faults, but this has changed. The new technical requirements for decentralised production plants (<30kVA) necessitate that the DERs are able to overcome voltage variations and keep exchanging energy with the grid for 160 ms [12]. This is also required by more and more network operators. Elia, the Belgian TSO, in [182] demands

DERs to remain connected to the utility grid for 150 ms during faults. More grid codes of different European countries can be found in [183]. To maintain high reliability and good power quality standards to the end customer, the DERs can be used to provide support during voltage dips. Therefore, novel control strategies are needed that are capable of minimising the negative influence of the voltage dip to the sensitive loads.

In [17], the authors propose a solution for DERs that are interfaced with the LV grid by means of a three-phase three-wire inverter. The control strategy involves injecting reactive power into the distribution grid during fault conditions. However, since the R/X ratio of the LV grid is between 2 and 10, the injected reactive power will not have the needed positive effect towards the voltage dip as the DERs will have to inject significantly more reactive power to support the grid voltage compared to when they would inject active power. In addition, the power ratings of the inverters often do not allow for these high current, which diminishes the voltage support effect of the DERs.

In [179, 184], the voltage dip mitigation capabilities of single-phase damping DERs under voltage dips were studied. The developed single-phase control strategy with voltage dip mitigation has a resistive behaviour towards grid voltage disturbances [179]. This means that DER acts resistively towards voltage dips and harmonic distortions instead of behaving as an open circuit towards them. More information about the control strategy can be found in [179]. The theoretical analysis and experimental results show that the voltage dip mitigation abilities of single-phase inverters equipped with the single-phase damping control strategy is better than that of classically controlled inverters. In the event of a voltage dip, the inverter injects an additional fundamental current in phase with the grid voltage.

Further development of the single-phase damping control strategy is made in [46], where the control strategy is extended to a three-phase one. The proposed three-phase control strategy is able to mitigate voltage unbalance in three-phase LV grids. In [46], it was already shown that, this resistive behaviour enables voltage unbalance mitigation. The resistive behaviour enables DERs to inject different currents in the three phases acting on the unbalance and, thus, supporting the weakest phase, where the conventional control reacts as open circuit towards this and has no (beneficial) effect towards the unbalance. Opposite to the classical control, the damping control strategy also has a beneficial effect on the voltage profile because of its ability to control the zero- and negative sequence component. Therefore, in this chapter, the behaviour of three-phase grid-connected DERs with the damping control strategy during voltage dips will be investigated and the damping performance of the DERs will be studied. This work focuses on small-scale three-phase (commercial < 12 kW) and medium-scale (12 kVA < 100 kVA) DERs units, which are inverter-connected to the LV distribution grid.

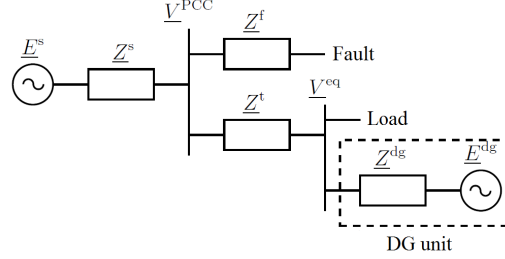


Figure 7.6: Voltage divider model used to investigate the residual voltage at the PCC

### 7.3 Voltage dip analysis

In order to calculate the residual voltage during a voltage dip due to a short-circuit elsewhere in the grid, at any given point in the distribution grid, the voltage divider model presented in [153] can be used. The model is presented in Fig.7.6 and it is based on the source impedance  $Z_1^s$ , which represents the internal impedance of the grid up to the PCC and the impedance  $Z_1^f$  between the PCC and the fault. All loads are modelled as constant impedance loads, so their contribution to the impedances above can be calculated easily by using the approach proposed in [153]. Since most of the voltage dips are three-phase asymmetrical, the impedance and voltage sources are replaced by their equivalent in symmetrical components. The positive-sequence voltage component  $V_1^{PCC}$  at the PCC is given by:

$$V_1^{PCC} = \frac{Z_1^f}{Z_1^f + Z_1^s} E_1^s \quad (7.8)$$

where  $E_1^s$  is the positive-sequence voltage of the grid. Because of the small impedance of the fault it can be assumed that the current flowing through  $Z_1^t$  is negligible compared to the fault current. From (7.8), it appears that not only the rms value of the voltage is affected during the voltage dip but also the phase angles. Since  $Z_1^s$  and  $Z_1^f$  are complex quantities, this can also lead to phase jumps in the PCC.

The calculation of the residual voltage experienced by a (sensitive) load is based on the voltage divider model shown in Fig. 7.6. If no DERs are present in the system, the remaining voltage level of the (sensitive) load  $V^{eq}$  is equal to the residual voltage at the point of common coupling  $V^{PCC}$  because the load impedance is much larger than the fault impedance, which is a common approximation in fault-analysis. Therefore, it can be also assumed that the load current causes negligible voltage drop across  $Z_1^t$ . If there are DERs present in the system, they could influence the residual voltage at the level  $V^{eq}$  of the sensitive load. Therefore, the voltage at the point of common coupling  $V^{eq}$  can be calculated by using the voltage source  $E_1^s$ .

## 7.4 Analytical comparison between the positive and damping control strategy

### 7.4.1 Positive-sequence control strategy

As mentioned in §2.3.2 the positive-sequence control strategy is one of the most common control strategies for DERs. The analytical model of it is given in §2.3.2, however for more clarity the injected currents are listed below:

$$\begin{aligned} \underline{i}_0 &= 0 \\ \underline{i}_1 &= g_1 \frac{\underline{v}_1}{|\underline{v}_1|} \\ \underline{i}_2 &= 0 \end{aligned} \quad (7.9)$$

where  $i_0$ ,  $i_1$  and  $i_2$  are the injected zero-, positive- and the negative sequence currents. The corresponding equivalent circuit toward the zero-, positive- and the negative-sequence components is presented in Fig. 7.9. From the analytical model and the equivalent circuit diagram it can be seen that the positive-sequence control strategy behaves as a closed circuit to the positive-sequence component and open circuit for the zero- and negative voltage components, hence it does not have any impact on the last two components.

### 7.4.2 Three-phase damping control strategy

In §2.6, a detailed description of the three-phase damping control strategy is given. Without loss of generality, the injected currents by this control strategy are used again as follows:

$$\begin{aligned} \underline{i}_a &= \frac{1}{3} \left\{ g_1 \left[ |\underline{v}_a| e^{j\theta_a} + |\underline{v}_b| e^{j(\theta_b + \frac{2\pi}{3})} + |\underline{v}_c| e^{j(\theta_c - \frac{2\pi}{3})} \right] \right. \\ &\quad \left. + g_d \left[ 2|\underline{v}_a| e^{j\theta_a} - |\underline{v}_b| e^{j(\theta_b + \frac{2\pi}{3})} - |\underline{v}_c| e^{j(\theta_c - \frac{2\pi}{3})} \right] \right\} \\ \underline{i}_b &= \frac{1}{3} \left\{ g_1 \left[ |\underline{v}_b| e^{j\theta_b} + |\underline{v}_a| e^{j(\theta_a - \frac{2\pi}{3})} + |\underline{v}_c| e^{j(\theta_c + \frac{2\pi}{3})} \right] \right. \\ &\quad \left. + g_d \left[ 2|\underline{v}_b| e^{j\theta_b} - |\underline{v}_a| e^{j(\theta_a - \frac{2\pi}{3})} - |\underline{v}_c| e^{j(\theta_c + \frac{2\pi}{3})} \right] \right\} \\ \underline{i}_c &= \frac{1}{3} \left\{ g_1 \left[ |\underline{v}_c| e^{j\theta_c} + |\underline{v}_a| e^{j(\theta_a + \frac{2\pi}{3})} + |\underline{v}_b| e^{j(\theta_b - \frac{2\pi}{3})} \right] \right. \\ &\quad \left. + g_d \left[ 2|\underline{v}_c| e^{j\theta_c} - |\underline{v}_a| e^{j(\theta_a + \frac{2\pi}{3})} - |\underline{v}_b| e^{j(\theta_b - \frac{2\pi}{3})} \right] \right\} \end{aligned} \quad (7.10)$$

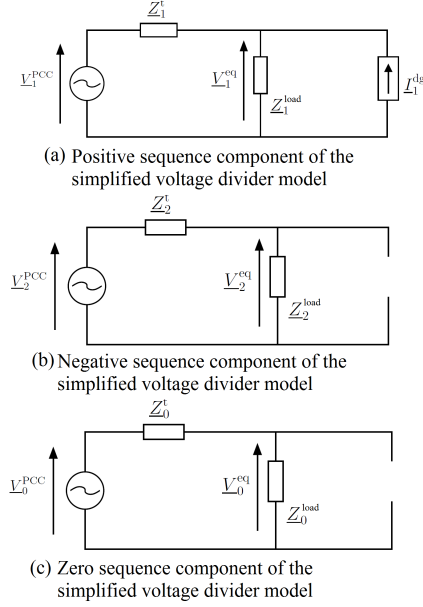


Figure 7.7: Equivalent circuit of the positive-sequence control strategy, expressed by symmetrical components

The terms in (7.10) that are related to  $g_1$  can be interpreted to represent the steady-state value of the fundamental component of the injected current. These terms are adapted by the dc-bus voltage controller in order to balance the power exchanged with the grid. The terms related to  $g_d$  emulate the resistive behaviour towards the zero- and negative-sequence voltage components. In order to react on the instantaneous changes of the phase voltages  $v_x(t)$ , which can vary faster than the terms in the curly brackets, as it reacts on every deviation of the fundamental grid voltage from the reference value, an additional term is included in the final equation [79]. The final equations in the time domain of the injected phase currents are written as follows:

$$\begin{aligned}
 i_{a,\text{ref}}(t) = & \frac{1}{3} \left\{ g_1 [v_a \sin(A) + v_b \sin(B) + v_c \sin(C)] \right. \\
 & \left. + g_d [2v_a \sin(A) - v_b \sin(B) - v_c \sin(C)] \right\} \\
 & + g_d (v_{a,1} \sin(\omega t + \theta_a) - v_{a,m} \sin(\omega t + \phi_a))
 \end{aligned}$$

$$i_{b,\text{ref}}(t) = \frac{1}{3} \left\{ \begin{aligned} &g_1 [v_b \sin(D) + v_a \sin(E) + v_c \sin(F)] \\ &+ g_d [2v_b \sin(D) - v_a \sin(E) - v_c \sin(F)] \\ &+ g_d (v_{b,1} \sin(\omega t + \theta_b) - v_{b,m} \sin(\omega t + \phi_b)) \end{aligned} \right\} \quad (7.11)$$

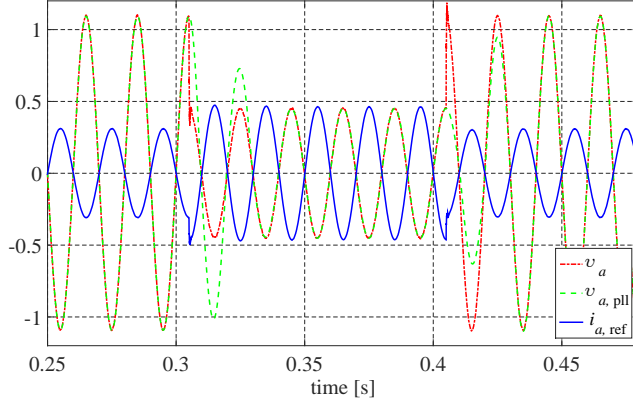
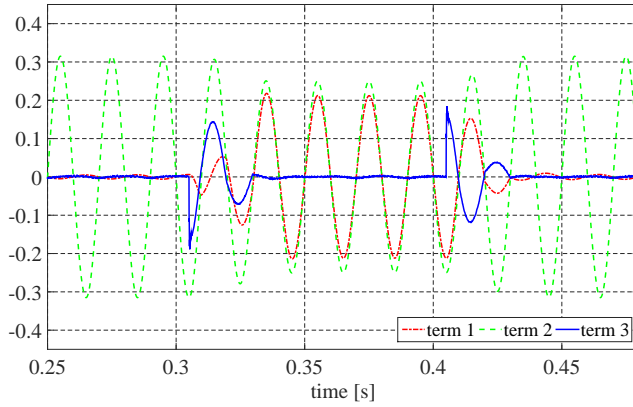
$$i_{c,\text{ref}}(t) = \frac{1}{3} \left\{ \begin{aligned} &\underbrace{g_1 [v_c \sin(G) + v_a \sin(H) + v_b \sin(I)]}_{\text{term1}} \\ &+ \underbrace{g_d [2v_c \sin(G) - v_a \sin(H) - v_b \sin(I)]}_{\text{term2}} \\ &+ \underbrace{g_d (v_{c,1} \sin(\omega t + \theta_c) - v_{c,m} \sin(\omega t + \phi_c))}_{\text{term3}} \end{aligned} \right\}$$

where:

$$\begin{aligned} A &= \omega t + \theta_a, & B &= \omega t + \theta_b + \frac{2\pi}{3}, & C &= \omega t + \theta_c - \frac{2\pi}{3} \\ D &= \omega t + \theta_b, & E &= \omega t + \theta_a - \frac{2\pi}{3}, & F &= \omega t + \theta_c + \frac{2\pi}{3} \\ G &= \omega t + \theta_c, & H &= \omega t + \theta_a + \frac{2\pi}{3}, & I &= \omega t + \theta_b - \frac{2\pi}{3} \end{aligned}$$

and  $v_{a,1} \sin(A)$ ,  $v_{b,1} \sin(D)$ ,  $v_{c,1} \sin(G)$  are the reference grid voltages that represent ideal sinusoidal fundamental signal while  $v_{a,m} \sin(\phi_a)$ ,  $v_{b,m} \sin(\phi_b)$  and  $v_{c,m} \sin(\phi_c)$  are the measured instantaneous values of the phase voltages.

An example of the reference current calculation is presented in Fig. 7.8 (a) and (b). The input conditions of the simulations are:  $|v_a| = 1.04$  p.u.  $|v_b| = 1.04$  p.u.  $|v_c| = 1.02$  p.u.  $g_d = 3$  p.u. and  $g_1 = 0.32$  p.u. Phase voltage  $v_a$  is subjected to a fault at time instance 0.305 s and the residual voltage is set to be 0.4 p.u. The fault is cleared at time 0.405s. Both instances are chosen such that the fault event occurs at the top of the sine of phase voltage  $v_a(t)$ . For more clarity, phase voltages  $v_b(t)$  and  $v_c(t)$  as well as reference currents  $i_{b,\text{ref}}(t)$  and  $i_{c,\text{ref}}(t)$  are not present. From Fig. 7.8 (a) it can be seen that between the two time instances 0.25s till 0.305s the DER operates in steady-state mode (the normalised phase locked loop voltage  $v_{a,\text{pll}}(t)$  matches with phase voltage  $v_a$ ) and the reference current is almost equal to its nominal value of 0.33 p.u. In Fig. 7.8 (b) the three terms of (7.11) are present individually and within the time interval under consideration, term 1 is dominant because there is very little voltage unbalance present at the PCC. At time instance 0.305s the fault occurs and the residual voltage drops to 0.4 p.u. Term 3 is then activated due to the difference between the instantaneous value of  $v_a(t)$

(a) Calculated reference current  $i_{a,\text{ref}}(t)$  according to (7.11) during voltage dip conditions

(b) Decomposition of the reference current by different terms

Figure 7.8: Calculation of the reference currents at voltage dips

and the normalised PLL voltage  $v_{a,\text{pll}}(t)$ . Term 3 is added to the reference current and it contributes for the fast response of the control strategy as shown in Fig. 7.8 (a) and (b). The PLL needs approximately 1.5 grid cycles to update correctly the new value of  $v_a(t)$ . During the voltage dip term 1 decreases because the positive-sequence component decreases. However, there is a significant voltage unbalance at the PCC and term 2 has more weight in the reference current calculation. After 1.5 cycles term 3 becomes very small and the voltage dip is mitigated entirely by term 2. At the end of the voltage dip at time instance 0.405s, the fault is cleared and term 3 has a non zero value due to the difference between  $v_a(t)$  and  $v_{a,\text{pll}}(t)$ . At this instance  $i_{a,\text{ref}}(t)$  decreases with a step and it decays until the difference

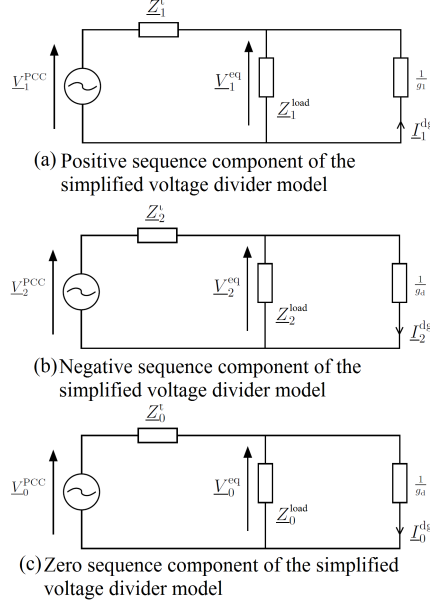


Figure 7.9: Equivalent circuit of the three-phase damping control strategy, expressed by symmetrical components

between  $v_a(t)$  and the reconstructed voltage  $v_{a,pll}(t)$  becomes zero.

By adding the last term in (7.11) the three-phase damping control strategy that is able to react on the instantaneous changes of the grid voltage, the final symmetrical component equivalent circuit is obtained as presented in Fig. 7.9. The term responsible for the voltage unbalance mitigation together with the last term of (7.11) provide a closed path for the zero- and negative sequence components. Thus, these components are mitigated.

Term 3 can be used for two different purposes. The first one is harmonic mitigation in grid-connected applications as used in [116] and also in microgrid applications as demonstrated in [185]. The other function can be voltage dip mitigation as studied in [179, 184]. In [116, 185], only the harmonic mitigation is considered and voltage dips are not considered whereas [46, 179, 184] the grid voltage is considered harmonic free and only dips are considered. Term 3 reacts on the instantaneous variation of the grid voltage from the nominal  $v_{1,x}(t)$ , which includes both harmonics and voltage dips. In this thesis, harmonic mitigation is not considered regardless the ability of term 3 to mitigate them. Therefore, a special algorithm could be used to enable this term only when voltage dip occurs.

### 7.4.3 Analytical analysis of voltage dips in LV feeders

To illustrate the damping performance of the control strategy a voltage dip of Type B [153] will be studied. This voltage dip affects only phase  $a$  and no phase shift in the other two phases is present. Voltage dip of Type A, is a fault between the three lines and it is not studied due to its symmetrical nature. Type C and D require phase shift between the phases, which are not under the fault condition. To easily explain the effect of the damping control strategy on the residual voltage, it is preferred that only change in the amplitude is considered.

It is assumed that the voltage asymmetry is present only at the PCC, see Fig. 7.6. The rest of the network is balanced such that the different schemes are decoupled in symmetrical components. The simplified model in symmetrical components is depicted in Fig. 7.7, in the case of the three-phase positive-sequence control strategy and in Fig. 7.9, in case of the three-phase damping control strategy.

The three-phase positive-sequence control strategy uses a reference current described by  $i_a^{\text{ref}} = g_1 \cdot \sin(\phi_a)$ ,  $i_b^{\text{ref}} = g_1 \cdot \sin(\phi_a - 2\pi/3)$  and  $i_c^{\text{ref}} = g_1 \cdot \sin(\phi_a + 2\pi/3)$ , where  $\phi_a$  is the instantaneous phase angle of phase  $a$  while  $g_1$  represents the fundamental input conductance. Therefore, the positive-sequence three-phase control strategy injects only positive-sequence current in the grid.

The voltage divider model in Fig. 7.6 may then be used to study the influence of the damping three-phase control strategy towards the residual voltage. By assuming that the asymmetry is only present at the PCC location, the three symmetrical components networks become independent of each other. The negative-sequence and zero-sequence component equivalent circuits in case of the three-phase damping control strategy of the simplified model are depicted in Fig. 7.9 (b) and Fig. 7.9 (c), respectively. The negative-sequence and zero-sequence component of the residual voltage at the location of the sensitive load are then given by:

$$\begin{aligned} \underline{v}_2^{\text{eq}} &= \frac{\underline{z}_2^{\text{load}} \parallel \frac{1}{g_d}}{\underline{z}_2^t + \left( \underline{z}_2^{\text{load}} \parallel \frac{1}{g_d} \right)} \underline{v}_2^{\text{PCC}} \\ \underline{v}_0^{\text{eq}} &= \frac{\underline{z}_0^{\text{load}} \parallel \frac{1}{g_d}}{\underline{z}_0^t + \left( \underline{z}_0^{\text{load}} \parallel \frac{1}{g_d} \right)} \underline{v}_0^{\text{PCC}} \end{aligned} \quad (7.12)$$

where  $\parallel$  denotes “in parallel with”. As it can be seen the damping conductance provides a higher admittance flowing path for the zero-sequence and the negative-sequence components. Therefore, the damping conductance behaves as a closed circuit for these components.

For the positive-sequence control strategy, the negative- sequence and zero-sequence components of the simplified voltage divider model are shown in Fig.

7.9 (b), and Fig. 7.9 (c), respectively. The negative-sequence and zero-sequence component of the retained voltage at the level of the load can be given by:

$$\begin{aligned} \underline{V}_{-2}^{\text{eq}} &= \frac{\underline{Z}_2^{\text{load}}}{\underline{Z}_2^{\text{t}} + (\underline{Z}_2^{\text{load}})} \underline{V}_2^{\text{PCC}} \\ \underline{V}_0^{\text{eq}} &= \frac{\underline{Z}_0^{\text{load}}}{\underline{Z}_0^{\text{t}} + \underline{Z}_0^{\text{load}}} \underline{V}_0^{\text{PCC}} \end{aligned} \quad (7.13)$$

In practice, the term  $\frac{\underline{Z}_2^{\text{load}} \|\frac{1}{g_d}\|}{\underline{Z}_2^{\text{t}} + \underline{Z}_2^{\text{load}} \|\frac{1}{g_d}\|}$  in (7.12) is smaller than the term  $\frac{\underline{Z}_2^{\text{load}}}{\underline{Z}_2^{\text{t}} + \underline{Z}_2^{\text{load}}}$  in (7.13). Therefore, both the negative-sequence and zero-sequence voltage components will decrease when the three-phase damping control strategy is used compared to the positive-sequence control. This will have a positive effect on the residual voltage at the level of the sensitive load, which will be closer to its nominal value in case of the three-phase damping control. Therefore, it can be concluded that the grid is supported by the damping control strategy during voltage dips.

This conclusion is further illustrated by analysing a specific voltage dip. A voltage dip Type B, in phase  $a$  can be described with:

$$\begin{aligned} v_a &= \alpha_1 |v| \\ v_b &= a^2 |v| \\ v_c &= a |v| \end{aligned} \quad (7.14)$$

where  $\alpha_1$  is a factor defining the depth of the voltage dip in phase  $a$  and  $|v|$  is the amplitude of the pre-fault voltage at the terminals of the inverter. Translated into symmetrical components, the following expressions are obtained:

$$\begin{aligned} \underline{v}_0 &= \frac{1}{3}(\alpha_1 - 1)|v| \\ \underline{v}_1 &= \frac{1}{3}(\alpha_1 - 2)|v| \\ \underline{v}_2 &= \frac{1}{3}(\alpha_1 - 1)|v| \end{aligned} \quad (7.15)$$

Hence, the desired value for the current injected by the three-phase damping inverter into the grid can be written in symmetrical components:

$$\begin{aligned} \underline{i}_0 &= g_d \frac{1}{3}(\alpha_1 - 1)|v| \\ \underline{i}_1 &= g_1 \frac{1}{3}(\alpha_1 - 2)|v| \end{aligned} \quad (7.16)$$

$$\underline{i}_2 = g_d \frac{1}{3} (\alpha_1 - 1) |\underline{v}|$$

These equations are then translated into phase quantities and the following expressions are obtained:

$$\begin{aligned} \underline{i}_a &= \left[ \frac{2}{3} g_d \frac{1}{3} (\alpha_1 - 1) + g_1 \frac{1}{3} (\alpha_1 + 2) \right] |\underline{v}| \\ \underline{i}_b &= \left[ (1 + a) g_d \frac{1}{3} (\alpha_1 - 1) + a^2 g_1 \frac{1}{3} (\alpha_1 + 2) \right] |\underline{v}| \\ \underline{i}_c &= \left[ (1 + a^2) g_d \frac{1}{3} (\alpha_1 - 1) + a g_1 \frac{1}{3} (\alpha_1 + 2) \right] |\underline{v}| \end{aligned} \quad (7.17)$$

If the DER injects its nominal power into the grid then  $g_1$  is negative, so the second term in the reference value for the current of phase  $a$  is negative. When  $\alpha_1 < 1$  and  $g_d$  is positive then the first term is negative. Consequently, this leads to the resistive behaviour with respect to the zero-sequence and the negative-sequences voltage component and also to current increasing in the phase where the voltage dip occurs.

Below, a brief numerical example is given to analytically show that the current will be different in the different phases and the phase with the lowest voltage will have the highest current. In case  $\alpha_1 = 0.7$ ,  $g_d = 1$ ,  $|v| = 1$  and  $g_1 = -0.5$ , then (7.17) gives  $\underline{i}_a = -0.517$ ,  $\underline{i}_b = 0.175 + j0.3031$  and  $\underline{i}_c = 0.175 - j0.3031$ . The rms value of  $|\underline{i}_a|$  is 0.517 A while  $|\underline{i}_b|$  and  $|\underline{i}_c|$  0.35 A versus 0.45 A (when  $g_d = 0$ ) for the duration of the voltage dip. Hence, the resistive behaviour of the three-phase damping inverter indeed leads to the injection of higher current in phase  $a$  where the voltage dip has occurred and lower current in the other two phases. Thus the faulty phase is supported and the residual voltage is increased.

#### 7.4.4 Simulation results

Reference [83] presents measurements of voltage dips and 1175 monitoring sites. The measurements are conducted in 2006 to 2009. The measurements are performed as suggested in IEC 61000-4-34 and the results showed that only voltage dips Type A, Type C and Type D are measured at the LV level (star connected loads). The statistical measurements also showed that Type A are about 20% of the total dips. Voltage dips Types C occur at HV and MV level and it accounts for 51 - 63% of the total dips. According to Fig. 7.4 and Table 7.1 voltage dip Type C is transformed into Type D at LV level for star connected loads. Besides voltage drop, this dip is characterised also by a phase jump, which will result in transients in the PLL units. Therefore, the influence of the voltage dip Type D in LV grids will be further investigated. Table 7.1 shows the typical voltage dips that are most likely to be present at the level of the sensitive load. To limit the volume of the

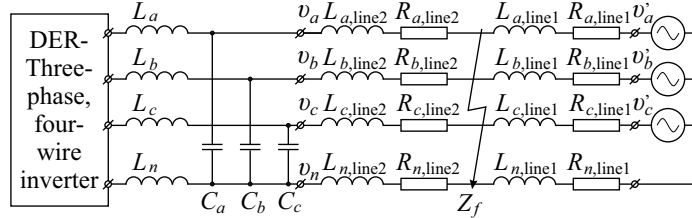


Figure 7.10: Set-up configuration to test voltage dip Type B

study Type C, Type E and Type G are not examined regardless of the phase jumps they exhibit.

In order to illustrate the behaviour of the examined control strategies, a simpler voltage dip is needed. As suggested in [79], a Type B voltage dip is used to examine the considered control strategies because it is a phase-to-ground dip. In summary, voltage dips Type B and Type D will be examined at the levels of residual voltages recommended by IEC 61000-4-34. The levels of the residual voltages are listed in Table 7.2. In addition, different values of the damping conductance will be investigated in order to assess the voltage dip mitigation abilities of the positive-sequence and the three-phase damping control strategies.

To assess the performance of the control strategies, the simulation model presented in Chapter 5 is used. The connection diagram of the DER is the same as the one depicted in Fig. 4.49. To calculate adequately the residual voltages and the phase jump of a dip Type D it is assumed that the grid topology is as the presented in Fig. 7.4 and a dip of Type B is present at the HV level with residual voltages of 40%, 70% and 80%. By using (7.2), (7.3) and (7.4) the residual voltages  $v'_a, v'_b$  and  $v'_c$  and their corresponding phase angle jumps are calculated. These values are then used in the simulation model.

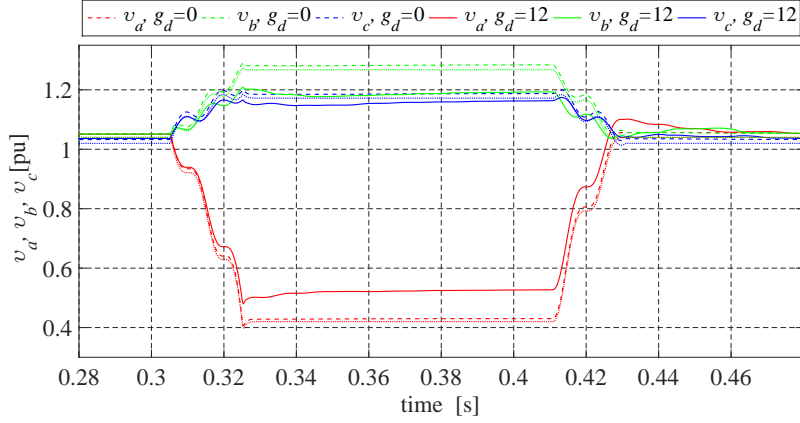
Voltage dip Type B is tested by creating a fault in the middle of the feeder between the phase and the neutral conductor. The fault impedance is selected such that the desired levels of residual voltages are achieved. Reference [81] suggests that the zero-sequence component does not propagate to the equipment terminals because there is at least one transformer, which blocks the zero-sequence component. This source also states that the fault rarely occurs at the same level of the sensitive load. In [164], it is stated that the zero-sequence impedance could cause voltage rise in the non-faulted phases to rise up to 1.2 to 1.3 p.u. This phenomenon is called voltage swells and it lasts as long as the fault is not cleared. Therefore, it is an interesting case to examine what would be the behaviour the LV grid if such a fault is present. Fig. 7.10 shows the set-up that is used to examine the residual voltages at the DER level. The feeder is split in two equal parts, which gives impedance of  $(0.235 + j0.1)\Omega$ .

### 7.4.5 Examination of voltage dips at nominal input power

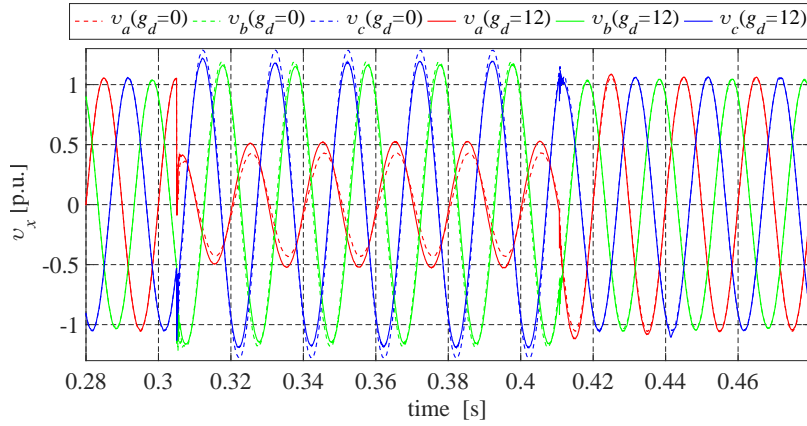
At first, voltage dip Type B is simulated by emulating a fault in the middle of the feeder so that residual voltage of about 40% is achieved. In this particular case, the fault impedance is  $0.325 \Omega$  while for the faults with residual voltages 70 and 80% this impedance is 1 and  $1.75\Omega$ , respectively. The dip is introduced in the feeder at time instance 0.305 s where the top of the sine wave in phase  $a$  is present. The dip is cleared out at time instance 0.41s, which happens to be the zero-crossing of  $v_a(t)$ . This dip type is also called a rectangular single stage dip. Non-rectangular dips are present when a transformer or large electrical machines are energised. Whereas multi-stage dips can occur due to two, and rarely more than four, consecutive faults [164]. Before and after the fault, the grid is considered to be  $v'_a = 1.04$  p.u.  $v'_b = 1.02$  p.u. and  $v'_c = 1.02$  p.u. and all phase angles are kept to their nominal values. These initial conditions are also used in the other sub-cases where the zero-input and power consumption modes are examined.

In this simulation, the input power of the DER is equal to its nominal value. The simulation results where the positive-sequence and three-phase damping control strategies are presented in Fig. 7.11. In Fig. 7.11 (a) are shown the phase voltages at the DER terminal and three cases are considered. By using dotted lines, the phase voltages are depicted when no DER unit is connected to the feeder. With dashed and solid lines are depicted the phase voltages when the positive-sequence and the three-phase damping control strategies are employed in the DER. The damping control strategy uses an initial value of the damping conductance of 12 p.u. and the local control is disabled. As it can be seen, due to the zero-sequence component, the non-faulty phases ( $b$  and  $c$ ) do experience voltage swells. Phase voltage  $|v_b|$  is almost 1.25 p.u. During the dip, the residual voltage in phase  $a$  is almost 40% while in phase  $b$  and  $c$  these voltages are 1.19 p.u. and 1.25 p.u. respectively. The positive-sequence control strategy slightly increases the residual voltage in phase  $a$  during the voltage dip but it also increases the rms values in the other two phases, which leads to even more severe overvoltages in them. On contrary, the three-phase damping control strategy is able to increase the residual voltage from approximately 0.4 p.u. to 0.5 p.u. by injecting larger current in this phase and thus supports the grid. In addition, the phase voltages in the phases that experience voltage swells are lowered as well. Voltage  $|v_c|$  is lowered down to 1.19 p.u. while  $|v_b|$  is decreased to 1.17 p.u.

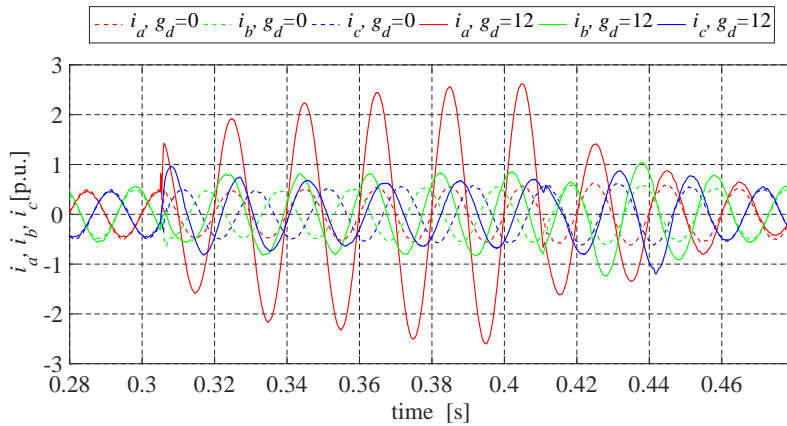
Fig. 7.11 (b) depicts the instantaneous three-phase voltages when both control strategies are compared. As it can be seen the dip indeed occurs on the top of the sine of  $v_a(t)$  but it can be also noticed a considerable difference between the positive-control strategy and the three-phase damping control strategy.



(a) rms voltages of the phase voltages during a voltage dip with a residual voltage of 40%



(b) Instantaneous values of the phase voltages at voltage dip Type B



(c) Injected current by DER during voltage dip at  $g_d = 0$  and 12 p.u.

Figure 7.11: Phase voltages and injected phase currents by the positive-sequence and three-phase damping control strategies at  $p_{dc} = -1$  p.u. when voltage dip Type B is investigated

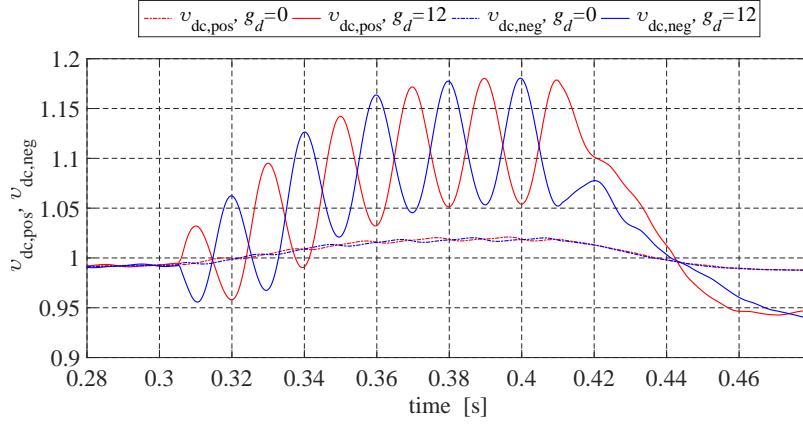
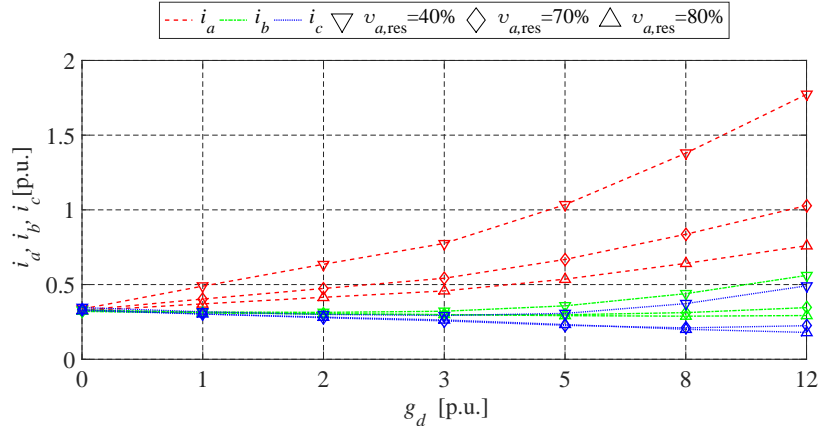


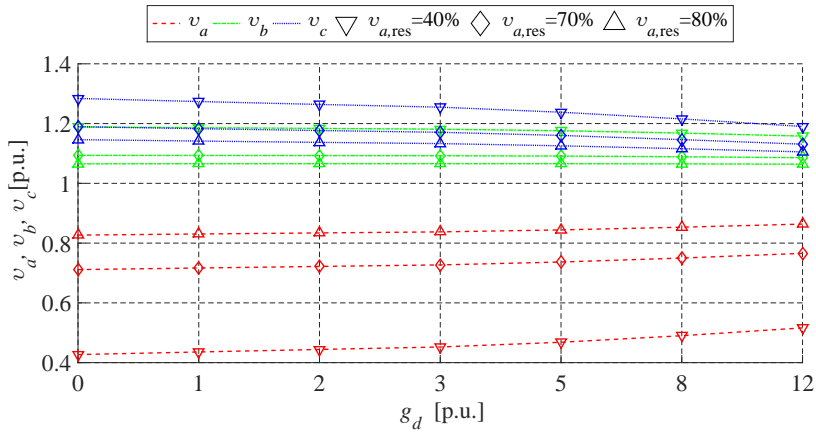
Figure 7.12: Positive and negative dc-bus voltages at  $g_d = 0$  p.u. and 12 p.u.

The injected phase currents are presented in Fig. 7.11 (c), where it can be seen that at the initiation of the voltage dip, severe distortions in the injected currents are not present. To achieve the difference of almost 10% in the residual voltages, the three-phase damping control strategy injects almost 5 times the nominal current in phase  $a$  while less current is been injected in phases  $b$  and  $c$ . When the fault is cleared, the phase currents need about 2.5 cycles to reach their nominal steady-state values. The dynamic of the phase currents is also dependent on the dc-bus controllers, which are slower compared to the current PI controllers. The positive and negative dc-bus voltages are depicted in Fig. 7.12 where the dynamics of the dc link during voltage dips is observed. Indeed, the dip ends at 0.41s but the dc-bus controller settles down slowly as mentioned in §5.4.3 and §5.4.4. In addition, it can be observed that both dc-bus voltages have the same path when positive-sequence control strategy is used and the same trend (when the ac ripple is neglected) when the damping control strategy is employed.

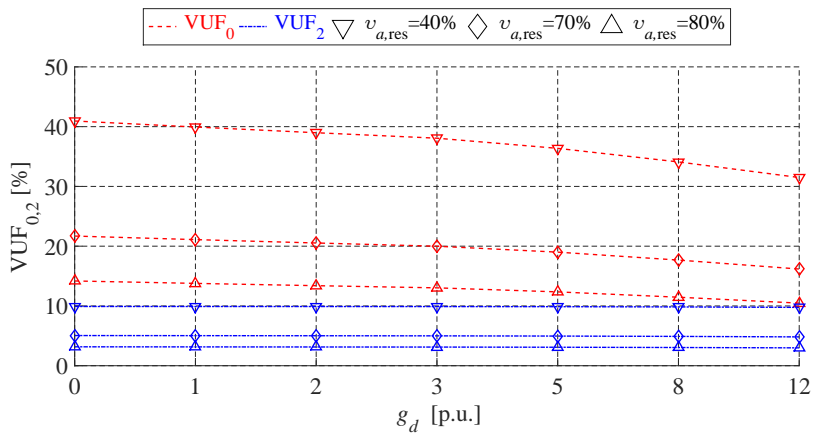
The injected phase currents as a function of the damping conductance are depicted in Fig. 7.13 (a). On top of that, this figure also depicts the injected currents as a function of the residual voltage in phase  $a$ . A distinction between the different residual voltages is made by using different markers and different colours are used for the different phase currents. As expected the higher divergence in the phase current is observed at the larger dip and damping conductance value. Almost none divergence is observed when the positive-sequence control strategy is used, regardless of the severity of the voltage dip. This figure also shows how many times the power electronic inverter should be oversized in order to achieve relatively good voltage dip mitigation.



(a) Injected rms phase currents as a function of  $g_d$  and residual voltage



(b) Residual phase voltages as a function of  $g_d$



(c) Voltage unbalance factors as a function of  $g_d$  and residual voltage

Figure 7.13: dc-bus voltages transient, rms current injection and voltage unbalance factor dependency on the damping conductance and residual voltages caused by a dip Type B at  $p_{dc} = -1$  p.u.

| Standard values         | 40%     |         |         | 70%     |         |         | 80%     |         |         |
|-------------------------|---------|---------|---------|---------|---------|---------|---------|---------|---------|
| Phase voltage           | $ v_a $ | $ v_b $ | $ v_c $ | $ v_a $ | $ v_b $ | $ v_a $ | $ v_c $ | $ v_b $ | $ v_c $ |
| Type D                  |         |         |         |         |         |         |         |         |         |
| Residual voltage [p.u.] | 0.601   | 0.901   | 0.901   | 0.786   | 0.934   | 0.934   | 0.854   | 0.954   | 0.954   |
| Phase jump [°]          | 0       | -17     | 17      | 0       | -8      | 8       | 0       | -3.2    | 3.2     |

Table 7.3: Comparison between voltage dips Type D and Type C in terms of residual voltages and phase jumps

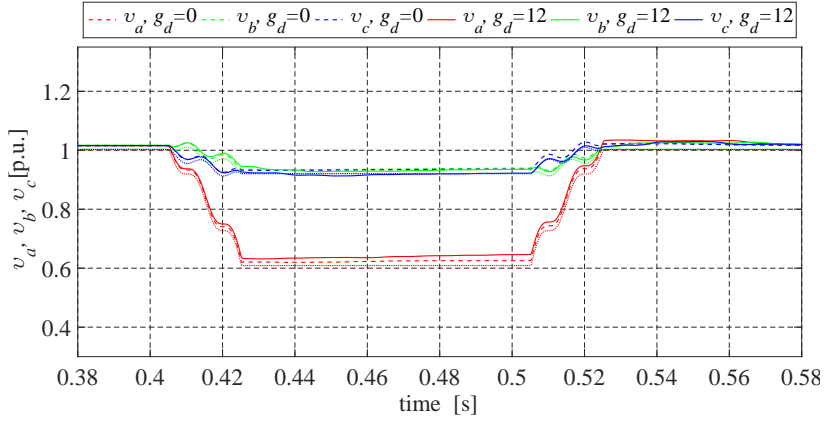
However, oversizing of about 5 times the power electronic inverter is enormously costly and compromises should be made regarding the voltage dip mitigation. Nevertheless, in LV grids there are more than one DER connected to the distribution feeder, therefore, later in this chapter the effect of three DERs connected at the same feeder will be further examined.

The residual phase voltages as a function of the damping conductance are depicted in Fig. 7.13 (b). To distinguish the different residual voltage levels and phase voltages, the approach used in Fig. 7.13 (a) is adopted. As it can be seen from the obtained results, the impact on the residual voltages is higher when the residual voltages are lower and vice versa especially at high values of the damping conductance. The effect is a consequence of the injected higher current in the faulty phase and less currents in the intact ones.

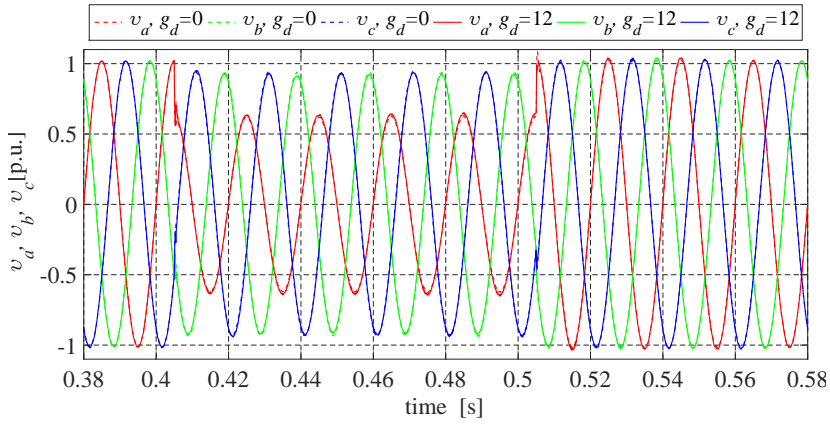
The zero- and negative-sequence voltage unbalance factors are shown in Fig. 7.13 (c). The same distinction between the residual voltages is applied as in Fig. 7.13 (a). This figure shows that the control strategy is able to affect  $VUF_0$  while  $VUF_2$  is barely impacted. The reason for this effect is that the term 2 of (7.10) contains both zero- and negative-sequence components, which are summed up. Therefore, the damping conductance impacts the one with the most weight, which in this particular case is the zero-sequence component.

The most common voltage dip in LV grids is Type D. This dip is a consequence of a single-phase-to-ground fault. The calculated residual voltages, which are used in the voltage sources in the simulation model are listed Table 7.3. As it can be seen for the calculated residual voltages, phases  $b$  and  $c$  are also affected by the fault and their rms voltages are not equal to the nominal values. In this simulation, the dip initiation and clear are chosen to be at times 0.405s and 0.505s, which in both times happens to be at the top of the sine of  $v_a(t)$ .

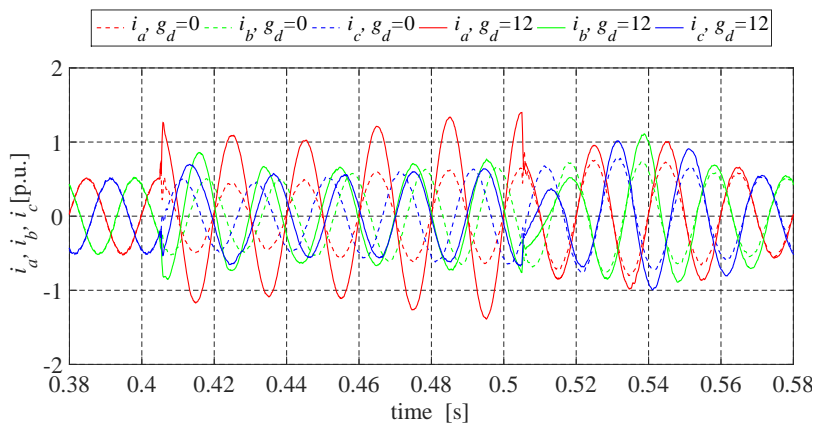
Fig. 7.14 (a) depicts three scenarios of the residual voltages during the fault. The dotted line represents the scenario when no DER is connected to the grid while the dashed line shows how the voltage profile changes if the positive-sequence control strategy is used and finally the solid line depicts the scenario when the three-phase damping control strategy is employed and damping conductance value of 12 p.u. is applied. The positive-sequence control strategy is able to slightly increase the residual voltage in phase  $a$  and also in phase  $c$  while  $|v_b|$  remains rather the same. If the three-phase damping control strategy is used, the residual voltage of phase  $a$  is increased almost as twice as much compared to the positive-sequence control strategy while the other two phase voltages are rather the same.



(a) rms voltages and their residual values during a voltage dip with a residual voltage of 40%

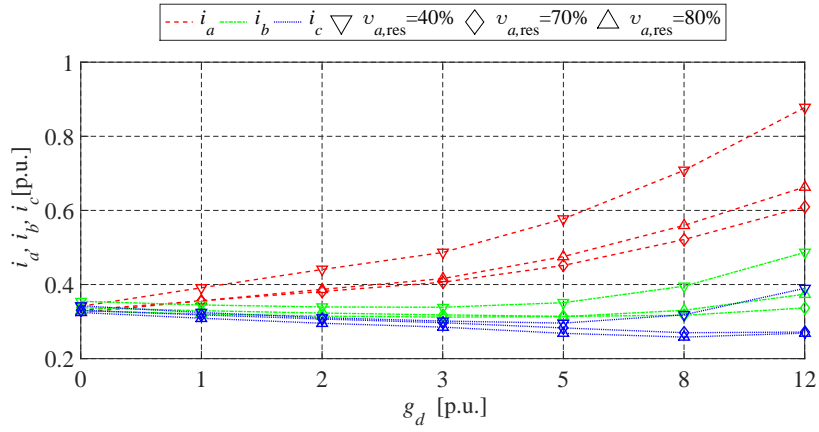


(b) Instantaneous values of the phase voltages at voltage dip Type D

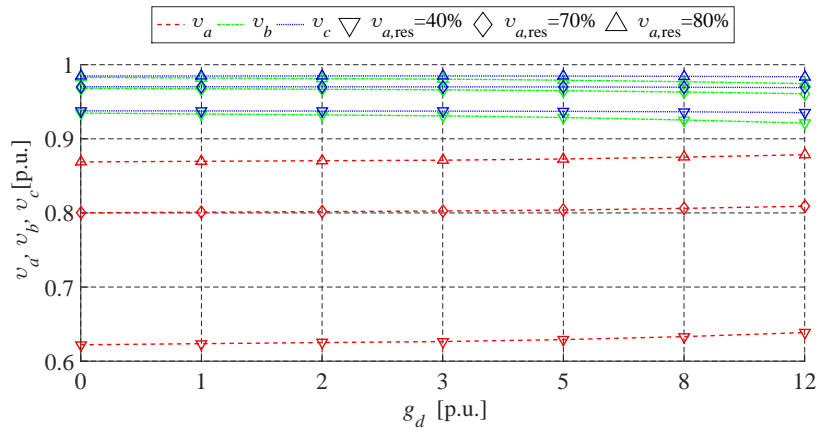


(c) Injected current by DER during voltage dip at  $g_d = 0$  and 12 p.u.

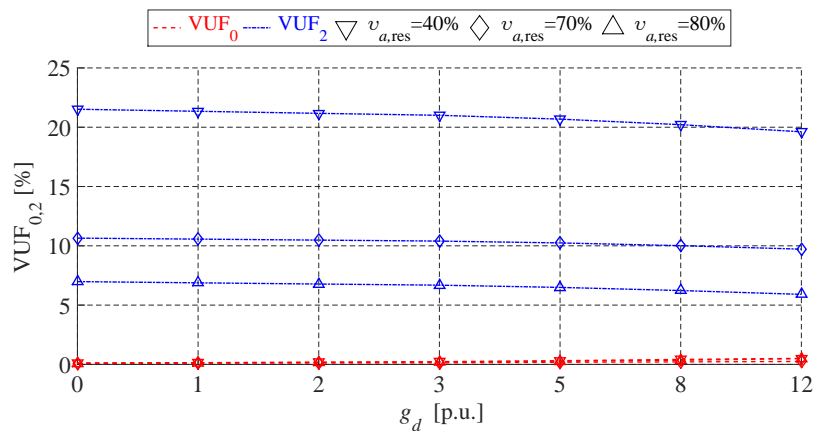
Figure 7.14: Phase voltages and injected phase currents by the positive-sequence and three-phase damping control strategies at  $p_{dc} = -1$  p.u. when voltage dip Type D is investigated



(a) Injected rms phase currents as a function of  $g_d$  and residual voltage



(b) Residual voltages as a function of  $g_d$



(c) Voltage unbalance factors as a function of  $g_d$  and residual voltage

Figure 7.15: dc bus voltages transient, rms current injection and voltage unbalance factor dependency on the damping conductance and residual voltages caused by a dip Type D at  $p_{dc} = -1$  p.u.

The instantaneous phase voltages are shown in Fig. 7.14 (b) and the exchanged phase currents are presented in Fig. 7.14 (c). The three-phase damping control strategy is able to increase the residual voltage with almost 0.1 p.u. if type B is present in the LV feeder but when Type D is examined. The results reveal that there is a very small difference in the residual voltages (about 4%) when the three-phase damping control strategy is used, despite the high value of the damping conductance of 12 p.u. This small effect is due to the fact the smaller current is injected in phase  $a$ , which is shown in Fig. 7.14 (c). In this particular case, the injected phase current  $|\dot{i}_a|$  is only 2.5 times the nominal value while the mitigation of dip Type B resulted in almost 5 times the nominal value.

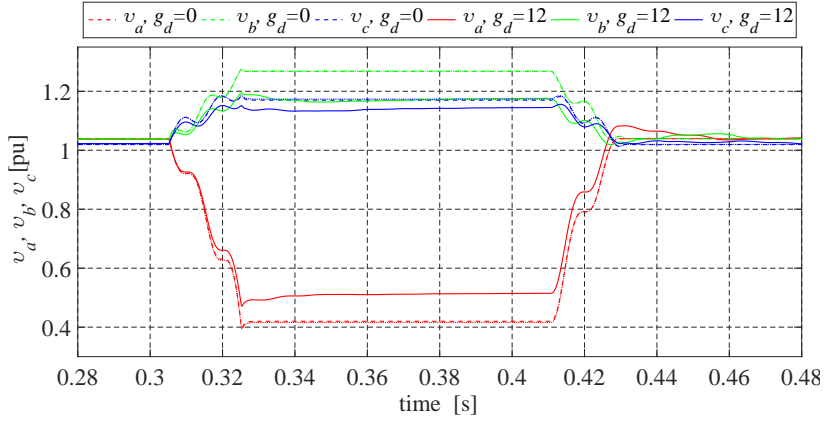
The exchanged phase currents as a function of the damping conductance and at different levels of the residual voltages are shown in Fig. 7.15 (a) and the residual voltages are depicted in Fig. 7.15 (b). At the maximum value of  $g_d$  of 12 p.u. and the lowest considered residual voltage, the maximum current injected in phase  $a$  is almost 0.9 p.u. In order to achieve higher voltage dip mitigation as obtained for the Type B, the value of the damping conductance must be increased.

The zero- and negative-sequence voltage unbalance factors are shown in Fig. 7.15 (b) and as it can be seen the negative-sequence component is more affected and at high values of the damping conductance and high residual voltages, the effect is more prominent and a decrease of about 3% is observed. Although the voltage dip Type D does not introduce any zero-sequence voltage at the DER terminals, the value of the zero-sequence voltage unbalance factor is not 0%, especially at high values of the damping conductance. This effect is caused by the transient in the PLLs, which introduces some zero-sequence current injection at the beginning and the end of the voltage dip.

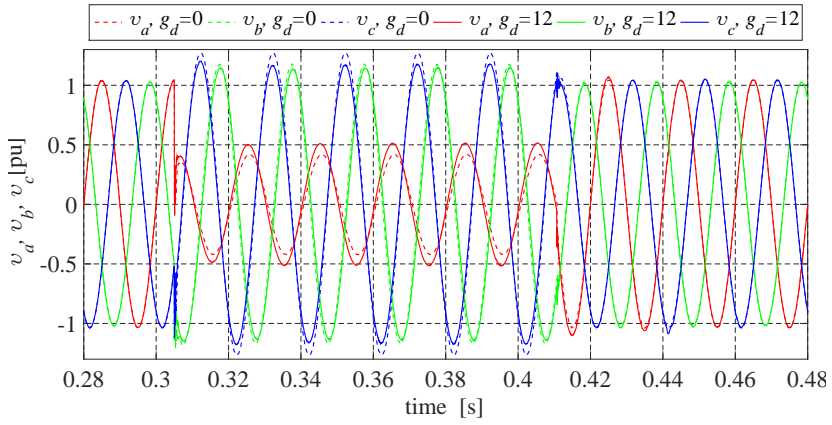
#### 7.4.6 Examination of voltage dips at zero input power

In this section, the voltage dip mitigation abilities of the positive-sequence and the three-phaser damping control strategies are investigated. The input data are the same as the ones used in §7.4.5.

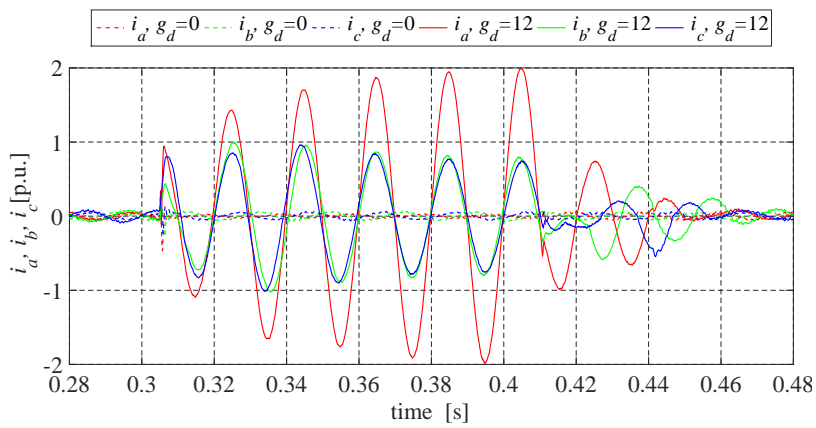
The residual voltages during the voltage dip Type B are depicted in Fig. 7.16 (a). In this examination three cases are considered such as no DER (it is depicted by using dotted lines), DER equipped with the positive-sequence control strategy (it is depicted by using dashed lines) and finally, a DER equipped with the three-phase damping control strategy (it is depicted by using solid lines). Since the DER input power is zero, the obtained results when no DER is connected and a DER that is equipped with the positive-sequence control strategy do overlap and give the same residual voltages. In contrast, the three-phase damping control strategy is able to increase the residual voltage with 10% as well as reducing the swell voltages in phases  $b$  and  $c$  with 7% and 3%, respectively.



(a) rms voltages of the phase voltages during a voltage dip with a residual voltage of 40%



(b) Instantaneous values of the phase voltages at voltage dip Type B



(c) Injected current by DER during voltage dip at  $g_d = 0$  and 12 p.u.

Figure 7.16: Phase voltages and injected phase currents by the positive-sequence and three-phase damping control strategies at  $p_{dc} = 0$  p.u. when voltage dip Type B is investigated

All phase voltages are depicted in Fig. 7.16 (b). The beneficial effect of the three-phase damping control strategy can be clearly seen compared to the positive-sequence control strategy. This beneficial effect is achieved by the injected phase currents, which are depicted in Fig. 7.16 (c). There are some phase currents that are flowing when the positive-sequence control strategy is used, but these currents are due to the capacitors  $C_a$ ,  $C_b$  or  $C_c$ . In general, before, during or after the transient, the positive-sequence does not exchange any phase currents. On contrary, the three-phase damping control strategy exchanges asymmetrical currents with the grid. In this mode, the control strategy consumes active power from phases  $b$  and  $c$  and injects it back in phase  $a$ . This active current is almost 1.4 p.u. and it is able to increase its residual voltage to 0.52 p.u. Besides active current, reactive currents are also exchanged with phases  $b$  and  $c$ . Phase current  $i_b(t)$  is slightly lagging  $v_b(t)$  while  $i_c(t)$  is slightly leading  $v_c(t)$ . Despite the lagging and leading of these phase currents, the residual phase voltages  $v_b$  and  $v_c$  are decreased.

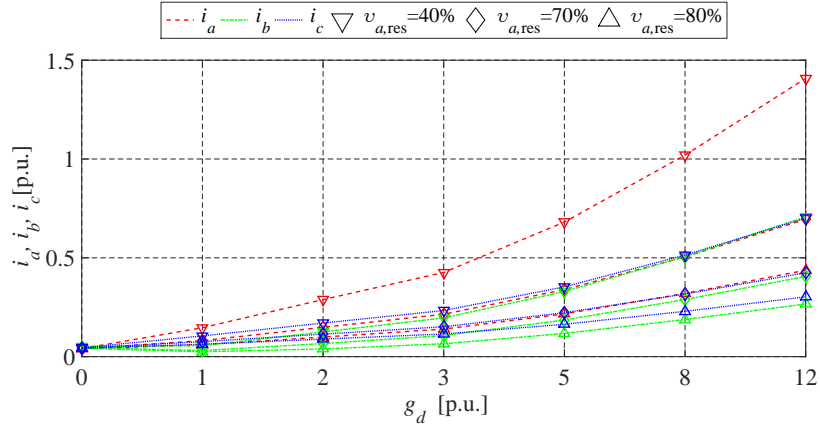
Since there is no power at the dc bus, the transient on the positive and the negative dc bus voltages will be smaller compared to Fig. 7.13. Therefore, these voltages are not considered interesting in this section.

The rms values of the phase currents as a function of the damping conductance at different residual voltages are depicted in Fig. 7.17 (a). These results show that the phase current  $|i_a|$  breaches the nominal current of the inverter current already at  $g_d = 2$  p.u. and 40% residual voltage, almost 50% oversizing is needed if  $g_d = 3$  p.u. is considered and so on. Ultimately, oversizing of 4 times is needed if the highest examined value of this study is applied.

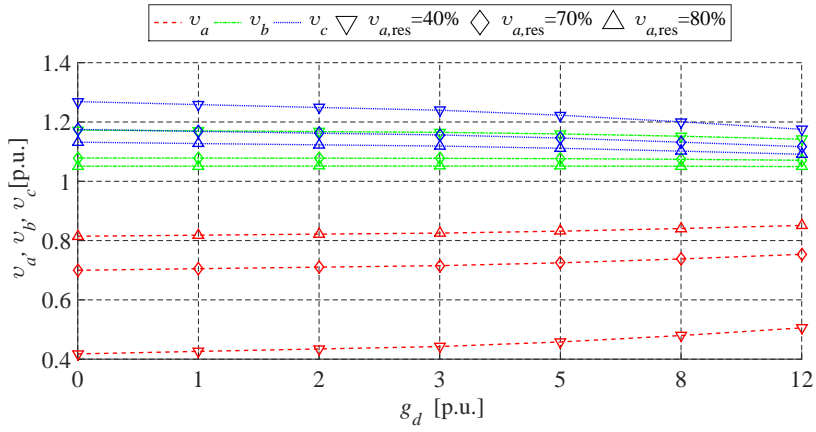
The rms values of the phase voltages as a function of the damping conductance at different residual voltages are depicted in Fig. 7.17 (b). Despite the fact that DER is not supplied by the primary source, the three-phase damping control strategy is able to mitigate the voltage dip by increasing the residual voltage in phase  $a$ . In Chapter 4, this valuable quality of the three-phase damping control strategy is studied when voltage unbalance is mitigated but the obtained results in this examination show that this quality can be successfully applied to voltage dip mitigation. If the lowest residual voltage is considered (residual voltage of 40%) in this mode ( $p_{dc} = 0$  p.u.) the nominal power ratings are already breached at  $g_d = 2$  p.u. while the dip mitigation provides only 2% to the residual voltage and 50% oversizing yields about 3% to the residual voltage at  $g_d = 3$  p.u. Since the voltage dip mitigation capabilities of the DER are determined by its power ratings in the end, it is a trade off between the desired voltage dip capability and inverter sizing.

As of the voltage unbalance mitigation, the results are presented in Fig. 7.17 (c) and they resemble the results in Fig. 7.13 (c). The major impact is on the zero-sequence unbalance factor while the negative-sequence unbalance factor is

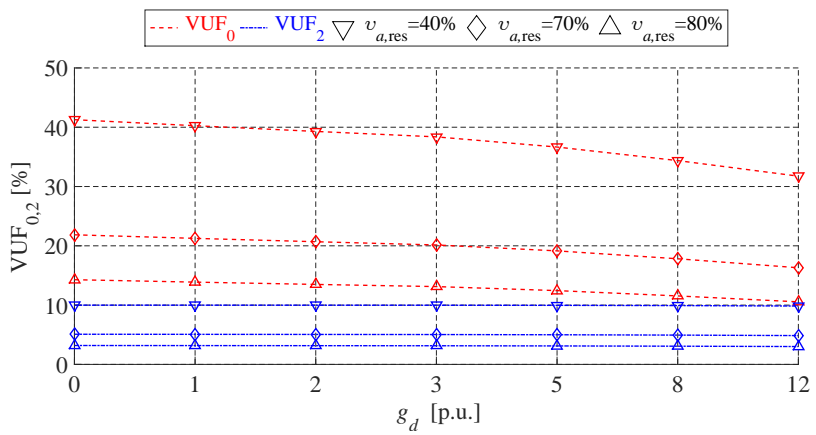
affected very little. The reason for this effect is given earlier in this section.



(a) Injected rms phase currents as a function of  $g_d$  and residual voltage

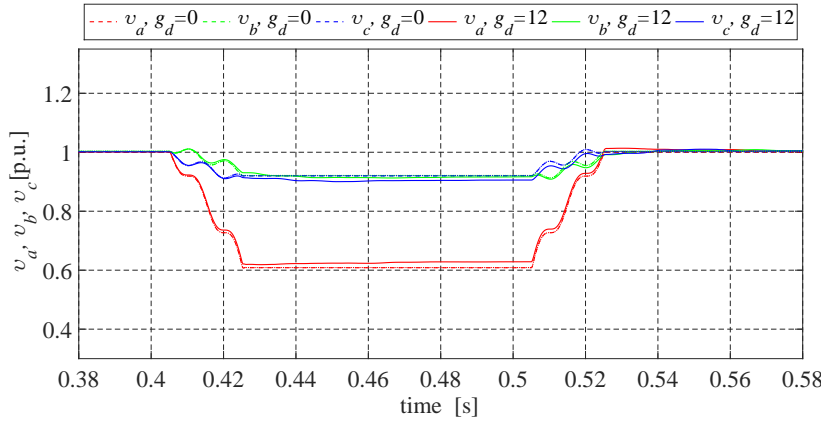


(b) Residual phase voltages as a function of  $g_d$

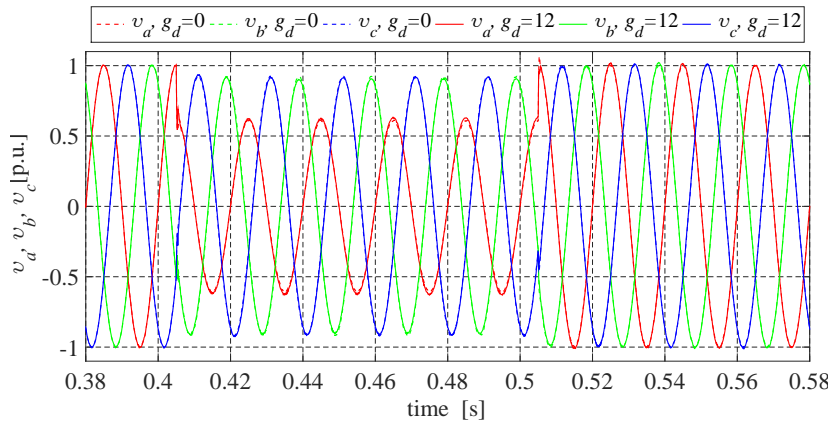


(c) Voltage unbalance factors as a function of  $g_d$  and residual voltage

Figure 7.17: dc bus voltages transient, rms current injection and voltage unbalance factor dependency on the damping conductance and residual voltages caused by a dip Type B at  $p_{dc} = 0$  p.u.



(a) rms voltages of the phase voltages during a voltage dip with a residual voltage of 40%



(b) Instantaneous values of the phase voltages at voltage dip Type B

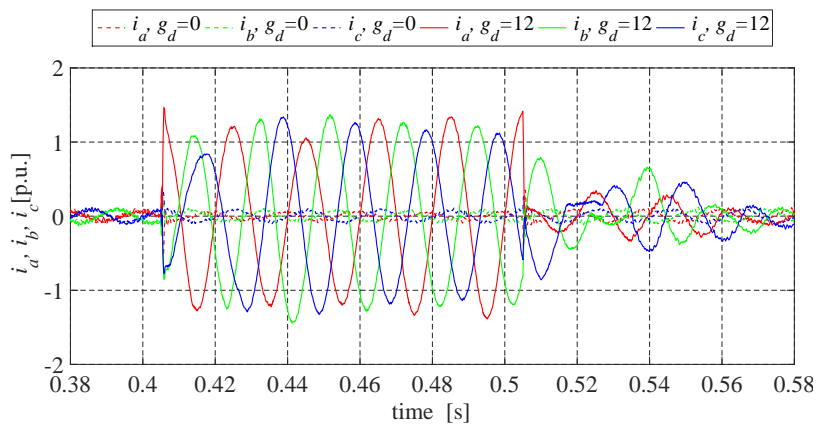
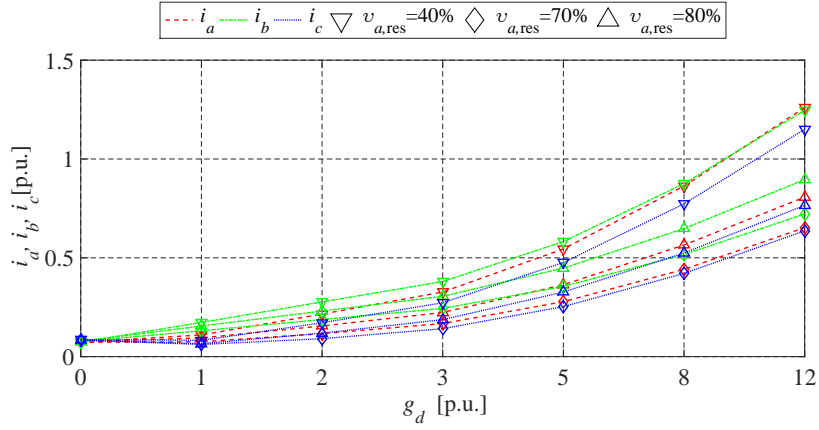
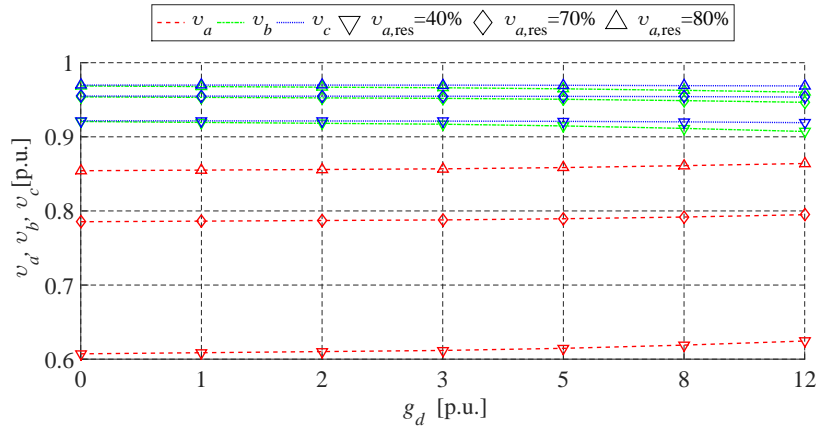
(c) Injected current by DER during voltage dip at  $g_d = 0$  and 12 p.u.

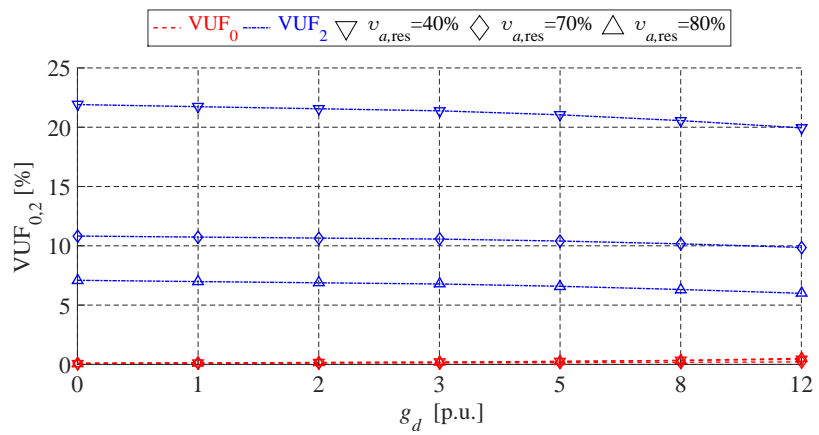
Figure 7.18: Phase voltages and injected phase currents by the positive-sequence and three-phase damping control strategies at  $p_{dc} = 0$  p.u. when voltage dip Type D is investigated



(a) Injected rms phase currents as a function of  $g_d$  and residual voltage



(b) Residual voltages as a function of  $g_d$



(c) Voltage unbalance factors as a function of  $g_d$  and residual voltage

Figure 7.19: dc bus voltages transient, rms current injection and voltage unbalance factor dependency on the damping conductance and residual voltages caused by a dip Type D at  $p_{dc} = 0$  p.u.

The voltage dip Type D affects all three phase voltages but the most critical one is phase  $a$ , which has the lowest residual voltage. As mentioned earlier, in this mode the control strategy draws currents from the phases with the highest voltage and injects it back in the phase with the lowest voltage to support the faulty phase and thus rise the residual voltage. The rms values of the phase voltages are depicted in Fig. 7.18 (a). This figure depicts also three scenarios where a DER is not connected, a DER equipped with the positive-sequence control strategy and finally, the three-phase damping control strategy is used by the DER. Since the primary source does not deliver any power to the DER, the voltage profiles of scenarios one and two do overlap completely. Hence, it is confirmed that the positive-sequence control strategy is unable to influence the residual voltages when voltage dip of Type D is present at the point of common connection. In contrast, the three-phase damping control strategy is able to increase the residual voltage in phase  $a$  with about 2%. Because of the power consumption from the other two phases, their residual voltage is slightly decreased.

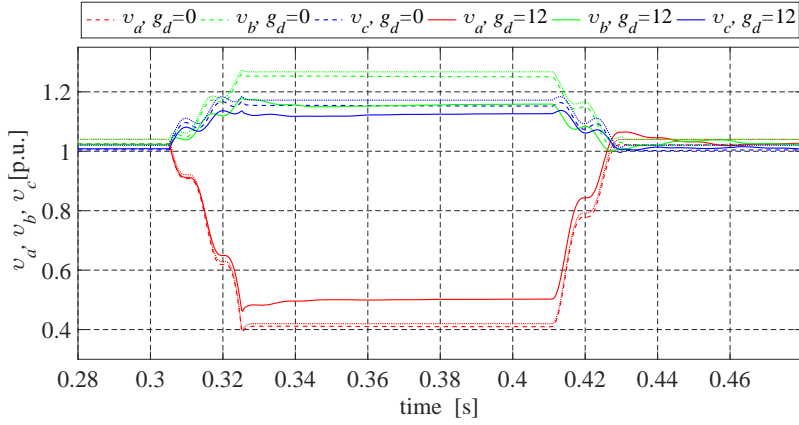
Fig. 7.18 (b) and (c) depict the waveforms of the phase voltages and exchanged phase currents, respectively. The dashed lines depict the reaction of the positive-sequence control strategy while the solid lines depict the three-phase damping control strategy. From Fig. 7.18 (b) it is difficult to distinguish the difference between both control strategies and the effect of the voltage dip mitigation is not that pronounced as in case of dip Type B. As mentioned earlier, this effect is because of the lower rms currents that are injected when this type of voltage dip is present.

The exchanged phase currents and residual phase voltages as a function of the damping conductance at different residual voltages is presented in Fig. 7.19 (a) and (b) respectively. In this mode, the maximum rms values of the phase currents is 1.3 p.u. and the effect on the residual voltages is very similar as explained in §7.4.5.

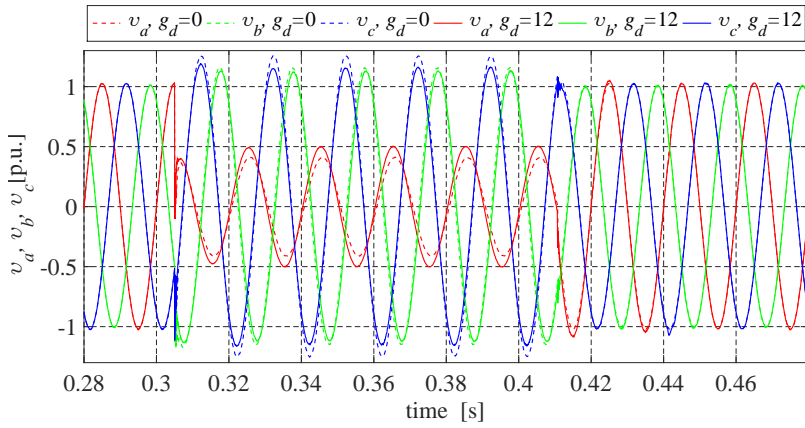
The results regarding the zero- and negative-sequence voltage unbalance factors are shown in Fig. 7.19 (c) and they can be interpreted in the same manner as the results presented in §7.4.5, which are related to Fig. 7.15 (c).

#### 7.4.7 Examination of voltage dips at nominal consumed power

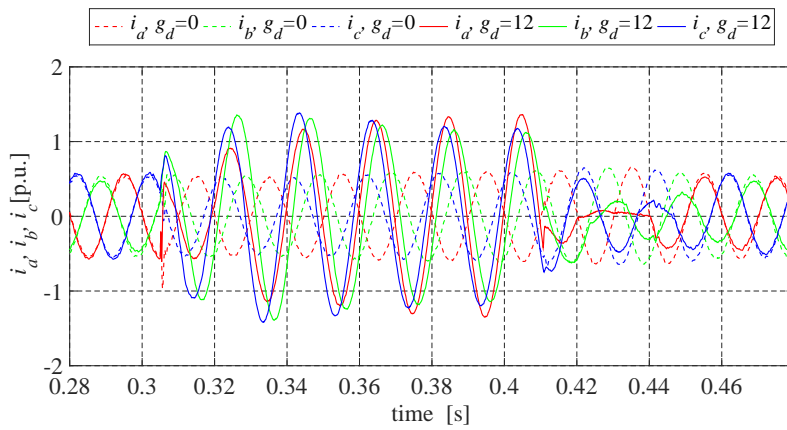
In this mode, the control strategy operates as an active rectifier to supply a load that is connected at the dc bus. The input conditions used by the simulation model are the same as ones that were used for the nominal input power and zero input power modes. A DER which is operated in this mode will draw positive-sequence current if it is equipped with the positive-sequence control strategy whether or not voltage unbalance is present at the inverter terminals. However, the three-phase damping control strategy will draw smaller current from the phase with the lower voltage and higher currents will be drawn from the phases with the highest voltages. In this way, the control strategy will mitigate the voltage unbalance.



(a) rms voltages of the phase voltages during a voltage dip with a residual voltage of 40%



(b) Instantaneous values of the phase voltages at voltage dip Type B



(c) Injected current by DER during voltage dip at  $g_d = 0$  and 12 p.u.

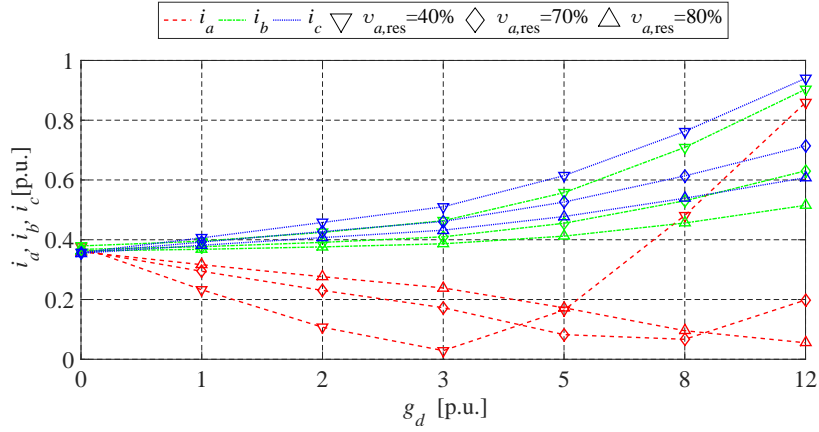
Figure 7.20: Phase voltages and injected phase currents by the positive-sequence and three-phase damping control strategies at  $p_{dc} = 1$  p.u. when voltage dip Type B is investigated

The residual voltages at the DER terminals are depicted in Fig. 7.20 (a) where three scenarios are depicted. In the first scenario a DER (or other device that draws current) is not connected to the feeder is examined and the obtained phase voltages are plotted by using dotted lines. In the second scenario a DER that is equipped with the positive-sequence control strategy is examined and its results are depicted by using a dashed line. Finally, the results of the third scenario, where a DER that is equipped with the three-phase damping control strategy is used, are depicted by solid lines. The obtained simulation results show that the positive-sequence control strategy is able to decrease the swell rms values in the none-faulty phases, which is also important to decrease the overvoltages due to the dip. However, the residual voltage in phase  $a$  is also decreased. Unlike the positive-sequence control strategy, the three-phase damping control strategy is able to increase the residual voltage in the faulty phase and decrease the swell rms voltages in phases  $b$  and  $c$ . In this mode, the later one is able to increase the residual voltage with almost 8% while the former one is decreasing it with about 1%.

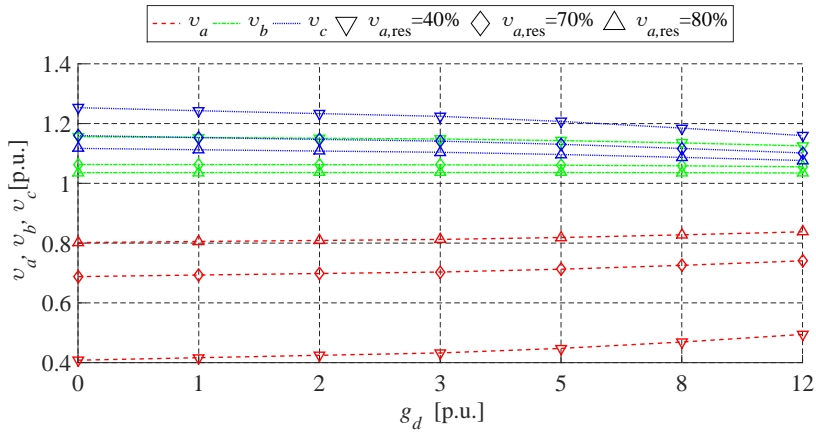
In Fig. 7.20 (b) and (c) the instantaneous values of the phase voltages and exchanged currents at  $g_d = 0$  p.u. and 12 p.u. are depicted. The decrease of the swell voltages and the increase of the residual voltages is achieved by active and reactive currents exchange with phases  $b$  and  $c$  while current is injected in phase  $a$ . Fig. 7.21 (a) depicts the rms values of phase currents as a function of the damping conductance value at different residual voltages and as it can be seen, at  $v_{a,res} = 40\%$ ,  $i_a$  experiences border mode around  $g_d = 3$  p.u. where current becomes nearly zero and above this value the three-phase damping control strategy starts to actively mitigate the voltage unbalance by consuming power from phases  $b$  and  $c$  and injecting it back into phase  $a$ . A similar statement can be made for the scenario where  $v_{a,res} = 70\%$  but the border mode occurs for higher values of the damping conductance, which is between 5 and 8 p.u. In conclusion, the three-phase damping control strategy requires about three times oversizing at  $g_d = 12$  p.u. to achieve the voltage dip mitigation capabilities that are presented in Fig. 7.20 (a), which is a significant cost for the prosumer.

Fig. 7.21 (b) depicts the rms values of phase voltages as a function of the damping conductance value at different residual voltages. The obtained simulation results show that the residual voltages are still impacted even if small values of  $g_d$  are used and the effect is more pronounced at lower residual voltages.

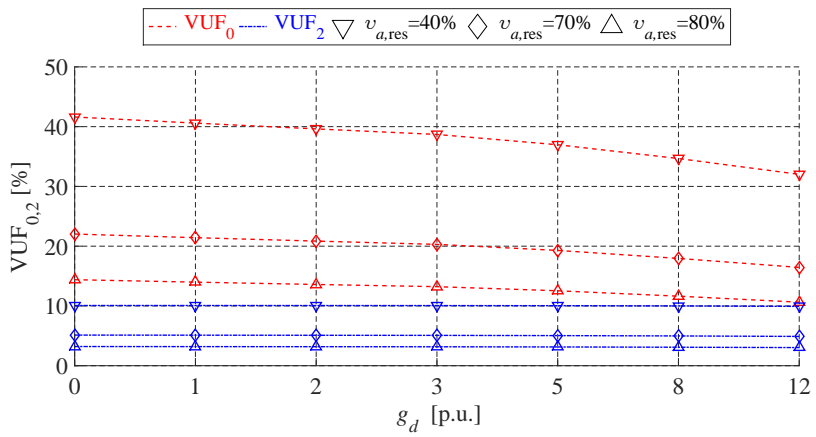
Finally, Fig. 7.21 (c) depicts the zero- and negative-sequence voltage unbalance factors as a function of the damping conductance value at different residual voltages. The obtained simulation results for the voltage unbalance factors are very similar to the results obtained in §7.4.5 and §7.4.6 where the dip Type B is examined. Hence, the same interpretation of the results obtained for the previous modes can be applied here.



(a) Injected rms phase currents as a function of  $g_d$  and residual voltage

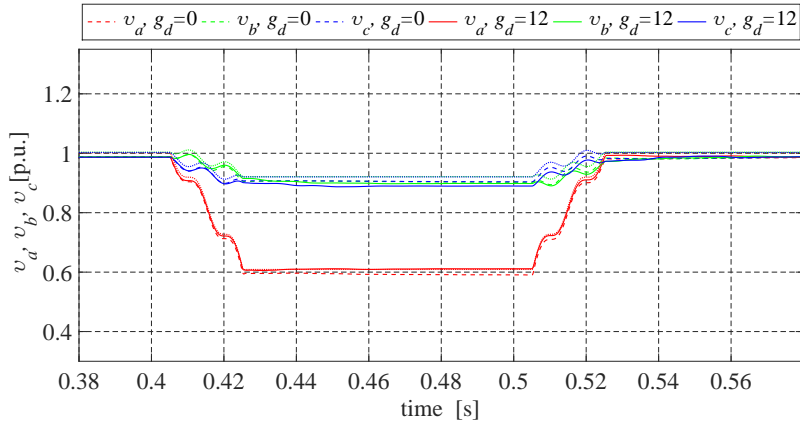


(b) Residual phase voltages as a function of  $g_d$

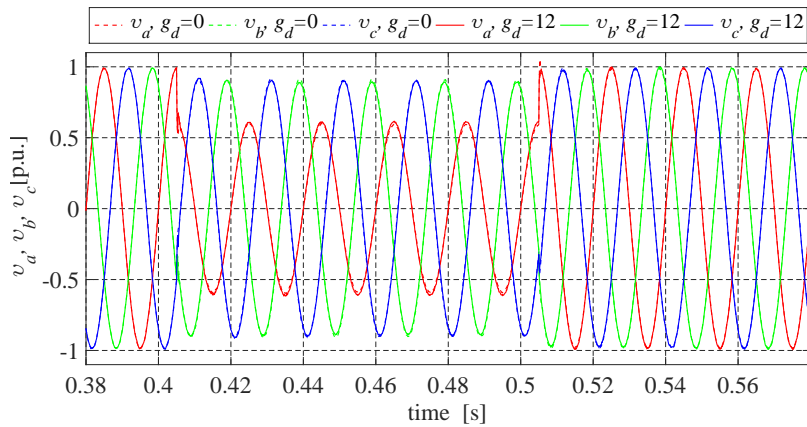


(c) Voltage unbalance factors as a function of  $g_d$  and residual voltage

Figure 7.21: dc bus voltages transient, rms current injection and voltage unbalance factor dependency on the damping conductance and residual voltages caused by a dip Type B at  $p_{dc} = -1$  p.u.



(a) rms voltages and their residual values during a voltage dip with a residual voltage of 40%



(b) Instantaneous values of the phase voltages at voltage dip Type D

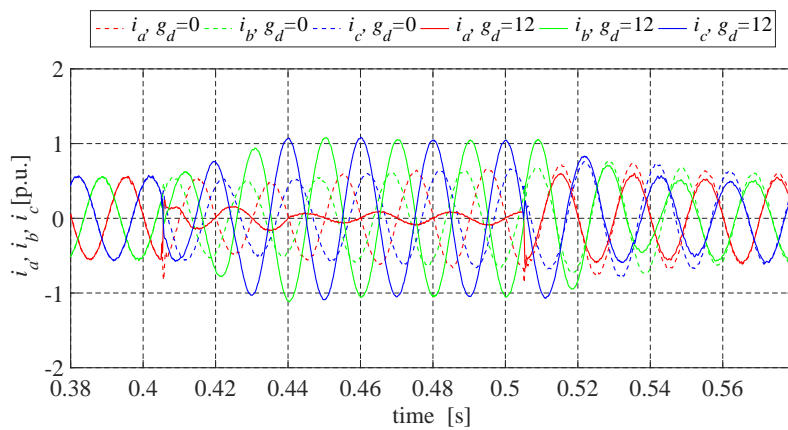
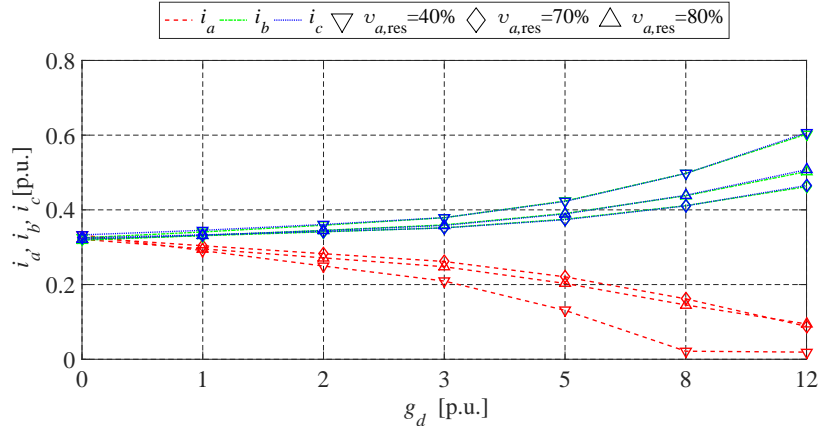
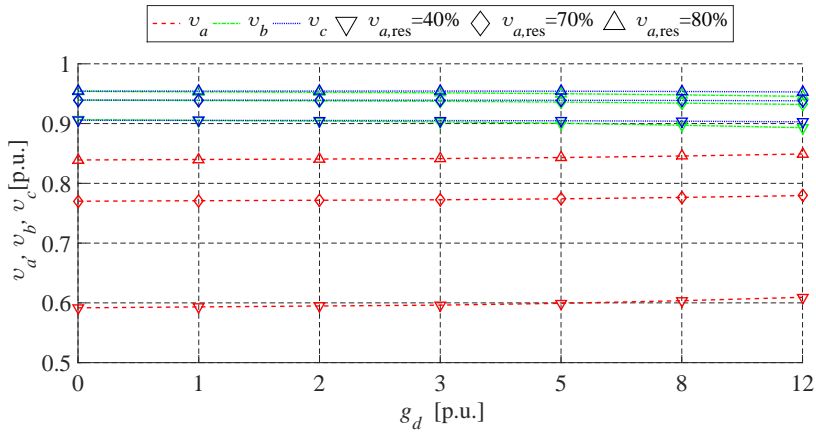
(c) Injected current by DER during voltage dip at  $g_d = 0$  and 12 p.u.

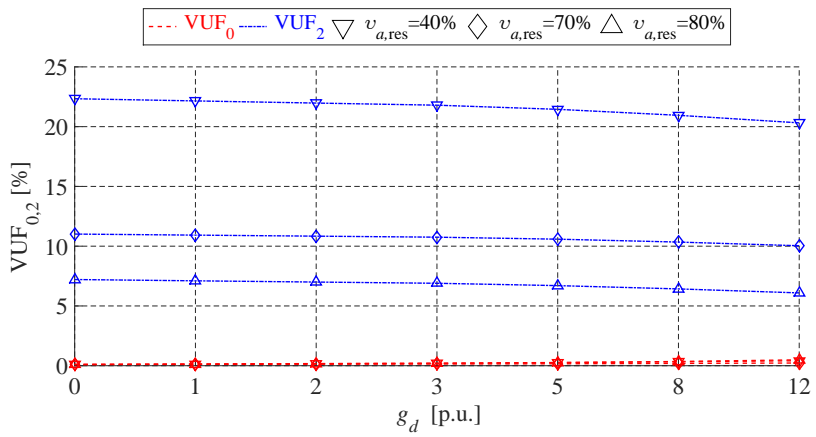
Figure 7.22: Phase voltages and injected phase currents by the positive-sequence and three-phase damping control strategies at  $p_{dc} = 1$  p.u. when voltage dip Type D is investigated



(a) Injected rms phase currents as a function of  $g_d$  and residual voltage



(b) Residual voltages as a function of  $g_d$



(c) Voltage unbalance factors as a function of  $g_d$  and residual voltage

Figure 7.23: RMS current injection, residual phase voltages and voltage unbalance factors dependency on the damping conductance and residual voltages caused by a dip Type D at  $p_{dc} = 1$  p.u.

This mode is also examined when a voltage dip Type D is considered. The residual voltages of the obtained simulation results are depicted in Fig. 7.22 (a). Three scenarios are considered in this study. In the first scenario a DER (or other device that draws current) is not connected to the feeder is examined and the obtained phase voltages are plotted by using dotted lines. In the second scenario a DER that is equipped with the positive-sequence control strategy is examined and its results are depicted by using a dashed line. Finally, the results of the third scenario, where a DER that is equipped with the three-phase damping control strategy is used, are depicted by solid lines. The obtained simulation results show that the DER that is equipped with the three-phase damping control strategy provides higher residual voltage in the faulty phase  $a$ . However, most of the load power is satisfied by phases  $b$  and  $c$ , which make their residual voltages slightly lower compared to the positive-sequence control strategy.

Fig. 7.22 (b) and (c) show the instantaneous waveforms of the phase voltages and exchanged phase currents, respectively. The results presented in Fig. 7.22 (b) show that the waveforms of the phase voltages almost overlap when both positive-sequence and three-phase damping control strategies are compared. To impact the residual voltages, more current must be consumed from the faulty phase(s). From the obtained results for the exchanged currents it can be seen that the three-phase damping control strategy does consume very little current from phase  $a$  and in order to mitigate the voltage unbalance besides drawing active currents, some additional reactive currents are exchanged with phases  $b$  and  $c$ .

The rms values of the exchanged currents by the DER as a function of the damping conductance value at different initial residual voltages are depicted in Fig. 7.23 (a). In this particular case, the higher drawn currents of 0.6 p.u. are present at the lower initial value of the residual voltage of 40% and  $g_d = 12$  p.u. Note that in this mode, the drawn rms currents are about 2 times smaller when compared to §7.4.5 and §7.4.6. This is because the bigger part of the power flow is through two phase ( $b$  and  $c$ ) where the voltages are the highest and very little part is provided by phase  $a$ . In the other two modes, the main power flow is through phase  $a$  where the phase voltage is the highest and very little is provided by phases  $b$  and  $c$ .

Finally, Fig. 7.23 (b) and (c) depict the residual voltage and zero- and negative-sequence voltage unbalance factors as a function of the damping conductance value at different residual voltages, respectively. The obtained simulation results for the residual voltages and voltage unbalance factors are very similar to the results obtained in §7.4.5 and §7.4.6 where the dip Type D is examined. Hence, the same interpretation of the results obtained for the previous modes can be applied here.

### 7.4.8 Discussion

The theoretical examination of the three-phase damping control strategy conducted in Chapter 4 showed that the value of  $g_d$  plays significant role on the magnitude of the injected currents. Furthermore, in §4.2 the maximum values of  $g_d$  were studied under different values of the phase voltages (for which type of the voltage dip) and different power electronic inverter over-sizing. The result showed that if the value of the damping conductance is high and low residual voltages are present, the injected current in the affected phase can reach very high values. Therefore, a decoupling of the damping conductances for the voltage unbalance and voltage dip mitigation can be employed to segregate the reaction of the control strategy towards these two problems. This can be achieved by using a voltage dip detection technique that will enable the last term of (7.11) only when certain grid conditions are present i.e. voltage dips with certain residual voltage and phase jump.

Moreover, the control of the last term of (7.11) will allow adding a fourth term in this equation that will be the same as the third one, however this term can be dedicated to mitigate harmonics, which extends further the beneficial effects of the three-phase damping control strategy to improve the power quality in LV grids.

If the full local control is applied and the DER is subjected to voltage dips, the reaction of the DER will be to turn off all the power coming from the primary source and it will continue to mitigate the dip by injecting less or consuming more depending on the operation mode if voltage dip Type B is present.

## 7.5 Voltage dip mitigation in an extended low voltage distribution feeder

In this section, the three-phase damping control strategy is tested by means of simulations on real feeder data. In addition, a combination of voltage dip detection algorithm and the three-phase damping control strategy is proposed.

### 7.5.1 Voltage dip characterisation algorithms

The voltage dip characterisation algorithms are used to extract and quantify the different parameters of the voltage dip. The goal of this thesis is not to develop a new voltage characterisation algorithm but to use already existing ones and possibly to combine them with the three-phase damping control strategy. In literature, there are many solutions that can provide satisfying performance when dip detection is needed. According to [186], the characterisation parameters of voltage dips can be split into 4 major groups: pre-event, during event, transition part and post event. In order for the three-phase damping control strategy to provide ride-through capabilities, the precision and fast detection are essential parameters. However,

the three-phase damping control strategy does not need all 4 groups but only the during event and the transition parts.

The voltage characterisation algorithms are documented and studied a lot in the literature. Some of the most common are listed below:

- Fourier transformation (FT) [187] - this method can characterise accurately the voltage parameters such as residual voltage and phase angles, which are needed for the three-phase damping control strategy, but the response time is more than 10 ms, which makes it unsuitable.
- Numerical Matrix Sag Detection Method (NMSD) - the proposed method in [188, 189], calculates the magnitude and angle of the phase voltage plus additional harmonics present in it. This method provides small latency, however, the disadvantage of it is that the number of the equation that must be calculated to compute the magnitude and phase angle, are proportional to the harmonics, “found” in the grid voltage. This makes NMSD difficult to implement in practice and also may require more computational time.
- Peak Value Evaluation Method (PVEM) [187] - it uses Clark transformations of the phase voltages (it is a single phase method). It is able to provide very fast response ( $< 1$  ms) and it has low complexity, which makes it appropriate for the three-phase damping control strategy.
- RMS evaluation method (REM) [188]-this approach monitors the rms values of the grid voltages and it is easy to implement, but it is unable to extract the phase angle and the latency is more than 10 ms.
- Park Vector DQ Transform (PVDQ) - Park’s vector is based on the instantaneous vector sum of all phase vectors. It is also easy to implement and provides very small latency.
- Wavelet analysis (WA) [187]- The wavelet transformation is based on the decomposition into daughter wavelets derived from the mother wavelet. The operating principle is similar to FT method and it also suffers from the same latency problem.
- Multi-resolution S-Transform (MRST) [190]- This method is also based of Fourier transform but a variable window is used instead of a continuous transformation and it is able to simultaneously localise the real and imaginary spectra of the grid voltage. The main drawback is the latency as all Fourier-based methods.
- Extended Kalman filter (EKF) [190]- The extended Kalman filter is able to process non-linear input signals (unlike the pure Kalman filter) such as

| Type             | FT | NMSD | PVEM | REM | PVDQ | WA | MRST | EKF | ESP |
|------------------|----|------|------|-----|------|----|------|-----|-----|
| Latency [ms]     | 10 | 3.4  | <1   | 5   | <1   | <4 | 3.4  | 5   | 5   |
| Computation cost | H  | VH   | L    | L   | L    | H  | M    | M   | H   |
| Sensitivity      | M  | L    | H    | L   | H    | M  | H    | H   | H   |

Legend:

VH- very high, H-high, M- moderate, L-low

FT - Fourier transform, NMSD - Numeral matrix sag detection method, PVE - Peak value evaluation, RMS- RMS-based evaluation, PVDQ - Clark transformation for peak value detection, WA - wavelet analysis, MRST - Multi-resolution S-transform, Extended Kalman filter, ESP - Enhanced SOGI PLL technique

Table 7.4: Most commonly used voltage dip characterization algorithms

voltage dips. According to [190], it provides very good performance of detecting the voltage dip residual voltage and the dip duration.

- Enhanced second order generalised integrators PLL (ESP) - In [191], PLL-based method is used to characterise the voltage dip with very good sensitivity in the magnitude range but the latency is still rather high - 5 ms.

In literature, other voltage dip characterisation techniques such as Phasor dip detection-based studied in [192, 193], Method of Ziarani and Konrad [194] based on non-periodic signals, missing voltage detector [195] and many more do exist as well. However, they are not so commonly used in practice and well known. In summary, the above described voltage characterisation techniques are listed in Table 7.4 and compared in terms of latency, complexity and sensitivity.

As it can be seen from the presented overview, the two methods PVEM and PVDQ have low latency, low complexity and high sensitivity. In §5.3, the selected PLL already uses Clark transformation in its structure, so adding the PVEM algorithm to the three-phase damping control strategy will be done easily and it will not introduce any additional complexity to the system. PVEM can be described mathematically as follows:

$$\begin{aligned} v_{\alpha}(t) &= v_a \sin(\omega t + \theta_x) \\ v_{\beta}(t) &= v_a \sin(\omega t + \theta_x - \frac{\pi}{2}) \end{aligned} \quad (7.18)$$

To obtain the peak value evaluation, the pair of orthogonal signals  $v_{\alpha}(t)$  and  $v_{\beta}(t)$  is then further processed:

$$\begin{aligned} v_{\text{PVEM}}(t) &= \sqrt{(v_{\alpha}(t))^2 + (v_{\beta}(t))^2} \\ &= \sqrt{v_a^2 \sin^2(\omega t) + v_a^2 \sin^2(\omega t - \frac{\pi}{2})} \end{aligned} \quad (7.19)$$

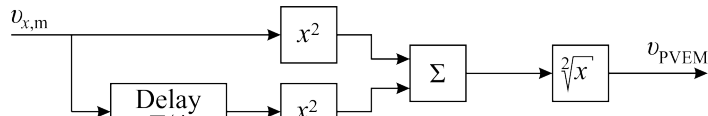


Figure 7.24: Voltage dip detection block diagram

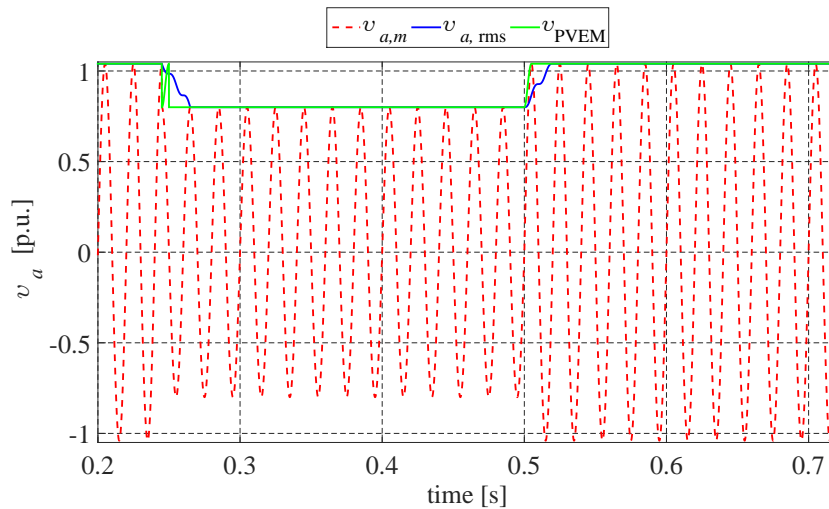


Figure 7.25: Voltage dip detection performance of the improved algorithm

The block diagram of the implemented PVEM in Matlab&Simulink shown in Fig. 7.24 and it is simulated under a voltage dip with a residual voltage of 0.8 p.u. and the simulation results are presented in Fig. 7.25. The dip initiation starts at time 0.145 s and it stops at 0.24 s. The obtained simulation results confirm that the algorithm is very fast and the latency at the start and the end of the dip is very small. Nevertheless, at the voltage dip initiation, the voltage dip occurs at the top of the sine and the output signal of the PVEM has a secondary glitch. If the output signal is compared with a threshold, this will disable and enable the dip term of (7.11), which will lead to undesired behaviour of the control strategy. The end of the dip occurs at the zero-crossing of the grid voltage and the secondary glitch problem is not present but it is important to note that the response time is about 5 ms.

In order for the dip detection algorithm to identify sudden changes in the phase voltage, the output signal from the PVEM is compared with a constant. A sudden change of the phase voltages below a certain value is considered as voltage dip. In [8] this value is 0.9 p.u. while in [9] this value is recommended to be 0.85

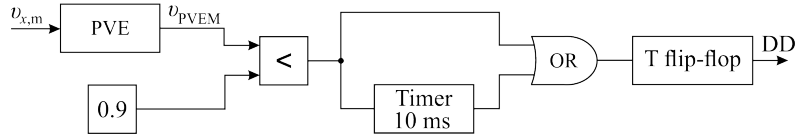


Figure 7.26: Voltage dip detection block diagram

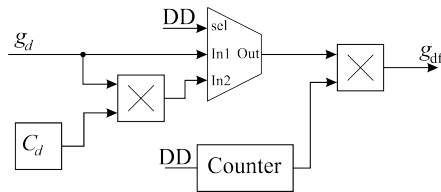


Figure 7.27: Damping conductance reduction during voltage dips

p.u. Therefore, a signal to detect the fault is generated that is driven by the falling edge of the output signal of the PVEM. This signal is used to enable the damping conductance reduction to a certain value. When the fault is cleared and the grid voltage has recovered above the rms values suggested by the standards considered earlier, the enabling signal is stopped and the damping conductance is ramped up to its nominal value with a certain slew rate.

Fig. 7.25 shows that the output signal of PVEM has very steep edge if a dip is encountered at the top of the sine. However, if the dip occurs at the top of the sine, a secondary rising edge is generated shortly after the dip. This will lead to a false triggering if the PVEM signal is compared with 0.9 p.u. (0.85 p.u.). In order to avoid such false triggers, a waiting timer of 10 ms is incorporated such that once the threshold of 0.9 p.u. is breached, the PVEM signal is blocked for 10 ms until one cycle of the grid voltage passes and the transient of the secondary triggering is over. This method is used for all phase voltages and the outputs are combined by logic OR. In this way, the voltage dip can be registered in any phase.

The output signal of the voltage dip detection DD (see Fig. 7.26) is used to drive a selector to switch between  $g_d$  and a down scaled value of it during a voltage dip. The block diagram of this scaling algorithm is depicted in Fig. 7.27 where  $C_d$  is down scaling coefficient and its value is set between 0 and 100%. It is chosen such that at most severe dip voltage level, the rms exchanged rms currents do not exceed the maximum allowed by the power electronic inverter. The down scaled value of the damping conductance is used during the voltage dip. After the grid recovery, signal DD assumes logic level 0 and the selector switches back to the pre-set value of  $g_d$ . However, after such events, step changes of the injected power are highly undesired and therefore, the damping conductance is ramped up from the downscaled value to its nominal value by using an incremental counter, which

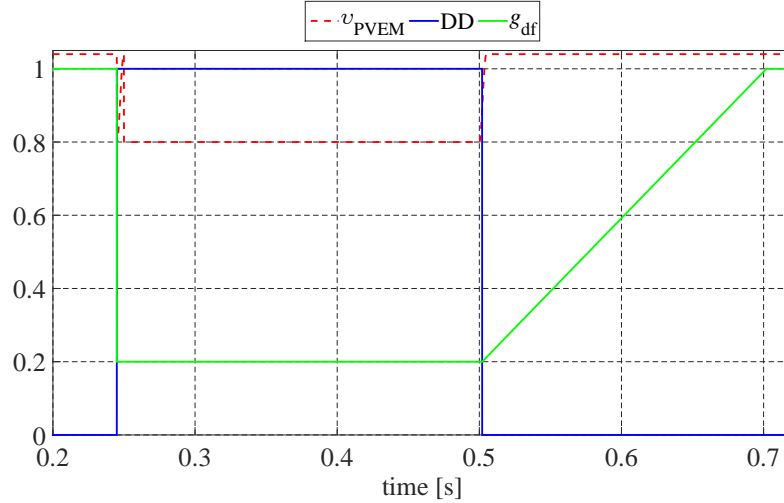


Figure 7.28: Voltage dip detection performance of the improved algorithm

output changes from  $C_d$  to 100%.

It is worth mentioning that the PVEM has some disadvantages such as:

- it is vulnerable to flickers, a threshold must be added not to react on changes within the standard voltage band.
- it is susceptible to voltage dips with duration shorter than 10 ms.
- if harmonics are present or the frequency is not exactly 50 Hz, then some pulsations will be present in the output signal of PVEM.

All of these factors may cause false triggering or lack of it, which will lead to very high values of  $g_d$  during voltage dips and therefore, excessive currents must be injected. The former ones may be much higher than the maximum allowed by the inverter. This motivates to explore in the future the performance of other more sophisticated techniques for dip characterisation that are less susceptible to the above mentioned disadvantages.

### 7.5.2 Simulation results of a 7 node LV feeder and multiple DERs connection

In this section, the PVEM algorithm is tested by means of simulation on a real LV feeder. These simulations are performed with disabled local control i.e. the injected power is invariant of the grid voltage as well as the damping conductance.

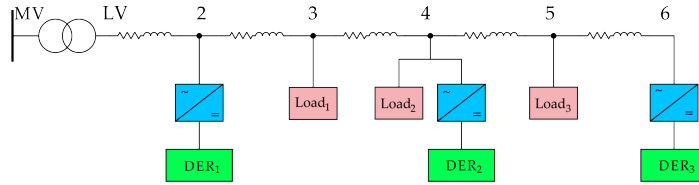


Figure 7.29: Feeder topology used to access the performance the examined control strategies

| LINE  | $R_1$ ( $\Omega/\text{km}$ ) | $X_1$ ( $\Omega/\text{km}$ ) | $C_1$ (nF/km) | $R_0$ ( $\Omega/\text{km}$ ) | $X_0$ ( $\Omega/\text{km}$ ) | Length (km) |
|-------|------------------------------|------------------------------|---------------|------------------------------|------------------------------|-------------|
| LV-2  | 0.456                        | 0.088                        | 250           | 4                            | 0.0877                       | 0.057       |
| 2 - 3 | 0.468                        | 0.085                        | 250           | 4                            | 0.0851                       | 0.094       |
| 3 - 4 | 0.48                         | 0.08                         | 250           | 4                            | 0.08                         | 0.025       |
| 4 - 5 | 0.462                        | 0.083                        | 250           | 4                            | 0.0833                       | 0.132       |
| 5 - 6 | 0.924                        | 0.076                        | 200           | 4                            | 0.0758                       | 0.066       |

Table 7.5: Properties of the LV feeder.

This is necessary because the simulated voltage dip is Type A and as it will be seen later it causes overvoltages in the least affected phases. If the local control is used, the overvoltages will reduce the damping conductance as well as the injected power down to zero. Such a behaviour however, is not allowed by grid codes [12, 196], which recommend the DERs to remain connected to the grid and provide support during voltage dips. It is possible not to droop the damping conductance in such circumstance as described in Chapter 4 and the DER will react as a zero-powered inverter and keep the local control (the active power drooping) active but still the local control will not be compatible with the grid codes. This incompatibility of the local control and grid codes is present only when voltage dip of Type A is present. At all other voltage dip types do not introduce voltage rise in the non-affected phases and therefore the local control functions normally.

In this section, the feeder presented in Fig. 7.29 is used to examine the behaviour of DERs during voltage dips. This feeder is a small part of an 80 node LV network located in Suha, Slovenia. The MV/LV transformer of Dyn5 type and it has a nominal power of 250 kVA, short circuit voltage of 4% while the no load losses are 325 W and 3250 W, respectively. The primary and secondary nominal voltages are 20 kV and 0.4 kV, respectively. The voltages at the secondary side are set to be 1.04 p.u., which is a typical setting used by the DSO in order to avoid undervoltages to the most remote customers when high loading conditions are present. The zero- and positive-sequence impedances of the cables in the feeder as well as their lengths are listed in Table 7.5.

The feeder is loaded with three-phase unbalanced loads and their nominal active and reactive power are listed in Table 7.6. The power factor of all loads is 0.9. Finally, there are three DERs connected to the feeder. Their nominal power

| Load              | Rated Active power | Rated reactive power |
|-------------------|--------------------|----------------------|
| Node 3 Load 1 (Y) | 4.5/2.7/2.7 kW     | 2.17/1.3/1.3 kvar    |
| Node 4 Load 2 (Y) | 3.6/3.6/3.6 kW     | 1.74/1.74/1.74 kvar  |
| Node 5 Load 3 (Y) | 5.4/3.6/3.6 kW     | 2.61/1.74/1.74kvar   |

Table 7.6: Nominal power of the loads and type of connection

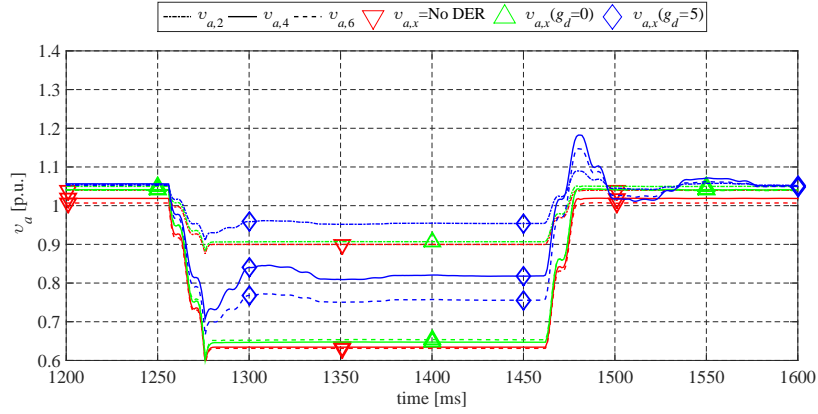
| DRES                    | Rated Active Power |
|-------------------------|--------------------|
| Node 2 DER <sub>1</sub> | 20 kW (Y)          |
| Node 4 DER <sub>2</sub> | 25 kW (Y)          |
| Node 6 DER <sub>3</sub> | 15 kW(Y)           |

Table 7.7: Nominal power of DERs and node connection

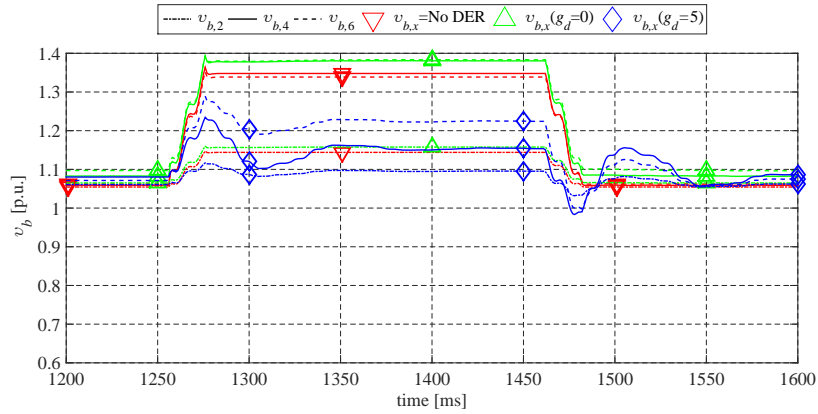
and connection node are listed in Table 7.7. To further examine the effect of the voltage dips over the DERs, the positive-sequence control strategy is used as a reference case. Then all DERs are equipped with the three-phase damping control strategy and finally, all DERs are equipped with the three-phase damping control strategy in, which the PVEM is incorporated. The damping conductance for the tests of all DREs is selected to be 5 p.u., which is sufficiently high enough to force the three-phase damping control strategy to inject very large currents into the grid.

Finally, the voltage dip is emulated by short-circuiting phase  $a$  to the neutral at node 4. The fault is created by an impedance of  $0.4 \Omega$ , which results in a residual voltage of about 0.63 p.u when no DERs are connected.

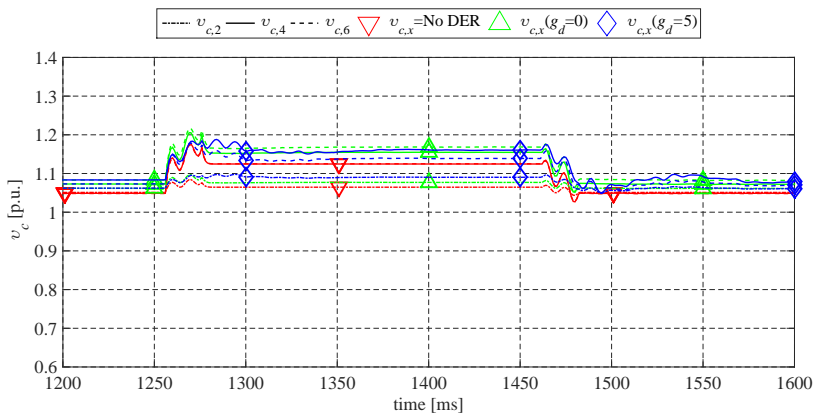
The obtained simulation results of the voltage dip mitigation in the considered LV feeder are depicted in Fig. 7.30. All voltages of the affected phase  $a$  are depicted in Fig. 7.30 (a). Different line styles are used to depict the voltages at the nodes where DERs are connected and different marker type are used to denote the cases of No DER, positive-sequence and three-phase damping control strategies. A solid line is used to indicate the rms values of the voltages at node 4 while for node 2 and 6, dash-dot and dash combinations are applied, respectively. As it can be seen from the obtained results, the No DER and positive-sequence cases provide similar results and the residual voltages are about 0.63 and 0.65 p.u. respectively. Since no voltage unbalance is provided by the other DERs, the residual voltages at node 6 (after the fault) remain more or less with the same residual voltages. On the other hand, when voltage unbalance mitigation is present by the DERs, the residual voltages at the faulty node is already 0.82 p.u. while the residual voltage  $v_{a,6}$  has increased up to 0.76 p.u. Note that these values are taken 150 ms after the fault where all the inverter transients are overcome and steady-state operation is achieved.



(a) rms voltage of phase a during a voltage dip



(b) rms voltage of phase b during a voltage dip



(c) rms voltage of phase c during a voltage dip

Figure 7.30: Phase voltages during pre-fault, fault and post-fault conditions when cases No DER, positive-sequence and three-phaser damping control strategies are applied without dip detection algorithm

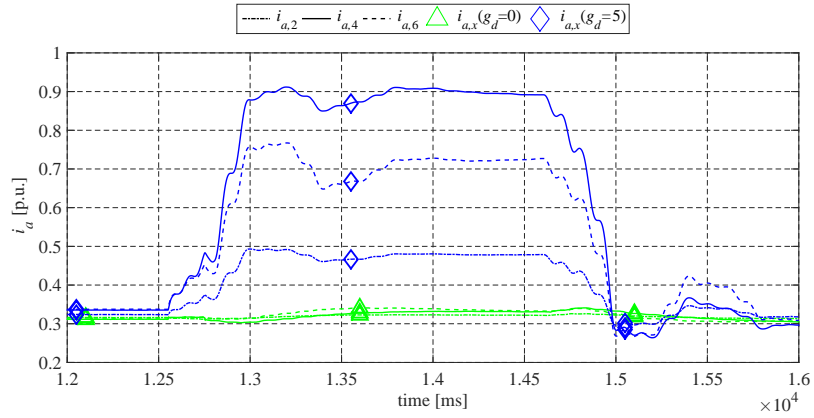
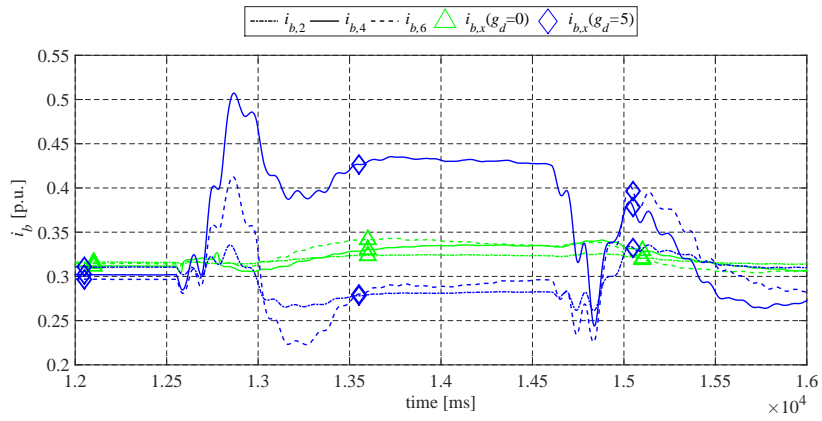
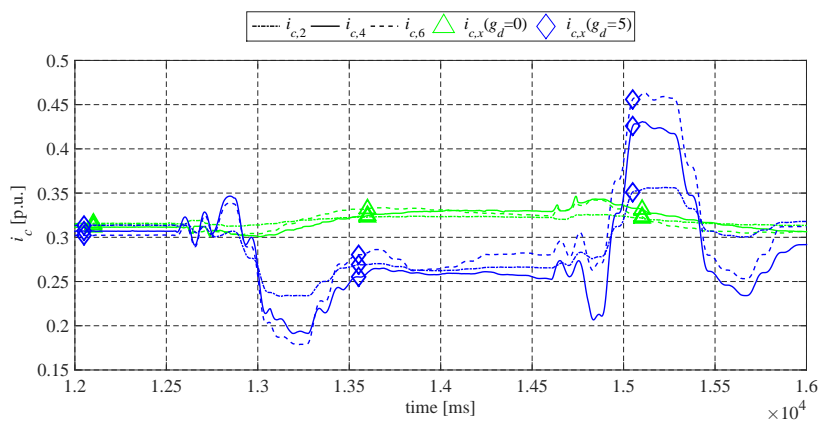
(a) Injected rms currents into phase  $a$  during a voltage dip(b) Injected rms currents into phase  $b$  during a voltage dip(c) Injected rms currents into phase  $c$  during a voltage dip

Figure 7.31: Injected currents by the DERs during pre-fault, fault and post-fault conditions when cases No DER, positive-sequence and three-phaser damping control strategies are applied without dip detection algorithm

Because of the fact that the fault is phase-to-neutral in the LV side, the zero-sequence component is propagating to the inverter terminals. In addition, it also causes swells (overvoltages) in the least affected phases. This effect can be seen from the obtained simulation results of phase voltages  $v_b$  and  $v_c$ , which are presented in Fig. 7.30 (b) and (c), respectively. In phase  $b$  the fault causes a voltage swell, which has an rms value of 1.35 p.u. and 1.38 p.u. when No DERs and positive-sequence cases are examined. This swell also propagates further down the feeder and more or less the same rms voltage levels are experienced at node 6. In contrast, the DERs equipped with the three-phase damping control strategy are able to decrease the swell magnitude to 1.23 p.u. at node 6 to 1.15 p.u. at node 4 to less than 1.1 p.u. at node 2. Similar results are obtained for phase voltage  $v_c$ .

This performance of the damping control strategy is achieved by the resistive behaviour explained earlier in this chapter. As it can be seen in Fig. 7.31 (a), the exchanged rms current (including active and reactive components) by DER<sub>2</sub> reaches almost 0.9 p.u., which is 2.7 times the nominal current at balanced voltage conditions. The results are less critical for the other the phases. Nevertheless, an oversizing of almost 3 times is a very expensive solution. In order to prevent such excessive currents, very low values of the damping conductance must be used. However, this will result in a poor voltage unbalance mitigation at normal operation conditions.

The exchanged rms currents phase  $|\dot{i}_a|$ ,  $|\dot{i}_b|$  and  $|\dot{i}_c|$  are depicted in Fig. 7.32 (a), (b) and (c), respectively. As it can be seen, by decreasing the value of  $g_d$  by 5 during voltage dips, the maximum exchanged current in phase  $a$  is decreased to less than 2 times the nominal current, which is comparable with the oversizing needed for voltage unbalance mitigation in Chapters 3 and 6. As of the current rms values of the other phases, maximum values of 0.38 p.u. and 0.36 p.u. are obtained, which is very low compared to the maximum rms values of  $|\dot{i}_a|$ .

The lower injected currents however, lead to a smaller impact on the residual voltages. As it can be seen from the simulation results of the phase voltages presented in Fig. 7.33, the residual voltage at the faulty node is 0.7 p.u. and 0.68 p.u. at node 6. In comparison, the residual voltages if  $g_d$  is not decreased are 0.82 p.u. and 0.76 p.u.

This algorithm decreases the voltage dip mitigation abilities of the three-phase damping control strategy but it allows to use higher value of  $g_d$ , which is crucial for voltage unbalance mitigation caused by asymmetrical loading and injection.

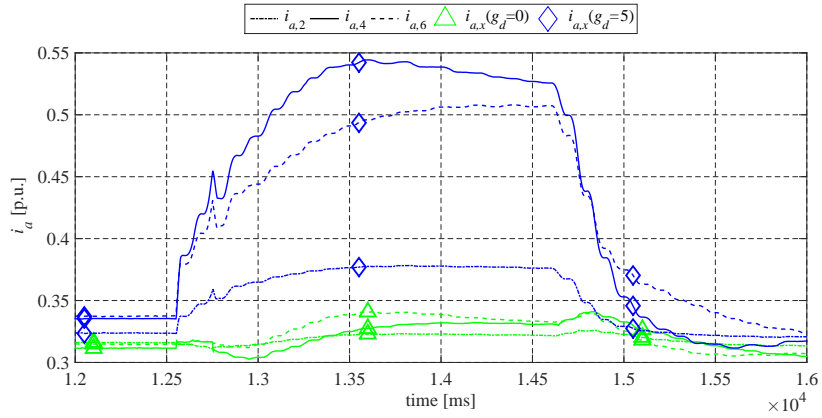
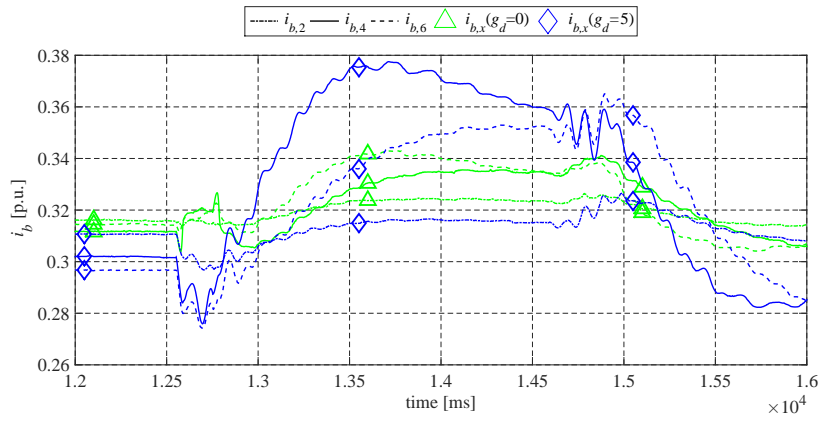
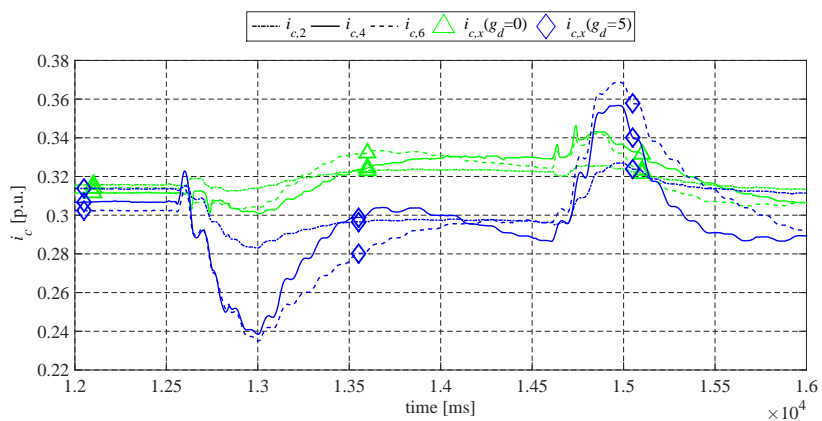
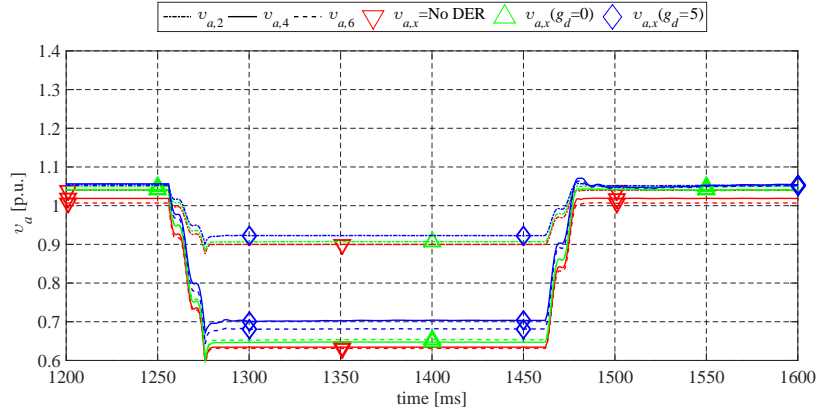
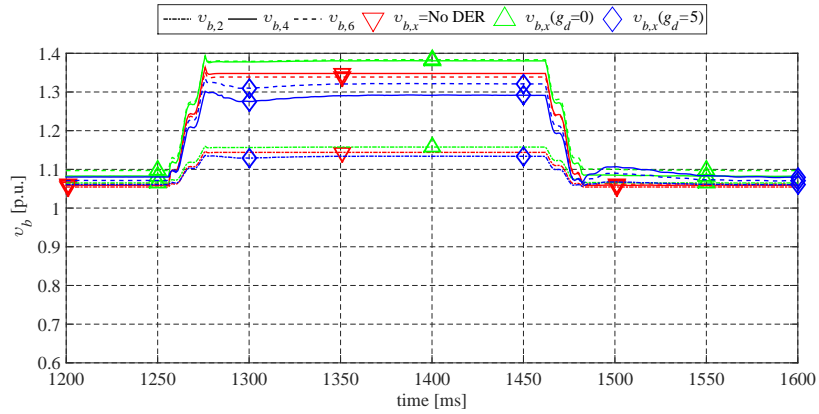
(a) Injected rms currents into phase  $a$  during a voltage dip(b) Injected rms currents into phase  $b$  during a voltage dip(c) Injected rms currents into phase  $c$  during a voltage dip

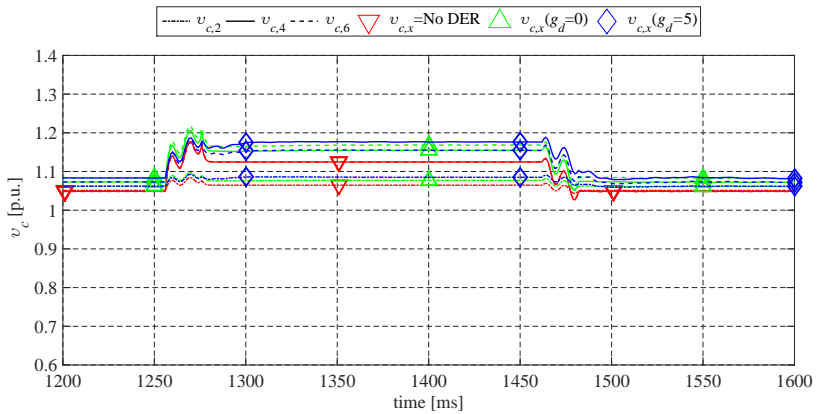
Figure 7.32: Injected currents by the DERs during pre-fault, fault and post-fault conditions when cases No DER, positive-sequence and three-phaser damping control strategies are applied with dip detection algorithm



(a) rms voltage of phase a during a voltage dip



(b) rms voltage of phase b during a voltage dip



(c) rms voltage of phase c during a voltage dip

Figure 7.33: Phase voltages during pre-fault, fault and post-fault conditions when cases No DER, positive-sequence and three-phaser damping control strategies are applied with dip detection algorithm

## 7.6 Conclusions

In this chapter, two control strategies were studied and it was analytically illustrated that the damping control strategy is able to support the grid during voltage dips better than the positive-sequence control strategy. During voltage dips, the three-phase damping control strategy emulates a resistive behaviour towards the zero-sequence and negative-sequence voltage components, which has a positive effect on the retained voltage. Additionally, this control strategy responds instantaneously to perturbations in the grid voltage. The control strategy shows to be equally effective both when the converter operates as inverter (connecting a DER unit to the grid) and when it operates as a rectifier (connecting, for example, a distributed battery or a load to the grid).

The influence of the three-phase damping control strategy during the occurrence of a voltage dip was described analytically and the positive effect was demonstrated. When a voltage dip occurs in the fault phase(s) the control strategy alters the injected phase currents so that the residual voltage is closer to the nominal value.

In addition, a combination of the three-phase damping control strategy with a voltage dip detection algorithm is proposed. The dip detection is used to reduce the value of the damping conductance, which leads to lower phase currents exchange. On the one hand, this combination slightly deteriorates the impact on the residual voltages but on the other hand it allows the inverter to operate with higher values of the damping conductance at normal conditions.

# 8

## Conclusions and future work

In this chapter, the main conclusions of this thesis are summarised. In the end, some suggestions for future research are given.

### 8.1 Concluding remarks

The increase of the installed capacity of DER imposes significant challenges to the DSO which limit the further penetration of renewables. One of the reasons for these problems is that the DERs are not connected in a coordinated manner. A more sophisticated approach is to make the DER more intelligent, by including local measurements and allowing them to improve the power quality. Thus the power quality problems will be solved locally with less or no actions needed by the DSO.

Existing control strategies for DER applications are discussed in Chapter 2. The main contribution of this chapter is that the control strategies are analytically described, making it easy to compare the strategies and this chapter points out some specific advantages and disadvantages. It is concluded that a combination of control strategies is required in order to consolidate a smart and sophisticated control strategy which is able to cover some important aspects of the power quality in low voltage distribution grids.

In Chapter 3, the modified three-phase damping control strategy is proposed which consists of active power drooping (part of the VBDC), a damping controller and the three-phase damping control strategy itself. The performance of differ-

ent control strategies is examined and different aspects such as exchanged power, zero- and negative-sequence voltage unbalance mitigation as well as grid loss are concerned. The modified three-phase damping control strategy demonstrated a better ability to improve the power quality compared to the original damping control strategy and excellent performance compared the positive-sequence control strategy (with and without PF control).

A throughout analytical examination of the three-phase damping control strategy is performed in Chapter 4. From the conducted analysis three operating modes are defined: current injection, zero-power and consumption mode. These modes are examined on the modified three-phase damping control strategy by means of simulation and experiments. The results revealed that the system performance can be greatly improved in all three operating modes compared the the positive-sequence control strategy. A remarkable performance of the modified three-phase damping control strategy is observed in zero-powered inverter mode. Even though is no power delivered by the primary source the power quality and system performance are improved. In this chapter, some recommendations are also given regarding the needed oversizing of the power electronic inverter.

Chapter 5 describes some practical guidelines regarding the implementation of the modified three-phase damping control strategy. Important aspects such as proper sampling of the measured signals, PLL selection as well as the stabilisation of the split dc-link capacitor voltages are examined. The proposed stabilisation of the dc-bus capacitor voltages showed very good performance for stabilising the voltages as well as delivering very little THD into the exchanged currents and dc current injection. The response order of the different controllers is also tested by enabling the droop and damping controllers during maximum generation. The same tests are performed also for the input power transient and the results showed that the proposed response order of the controllers does not lead to excessive overshoots or undershoots in the injected currents and also power oscillations are not present. In addition, the proposed dc-bus capacitor stabilisation scheme showed very good performance during the transients both capacitor voltages were experiencing very similar transient profiles, which confirms that the voltage stabilisation will guarantee equal voltages during power changes and disturbances. Finally, the three-phase damping control strategy and the positive-sequence control strategies are experimentally tested on a field trial in Austria and the results showed that the three-phase damping control strategy is able to mitigate the voltage unbalance and prevent overvoltages in three-phase low voltage grids as well as reduce the neutral current. This makes the modified three-phase damping control very suitable for integration onto DERs in areas with high penetration of renewable energy and power quality issues.

The integration of BESS into DERs and its benefits towards drooped energy and system performance are examined in Chapter 6. In this chapter, a comparison

of the positive-sequence control strategy and the modified three-phase damping control strategy is performed. BESS integration is examined in both: decentralised and centralised applications. From the conducted simulation results for the decentralised and experimental results of the centralised storage, it can be seen that in unbalanced grids, the three-phase damping control strategy is able to improve the power quality with a lower size of the BESS compared with the positive-sequence control strategy. In addition, the damping conductance influence on the needed storage capacity is examined and the results showed that a BESS with a smaller capacity compared to the positive-sequence control strategy is needed if the value of the damping conductance is higher.

In this chapter, two control strategies were studied and it was analytically proven that the damping control strategy is able to support the grid during voltage dips better than the positive-sequence control strategy. The behaviour of the three-phase damping control strategy is examined in all three modes. The obtained simulation results showed that the three-phase damping control strategy is able to increase the residual voltages and thus decrease the risks of damaging sensitive equipment. Furthermore, a combination of the three-phase damping control strategy with a voltage dip detection algorithm is proposed. This combination is used to decrease the value of the damping conductance and thus excessive phase currents will be avoided. This combination reduces the residual voltages but on the other hand the control strategy has a better voltage unbalance mitigation performance at normal conditions.

## 8.2 Future research

The local control concept is relatively new and there still a lot of research that must be conducted to solve the different issues that the distribution operators are facing. Some suggestions of the future work and possible improvements are given below:

- The proposed local control is using four grid voltages to calculate the active power drooping and  $g_d$  value. Two of these voltages are set by standards and it cannot be changed. However, the constant damping band ( $v_{cdb}$ ) and the constant power band ( $v_{cpb}$ ) of the modified damping control strategy can be variables. In this thesis, they are chosen to be 1.04 and 1.06 p.u. which may not be always the optimal values if applied in practice. Further research can be done to decouple the droop and damping controller. The damping controller uses  $v_{cpb}$  to calculate  $g_d$ . However, this limits the possible reference values which the damping conductance can assume. Different curves are also of interest to be examined. Currently, the damping conductance is decreased when  $v_{cpb} > 1.06$  p.u. but it might be better to keep it at maximum for bigger voltage interval around  $v_{cpb}$ . In addition, to comply with

the current standards, the DER is disconnected from the grid if the grid voltage is greater than 1.1 p.u. and  $g_d = 0$  p.u. It could be better if the damping conductance differs from zero if the grid voltage is above 1.1 p.u. because the DER will be able to improve the power quality although power from the primary source will not be injected.

- Splitting the damping conductance in zero-sequence and negative sequence damping conductances in Chapter 4 allows for performing grid impedance measurements. The grid impedance can then be used together with the mathematical analysis performed in Chapter 4 §4.4.3 to solve power flow equations and determine an optimal value of the damping conductance. Optimisations can also be performed with different objectives such as minimising grid losses, optimal power flow, equal power sharing, optimal power quality, etc. These calculations can be fed to a multi-agent system acting as a secondary control. Based on the data received from the DER, different power set-points can be set to different DERs. The objective of the multi-agent system is to control the entire low-voltage grid and perform equal power sharing, power quality optimisations, etc.
- In Chapter 4, it was theoretically and experimentally demonstrated that the DER is able to operate when power from the primary source is not available. In this operating mode, the DER is still able to improve the power quality of the grid voltage and this feature is useful when at night time (if PV is considered) or in times when the primary source does not deliver any power. Nevertheless, the constant operation of the power electronic inverter will decrease its life time which is mainly determined by the electrolytic capacitors in its dc-bus. To avoid this problem, future research can be conducted in the field of power electronics and electrolyticless inverters. These inverters are able to achieve similar lifespan as the PV panels which is an advantage in terms of cost for new inverter and maintenance.

# Bibliography

- [1] Yvo de Boer, “Kyoto protocol reference manual on accounting of emissions and assigned amount,” in *United Nations Framework Convention on Climate Change*, Rio de Janeiro 2008.
- [2] European Commission. in <https://ec.europa.eu/clima/policies/>, 2018.
- [3] International Energy Agency. in <https://www.iea.org/statistics/co2emissions/>, 2018.
- [4] International Energy Agency in <https://www.iea.org/geco/>, 2019.
- [5] Adnan Z. Amin., “Renewable power generation costs in 2017,” 2018.
- [6] KPMG, “Global trends in renewable energy,” 2019.
- [7] P. N. Vovos, A. E. Kiprakis, A. R. Wallace, and G. P. Harrison, “Centralized and distributed voltage control: Impact on distributed generation penetration,” *IEEE Transactions on Power Systems*, vol. 22, pp. 476–483, Feb 2007.
- [8] “Voltage characteristics of electricity supplied by public distribution networks,” *EN Standard 50160-2008*, 2008.
- [9] “IEC standard voltages,” *IEC standard*, 2009.
- [10] RWE AG and ABB AG and Consentec GmbH and Technische Universität Dortmund, “Abschlussbericht - BMWi-förderprojekt netze für die stromversorgung der Zukunft,” Oct. 2011.
- [11] “Generating plants connected to the medium-voltage network,” *BDEW-2008*, 2008.
- [12] IEEE Std 1547-2003, “Standard for interconnecting distributed resources with electric power systems.” IEEE, July 2003.
- [13] IEEE Std 1547.1-2005, “Standard conformance test procedures for equipment interconnecting distributed resources with electric power systems.” IEEE, July 2005.

- [14] IEC 61727 Ed. 2, "Photovoltaic (PV) Systems Characteristics of the utility interface," Dec 2004.
- [15] L. Degroote, B. Renders, B. Meersman, and L. Vandeveldel, "Neutral-point shifting and voltage unbalance due to single-phase dg units in low voltage distribution networks," in *2009 IEEE Bucharest PowerTech*, June 2009.
- [16] G. Mokhtari, A. Ghosh, G. Nourbakhsh, and G. Ledwich, "Smart robust resources control in lv network to deal with voltage rise issue," *IEEE Transactions on Sustainable Energy*, vol. 4, pp. 1043–1050, Oct 2013.
- [17] A. Camacho, M. Castilla, J. Miret, J. C. Vasquez, and E. Alarcon-Gallo, "Flexible voltage support control for three-phase distributed generation inverters under grid fault," *IEEE Transactions on Industrial Electronics*, vol. 60, pp. 1429–1441, April 2013.
- [18] B. Meersman, B. Renders, L. Degroote, T. Vandoorn, and L. Vandeveldel, "Three-phase inverter-connected dg-units and voltage unbalance," *Electric Power Systems Research*, vol. 81, no. 4, pp. 899 – 906, 2011.
- [19] A. Haque, P. Nguyen, T. Vo, and F. Blied, "Agent-based unified approach for thermal and voltage constraint management in LV distribution network," *Electric Power Systems Research*, vol. 143, pp. 462 – 473, 2017.
- [20] Y. Tang, R. Burgos, C. Li, and D. Boroyevich, "Assessment of medium voltage distribution feeders under high penetration of PV generation," in *2015 IEEE 16th Workshop on Control and Modeling for Power Electronics (COMPEL)*, Vancouver, Canada, July, 2015.
- [21] G. Loren and P. Mandatova, "Active distribution system management: A key tool for the smooth integration of distributed generation," in *EURELECTRIC paper*, Feb 2013.
- [22] X. Su, M. A. S. Masoum, and P. J. Wolfs, "Optimal pv inverter reactive power control and real power curtailment to improve performance of unbalanced four-wire LV distribution networks," *IEEE Transactions on Sustainable Energy*, vol. 5, pp. 967–977, July 2014.
- [23] S. Weckx, C. Gonzalez, and J. Driesen, "Combined central and local active and reactive power control of PV inverters," *IEEE Transactions on Sustainable Energy*, vol. 5, pp. 776–784, July 2014.
- [24] E. Demirok, P. C. Gonzalez, K. H. B. Frederiksen, D. Sera, P. Rodriguez, and R. Teodorescu, "Local reactive power control methods for overvoltage prevention of distributed solar inverters in low-voltage grids," *IEEE Journal of Photovoltaics*, vol. 1, pp. 174–182, Oct 2011.

- [25] E. Demirok, D. Sera, R. Teodorescu, P. Rodriguez, and U. Borup, "Evaluation of the voltage support strategies for the low voltage grid connected pv generators," in *2010 IEEE Energy Conversion Congress and Exposition*, pp. 710–717, Sept 2010.
- [26] W. A. Omran, M. Kazerani, and M. M. A. Salama, "Investigation of methods for reduction of power fluctuations generated from large grid-connected photovoltaic systems," *IEEE Transactions on Energy Conversion*, vol. 26, pp. 318–327, March 2011.
- [27] T. Stetz, F. Marten, and M. Braun, "Improved low voltage grid-integration of photovoltaic systems in germany," in *2013 IEEE Power Energy Society General Meeting*, July 2013.
- [28] J. W. Smith, W. Sunderman, R. Dugan, and B. Seal, "Smart inverter volt/var control functions for high penetration of PV on distribution systems," in *2011 IEEE/PES Power Systems Conference and Exposition*, March Phoenix, USA, 2011.
- [29] R. Dugan, W. Sunderman, and B. Seal, "Advanced inverter controls for distributed resources," in *22nd International Conference and Exhibition on Electricity Distribution (CIRED 2013)*, June Stockholm, Sweden, 2013.
- [30] Y. Chistyakov, E. Kholodova, K. Natreba, A. Szabo, and M. Metzger, "Combined central and local control of reactive power in electrical grids with distributed generation," in *2012 IEEE International Energy Conference and Exhibition (ENERGYCON)*, pp. 325–330, Sept 2012.
- [31] C. Demoulias, "A new simple analytical method for calculating the optimum inverter size in grid-connected PV plants," *Electric Power Systems Research*, vol. 80, no. 10, pp. 1197 – 1204, 2010.
- [32] R. Tonkoski, L. A. C. Lopes, and T. H. M. El-Fouly, "Coordinated active power curtailment of grid connected pv inverters for overvoltage prevention," *IEEE Transactions on Sustainable Energy*, vol. 2, pp. 139–147, April 2011.
- [33] T. L. Vandoorn, J. D. Kooning, B. Meersman, and L. Vandeveldel, "Voltage-based droop control of renewables to avoid on-off oscillations caused by overvoltages," *IEEE Transactions on Power Delivery*, vol. 28, pp. 845–854, April 2013.
- [34] K. D. Brabandere, A. Woyte, R. Belmans, and J. Nijs, "Prevention of inverter voltage tripping in high density PV grids," in *19th EU-PVSEC, Paris, France*, June 2004.

- [35] R. Kabiri, D. G. Holmes, and B. P. McGrath, "The influence of pv inverter reactive power injection on grid voltage regulation," in *2014 IEEE 5th International Symposium on Power Electronics for Distributed Generation Systems (PEDG)*, June 2014.
- [36] T. L. Vandoorn, B. Meersman, L. Degroote, B. Renders, and L. Vandeveldel, "A control strategy for islanded microgrids with dc-link voltage control," *IEEE Transactions on Power Delivery*, vol. 26, pp. 703–713, April 2011.
- [37] M. J. Dolan, E. M. Davidson, I. Kockar, G. W. Ault, and S. D. J. McArthur, "Reducing distributed generator curtailment through active power flow management," *IEEE Transactions on Smart Grid*, vol. 5, pp. 149–157, Jan 2014.
- [38] R. Tonkoski and L. A. Lopes, "Impact of active power curtailment on over-voltage prevention and energy production of pv inverters connected to low voltage residential feeders," *Renewable Energy*, vol. 36, no. 12, pp. 3566 – 3574, 2011.
- [39] C. H. Lin, W. L. Hsieh, C. S. Chen, C. T. Hsu, and T. T. Ku, "Optimization of photovoltaic penetration in distribution systems considering annual duration curve of solar irradiation," *IEEE Transactions on Power Systems*, vol. 27, pp. 1090–1097, May 2012.
- [40] A. C. Rueda-Medina and A. Padilha-Feltrin, "Distributed generators as providers of reactive power support - 2014; a market approach," *IEEE Transactions on Power Systems*, vol. 28, pp. 490–502, Feb 2013.
- [41] B. Meersman, *Control of 3-phase inverter-connected distributed generators regarding the improvement of the power quality*. Doctoral thesis, Universiteit Gent, Faculteit Ingenieurswetenschappen en Architectuur, Ghent, Belgium, Feb. 2012.
- [42] B. Bletterie, S. Kadam, R. Pitz, and A. Abart, "Optimisation of lv networks with high photovoltaic penetration 2014; balancing the grid with smart meters," in *2013 IEEE Grenoble Conference*, June 2013.
- [43] B. Bletterie, S. Kadam, R. Pitz, and A. Abart, "Understanding the effect of unsymmetrical infeed on the voltage rise for the design of stable voltage control algorithms with pv inverters," in *2013 IEEE Grenoble Conference*, June 2013.
- [44] "Specifieke technische voorschriften voor decentrale productie-installaties die in parallel werken met het distributienet, c10/11," in *www.synergrid.be*, May 2009.

- [45] F. Blaabjerg, R. Teodorescu, M. Liserre, and A. V. Timbus, "Overview of control and grid synchronization for distributed power generation systems," *IEEE Transactions on Industrial Electronics*, vol. 53, pp. 1398–1409, Oct 2006.
- [46] B. Meersman, B. Renders, L. Degroote, T. Vandoorn, and L. Vandeveldel, "The influence of grid-connected three-phase inverters on voltage unbalance," in *IEEE PES General Meeting*, July Providence, RI, USA, 2010.
- [47] A. V. Timbus, R. Teodorescu, F. Blaabjerg, M. Liserre, and A. Dell'Aquila, "Independent synchronization and control of three phase grid converters," in *International Symposium on Power Electronics, Electrical Drives, Automation and Motion, 2006. SPEEDAM 2006.*, pp. 1246–1251, May 2006.
- [48] A. V. Timbus, R. Teodorescu, F. Blaabjerg, M. Liserre, and P. Rodriguez, "PII algorithm for power generation systems robust to grid voltage faults," in *2006 37th IEEE Power Electronics Specialists Conference*, June 2006.
- [49] S.-K. Chung, "A phase tracking system for three phase utility interface inverters," *IEEE Trans. on Power Electron.*, vol. 15, pp. 431–438, May 2000.
- [50] T. Vandoorn, *Voltage-based droop control of converter-interfaced distributed generation units in microgrids*. Doctoral thesis, Gent University, Faculty of Engineering and Architecture, Ghent, Belgium, 2013.
- [51] VDE V 0126-1-1, "Automatic disconnection device between a generator and the public low-voltage grid," 2006.
- [52] T. L. Lee, S. H. Hu, and Y. H. Chan, "D-STATCOM with positive-sequence admittance and negative-sequence conductance to mitigate voltage fluctuations in high-level penetration of distributed-generation systems," *IEEE Transactions on Industrial Electronics*, vol. 60, pp. 1417–1428, April 2013.
- [53] M. Singh, V. Khadkikar, A. Chandra, and R. K. Varma, "Grid interconnection of renewable energy sources at the distribution level with power-quality improvement features," *IEEE Transactions on Power Delivery*, vol. 26, pp. 307–315, Jan 2011.
- [54] B. Renders, K. De Gussemé, W. R. Ryckaert, and L. Vandeveldel, "Input impedance of grid-connected converters with programmable harmonic resistance," *IET Electric Power Applications*, vol. 1, pp. 355–361, May 2007.
- [55] W. R. Ryckaert, K. De Gussemé, D. M. Van de Sype, J. A. Ghijselen, and J. A. Melkebeek, "Reduction of the voltage distortion with a converter employed as shunt harmonic impedance," in *Twentieth Annual IEEE Applied*

- Power Electronics Conference and Exposition, 2005. APEC 2005.*, vol. 3, pp. 1805–1810, March Austin, TX, USA, 2005.
- [56] B. Renders, *Convertor-gekoppelde decentrale generatoren en netkwaliteit in laagspanningsnetten*. Doctoral thesis, Universiteit Gent, Faculteit Ingenieurswetenschappen, Gent, Belgium, June 2009.
- [57] G. H. Oettinge, “European commission, 2011a european commission, 2011a. energy roadmap 2050,” in *www.ec.europa.eu*, June 2012.
- [58] M. van Werven and M. Scheepers, “The changing role of distribution system operators in liberalized and decentralizing electricity markets,” in *International Conference on Future Power Systems*, June Amsterdam, Netherlands, 2005.
- [59] L. Vandeveld and B. Meersman, “Increasing the penetration of the renewable energy sources in the distribution grid by developing control strategies and using ancillary services (increase),” in *EC-FP7 Project, Grant Agreement no.: 608998*.
- [60] “<http://www.project-increase.eu/>,”
- [61] A. F. Gubina, T. Medved, B. Prislan, and J. Zupani, “A method for optimal schedule balancing in distribution network using multi agent control strategy,” in *2016 13th International Conference on the European Energy Market (EEM)*, June Porto, Portugal, 2016.
- [62] J. Desmet, B. Verhelst, L. Vandeveld, and C. Debruyne, “Test field for lv distribution systems,” in *22nd International Conference and Exhibition on Electricity Distribution (CIRED 2013)*, pp. 1–4, June Stockholm, Sweden, 2013.
- [63] J. V. Ryckeghem, T. Delerue, A. Bottenberg, J. Rens, and J. Desmet, “Decongestion of the distribution grid via optimised location of pv-battery systems,” in *26nd International Conference and Exhibition on Electricity Distribution (CIRED 2013)*, vol. 2017, pp. 573–576, October 2017.
- [64] W. H. Kersting and R. K. Green, “The application of carson’s equation to the steady-state analysis of distribution feeders,” in *2011 IEEE/PES Power Systems Conference and Exposition*, March Phoenix, AZ, USA, 2011.
- [65] W. H. Kersting, *distribution system modeling and analysis, 2nd E.* 2007.
- [66] G. C. Kryonidis, E. O. Kontis, A. I. Chrysochos, C. S. Demoulias, D. Bozalakov, B. Meersman, T. L. Vandoorn, and L. Vandeveld, “A simulation tool for extended distribution grids with controlled distributed generation,” in *2015 IEEE Eindhoven PowerTech*, June 2015.

- [67] H. Saadat, *Power System Analysis, 3rd E.* 2010.
- [68] D. V. Bozalakov, T. L. Vandoorn, B. Meersman, G. K. Papagiannis, A. I. Chrysochos, and L. Vandeveldel, "Damping-based droop control strategy allowing an increased penetration of renewable energy resources in low-voltage grids," *IEEE Transactions on Power Delivery*, vol. 31, pp. 1447–1455, Aug 2016.
- [69] D. V. Bozalakov, M. J. Mnati, J. Laveyne, A. V. d. Bossche, and L. Vandeveldel, "Voltage unbalance and overvoltage mitigation by using the three-phase damping control strategy in battery storage applications," in *7th International Conference on Renewable Energy Research and Applications (ICRERA)*, pp. 753–759, Paris, France, Oct 2018.
- [70] F. Olivier, R. Fonteneau, and D. Ernst, "Modelling of three-phase four-wire low-voltage cables taking into account the neutral connection to the earth," *CIREN - Open Access Proceedings Journal*, vol. 2018, no. 1, 2018.
- [71] D. Bozalakov, J. Laveyne, J. Desmet, and L. Vandeveldel, "Overvoltage and voltage unbalance mitigation in areas with high penetration of renewable energy resources by using the modified three-phase damping control strategy," *Electric Power Systems Research*, vol. 168, pp. 283 – 294, 2019.
- [72] L. S. Xavier, A. F. Cupertino, and H. A. Pereira, "Ancillary services provided by photovoltaic inverters: Single and three phase control strategies," *Computers & Electrical Engineering*, vol. 70, pp. 102 – 121.
- [73] A. Safa, E. M. Berkouk, Y. Messlem, and A. Gouichiche, "A robust control algorithm for a multifunctional grid tied inverter to enhance the power quality of a microgrid under unbalanced conditions," *International Journal of Electrical Power & Energy Systems*, vol. 100, pp. 253 – 264, 2018.
- [74] B. Olek and M. Wierzbowski, "Local energy balancing and ancillary services in low-voltage networks with distributed generation, energy storage, and active loads," *IEEE Transactions on Industrial Electronics*, vol. 62, pp. 2499–2508, April 2015.
- [75] J. V. d. V. L. V. T. Vandoorn, J. De Kooning, "Three-phase primary control for unbalance sharing between distributed generation units in a microgrid," *Smart Grid and the Future Electrical Network*, vol. 6, Dec 2013.
- [76] M. V. M. Ali, M. Babar, P. Nguyen, and J. Cobben, "Overlaying control mechanism for solar pv inverters in the lv distribution network," *Electric Power Systems Research*, vol. 145, pp. 264 – 274, 2017.

- [77] M. M. V. M. Ali, P. H. Nguyen, W. L. Kling, A. I. Chrysochos, T. A. Papadopoulos, and G. K. Papagiannis, "Fair power curtailment of distributed renewable energy sources to mitigate overvoltages in low-voltage networks," in *2015 IEEE Eindhoven PowerTech*, June 2015.
- [78] M. Kaspirek, D. Mezera, and J. Jiricka, "Problems of voltage stabilization in MV and LV distribution grids due to the operation of renewable energy sources," in *22nd International Conference and Exhibition on Electricity Distribution (CIRED 2013)*, Stockholm, Sweden, June 2013.
- [79] D. Bozalakov, T. Vandoorn, B. Meersman, C. Demoulias, and L. Vandevelde, "Voltage dip mitigation capabilities of three-phase damping control strategy," *Electric Power Systems Research*, vol. 121, pp. 192–199, 2015.
- [80] D. Bozalakov, M. J. Mnati, A. Van den Bossche, and L. Vandevelde, "Voltage unbalance mitigation by using the three-phase damping control strategy in active rectification mode," in *IEEE Young Researchers Symposium (YRS2018)*, May 2018.
- [81] M. H. Bollen, *Understanding Power Quality Problems: Voltage Sags and Interruptions*, pp. 465–476. Wiley-IEEE Press, 2000.
- [82] "Preface," in *Practical Power Distribution for Industry* (J. de Kock and K. Strauss, eds.), p. viii, Oxford: Newnes, 2004.
- [83] M. H. Bollen, S. Z. Djokic, K. Stockman, R. Neumann, and G. Ethier, "Voltage-dip immunity: statistics and need for further work," in *International Conference of Renewable Energy and Power Quality (ICREPO)*, Granada, Spain, March 2010.
- [84] M. Bollen, J. R. Gordon, S. Djokic, K. Stockman, J. Milanovic, R. Neumann, G. Ethier, and F. Zavoda, "Voltage dip immunity of equipment and installations - status and need for further work," in *CICED 2010 Proceedings*, Nanjing, China, Sept 2010.
- [85] IEC 61000-4-11, "Testing and measurement techniques Voltage dips, short interruptions and voltage variations immunity tests," 2004.
- [86] J. Cappelle, J. Vanalme, S. Vispoel, T. V. Maerhem, B. Verhelst, C. Debruyne, and J. Desmet, "Introducing small storage capacity at residential pv installations to prevent overvoltages," in *2011 IEEE International Conference on Smart Grid Communications (SmartGridComm)*, pp. 534–539, Brussels, Belgium, Oct 2011.

- [87] W. Labeeuw and G. Deconinck, "Residential electrical load model based on mixture model clustering and markov models," *IEEE Transactions on Industrial Informatics*, vol. 9, pp. 1561–1569, Aug 2013.
- [88] A. V. Oppenheim and A. S. Willsky, *Signals and Systems (2nd Edition)*. Pearson, 1996.
- [89] M. G. Simoes and F. A. Farret, *Modeling power electronics and interfacing energy conversion systems*. Wiley, 2017.
- [90] R. R. Behera and A. N. Thakur, "An overview of various grid synchronization techniques for single-phase grid integration of renewable distributed power generation systems," in *2016 International Conference on Electrical, Electronics, and Optimization Techniques (ICEEOT)*, pp. 2876–2880, Chennai, India, March 2016.
- [91] R. Teodorescu, M. Liserre, and P. Rodriguez, "Grid converters for photovoltaic and wind power systems," in *John Wiley & Sons*, 2011.
- [92] B. Meersman, J. D. Kooning, T. Vandoorn, L. Degroote, B. Renders, and L. Vandeveld, "Overview of PLL methods for distributed generation units," in *45th International Universities Power Engineering Conference UPEC2010*, Cardiff, Wales, UK, Aug 2010.
- [93] S. A. O. da Silva, R. Novochadlo, and R. A. Modesto, "Single-phase pll structure using modified p-q theory for utility connected systems," in *2008 IEEE Power Electronics Specialists Conference*, pp. 4706–4711, June 2008.
- [94] A. Luna, J. Rocabert, I. Candela, P. Rodriguez, R. Teodorescu, and F. Blaabjerg, "Advanced structures for grid synchronization of power converters in distributed generation applications," in *2012 IEEE Energy Conversion Congress and Exposition (ECCE)*, pp. 2769–2776, Sept 2012.
- [95] F. Xiao, L. Dong, L. Li, and X. Liao, "A frequency-fixed sogi-based pll for single-phase grid-connected converters," *IEEE Transactions on Power Electronics*, vol. 32, pp. 1713–1719, March 2017.
- [96] P. Cossutta, S. Raffo, A. Cao, F. Ditaranto, M. P. Aguirre, and M. I. Valla, "High speed single phase sogi-pll with high resolution implementation on an fpga," in *2015 IEEE 24th International Symposium on Industrial Electronics (ISIE)*, pp. 1004–1009, June 2015.
- [97] H. K. Yada and M. S. R. Murthy, "An improved control algorithm for DSTATCOM based on single-phase SOGI-PLL under varying load conditions and adverse grid conditions," in *2016 IEEE International Conference*

- on *Power Electronics, Drives and Energy Systems (PEDES)*, pp. 1–6, Dec 2016.
- [98] Y. Huang, X. Yuan, J. Hu, P. Zhou, and D. Wang, “Dc-bus voltage control stability affected by ac-bus voltage control in vscs connected to weak ac grids,” *IEEE Journal of Emerging and Selected Topics in Power Electronics*, vol. 4, pp. 445–458, June 2016.
- [99] L. Moran, P. D. Ziogas, and G. Joos, “Design aspects of synchronous pwm rectifier-inverter systems under unbalanced input voltage conditions,” *IEEE Transactions on Industry Applications*, vol. 28, pp. 1286–1293, Nov 1992.
- [100] T. C. Green and J. H. Marks, “Control techniques for active power filters,” *IEE Proceedings - Electric Power Applications*, vol. 152, pp. 369–381, March 2005.
- [101] B. Meersman, B. Renders, L. Degroote, T. Vandoorn, and L. Vandeveldel, “DC-bus voltage controllers for a three-phase voltage-source inverter for distributed generation,” in *ICREPQ09, Valencia (Spain), 15-17, April 2009*.
- [102] J. De Kooning, *Balancing van het middelpunt van de busspanning bij driefasige netgekoppelde invertoren met neutrale geleider*. Ms. thesis, Universiteit Gent, Faculteit Ingenieurswetenschappen, Gent, Belgium, June 2010.
- [103] M. Pahlevani, S. Eren, A. Bakhshai, and P. Jain, “A DC-bus voltage control technique for grid-connected ac/dc converters used in smart energy storage units,” in *2015 IEEE 6th International Symposium on Power Electronics for Distributed Generation Systems (PEDG)*, pp. 1–7, Aachen, Germany, June 2015.
- [104] Y. Jiao, F. C. Lee, and S. Lu, “Space vector modulation for three-level npc converter with neutral point voltage balance and switching loss reduction,” *IEEE Transactions on Power Electronics*, vol. 29, pp. 5579–5591, Oct 2014.
- [105] X. Xing, A. Chen, W. Wang, C. Zhang, Y. Li, and C. Du, “Space-vector-modulated for z-source three-level t-type converter with neutral voltage balancing,” in *2015 IEEE Applied Power Electronics Conference and Exposition (APEC)*, pp. 833–840, March 2015.
- [106] N. M. R. Santos, J. F. Silva, J. Verweckken, V. M. F. Pires, and R. Castro, “Enhancing the ride-through capability of dc-link voltage in npc multilevel unified power-flow controllers,” *IEEE Transactions on Power Delivery*, vol. 29, pp. 1542–1550, Aug 2014.

- [107] Q.-C. Zhong, L. Hobson, and M. Jayne, "Classical control of the neutral point in 4-wire 3-phase dc-ac converters," *Electrical Power Quality and Utilisation Journal*, vol. 2, no. 11, pp. 111–119, 2005.
- [108] Q. C. Zhong, J. Liang, G. Weiss, C. M. Feng, and T. C. Green, " $H^\infty$  control of the neutral point in four-wire three-phase dc-ac converters," *IEEE Transactions on Industrial Electronics*, vol. 53, pp. 1594–1602, Oct 2006.
- [109] K. Hasegawa and H. Akagi, "A new dc-voltage-balancing circuit including a single coupled inductor for a five-level diode-clamped pwm inverter," *IEEE Transactions on Industry Applications*, vol. 47, pp. 841–852, March 2011.
- [110] S. Busquets-Monge, S. Alepuz, J. Bordonau, and J. Peracaula, "Voltage balancing control of diode-clamped multilevel converters with passive front-ends," *IEEE Transactions on Power Electronics*, vol. 23, pp. 1751–1758, July 2008.
- [111] R. Stala, "A natural dc-link voltage balancing of diode-clamped inverters in parallel systems," *IEEE Transactions on Industrial Electronics*, vol. 60, pp. 5008–5018, Nov 2013.
- [112] N. Gupta, A. Swarnkar, and K. Niazi, "A novel method for simultaneous phase balancing and mitigation of neutral current harmonics in secondary distribution systems," *International Journal of Electrical Power & Energy Systems*, vol. 55, pp. 645 – 656, 2014.
- [113] J. Zaragoza, J. Pou, S. Ceballos, E. Robles, C. Jaen, and M. Corbalan, "Voltage-balance compensator for a carrier-based modulation in the neutral-point-clamped converter," *IEEE Transactions on Industrial Electronics*, vol. 56, pp. 305–314, Feb 2009.
- [114] J. Shen, S. Schroder, B. Duro, and R. Roesner, "A neutral-point balancing controller for a three-level inverter with full power-factor range and low distortion," *IEEE Transactions on Industry Applications*, vol. 49, pp. 138–148, Jan 2013.
- [115] J. Pou, J. Zaragoza, S. Ceballos, M. Saeedifard, and D. Boroyevich, "A carrier-based pwm strategy with zero-sequence voltage injection for a three-level neutral-point-clamped converter," *IEEE Transactions on Power Electronics*, vol. 27, pp. 642–651, Feb 2012.
- [116] D. M. V. de Sype, K. De Gussemé, A. P. M. V. den Bossche, and J. A. Melkebeek, "Duty-ratio feedforward for digitally controlled boost pfc converters," *IEEE Transactions on Industrial Electronics*, vol. 52, pp. 108–115, Feb 2005.

- [117] “Electromagnetic compatibility (EMC) part 3-2: Limits for harmonic current emissions (equipment input current 16 a per phase),” *IEC Standard 61000-3-2, 2009*, 2009.
- [118] A. Timbus, M. Liserre, R. Teodorescu, P. Rodriguez, and F. Blaabjerg, “Evaluation of current controllers for distributed power generation systems,” *IEEE Transactions on Power Electronics*, vol. 24, pp. 654–664, March 2009.
- [119] R. P. Aguilera, P. Acua, P. Lezana, G. Konstantinou, B. Wu, S. Bernet, and V. G. Agelidis, “Selective harmonic elimination model predictive control for multilevel power converters,” *IEEE Transactions on Power Electronics*, vol. 32, pp. 2416–2426, March 2017.
- [120] K. Zhou, Y. Yang, F. Blaabjerg, and D. Wang, “Optimal selective harmonic control for power harmonics mitigation,” *IEEE Transactions on Industrial Electronics*, vol. 62, pp. 1220–1230, Feb 2015.
- [121] B. Renders, L. Degroote, J. Driesen, and L. Vandeveldel, “Profits of power-quality improvement by residential distributed generation,” in *2007 42nd International Universities Power Engineering Conference*, pp. 377–381, Brighton, UK, Sept 2007.
- [122] J. Morales, L. G. de Vicua, R. Guzman, M. Castilla, and J. Miret, “Modeling and sliding mode control for three-phase active power filters using the vector operation technique,” *IEEE Transactions on Industrial Electronics*, vol. 65, pp. 6828–6838, Sep. 2018.
- [123] L. Feng and Y. Wang, “Modeling and resonance control of modular three-level shunt active power filter,” *IEEE Transactions on Industrial Electronics*, vol. 64, pp. 7478–7486, Sept 2017.
- [124] A. V. Barva and P. R. Bhavsar, “Design and simulation of split-capacitor based three-phase four-wire shunt active power filter,” in *2017 2nd IEEE International Conference on Recent Trends in Electronics, Information Communication Technology (RTEICT)*, pp. 1106–1110, May 2017.
- [125] P. S. and K. S. Thampatty, “Dynamic modeling and control of upfc for power flow control,” *Procedia Technology*, vol. 21, pp. 581 – 588, 2015. SMART GRID TECHNOLOGIES.
- [126] E. O. Kontis, G. C. Kryonidis, A. I. Chrysochos, C. S. Demoulias, and G. K. Papagiannis, “Long-term evaluation of dres penetration in lv networks using droop control techniques,” in *2016 IEEE PES Innovative Smart Grid Technologies Conference Europe (ISGT-Europe)*, Ljubljana, Slovenia, Oct 2016.

- [127] H. Zsiborács, N. Hegedüsne Baranyai, A. Vincze, I. Háber, and G. Pintér, “Economic and technical aspects of flexible storage photovoltaic systems in Europe,” *Energies*, vol. 11, no. 6, 1445, 2018.
- [128] S. Weckx and J. Driesen, “Load balancing with EV chargers and PV inverters in unbalanced distribution grids,” *IEEE Transactions on Sustainable Energy*, vol. 6, pp. 635–643, April 2015.
- [129] H. B. Tolabi, M. H. Ali, and M. Rizwan, “Simultaneous reconfiguration, optimal placement of DSTATCOM, and photovoltaic array in a distribution system based on fuzzy-ACO approach,” *IEEE Transactions on Sustainable Energy*, vol. 6, pp. 210–218, Jan 2015.
- [130] P. Chaudhary and M. Rizwan, “Voltage regulation mitigation techniques in distribution system with high PV penetration: A review,” *Renewable and Sustainable Energy Reviews*, vol. 82, pp. 3279 – 3287, 2018.
- [131] D. Shaw-Williams, C. Susilawati, and G. Walker, “Value of residential investment in photovoltaics and batteries in networks: A techno-economic analysis,” *Energies*, vol. 11, no. 4, 1022, 2018.
- [132] Y. Yang, H. Li, A. Aichhorn, J. Zheng, and M. Greenleaf, “Sizing strategy of distributed battery storage system with high penetration of photovoltaic for voltage regulation and peak load shaving,” *IEEE Transactions on Smart Grid*, vol. 5, pp. 982–991, March 2014.
- [133] G. Hilton, A. Cruden, and J. Kent, “Comparative analysis of domestic and feeder connected batteries for low voltage networks with high photovoltaic penetration,” *Journal of Energy Storage*, vol. 13, pp. 334 – 343, 2017.
- [134] K. H. Chua, Y. S. Lim, P. Taylor, S. Morris, and J. Wong, “Energy storage system for mitigating voltage unbalance on low-voltage networks with photovoltaic systems,” *IEEE Transactions on Power Delivery*, vol. 27, pp. 1783–1790, Oct 2012.
- [135] B. Faessler, M. Schuler, M. Preiinger, and P. Keplinger, “Battery storage systems as grid-balancing measure in low-voltage distribution grids with distributed generation,” *Energies*, vol. 10, no. 12, 2161, 2017.
- [136] H. C. Hesse, R. Martins, P. Musilek, M. Naumann, C. N. Truong, and A. Jossen, “Economic optimization of component sizing for residential battery storage systems,” *Energies*, vol. 10, no. 7, 835, 2017.
- [137] P. L. J. Paatero, “Impacts of energy storage in distribution grids with high penetration of photovoltaic power,” in *International Journal of Distributed Energy Sources*, pp. 534–539, Oct 2011.

- [138] S. Gortz, *Battery energy storage for intermittent renewable electricity production*,. Master thesis, Umea University, Sweden, 2015.
- [139] M. J. Zangs, P. B. E. Adams, T. Yunusov, W. Holderbaum, and B. A. Potter, “Distributed energy storage control for dynamic load impact mitigation,” *Energies*, vol. 9, no. 8,647, 2016.
- [140] B. Idlbi, J. von Appen, T. Kneiske, and M. Braun, “Cost-benefit analysis of battery storage system for voltage compliance in distribution grids with high distributed generation,” *Energy Procedia*, vol. 99, 2016. 10th International Renewable Energy Storage Conference, IRES 2016, 15-17 March 2016, Düsseldorf, Germany.
- [141] S. Rodrigues, R. Torabi, H. G. Ramos, and F. Morgado-Dias, “Powerwall 2.0 economic feasibility in Australia,” in *2017 International Conference in Energy and Sustainability in Small Developing Economies (ES2DE)*, Funchal, Portugal, July 2017.
- [142] A. Zeh and R. Witzmann, “Operational strategies for battery storage systems in low-voltage distribution grids to limit the feed-in power of roof-mounted solar power systems,” *Energy Procedia*, vol. 46, pp. 114 – 123, 2014. 8th International Renewable Energy Storage Conference and Exhibition (IRES 2013).
- [143] S. Nguyen, W. Peng, P. Sokolowski, D. Alahakoon, and X. Yu, “Optimizing rooftop photovoltaic distributed generation with battery storage for peer-to-peer energy trading,” *Applied Energy*, vol. 228, pp. 2567 – 2580, 2018.
- [144] F. Marra, G. Yang, C. Trholt, J. stergaard, and E. Larsen, “A decentralized storage strategy for residential feeders with photovoltaics,” *IEEE Transactions on Smart Grid*, vol. 5, pp. 974–981, March 2014.
- [145] M. J. E. Alam, K. M. Muttaqi, and D. Sutanto, “Distributed energy storage for mitigation of voltage-rise impact caused by rooftop solar PV,” in *2012 IEEE Power and Energy Society General Meeting*, San Diego, CA, USA, July 2012.
- [146] M. Liserre, R. Teodorescu, P. Rodriguez, F. Blaabjerg, and A. Timbus, “Independent synchronization and control of three phase grid converters,” in *Proc. of the International Symposium on Power Electronics, Electrical Drives, Automation and Motion (SPEEDAM)*, (Naples, Italy), May 23-26 2006.
- [147] M. Liserre, R. Teodorescu, P. Rodriguez, F. Blaabjerg, and A. Timbus, “PLL algorithm for power generation systems robust to grid voltage faults,” in

- Proc. of the 37th IEEE Power Electronics Specialist Conference (PESC 2006)*, (Cheju Isl, South Korea), Jun. 18-22 2006.
- [148] D. Bozalakov, B. Meersman, A. Bottenberg, J. Rens, J. Desmet, and L. Vandevelde, "Dc-bus voltage balancing controllers for split dc-link four-wire inverters and their impact on the quality of the injected currents," *CIREC - Open Access Proceedings Journal*, vol. 2017, no. 1, pp. 564–568, 2017.
- [149] S. Vavilapalli, S. Padmanaban, U. Subramaniam, and L. Mihet-Popa, "Power balancing control for grid energy storage system in photovoltaic applications real time digital simulation implementation," *Energies*, vol. 10, no. 7, 928, 2017.
- [150] S. Hashemi and J. Stergaard, "Efficient control of energy storage for increasing the pv hosting capacity of lv grids," *IEEE Transactions on Smart Grid*, vol. 9, pp. 2295–2303, May 2018.
- [151] "Tesla powerwall 2 dc," [https://www.solahart.com.au/media/2849/powerwall-2-dc\\_datasheet\\_english.pdf](https://www.solahart.com.au/media/2849/powerwall-2-dc_datasheet_english.pdf)," Last visited: July 2018.
- [152] J. C. Gomez, M. M. Morcos, C. A. Reineri, and G. N. Campetelli, "Behavior of induction motor due to voltage sags and short interruptions," *IEEE Transactions on Power Delivery*, vol. 17, pp. 434–440, Apr 2002.
- [153] M. H. J. Bollen, "Characterisation of voltage sags experienced by three-phase adjustable-speed drives," *IEEE Transactions on Power Delivery*, vol. 12, pp. 1666–1671, Oct 1997.
- [154] L. Zhan and M. H. J. Bollen, "Characteristic of voltage dips (sags) in power systems," *IEEE Transactions on Power Delivery*, vol. 15, pp. 827–832, Apr 2000.
- [155] M. Bollen and L. Zhang, "Different methods for classification of three-phase unbalanced voltage dips due to faults," *Electric Power Systems Research*, vol. 66, no. 1, pp. 59 – 69, 2003.
- [156] Y. H. Chen, C. Y. Lin, J. M. Chen, and P. T. Cheng, "An inrush mitigation technique of load transformers for the series voltage sag compensator," *IEEE Transactions on Power Electronics*, vol. 25, pp. 2211–2221, Aug 2010.
- [157] M. H. J. Bollen, S. Cundeva, J. R. Gordon, S. Z. Djokic, K. Stockman, J. V. Milanovic, R. Neumann, and G. Ethier, "Voltage dip immunity aspects of power-electronics equipment recommendations from cigre/cired/uie jwg

- c4.110,” in *11th International Conference on Electrical Power Quality and Utilisation*, Lisbon, Portugal, Oct 2011.
- [158] A. D. Fazio, V. Duraccio, P. Varilone, and P. Verde, “Voltage sags in the automotive industry: Analysis and solutions,” *Electric Power Systems Research*, vol. 110, pp. 25 – 30, 2014.
- [159] J. Manson and R. Targosz, “European power quality survey report - report,” *Leonardo ENERGY*, 2008.
- [160] J. C. Gomez and M. Morcos, “Contactor immunity related to voltage sags,” *CIREN-19th International Conference on Electricity Distribution*, vol. 2007, no. 1, 2007.
- [161] S. Z. Djokic, J. V. Milanovic, and D. S. Kirschen, “Sensitivity of ac coil contactors to voltage sags, short interruptions, and undervoltage transients,” *IEEE Transactions on Power Delivery*, vol. 19, pp. 1299–1307, July 2004.
- [162] D. Yang, X. Gao, Z. Ma, E. Cui, and H. Zhang, “Novel voltage sag protection topology of contactors for uninterrupted switching capability,” *IEEE Transactions on Industry Applications*, pp. 1–1, 2018.
- [163] A. Honrubia-Escribano, E. Gomez-Lázaro, A. Molina-Garca, and J. Fuentes, “Influence of voltage dips on industrial equipment: Analysis and assessment,” *International Journal of Electrical Power & Energy Systems*, vol. 41, no. 1, pp. 87 – 95, 2012.
- [164] Working Group C4.110, *Voltage Dip Immunity of Equipment and Installations*. Report, April 2010.
- [165] S. Z. Djokic, K. Stockman, J. V. Milanovic, J. J. M. Desmet, and R. Belmans, “Sensitivity of ac adjustable speed drives to voltage sags and short interruptions,” *IEEE Transactions on Power Delivery*, vol. 20, pp. 494–505, Jan 2005.
- [166] IEC 61000-4-34, “Testing and measurement techniques - Voltage dips, short interruptions and voltage variations immunity tests for equipment with input current more than 16 A per phase,” 2005.
- [167] M. H. Bollen, *Signal Processing of Power Quality Disturbances*. Wiley-IEEE Press, 2006.
- [168] O. Ipinnimo, S. Chowdhury, S. Chowdhury, and J. Mitra, “A review of voltage dip mitigation techniques with distributed generation in electricity networks,” *Electric Power Systems Research*, vol. 103, pp. 28 – 36, 2013.

- [169] K. J. P. Macken, M. H. J. Bollen, and R. J. M. Belmans, "Mitigation of voltage dips through distributed generation systems," *IEEE Transactions on Industry Applications*, vol. 40, pp. 1686–1693, Nov 2004.
- [170] SEMI F47-0706, "SEMI F47-0706 (Reapproved 0812) - Specification for Semiconductor Processing Equipment Voltage Sag Immunity," 2012.
- [171] J. Cobben, *Power Quality Implications at the Point of Connection*. Doctoral thesis, Technical University of Eindhoven, Eindhoven, The Netherlands, 2007.
- [172] C. Kumar and M. K. Mishra, "A multifunctional DSTATCOM operating under stiff source," *IEEE Transactions on Industrial Electronics*, vol. 61, pp. 3131–3136, July 2014.
- [173] D. Ananth and G. N. Kumar, "Mitigation of voltage dip and power system oscillations damping using dual STATCOM for grid connected DFIG," *Ain Shams Engineering Journal*, vol. 8, no. 4, pp. 581 – 592, 2017.
- [174] J. V. Milanovic and Y. Zhang, "Global minimization of financial losses due to voltage sags with facts based devices," *IEEE Transactions on Power Delivery*, vol. 25, pp. 298–306, Jan 2010.
- [175] S. Hsieh, "Economic evaluation of the hybrid enhancing scheme with DSTATCOM and active power curtailment for pv penetration in taipower distribution systems," *IEEE Transactions on Industry Applications*, vol. 51, pp. 1953–1961, May 2015.
- [176] M. Farhadi-Kangarlu, E. Babaei, and F. Blaabjerg, "A comprehensive review of dynamic voltage restorers," *International Journal of Electrical Power & Energy Systems*, vol. 92, pp. 136 – 155, 2017.
- [177] D. Patel, A. K. Goswami, and S. K. Singh, "Voltage sag mitigation in an indian distribution system using dynamic voltage restorer," *International Journal of Electrical Power & Energy Systems*, vol. 71, pp. 231 – 241, 2015.
- [178] P. Fernandez-Comesana, F. D. Freijedo, J. Doval-Gandoy, O. Lopez, A. G. Yepes, and J. Malvar, "Mitigation of voltage sags, imbalances and harmonics in sensitive industrial loads by means of a series power line conditioner," *Electric Power Systems Research*, vol. 84, no. 1, pp. 20 – 30, 2012.
- [179] B. Renders, K. De Gussemé, W. R. Ryckaert, K. Stockman, L. Vandeveldel, and M. H. J. Bollen, "Distributed generation for mitigating voltage dips in low-voltage distribution grids," *IEEE Transactions on Power Delivery*, vol. 23, pp. 1581–1588, July 2008.

- [180] ENTSO-e, “Network code requirements for grid connection applicable to all generators (8.3.2013).,” 2016.
- [181] ENTSO-e, “Implementation guideline for network code-requirements for grid connection applicable to all generators (16.10.2013).,” 2016.
- [182] Elia Group, “<http://www.elia.be/media/files/Elia/users-group/20160325%20-%20Belgian%20Grid/23robustnessFTRWGBG25032016.pdf>,” 2016.
- [183] ENTSO-e, “Recommendations for unified technical regulations for grid-connected pv systems, SUNRISE project,” 2016.
- [184] B. Renders, K. De Gussemé, W. R. Ryckaert, and L. Vandeveld, “Converter-connected distributed generation units with integrated harmonic voltage damping and harmonic current compensation function,” *Electric Power Systems Research*, vol. 79, no. 1, pp. 65 – 70, 2009.
- [185] T. Vandoorn, B. Meersman, J. D. Kooning, and L. Vandeveld, “Controllable harmonic current sharing in islanded microgrids: DG units with programmable resistive behavior toward harmonics,” *IEEE Transactions on Power Delivery*, vol. 27, pp. 831–841, April 2012.
- [186] S. Z. Djokic and M. H. J. Bollen, “Dip segmentation method,” in *2008 13th International Conference on Harmonics and Quality of Power*, pp. 1–8, Sept 2008.
- [187] M. A. Alonso, J. F. Sanz, J. Salln, and J. L. Villa, “Comparison of different voltage dip detection techniques,” in *ICREPQ09, Valencia (Spain)*, April 2009.
- [188] C. Fitzer, M. Barnes, and P. Green, “Voltage sag detection technique for a dynamic voltage restorer,” in *Conference Record of the 2002 IEEE Industry Applications Conference. 37th IAS Annual Meeting (Cat. No.02CH37344)*, vol. 2, pp. 917–924 vol.2, Oct 2002.
- [189] C. Fitzer, M. Barnes, and P. Green, “Voltage sag detection technique for a dynamic voltage restorer,” *IEEE Transactions on Industry Applications*, vol. 40, pp. 203–212, Jan 2004.
- [190] E. Perez and J. Barros, “Voltage event detection and characterization methods: A comparative study,” in *2006 IEEE/PES Transmission Distribution Conference and Exposition: Latin America*, p. 1, Caracas, Venezuela, Aug 2006.

- [191] J. L. Dantas, F. K. A. Lima, C. G. C. Branco, J. M. Guerrero, and J. C. Vasquez, "A robust and fast generic voltage sag detection technique," in *2015 IEEE 13th Brazilian Power Electronics Conference and 1st Southern Power Electronics Conference (COBEP/SPEC)*, Fortaleza, Brazil, Nov 2015.
- [192] M. P. Antunes, I. D. de Melo, J. L. R. Pereira, M. A. de Souza, and N. de Lima Silva, "Voltage sag detection methods based on synchronized phasor measurements using RTDS," in *2017 IEEE 26th International Symposium on Industrial Electronics (ISIE)*, pp. 180–185, Edinburgh, UK, June 2017.
- [193] A. Bagheri, M. H. Bollen, and I. Y. Gu, "Improved characterization of multi-stage voltage dips based on the space phasor model," *Electric Power Systems Research*, vol. 154, pp. 319 – 328, 2018.
- [194] A. Ziarani and A. Konrad, "A method of extraction of nonstationary sinusoids," *Signal Processing*, vol. 84, no. 8, pp. 1323 – 1346, 2004.
- [195] A. Moschitta, P. Carbone, and C. Muscas, "Performance comparison of advanced techniques for voltage dip detection," *IEEE Transactions on Instrumentation and Measurement*, vol. 61, pp. 1494–1502, May 2012.
- [196] Verband der Elektrotechnik Elektronik Informationstechnik, "Utility-scale PV systems: grid connection requirements, test procedures and European harmonisation," 2011.
- [197] "<http://www.europe-solarshop.com/inverters/sma.html>,"
- [198] "<https://zerohomebills.com/product/sma-sunny-tripower-30000tl-us-10-30kw-solar-inverter/>,"
- [199] "<https://zerohomebills.com/product/tesla-powerwall-7-kw-with-storedge-dc-system/>,"
- [200] "<https://zerohomebills.com/product/tesla-powerwall-7-kw-with-storedge-dc-system/>,"



# Publications list of D. V. Bozalakov

## International journal publications

- [1] **Dimitar Bozalakov**, Mohannad M. J. Al-Rubaye, Joannes Laveyne, Jan Desmet and Lieven Vandevelde, “Battery storage integration in voltage unbalance and overvoltage mitigation control strategies and its impact on the power quality,” *Energies*, vol. 12, No. 8, 2019.
- [2] **Dimitar Bozalakov**, Joannes Laveyne, Jan Desmet and Lieven Vandevelde, “Overvoltage and voltage unbalance mitigation in areas with high penetration of renewable energy resources by using the modified three-phase damping control strategy,” *Electric Power System Research*, Vol. 168, pp. 283-294, 2019.
- [3] Mohannad Jabbar Mnati, **Dimitar V. Bozalakov**, Alex Van den Bossche, “PID Control of a Three Phase Photovoltaic Inverter Tied to a Grid Based on a 120-Degree Bus Clamp PWM,” *IFAC*, Volume 51, Issue 4, 2018.
- [4] Mohannad Jabbar Mnati, **Dimitar V. Bozalakov**, and Alex Van den Bossche, “A New Synchronization Technique of a Three-Phase Grid Tied Inverter for Photovoltaic Applications, Mathematical Problems in Engineering, vol. 2018, 2018.
- [5] Mohannad Jabbar Mnati, **Dimitar V. Bozalakov**, and Alex Van den Bossche, “New Pulse Width Modulation Technique to Reduce Losses for Three-Phase Photovoltaic Inverters, Active and Passive Electronic Components, vol. 2018, Article ID 4157614, 10 pages, 2018.
- [6] **Dimitar V. Bozalakov**, Tine L. Vandoorn, Bart Meersman, Grigoris K. Papagiannis, Andreas I. Chrysochos and Lieven Vandevelde, “Damping-Based Droop Control Strategy Allowing an Increased Penetration of Renewable Energy Resources in Low-Voltage Grids,” in *IEEE Transactions on Power Delivery*, vol. 31, no. 4, pp. 1447-1455, Aug. 2016.
- [7] Vasiliki Klonari, Bart Meersman, **Dimitar Bozalakov**, Tine L. Vandoorn, Lieven Vandevelde, Jacques Lobry, François Vallée, “A probabilistic frame-

work for evaluating voltage unbalance mitigation by photovoltaic inverters,” Sustainable Energy, Grids and Networks, vol. 8, pp. 1-11, 2016.

- [8] **Dimitar Bozalakov**, Tine L. Vandoorn, Bart Meersman, Charis Demoulias, Lieven Vandeveldel, “Voltage dip mitigation capabilities of three-phase damping control strategy,” Electric Power Systems Research, vol. 121, pp. 192-199, 2015.

## International conferences

- [9] **Dimitar Bozalakov**, Mohannad Jabbar Mnati Al-Rubaye, Joannes Laveyne, Alex Van den Bossche and Lieven Vandeveldel, “Voltage unbalance and overvoltage mitigation by using the three-phase damping control strategy in battery storage applications,” 7th International Conference on Renewable Energy Research and Applications (ICRERA), Paris, France, 2018.
- [10] **Dimitar Bozalakov**, Mohannad Jabbar Mnati Al-Rubaye, Alex Van den Bossche and Lieven Vandeveldel, “Voltage unbalance mitigation by using the three-phase damping control strategy in active rectification mode,” Young Researchers Symposium 2018, May, Brussels, Belgium.
- [11] **Dimitar Bozalakov**, Bart Meersman, Agkaton Bottenberg, Johan Rens, Jan Desmet and Lieven Vandeveldel, “Dc-bus voltage balancing controllers for split dc-link four-wire inverters and their impact on the quality of the injected currents,” in CIREN - Open Access Proceedings Journal, vol. 2017, no. 1, pp. 564-568, 2017
- [12] Vasiliki Klonari, Bart Meersman, **Dimitar Bozalakov**, Tine Vandoorn, Jacques Lobry and François Vallée, “Long term assessment of a voltage unbalance mitigation scheme implemented by photovoltaic inverters,” Energycon 2016.
- [13] G.C. Kryonidis, E.O. Kontis, A.I. Chrysochos, C.S. Demoulias, **D. Bozalakov**, B. Meersman, T. Vandoorn and Lieven Vandeveldel, “A simulation tool for extended distribution grids with controlled distributed generation,” PowerTech, Eindhoven, The Netherlands, 2015.
- [14] **Dimitar Bozalakov**, Tine Vandoorn, Bart Meersman and Lieven Vandeveldel, “Overview of increasing the penetration of renewable energy sources in the distribution grid by developing control strategies and using ancillary services,” Young Researchers Symposium (YRS -2014), May, Gent, Belgium, 2014.

# A

## Additional measurements conducted in Chapter 3

Zero-sequence and negative-sequence voltage unbalance factors measured for Case 1 sub-case 2 are presented in Table A.1. The data are obtained under different values of  $v_a$  and  $g_d$ .

|                 |                  |                  |                  |                  |                  |                  |                  |                  |                  |                  |                  |                  |                  |                  |                  |                  |                  |                  |                  |                  |
|-----------------|------------------|------------------|------------------|------------------|------------------|------------------|------------------|------------------|------------------|------------------|------------------|------------------|------------------|------------------|------------------|------------------|------------------|------------------|------------------|------------------|
| No DER          | VUF <sub>0</sub> | VUF <sub>2</sub> |
| $g_d = 0$ p.u.  | 17.770           | 17.770           | 13.724           | 13.724           | 10.017           | 10.017           | 6.454            | 6.456            | 3.164            | 3.166            | 0.091            | 0.143            | 2.919            | 2.921            | 2.867            | 2.867            | 2.867            | 2.867            | 2.867            | 2.867            |
| $g_d = 1$ p.u.  | 17.602           | 17.484           | 12.568           | 13.510           | 9.105            | 9.806            | 6.420            | 6.314            | 3.152            | 3.048            | 0.092            | 0.143            | 2.867            | 2.867            | 2.866            | 2.864            | 2.831            | 2.831            | 2.831            | 2.831            |
| $g_d = 2$ p.u.  | 15.174           | 16.693           | 11.725           | 12.970           | 8.525            | 9.404            | 5.534            | 6.069            | 2.722            | 2.929            | 0.090            | 0.118            | 2.439            | 2.439            | 2.352            | 2.745            | 2.745            | 2.745            | 2.745            | 2.745            |
| $g_d = 3$ p.u.  | 14.161           | 16.368           | 10.989           | 12.680           | 8.007            | 9.212            | 5.188            | 5.933            | 2.530            | 2.842            | 0.088            | 0.140            | 2.064            | 2.064            | 2.656            | 2.656            | 2.656            | 2.656            | 2.656            | 2.656            |
| $g_d = 5$ p.u.  | 12.539           | 15.760           | 9.726            | 12.186           | 7.036            | 8.886            | 4.630            | 5.690            | 2.243            | 2.761            | 0.088            | 0.140            | 2.064            | 2.064            | 2.656            | 2.656            | 2.656            | 2.656            | 2.656            | 2.656            |
| $g_d = 8$ p.u.  | -                | -                | 8.382            | 11.484           | 6.070            | 8.339            | 3.929            | 5.407            | 1.925            | 2.648            | 0.071            | 0.131            | 1.796            | 1.796            | 2.490            | 2.490            | 2.490            | 2.490            | 2.490            | 2.490            |
| $g_d = 12$ p.u. | -                | -                | -                | -                | 5.117            | 7.800            | 3.287            | 5.072            | 1.629            | 2.452            | 0.088            | 0.140            | 1.402            | 1.402            | 2.392            | 2.392            | 2.392            | 2.392            | 2.392            | 2.392            |

Table A.1: Zero- and negative-sequence voltage unbalance factors, measured at the PCC when  $p_{ac} = -1$  p.u.

|                 |                  |                  |                  |                  |                  |                  |                  |                  |                  |                  |                  |                  |                  |                  |                  |                  |                  |                  |                  |                  |
|-----------------|------------------|------------------|------------------|------------------|------------------|------------------|------------------|------------------|------------------|------------------|------------------|------------------|------------------|------------------|------------------|------------------|------------------|------------------|------------------|------------------|
| No DER          | VUF <sub>0</sub> | VUF <sub>2</sub> |
| $g_d = 1$ p.u.  | 17.770           | 17.770           | 13.805           | 13.806           | 10.017           | 10.017           | 6.440            | 6.441            | 3.105            | 3.111            | 0.091            | 0.143            | 2.919            | 2.921            | 2.875            | 2.875            | 2.875            | 2.875            | 2.875            | 2.875            |
| $g_d = 2$ p.u.  | 16.559           | 17.503           | 12.809           | 13.493           | 9.323            | 9.766            | 6.007            | 6.328            | 2.928            | 3.033            | 0.116            | 0.116            | 2.677            | 2.677            | 2.856            | 2.856            | 2.856            | 2.856            | 2.856            | 2.856            |
| $g_d = 3$ p.u.  | 15.411           | 16.933           | 11.956           | 13.204           | 8.701            | 9.582            | 5.621            | 6.155            | 2.730            | 3.043            | 0.091            | 0.143            | 2.374            | 2.374            | 2.769            | 2.769            | 2.769            | 2.769            | 2.769            | 2.769            |
| $g_d = 5$ p.u.  | 14.467           | 16.680           | 11.219           | 12.913           | 8.100            | 9.416            | 5.270            | 6.016            | 2.605            | 2.917            | 0.091            | 0.143            | 2.100            | 2.100            | 2.692            | 2.692            | 2.692            | 2.692            | 2.692            | 2.692            |
| $g_d = 8$ p.u.  | 12.828           | 16.058           | 9.888            | 12.465           | 7.237            | 8.981            | 4.711            | 5.773            | 2.267            | 2.787            | 0.090            | 0.119            | 2.100            | 2.100            | 2.692            | 2.692            | 2.692            | 2.692            | 2.692            | 2.692            |
| $g_d = 12$ p.u. | 10.962           | 15.178           | 8.460            | 11.790           | 6.205            | 8.477            | 4.009            | 5.488            | 1.982            | 2.602            | 0.035            | 0.086            | 1.766            | 1.766            | 2.556            | 2.556            | 2.556            | 2.556            | 2.556            | 2.556            |
| $g_d = 12$ p.u. | 9.203            | 14.156           | 7.120            | 10.967           | 4.847            | 8.281            | 3.347            | 5.134            | 1.646            | 2.471            | 0.090            | 0.119            | 1.493            | 1.493            | 2.386            | 2.386            | 2.386            | 2.386            | 2.386            | 2.386            |

Table A.2: Zero- and negative-sequence voltage unbalance factors, measured at the PCC when  $p_{ac} = 0$  p.u.

|                 |                  |                  |                  |                  |                  |                  |                  |                  |                  |                  |                  |                  |                  |                  |                  |                  |                  |                  |                  |                  |
|-----------------|------------------|------------------|------------------|------------------|------------------|------------------|------------------|------------------|------------------|------------------|------------------|------------------|------------------|------------------|------------------|------------------|------------------|------------------|------------------|------------------|
| -               | VUF <sub>0</sub> | VUF <sub>2</sub> |
| $g_d = 1$ p.u.  | 17.770           | 17.770           | 13.818           | 13.818           | 10.017           | 10.017           | 6.454            | 6.456            | 3.135            | 3.137            | 0.091            | 0.143            | 2.919            | 2.921            | 2.935            | 2.935            | 2.935            | 2.935            | 2.935            | 2.935            |
| $g_d = 2$ p.u.  | 16.858           | 17.686           | 12.991           | 13.677           | 9.392            | 9.945            | 6.077            | 6.400            | 2.906            | 3.116            | 0.070            | 0.131            | 2.737            | 2.737            | 2.899            | 2.899            | 2.899            | 2.899            | 2.899            | 2.899            |
| $g_d = 3$ p.u.  | 15.674           | 17.318           | 12.064           | 13.428           | 8.735            | 9.726            | 5.702            | 6.237            | 2.792            | 3.002            | 0.091            | 0.144            | 2.507            | 2.507            | 2.810            | 2.810            | 2.810            | 2.810            | 2.810            | 2.810            |
| $g_d = 5$ p.u.  | 14.580           | 17.031           | 11.319           | 13.129           | 8.209            | 9.526            | 5.348            | 6.095            | 2.629            | 2.941            | 0.091            | 0.144            | 2.418            | 2.418            | 2.731            | 2.731            | 2.731            | 2.731            | 2.731            | 2.731            |
| $g_d = 8$ p.u.  | 12.972           | 16.323           | 10.032           | 12.613           | 7.284            | 9.139            | 4.718            | 5.886            | 2.298            | 2.818            | 0.070            | 0.131            | 2.142            | 2.142            | 2.559            | 2.559            | 2.559            | 2.559            | 2.559            | 2.559            |
| $g_d = 12$ p.u. | 11.151           | 15.375           | 8.603            | 11.937           | 6.267            | 8.650            | 4.072            | 5.552            | 2.025            | 2.646            | 0.070            | 0.131            | 1.867            | 1.867            | 2.421            | 2.421            | 2.421            | 2.421            | 2.421            | 2.421            |
| $g_d = 12$ p.u. | 9.324            | 14.399           | 7.202            | 11.164           | 5.196            | 8.099            | 3.411            | 5.198            | 1.671            | 2.496            | 0.005            | 0.111            | 1.531            | 1.531            | 2.421            | 2.421            | 2.421            | 2.421            | 2.421            | 2.421            |

Table A.3: Zero- and negative-sequence voltage unbalance factors, measured at the PCC when  $p_{ac} = 0.6666$  p.u.

# B

## Developed inverter prototype and experimental set-up

Short description of the different blocks used in three-phase four wire inverter prototype presented in Fig. B.1

- 1 - dc-bus capacitor bank
- 2 - power electronics part of the inverter
- 3 - measurements block
- 4 - differential inductive filter
- 5 - common mode filter
- 6 - contactor for grid and load connection
- 7 - emergency stop
- 8 - automatic circuit breaker

to give some explanation

- DSP - digital signal processor
- PA - protective algorithm
- CAN - control area network

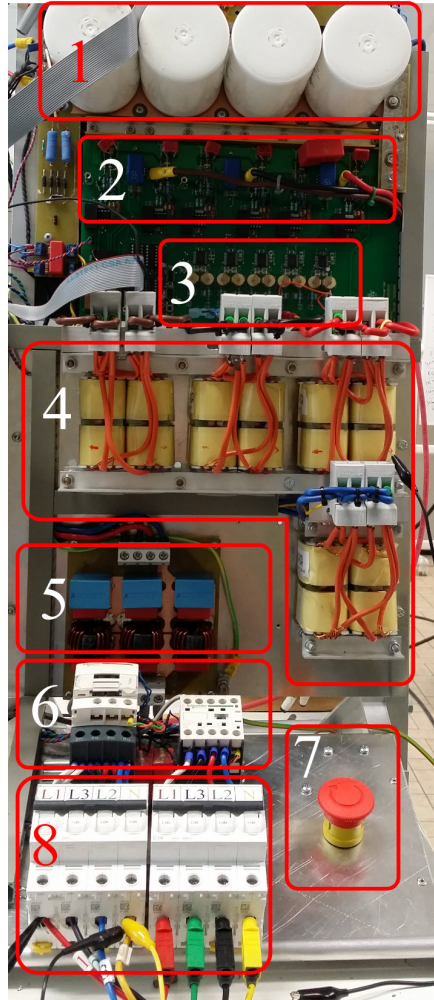


*Figure B.1: Three-phase inverter prototype used for the experimental validation of the proposed control algorithms*

- SCI - serial communication interface
- I2C - inter integrated communication

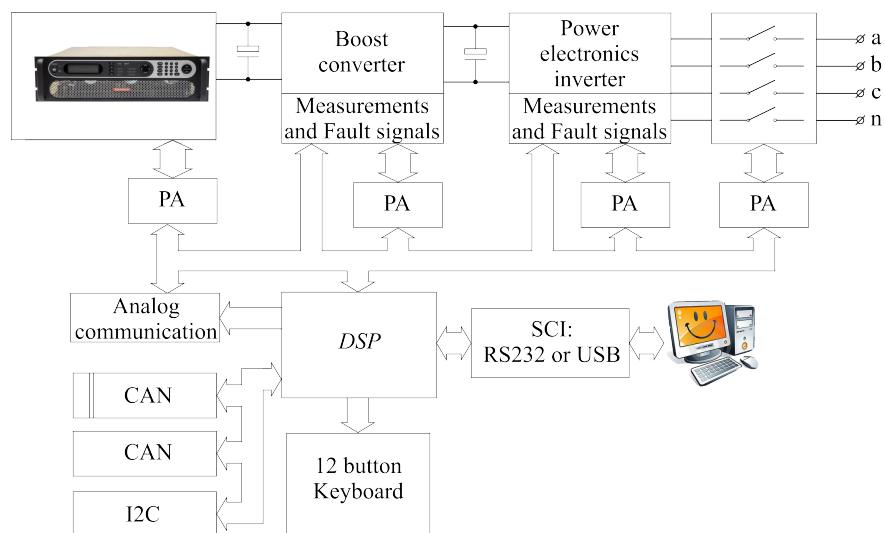


Figure B.2: Block diagram of the developed DSP-based controller used in the experimental set-up

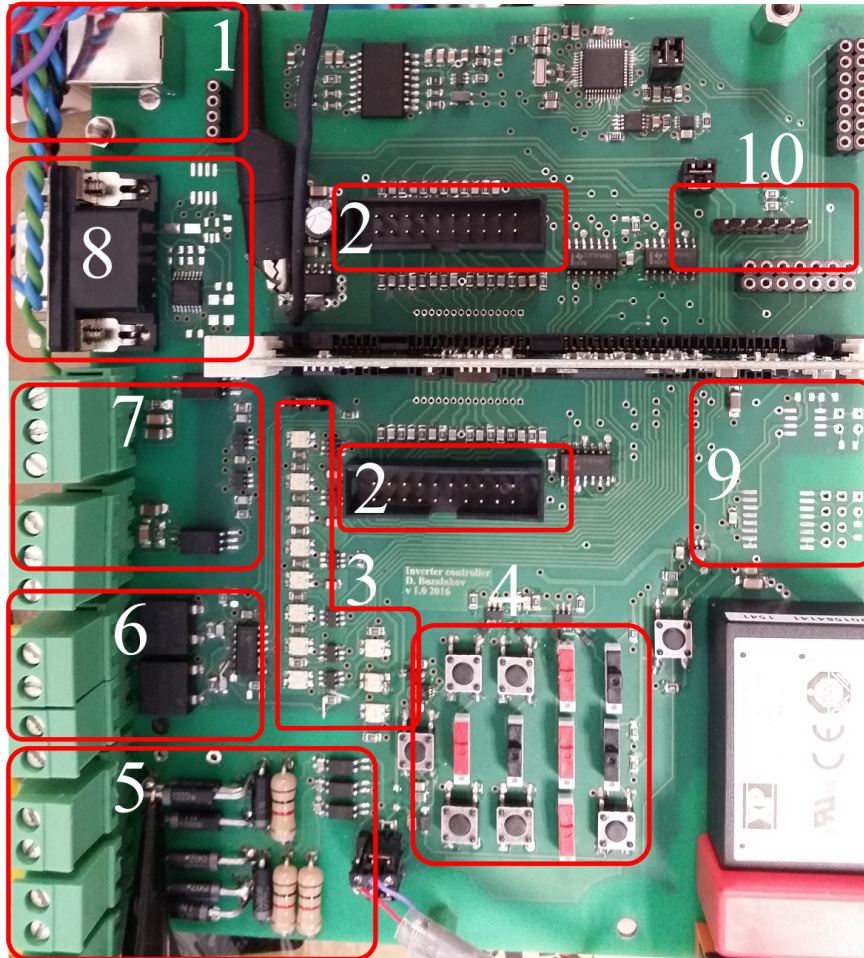


Figure B.3: A picture of the developed DSP-based controller used in the experimental set-up

# C

Price comparison of BESS and PV  
inverters

Table C.1: Maximum current ratings of the power electronic inverters as a function of the damping conductance and storage

| <b>Parameter</b>           | $g_d = 0$ <b>p.u.</b> | $g_d = 5$ <b>p.u.</b> | $g_d = 10$ <b>p.u.</b> | $g_d = 20$ <b>p.u.</b> | $g_d = 40$ <b>p.u.</b> |
|----------------------------|-----------------------|-----------------------|------------------------|------------------------|------------------------|
| $I_{\max}$ [A]             | 32                    | 38                    | 42                     | 45                     | 47                     |
| $P$ [kW]                   | 20                    | 23.6                  | 26.1                   | 28                     | 29.2                   |
| Inverter type              | SMA Tripower<br>Sunny | SMA Tripower<br>Sunny | SMA Tripower<br>Sunny  | SMA Tripower<br>Sunny  | SMA Tripower<br>Sunny  |
| Inverter $S_{\max}$ [kVA]  | 20000TL-30<br>20      | 25000TL-30<br>25      | 30000TL-US-10<br>30    | 30000TL-US-10<br>30    | 30000TL-US-10<br>30    |
| Inverter cost [Euro]       | 2769.00 [197]         | 2799.00 [197]         | 3593.60 [198]          | 3593.60 [198]          | 3593.60 [198]          |
| TeslaWall 1.0 price [Euro] | 4522.3 [199]          | 4522.3 [199]          | 4522.3 [199]           | 4522.3 [199]           | 4522.3 [199]           |
| TeslaWall 2.0 price [Euro] | 7740 [200]            | 7740 [200]            | 7740 [200]             | 7740 [200]             | 7740 [200]             |
| Total                      | 7291.3*               | 7321.3*               | 8115.9*                | 8115.9*                | 8115.9*                |
|                            | 10509**               | 10549**               | 11333.6**              | 11333.6**              | 11333.6**              |

\*Solar inverter + TeslaWall 1.0

\*\*Solar inverter + TeslaWall 2.0



Thank to European Commission and FP 7 programme for funding the project INCREASE - Grant agreement: 608998, in which this thesis is funded.